Vapor-Liquid Interfaces: Molecular Simulation, Density Gradient Theory, and Experiments

Vom Fachbereich Maschinenbau und Verfahrenstechnik

der Technischen Universität Kaiserslautern

zur Verleihung des akademischen Grades

Doktor-Ingenieur (Dr.-Ing.)

genehmigte

Dissertation

von

Dipl.-Ing. Simon Stephan

aus Darmstadt

Dekan:	Prof. Dr.-Ing. Tilmann Beck
Berichterstatter:	Prof. Dr.-Ing. Hans Hasse
	Prof. Dr.-Ing. Jadran Vrabec

Tag der mündlichen Prüfung: 24.06.2020

D 386

Simon Stephan
Vapor-Liquid Interfaces:
Molecular Simulation, Density Gradient Theory, and Experiments
Scientific Report Series Volume 33
2020

Abstract

Properties of vapor-liquid interfaces play an important role in many processes, but corresponding data is scarce, especially for mixtures. Therefore, two independent routes were employed in the present work to study them: molecular dynamics (MD) simulations using classical force fields as well as density gradient theory (DGT) in combination with theoretically-based equations of state (EOS). The investigated interfacial properties include: interfacial tension, adsorption, and the enrichment of components, which quantifies the interesting effect that in many systems the density of certain components in the interfacial region is much higher than in either of the bulk phases. As systematic investigations of the enrichment were lacking, it was comprehensively studied here by considering a large number of Lennard-Jones (LJ) mixtures with different phase behavior; also the dependence of the enrichment on temperature and concentration was elucidated and a conformal solution theory for describing the interfacial properties of LJ mixtures was developed. Furthermore, general relations of interfacial properties and the phase behavior were revealed and the relation between the enrichment and the wetting behavior of fluid interfaces was elucidated. All studies were carried out by both MD and DGT, which were found to agree well in most cases. The results were extended to real mixtures, which were studied not only by simulations but also in laboratory experiments. In connection with these investigations, three literature reviews were prepared which cover: a) simulation data on thermophysical properties of the LJ fluid; b) the performance of different EOS of the LJ fluid on that simulation data; c) data on the enrichment at vapor-liquid interfaces. Electronic databases were established for a) - c). Based on c), a short-cut method for the prediction of the enrichment from readily available vapor-liquid equilibrium data was developed. Last not least, an MD method for studying the influence of mass transfer on interfacial properties was developed and applied to investigate the influence of the enrichment on the mass transfer.

Kurzfassung

Grenzflächeneigenschaften von Flüssigkeiten, wie die Grenzflächenspannung und die Adsorption, spielen eine wichtige Rolle in vielen technischen Anwendungen, entsprechende Daten sind jedoch – insbesondere für Gemische – vergleichsweise rar. In der vorliegenden Arbeit werden deshalb zwei unabhängige prädikative Methoden zu deren Untersuchung eingesetzt: Molekulardynamik (MD) Simulationen auf der Basis klassischer Kraftfelder sowie die Dichtegradiententheorie (DGT) in Kombination mit theoretisch basierten Zustandsgleichungen. Zu den untersuchten Eigenschaften gehören: Grenzflächenspannung, Adsorption und die Anreicherung von Komponenten an der Grenzfläche, welche den interessanten Effekt beschreibt, dass in vielen Systemen die Dichte einzelner Komponenten an der Grenzfläche höher ist als in den beiden Bulkphasen. Da systematische Studien der Anreicherung nicht verfügbar sind, wurde sie in dieser Arbeit umfassend anhand einer Vielzahl von Lennard-Jones (LJ) Mischungen mit unterschiedlichem Phasenverhalten untersucht; dies beinhaltet die Untersuchung der Abhängigkeit der Anreicherung von Temperatur und Konzentration sowie die Entwicklung einer *conformal solution theory* zur Beschreibung der Grenzflächeneigenschaften von LJ-Mischungen im Allgemeinen. Weiterhin wurden allgemeine Beziehungen zwischen Grenzflächeneigenschaften und dem Phasenverhalten aufgestellt. Dabei wurde ein Zusammenhang zwischen der Anreicherung und dem Benetzungsverhalten fluider Grenzflächen offengelegt. Alle Studien wurden sowohl mit MD als auch DGT durchgeführt, deren Ergebnisse in den meisten Fällen gut übereinstimmen. Die Untersuchungen wurden weiterhin auf reale Mischungen ausgedehnt, welche neben Simulationen auch mittels Laborexperimenten erfolgten. Im Zusammenhang mit diesen Untersuchungen wurden ferner drei elektronische Datenbanken erstellt: a) Simulationsdaten von thermodynamischen Stoffdaten des LJ-Fluids; b) die Auswertung einer Vielzahl von Zustandsgleichungen des LJ-Fluids anhand dieser Simulationsdaten; c) Daten über die Anreicherung an Dampf-Flüssigkeit-Grenzflächen. Auf der Grundlage von c) wurde weiterhin eine short-cut Methode zur Vorhersage der Anreicherung von Komponenten an Grenzflächen aus vielfältig verfügbaren Dampf-Flüssigkeit-Gleichgewichtsdaten entwickelt. Nicht zuletzt wurde eine MD-Methode zur Untersuchung des Einflusses des Stofftransports auf Grenzflächeneigenschaften entwickelt und angewandt, um den Einfluss der Anreicherung auf den Stofftransport zu untersuchen.

Contents

List of Symbols

Latin symbols

a_i, b_i, c_i	parameters
a, b, c, d	indices of interaction sites
$\underline{a}$	parameter vector
a	Helmholtz energy
A	peak area
A	geometric parameter
c_p	isobaric heat capacity
c_v	isochoric heat capacity
d	temperature-dependent diameter
$Đ$	Maxwell-Stefan diffusion coefficients
E	enrichment
f_a, f_b	terms in enrichment model
f	angle-dependent expressions for point dipoles
$g(r)$	radial distribution function
g	gravitational constant
g_{I}, g_{II}	terms in enrichment model
H	Henry's law constant
Δh_{v}	enthalpy of vaporization
i	component index
i	parameter index
I	integral
K	parameter
K	partition coefficient
k_j	parameters
k_{B}	Boltzmann constant
L_{10}^{90}	interfacial thickness
l_λ	filter width
l	length
m	chain parameter in SAFT
M	particle mass
M	number of data points
N	number of particles
n	number of interaction sites
n	mixture index
p	pressure
p^{s}	vapor pressure

p_{N}	normal pressure at interface
p_{T}	tangential pressure at interface
P	uncertainty measure
Q	quadrupole moment
R	universal gas constant
$\tilde{\delta}R$	radial distance
$\mathcal{R}$	spectrum in Fourier space
r	distance between particles
r_{c}	cut-off radius
S	surface area
T	temperature
u	standard uncertainty
u	internal energy
$u(r)$	intermolecular potential energy
V	volume
w	speed of sound
x_i	mole fraction of component i
x	spatial coordinate
y	spatial coordinate
Y	fit functions
z	spatial coordinate
Z	compressibility factor

Superscripts

0	homogeneous state contribution in DGT
0	reference point at interface
00	hypothetical pure fluid
1	component 1
2	component 2
97	97% of liquid density
c	critical
CP	critical point
config	configurational contribution
corr	correlation
disp	dispersion
DP	data point
end	final
exp	experimental
hs	hard sphere
id	ideal gas
IP	intersection point in density profiles
i	particle index
i	component index
j	particle index
j	component index

k	particle index
l	particle index
kin	kinetic energy contribution
L	liquid phase
mod	model
oscill	oscillatory contribution
pert	perturbation
res	residual with respect to ideal gas
ref	reference
s	saturation
shape	contribution from the shape of the density profile
sim	simulation
trip	triple point
V	vapor phase
*	special density profiles
$'$	saturated phase $'$
$''$	saturated phase $''$

Greek symbols

α	parameter
α	thermal expansion coefficient
β	isothermal compressibility
γ	thermal pressure coefficient
γ	surface tension
Γ	Grüneisen parameter
$\Gamma_i^{(j)}$	relative adsorption of component i
Δ	deviation or difference
δ	increment
ε	Lennard-Jones energy parameter
ζ_n	abbreviation
ζ	abbreviation
η	packing fraction
κ	density gradient theory influence parameter
λ	step square well parameter
λ_{struc}	wavelength of structuring
μ	chemical potential
μ	dipole moment
μ_{JT}	Joule-Thomson coefficient
ρ	density
ρ_{tot}	total density
σ	Lennard-Jones size parameter
τ	time
ξ	binary interaction parameter
ω_i	relative orientation of molecule i
ω	angular frequency

Ω grand thermodynamic potential

Abbreviations

AAD	absolute average deviation
BICEP	bicritical end point
CK-SAFT	Chen-Kreglewski SAFT EOS
CST	conformal solution theory
DFT	density functional theory
DGT	density gradient theory
RF-DGT	reference density gradient theory algorithm
sDGT	stabilized density gradient theory algorithm
EOS	equation of state
FFE	fluid-fluid equilibrium
FW	Fisher-Widom line
PeTS	perturbed truncated and shifted
PeTS-i	perturbed truncated and shifted interface functional
PC-SAFT	Perturbed-chain statistical associating fluid theory
PCP-SAFT	Perturbed-chain polar statistical associating fluid theory
PR	Peng-Robinson EOS
LFT	lattice fluid theory
LJ	Lennard-Jones
LJTS	Lennard-Jones truncated and shifted
LLE	liquid-liquid equilibrium
MC	Monte Carlo
MD	molecular dynamics
NVT	canonical ensemble
NpT	isobaric-isothermal ensemble
QCHB	quasi-chemical hydrogen bonding
SAFT	statistical associating fluid theory
SAFT-VR Mie	SAFT variable range Mie EOS
SAFT-γ Mie	group contribution SAFT-VR Mie EOS
SRK	Soave-Redlich-Kwong EOS
UCEP	upper critical end point
VDW	van der Waals EOS
VLE	vapor-liquid equilibrium
VLLE	vapor-liquid-liquid equilibrium

1 Introduction

Properties of vapor-liquid interfaces play a crucial role in many technological an natural processes. Experimental data on interfacial properties are in most cases limited to the surface tension of pure substances [1, 381]. Hence, reliable and predictive models for interfacial properties – especially for mixtures – are important. Molecular thermodynamics has become a well established alternative to experiments for predicting thermophysical properties of fluids, including their interfacial properties. Furthermore, applying molecular thermodynamics provides insight into the nanoscopic structure of interfaces that is currently not accessible by experiments. Two independent routes from molecular thermodynamics were employed in the present work: first, molecular dynamics (MD) simulations based on classical force fields and, second, density gradient theory (DGT) in combination with theoretically-based equations of state (EOS). Furthermore, also measurements of the surface tension of mixtures were carried out with the pendant drop method. The general aim of the present work is to establish relations between nanoscopic and macroscopic properties of vapor-liquid interfaces.

In macroscopic models, the fluid interface is generally considered as a two-dimensional boundary, where thermodynamic properties exhibit a discontinuous change, cf. Fig. 1 - left. On the nanoscopic scale, however, fluid interfaces are three-dimensional objects, where thermodynamic properties continuously change over a small range from one bulk phase value to the other, cf. Fig. 1 - right. This results in large gradients in the pressure, density, and composition that influence the macroscopic behavior of the system. Due to fluctuations present at fluid interfaces, the transition of thermodynamic properties across fluid interfaces on the molecular level can currently only be studied by theoretical methods [17, 168, 186, 573], e.g. molecular simulations, density gradient theory, or density functional theory (DFT).

Vapor-liquid interfaces are characterized by large gradients of thermodynamic properties. In the interfacial region, which is generally only a few nanometers wide, the total density usually changes smoothly from the value in one bulk phase to that in the other. Unexpected effects are, however, observed for the individual component density profiles in mixtures: they can exhibit a non-monotonic behavior with a maximum that can be several times larger than the densities in the bulk phases, cf. Fig. 1 - right. This is called *enrichment* [50] and is usually only observed for low-boiling components. This interesting phenomenon has been reported since the early days of computational studies on fluid interfaces of mixtures [91, 173, 192, 194, 195, 361, 362] and has been confirmed since then by different independent theoretical methods [50, 116, 198, 205, 362, 445, 453, 459, 483, 624, 630, 705]. The enrichment describes a special feature of the surface excess at the interface. The relative adsorption – as defined by Gibbs [211] – and the enrichment both characterize the surface excess and are thereby related, but have
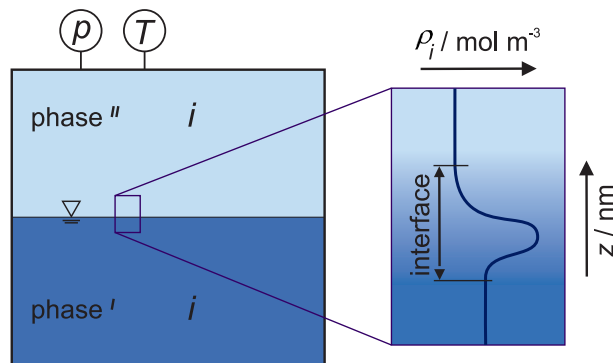
Figure 1: Classical scheme of a vapor-liquid equilibrium of a phase $'$ and a phase $''$ of a
mixture with $i = 1 .. N$ components (left) and a zoom to the interface between
the two phases (right). The thickness of fluid interfaces is on the nanoscopic
scale. Density profiles $\rho_i(z)$ of a component i in mixtures can exhibit a non-
monotonic transition across the interface with a distinct maximum. The
color indicates the total density.

different features. In particular, adsorption may be present without the presence of
an enrichment. Mixtures that exhibit an interfacial enrichment have been investigated
many times in the literature [32–34, 50, 56, 57, 130, 153, 184, 192–195, 328, 354, 361,
362, 373, 379, 390, 391, 412, 446, 483, 492, 501–504, 522, 533, 551, 552, 583, 634], but
no systematic evaluation of the phenomenon has been conducted so far.

Furthermore, no theoretical framework for the enrichment has been established yet
that would describe its dependence on the molecular interaction parameters, on the
temperature, and the composition or its relation to the phase behavior. Also the
relation between the relative adsorption and the enrichment is not yet fully under-
stood. Nevertheless, the enrichment has attracted much attention in the past, e.g. Refs.
[89, 121, 161, 173, 192, 361, 458], not least because it is believed to have an influence on
the mass transfer across the interface [159, 194, 199, 312, 328, 361, 488, 634] and might
therefore be important for many technical applications like fluid separation processes.
Nevertheless, a proof or refute for an influence of the enrichment on the macroscopic
mass transfer is still lacking.

In some studies, density profiles of vapor-liquid interfaces of mixtures were computed
from MD and DGT and compared [50, 116, 205, 362, 445, 446, 453, 459, 483, 705].
The results from the two methods usually agree qualitatively well, despite the fact
that MD simulations yield a picture of the interfacial region that is three-dimensional
and shows fluctuations, whereas DGT usually considers only a one-dimensional gradient
and does not take fluctuations into account. For a quantitative comparison, the different
approaches must be applied to the same fluid. This is not trivial, even for simple fluids, as
MD simulations are based on force fields, while DGT is based on an equation of state and
both should at least yield conformal descriptions of the bulk phases of the vapor-liquid
equilibrium (VLE). The molecular simulation (also called *computer experiment*) results
are considered as reference to which the DGT results are compared. Both molecular
simulation and DGT were used in the present work to systematically study vapor-liquid
interfacial properties. This approach was applied on two types of Lennard-Jones fluids:

the classical Lennard-Jones fluid – including long-range interactions – and the Lennard-Jones truncated & shifted fluid.

In the present work, vapor-liquid interfaces of pure fluids and mixtures were studied; with a clear focus on the latter. Two different approaches for carrying out these studies can be distinguished: in the first approach, model fluids are studied and the effect of a variation of molecular interaction parameters on the properties of the interface and the corresponding vapor-liquid equilibrium is elucidated. These systematic studies yield generic insights on the interplay of the molecular interactions, the phase behavior, and the interfacial properties that is subsequently generalized for selected properties to real mixtures. In the second approach, real fluids are studied directly, which has obvious advantages, but the drawback that it is difficult to gain generic insights as the findings are primary restricted to the given system. Both approaches are complementary and both were applied in the present work: in the chapters 2 - 6, studies on fluid interfacial properties of Lennard-Jones model fluids are presented, whereas the chapters 7 - 9 focus on interfacial properties of real fluids. The investigated properties include: the surface tension, the relative Gibbs adsorption, the interfacial thickness, and the enrichment of components, which quantifies the non-monotonicity of component density profiles in mixtures, cf. Fig. 1 - right. Different characteristics of vapor-liquid interfaces are thereby addressed: structuring effects at the interface, the relation of the phase behavior and interfacial properties, the applicability of conformal solution theory to interfacial properties, the wetting behavior at vapor-liquid-liquid fluid interfaces, the influence of long-range interactions on interfacial properties, the mass transfer though vapor-liquid interfaces, the relation of the relative adsorption and the enrichment, and the generalization of the findings for the enrichment in a novel short-cut method for its prediction. This work mainly addresses vapor-liquid interfaces, but also liquid-liquid and gas-gas interfaces are briefly discussed.

Furthermore, several data repositories were established in the present work, which make research data that is relevant in this field, but was previously tedious to access, readily available in electronic form: a consolidated database of 35,000 data points of molecular simulation results of thermophysical properties of the LJ fluid was compiled and published [640]. It was used for a comparison of 20 different LJ EOS. Also the results from all these EOS for each property and state point are made available in electronic form [639]. Additionally, based on a comprehensive review of the literature on component density profiles at vapor-liquid interfaces, the available data on the enrichment was retrieved from the corresponding publications. The 2,000 data points on the enrichment, to which the present work has contributed substantially, are readily available in electronic form [627].

The present work is essentially a cumulative dissertation, which summarizes results from work that has already published in scientific journals or are submitted for publication. The Appendix contains an overview of the individual papers and the contributions of the author. The state of the art and the scope of each study is presented at the beginning of each chapter.

In chapter 2, homogeneous and interfacial properties of the Lennard-Jones truncated and shifted (LJTS) fluid are studied. The PeTS equation of state from a previous work of our group [249] is compared to computer experiment data and the best currently available EOS for that fluid from the literature [662]. The vapor-liquid interface of the LTJS fluid

is investigated in a wide temperature range. Results from three different approaches to model the vapor-liquid interface are compared: molecular dynamics (MD) simulations, DGT+PeTS EOS, and DFT. The DFT results are taken from Ref. [637]. The surface tension, pressure and density profiles, including structuring effects at the interface, are investigated. A new method for the examination of the oscillatory layering structure at vapor-liquid interfaces is developed and tested on the results from the different methods. It is shown that an oscillatory layering structure is present in the results from MD and DFT.

A systematic study on the fluid interfacial properties of binary Lennard-Jones mixtures by MD and DGT is carried out in chapter 3. As in chapter 2, the fluids are described by the LJTS potential. The PeTS EOS was extended to mixtures and then used as base in the DGT to predict interfacial properties of binary LJTS mixtures. The molecular interaction parameters of the LJTS mixtures were used in MD and the EOS+DGT without any adjustment. The following interfacial properties were studied: density profiles, surface tension, relative adsorption, enrichment, and interfacial thickness. Furthermore, the corresponding phase equilibrium properties were studied (isothermal phase diagrams, Henry's law constants, and characteristic lines in the $p - T$ diagram). In section 3.3, six binary LJTS mixtures are examined at a constant temperature, which was chosen such that the high-boiling component 1 is subcritical while the low-boiling component 2 is either subcritical or supercritical. Furthermore, the parameter ξ in the combination rule for the unlike dispersive interaction was varied such that the resulting mixtures showed three types of behavior: high-boiling azeotropic, ideal, and low-boiling azeotropic. In section 3.4 and 3.5, a large number of different LJTS mixtures are investigated at constant liquid phase composition and temperature. By varying ξ and the ratio of the dispersion energies of the two components $\varepsilon_2/\varepsilon_1$, a variety of types of phase behavior is covered by the study. The results elucidate the influence of the liquid phase interactions on the interfacial properties. The dependence of the interfacial properties on the variables ξ and $\varepsilon_2/\varepsilon_1$ reveals regularities that are explained by conformal solution theory of the liquid phase. It is thereby shown that the interfacial properties of the mixtures are dominated by the mean liquid phase interactions, whereas the vapor phase has only a minor influence. In section 3.6, interfacial properties of two binary LJTS mixtures are studied in detail: a highly asymmetric mixture (type III), which exhibits vapor-liquid equilibria (VL_1E and VL_2E), liquid-liquid equilibria (L_1L_2E), a three-phase equilibrium (VL_1L_2E), and supercritical fluid-fluid equilibria (F_1F_2E), and, as a reference, an ideal mixture (type I). The focus of this study is on the relation of the interfacial properties to the phase behavior of the mixture. It is shown that a direct relation exists between the enrichment found at VL_1 interfaces and the wetting behavior at the VL_1L_2E three-phase line in the type III mixture. Based on the systematic study on binary LJTS mixtures in chapter 3, conditions that favor strong enrichment of components at vapor-liquid interfaces are identified. Also, the relation between the enrichment and the relative Gibbs adsorption is elucidated.

While the chapters 2 and 3 consider the Lennard-Jones truncated and shifted (LJTS) fluid, chapter 4 considers the classical 'full' Lennard-Jones (LJ) fluid. The LJ fluid is probably the most frequently studied model fluid in the literature. Accordingly, a large number of computer experiment data and equations of state are available for the LJ fluid. First, available simulation data (35,000 data points) of the LJ fluid is reviewed and evaluated by different thermodynamic tests. Based on that assessment,

a consolidated electronic database is established [640]. Subsequently, 20 Equations of state for the LJ fluid are systematically assessed in section 4.3 and 4.4, by comparing their results with the consolidated molecular simulation data. Also these results are compiled in an electronic database [639], which enables a straightforward application of the test procedure as a benchmark for the development of new LJ EOS. Furthermore, to enable a meaningful comparison of the DGT results for the LJ and LJTS fluid, a new LJ EOS is parametrized using the same framework that the PeTS EOS [249] is built on. The parametrization of the new LJ EOS (presented in the Appendix) is guided by the idea that its performance on the VLE properties should be in the range of the mutual agreement of the best available computer experiment datasets, while also homogeneous state properties are represented well. For the evaluation of both the simulation data and the LJ EOS, a large variety of thermophysical properties were considered: vapor pressure; saturated densities; enthalpy of vaporization; critical properties; and thermal, caloric, and entropic properties at homogeneous state points. In section 4.4, the comparison is extended to *Brown's* characteristic curves and the second and third virial coefficient. Overall, it was found that none of the available LJ EOS meets the following two criteria: (1) it does not yield unphysical artifacts when used for extrapolations, and (2) it describes data from computer experiments within their statistical uncertainty in most fluid regions. The new LJ EOS developed in this work yields good results for the LJ fluid, but does not outperform the best existing LJ EOS. However, among the LJ EOS that show no artifacts in the unstable region, the LJ EOS from the present work gives the best description of the molecular simulation VLE data. It is therefore a good choice for applications within DGT. Furthermore, the rigorous assessment of both simulation data and LJ EOS provides a conformal representation of known quality in molecular simulation and the theory – especially regarding the VLE properties.

In chapter 5, results of a study on the influence of the dispersive long-range interactions on phase equilibria and interfacial properties in binary Lennard-Jones mixtures are reported. As in chapters 2 and 3, MD simulations and EOS+DGT were used. To assess the influence of the long-range interactions, properties of LJTS mixtures (cf. section 3.3) are compared with results from LJ mixtures. The results from the LJTS mixtures and the LJ mixtures are compared applying the corresponding states principle.

The mass transfer through vapor-liquid interfaces of mixtures is of fundamental importance in many technical processes, for example fluid separation techniques like distillation and absorption. The enrichment of components would be an insurmountable obstacle to mass transfer according to Fickian theory. Hence, the enrichment is believed to influence the mass transfer across interfaces. A new molecular simulations method is therefore developed in this work to study a stationary mass flux through vapor-liquid interfaces. It is presented in chapter 6 together with first results, in which the method was applied to two different systems; one exhibiting a large enrichment at the interface and the other exhibiting no enrichment. The results reinforce the assumption that the enrichment acts as a hindrance to mass transfer through fluid interfaces.

While the chapters 2 - 5 are limited to properties of model fluids, the chapters 7 - 9 consider real substance mixtures. All three studies in the chapters 7 - 9 focus on the interfacial structure and the surface excess – especially the enrichment of the low-boiling component. Chapter 7 presents a combined study using molecular simulation, density gradient theory as well as experiments on an exemplary chosen mixture (cyclohexane +

CO_2). Results for the enrichment predicted from MD and DGT from different mixtures of the type solvent + supercritical solute are compared in chapter 8. In chapter 9, the results from the previous chapters are brought together by developing an empirical model for the prediction of the enrichment from bulk VLE properties solely. Literature data on the enrichment is reviewed, digitalized, and compiled in an electronic database [627]. An empirical model is proposed to establish a link between the nanoscopic enrichment and macroscopic properties – namely vapor-liquid equilibrium data. The model parameters were determined from a fit to the dataset on the enrichment in about 100 binary LJTS model mixtures (presented in chapter 3) that exhibit different types of phase behavior. The model is then tested on the entire set of other enrichment data available in the literature (approximately 2,000 data points), which includes also mixtures containing non-spherical, polar, and H-bonding components. It is shown that the model practically predicts the enrichment within the uncertainty of the enrichment data, which enables predictions of the enrichment at vapor-liquid interfaces from macroscopic data alone.

Finally, chapter 10 summarizes the present work. The Appendix provides additional information and numeric values of the data discussed in the individual chapters in the main body of this work.

In the chapters 2 - 6 that consider model fluids, all physical properties are conveniently reduced using the Lennard-Jones potential parameters ε and σ as well as the mass of the particle M and the Boltzmann constant k_B [17]. All intensive properties indicate the respective quantity per particle. In the case of binary Lennard-Jones mixtures (cf. chapter 3, 5, and 6), the high-boiling component 1 is used as a reference throughout.

2 Lennard-Jones Truncated & Shifted Fluid: Equation of State and Interfacial Properties

2.1 Introduction

The LJTS potential is probably the simplest and computationally least expensive potential that describes properties of simple fluids well [49, 251, 275, 360, 409, 576, 611, 687]. The vapor-liquid interfacial properties of the Lennard-Jones (LJ) and the LJTS fluid have been investigated many times in the literature [31, 230, 397, 440, 507, 672, 687, 693, 698]. However, to the best of our knowledge, no systematic comparison between the three different methods MD, DGT, and DFT has yet been conducted for this fluid or any other fluid on a consistent basis (force field, EOS, and functional). The truncation of the Lennard-Jones potential in the LJTS potential affects both the thermodynamic bulk [148, 395, 611, 628, 672] and interfacial properties [31, 169, 170, 230, 507, 628, 706]. Only the LJTS potential is considered in this chapter.

The Perturbed Truncated and Shifted (PeTS) EOS [249] provides a foundation to perform a comparison of interfacial properties obtained from different theoretical approaches in a rigorous way. The PeTS EOS provides an excellent description of the LJTS fluid not only for stable but also for metastable states and interfacial properties such as the surface tension. The vapor-liquid interface of the LJTS fluid is investigated in detail here: the pressure and density profiles obtained with the three methods are reported for temperatures covering the range between the triple point and the critical point. Also, an empirical correlation for the density profiles is used – mainly for the curve deconvolution (see below) – that was adopted from *Vrabec et al.* [687].

Besides the comparison of the three methods, a second focus of this work lies on the investigation of the oscillatory layering structure [171, 520] on the liquid side of the vapor-liquid density profiles, which has been investigated in the literature by integral equation theory [75, 145, 170, 171, 369, 651, 653, 654, 675], density functional theory [169, 170, 257, 697], and molecular simulations [145, 651, 653, 654] for some model fluids. The vapor phase of a vapor-liquid interface can be regarded as an external field [170] that causes a structuring of the molecules in the liquid phase – similar to what is observed at wall-liquid interfaces. *Evans* and co-workers [170] have shown that the density of an inhomogeneous fluid $\rho(z)$ of a short-ranged potential decays from the liquid surface into the bulk in the same way as the radial distribution function $g(r)$ does for $r \to \infty$, i.e. either with exponentially damped oscillations or with a monotonic decay.

The occurrence and magnitude of an oscillating decay at different state points is directly related to the *Fisher-Widom* (FW) line [179], that describes the crossover between the oscillatory and monotonic decay of the radial distribution function for short-ranged potentials in the bulk fluid [170, 369, 520, 653]. The oscillatory decay occurs when the repulsive forces dominate, whereas the monotonic decay occurs when attractive forces dominate. The *Fisher-Widom* line of the LJTS fluid with a cut-off radius of $2.5\,\sigma$ has been investigated in the literature [145, 369, 675] and its intersection point with the vapor-liquid coexistence curve was found to be at about T/T_c = 0.9 and ρ/ρ_c = 1.9 [145, 170, 369, 675]. Density oscillations at vapor-liquid interfaces should therefore be expected up to that temperature.

A new method for analyzing the oscillatory layering structure on the liquid side of vapor-liquid interfaces based on a Fourier transform and curve deconvolution is proposed in the present work. It is thereby shown that the density oscillations are found in molecular simulation data of the LJTS fluid. To the best of our knowledge such oscillations have been observed only for force fields that were trained for that feature [651, 653, 654]. The temperature dependency of the amplitude of the layering structure is investigated. It decreases with increasing temperature until it vanishes at about T/T_c = 0.88 which confirms predictions from the literature [145, 675].

This chapter is organized as follows: the equations and the performance of the PeTS EOS [249] are briefly discussed, the employed theoretical methods (MD, DGT, and DFT) are introduced, and then the results for the surface tension, the pressure profiles, and the density profiles are presented and discussed. Subsequently, a new method for the examination of the oscillatory layering structure at vapor-liquid interfaces is introduced and applied to the results for the LJTS fluid from the different methods.

2.2 Perturbed Truncated and Shifted (PeTS) Equation of State

2.2.1 Theory

The perturbed truncated and shifted (PeTS) EOS was developed to describe the thermodynamic behavior of the LJTS fluid [249]. It is based on the perturbation theory of *Barker and Henderson* [41]. The dispersion contribution in the PeTS EOS is modeled as a series expansion in the density as proposed by *Gross and Sadowski* [223]. The PeTS-i functional (see below) reduces to the PeTS EOS in the bulk and is also described in detail by *Heier et al.* [249].

The PeTS EOS is given here in reduced units with respect to the potential parameters and the Boltzmann constant. It uses the perturbation theory of *Barker and Henderson* [41], which splits the residual free energy $\tilde{a}^{\mathrm{res}}$ into the free energy of a reference potential a^{ref} and a part due to the perturbation $\tilde{a}^{\mathrm{pert}}$

$$\tilde{a}^{\mathrm{res}} \equiv \tilde{a} - \tilde{a}^{\mathrm{id}} = \tilde{a}^{\mathrm{ref}} + \tilde{a}^{\mathrm{pert}} \tag{1}$$

where $\tilde{a} = a/k_{\mathrm{B}}T$ is the free energy per particle and $\tilde{a}^{\mathrm{id}}$ is the free energy per particle of the ideal gas. The LJTS potential is discretized with the modified step-square-well potential proposed by *Chen and Kreglewski* [108]

$$u\left(r\right) = \begin{cases} \infty & r < \left(1 - c_1\right) \\ c_2 & \left(1 - c_1\right) \leq r < 1 \\ -1 & 1 \leq r < \lambda \\ 0 & r \geq \lambda \end{cases} \tag{2}$$

which has three parameters: c_1 and c_2 which characterize the repulsive part and λ which characterizes the attractive part. Only the repulsive part of the potential is used in the following, i.e. the parameter λ is not used. The attraction is handled implicitly by the PeTS EOS.

Using the approach of *Barker and Henderson* [41], the repulsive part of a potential can be described by an effective hard sphere diameter d

$$d(T) = \int_0^1 \left(1 - \exp\left(-\frac{u(r)}{k_{\mathrm{B}}T}\right)\right) \mathrm{d}r. \tag{3}$$

Applied to the potential Eq. (2) this yields

$$d\left(T\right) = 1 - c_1 \exp\left(-\frac{c_2}{k_{\mathrm{B}}T}\right). \tag{4}$$

Following this approach, the reference term in equation Eq. (1) is the free energy of the hard sphere which is according to *Boublík* [67] and *Mansoori et al.* [407]

$$\tilde{a}^{\mathrm{ref}} = \tilde{a}^{\mathrm{hs}} = \frac{3\eta}{1 - \eta} + \frac{\eta}{(1 - \eta)^2} \tag{5}$$

where η is the reduced packing fraction

$$\eta = \frac{\pi}{6}\rho\,d^3 \tag{6}$$

and ρ is the number density. According to *Barker and Henderson* [41], the perturbation contribution in equation Eq. (1), which describes only dispersion here, is

$$\tilde{a}^{\mathrm{pert}} = \tilde{a}_1 + \tilde{a}_2 \tag{7}$$

up to second-order, where $\tilde{a}_1$ is the first-order dispersion contribution and $\tilde{a}_2$ the second-order dispersion contribution. These contributions are given by Ref. [223] as

$$\tilde{a}_1 = -2\pi\rho\frac{1}{T}\underbrace{\int_1^\infty u(r)g\left(\frac{r}{d}\right)r^2\mathrm{d}r}_{I_1} \tag{8}$$

and

$$\tilde{a}_2 = -\pi\rho\left(1 + \frac{8\eta - 2\eta^2}{(1-\eta)^4}\right)^{-1}\left(\frac{1}{T}\right)^2\frac{\partial}{\partial\rho}\underbrace{\left[\int_1^\infty u(r)^2 g\left(\frac{r}{d}\right)r^2\mathrm{d}r\right]}_{I_2}. \tag{9}$$

In analogy to the approach of *Gross and Sadowski* [223], the integrals I_1 and I_2 in the equations Eq. (8) and Eq. (9) are developed into a Taylor series as functions of the packing fraction only

$$I_1 = \sum_{i=0}^{6} a_i\eta^i \tag{10}$$

$$I_2 = \sum_{i=0}^{6} b_i\eta^i \tag{11}$$

for which 14 state independent parameters are used: a_i and b_i with $i \in \{0,1,2,3,4,5,6\}$. Additionally, the parameters c_1 and c_2 characterize the repulsive part of the potential Eq. (2).

The resulting 16 parameters were fitted to saturated liquid and vapor densities ρ' and ρ'' and vapor pressures p^{s} of the LJTS fluid for temperatures T between 0.64 and $1.06\,\varepsilon k_{\mathrm{B}}^{-1}$ [249]. The data was taken from *Vrabec et al.* [687]. The data from the metastable region was not used for fitting. The resulting parameters are given in Table 1.

Table 1: Parameters of the PeTS EOS and the DGT influence parameter.

Parameter	Value	Parameter	Value	Parameter	Value
a_0	0.690603404	b_0	0.664852128	c_1	0.127112544
a_1	1.189317012	b_1	2.10733079	c_2	3.052785558
a_2	1.265604153	b_2	-9.597951213		
a_3	-24.34554201	b_3	-17.37871193	κ_{PeTS}	2.7334
a_4	93.67300357	b_4	30.17506222		
a_5	-157.8773415	b_5	209.3942909		
a_6	96.93736697	b_6	-353.2743581		

2.2.2 Comparison to Computer Experiment Data

Vapor-Liquid Equilibrium

In Fig. 2, the results of the PeTS EOS (solid lines) and the vapor-liquid equilibrium (VLE) data of *Vrabec et al.* [687] (squares) are compared. The results from the PeTS EOS are in very good agreement with the computer experiment data – since that was used for the fitting. This can also be seen in Fig. 3, where the deviation of the results obtained from the PeTS EOS from the simulation data of *Vrabec et al.* [687] is displayed. Fig. 3 also includes the deviation of the results from the EOS of *Thol et al.* [662] from the simulation data. In most cases, the deviations do not exceed the statistical uncertainty of the simulation data. This holds for both EOS.

The PeTS EOS has an average absolute deviation (AAD) to such data [687] in the vapor pressure $\overline{\delta p^s_{\mathrm{PeTS}}}$ = 0.00026 and $\overline{\delta \rho'_{\mathrm{PeTS}}}$ = 0.00091 and $\overline{\delta \rho''_{\mathrm{PeTS}}}$ = 0.00049 in the saturated liquid and vapor density respectively [249].
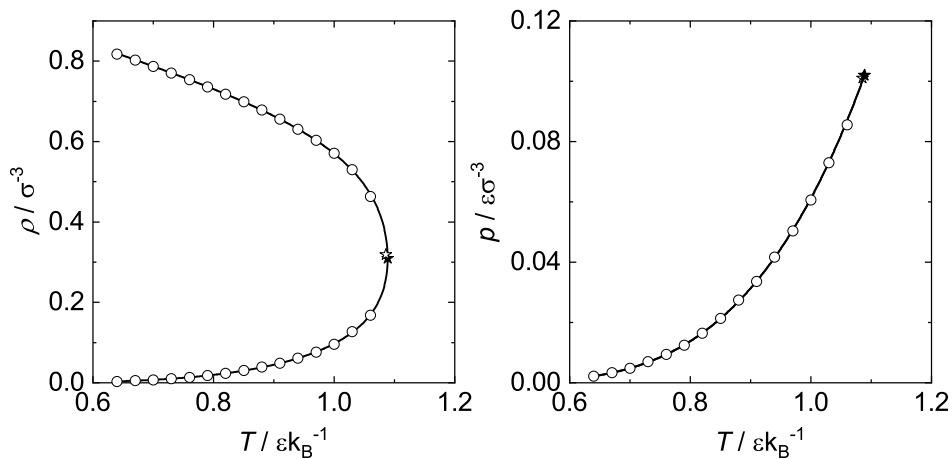
Figure 2: Saturated densities (left) and vapor pressure curve (right) of the LJTS fluid obtained with the PeTS EOS (line) and with molecular simulation data from Ref. [687] (squares).
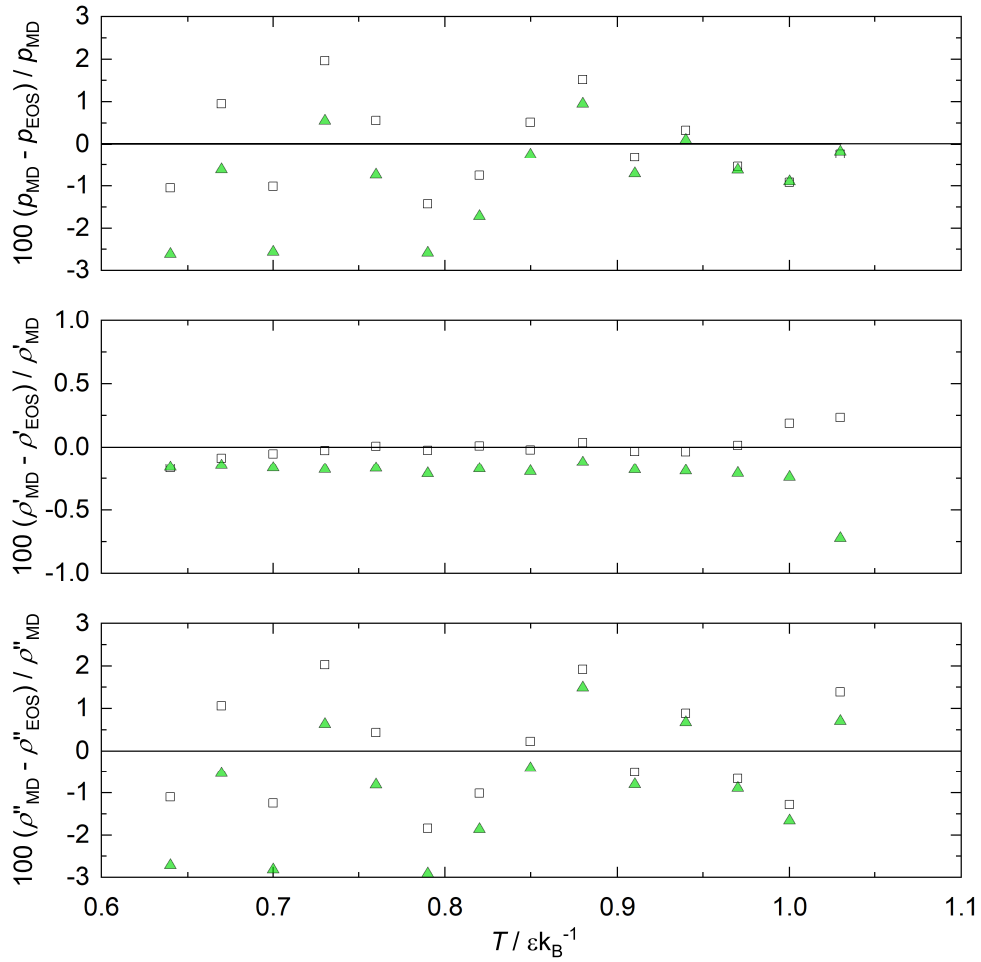
Figure 3: Deviations of results obtained with the PeTS EOS (squares) and the EOS
from *Thol et al.* [662] (triangles) from molecular simulation data of *Vrabec
et al.* [687] for the vapor pressure (top), saturated liquid density (middle)
and saturated vapor density (bottom) of the LJTS fluid.

Homogeneous Stable States

Thol et al. [662] report simulation data for the pressure as a function of temperature and density for homogeneous stable states for a wide range of conditions. That data, even though it was not included in the fit, is represented well by the PeTS EOS, cf. Fig. 4. For given temperature and density, the relative deviation in the pressure is in most cases below 5%. Three simulation data points of *Thol et al.* [662] are not included in Fig. 4. They show very high deviations from both the PeTS EOS and the EOS of *Thol et al.* [662] and are probably erroneous.

The EOS of *Thol et al.* [662] describes the simulation data, to which it was fitted, better than the PeTS EOS. Still the predictions of the PeTS EOS for that data are good.
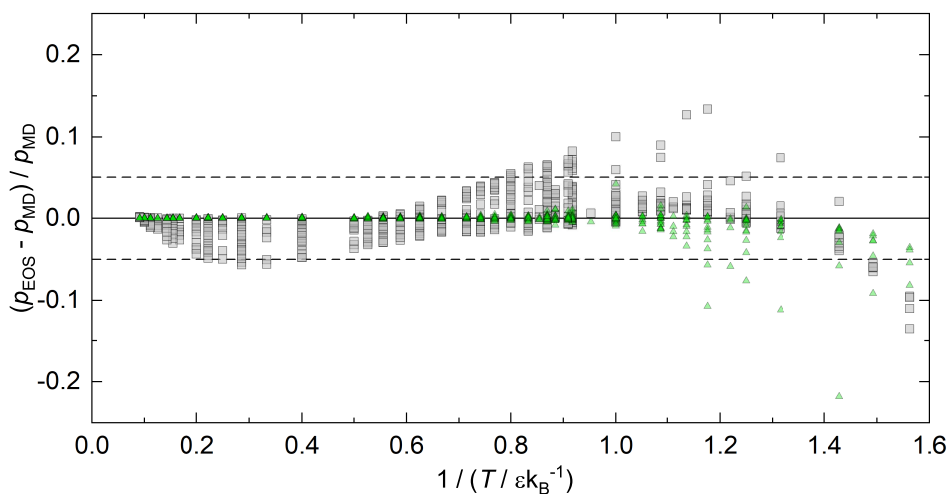
Figure 4: Deviation of results for the pressure obtained with the PeTS EOS (squares) and the EOS of *Thol et al.* [662] (triangles) from the simulation data of homogeneous states of the LJTS fluid [662] plotted as a function of the inverse temperature. All states given by *Thol et al.* [662] are used for the comparison except for three state points as described in the text. The dashed lines show the deviation of ±5%.

Homogeneous Metastable States

The results of computer experiment data for metastable states [249] are compared to the results of the PeTS EOS and to those of the EOS of *Thol et al.* [662] in Fig. 5. Besides the overall picture (left), Fig. 5 also contains a zoomed plot of the gas side (right). The binodal as obtained from the PeTS EOS does not differ significantly from that obtained from the EOS of *Thol et al.* [662]. The error bars of the simulation results are mostly within symbol size. Only close to the spinodal on the liquid side of the phase equilibrium the error bars are relatively large due to low particle numbers in these simulations. While in the homogeneous region both EOS perform equally well, there are important differences in the metastable region. The subcritical isotherms of the EOS of *Thol et al.* [662] have two minima and two maxima whereas those from the PeTS EOS have only one minimum and one maximum, so that only the latter can be used together with DGT for studying properties of fluid interfaces. Also the spinodals

found from both EOS differ significantly. The metastable region predicted by the EOS of *Thol et al.* [662] is significantly smaller than that predicted by the PeTS EOS, i.e. the spinodal predicted by the EOS of *Thol et al.* [662] encloses four of the state points for which simulation results were obtained here, thereby erroneously predicting instability. The simulation data for the metastable region confirms the results of the PeTS EOS.
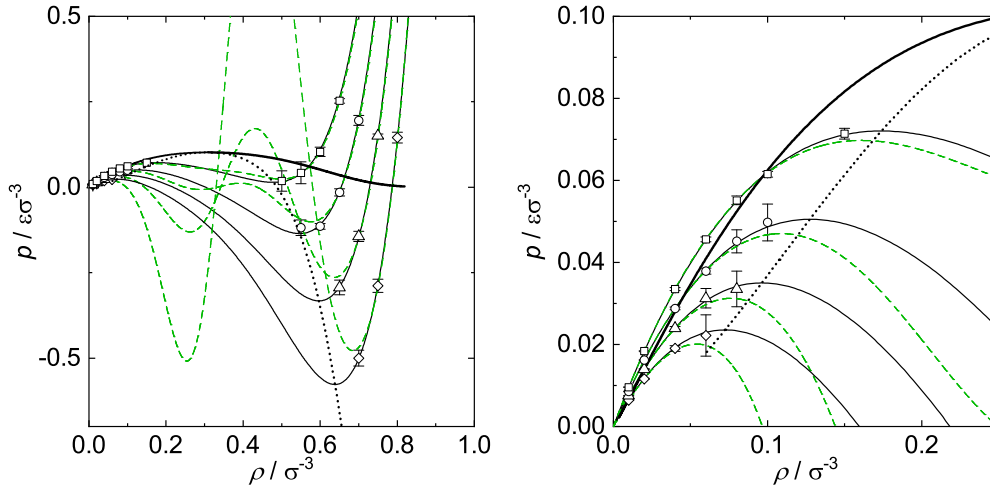
Figure 5: Thermal properties of the LJTS fluid: isotherms obtained with the PeTS EOS (black solid line), the EOS of *Thol et al.* [662] (green dashed line), and from MD simulations for $T = 1.0\,\varepsilon k_{\mathrm{B}}^{-1}$ (squares), $T = 0.9\,\varepsilon k_{\mathrm{B}}^{-1}$ (circles), $T = 0.8\,\varepsilon k_{\mathrm{B}}^{-1}$ (triangles), and $T = 0.7\,\varepsilon k_{\mathrm{B}}^{-1}$ (diamonds). The thick solid line is the binodal and the dotted line is the spinodal from the PeTS EOS. The binodal from the EOS of *Thol et al.* [662] is practically identical with the depicted one. The spinodal from the EOS of *Thos et al.* [662] is not shown for clarity, but differs significantly. Symbols are simulation results from Ref. [249].

In Fig. 6, results of the PeTS EOS (line) and the simulations (symbols) of $\mu - p - T$ behavior are shown. In the $\mu - p$ projection of the phase space, equilibrium points are given by the self-intersection of the isotherm. Vapor states are found on the almost vertical part of the isotherm, where stable points are below the intersection and metastable points are above it. Liquid states are on the other linear branch of the isotherm, where pressures higher than that at the intersection indicate stable states and lower pressures indicate metastable states. Unstable states are found on the curved part of the isotherm connecting the vapor and liquid line. The latter can only be obtained from the PeTS EOS. Simulation data and results from PeTS EOS agree very well.
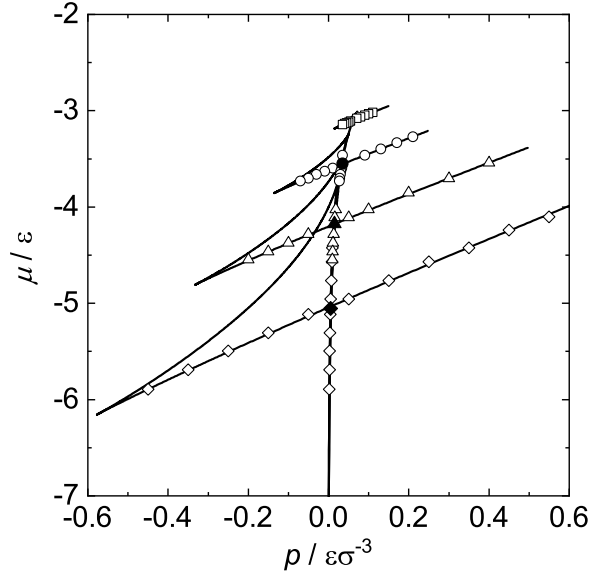
Figure 6: Chemical potential of the LJTS fluid as a function of pressure obtained from the PeTS EOS (lines) and from molecular simulations (symbols) [249] for $T = 1.0\,\varepsilon k_{\mathrm{B}}^{-1}$ (squares), $T = 0.9\,\varepsilon k_{\mathrm{B}}^{-1}$ (circles), $T = 0.8\,\varepsilon k_{\mathrm{B}}^{-1}$ (triangles), and $T = 0.7\,\varepsilon k_{\mathrm{B}}^{-1}$ (diamonds). Vapor states are found on the steep branch in the middle and coincide for all temperatures. The almost straight flat branches correspond to liquid states and the curved branches, which can only be determined by the EOS, correspond to unstable states. VLE points are marked with filled symbols.

2.3 Vapor-Liquid Interfacial Properties

2.3.1 Modeling and Simulation of Interfacial Properties

The methods used for calculating the surface tension, density, and pressure profiles of the planar interface from MD, DGT, and DFT are briefly described in the following. The vapor-liquid interfacial properties were investigated in the temperature range from $T = 0.65\,\varepsilon k_{\mathrm{B}}^{-1}$ to $1.05\,\varepsilon k_{\mathrm{B}}^{-1}$ with an increment of $\Delta T = 0.05\,\varepsilon k_{\mathrm{B}}^{-1}$. The upper and lower bounds of that range are close to the critical point temperature and the triple tempe-rature, respectively, of the LJTS fluid with a cut-off at $2.5\,\sigma$. Table 2 reports literature data [61, 148, 244, 442, 603, 611, 662, 667, 672, 687] for these temperatures. In the present work, values of *Vrabec et al.* [687] for the critical point and van *Meel et al.* [442] for the triple point are used.

2.3.1.1 Molecular Simulations

The molecular dynamics (MD) simulations were performed with the MD code *ls1 mardyn* [506] in the NVT ensemble with 16,000 particles in a rectangular box. Periodic boundary conditions were applied in all directions. In the studied scenario, the vapor phase coexists with a liquid phase. The liquid slab is in the middle of the box, resulting in two vapor-liquid interfaces, which are oriented perpendicular to the z-axis [706]. For the calculation of the interfacial thickness and the oscillatory layering structure, only one side of the

Table 2: Critical parameters (top) and triple parameters (bottom) of the LJTS fluid. The bold values indicate the values that were used in the present work.

	$T_c / \varepsilon k_B^{-1}$	ρ_c / σ^{-3}	$p_c / \varepsilon \sigma^{-3}$
Dunikov et al. [148]	1.06	0.3173	0.097
Haye and Bruin [244]	1.08	–	–
PeTS EOS	1.089	0.3092	0.102
Shi and Johnson [603]	1.08	0.3211	–
Smit [611]	1.09	0.317	–
Thol et al. [662]	1.086	0.319	0.101
Trokymchuk and Alejandre [672]	1.073	0.323	0.0908
	1.186	0.319	0.1098
Vrabec et al. [687]	**1.0779**	**0.319**	–

	$T_{trip} / \varepsilon k_B^{-1}$	$p_{trip} / \varepsilon \sigma^{-3}$
Bolhius and Chandler [61]	0.55	–
Toxvaerd [667]	0.62	–
van Meel et al. [442]	**0.62**	0.00271

liquid slab was taken into account. Also, only one side of the pressure and density profiles is considered for the comparison with the other methods. The elongation of the simulation box in the z-direction, i.e. normal to the interface, is $l_z = 80\,\sigma$ and in the tangential direction at least $l_x = l_y = 24\,\sigma$. The pressure and density profiles were calculated at $N = 1{,}200$ bins, each with a width of $\Delta z = 0.0667\,\sigma$.

The equation of motion was solved by a leapfrog integrator [17]. The temperature was kept constant by a slab-wise velocity scaling thermostat. A time step of $\Delta \tau = 0.001\,\sigma\sqrt{M/\varepsilon}$ was used. The equilibration was conducted for 2 million time steps, while the production ran for further 3 million time steps. The statistical errors given in the present study are equal to three times the standard deviation of all sampled block averages, each over 1 million time steps. Also the density and pressure profiles from each state point were averaged over that block interval. Since the interaction potential is truncated at $2.5\,\sigma$, no long-range correction for the forces and the pressure is necessary.

The Lennard-Jones truncated and shifted potential u_{LJTS} used for the molecular simulations is [17]

$$u_{LJ}(r) = 4\varepsilon\left[\left(\frac{\sigma}{r}\right)^{12} - \left(\frac{\sigma}{r}\right)^{6}\right] \quad \text{and} \tag{12}$$

$$u_{LJTS}(r) = \begin{cases} u_{LJ}(r) - u_{LJ}(r_c) & r \leq r_c \\ 0 & r > r_c, \end{cases} \tag{13}$$

with u_{LJ} being the full Lennard-Jones potential, ε and σ being the energy and size parameter, respectively. The distance between two particles is denoted by r. The cut-off radius r_c of the potential was set to $2.5\,\sigma$ throughout this study.

The surface tension was computed from the difference between the normal and the tangential diagonal components of the overall pressure tensor [695], i.e. the mechanical route

$$\gamma_{\mathrm{MD}} = \frac{1}{2} \int_{-\infty}^{\infty} (p_{\mathrm{N}} - p_{\mathrm{T}}) \mathrm{d}z \,. \tag{14}$$

Thereby, the normal pressure p_{N} is given by the z-component of the diagonal of the pressure tensor, and the tangential pressure p_{T} was determined by averaging over the x and y-components of the diagonal of the pressure tensor. The pressure calculation is based on the method proposed by *Irving and Kirkwood* [325].

2.3.1.2 Density Gradient Theory

Density gradient theory [81, 82, 690] is a widely used framework for calculating surface tensions for pure substances [91, 121, 455] and mixtures [78, 90, 305, 404, 456, 458, 477] based on an EOS, especially for real substances. For a comprehensive introduction, we refer to Ref. [455]. In density gradient theory, the free energy of the heterogeneous system is developed around the free energy of the homogeneous system $a_0(\rho)$. For a planar interface of a pure substance, the free energy can thereby be written as:

$$a(\rho, \nabla\rho) = a_0(\rho) + 1/2 \; \kappa \left(\frac{\mathrm{d}\rho}{\mathrm{d}z} \right)^2 . \tag{15}$$

To model fluid interfaces, density gradient theory only requires the free energy of the bulk fluid and the so-called influence parameter κ, which describes the resistance to the density gradient. In general, κ is a function of the substance, the temperature, and the density [573] and can be related to the direct correlation function of the uniform fluid via linear response theory [37, 121, 168, 428]. Nevertheless, in many applications, the influence parameter is treated as a state-independent parameter [50, 305, 705], which is also done in the present study.

Density profiles and the surface tension at the interface were calculated from the Euler-Lagrange equation as

$$z - z_0 = \int_{\rho_0}^{\rho} \sqrt{\frac{\kappa}{2\Delta\Omega(\rho)}} \, \mathrm{d}\rho \,, \tag{16}$$

$$\gamma_{\mathrm{DGT}} = \int 2\Delta\Omega \, \mathrm{d}z \,. \tag{17}$$

where $\Delta\Omega$ is the grand thermodynamic potential defined as $\Delta\Omega(\rho) = \rho a_0(\rho) - \rho\mu^{\mathrm{s}} + p^{\mathrm{s}}$ and $a_0(\rho)$ the homogeneous free energy at the local density ρ, μ^{s} the saturated bulk phase chemical potential, and p^{s} the saturated bulk pressure. The pressure profiles $p_{\mathrm{N}} - p_{\mathrm{T}}(z)$ were calculated from comparing the integrand of Eqs. (14) and (17) and identifying $2\Delta\Omega(z) = p_{\mathrm{N}} - p_{\mathrm{T}}(z)$. This expression can also be derived in a rigorous way for DGT [119, 231, 248, 511, 720].

The PeTS EOS was employed here for calculating the free energy in Eqs. (16) and (17). The DGT density profiles were calculated in a $20\,\sigma$ domain with finite $\Delta z = 0.01\,\sigma$, resulting in $N = 2{,}000$ bins.

Using the PeTS EOS, the influence parameter κ for DGT is fitted here to surface tension data of the LJTS fluid obtained from molecular dynamics simulation [687]. First, each of the 18 data points for $\gamma_{\mathrm{MD}}(T)$ provided by Ref. [687] was used to calculate the influence parameter individually. The results are shown as symbols in Fig. 7. These κ values reproduce the exact molecular simulation surface tension results. The error bars of the surface tension from molecular simulations, specified by *Vrabec et al.* [687], are transferred to error bars in κ, as shown in Fig. 7.
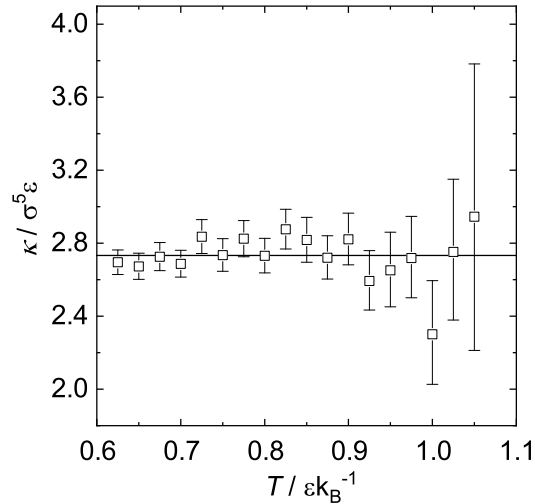
Figure 7: Influence parameter κ of the DGT calculated from molecular simulation data of the surface tension of the LJTS fluid [687]. The error bars are calculated from the surface tension error bars [687]. The horizontal line shows the chosen temperature-independent κ_{PeTS} value.

The horizontal line in Fig. 7 is an error weighted average of the influence parameters with the value $\kappa_{\mathrm{PeTS}} = 2.7334\,\varepsilon\sigma^5$. This value is used in the following, since it is constant within error bars for all but one single simulation data point (cf. Fig. 7). The resulting numeric value $\kappa_{\mathrm{PeTS}} = 2.7334\,\varepsilon\sigma^5$ was used throughout the present work.

2.3.1.3 Density Functional Theory

The DFT results used for comparison in this study are taken from Ref. [637]. They were computed using the following formalism.

The free energy in density functional theory is written as a sum of contributions [637]

$$A[\rho(\mathbf{r})] = A_{\mathrm{id}}[\rho(\mathbf{r})] + A_{\mathrm{hs}}[\rho(\mathbf{r})] + A_{\mathrm{disp}}[\rho(\mathbf{r})], \tag{18}$$

where the squared brackets indicate a functional dependency on the local density $\rho(\mathbf{r})$ and $\mathbf{r}$ is the location.

The PeTS-i functional from a previous work of our group is used in the density functional theory [249]. To be consistent with the PeTS EOS, the PeTS-i functional uses the white-bear version of fundamental measure theory (FMT) from *Roth et al.* [570], which reduces in the bulk fluid to the Carnhan-Starling hard sphere EOS. The dispersion contribution according to *Sauer and Gross* [588] is applied. *Heier et al.* [249] have

fitted the parameter of the dispersion contribution to the surface tension value from computer experiment at $T = 0.8\,\varepsilon k_{\mathrm{B}}^{-1}$. The equations and assumptions made in the theory are summarized in the Supplementary Information of Refs. [249, 637].

DFT density profiles were calculated [671] by solving the Euler-Lagrange equation obtained from functional minimization of the free energy.

The surface tension of a planar interface was calculated from

$$\gamma_{\mathrm{DFT}} = \int \left(a[\rho(z)] + p^{\mathrm{s}} - \rho(z)\mu^{\mathrm{s}} \right)\,\mathrm{d}z, \tag{19}$$

where $a[\rho(z)]$ is defined from Eq. (18) and

$$A[\rho(z)] = S \int a[\rho(z)]\,\mathrm{d}z, \tag{20}$$

with S being the area of the surface perpendicular to z. Calculations were performed on a $20\,\sigma$ domain with finite $\Delta z = 0.01\,\sigma$, i.e. $N = 2{,}000$ bins [637].

The DFT pressure profiles $p_{\mathrm{N}} - p_{\mathrm{T}}(z)$ were calculated from comparing the integrand of Eqs. (14) and (19) and identifying $p_{\mathrm{N}} - p_{\mathrm{T}}(z) = a[\rho(z)] + p^{\mathrm{s}} - \rho(z)\mu^{\mathrm{s}}$. Since any functional can be derived in a gradient expansion, the arguments from [119, 231, 248, 511, 720] also hold for this formula.

2.3.1.4 Empirical Correlation

A simple analytical function for the density profiles is required for the curve deconvolution described below for the investigation of the oscillatory layering structure. Many empirical functions have been proposed in the past [76, 180, 365, 561, 687]. *Vrabec et al.* [687] came to the conclusion, that the hyperbolic tangent profile

$$\rho(z) = \frac{1}{2}(\rho' + \rho'') - \frac{1}{2}(\rho' - \rho'')\tanh\left(\frac{2z}{K}\right), \tag{21}$$

originally proposed by *van der Waals* [691], matches the LJTS density profiles from computer experiments best. The parameter K can be understood as a measure for the interfacial thickness. *Vrabec et al.* [687] used a temperature dependent K-parameter, defined by[1]

$$K = -1.720\left(\frac{T_{\mathrm{c}} - T}{T_{\mathrm{c}}}\right)^{1.89} + 1.103\left(\frac{T_{\mathrm{c}} - T}{T_{\mathrm{c}}}\right)^{-0.62}. \tag{22}$$

It is known [167, 397] that density profiles obey a different decay into both bulk phases, which can be related to the bulk isothermal compressibility [45]. The decay towards the gas bulk phase is therefore more rapid than to the liquid bulk phase. This feature is not captured by the purely empirical correlation.

Also the density profiles from the empirical correlation were calculated on a $20\,\sigma$ domain with finite $\Delta z = 0.01\,\sigma$, i.e. $N = 2{,}000$ bins.

---

[1]In the publication of *Vrabec et al.* [687] is a misprint in Eq. (13) in the first term, which is corrected here. [correspondence with the author]

Vrabec et al. [687] also give a correlation for the surface tension of the LJTS fluid:

$$\gamma = 2.08 \left(1 - T/T_c\right)^{1.21}, \tag{23}$$

which is used for comparison. This power law is strictly only valid in the vicinity of the critical point. However, it has been shown to be within the error bars of simulation data in the whole temperature range [687, 702, 703].

2.3.1.5 Characterization and Comparison of Density Profiles

Density Profiles

Four types of density profiles are compared in this study:

1. Molecular dynamics simulations (MD)

2. Density gradient theory + PeTS EOS (DGT)

3. Density functional theory + PeTS-i functional (DFT)

4. Empirical correlation of the MD data (Corr)

where 4 is only used as a simple reference. The brackets indicate the corresponding abbreviation used in the following. The origin on the z-axis of each density profile is arbitrarily chosen such that $z(\rho_0) = 0$ with $\rho_0 = \rho'' + 0.5(\rho' - \rho'')$.

Average Difference to Computer Experiment

The average absolute deviation (AAD) between the density profiles from molecular simulations and those obtained via the theoretical route (DGT and DFT) or the empirical correlation were calculated by:

$$\overline{\delta\rho_j} = \frac{1}{N} \sum_i^N \left|\rho_{\mathrm{MD}}(z_i) - \rho_j(z_i)\right| \quad \text{with} \quad j = \mathrm{DGT}, \mathrm{DFT}, \mathrm{Corr} , \tag{24}$$

where N is the number of bins on the z-axis. A piecewise cubic interpolation scheme is used to calculate the density at corresponding z positions.

Also the differences between the empirical correlation [687] and molecular simulations are reported for the sake of completeness.

Interfacial Thickness

We use the 90-10% definition for the effective interfacial thickness L_{10}^{90} according to *Lekner and Henderson* [365]. It is defined as the distance between the points, where the local density reaches 10% and 90% of the corresponding bulk densities:

$$
\begin{aligned}
L_{10}^{90} &= z(\rho_{90}) - z(\rho_{10}), \\
\rho_{10} &= \rho'' + 0.1\left(\rho' - \rho''\right), \\
\rho_{90} &= \rho'' + 0.9\left(\rho' - \rho''\right).
\end{aligned}
\tag{25}
$$

2.3.2 Results for the Surface Tension

Fig. 8 shows the results for the surface tension γ of the LJTS fluid as a function of the temperature obtained from the different methods. The molecular simulations results stem from the present study as well as from Ref. [687]. Furthermore, results from DGT and DFT using the PeTS EOS and PeTS-i functional, respectively, are shown. The surface tension values from DGT and DFT lie within the error bars of the computer experiment data for most temperatures. All methods agree within 5% up to $T = 1.0\,\varepsilon k_\mathrm{B}^{-1}$. The surface tension values by molecular simulations from *Vrabec et al.* [687] and this work are in good agreement. The numerical results for the surface tension from MD, DGT, and DFT are reported in Table 3.
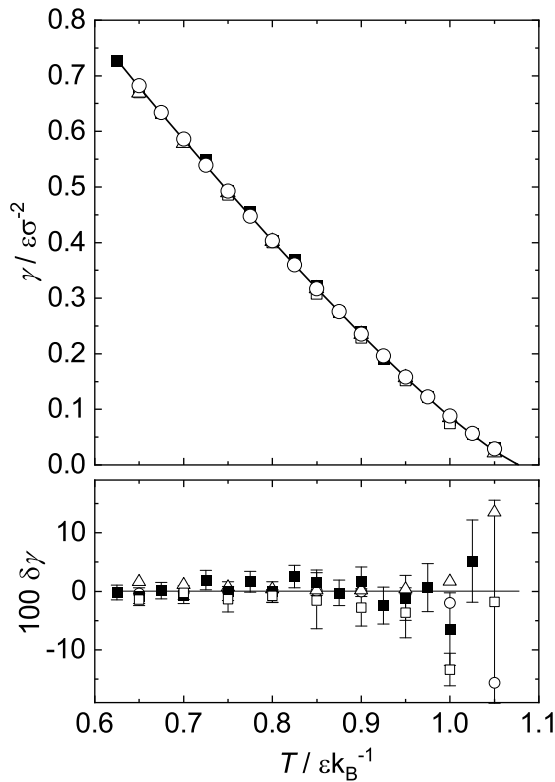
Figure 8: Top: surface tension of the LJTS fluid as a function of the temperature. Data obtained from molecular simulations (filled squares: Ref. [687], empty squares: this work), DGT (circles), and DFT (triangles). The solid line is an empirical correlation for the surface tension proposed in Ref. [687], cf. Eq. (23). Bottom: relative deviation for the surface tension from the empirical correlation: values by DGT (circles), DFT (triangles), MD from this work (empty squares), and *Vrabec et al.* [687] (full squares) as a function of temperature.

Table 3: Surface tension data of the LJTS fluid from MD, DGT, and DFT.

$T / \varepsilon k_{\mathrm{B}}^{-1}$	$\gamma / \varepsilon \sigma^{-2}$		
	MD	DGT	DFT
0.65	0.670(7)	0.683	0.669
0.7	0.584(7)	0.586	0.579
0.75	0.486(11)	0.493	0.489
0.8	0.400(4)	0.403	0.402
0.85	0.312(15)	0.317	0.317
0.9	0.229(7)	0.235	0.235
0.95	0.152(7)	0.158	0.157
1	0.075(2)	0.088	0.085
1.05	0.025(4)	0.029	0.022

2.3.3 Results for the Pressure Profiles

Fig. 9 shows the pressure profiles obtained with MD, DGT, and DFT for $T = 0.65 \, \varepsilon k_{\mathrm{B}}^{-1}$, $0.85 \, \varepsilon k_{\mathrm{B}}^{-1}$, and $1.05 \, \varepsilon k_{\mathrm{B}}^{-1}$. The results from the different methods agree qualitatively well, but clear differences can be identified. The maximum pressure position is shifted between the methods and also the maximum pressure differs. Furthermore, a minimum pressure occurs in DFT and MD but not in DGT.

The effect of the oscillatory layering structure on the pressure profiles is clearly noticeable at low temperatures for DFT in the form of two shoulders on the right side of the pressure difference peak. Also in the molecular simulation pressure profile this can bee seen, but to a smaller extent than in the DFT results.
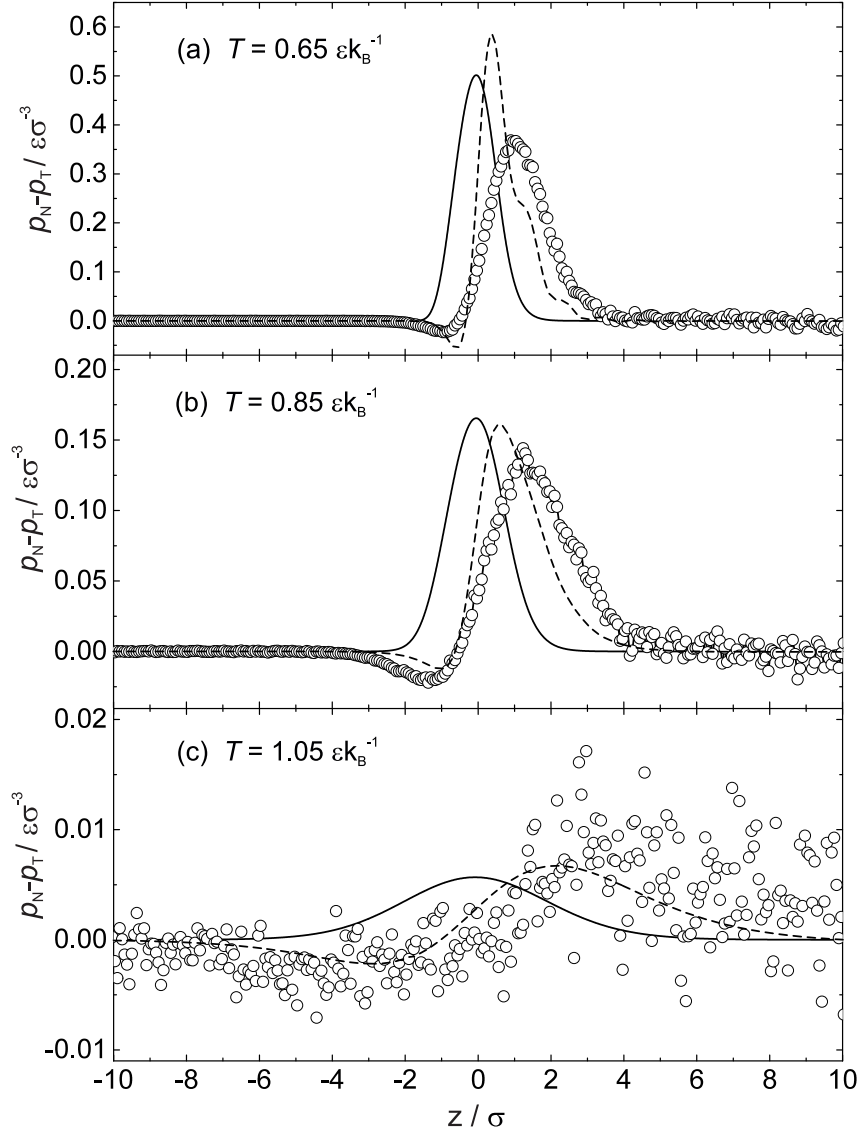
Figure 9: Difference between normal and tangential pressure at the interface of the LJTS fluid at $T = 0.65\,\varepsilon k_B^{-1}$ (top); $T = 0.85\,\varepsilon k_B^{-1}$ (center) and $T = 1.05\,\varepsilon k_B^{-1}$ (bottom): molecular simulations (symbols), DGT (solid line), and DFT (dashed line).

2.3.4 Results for the Density Profiles

The obtained density profiles from DGT and DFT are individually compared with those from computer experiment in Fig. 10.
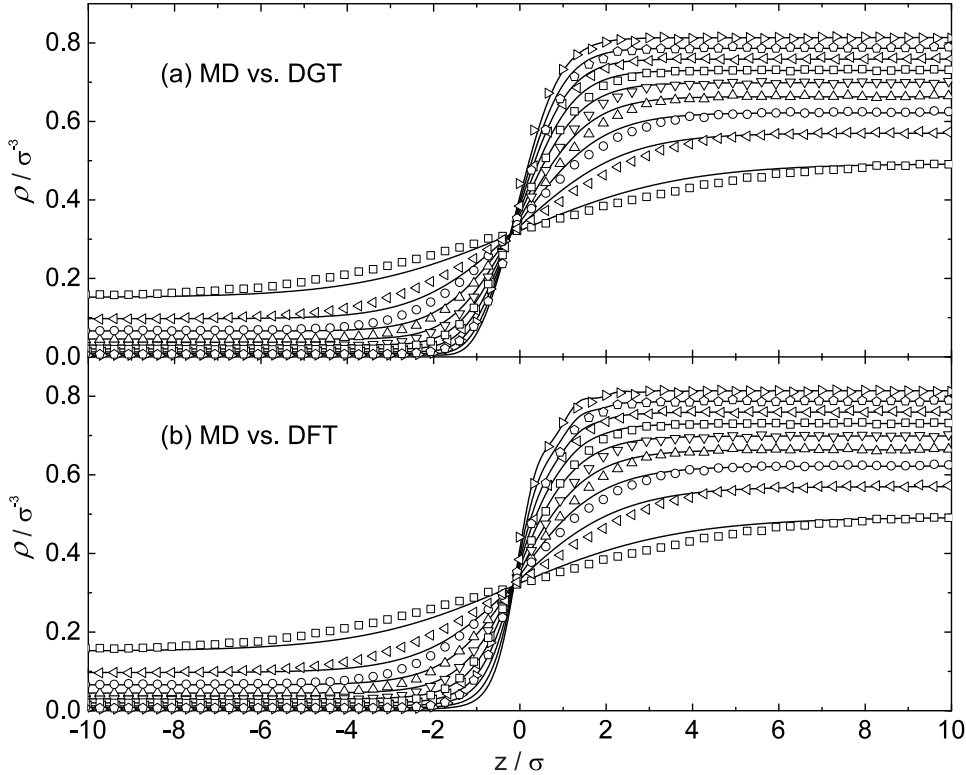
Figure 10: Density profiles of the planar interface: results from molecular simulations (symbols) are compared to (a) DGT and (b) DFT, which are indicated as solid lines. The density profiles are compared at $T/\varepsilon k_\mathrm{B}^{-1}$ = 0.65 ($\triangleright$); 0.7 ($\circ$); 0.75 ($\triangleleft$); 0.8 ($\square$); 0.85 ($\triangledown$); 0.9 ($\triangle$); 0.95 ($\circ$); 1.0 ($\triangleleft$); 1.05 ($\square$).

The agreement between the computer experiment and both DFT and DGT is better for lower temperatures while discrepancies increase towards the critical point. The deviations are highest in the 'knee' of the liquid and the vapor side of the density profile where the curvature is highest. None of the theoretical methods stand out in their capability of describing the computer experiment density profiles. The oscillatory layering structure of the fluid on the liquid side, especially in the DFT density profile at $T = 0.65\,\varepsilon k_\mathrm{B}^{-1}$ and $0.7\,\varepsilon k_\mathrm{B}^{-1}$ will be discussed in detail below.

The density profiles from all employed methods and temperatures coincide at approximately $z = -0.2\,\sigma$ through $\rho = 0.31 \pm 0.01\,\sigma^{-3}$ which is in very good agreement with the critical density $\rho_\mathrm{c} = 0.318\,\sigma^{-3}$. This interesting finding was already reported by *Bongiorno and Davis* [63]. A further investigation of this phenomenon is out of the scope of this work.

Fig. 11 shows the deviation of the density profiles at $T = 0.65\,\varepsilon k_\mathrm{B}^{-1}$ (a), $0.85\,\varepsilon k_\mathrm{B}^{-1}$ (b), and $1.05\,\varepsilon k_\mathrm{B}^{-1}$ (c) respectively. Molecular simulations, which we consider as a reference, shows stochastic fluctuations in the density throughout the profile. Therefore, the differences to the empirical correlation ($\delta\rho_m(z) = \rho_\mathrm{Corr}(z) - \rho_m(z)$ with m = MD, DGT, DFT) are plotted, i.e. the baseline $\delta\rho = 0$ corresponds to the empirical correlation.
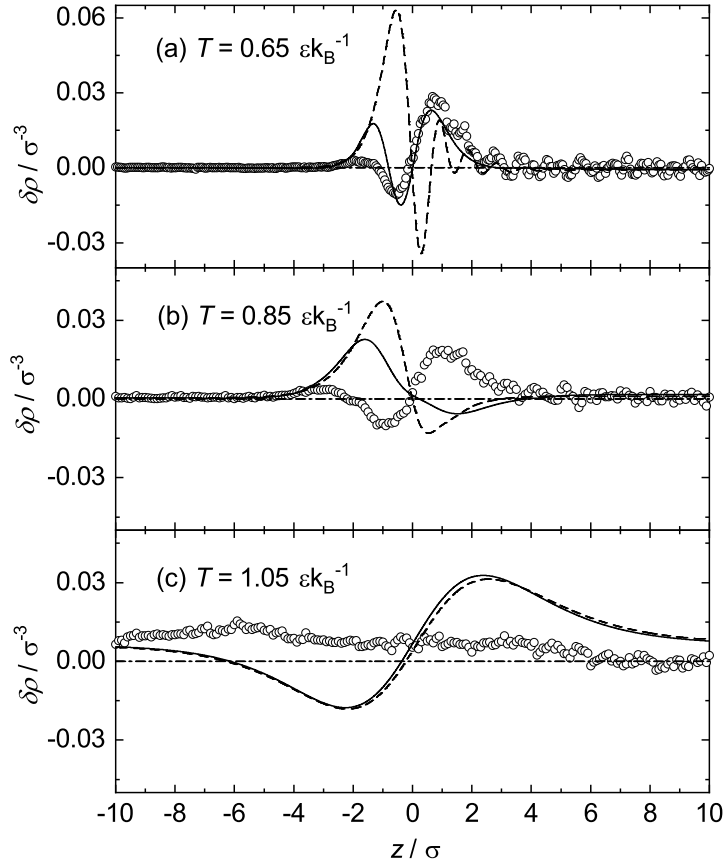
Figure 11: Deviation plots of density profiles at $T = 0.65\,\varepsilon k_{\mathrm{B}}^{-1}$ (top), $T = 0.85\,\varepsilon k_{\mathrm{B}}^{-1}$ (center), and $T = 1.05\,\varepsilon k_{\mathrm{B}}^{-1}$ (bottom). The baselines represent the empirical correlation (Eq. (21) to Eq. (22)). The solid line indicates DGT, the dashed line DFT, and symbols molecular simulations. $\delta\rho$ indicates the absolute deviation between the empirical correlations and the different theoretical methods.

The DGT and DFT density profiles essentially coincide close to the critical point. The deviations between the theoretical methods and the computer experiment are of the same order of magnitude as the deviations between the empirical correlation and the computer experiment. This is remarkable, since DGT and DFT are predictions. At $T = 0.65\,\varepsilon k_{\mathrm{B}}^{-1}$, the DFT density profile shows a strong oscillatory behavior compared to the empirical correlation at $z > 0$ in Fig. 11 (a), which is a result of the oscillatory layering structure at the interface. Such oscillations are expected in DFT density profiles at $T < T_{\mathrm{FW}}$ [145]. The oscillations are also present in the computer experiment (same figure), but to a much smaller extent.

The average absolute deviation in the density profile with respect to the MD results (cf. Eq. (24)) is shown in Fig. 12. The difference between the empirical correlation and molecular simulation results remains rather constant in a broad temperature range $(0.65 < T/\varepsilon k_{\mathrm{B}}^{-1} < 1)$ and increases close to the critical point, while the differences between the theoretical methods (DGT and DFT) and molecular simulations increase monotonically with the temperature. DGT is theoretically only valid in the limit of slowly changing densities, i.e. close to the critical point [167, 168]. The increasing deviation with the temperature can therefore be attributed to the increasing differences
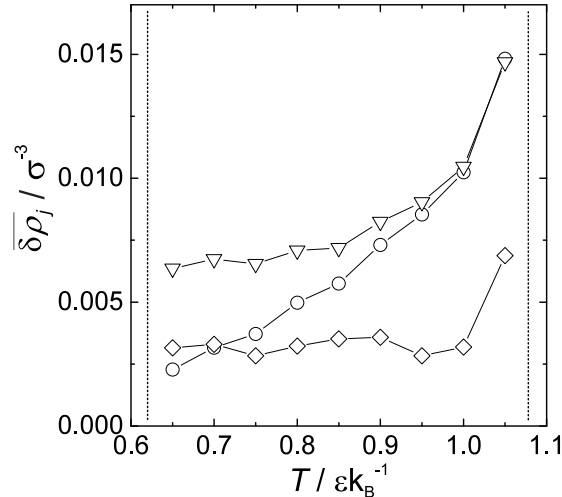
Figure 12: Average absolute deviation of density profiles to molecular simulations results, cf. Eq. (24): circles indicate DGT, triangles DFT, and diamonds the empirical correlation. Dotted lines indicate triple temperature and critical temperature. Solid lines are a guide for the eye.

between the EOS and the LJTS force field approaching the critical point. Approaching the critical point, DGT and DFT density profiles show a very similar deviation from molecular simulations. This might be due to the classical scaling of the underlying EOS compared to the expected Ising scaling of molecular simulations. The density profiles average absolute deviation between the theory and the computer experiments $\overline{\delta\rho_j}$ lies about one order of magnitude higher than the AAD of the bulk saturated densities between the PeTS EOS and the corresponding computer experiments, cf. section 2.2.

The temperature dependence of the 90-10% interfacial thickness, as defined by Eq. (25) is shown in Fig. 13. The interfacial thickness increases monotonically with the temperature approaching a pole at the critical temperature. The theoretical methods agree with each other well at high temperatures, while they differ at lower temperatures. The 90-10% interfacial thickness obtained from the theoretical methods is in the entire temperature range smaller than that from molecular simulations.

This is probably due to the fact that molecular dynamics is a three-dimensional and dynamical method, in which the resulting density profiles are gained by averaging over the two dimensions parallel to the interface and the time. The breathing and moving of the liquid slab normal to the interface and so-called capillary waves, i.e. fluctuations of the liquid surface [267, 293, 513, 573, 713] lead to a broadening of the density profiles [592, 598, 652, 653, 714]. These are shown in Fig. 14 as snapshots from molecular simulations of one σ thick slices perpendicular to the interface at two temperatures. The liquid surface has an undulation (parallel to the surface – here in x- and y-direction) that increases with the temperature. DGT and DFT are static and one-dimensional methods and therefore describe the density change at a perfectly planar interface or through one point on the so-called intrinsic surface.
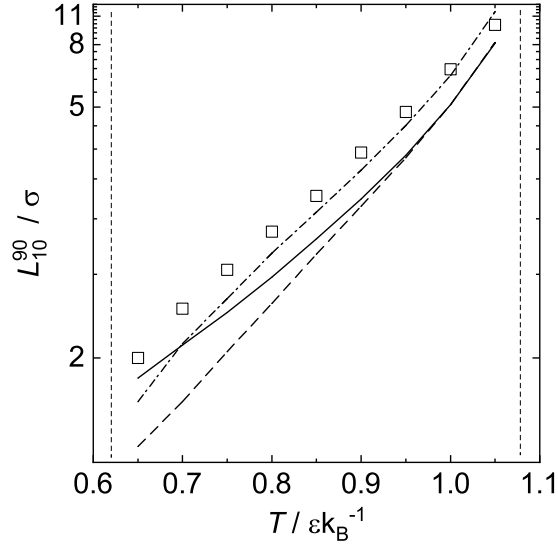
Figure 13: Temperature dependency of the 90-10% interfacial thickness (cf. Eq. (25)) from molecular simulations (symbols), and DGT (solid line), DFT (dashed line), and the empirical correlation (dashed-dotted line). Dotted vertical lines indicate triple temperature and critical temperature. The ordinate has a reciprocal scaling.
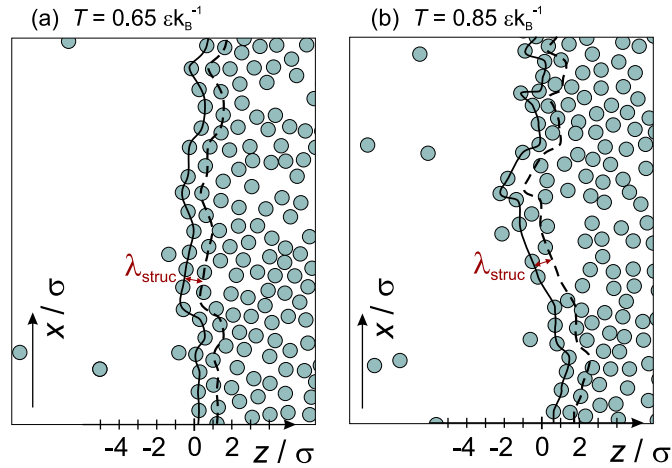
Figure 14: Snapshots of vapor-liquid interface from molecular simulations of the LJTS fluid at (a) $T = 0.65\,\varepsilon k_{\mathrm{B}}^{-1}$ and (b) $T = 0.85\,\varepsilon k_{\mathrm{B}}^{-1}$. The slice that is shown has a width of $\Delta y = 1\,\sigma$. The solid black line schematically indicates the intrinsic surface from the current molecular configuration. The black dotted line indicates the equidistant surface for the layering structure at the distance λ_{struc} from the intrinsic surface.

2.4 Oscillatory Layering Structure at Vapor-Liquid Interfaces

2.4.1 New Method for Analyzing the Oscillatory Layering Structure at Vapor-Liquid Interfaces

For the analysis of the oscillatory layering structure on the liquid side of the vapor-liquid interface, a Fourier transform [68] is applied. Thereby, the wavelength and average amplitude of the oscillatory layering structure can be analyzed.

To extract the sinusoidal part of the density profile $\rho(z)$, a Laplace filter [68] is applied to the density profiles by double numerical differentiation. The Laplace filter suppresses the average value of the signal and increases the sinusoidal part of the signal. To suppress the high frequency noise in the MD density profiles, a Gaussian filter with a variance of $l_\lambda = 0.04\,\sigma$ was applied to those profiles. The Fourier transform of $\nabla^2\rho$ then reads

$$\mathcal{R}_j(\omega) = \int\limits_0^\infty \nabla^2\rho_j(z)e^{iz\omega}\mathrm{d}z \; , \tag{26}$$

with ω being the angular frequency and j = MD, DGT, DFT, Corr. Only the density profile for $z > z_0$ was evaluated since an oscillatory layering structure is only expected on the liquid side [169]. Since the Fourier transform spectra $\mathcal{R}(\omega)$ contains information on the shape of the density profile itself as well as on the oscillations that are of interest here, a curve deconvolution scheme is applied [20]. The spectra $\mathcal{R}_j(\omega)$ are approximated by a linear combination of bell-shaped curves. The part of the Fourier transform that results from the oscillations in the density profile $\mathcal{R}^{\mathrm{oscill}}(\omega)$ can thereby be distinguished from the part that results from the shape of the density profile $\mathcal{R}^{\mathrm{shape}}(\omega)$.

$$\mathcal{R}_j(\omega) = a_j(T)\,\mathcal{R}^{\mathrm{oscill}}(\omega) + k_j(T)\,\mathcal{R}^{\mathrm{shape}}(\omega) \tag{27}$$

In this linear combination, a_j and k_j are adjustable parameters for each spectrum. The Fourier transform that describes the shape of the density profile $\mathcal{R}^{\mathrm{shape}}$ is approximated by eight Gaussian curves and the Fourier transform that describes the oscillatory layering structure $\mathcal{R}^{\mathrm{oscill}}$ by a single Gaussian curve. The deconvolution model parameters, i.e. the frequency of each Gaussian curve, its mean value, and its variance are kept constant throughout this work. The deconvolution model is parametrized in two steps: first, by fitting $\mathcal{R}^{\mathrm{shape}}(\omega)$ to the Fourier transform of the empirical correlation $\mathcal{R}^{\mathrm{shape}}_{\mathrm{Corr}}$ at $T = 0.65\,\varepsilon k_{\mathrm{B}}^{-1}$ with $k = 1$, since the empirical correlation density profile Eq. (21) - (22) has no oscillating content ($\mathcal{R}_{\mathrm{Corr}}(\omega) = 0$). Second, by fitting the frequency and the variance of the Gaussian curve $\mathcal{R}^{\mathrm{oscill}}$ to the Fourier transform j = DFT at $T = 0.65\,\varepsilon k_{\mathrm{B}}^{-1}$ and $a = 1$. For other temperatures and density profile types j =DFT, DGT, MD only a_j and k_j are adjusted by a least square fit. The peak $\mathcal{R}^{\mathrm{oscill}}(\omega)$ in the spectrum can thereby be identified as a result of the oscillatory layering structure in the interface.

The peak area A of the peak $\mathcal{R}^{\mathrm{oscill}}$ is calculated for all types of density profiles and temperatures, since it is proportional to the average amplitude of the sinusoidal content resulting from the oscillatory layering structure.

2.4.2 Comparison of Results from different Methods

Fig. 15 shows the 2nd derivative of the density profile $\nabla^2\rho(z)$ at $T = 0.65\,\varepsilon k_{\mathrm{B}}^{-1}$ (top) and $T = 0.7\,\varepsilon k_{\mathrm{B}}^{-1}$ (bottom). While the gas side of the density profiles has a smooth trend for all investigated methods (MD, DGT, DFT, and Corr), the liquid side of the density profiles shows strong oscillations for DFT and damped oscillations for MD. These oscillations are due to a layering structure of the dense liquid phase at a narrow interface. The density profiles from DGT and the empirical correlation do not show this feature at all.
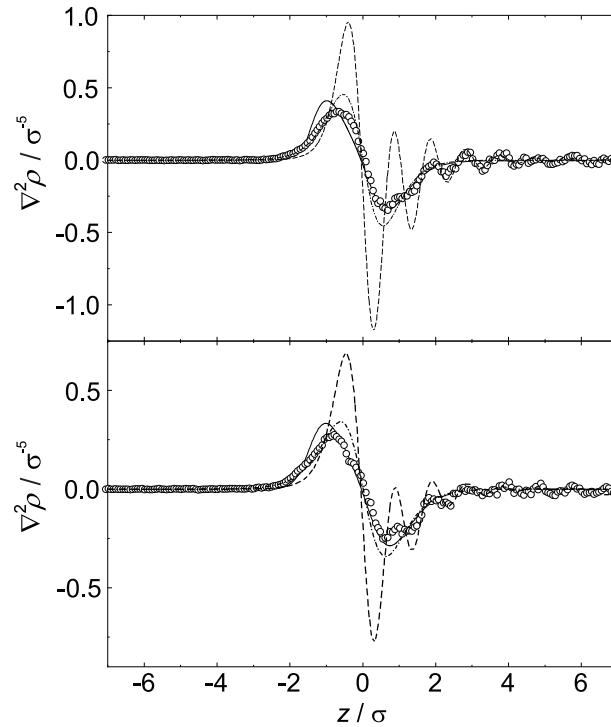
Figure 15: Second derivative of density profiles $\rho(z)$ at $T = 0.65\,\varepsilon k_{\mathrm{B}}^{-1}$ and $T = 0.7\,\varepsilon k_{\mathrm{B}}^{-1}$: results from molecular simulations (symbols), DGT (solid line), DFT (dashed line), and the empirical correlation (dashed-dotted line).

The z-positions of the maxima and minima of DFT and MD agree well. We refer to this phenomenon as 'oscillatory layering structure'. The DFT density profiles show a higher amplitude of the oscillatory layering structure than those from molecular simulations.

The Fourier transform of $\nabla^2\rho(z)$ for $z > 0$ is shown in Fig. 16 as a function of the wavelength λ for the two lowest investigated temperatures $T = 0.65\,\varepsilon k_{\mathrm{B}}^{-1}$ (top) and $T = 0.7\,\varepsilon k_{\mathrm{B}}^{-1}$ (bottom). The density profiles from the square gradient model in DGT, cf. Eq. (15), can not contain any oscillation for a pure substance due to the simplified description of the repulsion between molecules. The density profiles from the empirical correlation can not contain any oscillation for mathematical reasons, cf. Eqs. (21) and (22). Accordingly, the spectra $\mathcal{R}^{\mathrm{DGT}}$ and $\mathcal{R}^{\mathrm{corr}}$ can be used to identify $\mathcal{R}^{\mathrm{shape}}$ as the long bow in Fig. 16, which increases monotonically with λ. Following the curve deconvolution ansatz in Eq. (27), the peak at $\lambda_{\mathrm{struc}} \approx \sigma$ in the Fourier transform of DFT and MD (Fig. 16) can be attributed to the oscillatory layering structure on the liquid side of the interface. The wavelength of the oscillations in the DFT density profiles can
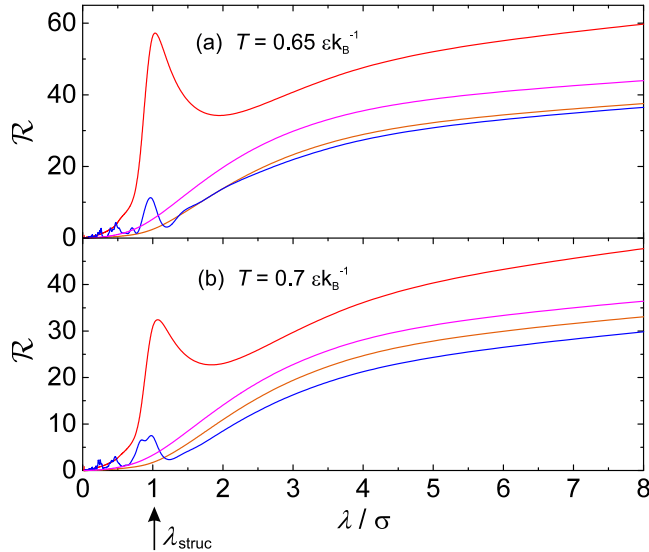
Figure 16: Fourier transform $\mathcal{R}$ of the second derivative of density profiles as a function of the wavelength λ at $T = 0.65\,\varepsilon k_{\mathrm{B}}^{-1}$ and $T = 0.7\,\varepsilon k_{\mathrm{B}}^{-1}$: molecular simulations (blue), DGT (orange), DFT (red), and the empirical correlation (pink). λ_{struc} indicates the wavelength from the oscillatory layering structure.

also be examined visually in Fig. 15 to be approximately one σ. The wavelength of the layering structure for both MD and DFT is almost constant over all temperatures even though the amplitude decreases with increasing temperature.

Even though a Gaussian filter was applied to the MD density profiles, as described above, to suppress stochastic fluctuations, the Fourier transform from MD density profiles show noise at about $\lambda < 0.7\,\sigma$. Due to the applied narrow filter width, an interference of the filter with the band at λ_{struc} can be excluded.

The Fourier transforms were deconvoluted as described above and the obtained peak due to the oscillatory layering structure at λ_{struc} was integrated. This results in the peak area A, which is proportional to the average amplitude of the density oscillations in each density profile. The peak area A is plotted in Fig. 17 for MD and DFT in the entire temperature range between the triple and critical temperature of the LJTS fluid. The relative peak area with respect to that in the spectrum of the MD results at $T = 0.65\,\varepsilon k_{\mathrm{B}}^{-1}$ is plotted. DFT and molecular simulations density profiles have their maximum peak area at low temperatures close to the triple point as expected [145, 169, 369, 653]. This is due to an increased structuring of particles at the rapidly changing density with respect to z at the interface at lower temperatures. The peak area of $\mathcal{R}^{\mathrm{oscil}}$ decreases monotonically with the temperature for these types of density profiles. While the temperature dependency of A agrees well between DFT and MD, the magnitude differs significantly. The maximum relative peak area at $T = 0.65\,\varepsilon k_{\mathrm{B}}^{-1}$ is about 6.69 for DFT. The relatively high amplitude in the DFT density profiles compared to the MD results is mainly due to the fact that MD density profiles are averaged over two spatial coordinates (x and y), cf. Fig. 14.

Surface fluctuations are present in molecular simulations [267, 713] and smear the oscillatory layering structure in the density profiles due to the spatial and time averaging. This results in a much lower amplitude of the layering in the MD density profiles. The
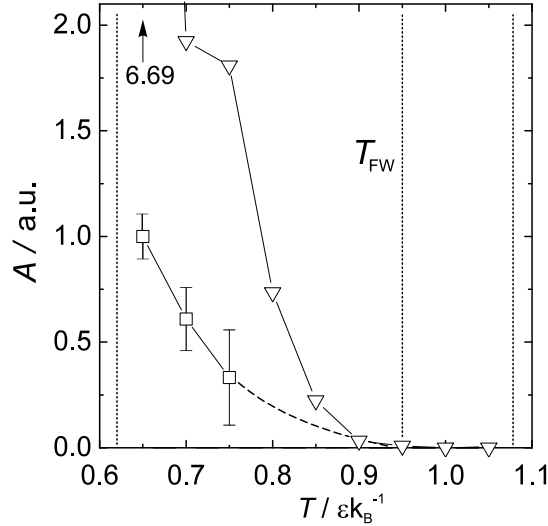
Figure 17: Temperature dependency of the relative peak area of $\mathcal{R}^{\mathrm{oscill}}$ at λ_{struc} calculated by the curve deconvolution: molecular simulations (squares) and DFT (triangles). The dashed line is a $\propto 1/T$ extrapolation for the MD results to higher temperatures. The normalization is done with respect to A_{MD} at $T = 0.65\,\varepsilon k_{\mathrm{B}}^{-1}$. The error bars from molecular simulations are estimated from the signal-to-noise ratio in the Fourier transform, cf. Fig. 16. The dotted lines indicate the triple temperature, the temperature $T/T_{\mathrm{c}} = 0.88$ at which the *Fisher-Widom* (FW) line crosses the dew line [145], and the critical temperature respectively. Solid lines are a guide for the eye.

layering at the intrinsic surface (black solid line) is visible in Fig. 14 but decreases with an increasing temperature. It is therefore likely that the layering at the intrinsic surface is more pronounced than the layering in the time and space-averaged MD density profiles. The influence of surface fluctuations, i.e. capillary waves, has been discussed in the literature numerous times [69, 169–171, 174, 454, 651–653, 669]. Hence, capillary waves that are present in 3D molecular simulations but are not captured by DGT and DFT lead to a Gaussian broadening of the interface, which also smears the oscillatory layering structure. It is expected that capillary wave fluctuations reduce the amplitude of the oscillatory layering structure, but their wavelength and temperature decay remains unchanged – the decay is expected to be exponential with the surface roughness [169, 653, 669]. This is in line with our finding that the oscillatory layering structure in computer experiment is much less prominent than that in DFT while the wavelength is the same, i.e. neither capillary waves nor the temperature affects the wavelength of the layering structure.

The error bars shown for molecular simulations in Fig. 17 were estimated from the signal-to-noise ratio, i.e. the average noise peak height at $0 < \lambda < 0.7\,\sigma$ and the peak height at $\lambda = 1\,\sigma$. Only data points for which the numerical value exceeds the corresponding error bar are plotted in Fig. 17, which is only the case for the three temperatures $T/\varepsilon k_{\mathrm{B}}^{-1} = 0.65$, 0.7, and 0.75. Hence, the oscillatory layering structure in the molecular simulations can only be detected with the applied method up to a temperature of $T \simeq 0.75\,\varepsilon k_{\mathrm{B}}^{-1}$. The shown dashed line is an extrapolation for the MD results with a simple $1/T$ function that also nicely reproduces the temperature dependency of A for DFT.

The dotted vertical line in Fig. 17 indicates the temperature T/T_c = 0.88, where the *Fisher-Widom* (FW) line for the LJTS fluid intersects the dew line according to Refs. [145, 369, 675]. This is in very good agreement with the temperature decay and vanishing of the oscillatory layering structure for DFT and MD results found in this work.

2.5 Conclusions

The vapor-liquid interface of the Lennard-Jones truncated and shifted (LJTS) fluid was investigated in the present work by molecular simulations, density gradient theory, and density functional theory. The PeTS (perturbed truncated and shifted) EOS and PeTS-i functional, developed in a previous work of our group [249, 637], were applied.

Equations of state from the literature for the LJTS fluid [302, 662] cannot be used in interfacial theories due to lacking accuracy [302] or unphysical behavior in the unstable region [662]. An Equation of state for the LJTS fluid was therefore developed based on perturbation theory [249]: the perturbed truncated and shifted (PeTS) EOS. It gives similar results for the vapor-liquid equilibrium (VLE) as the best existing EOS for the LJTS fluid, that of *Thol et al.* [662], but shows no unphysical behavior in the metastable or unstable region.

The PeTS EOS has a simple structure and was parameterized only to VLE data [249]. That data is well described by the PeTS EOS. But the PeTS EOS also predicts accurately molecular simulation results in the metastable region, as well as data on homogeneous stable states, including states far above the critical point. The PeTS EOS was applied in a DGT and a DFT approach for modeling the surface tension of the vapor-liquid interface. The DGT influence parameter κ is found to be constant within the error bars of the molecular simulations data. The DFT interaction averaging diameter is only fit to one surface tension value. The resulting surface tension of the LJTS fluid calculated by DGT and DFT lies within the error bars of the molecular simulation results.

DGT and DFT describe the interfacial properties, i.e. the density and pressure profiles and the surface tension, of the LJTS fluid from molecular simulations similarly well. The results for the surface tension from DGT and DFT lie mostly within the error bars of the molecular simulations results. It is thereby shown that the use of a very accurate EOS in density gradient theory or functional in density functional theory leads to good agreement between those theoretical methods and molecular simulations regarding the interfacial structure.

However, the comparison of molecular simulations, density gradient theory, and density functional theory reveals some significant differences, i.e. DGT does not generate the drop in the pressure profile on the vapor side of the interface [714] and the oscillatory layering structure on the liquid side of the density profile.

The post-processing method that was developed here for the investigation of the oscillatory layering structure reveals that density oscillations, as predicted by DFT, are also present in the molecular simulations density profiles for the LJTS fluid, however, with a lower amplitude. The decay of the amplitude of the oscillatory layering structure with an increasing temperature is found to be in very good agreement with predictions

for the *Fisher-Widom* line by *Dijkstra and Evans* [145]. The amplitude of the density oscillations decreases with an increasing temperature while the wavelength stays constant. Since the MD density profiles are smeared by surface fluctuations which are not present in DFT, the density oscillations are significantly smaller in their amplitude, as also discussed in Ref. [170, 652, 653]. Investigating the influence of a Gaussian convolution on the DFT density profiles, which considers the temperature-dependent surface fluctuation amplitudes and the statistical distribution of interface positions, could be helpful for future work.

The fact that density profiles from different temperatures seem to coincide at the critical density, if the origin of the spatial axis is set to the density of the rectilinear diameter at each temperature might be an interesting topic for future systematic investigations.

3 Binary Mixtures of Lennard-Jones Truncated & Shifted Fluids: Molecular Simulation and Density Gradient Theory

3.1 Introduction

In the present work, a systematic study of interfacial properties of mixtures of Lennard-Jones truncated and shifted (LJTS) fluids was carried out. The PeTS EOS [249] (cf. section 2.2) was used to describe the LJTS fluid within DGT. The PeTS EOS describes the properties of the LJTS fluid well both for stable and metastable fluid states [249]. Also the results for the density profiles in the interfacial region obtained by the PeTS EOS in combination with DGT agree well with those from MD simulations of the LJTS fluid, cf. section 2.3 [637]. For this purpose, the influence parameter κ of the DGT was adjusted to results from the surface tension from MD simulations of the LJTS fluid. Remaining differences between the results from MD and those from DGT probably mainly stem from the fact that fluctuations occur in MD but not in DGT, cf. chapter 2.

In the present work, the PeTS EOS [249] was applied for the first time to mixtures. The extension is based on van der Waals one-fluid theory. The molecular interaction parameters of the LJTS model were simply adopted in the PeTS EOS, including those in the combination rule. The results from both approaches are compared for phase equilibria and interfacial properties of the studied mixtures.

As outlined in introduction, a maximum of the component density in the interfacial region is observed in many cases for the low-boiling component in mixtures, which can reach values several times larger than the largest value of the two bulk densities of that component [50, 635], cf. Fig. 1. This is called *enrichment*. Significant enrichment has been reported for water + CO_2 mixtures, where the component density of CO_2 were reported to be up to 7 times higher at the interface than in the bulk phases [354, 373, 391, 504]. In water + alcohols mixtures [305], as well as alkanes + dimethylformamide mixtures [589], component densities were found which were up to 10 times higher than the highest corresponding component density in the bulk phase. Only minor enrichments are reported for mixtures of alkanes [87, 533], mixtures of poly(dimethylsiloxane) + acid gases [604], mixtures of carbon dioxide + sulfur dioxide, mixtures of carbon dioxide + hydrogen sulfide [77, 78], mixtures of acetone + nitrogen and of acetone + oxygen [153],

and mixtures of R32 and R290 [184]. Overall, a strong enrichment is reported in many cases where the VLE exhibits a wide-boiling behavior [50, 56, 379, 459, 483, 492, 504, 583, 634, 705]. No systematic evaluation of the phenomenon of interfacial enrichment has been conducted so far to elucidate its dependency on the type of the mixture. This is done in the present work.

This chapter reports on results from four studies on binary LJTS mixtures. First, the employed simulation methods and theory are introduced in section 3.2. Then, the four studies are subsequently discussed: (1) six binary LJTS mixtures were studied at one temperature but in the entire composition range (section 3.3). (2) 90 LJTS mixtures were studied at constant temperature and liquid phase composition (section 3.4). (3) A conformal solution theory for interfacial properties of vapor-liquid interfaces is developed and applied to the data from (2) (section 3.5). (4) Two binary LJTS mixtures were studied in a wide temperature and composition range (section 3.6). While (1) - (3) are restricted to vapor-liquid equilibria and interfaces, (4) also considers vapor-liquid-liquid, liquid-liquid, and fluid-fluid equilibria and interfaces. The four studies focus on different aspects of fluid interfaces, but all contribute to a comprehensive understanding of interfacial properties of simple fluid mixtures.

3.2 Modeling and Simulation

3.2.1 Binary Lennard-Jones Truncated & Shifted Mixtures

The Lennard-Jones truncated and shifted (LJTS) potential with a truncation radius of $2.5\,\sigma$ is a simple and computationally efficient intermolecular potential that still gives a reasonable picture of the behavior of simple fluids. Therefore, it is often used as a model fluid for studies of physical phenomena and the development of methods in molecular simulations [50, 154, 272–274, 626, 636, 637, 662].

The LJTS potential u_{LJTS} used for the molecular simulations in this work is

$$u_{\mathrm{LJ}}(r) = 4\varepsilon\left[\left(\frac{\sigma}{r}\right)^{12} - \left(\frac{\sigma}{r}\right)^{6}\right] \quad \text{and} \tag{28}$$

$$u_{\mathrm{LJTS}}(r) = \begin{cases} u_{\mathrm{LJ}}(r) - u_{\mathrm{LJ}}(r_{\mathrm{c}}) & r \le r_{\mathrm{c}} \\ 0 & r > r_{\mathrm{c}}. \end{cases} \tag{29}$$

with u_{LJ} being the full Lennard-Jones potential, ε and σ being the energy and size parameter, respectively. The distance between two particles is denoted by r. The truncation radius r_{c} of the potential is set to $2.5\,\sigma$ throughout this chapter. The truncation of the potential has an influence on the fluid's thermodynamic bulk [148, 395, 611, 672] and interfacial properties [31, 169, 170, 230, 507, 706]. Since the interaction potential is truncated at $2.5\,\sigma$, no long-range correction for the forces and the pressure is necessary.

In the present study binary LJTS mixtures were investigated. The high-boiling component (i.e. the component with the higher boiling point) is labeled with '1' and the low-boiling component (the component with the lower boiling point) with '2'. The size parameter of both components is the same in all mixtures, i.e. $\sigma_1 = \sigma_2 = \sigma$. Also the mass of both components is the same.

The modified Lorentz-Berthelot combination rules are employed [52, 394] for the modeling of the interaction between unlike LJTS particles:

$$\sigma_{ij} = \frac{\sigma_i + \sigma_j}{2}\,, \tag{30}$$

$$\varepsilon_{ij} = \xi\sqrt{\varepsilon_i\varepsilon_j}\,. \tag{31}$$

Here, indices i and j stand for the interaction of two particles of the same component and ij for the cross interaction between the different components, and ξ is a state-independent interaction parameter. The binary interaction parameter ξ_{12} is often adjusted to VLE data of the binary mixture and found to be state-independent in many cases [594]. The goal of the present work is to carry out a systematic study of the influence of the molecular interactions on the interfacial properties. Hence, binary systems were considered in this work with different values for the interaction parameters ξ and ε_2.

3.2.2 Extending the PeTS EOS to Mixtures

The PeTS EOS was developed to model the thermodynamic properties of the LJTS fluid [249], cf. chapter 2. It is based on the perturbation theory of *Barker and Henderson* [41], which splits the free energy per particle $\tilde{a} = a/k_{\mathrm{B}}T$ into the ideal gas contribution $\tilde{a}_{\mathrm{id}}$, the free energy of a hard sphere potential $\tilde{a}_{\mathrm{hs}}$ and a perturbation $\tilde{a}_{\mathrm{pert}}$ contribution due to dispersion, i.e.

$$\tilde{a} = \tilde{a}_{\mathrm{id}} + \tilde{a}_{\mathrm{hs}} + \tilde{a}_{\mathrm{pert}} \,. \tag{32}$$

The perturbation contribution is modeled as a sum of first- and second-order contributions, i.e. $\tilde{a}_{\mathrm{pert}} = \tilde{a}_1 + \tilde{a}_2$. In analogy to the approach of *Gross and Sadowski*, [223, 249] these are developed in a Taylor series as functions of the packing fraction η. The PeTS EOS was fitted to vapor-liquid equilibrium simulation data of the LJTS fluid and describes the vapor pressure and the saturated densities well [249], cf. chapter 2.

The PeTS EOS was extended in the present work to binary mixtures based on the van der Waals one-fluid theory [367], which is known to perform well as long as the size parameters σ_1 and σ_2 of both components are similar [222, 237, 605].

The free energy of the hard sphere fluid mixtures is [67, 223, 407]

$$\tilde{a}_{\mathrm{hs}} = \zeta_0^{-1}\left(\frac{3\zeta_1\zeta_2}{(1-\zeta_3)} + \frac{\zeta_2^3}{\zeta_3(1-\zeta_3)^2} + \left(\frac{\zeta_2^3}{\zeta_3^2} - \zeta_0 \right)\ln(1-\zeta_3) \right), \tag{33}$$

where ζ_n is defined as

$$\zeta_n = \frac{\pi}{6}\rho\sum_{i=1}^{2} x_i d_i^n \quad \text{with} \quad n = 0, 1, 2, 3 \,. \tag{34}$$

In Eq. (34) ρ is the total density of the mixture, x_i is the mole fraction of the component i and d_i the temperature dependent effective hard sphere diameter of component i. Considering that the packing fraction is $\eta = \zeta_3$, the total density of the mixture can be calculated from

$$\rho = \frac{6}{\pi}\eta \left(\sum_{i=1}^{2} x_i d_i^3 \right)^{-1} . \tag{35}$$

The temperature-dependent diameter d_i is calculated according [41, 108] to:

$$d_i = \sigma_i\left(1 - c_1 \exp\left(\frac{-c_2\varepsilon_i}{k_{\mathrm{B}}T} \right) \right), \tag{36}$$

where c_1 and c_2 are universal constants of the pure component PeTS EOS [249], cf. chapter 2. The first and second-order dispersion term are given by [223]

$$\tilde{a}_1 = -2\pi\rho\sum_{k=0}^{6} a_k\eta^k \sum_{i=1}^{2}\sum_{j=1}^{2} x_i x_j(\varepsilon_{ij}/k_{\mathrm{B}}T)\sigma_{ij}^3\,, \tag{37}$$

$$\tilde{a}_2 = -\pi\rho\left(1 + \frac{8\eta - 2\eta^2}{(1-\eta)^2} \right)^{-1} \sum_{k=0}^{6} b_k\eta^k \sum_{i=1}^{2}\sum_{j=1}^{2} x_i x_j(\varepsilon_{ij}/k_{\mathrm{B}}T)^2\sigma_{ij}^3. \tag{38}$$

In the series expansion in η (first sum in both terms) a_k and b_k are also universal constants of the pure component PeTS EOS [249]. The numeric values of the constants

c_1, c_2, a_k and b_k were adjusted to VLE data of the pure LJTS fluid. The equations are presented here for binary mixtures, but in a way that the extension to multicomponent mixtures is straightforward. For a comprehensive description of the implementation of the equations and derivatives see Ref. [223].

For the calculation of the cross interaction parameters σ_{ij} and ε_{ij} in Eq. (37) - (38) the modified combination rules of Lorentz and Berthelot were used – exactly in the same way as they were used in the molecular simulations, i.e. Eq. (30) and (31) also apply for the PeTS EOS.

3.2.3 Density Gradient Theory for Binary Mixtures

Density gradient theory (DGT) can be applied for the calculation of interfacial properties of pure components [81, 82, 91, 121, 455] and mixtures [78, 90, 159, 305, 404, 456, 458, 477]. It only requires a free energy model of the fluid and the numbers for the binary influence parameters κ_{ij}, which describe the influence of the density gradients on the free energy. For an introduction into DGT we refer the reader to Refs. [125, 455, 573].

In DGT, the free energy of the heterogeneous system is expanded in a Taylor series in the density derivative with respect to the spatial coordinate normal to the interface $\nabla^m \underline{\rho}$, $m = 1, 2, ..$ and usually truncated after the square gradient term. The free energy density $\hat{a} = A/V$ can thereby be written for a planar interface of a binary mixture with the components i and j as:

$$\hat{a}(\underline{\rho}, \nabla\underline{\rho}) = \hat{a}_0(\underline{\rho}) + \sum_{i=1}^{2}\sum_{j=1}^{2} 1/2 \; \kappa_{ij}\nabla\rho_i\nabla\rho_j \tag{39}$$

where $\hat{a}_0(\rho)$ is the free energy per volume of the homogeneous system at the local density and $\underline{\rho}$ indicates the vector of the number densities ρ_i and $\nabla\underline{\rho}$ the vector of the corresponding gradients. The influence parameters κ_{ij} generally depend on density and temperature [37, 121, 573]. However, in many applications they are treated as state-independent parameters [50, 305], which is also done in the present work.

In the remainder of this work, the following notation is used: κ_1 and κ_2 stand for the pure component influence parameters and κ_{12} stands for the cross-interaction influence parameter. The influence parameter of the pure LJTS fluid has been determined in Ref. [249] and is adopted here. This leads to: $\kappa_1 = 2.7334\,\sigma^5\varepsilon$ as well as to $\kappa_2 = \kappa_1 \frac{\varepsilon_2}{\varepsilon_1}$. It was shown in Refs. [249, 637] that this leads to an excellent description of the pure component interfacial tension of the pure LJTS fluid, but a slight systematic underestimation of the interfacial thickness predicted from molecular simulation [628, 637], cf. chapter 2. The cross-interaction influence parameter was calculated in the present work from

$$\kappa_{ij} = \sqrt{\kappa_i\kappa_j}\,. \tag{40}$$

In the literature, often an additional adjustable parameter is used in Eq. (40) to handle particularly complex and asymmetric mixtures [377, 504]. This was not done in the present work.

The equilibrium density profiles $\rho_i(z)$ in the planar interface were computed by minimizing Eq. (39). For solving the DGT equation for both components in the entire

interfacial domain, the numerically robust stabilized DGT (sDGT) algorithm proposed by *Mu et al.* [477] as well as the classical reference density method [91] were employed. The results from both methods were found to agree perfectly. The domain length was set to $30\,\sigma$ and a spatial discretization of $0.02\,\sigma$ was used.

The surface tension γ was calculated from [91, 573]

$$\gamma = \int \sum_{i=1}^{2} \sum_{j=1}^{2} \kappa_{ij} \nabla \rho_i \nabla \rho_j \ \mathrm{d}z. \tag{41}$$

Results obtained by DGT in combination with the PeTS EOS are referred to in the following as 'results from DGT' for brevity.

3.2.4 Molecular Simulations

Direct Vapor-Liquid Equilibrium Simulations

The molecular simulations were performed with the MD code *ls1 mardyn* [506] in the NVT ensemble with $N = 16{,}000$ particles. The simulation volume contained two phases, a slab of a first phase in the middle, surrounded by two slabs of a second phase. Periodic boundary conditions were applied, such that two fluid interfaces were obtained, which are planar, if the fluctuations are neglected. The interfaces were perpendicular to the z-axis. The elongation of the simulation box normal to the interface was $80\,\sigma$ and the thickness of the phase in the centre of the simulation box was about $40\,\sigma$, which is large enough to exclude finite size effects [706]. The elongation in the directions parallel to the interface was at least $20\,\sigma$. For the initialization, the bulk phase compositions were estimated with the PeTS EOS to ensure a stable simulation and fast equilibration. The equilibration was carried out for 2,500,000 time steps. The production was executed for 7,500,000 time steps to reduce statistical uncertainties. Density and pressure profiles were computed in block averages of 500,000 time steps during the production phase, resulting in 15 sampling points for each state point. The pressure and density profiles were calculated at $N = 1200$ bins, each with a width of $\Delta z = 0.0667\,\sigma$. The equation of motion was solved by a leapfrog integrator [176] with a time step of $\Delta \tau = 0.001\ \sigma\sqrt{M/\varepsilon}$. The statistical error was estimated to be twice the standard deviation of all block averages. The equilibrium densities and pressures were calculated as an average over the respective phases excluding the area close to the interface, i.e. the area where the first derivative of the density with respect to the z-coordinate deviates from zero significantly.

The position of the phase in the middle of the simulation box fluctuates. This fluctuation would result in a smearing of the averaged density profiles. To avoid this, the individual density profiles from one block average were shifted before the averaging. The shift was carried out such that the z-axis origin was set to the position, where $\rho_{\mathrm{tot}} = \rho_{\mathrm{tot}}'' + 0.5(\rho_{\mathrm{tot}}' - \rho_{\mathrm{tot}}'')$, where ρ_{tot} is the total number density $\rho_{\mathrm{tot}} = \rho_1 + \rho_2$.

The surface tension was computed from the deviation between the normal and the tangential diagonal components of the overall pressure tensor [325, 695], i.e. the mechanical route

$$\gamma = \frac{1}{2} \int_{-\infty}^{\infty} (p_{\mathrm{N}} - p_{\mathrm{T}}) \ \mathrm{d}z. \tag{42}$$

The normal pressure p_N is thereby given by the z-component of the diagonal of the pressure tensor, and the tangential pressure p_T is determined by averaging over x- and y-components of the diagonal of the pressure tensor. The interfacial area S of each planar fluid interface is given by the cross section of the simulation volume normal to the z-axis.

Henry's Law Constant Simulations

Henry's law constants $H_{2,1}$ of the low-boiling component 2 in the solvent 1 were determined in the NpT ensemble with 1372 solvent particles using *Widom*'s test particle method [712]. The simulations were performed with the program *ms2* [575]. In the simulations, the residual chemical potential μ_2^∞ of the solute is sampled, which is directly related to the Henry's law constant by [607]

$$H_{2,1} = \rho' k_B T \, \exp(\mu_2^\infty / k_B T) \,, \tag{43}$$

where ρ' is the saturated liquid density of the solvent and T is the temperature. Each simulation run consisted of 300,000 time steps for equilibration and 1,000,000 time steps for production. The time step was set to $\Delta\tau = 0.001\,\sigma\sqrt{M/\varepsilon}$. 5200 trial insertions were carried out per time step. The statistical uncertainty of the Henry's law constant is estimated to be three times the standard deviation of the ten block averages (the block size was 100,000 time steps).

3.2.5 Definition of Interfacial Properties

The relative adsorption and enrichment of the low-boiling component 2 and the interfacial thickness are used here to characterize the vapor-liquid interfaces. Both the MD simulations and the DGT calculations yield the component density profiles $\rho_i(z)$ for both the high-boiling and low-boiling component $i = 1, 2$ at the planar interfaces.

On the basis of the density profiles of both components, the relative adsorption defined by *Gibbs* [211] can be computed by the symmetric interface segregation according to *Telo da Gama and Evans* [194, 692] as

$$\Gamma_2^{(1)} = -\left(\rho_2' - \rho_2''\right) \int_{-\infty}^{\infty} \left[\frac{\rho_1(z) - \rho_1'}{\rho_1' - \rho_1''} - \frac{\rho_2(z) - \rho_2'}{\rho_2' - \rho_2''} \right] \mathrm{d}z \,, \tag{44}$$

where ρ_1', ρ_1'' and ρ_2', ρ_2'' are the component densities at saturation in the two coexisting bulk phases $'$ and $''$, respectively. $\Gamma_2^{(1)}$ is the relative adsorption of component 2 at the interface with respect to component 1.

A further property for describing the interfacial excess is the interfacial enrichment E_2 of the low-boiling component 2, which was introduced by *Becker et al.* [50] as the ratio between the maximum local density of component 2 in the interfacial region and the larger of the component densities in the two bulk phases ρ_2', ρ_2'',

$$E_2 = \frac{\max\left(\rho_2(z)\right)}{\max\left(\rho_2', \rho_2''\right)} \,. \tag{45}$$

The enrichment E_2 thereby quantifies the non-monotonicity of the density profiles at the interface. By definition, the enrichment assumes values equal to or larger than unity.

For the MD results, the numerator and denominator from Eq. (45) were computed for each block averaged density profile. The bulk densities in the denominator were obtained from a spatial averaging in the corresponding regions, while the maximum value in the denominator is simply the maximal ρ_2 value of the bins in the interfacial region. This can cause artefacts for the evaluation of molecular simulations density profiles, which are superimposed by a random noise: consider the extreme case that the density is uniform in both phases as well as in the interface, i.e. $\rho_2(z)$ = const. Then, obviously $E_2 = 1$. But, due to the fluctuations, the evaluation of Eq. (45) in the way that we have just described will always lead to $E_2 > 1$ as the maximal value of the bins in the interface is selected, which will be larger than the averaged values for the bulk phases ρ'_2, ρ''_2. The results from the previous studies [628, 630, 635], indicate that values below $E_2 = 1.1$ cannot be discerned for $E_2 = 1$ in the case of molecular simulations data.

Both the enrichment E_2 and the relative adsorption $\Gamma_2^{(1)}$ quantify the interfacial excess, but they do not contain the same information. The relative adsorption $\Gamma_2^{(1)}$ quantifies the interfacial excess in the sense of Gibbs [211]. It can not only be obtained from the interfacial density profiles but also from data on the concentration-dependence of the surface tension, i.e. from macroscopic data. The relation is given by the Gibbs adsorption equation $\Gamma_2^{(1)} = -(\partial\gamma/\partial\mu_2)_T$. It has been shown many times [16, 25, 33, 34, 50, 116, 354, 361, 441, 445, 483, 522, 624, 659, 692] that $\Gamma_2^{(1)}$ computed via Eq. (44) from the interfacial density profiles $\rho_i(z)$ is in good agreement with data obtained from the interfacial tension using the Gibbs adsorption equation. While $\Gamma_2^{(1)}$ is an integral measure of the interfacial excess, the enrichment E_2 simply quantifies the non-monotonicity of the interfacial density profile, i.e. the relative peak height of $\rho_2(z)$. E_2 is therefore dimensionless, whereas $\Gamma_2^{(1)}$ has the dimension number of particles per unit area. Furthermore, a relative adsorption $\Gamma_2^{(1)} > 0$ may be present when there is no enrichment ($E_2 = 1$), e.g. if the two component density profiles are shifted relative to each other [50, 630, 635]. But an enrichment $E_2 > 1$ will in general result in an adsorption $\Gamma_2^{(1)} > 0$.

To describe and compare the thickness of fluid interfaces, the 90-10% definition for the effective interfacial thickness L_{10}^{90} according to *Lekner and Henderson* [365] is used, which is the distance between the points where the total number density $\rho^{\text{tot}}(z) = \rho_1(z) + \rho_2(z)$ reaches 10% and 90% of the total bulk densities respectively:

$$
\begin{aligned}
L_{10}^{90} &= z(\rho_{90}^{\text{tot}}) - z(\rho_{10}^{\text{tot}})\,, \\
\rho_{10}^{\text{tot}} &= \rho''_{\text{tot}} + 0.1\,(\rho'_{\text{tot}} - \rho''_{\text{tot}})\,, \\
\rho_{90}^{\text{tot}} &= \rho''_{\text{tot}} + 0.9\,(\rho'_{\text{tot}} - \rho''_{\text{tot}}).
\end{aligned}
\tag{46}
$$

The origin on the z-axis of the interfacial profiles from both MD and DGT shown in the following was arbitrarily chosen such that $\rho_{\text{tot}}(z) = 0$ at $\rho_{\text{tot}} = \rho''_{\text{tot}} + 0.5\,(\rho'_{\text{tot}} - \rho''_{\text{tot}})$.

For the MD results, the enrichment E_2, the relative adsorption $\Gamma_2^{(1)}$, and the interfacial thickness L_{10}^{90} were calculated from each block averaged density profile. The reported value was computed from the mean of the block averages; the statistical uncertainty was estimated to be three times the standard deviation of all sampled block averages.

3.3 Study of Six Binary LJTS Mixtures

In this section, six binary LJTS mixtures were investigated at a single temperature. The temperature and the molecular interaction parameters were chosen such that different types of phase behavior were obtained: mixtures where the low-boiling component is subcritical and mixtures where it is supercritical. Furthermore, the study comprises mixtures with high-boiling and low-boiling azeotropic phase behavior. All mixtures were studied by molecular simulation and DGT.

The focus of the present study lies on the interfacial adsorption and enrichment and its dependency on the mixture type and the composition. Conditions that favor the enrichment are thereby identified. The obtained vapor-liquid equilibrium and interfacial properties are discussed in detail.

3.3.1 Specification of LJTS Mixtures A - F

For component 1, $\varepsilon_1 = 1$ and $\sigma_1 = 1$ in all mixtures. The low-boiling character of the component 2 is obtained by decreasing the dispersion energy with respect to component 1. Two different low-boiling components are investigated: $\varepsilon_2/\varepsilon_1 = 0.9$ and $\varepsilon_2/\varepsilon_1 = 0.5$. The resulting vapor pressure curves are shown in Fig. 18. They were calculated with the PeTS EOS, which has been shown to reproduce the LJTS vapor-liquid equilibrium very well [249], cf. section 2.2. The temperature for which the simulations of the present work were carried out is constant and indicated in Fig. 18 by a vertical dashed line. For that temperature, the component 2 with $\varepsilon_2/\varepsilon_1 = 0.9$ is subcritical (dashed line), while the component 2 with $\varepsilon_2/\varepsilon_1 = 0.5$ is supercritical (dotted line).
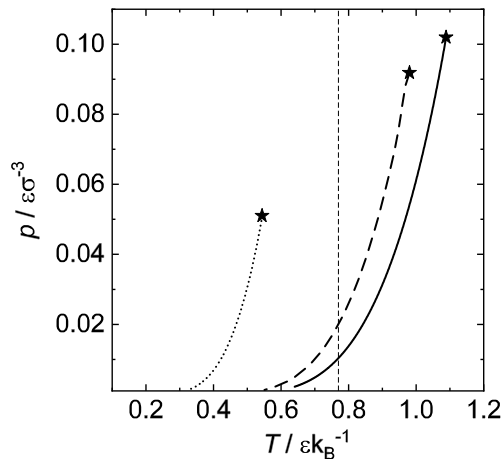
Figure 18: Vapor pressure curves for the three pure LJTS fluids that were considered in the present study. The temperature for which all simulations of the present work were carried out ($T = 0.77\,\varepsilon k_\mathrm{B}^{-1}$) is indicated by vertical dotted line. The high-boiling component 1 is the solid curve. The low-boiling components differ in the their dispersion energies: dashed line: $\varepsilon_2/\varepsilon_1 = 0.9$, dotted line: $\varepsilon_2/\varepsilon_1 = 0.5$. Critical points are indicated by stars.

Slightly different critical points are reported in the literature for the LJTS fluid with a cut-off at $2.5\,\sigma$ [61, 148, 244, 442, 603, 611, 662, 667, 672, 687]. We adopt the values of

Vrabec et al. [687] for the critical point of the LJTS fluid: $T_{\mathrm{c}} = 1.0779 \, \varepsilon k_{\mathrm{B}}^{-1}$; $\rho_{\mathrm{c}} = 0.319 \, \sigma^{-3}$. The temperature is chosen to be $T = 0.77 \, \varepsilon k_{\mathrm{B}}^{-1}$ throughout this study, which corresponds approximately $0.7 \, T_{\mathrm{c}}$. For a discussion of the influence of the temperature on vapor-liquid interfacial properties of the pure LJTS fluid, see section 2.3.

The binary interaction parameter in the Berthelot combination rule (31) was varied here as: $\xi_{12} = 1$, 1.2 and 0.85. These choices in combination with the varied dispersion energy result in six binary LJTS mixtures that were investigated in this study. They are summarized in Fig. 19 using sketches of the phase diagrams at the studied temperature. In three of the mixtures, component 2 is subcritical, and in the three others, it is supercritical, resulting in a critical point of the mixture. This depends on the choice of $\varepsilon_2/\varepsilon_1$. The parameter ξ_{12} is used to control the deviations from Raoult's law. For $\xi_{12} = 1$ the mixture is almost ideal, the value of $\xi_{12} = 1.2$ causes negative deviation from Raoult's law and $\xi_{12} = 0.85$ causes positive deviation from Raoult's law. The six systems are labeled A to F. For the subtrical systems, this leads to a low-boiling azeotrope and a high-boiling azeotrope, respectively.
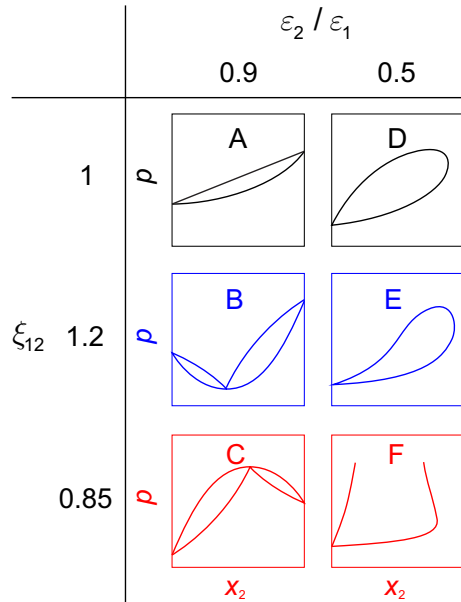
Figure 19: Sketches of the isothermal phase diagrams of the six studied binary mixtures 1 + 2 at the considered temperature. The different choices of the ratio of the LJTS dispersion energies $\varepsilon_2/\varepsilon_1$ and the binary interaction parameter ξ_{12} lead to different types of phase behavior (A - F).

3.3.2 Results and Discussion

3.3.2.1 Vapor-Liquid Equilibria

Fig. 20, panels A - F show the binary phase diagrams of the six investigated mixtures, for the studied temperature $T = 0.77 \, \varepsilon k_{\mathrm{B}}^{-1}$. The numerical results for the phase equilibria of the six studied systems obtained by MD and the PeTS EOS are given in the Appendix. The solid lines are the PeTS EOS and the symbols are the computer experiments. The

error bars are only shown where they exceed the symbol size. The left column shows the subcritical (A - C) and the right column the supercritical mixtures (D - F).
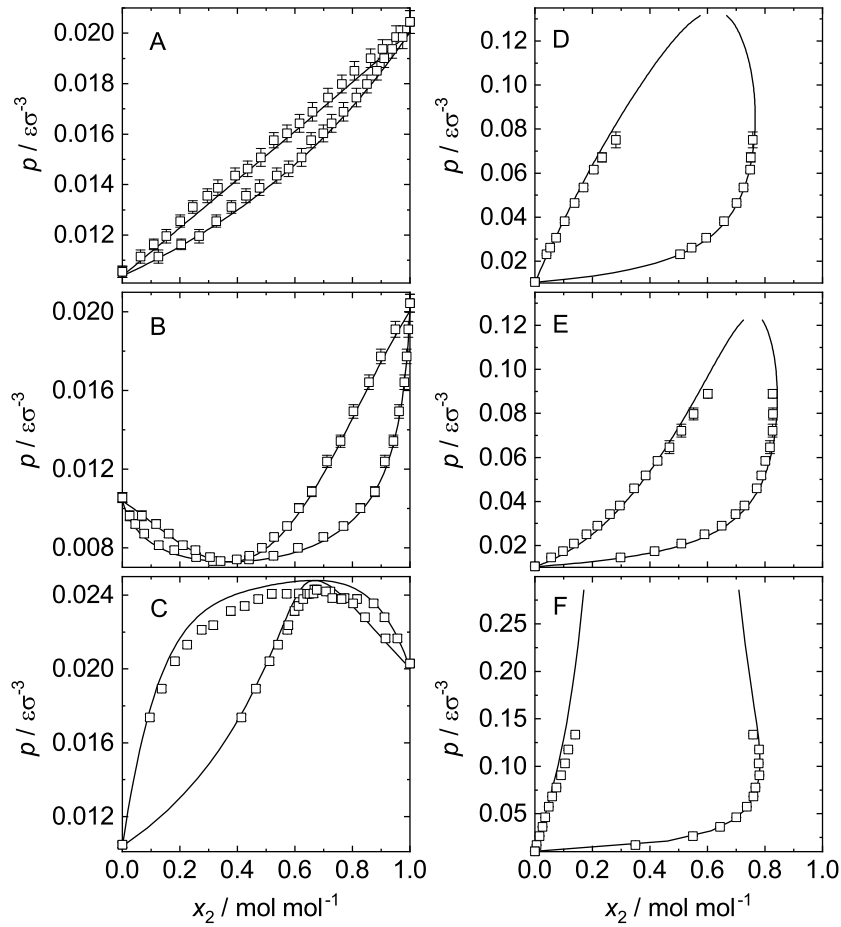
Figure 20: Vapor-liquid equilibria of the binary LJTS mixtures A - F at $T = 0.77 \, \varepsilon k_{\mathrm{B}}^{-1}$. Symbols are MD results and the lines are the PeTS EOS.

The molecular simulation results and those from the PeTS EOS agree generally very well, even though the parameters were simply transferred from the force field to the EOS and no adjustment was made. For mixture C some deviations in the pressure are observed, especially in the vicinity of the low-boiling azeotrope. For the supercritical mixtures D - F the equation of state overestimates the pressure close to the critical point compared to the computer experiment which is, however, a general feature of classical EOS.

The mixtures D and F show particularly wide two-phase regions. Table 4 shows the partition coefficients at infinite dilution

$$K_2^{\infty} = \lim_{x_2' \to 0} \frac{x_2''}{x_2'} \tag{47}$$

that were found from an extrapolation of the results of the PeTS EOS. The numbers of K_2^{∞} are high for wide-boiling mixtures. For mixtures D and F, high numbers of K_2^{∞} are found. For the azeotropic mixture B, the number for K_2^{∞} is below 1, meaning that the component 2 is enriched in the liquid and not in the vapor phase contrary to all other mixtures that were studied here.

Table 4: Partition coefficient K_2 and interfacial enrichment of low-boiling component E_2 at infinite dilution of the low-boiling component ($x'_2 \rightarrow 0$) in the six investigated binary mixtures from DGT+PeTS EOS.

System	K_2^∞	E_2^∞
A	1.8	1.00
B	0.2	1.00
C	8.8	1.53
D	22.8	2.39
E	4.8	1.32
F	87.8	2.90

3.3.2.2 Interfacial Properties

The vapor-liquid interface was investigated for all VLE state points shown in Fig. 20 by MD and DGT. The state points of the LJTS mixtures are specified in the following by the liquid phase composition x'_2. The numerical values for the surface tension γ, the relative adsorption $\Gamma_2^{(1)}$, the enrichment E_2, and the interfacial thickness L_{10}^{90} for all studied mixtures and state points are presented in the Appendix.

Density Profiles

In Figs. 21 and 22, results for density profiles from MD and DGT are compared. Fig. 21 shows results for two state points of the mixture C, Fig. 22 is similar, but for the mixture D. The shown state points are at low concentrations x'_2.

The density of the high-boiling component $\rho_1(z)$ changes monotonously from the vapor to the liquid phase, while the density of the low-boiling component $\rho_2(z)$ exhibits a maximum at the interface in all four cases shown in Figs. 21 and 22. Overall, the results from MD and DGT are in good agreement. The density maximum is predicted by both MD and DGT, but its height is slightly larger for DGT than for MD. As already discussed by *Becker et al.* [50] and *Werth et al.* [705] this is due to fluctuations at the interface that are present in MD but not in DGT. Such fluctuations might also be the reason for the slightly shifted position of the density maximum in both interfacial profiles of the mixture C shown in Fig. 21. Also, some differences in the interfacial thickness are observed: the MD density profiles are broader than those from DGT in all cases shown in Figs. 21 and 22. This can also be attributed to these fluctuations [637]. Considering the fact that the parameters $\varepsilon_2/\varepsilon_1$ and ξ_{12} of the LJTS force field model were simply adopted in the EOS and no mixture data was used for the adjustment of both methods, the results agree remarkably well. Good agreement was also observed for the other state points of the mixtures C and D as well as for all other studied mixtures (not shown).

Figs. 23 and 24 show the density profiles for the mixtures A - F for all studied state points. Since MD and DGT results agree very well in all cases, only the DGT results are shown here (the corresponding plots for the MD results are presented in the Appendix).

An enrichment of the low-boiling component, i.e. a maximum in the corresponding density profile, is observed not only in the mixtures C and D but also in the mixtures E
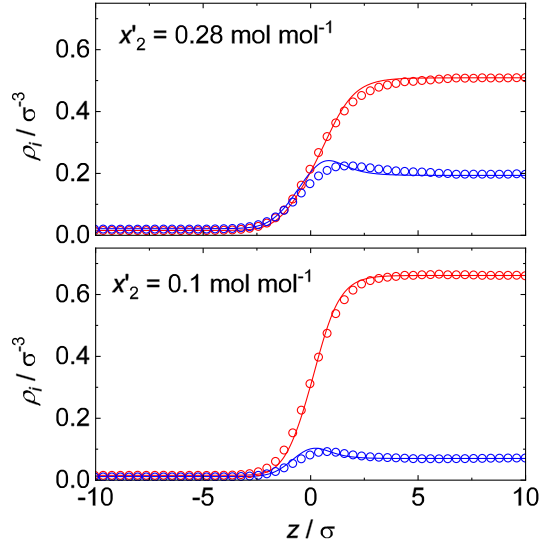
Figure 21: Comparison of the component density profiles in the interface of the binary LJTS mixture C at x'_2 = 0.28 mol mol^{-1} (top) and x'_2 = 0.1 mol mol^{-1} (bottom). Symbols: MD simulation; lines: DGT + PeTS EOS. Red: component 1 (high-boiling); blue: component 2 (low-boiling).
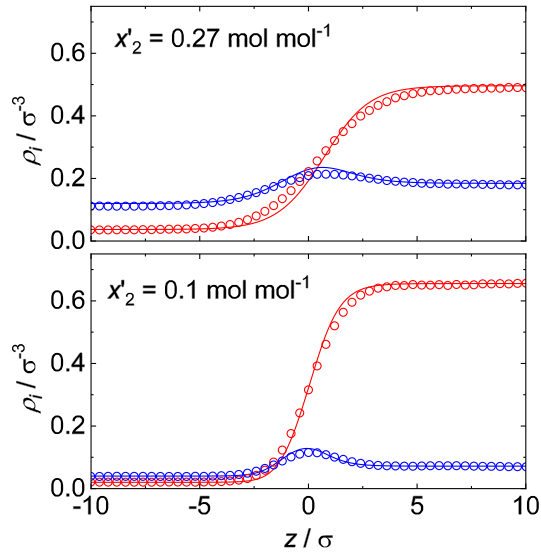
Figure 22: Comparison of the component density profiles in the interface of the binary LJTS mixture D at x'_2 = 0.27 mol mol^{-1} (top) and x'_2 = 0.1 mol mol^{-1} (bottom). Symbols: MD simulation; lines: DGT + PeTS EOS. Red: component 1 (high-boiling); blue: component 2 (low-boiling).

and F (cf. Fig. 24). No enrichment of the low-boiling component is found in the quasi ideal mixture A and in mixture B that exhibits a high-boiling azeotrope (cf. Fig 23). No enrichment of the high-boiling component 1 is found in any of the six investigated mixtures.
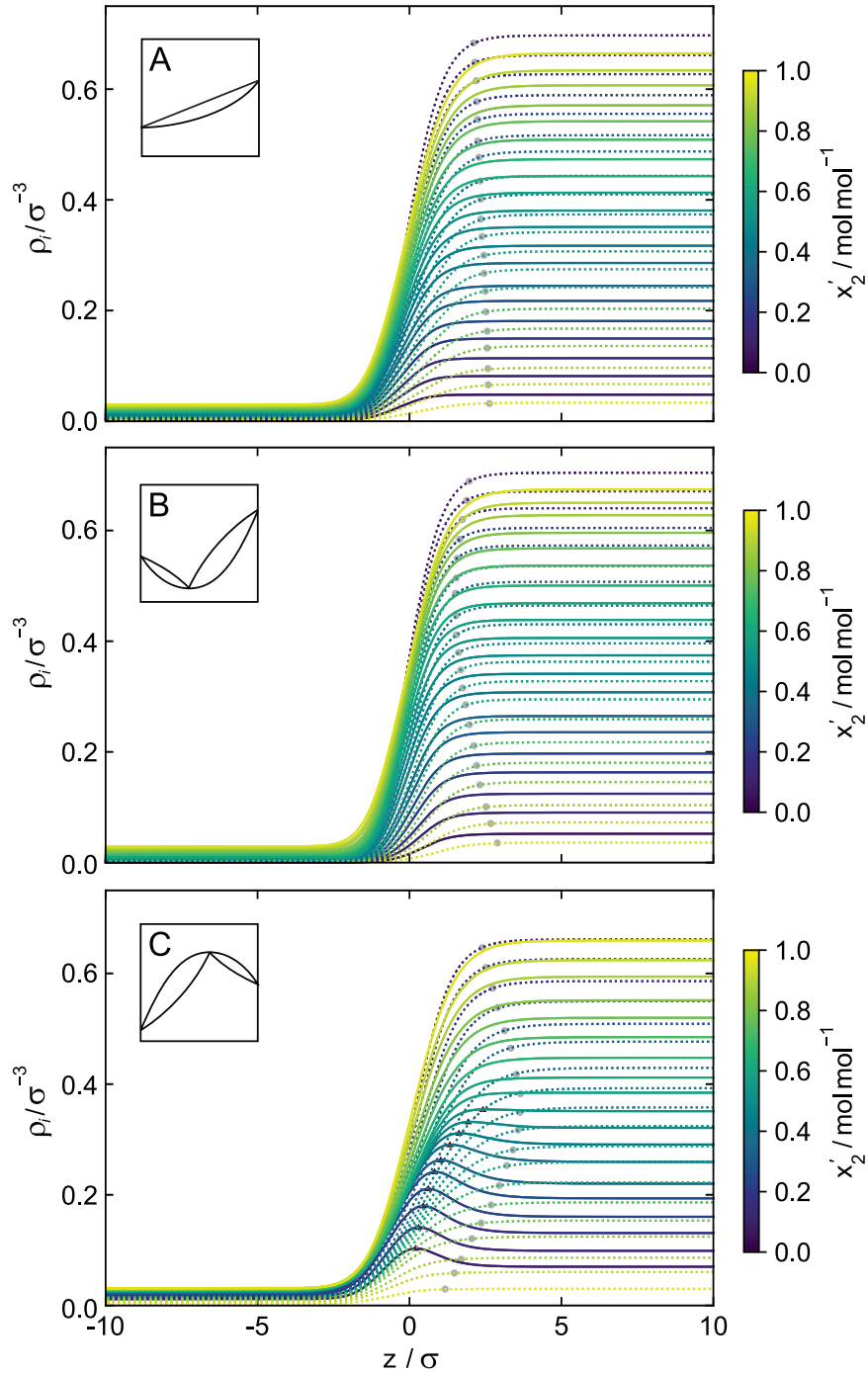
Figure 23: Density profiles of the binary LJTS mixtures A, B, and C at $T = 0.77\,\varepsilon k_{\mathrm{B}}^{-1}$. Results from DGT. Dashed lines: high-boiling component 1; solid lines: low-boiling component 2. The color indicates the liquid phase composition. Triangles indicate the position of the density maximum. Grey points indicate the z-coordinate, where the density of the high-boiling component 1 reaches 97% of the bulk value, cf. Eq. (48).
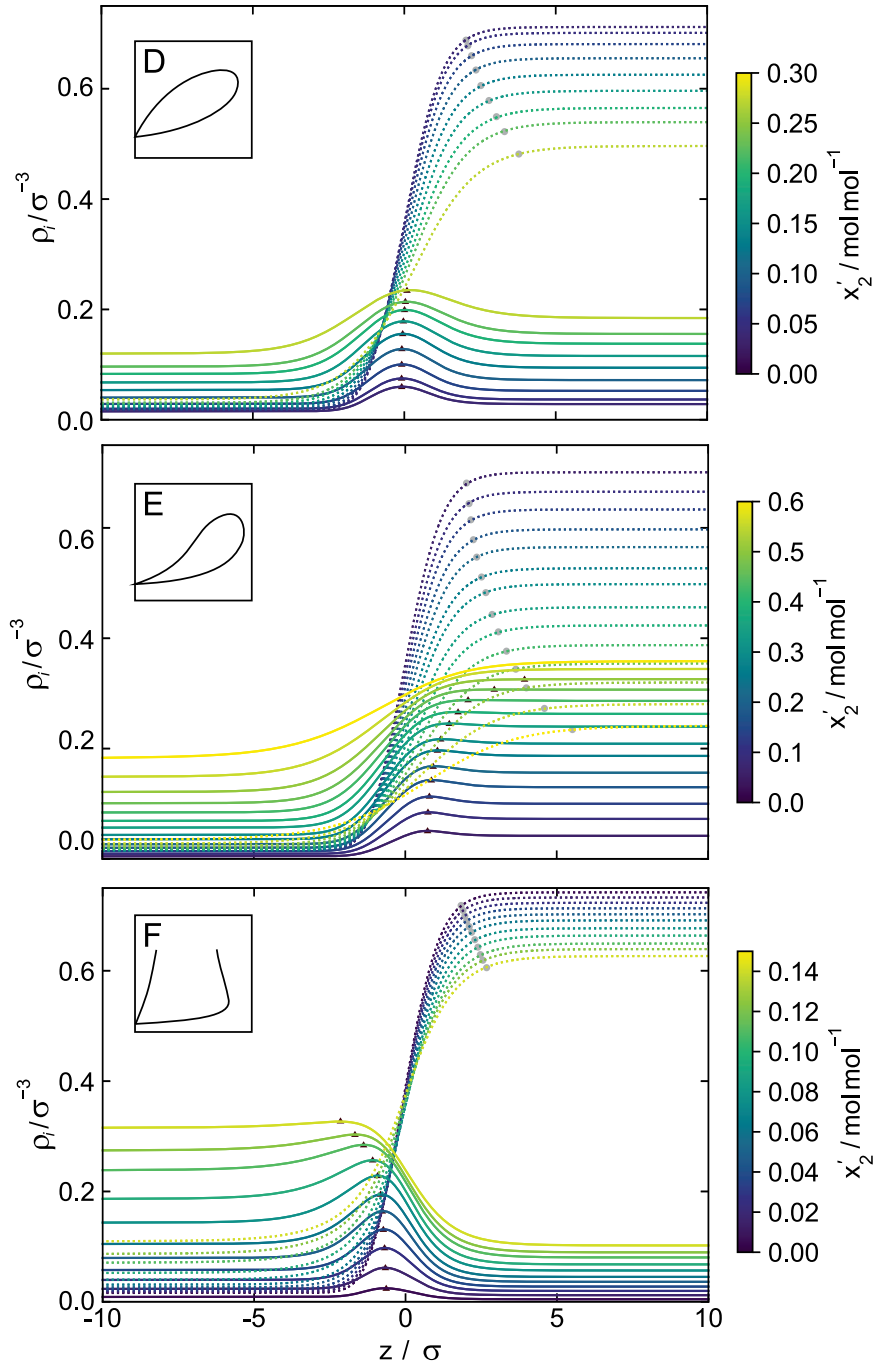
Figure 24: Density profiles of the binary LJTS mixtures D, E, and F at $T = 0.77\,\varepsilon k_{\mathrm{B}}^{-1}$. Results from DGT. Dashed lines: high-boiling component 1; solid lines: low-boiling component 2. The color indicates the liquid phase composition. Triangles indicate the position of the density maximum. Grey points indicate the z-coordinate, where the density of the high-boiling component 1 reaches 97% of the bulk value, cf. Eq. (48).

Surface Tension, Relative Adsorption and Enrichment

Fig. 25 shows the surface tension (top), interfacial adsorption (middle), and enrichment of the low-boiling component 2 (bottom) as a function of the liquid phase composition x_2' for all six studied mixtures. The panels on the left show the results for the three subcritical mixtures A, B, and C; the panels on the right the three supercritical mixtures D, E, and F. The surface tension of the pure components 1 and 2 calculated by MD and DGT agree very well, since the influence parameter for the pure LJTS fluid was fitted to such data [249, 637]. The pure low-boiling component has a lower surface tension than the high-boiling component due to the reduced dispersion energy.
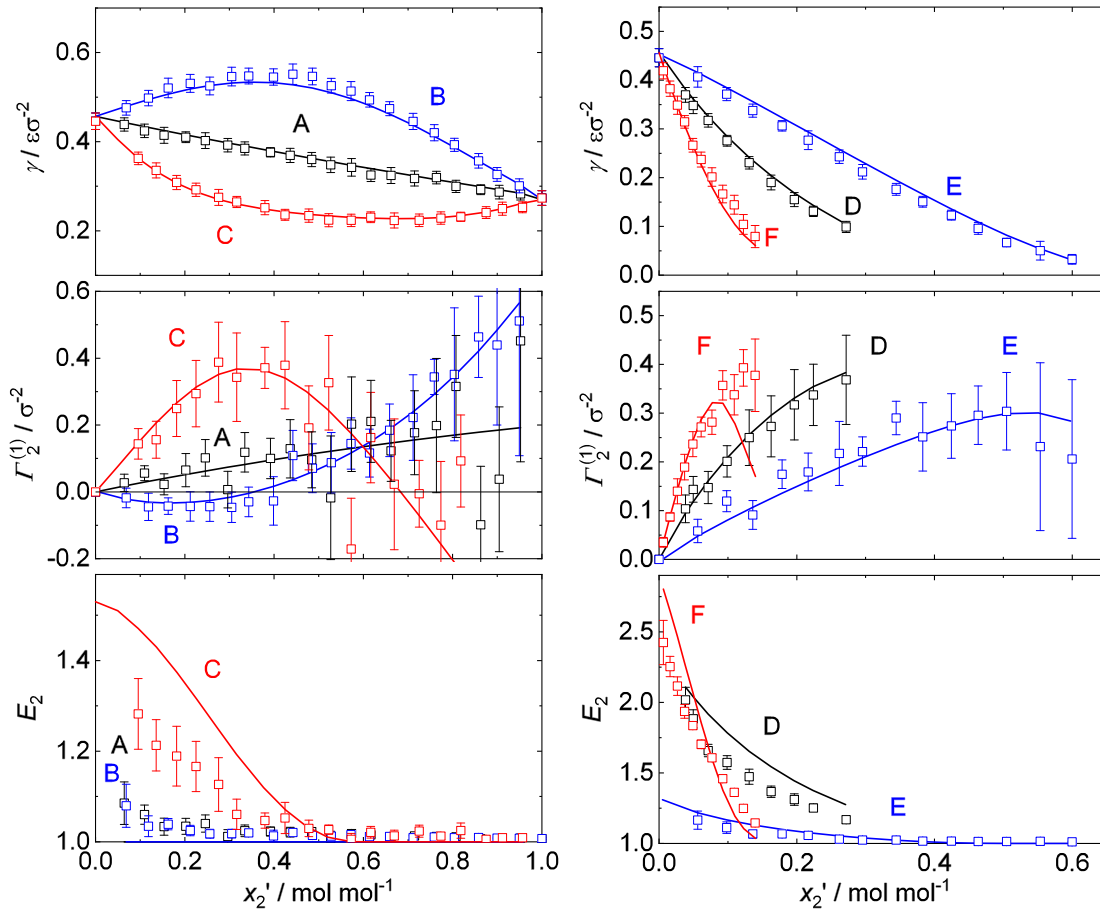
Figure 25: Interfacial properties of the binary mixtures A, B, C (left plots) and D, E, F (right plots). Plots show the interfacial tension (top row), relative adsorption (middle row), and interfacial enrichment of the low-boiling component (bottom row) as a function of the liquid phase composition x_2'. The temperature is $T = 0.77\,\varepsilon k_{\mathrm{B}}^{-1}$. Symbols: MD; lines: DGT.

The surface tension of the ideal mixture A decreases linearly with increasing mole fraction x_2'. The surface tension of mixture B, which exhibits a high-boiling azeotrope, has a maximum, which is found close to the azeotropic composition, cf. Fig. 20 - middle. The surface tension of mixture C shows a minimum of the surface tension, again close to the azeotropic composition, cf. Fig. 20 - bottom. The results for the surface tension from

DGT agree almost always within the error bars with the MD results. This is remarkable as in the model development no data on interfacial properties of mixtures was used.

The relative adsorption $\Gamma_2^{(1)}$ of the low-boiling component 2 (cf. Fig. 25 - middle) is zero for infinite dilution of component 2. In the ideal mixture A, starting at $x_2' = 0$, the relative adsorption of component 2 increases linearly with the mole fraction x_2', which is in good agreement with the expectations from the Gibbs adsorption equation since the surface tension decreases monotonously. The relative adsorption $\Gamma_2^{(1)}$ of component 2 in mixture B, which has a high-boiling azeotrope, exhibits a minimum. On the contrary, the relative adsorption of component 2 in mixture C, which has a low-boiling azeotrope, exhibits a maximum. The composition at which the relative adsorption $\Gamma_2^{(1)}$ is zero – which also corresponds to the extrema in the surface tension according to the Gibbs adsorption equation – has been called *aneotropic concentration* [434]. The component adsorbing at the interface therefore changes from 2 to 1 upon passing through the aneotropic point with increasing x_2'. No proof has been found yet, that the aneotropic and azeotropic point must coincide [184], nevertheless the aneotropic concentration agrees well with the azeotropic concentration for both mixtures B and C (cf. Figs. 20 and 25). This has already been reported in the literature for mixtures with a low-boiling azeotrope, e.g. Refs. [133, 184, 194, 195, 435]. A further interesting finding is that the curves for the relative adsorption $\Gamma_2^{(1)}(x_2')$ of the three investigated mixtures have a common intersection point at approximately $x_2' = 0.6 \, \text{mol mol}^{-1}$. The relative adsorption results from DGT and MD agree within the MD error bars for all three mixture A, B, and C until this intersection point. Beyond this intersection point, the results from MD show an increasing scattering and increasing error bars, which is likely due to the fact that only few particles of component 1 are present.

The enrichment E_2, cf. Eq. (45), for the three subcritical mixtures A, B, and C is shown as a function of the mole fraction x_2' in Fig. 25 - bottom. A significant enrichment of the low-boiling component is only found in the mixture C, i.e. the mixture with the low-boiling azeotrope. At the vapor-liquid interface of that mixture, the component density ρ_2 is up to 1.5 times higher than the highest of the bulk component density (the liquid phase in this case). The enrichment E_2 is highest at infinite dilution of the low-boiling component and decreases with an increasing mole fraction x_2'. The DGT results for the enrichment E_2 of the mixture C are higher than those from MD. DGT predicts no enrichment, i.e. $E_2 = 1$ for both mixtures A and B, while the molecular simulations show a slight enrichment in those two mixtures at low mole fractions of component 2 in the liquid phase. This is due to the fact that the fluctuations of the density ρ_2 in the MD results become more important at low concentrations x_2'. Since the maximum of a fluctuating curve divided by its average value must be larger than unity Eq. (45) always predicts an enrichment $E_2 \geq 1$ and this artifact from the fluctuations becomes more important at low concentrations x_2'. In principle, other definitions of the enrichment could be applied to avoid such problems. But we prefer to keep the simple definition by Eq. (45) as the artifacts mentioned above are generally not important. The enrichment of the low-boiling component E_2 converges to unity at higher mole fractions x_2' for all subcritical mixtures A, B, and C.

Fig. 25 - right panel shows the predicted surface tension γ (top), interfacial adsorption $\Gamma_2^{(1)}$ (middle), and enrichment of the low-boiling component E_2 (bottom) for the mixtures D, E, and F as a function of the mole fraction of the low-boiling component 2 in the liquid phase x_2'. The surface tension of all three mixtures for which the low-boiling

component is supercritical decreases almost linearly with x_2', except in the vicinity of the critical point, where the surface tension goes to zero. The decay of the surface tension becomes steeper with a decreasing binary interaction parameter ξ_{12}. The results for the surface tension γ of the mixtures D, E, and F (Fig. 25 - right panel) from DGT agree almost always within the error bars with the MD results, as for the mixtures A, B, and C (cf. Fig. 25 - left panel).

The relative adsorption of the low-boiling component $\Gamma_2^{(1)}$ as a function of the mole fraction x_2' in mixture D, E, and F is shown in Fig. 25 - right panel. Starting at infinite dilution of the low-boiling component 2, the relative adsorption $\Gamma_2^{(1)}$ of the low-boiling component 2 increases with the mole fraction x_2'. For mixture F, close to the critical point, i.e. approximately at the composition x_2' where the surface tension decay changes from a linear decay to a non-linear decay, the relative adsorption exhibits a maximum for all three mixtures and then decreases to zero at the critical point. The steepness of $\Gamma_2^{(1)}$ increases with a decreasing binary interaction parameter ξ_{12}, which goes in line with the decay of the surface tension. This is again consistent with the expectations from the Gibbs adsorption equation. The agreement between the MD and DGT results for the relative adsorption is better in the linear-decay regime of the surface tension than close to the critical point. Close to the critical point only the trends are consistently predicted by both methods.

The enrichment of the low-boiling component E_2, cf. Eq. (45), in mixture D, E, and F is shown in Fig. 25 - right panel as a function of the mole fraction x_2'. In the mixture D, the component density ρ_2 is up to 2.1 times higher in the interface than in the bulk liquid phase, cf. Fig. 24. Such values have also been reported in the literature for supercritical systems, e.g. ethanol + CO_2 [50] and toluene + CO_2 [705]. The mixture F shows a maximum enrichment of the low-boiling component of up to 2.8. The mixture E on the other side has only a slight enrichment of up to 1.3. All three mixtures D, E, and F, for which the low-boiling component is supercritical, have a monotonously decreasing enrichment E_2 with increasing mole fraction x_2', which goes to unity at the critical point. This has already been reported by *Becker et al.* [50] and *Werth et al.* [705]. An interesting fact is that the relative steepness of the surface tension observed for the mixtures D, E, and F seems to correlate with the relative steepness of the interfacial enrichment. Furthermore, the numeric values of the enrichment differs significantly among the investigated mixtures D, E and F, whereas the numeric values of the relative adsorption $\Gamma_2^{(1)}$ lie in the same range for these mixtures (cf. Fig. 25). The agreement between the MD and DGT results for the interfacial enrichment is very good for the mixture E, while for the mixtures D and F only the trend of the composition dependency of the enrichment is predicted consistently by both methods.

All six studied LJTS mixtures show the highest enrichment E_2 at low concentrations of component 2. The enrichment at infinite dilution E_2^∞ was computed by DGT, as the corresponding numbers are difficult to obtain from molecular simulations due to large statistical uncertainties if only few particles of component 2 are present. The resulting numeric values of E_2^∞ for the mixtures and conditions studied in the present work are listed in Table 4. For the ideal mixture A, E_2^∞ is basically unity, i.e. there is almost no enrichment. However, this does not hold in a mathematical sense. A closer inspection of the DGT results for this system shows a slight positive number of 1.001. The high-boiling azeotropic mixture B has no enrichment, i.e. $E_2^\infty = 1$ to the last digit. The enrichment of the low-boiling component at infinite dilution E_2^∞ from the six investigated LJTS

mixtures is plotted as a function of the partition coefficient at infinite dilution K_2^∞ in Fig. 26. For $K_2^\infty > 1$ the enrichment is found to increase fairly linearly with $\ln(K_2^\infty)$.
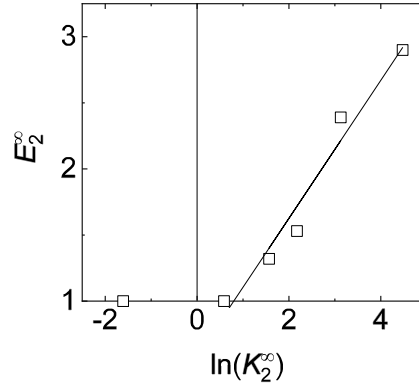
Figure 26: Enrichment of the low-boiling component 2 at infinite dilution E_2^∞ computed from DGT as a function of the the partition coefficient at infinite dilution K_2^∞, cf. Eq. (47), for the six investigated LJTS mixtures A - F. The temperature is $T = 0.77\,\varepsilon k_{\mathrm{B}}^{-1}$. Line: linear fit of the data for mixtures with positive partition coefficients.

Relative Adsorption and Enrichment of the High-Boiling Component

For the sake of completeness the relative adsorption $\Gamma_1^{(2)}$ and enrichment E_1 of the high-boiling component 1 at the interface are shown in Fig. 27 for the three investigated subcritical mixtures A, B, and C. The high-boiling component 1 shows no enrichment in the DGT results. The MD results show a slightest enrichment, which is due to the numerical artifact as discussed above.

Interfacial Thickness

Fig. 28 shows the interfacial thickness L_{10}^{90} as a function of the mole fraction of the low-boiling component in the liquid phase x_2' as obtained from the MD and DGT data using Eq. (46). Fig. 28 - top shows the results of the interfacial thickness of the mixtures A, B, and C and Fig. 28 - bottom of the mixtures D, E, and F.

The interfacial thickness for the ideal mixture A follows a linear trend with increasing x_2'. The mixture B exhibits a minimum in the interfacial thickness. Mixture C has a maximum in the interfacial thickness. Comparing these findings to the results for the surface tension, shows that wider interfaces of a Lennard-Jones mixture have a lower surface tension, while narrower interfaces have higher surface tension.

The interfacial thickness L_{10}^{90} of the mixtures D, E, and F, where the low-boiling component is supercritical, exhibits a pole at the critical point, because the interface becomes infinitely broad.

The density profiles in MD are broader than those from DGT which is in line with the results from the pure LJTS substance, cf. chapter 2. This has been attributed to fluctuations at the interface that are present in MD as a dynamical method but not in
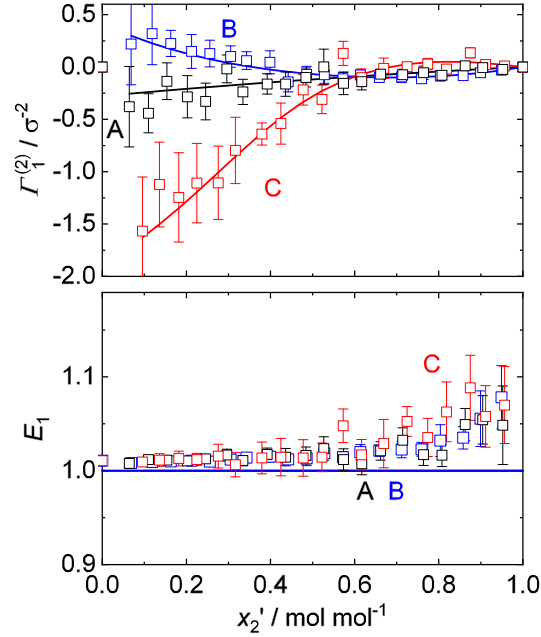
Figure 27: Relative adsorption (top) and interfacial enrichment (bottom) of the high-
boiling component of the mixtures A, B, and C as a function of the liquid
phase composition x_2'. The temperature is in all cases $T = 0.77\,\varepsilon k_{\mathrm{B}}^{-1}$. Sym-
bols: MD; lines: DGT. Black corresponds to system A, blue to system B
and red to system C.

DGT [637]. Such deviations of results for the interfacial thickness obtained by DGT
and MD have also been reported in the literature for other substances [50, 705]. The
results obtained in the present work show that the trend of the composition dependency
of the interfacial thickness is predicted consistently by both methods. Increasing the
interfacial thickness predicted by DGT by about 15% would lead to a good agreement
between MD and DGT for all six investigated mixtures.

3.3.2.3 Detailed Discussion of the Density Profiles

While the density profiles of the mixtures A and B are similar (cf. Fig. 23), the structure
of the fluid interfaces in the mixtures C, D, E, and F (cf. Fig. 23 and 24) have unique
attributes which are discussed in the following. To illustrate these attributes, we use the
'knee on the liquid side of the density profiles' of the high-boiling component 1, which is
defined as the z-coordinate $z_{1,97}$ where the density $\rho_1(z)$ reaches 97% of the liquid bulk
density ρ_1':

$$\rho_{1,97}(z_{1,97}) = \rho_1'' + 0.97\,(\rho_1' - \rho_1''). \tag{48}$$

For the subcritical mixtures A (Fig. 23 - top) and B (Fig. 23 - middle), the density
profiles of the low-boiling component 2 have a similar composition dependency, while
differences in the density profiles of the high-boiling component 1 are found. In the ideal
mixture A (Fig. 23 - top), the knee on the liquid side of the density profiles of the high-
boiling component $z_{1,97}$ moves slightly monotonously to the right with increasing x_2'.
This results in a slight positive adsorption of the low-boiling component with respect to
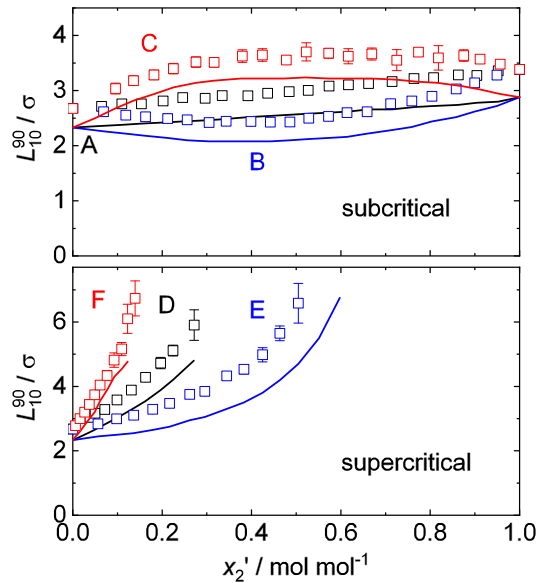
Figure 28: Interfacial thickness of the mixtures A, B, and C (top) and mixtures D, E, and F (bottom) at $T = 0.77\,\varepsilon k_B^{-1}$. Symbols: MD; lines: DGT. Black corresponds to systems with $\xi_{12} = 1$; blue to systems with $\xi_{12} = 1.2$ and red to systems with $\xi_{12} = 0.85$.

the high-boiling component (cf. Fig. 25 - middle) and an increasing interfacial thickness with an increasing mole fraction x_2' (cf. Fig. 28 - top).

The high-boiling component 1 in mixture B (cf. Fig. 23 - middle) behaves differently, i.e. its liquid phase knee $z_{1,97}$ moves first left with increasing mole fraction x_2' and than back right. The turning point can be estimated to be the azeotropic composition. This results in a minimum in the composition dependency of the interfacial thickness (cf. Fig. 28 - top) and a negative adsorption of the low-boiling component until the azeotropic composition (cf. Fig. 25 - middle).

The mixture C, that exhibits a low-boiling azeotrope, shows a completely different interfacial behavior (cf. Fig. 23 - bottom) than the mixtures A and B. The density profiles of the low-boiling component exhibit a maximum at low mole fractions x_2'. The z-position of the maximum shifts right with increasing x_2', which goes in hand with a significant broadening of the interface (cf. Fig. 28 - top). The liquid phase knee $z_{1,97}$ of the high-boiling component 1 in mixture C (Fig. 23 - bottom) shows the opposite behavior as in the mixture B (Fig. 23 - middle), i.e. it moves first right with increasing x_2' and than left, which is the reason for a positive relative adsorption of the low-boiling component 2 (cf. Fig. 25 - middle) and a maximum of the composition dependency of the interfacial thickness (cf. Fig. 28 - top).

The density profiles of mixture D (cf. Fig. 24) show a strong enrichment of the low-boiling component 2, central in the interfacial region. Its maximum position stays at a constant z-position throughout the investigated composition range in contrast to the mixture C. The interfacial thickness in mixture D monotonously increases and the enrichment decreases with increasing mole fraction of the low-boiling component in the liquid phase x_2', cf. Fig. 28 and 25, respectively.

For the mixture E, the z-position of the enrichment slightly shifts right with increasing

x'_2, similar to mixture C (both have an elevated cross interaction, i.e. $\xi_{12} = 1.2$). The interfacial thickness of mixture E monotonously increases with increasing mole fraction x'_2, cf. Fig. 28 - bottom. The density profiles of mixture E in Fig. 24 furthermore reveal, that this broadening is dominated by the low-boiling component on the vapor side of the interface ($z < 0$), while it is dominated by the high-boiling component on the liquid side of the interface ($z > 0$).

While the low-boiling component's bulk liquid densities are higher than the bulk vapor densities in the mixtures D and E, i.e. $\rho'_2 > \rho''_2$ (cf. Fig. 24 - top and middle), this inverts for the mixture F (Fig. 24 - bottom). It is shown in section 3.4 and in chapter 9 that the relation of the densities ρ'_2 and ρ''_2 is of general importance for the enrichment at vapor-liquid interfaces in a given mixture.

The mixture F, which exhibits a particularly wide-boiling phase envelope ($K_2^\infty = 87.8$), shows a large enrichment of the low-boiling component 2 at the interface. The z-position of that maximum is about one σ left of the center of the interface at low x'_2 and shifts further left with increasing x'_2. Also in the mixture F, the interfacial thickness increases monotonously with increasing x'_2 (cf. Fig. 28 - bottom). This broadening is mainly located on the vapor side of the interface ($z < 0$).

The density profiles of the high-boiling component show the interesting feature of a common intersection point in all three supercritical mixtures D, E, and F (cf. Fig. 24). This common intersection point is one of the most noticeable features in the density profiles of the mixtures where the low-boiling component is supercritical. This phenomenon has already been reported for pure substance density profiles [63, 637], cf. chapter 2. The density at the intersection point for pure substance density profiles was identified as the critical density, which can be attributed to the law of the rectilinear diameter. In the three subcritical mixtures A, B, and C (cf. Fig. 23), no common intersection points of the density profiles are observed. The density ρ_1 at the intersection point of the mixtures D and E are slightly below the corresponding critical density. Common intersections are also found at fluid interfacial density profiles in other systems in this work: section 3.6.4.4 reports on different types of common intersection points in a type III mixture and chapter 7 reports on common intersection points in density profiles in the system cyclohexane + CO_2.

3.3.3 Conclusions

In this section, interfacial and bulk properties of six binary Lennard-Jones truncated and shifted mixtures were examined with molecular simulations and density gradient theory in combination with the PeTS EOS. The cross-interaction influence parameter in DGT is calculated by a geometric mixing rule. Six types of mixtures were investigated – all at the same temperature. Their phase behavior was set by the ratio of the two component's dispersion energies and the binary cross interaction parameter in the modified Lorentz-Berthelot combination rules.

The agreement of the results from MD and DGT+PeTS for both bulk and interfacial properties is found to be excellent. The DGT results for the surface tension and relative adsorption agree within the MD error bars. Slight deviations between the MD and DGT results for the enrichment are observed, but the trends are consistently predicted from

both methods. Significant deviations between MD and DGT are only found for the interfacial thickness, but the trends still agree well between both predictions. These deviations are attributed to surface fluctuations that broaden the interface present in MD but not in DGT [637].

A significant enrichment of the low-boiling component at the interface is found for mixtures where the low-boiling component is supercritical or that exhibit a low-boiling azeotrope. The local density of the low-boiling component at the interface is found to be up to three times the value in the bulk phase. Enrichment is in all cases only found for the low-boiling component. Furthermore, the enrichment is found to decrease monotonously with the mole fraction of the low-boiling component in the liquid phase in all investigated mixtures, i.e. the highest enrichment is found at infinite dilution of the low-boiling component. The magnitude of the enrichment is found to be related to the width of the phase boundary. Strong enrichment is therefore favored in mixtures that exhibit a wide boiling phase boundary, which reinforces observations in previous studies [50, 705]. The numeric values of the relative adsorption of the low-boiling component are similar in the investigated mixtures, although the enrichment of the low-boiling component differs significantly among the mixtures.

The present study focuses on the influence of dispersive interactions on interfacial properties. Future work could benefit from an extension to H-bonding molecules and polar interactions [101, 102, 225, 358].

3.4 Comprehensive Study of Binary LJTS mixtures

In this section both molecular dynamics simulation and density gradient theory are used to conduct a comprehensive study of binary Lennard-Jones truncated and shifted (LJTS) mixtures, regarding their vapor-liquid equilibrium and interfacial properties.

While the global phase behavior of Lennard-Jones mixtures or mixtures of other simple spherical molecules has been investigated several times in the literature [139, 339, 344, 426, 538], no systematic study of the global behavior of interfacial properties is available.

We have therefore carried out such a study using both molecular dynamics simulation and DGT. The focus lies on the interfacial adsorption and enrichment and its dependency on the molecular interactions. The studied fluid is described by the Lennard-Jones truncated and shifted (LJTS) potential. The PeTS EOS [249, 635] (Perturbed Lennard-Jones truncated and shifted) is used to describe the LJTS fluid within DGT. The planar vapor-liquid interface of 90 binary LJTS mixtures was investigated at constant temperature ($T = 0.77\,\varepsilon k_{\mathrm{B}}^{-1}$) and constant liquid phase composition ($x_2' = 0.05$ mol mol^{-1}). The temperature is 0.7 of the critical temperature of the high-boiling component.

The 90 investigated mixtures were obtained by varying the dispersion energies of the two components $\varepsilon_2/\varepsilon_1$ and the binary interaction parameter ξ in the modified Berthelot combination rule [52]. The size parameter of both components was the same and was not varied in this work. For the planar interfaces of these mixtures the surface tension, interfacial thickness, relative adsorption, and enrichment of the low-boiling component were determined, such that a large body of data for elucidating the influence of the different interactions on the interfacial properties became available.

All interfacial properties of different studied mixtures were found to have common regularities regarding their ξ, $\varepsilon_2/\varepsilon_1$ dependency. Using a CST, it is then shown in section 3.5 that these regularities can be explained in terms of the mean liquid phase interactions, i.e. the internal energy. This methodology is used to correlate the interfacial properties as functions of the internal energy of the liquid phase. CST has been applied to bulk properties (static [366, 367, 393, 406, 408, 463] and transport [462]) but to the best of our knowledge not to interfacial properties.

By computing the Henry's law constants of the investigated LJTS mixtures, the results and the physical insight from the interfacial properties behavior are furthermore put into relation with the gas solubility of the low-boiling component in the high-boiling component.

3.4.1 Specification of Binary LJTS Mixtures

90 binary LJTS mixtures were investigated in the present work. The high-boiling component is denoted as component 1 and the low-boiling component as 2. The size parameter of both components is the same for all investigated mixtures, i.e. $\sigma_1 = \sigma_2 = \sigma$. Also the mass of both components is the same. Component 1 is considered as reference component here and is the same for all mixtures with $\varepsilon_1 = 1$ and $\sigma_1 = 1$. The low-boiling character of component 2 is obtained by varying the dispersion energy with respect to component 1 between $\varepsilon_2/\varepsilon_1 = 0.5$ and 0.95 with a decrement of 0.05. The critical points

of the high-boiling component 1 and the ten different low-boiling components 2 are shown in Fig. 29 together with the vapor pressure curves of component 1 and two of the pure components 2 with the highest and lowest dispersion energy ratio $\varepsilon_2/\varepsilon_1$. The results shown in Fig. 29 were calculated with the PeTS EOS, which is known to reproduce the LJTS vapor-liquid equilibrium very well [249, 635], cf. chapter 2. Throughout the present study, the temperature is $T = 0.77\,\varepsilon k_\mathrm{B}^{-1}$, which corresponds to approximately 0.7 of the critical temperature of the pure component 1 (cf. dashed line in Fig. 29).
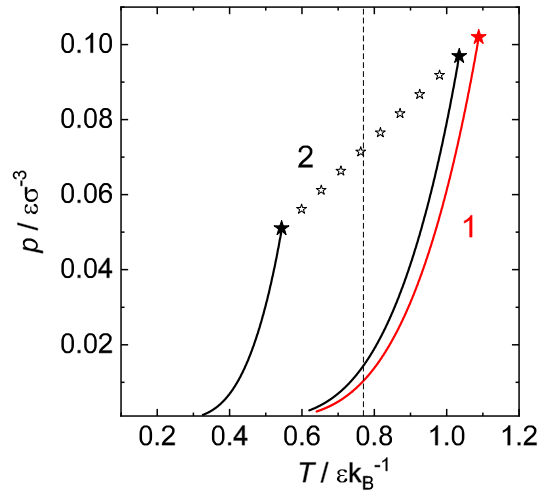
Figure 29: Vapor pressure curves for the pure LJTS fluids that were considered in the present work. The temperature for which all simulations of the present work were carried out is $T = 0.77\,\varepsilon k_\mathrm{B}^{-1}$ and is indicated as vertical dotted line. The high-boiling component 1 is indicated in red; the different low-boiling components 2 in black. The low-boiling components 2 with the lowest $(\varepsilon_2/\varepsilon_1 = 0.5)$ and highest $(\varepsilon_2/\varepsilon_1 = 0.95)$ dispersion energy used in this study are indicated as black lines. For clarity only two out of the 10 low-boiling components' vapor pressure curves are shown. Stars indicate the critical points of all 11 investigated pure substances. The empty stars indicate the critical points of the low-boiling fluids with $\varepsilon_2/\varepsilon_1 = 0.55, 0.6, ..0.85, 0.9$.

The modified Lorentz-Berthelot combination rules were employed [52, 394] for describing the interactions between unlike LJTS particles:

$$\sigma_{12} = \frac{\sigma_1 + \sigma_2}{2}\,, \tag{49}$$

$$\varepsilon_{12} = \xi\sqrt{\varepsilon_1\varepsilon_2}\,, \tag{50}$$

where the indices 1 and 2 indicate the interaction of two particles of the same component and the double index 12 the cross interaction between different components. The value of ε_{12} describes the cross affinity between the two components which is systematically varied by varying ξ. The binary interaction parameter ξ is used as adjustable parameter, which is considered to be state-independent. For the modeling of real fluid mixtures, its number is often obtained from a fit to experimental data [594]. The present work does not aim at reproducing the phase behavior of selected real mixtures. We are interested in studying the influence of the molecular interactions on the interfacial behavior of LJTS mixtures. Therefore, the binary interaction parameter is varied in the range $\xi = 0.85$ and 1.25 with a decrement of 0.05. This results in 90 binary LJTS mixtures as shown

in Fig. 30.
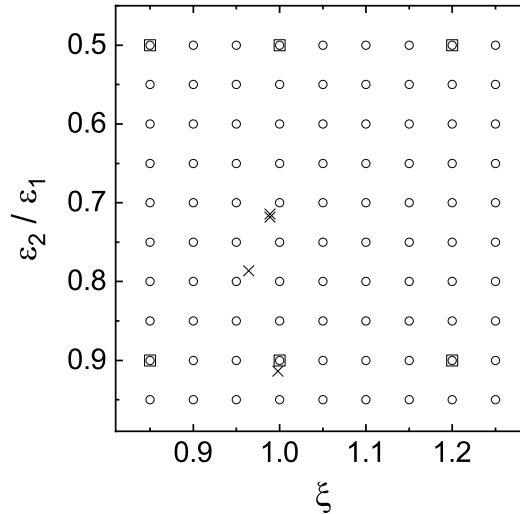
Figure 30: Overview of the investigated binary LJTS mixtures in the plane of the binary interaction parameter ξ and the ratio of the dispersion energies of the low and high-boiling component $\varepsilon_2/\varepsilon_1$. Circles indicate the 90 mixtures that were investigated in the present work. Squares mark the mixtures investigated in section 3.3 [635]. The stars indicate Lennard-Jones parameters of models of real binary mixtures proposed by *Vrabec et al.* [686] for argon + krypton, argon + methane, krypton + xenon, and methane + krypton.

The liquid phase composition is prescribed by setting $x'_2 = 0.05\,\mathrm{mol\,mol^{-1}}$ throughout this study. This composition was chosen based on the experience from our previous studies, which showed that the enrichment is strongest at low concentrations of the low-boiling component in the saturated liquid phase [50, 628, 634, 635].

The binary interaction parameter ξ and the ratio of the dispersion energies $\varepsilon_2/\varepsilon_1$ is not only used in the MD simulations, but the same number is also used in the PeTS EOS, and therefore also in the DGT calculations. It has been shown before that no adjustments are necessary: the phase behavior and interfacial properties that are obtained from both methods match well, when the same numbers for ξ and $\varepsilon_2/\varepsilon_1$ are used in MD and DGT, cf. section 3.3 [628, 635].

3.4.2 Results and Discussion

3.4.2.1 Vapor-Liquid Equilibria

The vapor-liquid equilibrium of LJTS mixtures (cf. Fig. 30) was investigated here at $T = 0.77\,\varepsilon k_{\mathrm{B}}^{-1}$ with both MD simulations and the PeTS EOS. The MD simulations were carried out for a liquid phase mole fraction of the low-boiling component 2 of $x'_2 = 0.05\,\mathrm{mol\,mol^{-1}}$. The numerical values of the VLE data at $x'_2 = 0.05\,\mathrm{mol\,mol^{-1}}$ and $T = 0.77\,\varepsilon k_{\mathrm{B}}^{-1}$ obtained from MD and the PeTS EOS are reported for all 90 mixtures in the Appendix (vapor pressure, gas phase composition, and saturated densities). The PeTS EOS was used to calculate the isothermal phase diagrams of all 90 mixtures.
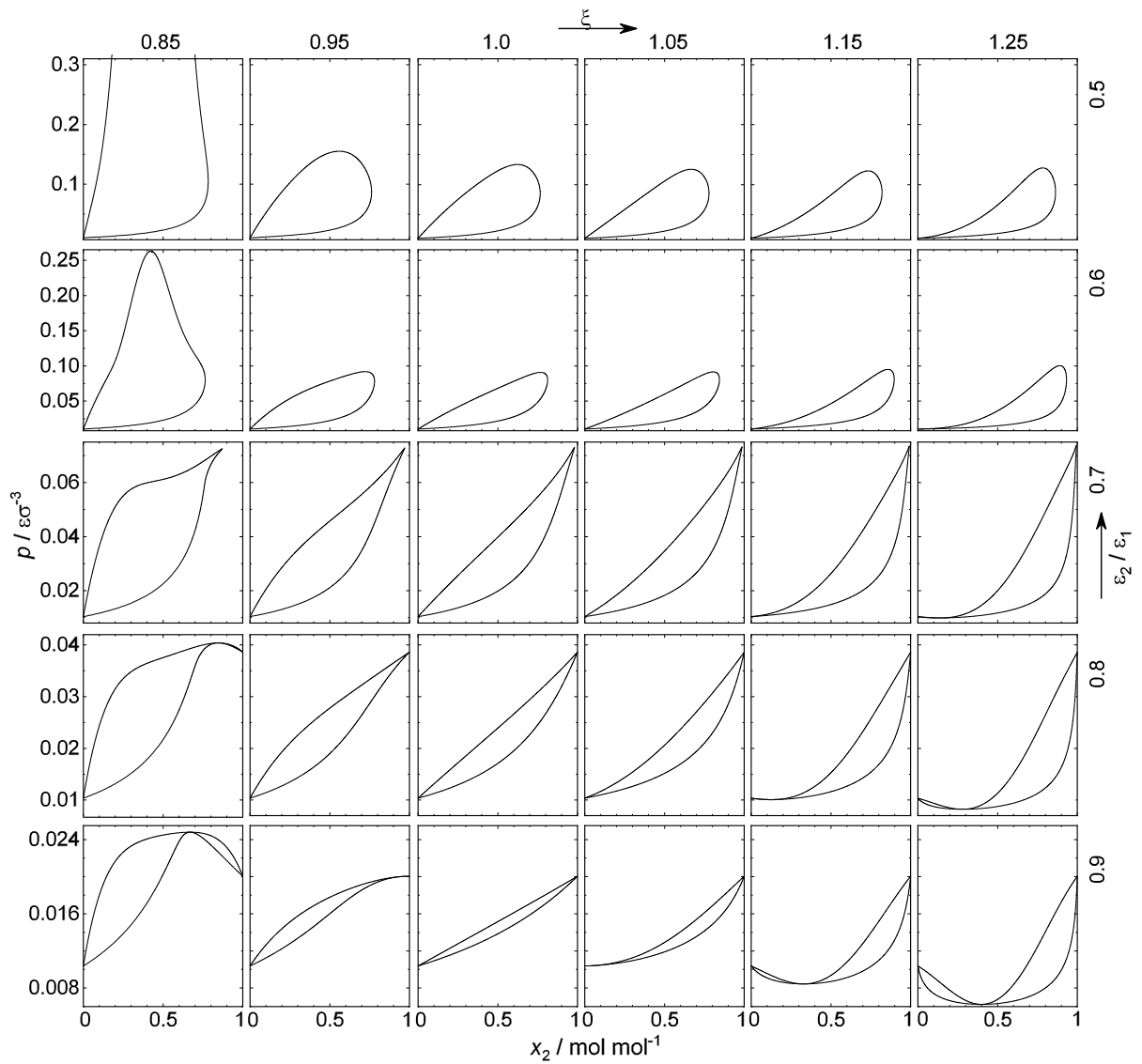
Figure 31: Selection of isothermal $p - x$ phase diagrams of binary LJTS mixtures at $T = 0.77\,\varepsilon k_{\mathrm{B}}^{-1}$ for different binary interaction parameter ξ and ratio of the dispersion energies of both components $\varepsilon_2/\varepsilon_1$. The phase diagrams were calculated by the PeTS EOS [249, 635]. Columns have constant binary interaction parameter as indicated at the top; rows have constant ratio of the dispersion energies as indicated on the right. *Corner A* is top left, *corner B* bottom right, see text.

Representative results for 30 systems are shown in Fig. 31. For all mixtures the high-boiling component 1 is the same. Its vapor pressure is $p^s = 0.0104\,\varepsilon\sigma^{-3}$ at $T = 0.77\,\varepsilon k_{\mathrm{B}}^{-1}$. The low-boiling component 2 in the mixtures varies. Results for different values of $\varepsilon_2/\varepsilon_1$ are shown in the different rows of the matrix depicted in Fig. 31. For high values of $\varepsilon_2/\varepsilon_1$, the component 2 is subcritical, for small values of $\varepsilon_2/\varepsilon_1$, it is supercritical. The critical temperature of the pure component 2 is $T_c = 0.77\,\varepsilon k_{\mathrm{B}}^{-1}$ for $\varepsilon_2/\varepsilon_1 = 0.71$. In the columns of the matrix shown in Fig. 31, results for different choices of ξ are presented. For $\xi = 1$ the mixtures are almost ideal in the sense of Raoult's law. For $\xi > 1$ attractive interactions prevail and the mixtures tend to form high-boiling azeotropes, while for $\xi < 1$ repulsive interactions prevail and the mixtures tend to form low-boiling azeotropes. Decreasing ξ below the lowest value that was studied in the present work ($\xi = 0.85$) leads to a liquid-liquid phase split at $T = 0.77\,\varepsilon k_{\mathrm{B}}^{-1}$. As studying liquid-liquid equilibria was out of the scope of this study, only mixtures with $\xi > 0.85$ were studied here. The critical pressures of the mixtures with small values of $\varepsilon_2/\varepsilon_1$ show an interesting behavior: they remain almost constant upon lowering ξ and increase only sharply for the lowest value of ξ shown in Fig. 31.

Qualitatively, the bubble lines of the mixtures in the ξ, $\varepsilon_2/\varepsilon_1$-plane differ more than the dew lines. This can be interpreted as a consequence of the fact that the interactions in the liquid phase are dominating the VLE behavior compared to a minor influence of the vapor phase. This is evident, since the self interactions and cross interactions have a stronger impact in the dense liquid phase.

The results for the Henry's law constants of all 90 investigated mixtures at $T = 0.77\,\varepsilon k_{\mathrm{B}}^{-1}$ that were obtained from the MD simulations as well as from the PeTS EOS are shown in Fig. 32 as a function of the binary interaction parameter ξ and the ratio of the dispersion energies $\varepsilon_2/\varepsilon_1$. The numeric values are reported in the Appendix. The results from the computer experiment and the theory are found to be in good agreement for all mixtures. As expected, the Henry's law constant $H_{2,1}$ increases steadily with decreasing ratio of dispersion energies $\varepsilon_2/\varepsilon_1$ as well as with decreasing values of ξ.

The plot of $H_{2,1}$ over $\varepsilon_2/\varepsilon_1$ and ξ shown in Fig. 32 has some interesting features. First, moving along the diagonal connecting the corner points ($\varepsilon_2/\varepsilon_1 = 0.5$, $\xi = 0.85$, labeled here as *corner A*) and ($\varepsilon_2/\varepsilon_1 = 0.95$, $\xi = 1.25$, labeled here as *corner B*), the Henry's law constant first increases only weakly but then steeply. This is due to the fact that towards *corner B* the mean dispersive interactions in the liquid phase become less attractive, which decreases the solubility of the low-boiling component 2 in the high-boiling component 1.

Furthermore, the surface $H_{2,1} = H_{2,1}(\varepsilon_2/\varepsilon_1, \xi)$ has a remarkably simple shape. The traces of the level curves in the $\varepsilon_2/\varepsilon_1$, ξ-plane can be approximated by segments of root functions (cf. Fig. 32), which results in an approximately radial symmetry of the function $H_{2,1} = H_{2,1}(\varepsilon_2/\varepsilon_1, \xi)$ in the investigated range of $\varepsilon_2/\varepsilon_1$ and ξ. As only a segment of the function is plotted in Fig. 32, the curvature can only be seen by inspecting the traces of the isolines. Going from *corner A* to *corner B* in a straight line follows the gradient of that function.

Fig. 33 shows the difference of the number density of the low-boiling component between the bulk vapor and bulk liquid phase $\Delta\rho_2 = \rho_2' - \rho_2''$ at $x_2' = 0.05\,\mathrm{mol\,mol}^{-1}$ and $T = 0.77\,\varepsilon k_{\mathrm{B}}^{-1}$ as a function of the binary interaction parameter ξ and the ratio of the
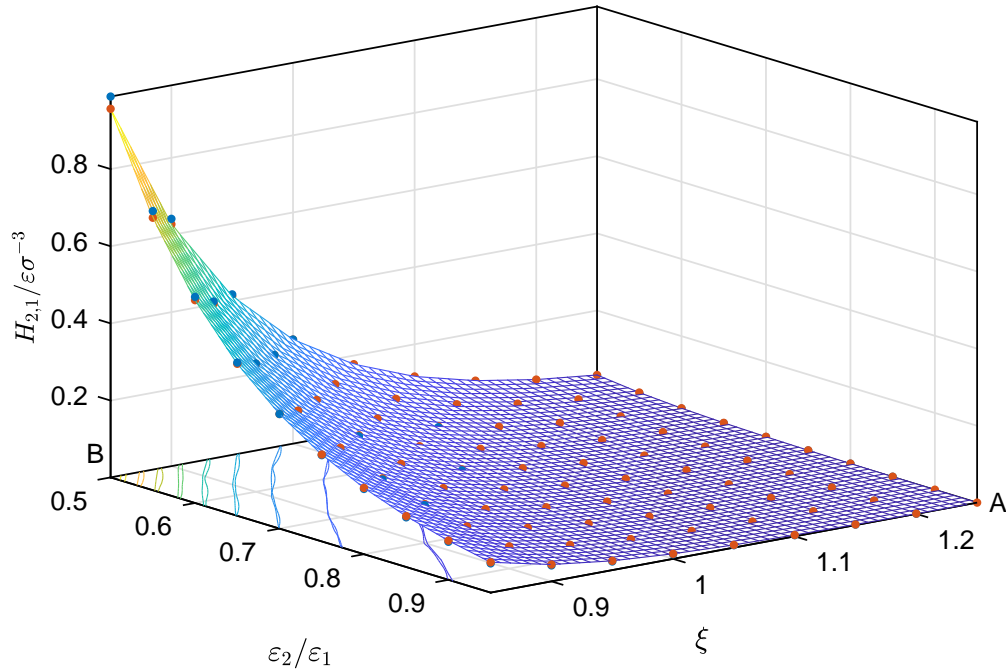
Figure 32: Henry's law constant $H_{2,1}$ of binary LJTS mixtures $1 + 2$ at $T = 0.77\,\varepsilon k_{\mathrm{B}}^{-1}$ as a function of the binary interaction parameter ξ and the ratio of the dispersion energies $\varepsilon_2/\varepsilon_1$. Results from MD: blue points; results from the PeTS EOS [249, 635]: orange points. The surface is a linear interpolation of the EOS results. The color of the surface is coded by its height.

dispersion energies $\varepsilon_2/\varepsilon_1$. The difference of the number density of the low-boiling component $\Delta\rho_2$ was calculated for all 90 LJTS mixtures using both MD simulation and the PeTS EOS. The computer experiments and the EOS have a distinct offset which vanishes in *corner B*, but the qualitative behavior of the results from both methods agrees well.

The deviations show that the VLE behavior of LJTS mixtures is not described perfectly by the PeTS EOS, but in assessing the deviations it has to be considered that $\Delta\rho_2$ is a very sensitive property. The same symmetry as for the Henry's law constant (cf. Fig. 32) is also found for $\Delta\rho_2(\varepsilon_2/\varepsilon_1, \xi)$ (Fig. 33) but the trends are inverse: $\Delta\rho_2$ is low where $H_{2,1}$ is high. This is not unexpected since both properties express the tendency of the low-boiling component to portion on both phases.

An interesting feature of $\Delta\rho_2(\varepsilon_2/\varepsilon_1, \xi)$ is the zero crossing line of $\Delta\rho_2$ close to *corner B*. In a wide range of investigated mixtures $\Delta\rho_2 > 0$, i.e. the the low-boiling component accumulates in the liquid phase. Vice versa, for $\Delta\rho_2 < 0$ the low-boiling component has a preferential residency in the vapor phase.

3.4.2.2 Vapor-Liquid Interfaces

Planar vapor-liquid interfaces were investigated by both MD and DGT at $T = 0.77\,\varepsilon k_{\mathrm{B}}^{-1}$ and $x_2' = 0.05\,\mathrm{mol\,mol^{-1}}$. Besides the density profiles, the interfacial enrichment (cf. Eq. (45)), relative adsorption (cf. Eq. (44)), interfacial tension (cf. Eq. (41) and (42)), and interfacial thickness (cf. Eq. (46)) were investigated for all 90 binary LJTS mixtures (cf.
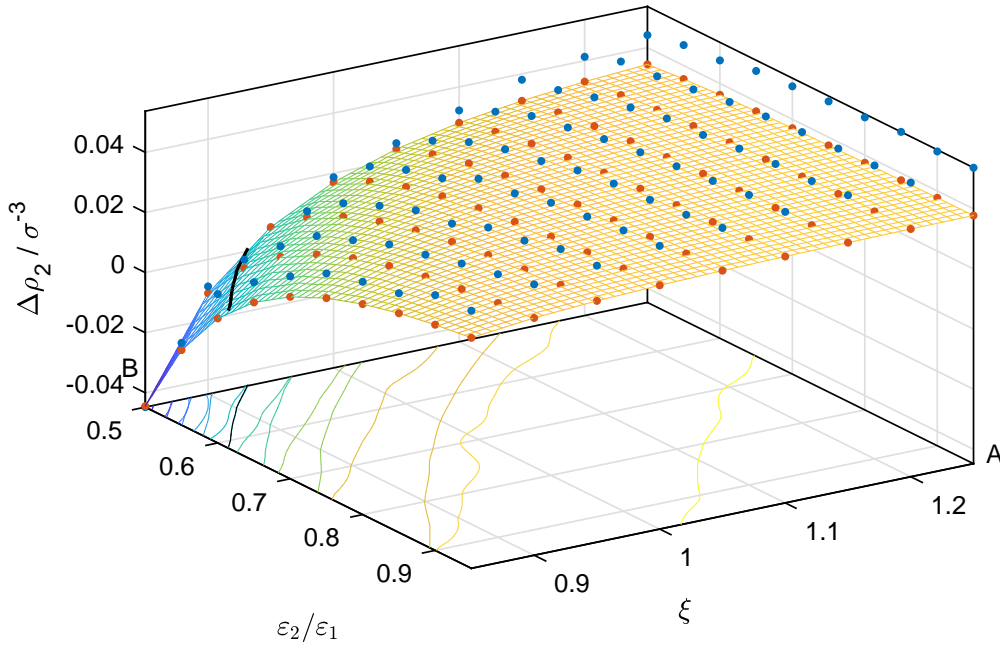
Figure 33: Difference in the bulk number density of the low-boiling component $\Delta\rho_2 = \rho_2' - \rho_2''$ at $T = 0.77\,\varepsilon k_\mathrm{B}^{-1}$ and $x_2' = 0.05\,\mathrm{mol\,mol^{-1}}$ as a function of the binary interaction parameter ξ and the ratio of the dispersion energies $\varepsilon_2/\varepsilon_1$. Results from MD: blue points; results from the PeTS EOS [249, 635]: orange points. The surface is a linear interpolation of the EOS results. The color of the surface is coded by its height position. The black line indicates the trace of the zero crossing line $\Delta\rho_2 = 0$ from the EOS results.

Fig. 30). Density profiles are shown in Fig. 34, the enrichment in Fig. 35, the relative adsorption in Fig. 36, the surface tension in Fig. 37, and the interfacial thickness in Fig. 38.

The prescribed liquid phase composition is exactly matched in DGT, but not by MD due to fluctuations. The mole fraction of the low-boiling component in the liquid phase obtained from the MD simulations is in the range $x_2' = 0.05 .. 0.07\,\mathrm{mol\,mol^{-1}}$. The numeric values of the interfacial properties from both MD and DGT as well as the actual liquid phase composition in MD are reported in Table 5. The error bars of the MD simulation results are not shown in the plots in Figs. 35 - 38 for clarity, but the statistical uncertainties are reported in Table 5.

Table 5: Interfacial properties of the investigated binary LJTS mixtures. Results from MD and DGT+PeTS EOS. The temperature is $T = 0.77\,\varepsilon k_{\mathrm{B}}^{-1}$. The DGT results are calculated at the liquid phase composition $x_2' = 0.05\,\mathrm{mol\,mol^{-1}}$. The exact MD liquid phase composition is given in the 2$^{\mathrm{nd}}$ column. The other columns are from left to right: the surface tension, the relative adsorption, the enrichment of the low-boiling component 2, and the interfacial thickness. The number in the parentheses indicates the statistical uncertainty in the last decimal digit.

$\varepsilon_2/\varepsilon_1$	x_2'	$\gamma\ /\ \varepsilon\sigma^{-2}$		$\Gamma_2^{(1)}\ /\ \sigma^{-2}$		E_2		$L_{10}^{90}\ /\ \sigma$	
		MD	DGT	MD	DGT	MD	DGT	MD	DGT
$\xi = 0.85$									
0.5	0.058(2)	0.23(3)	0.263	0.30(3)	0.248	1.71(3)	2.05	4.08(9)	3.24
0.55	0.058(1)	0.26(3)	0.287	0.28(2)	0.231	2.10(3)	2.53	3.8(1)	3.10
0.6	0.063(3)	0.28(2)	0.310	0.23(4)	0.207	2.3(2)	3.09	3.53(9)	2.96
0.65	0.062(2)	0.32(2)	0.330	0.18(4)	0.181	2.1(1)	2.91	3.37(8)	2.84
0.7	0.061(1)	0.32(2)	0.349	0.18(2)	0.156	1.92(8)	2.53	3.3(1)	2.76
0.75	0.063(2)	0.34(2)	0.365	0.15(3)	0.133	1.66(8)	2.20	3.16(7)	2.68
0.8	0.062(2)	0.35(2)	0.379	0.15(3)	0.112	1.6(1)	1.93	3.08(8)	2.62
0.85	0.061(1)	0.36(1)	0.392	0.15(2)	0.094	1.57(7)	1.70	3.03(8)	2.56
0.9	0.065(2)	0.38(2)	0.403	0.11(4)	0.077	1.3(1)	1.51	2.95(4)	2.52
0.95	0.064(1)	0.39(2)	0.413	0.11(4)	0.063	1.29(9)	1.34	2.91(5)	2.48
$\xi = 0.9$									
0.5	0.059(4)	0.27(2)	0.305	0.22(3)	0.195	2.16(5)	2.53	3.63(9)	2.96
0.55	0.059(3)	0.30(1)	0.326	0.23(2)	0.172	2.3(1)	2.83	3.44(7)	2.86
0.6	0.059(1)	0.31(2)	0.346	0.18(2)	0.149	2.0(1)	2.45	3.27(9)	2.76
0.65	0.062(1)	0.34(2)	0.363	0.14(3)	0.128	1.74(7)	2.13	3.19(7)	2.66
0.7	0.061(2)	0.35(2)	0.378	0.12(2)	0.108	1.6(1)	1.87	3.09(6)	2.60
0.75	0.062(2)	0.37(2)	0.391	0.11(3)	0.090	1.46(8)	1.65	3.02(6)	2.54
0.8	0.062(1)	0.38(2)	0.402	0.09(2)	0.074	1.38(6)	1.47	2.93(6)	2.50
0.85	0.063(2)	0.38(3)	0.413	0.10(1)	0.060	1.3(1)	1.32	2.89(4)	2.46
0.9	0.065(2)	0.40(2)	0.422	0.07(3)	0.048	1.20(7)	1.19	2.83(5)	2.44
0.95	0.066(1)	0.42(2)	0.429	0.03(3)	0.037	1.09(6)	1.09	2.80(4)	2.42
$\xi = 0.95$									
0.5	0.057(1)	0.30(2)	0.337	0.20(3)	0.152	2.22(5)	2.53	3.43(7)	2.78
0.55	0.059(1)	0.33(2)	0.355	0.17(2)	0.131	1.90(7)	2.19	3.27(8)	2.70
0.6	0.061(3)	0.34(2)	0.372	0.14(2)	0.111	1.7(1)	1.91	3.14(9)	2.62
0.65	0.061(1)	0.36(3)	0.386	0.13(1)	0.092	1.53(8)	1.68	3.05(8)	2.56
0.7	0.062(2)	0.37(3)	0.399	0.11(3)	0.076	1.4(1)	1.49	3.01(8)	2.50
0.75	0.061(1)	0.37(2)	0.410	0.10(2)	0.062	1.38(3)	1.34	3.00(5)	2.46
0.8	0.064(2)	0.40(2)	0.419	0.09(2)	0.049	1.21(8)	1.22	2.87(8)	2.44
0.85	0.065(1)	0.41(2)	0.428	0.05(3)	0.038	1.11(8)	1.12	2.84(7)	2.40
0.9	0.067(2)	0.42(2)	0.435	0.04(3)	0.028	1.07(6)	1.04	2.74(6)	2.38
0.95	0.067(1)	0.42(2)	0.442	0.07(2)	0.019	1.12(4)	1.00	2.76(7)	2.36
$\xi = 1$									
0.5	0.059(2)	0.32(2)	0.361	0.17(3)	0.119	1.82(8)	2.04	3.25(9)	2.66
0.55	0.062(1)	0.34(2)	0.377	0.14(3)	0.100	1.55(8)	1.78	3.13(7)	2.60
0.6	0.062(1)	0.36(1)	0.392	0.10(2)	0.082	1.43(7)	1.57	2.99(7)	2.52
0.65	0.062(2)	0.37(2)	0.404	0.11(2)	0.067	1.35(1)	1.40	2.95(6)	2.48
0.7	0.065(1)	0.39(3)	0.415	0.07(4)	0.053	1.12(7)	1.27	2.87(6)	2.44

$\varepsilon_2/\varepsilon_1$	x'_2	$\gamma \ / \ \varepsilon\sigma^{-2}$		$\Gamma_2^{(1)} \ / \ \sigma^{-2}$		E_2		$L_{10}^{90} \ / \ \sigma$	
		MD	DGT	MD	DGT	MD	DGT	MD	DGT
0.75	0.065(2)	0.41(2)	0.424	0.06(2)	0.041	1.13(5)	1.16	2.81(5)	2.42
0.8	0.066(2)	0.41(2)	0.433	0.04(3)	0.031	1.09(6)	1.08	2.81(6)	2.38
0.85	0.067(2)	0.43(3)	0.440	0.02(5)	0.022	1.05(7)	1.02	2.72(7)	2.36
0.9	0.068(2)	0.43(2)	0.446	0.05(3)	0.013	1.08(6)	1.00	2.72(8)	2.36
0.95	0.068(2)	0.45(2)	0.452	0.02(3)	0.006	1.08(7)	1.00	2.73(4)	2.34
$\xi = 1.05$									
0.5	0.059(2)	0.36(2)	0.380	0.15(3)	0.094	1.6(1)	1.71	3.13(6)	2.58
0.55	0.061(1)	0.36(2)	0.395	0.13(3)	0.076	1.44(7)	1.51	3.01(8)	2.50
0.6	0.063(1)	0.38(2)	0.407	0.09(2)	0.061	1.25(6)	1.36	2.92(7)	2.46
0.65	0.064(1)	0.40(2)	0.418	0.07(2)	0.048	1.17(6)	1.23	2.84(6)	2.42
0.7	0.065(2)	0.41(2)	0.428	0.07(3)	0.036	1.13(6)	1.14	2.80(4)	2.40
0.75	0.067(2)	0.42(3)	0.436	0.06(2)	0.026	1.11(7)	1.07	2.76(9)	2.38
0.8	0.067(1)	0.43(2)	0.443	0.02(2)	0.017	1.08(5)	1.02	2.73(6)	2.36
0.85	0.067(1)	0.44(2)	0.449	0.03(1)	0.010	1.08(3)	1.00	2.69(4)	2.34
0.9	0.068(2)	0.45(2)	0.455	0.04(4)	0.003	1.11(9)	1.00	2.70(9)	2.32
0.95	0.069(1)	0.45(2)	0.460	-0.01(2)	-0.003	1.07(4)	1.00	2.63(5)	2.32
$\xi = 1.1$									
0.5	0.061(1)	0.37(2)	0.396	0.08(3)	0.073	1.38(7)	1.49	3.05(5)	2.50
0.55	0.063(2)	0.39(2)	0.409	0.07(2)	0.058	1.24(9)	1.34	2.93(7)	2.44
0.6	0.065(2)	0.41(2)	0.420	0.06(3)	0.044	1.12(7)	1.22	2.86(6)	2.42
0.65	0.065(2)	0.41(2)	0.430	0.04(3)	0.033	1.08(5)	1.13	2.77(8)	2.38
0.7	0.066(1)	0.42(3)	0.438	0.01(3)	0.023	1.04(5)	1.06	2.77(4)	2.36
0.75	0.067(2)	0.43(2)	0.445	0.03(3)	0.014	1.08(4)	1.02	2.73(6)	2.34
0.8	0.068(1)	0.44(2)	0.452	0.01(2)	0.007	1.07(4)	1.00	2.67(5)	2.32
0.85	0.069(1)	0.46(2)	0.457	-0.02(4)	0.000	1.04(6)	1.00	2.68(6)	2.32
0.9	0.070(1)	0.46(2)	0.462	-0.01(3)	-0.006	1.07(3)	1.00	2.65(5)	2.30
0.95	0.070(2)	0.47(2)	0.466	0.01(3)	-0.011	1.09(4)	1.00	2.63(7)	2.30
$\xi = 1.15$									
0.5	0.063(2)	0.38(3)	0.409	0.07(2)	0.057	1.2(1)	1.33	2.89(3)	2.44
0.55	0.063(1)	0.40(2)	0.421	0.09(3)	0.043	1.17(6)	1.22	2.85(7)	2.40
0.6	0.065(1)	0.40(2)	0.431	0.07(2)	0.031	1.11(4)	1.13	2.82(7)	2.38
0.65	0.066(1)	0.43(2)	0.439	0.04(2)	0.021	1.08(5)	1.06	2.77(4)	2.36
0.7	0.068(2)	0.43(2)	0.447	0.00(5)	0.013	1.04(5)	1.02	2.71(7)	2.34
0.75	0.068(1)	0.45(3)	0.453	0.01(3)	0.005	1.06(5)	1.00	2.68(5)	2.32
0.8	0.069(1)	0.45(2)	0.459	0.00(3)	-0.001	1.06(3)	1.00	2.64(7)	2.30
0.85	0.070(2)	0.46(1)	0.464	0.01(3)	-0.007	1.09(6)	1.00	2.65(8)	2.30
0.9	0.070(1)	0.46(2)	0.468	-0.02(2)	-0.012	1.05(5)	1.00	2.65(7)	2.30
0.95	0.071(1)	0.47(2)	0.472	-0.05(2)	-0.017	1.04(4)	1.00	2.62(5)	2.28
$\xi = 1.2$									
0.5	0.064(2)	0.39(2)	0.420	0.07(3)	0.043	1.13(8)	1.23	2.87(9)	2.40
0.55	0.067(2)	0.42(2)	0.431	0.02(3)	0.031	1.07(6)	1.13	2.78(5)	2.38
0.6	0.066(2)	0.43(2)	0.440	0.06(2)	0.021	1.12(5)	1.07	2.76(6)	2.34
0.65	0.067(1)	0.43(2)	0.447	0.01(2)	0.012	1.06(3)	1.02	2.71(4)	2.34
0.7	0.069(1)	0.45(2)	0.454	0.00(2)	0.004	1.05(3)	1.00	2.69(5)	2.32
0.75	0.069(1)	0.45(2)	0.460	0.01(2)	-0.002	1.08(3)	1.00	2.67(4)	2.30
0.8	0.070(1)	0.47(3)	0.465	0.00(3)	-0.008	1.08(4)	1.00	2.63(5)	2.30
0.85	0.070(2)	0.46(3)	0.469	-0.03(2)	-0.013	1.05(4)	1.00	2.61(5)	2.28
0.9	0.070(1)	0.48(3)	0.473	-0.03(1)	-0.018	1.06(3)	1.00	2.58(7)	2.28

$\varepsilon_2/\varepsilon_1$	x_2'	$\gamma \, / \, \varepsilon\sigma^{-2}$		$\Gamma_2^{(1)} \, / \, \sigma^{-2}$		E_2		$L_{10}^{90} \, / \, \sigma$	
		MD	DGT	MD	DGT	MD	DGT	MD	DGT
0.95	0.070(1)	0.48(2)	0.476	-0.03(3)	-0.022	1.06(3)	1.00	2.62(7)	2.28
$\xi = 1.25$									
0.5	0.065(1)	0.41(2)	0.430	0.05(3)	0.032	1.09(4)	1.15	2.80(5)	2.36
0.55	0.067(1)	0.42(2)	0.439	0.02(2)	0.021	1.06(3)	1.08	2.79(8)	2.32
0.6	0.067(1)	0.43(2)	0.447	0.02(1)	0.012	1.06(2)	1.03	2.70(4)	2.30
0.65	0.069(1)	0.45(2)	0.454	0.00(3)	0.004	1.05(3)	1.00	2.65(7)	2.30
0.7	0.069(1)	0.45(2)	0.460	0.02(2)	-0.003	1.09(4)	1.00	2.63(4)	2.28
0.75	0.070(1)	0.47(2)	0.465	0.01(3)	-0.008	1.07(3)	1.00	2.61(8)	2.30
0.8	0.070(1)	0.48(2)	0.470	-0.02(1)	-0.014	1.06(2)	1.00	2.61(6)	2.28
0.85	0.071(1)	0.48(2)	0.474	-0.01(2)	-0.018	1.07(4)	1.00	2.62(7)	2.28
0.9	0.070(1)	0.49(2)	0.477	-0.03(2)	-0.022	1.07(3)	1.00	2.59(6)	2.28
0.95	0.071(1)	0.49(2)	0.481	-0.04(1)	-0.024	1.06(4)	1.00	2.58(8)	2.28

Density Profiles and Enrichment

Selected results for the density profiles are shown in Fig. 34. The plot is organized in the same way as Fig. 31, i.e. the selected systems are the same. The density profiles are plotted as a function of the spatial coordinate z normal to the planar interface. For clarity, only the DGT density profiles are shown here. It was already shown in section 3.3 that the density profiles of LJTS mixtures predicted by MD and DGT+PeTS agree very well. This is confirmed in this study. It can be seen from Fig. 34 that the enrichment of the low-boiling component E_2, i.e. the relative hight of the peak in $\rho_2(z)$, generally increases with decreasing $\varepsilon_2/\varepsilon_1$ and decreasing ξ. Details become clearer in Fig. 35, where E_2 is plotted as a function of $\varepsilon_2/\varepsilon_1$ and ξ. The layout of the plot is similar to that in Figs. 32 and 33.

In contrast to the density profile of the low-boiling component 2, which dramatically changes in the ξ, $\varepsilon_2/\varepsilon_1$-plane, the density profile of the high-boiling component 1 remains fairly similar among the different mixtures, as already discussed in our previous work [635]. No enrichment of the high-boiling component 1 is observed in any mixture.

Starting in *corner A*, no enrichment of the low-boiling component 2 is found. The enrichment increases with a decreasing $\Delta\rho_2$ towards the *corner B* (cf. Fig. 33). The density profiles in the region of the ξ, $\varepsilon_2/\varepsilon_1$-plane where $\Delta\rho_2$ is close to zero show a particularly high enrichment. A significant enrichment of the low-boiling component is found for mixtures that exhibit a low solubility of the low-boiling component in component 1, i.e. large Henry's law constants (cf. Fig. 32).

The predictions for the enrichment E_2 from the computer experiments and the theory are found to be in good qualitative agreement for all investigated mixtures. DGT overestimates the enrichment predicted by MD for mixtures close to *corner B*. Such an overestimation of the enrichment E_2 by DGT compared to MD results was also reported previously by *Becker et al.* [50] and *Stephan et al.* [634, 635] for mixtures where the low-boiling component is supercritical. The enrichment predicted by MD in *corner A* is slightly above unity, while DGT predicts no enrichment, i.e. $E_2 = 1$, in that region. As already discussed in section 3.3, the deviation of the MD results from $E_2 = 1$ is
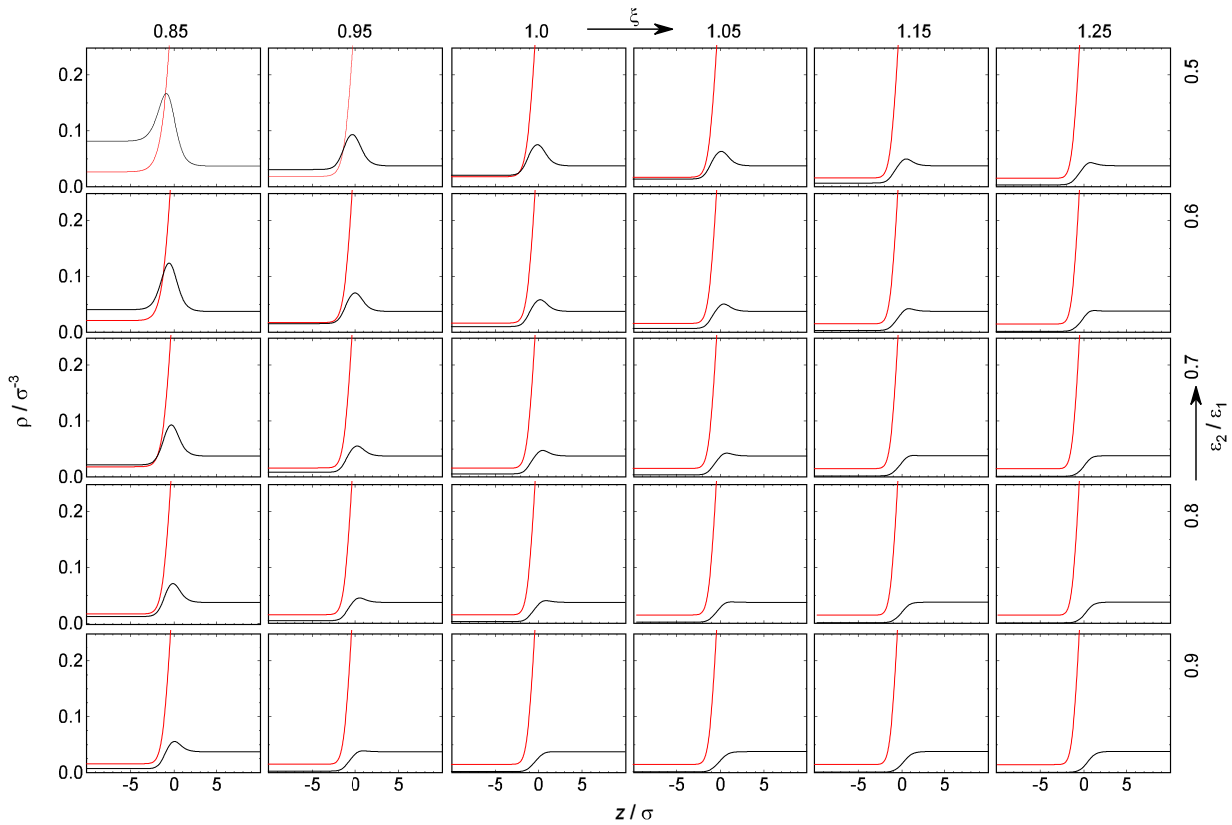
Figure 34: Selection of density profiles at planar vapor-liquid interfaces calculated by DGT: local density of the low-boiling component 2 (black line) and high-boiling component 1 (red line) as a function of the spatial coordinate z normal to the interface in the plane of the binary interaction parameter ξ and the ratio of the dispersion energies $\varepsilon_2/\varepsilon_1$. Columns have constant binary interaction parameter as indicated on the top; rows have constant ratio of the dispersion energies as indicated on the right. The temperature is always $T = 0.77\,\varepsilon k_B^{-1}$ and the liquid phase concentration is $x_2' = 0.05\,\mathrm{mol\,mol^{-1}}$. *Corner A* is top left, *corner B* bottom right, see text.

attributed to the fluctuations in connection with the definition of the enrichment (cf. Eq. (45)).

Again, the same symmetry as in the plots shown in Figs. 32 and 33 (Henry's law constant $H_{2,1}$ and density difference $\Delta\rho_2$) is also found for $E_2(\varepsilon_2/\varepsilon_1, \xi)$.

In the *corner A* (high mean dispersive interactions), practically no enrichment E_2 is found, while strong enrichment is found in *corner B*. Starting in *corner A* and going to *corner B* on a straight line, the enrichment E_2 remains around unity for a while, and then increases sharply. Interestingly, there is a drop in E_2, before *corner B* is reached.

The position of the line of the maximal enrichment E_2 in the ξ, $\varepsilon_2/\varepsilon_1$-plane, as indicated in Fig. 35, is in very good agreement with the zero crossing line of the difference of the number density of component 2 $\Delta\rho_2 = 0$, cf. Fig. 33. I.e. it corresponds to mixtures for which the density of the component 2 is equal in both phases. For mixtures on that line, any adsorption of the low-boiling component at the interface must result in an enrichment for geometric reasons. In contrast, for mixtures with $\Delta\rho_2 \neq 0$ a relative
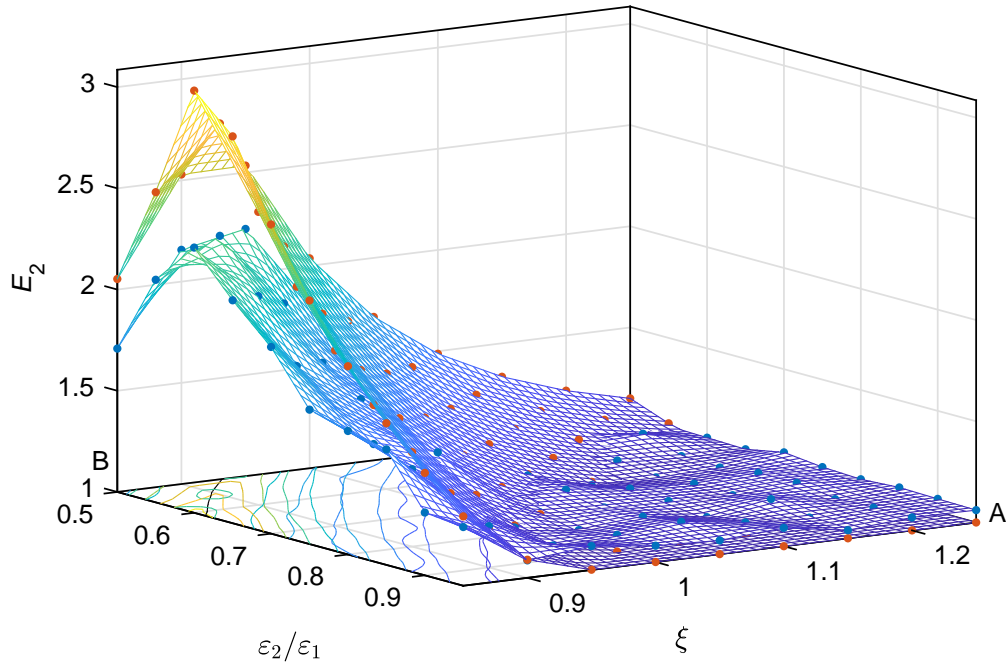
Figure 35: Enrichment E_2 of the low-boiling component 2, as defined by Eq. (45), at the interface as a function of the binary interaction parameter ξ and the ratio of the dispersion energies $\varepsilon_2/\varepsilon_1$ at $T = 0.77\,\varepsilon k_{\mathrm{B}}^{-1}$ and $x_2' = 0.05\,\mathrm{mol\,mol^{-1}}$. Results from MD: blue points; results from DGT: orange points. The surfaces are linear interpolations of the respective results. The color of the surfaces is coded by its height position. The black line indicates the trace of zero crossing line $\Delta\rho_2 = 0$ from the DGT results (see Fig. 33). The *corners A* and *B* to which the text refers are indicated.

adsorption can also arise from a relative shift of $\rho_2(z)$ with respect to $\rho_1(z)$. Even though the predicted magnitude of the enrichment by MD and DGT differs slightly, the position of the maximum line in the ξ, $\varepsilon_2/\varepsilon_1$-plane agrees perfectly.

Relative Adsorption

Fig. 36 shows the relative adsorption $\Gamma_2^{(1)}$ of the low-boiling component at the vapor-liquid interface, as defined by Eq. (44), as a function of the binary interaction parameter ξ and the ratio of the dispersion energies $\varepsilon_2/\varepsilon_1$. Again results from both MD and DGT are shown. The predictions from the computer experiment and the theory are found to be in good agreement for all investigated mixtures. The MD results show some scattering due to fluctuations in the simulations, while results from the theory are smooth. The symmetry that was observed in the previous plots of this type is also observed here. In contrast to the enrichment E_2, the relative adsorption increases steadily when going from *corner A* to *corner B*. The relative adsorption of the low-boiling component 2 is negative close to the *corner A*, i.e. high mean attractive interactions, and positive elsewhere. The zero crossing line of the relative adsorption (black line in Fig. 36) is roughly identical with the line that separates mixtures with high-boiling azeotropes from zeotropic mixtures, cf. Fig. 31. Hence, the relative adsorption $\Gamma_2^{(1)}$ is negative for mixtures with high-boiling azeotropes, while it is positive for other mixtures, which
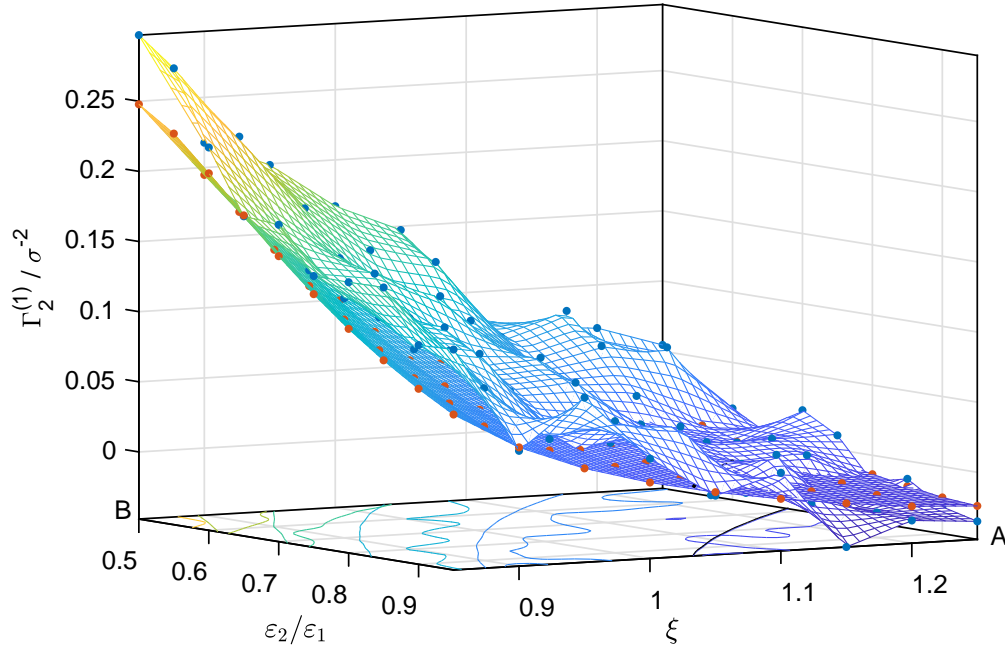
Figure 36: Relative adsorption $\Gamma_2^{(1)}$ of the low-boiling component 2, as defined by
Eq. (44), at the interface as a function of the binary interaction para-
meter ξ and the ratio of the dispersion energies $\varepsilon_2/\varepsilon_1$ at $T = 0.77\,\varepsilon k_\mathrm{B}^{-1}$ and
$x_2' = 0.05\,\mathrm{mol\,mol^{-1}}$. Results from MD: blue points; results from DGT: or-
ange points. The surfaces are linear interpolations of the respective results.
The color of the surfaces is coded by its height position. The black line
indicates the trace of the zero crossing line $\Gamma_2^{(1)} = 0$ from the DGT results.

reinforces findings for the relative adsorption in Ref. [184, 434, 435, 512, 635].

Furthermore, the relative adsorption dependency on ξ and $\varepsilon_2/\varepsilon_1$ can be split into two
characteristic regions: one region exhibiting a non-linear regime and one region exhibit-
ing a linear regime. Going from *corner A* to *corner B*, the relative adsorption exhibits
first a convex increase, whereas approaching *corner B* $\Gamma_2^{(1)}$ increases linearly. This can
only be seen in the results obtained from DGT, since the MD results are superimposed
by significant scattering. The breakup between the linear and non-linear regime of $\Gamma_2^{(1)}$
corresponds well with the region where the enrichment of the low-boiling component is
close to unity and the region of significant enrichment. This indicates again [50, 635],
that the enrichment and the relative adsorption contain different information and it is
emphasized that both should be discussed. Relative adsorption may occur even if there
is no enrichment, but an enrichment will in general result in an adsorption.

Surface Tension

Fig. 37 shows the surface tension as a function of the binary interaction parameter ξ and
the ratio of dispersion energies $\varepsilon_2/\varepsilon_1$. The results from both MD and DGT are shown.
The predictions from the computer experiments and the theory agree remarkably well
for all investigated mixtures, i.e. the DGT results mostly lie within the MD error bars
(cf. Table 5). Only slight systematic deviations are found in *corner B*, where the DGT
results overestimate those from computer experiments. The same type of symmetry
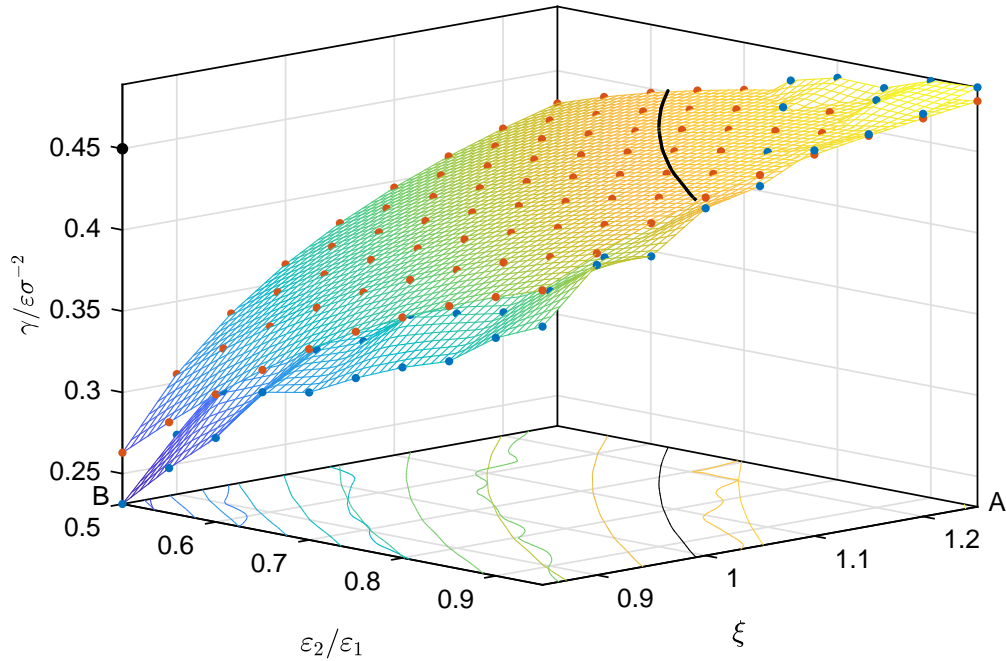
Figure 37: Interfacial tension γ, as defined by Eq. (41) and (42), as a function of the binary interaction parameter ξ and the ratio of the dispersion energies $\varepsilon_2/\varepsilon_1$ at $T = 0.77\,\varepsilon k_{\mathrm{B}}^{-1}$ and $x_2' = 0.05\,\mathrm{mol\,mol^{-1}}$. Results from MD: blue points; results from DGT: orange points. The surfaces are linear interpolations of the respective results. The color of the surfaces is coded by its height position. The black dot indicates the surface tension γ_1 of the pure component 1 at $T = 0.77\,\varepsilon k_{\mathrm{B}}^{-1}$ according to *Stephan et al.* [637], cf. chapter 2. The black line indicates the crossing line of $\gamma = \gamma_1$ from the DGT results.

as for the properties discussed above (cf. Figs. 32, 33, 35, 36), is also observed for $\gamma(\varepsilon_2/\varepsilon_1, \xi)$.

Going from *corner A* to *corner B*, the surface tension decreases steadily. It is found that the line, for which the surface tension of the mixture equals the surface tension of the pure component 1 (cf. Fig. 37) is in good agreement with the line for which the relative adsorption is zero (cf. Fig. 36). This is related to the Gibbs adsorption equation which relates the surface excess to the concentration dependence of the surface tension. Adding component 2 to the pure component 1 in *corner A*, i.e. the region of mixtures with the highest mean dispersive interactions, leads to an increase of the surface tension. This is a typical finding for mixtures with a high-boiling azeotrope [133, 184, 635]. For mixtures with a low-boiling azeotrope, on the other hand, adding component 2 usually results in a decreased surface tension [133, 184, 635], which is also found in our data.

Interfacial Thickness

Fig. 38 shows the interfacial thickness L_{10}^{90} as defined by Eq. (46) as a function of the binary interaction parameter ξ and the ratio of dispersion energies $\varepsilon_2/\varepsilon_1$ for both MD and DGT. The predictions from the computer experiments and the theory agree qualitatively very well, but are shifted significantly. The interfacial thickness predicted from DGT is systematically lower than that from the computer experiments. This could
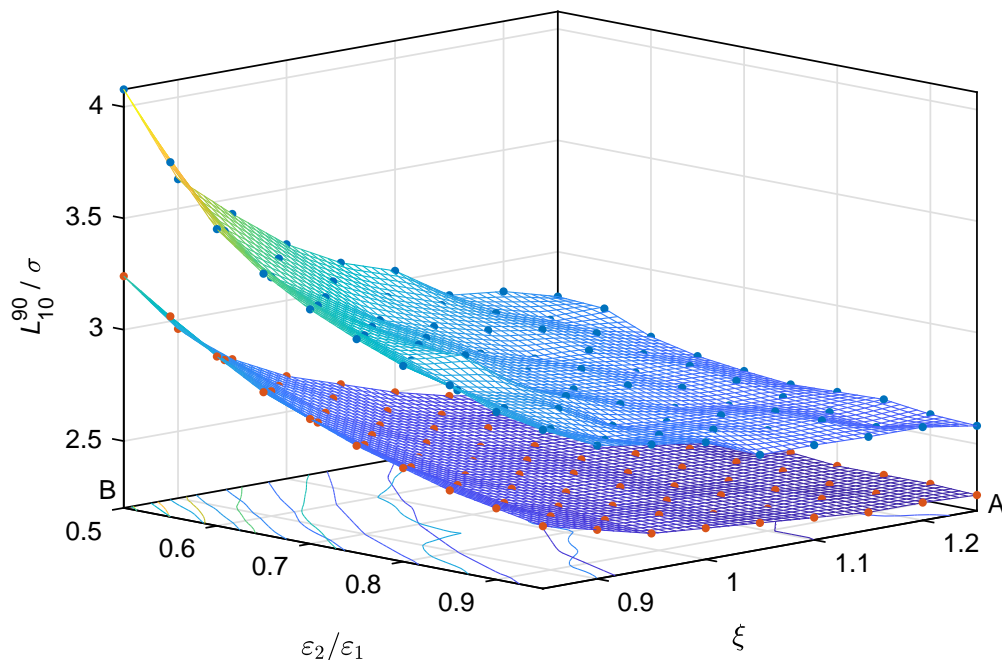
Figure 38: Interfacial thickness L_{10}^{90}, as defined by Eq. (46), as a function of the binary interaction parameter ξ and the ratio of the dispersion energies $\varepsilon_2/\varepsilon_1$ at $T = 0.77\,\varepsilon k_{\mathrm{B}}^{-1}$ and $x_2' = 0.05\,\mathrm{mol\,mol^{-1}}$. Results from MD: blue points; results from DGT: orange points. The surfaces are linear interpolations of the respective results. The color of the surfaces is coded by its height position.

be caused by fluctuations that are present in MD but not in DGT [50, 635, 637], but it could also be caused by differences between the PeTS EOS and the LJTS force field. The latter hypothesis is supported by the fact that in a recent study, no such differences were observed for the LJ fluid [628], cf. chapter 5.

On average, the DGT underestimates the MD interfacial thickness by approximately -15%, which is in line with results reported earlier for the corresponding pure substances, cf. chapter 2, as well as for selected LJTS mixtures in the entire composition range, cf. section 3.3.

Again, a symmetric behavior is found for $L_{10}^{90}(\varepsilon_2/\varepsilon_1, \xi)$. Going from *corner A* to *corner B*, the interfacial thickness increases steadily. This is in line with the decay of the surface tension, since broader and smoother density profiles result in a lower surface tension. The interfacial thickness is almost twice as high in *corner B* as in *corner A*.

3.4.3 Conclusions

The vapor-liquid equilibrium and interfacial properties (Henry's law constant, vapor pressure, composition, surface tension, relative adsorption, interfacial thickness, and enrichment) of binary Lennard-Jones mixtures were determined for a broad range of mixtures of different types (zeotropic, low-boiling azeotrope, high-boiling azeotrope; subcritical, supercritical) by MD and EOS+DGT. The study was carried out at constant temperature and liquid phase composition. The results from MD and EOS+DGT were found to be in good agreement. The relation of both the VLE bulk properties and the interfacial properties with the underlying molecular interactions was investigated.

The interfacial enrichment, which is assumed to have an influence on the mass transfer through interfaces, is found to be particularly high for Lennard-Jones mixtures that have low numbers for $\varepsilon_2/\varepsilon_1$ and for ξ. Furthermore, the enrichment exhibits a maximum for mixtures with $\Delta\rho_2 = \rho_2' - \rho_2'' = 0$, which forces all adsorption at the interface into an enrichment.

The comparison of Figs. 32, 34 - 38 shows that all investigated bulk and interfacial properties exhibit a regular behavior when plotted as a function of $\varepsilon_2/\varepsilon_1$ and ξ. For all properties, a symmetry is found. It is shown in the Appendix that this symmetry is likewise observed for the vapor pressure and vapor phase composition at constant temperature and liquid phase composition. The symmetry is also found in the matrix diagram of the density profiles in Fig. 34. This interesting regularity can be explained by a conformal solution theory, as presented in the following section.

3.5 Conformal Solution Theory of Fluid Interfaces

3.5.1 Modeling the Regularities of VLE and Interfacial Properties

The regularity of the properties of the studied binary LJTS mixtures (see previous section) can be explained with a conformal solution theory (CST) of the liquid phase. The regularity is thereby put into direct relation with the underlying molecular interactions. The employed CST is adopted from the literature and therefore only outlined here. For brevity, a mixture n is defined by its coordinates in the ξ, $\varepsilon_2/\varepsilon_1$-plane as

$$\underline{a}_n = \left(\xi_n, (\varepsilon_2/\varepsilon_1)_n\right). \tag{51}$$

Our starting hypothesis is that the observed regularity is due to the mean dispersive interactions in the liquid phase. To validate this assumption, the configurational contribution of the internal energy u'_{config} of the saturated liquid phase is studied, where the total internal energy u' is the sum of the kinetic energy contribution u'_{kin} and the configurational contribution u'_{config}. For a pairwise additive intermolecular potential v, the configurational internal energy for a given point in the configurational space $\underline{r}$ is $u'_{\text{config}}(\underline{r}) = \sum_{k=1}^{N} \sum_{k>l}^{N} v(r_{kl})$, where N is the number of particles and r_{kl} the distance between two particles k and l. The configurational internal energy u'_{config} of a binary mixture can be calculated from rigorous statistical mechanics from the pair potential v and the radial distribution function (RDF) $g(r)$ [237, 262, 406]:

$$u'_{\text{config}} = \frac{U'_{\text{config}}}{N} = \frac{1}{2}\rho' \sum_{i=1}^{2} \sum_{j=1}^{2} x'_i x'_j \int_0^\infty g_{ij}(r)v_{ij}(r)r^2 4\pi \, \mathrm{d}r \,, \tag{52}$$

where ρ' is the total number density and x'_i the mole fraction of component i, N the total number of particles, g_{ij} the radial distribution function between two components i and j, and v_{ij} the pair potential energy. To compute and evaluate u'_{config} for a given mixture $\underline{a}_n$ at a given $T = 0.77\,\varepsilon k_{\text{B}}^{-1}$ and $x'_2 = 0.05\,\text{mol}\,\text{mol}^{-1}$, the conformal solution theory of *Leland* and co-workers [177, 366, 367] is applied here, which goes back to the original work of *van der Waals* [406, 690] and *Longuet-Higgins* [393]. The CST of *Leland* and co-workers was developed to provide a statistical-mechanical framework to compute excess thermodynamic functions of mixing, from the intermolecular potentials and the radial distribution functions of the pure components [366, 393, 572]. The properties of the studied mixture are thereby approximated by those of a hypothetical pure fluid, indicated with the index $_{00}$.

The main assumptions of the employed conformal solution theory, cf. Eqs. (52) - (56), are summarized here briefly. In Eq. (52) $4\pi\rho'g(r)\,\mathrm{d}r = n'(r)\,\mathrm{d}r$ can be identified [262] as the mean number of particles n' in a range between r and $r + \mathrm{d}r$. The configurational internal energy u'_{config} is obtained by integrating $n'(r)\cdot v(r)$ over all r ranges and weighted by the respective mole fraction; the factor $1/2$ ensures that each pair interaction is only counted once. In general the three radial distribution functions g_{11}, g_{12}, and g_{22} are a function of the type of both components (ε, σ), the composition, the temperature, the density, and the distance r between two particles [279, 364, 406, 420], i.e.

$g_{ij} = g_{ij}(\varepsilon_{ij}, \sigma_{ij}, \underline{x}, T, \rho, r)$. It is known that the RDF is only weakly depending on the composition and the dispersion energies of the components [364, 420].

For the one-fluid CST, the properties of a mixture are approximated by those of a hypothetical pure fluid. The molecular interactions of that hypothetical fluid are to be *conformal* to those of the pure components that constitute the mixture, i.e. their pair potentials v_{ij} must be described [237] by the same mathematical function $v_{ij} = \varepsilon_{ij}\, v(r/\sigma_{ij})$. The hypothetical pure fluid – in our case a spherical Lennard-Jones pair potential – is then characterized by the two interaction parameters σ_{00} and ε_{00} and a single radial distribution function $g_{00} = g_{00}(\tilde{r}, T, \rho)$ [366, 406]. The central assumption in the 'one-fluid' CST is that the radial distribution functions $g_{ij}(r)$ scale with the respective size parameter σ_{ij}, i.e.

$$g_{ij}(r/\sigma_{ij}) = g_{00}(\tilde{r}/\sigma_{00}),\tag{53}$$

which includes a coordinate transformation [237] $r \to \tilde{r}$. Thereby, the internal energy of the liquid phase of a binary mixture can be written as

$$u'_{\text{config}} = u'_{\text{config},00} = \frac{1}{2}\rho' \sum_{i=1}^{2}\sum_{j=1}^{2} x'_i x'_j\, \varepsilon_{ij}\, \sigma_{ij}^3 \int_0^\infty g_{00}(\tilde{r})\; v_{00}(\tilde{r})\, \tilde{r}^2 4\pi\; \mathrm{d}\tilde{r}\,.\tag{54}$$

By identifying

$$\sum_{i=1}^{2}\sum_{j=1}^{2} x'_i x'_j\, \varepsilon_{ij}\, \sigma_{ij}^3 = \varepsilon_{00}\, \sigma_{00}^3\,,\tag{55}$$

Eq. (54) can then be written as

$$u'_{\text{config},00} = \varepsilon_{00}\, \sigma_{00}^3 \cdot \frac{1}{2}\rho' \int_0^\infty g_{00}(\tilde{r})\; v_{00}(\tilde{r})\, \tilde{r}^2 4\pi\; \mathrm{d}\tilde{r}\,.\tag{56}$$

Eq. (55) is the well-known first mixing rule of the van der Waals one-fluid theory, which is also used for modeling LJTS mixtures with the PeTS EOS, cf. section 3.2.2. Since $\sigma_{ij} = \sigma_1 = 1$ holds for the entire present study, a second mixing rule is obsolete here. The LJTS potential of the reference component 1 is used in Eq. (56), i.e. $v_{00} = v_{\text{LJTS}}$.

As the dependency of ρ' on ξ or $\varepsilon_2/\varepsilon_1$ can be neglected here in a good approximation, only the first term $\varepsilon_{00}\, \sigma_{00}^3$ in Eq. (56) depends on the mixture $\underline{a}_n$. The resulting configurational internal energy u'_{config} depends evidently directly on the chosen combination rule. In accordance with the MD, EOS, and DGT calculations, the modified Lorentz-Berthelot combination rule, cf. Eq. (49), was also employed for the CST.

A correlation for the radial distribution function of the Lennard-Jones fluid $g_{00} = g_{\text{LJ}}$ was adopted from *Morsali et al.* [476]. They propose an empirical correlation of the Lennard-Jones RDF as a function of the temperature and the density $g_{\text{LJ}} = g_{\text{LJ}}(\tilde{r}, T, \rho)$. *Morsali et al.* [476] developed an RDF correlation for the full Lennard-Jones fluid, whereas the present study investigates the Lennard-Jones truncated and shifted fluid. This is incorporated by employing a corresponding state principle, i.e. the Lennard-Jones RDF from *Morsali et al.* [476] was calculated at the same reduced temperature and density with respect to its critical quantity, i.e. $T_{\text{red}} = T^{\text{LJ}}/T_c^{\text{LJ}} = T^{\text{LJTS}}/T_c^{\text{LJTS}}$ and $\rho_{\text{red}} = \rho^{\text{LJ}}/\rho_c^{\text{LJ}} = \rho^{\text{LJTS}}/\rho_c^{\text{LJTS}}$. The critical parameters were adopted from *Vrabec et al.* [687] and *Lotfi et al.* [395] for the LJTS and LJ fluid, respectively. The influence of the potential truncation on the RDF is therefore neglected. *Morsali et al.* [476] compared

results from their RDF with a large number of computer experiment data and found excellent agreement. A comparison of u'_{config} obtained from the PeTS EOS and the outlined CST is given in the Appendix. They agree well; the absolute average deviation is 2%.

In summary, Eq. (56) enables the computation of the configurational internal energy of binary LJTS mixtures $u'_{\text{config}}(\underline{a})$ from CST, using only the RDF of the pure LJTS fluid $g_{\text{LJTS}}(\tilde{r}, T, \rho)$ and the potential function $v_{\text{LJTS}}(\tilde{r})$. $u'_{\text{config}}(\underline{a})$ is used here to characterize the mean interactions in the saturated liquid phase and subsequently put these in relation to the regularity of interfacial properties.

3.5.2 Evaluation of the CST Model

The configurational internal energy u'_{config} at $T = 0.77\,\varepsilon k_{\text{B}}^{-1}$ and $x'_2 = 0.05\,\text{mol}\,\text{mol}^{-1}$, computed by Eq. (56), is shown in Fig. 39 as a function of ξ and $\varepsilon_2/\varepsilon_1$ for all 90 investigated LJTS mixtures. Starting in *corner A*, the absolute value of the configurational internal energy $|u'_{\text{config}}|$, and thereby also the magnitude of the mean dispersive interactions, steadily decreases with decreasing ξ and decreasing $\varepsilon_2/\varepsilon_1$ towards *corner B*, which is a direct result of the molecular interactions. The internal energy of the liquid phase $u'_{\text{config}}(\varepsilon_2/\varepsilon_1, \xi)$ obeys the same regular behavior as the bulk and interfacial properties, cf. Figs. 32, 33 and 35 - 38, i.e. radially shaped traces for $u'_{\text{config}} = \text{const.}$ are found in the $\varepsilon_2/\varepsilon_1$, ξ-plane.
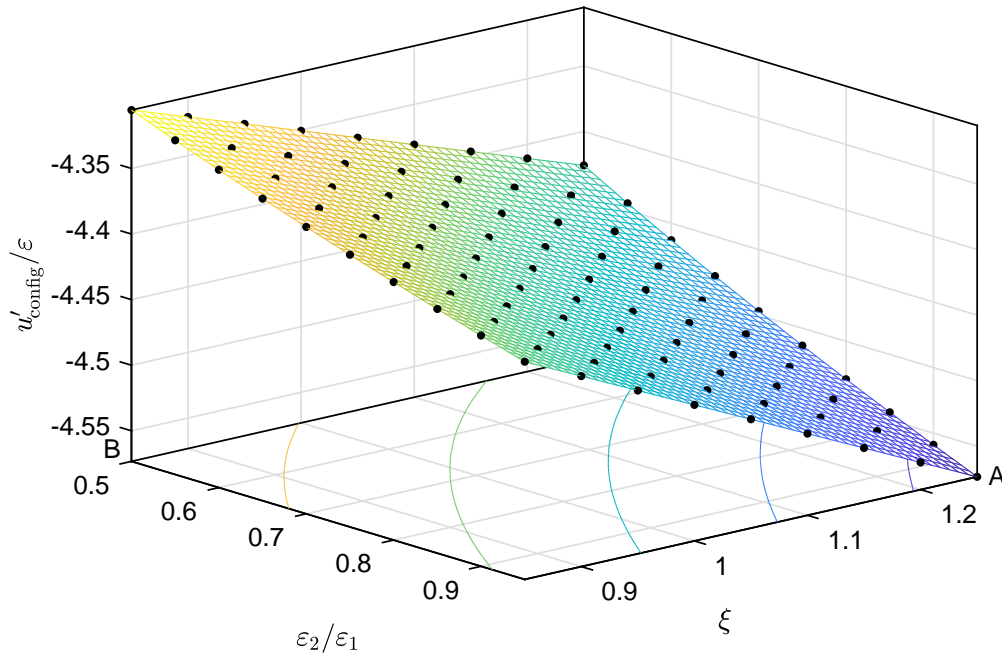
Figure 39: Configurational internal energy of the saturated liquid phase u'_{config} calculated from the conformal solution theory Eq. (56) as a function of the binary interaction parameter ξ and the ratio of the dispersion energies $\varepsilon_2/\varepsilon_1$ at $x'_2 = 0.05\,\text{mol}\,\text{mol}^{-1}$ and $T = 0.77\,\varepsilon k_{\text{B}}^{-1}$. The surface is a linear interpolation of the data points. The color of the surface is coded by its height position.

According to the discussion of Eq. (56), the configurational internal energy of a binary mixture u'_{config} at a given temperature and composition depends on the mixture type only via the term $\varepsilon_{00}\,\sigma_{00}^3$, that is defined by Eq. (55). Both the integral and the factor $\frac{1}{2}\rho'$ in Eq. (56) can be merged to a constant I at a given temperature and composition. Introducing $\zeta = \varepsilon_2/\varepsilon_1$, and employing the modified Berthelot combination rule, Eq. (56) can be written as

$$\frac{u'_{\text{config}}}{I} = \sum_{i=1}^{2}\sum_{j=1}^{2} x'_i x'_j \,\varepsilon_{ij}\,\sigma_{ij}^3 = x_1'^{\,2}\,\varepsilon_1 + 2\,x'_1 x'_2\,\varepsilon_1\,\xi\sqrt{\zeta} + x_2'^{\,2}\,\varepsilon_1\,\zeta \;. \tag{57}$$

The functional form of $u'_{\text{config}}(\xi, \zeta)$ described by Eq. (57) yields the regularity with the approximatively radial traces of $u'_{\text{config}} = \text{const.}$ in the $\varepsilon_2/\varepsilon_1$, ξ-plane, as depicted in Fig. 39. Eq. (57) indicates that the regular traces that were observed in Figs. 32, 33 and 35 - 38 are not strictly radial but obey a more complicated law.

In our case, x'_1, x'_2 and ε_1 are constant and the last term in Eq. (57) is small, as x'_2 is small. Hence, the traces depicted in Fig. 39 as well as Figs. 32, 33 and 35 - 38 are basically curves in which $\xi\sqrt{\zeta}$ are constant. They only appear to be approximately radial in the plots used here, due to the investigated $\varepsilon_2/\varepsilon_1$, ξ range.

The regular behavior found in $u'_{\text{config}}(\varepsilon_2/\varepsilon_1, \xi)$ is the same regular behavior as obtained for the bulk and interfacial properties, cf. Figs. 32 - 38. Hence, the observed regularity (for both bulk and interfacial properties) is a consequence of the employed mixing and combination rule in DGT+EOS and the combination rule in MD. However, the regularity and the shape of the traces evidently depend on the composition, cf. Eq. (57). The results from this work indicate that the van der Waals one-fluid theory mixing rule used in the PeTS EOS [249, 635], cf. section 3.2.2, yields an excellent description of molecular simulation results for both bulk and interfacial mixture properties. The fact that the bulk and interfacial properties in the VLE are dominated by the liquid phase interactions can be described by the CST and can be exploited to find simple correlations of all studied properties. The hypothesis is here that they can be described as simple functions of the internal energy of the liquid phase.

Figs. 40 and 41 show that this hypothesis is confirmed by the data from the present work: bulk and interfacial properties of the 90 LJTS mixtures are plotted as a function of the corresponding liquid phase configurational internal energy u'_{config}. All properties are at constant temperature and liquid phase composition. The results from both MD and DGT are shown. The investigated VLE bulk properties (Fig. 40) and interfacial properties (Fig. 41) from both MD and DGT are found to be a simple function of each mixture's liquid phase configurational internal energy, which strongly indicates that there is a direct link between them. For all studied properties, a simple relation is found, for both the results obtained from MD and those from EOS+DGT.

Instead of the internal energy from CST also the internal energy from the EOS or the force field could have been used for establishing plots like the ones shown in Figs. 40 and 41. The basic findings would have been the same, as the internal energies of the liquid phase determined by the three methods agree very well, see Appendix. However, using the CST gives further insight on the underlying mechanism, i.e. the fact that the choice of the combination rule is responsible for the regularity behavior, cf. Eq. (57).

A fit function $Y = Y(u'_{\text{config}})$ was parametrized to the DGT and EOS results for each
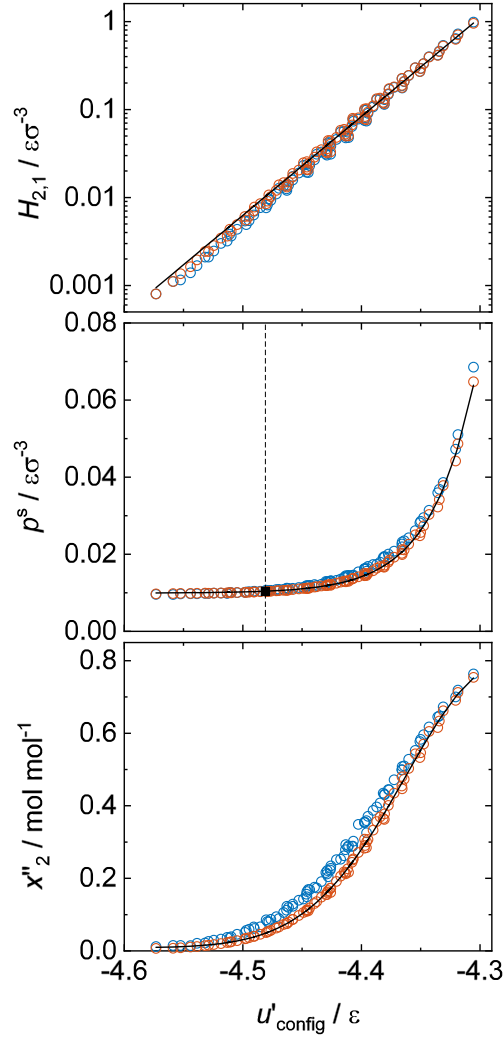
Figure 40: Results for the conformal solution theory applied to the VLE properties (Henry's law constant $H_{2,1}$, vapor pressure p^s, and vapor phase composition x_2''): the respective VLE property computed by MD (blue) and the EOS (orange) are shown as a function of the configurational internal energy of the saturated liquid phase u_{config}' as computed by Eq. (56). The black solid lines indicate the fitted functions (58) - (60) (fitted to the DGT results). All results are at $x_2' = 0.05\,\mathrm{mol\,mol^{-1}}$ and $T = 0.77\,\varepsilon k_B^{-1}$. The dashed line indicates u_{config}' of the high-boiling pure component 1 computed by Eq. (56). The black symbol indicates the vapor pressure of the pure component 1 obtained from the EOS.

bulk and interfacial property $Y = \langle H_{2,1}, p^s, x_2'', E_2, \Gamma_2^{(1)}, \gamma, L_{10}^{90} \rangle$. The mathematical forms and the parameters of the fitted functions are given in the following. The differences between the DGT and the MD results in Figs. 40 and 41 are due to differences in the data from these methods and not related to the CST, cf. Figs. 32, 33 and 35 - 38.

For each of the seven considered properties $Y = \langle H_{2,1}, p^s, x_2'', E_2, \Gamma_2^{(1)}, \gamma, L_{10}^{90} \rangle$, a simple correlation function was parameterized to describe $Y = Y(u'_{\text{config}})$. The DGT results were used for this fit since they do not exhibit stochastic scattering as the MD results do. Three function types were used:

$$Y/[Y] = \hat{Y} + a_1 \cdot \exp\left(\frac{u'_{\text{config}}/\varepsilon - a_2}{a_3}\right), \tag{58}$$

$$Y/[Y] = \hat{Y} + a_1 \cdot \exp\left(-0.5\left(\frac{u'_{\text{config}}/\varepsilon - a_2}{a_3}\right)^2\right), \tag{59}$$

$$Y/[Y] = \hat{Y} \cdot \exp\left(a_3\, u'_{\text{config}}/\varepsilon\right), \tag{60}$$

where $\hat{Y}$ and a_i are fitting parameters. $[Y]$ indicates the corresponding units of Y as $[Y] = \langle \varepsilon\sigma^{-3},\ \varepsilon\sigma^{-3},\ \text{mol mol}^{-1},\ 1,\ \sigma^{-2},\ \varepsilon\sigma^{-2},\ \sigma \rangle$. The obtained numeric values for $\hat{Y}$ and a_i are summarized in Table 6. Eq. (58) was used for correlating $p^s, \Gamma_2^{(1)}, \gamma, L_{10}^{90}$; Eq. (59) for x_2'', E_2; and Eq. (60) for correlating $H_{2,1}$. The absolute average deviations (AAD) between the fitted curves and the DGT results are also given in Table 6.

Fig. 40 shows the results for the Henry's law constant $H_{2,1}$, the vapor pressure p^s, and the vapor phase mole fraction x_2'' for the conditions studied in the present work as a function of the corresponding liquid phase configurational internal energy. The three properties increase with decreasing mean dispersive interactions in the liquid phase, i.e. with decreasing absolute value of u'_{config}. Fig. 41 shows that the same holds for the relative adsorption $\Gamma_2^{(1)}$ and interfacial thickness L_{10}^{90}. The enrichment of the low-boiling component E_2 also generally increases with decreasing mean dispersive interactions, with the exception of the region near *corner B*. This exception is due to the difference in the number density, cf. Fig. 33. Only the surface tension γ shows the inverse trend: it decreases with decreasing mean dispersive interactions. In all cases, simple functional relations between the studied properties and u'_{config} are found, which are however, of different types. The fitted functions for all seven investigated properties agree excellently with the underlying DGT results. Similar fits were obtained for the MD results, but are not shown in Figs. 40 and 41 for clarity. The DGT and EOS results for all properties exhibit only low scattering around the respective fitted curves, i.e. the investigated bulk and interfacial properties are highly correlated with the liquid phase mean interactions. The scattering of the MD results is larger than that of the DGT and EOS results due to the fluctuations from the sampling during the simulation. The absolute average deviation (AAD) from the DGT and EOS results from the corresponding fitted curves were calculated for each property and are reported in Table 6.

The scattering of the DGT and EOS results for the vapor pressure p^s and the vapor phase composition x_2'' around the respective fitted curve is fairly constant in the entire range of u'_{config}, i.e. the range of investigated mixtures. In contrast to this, the scattering of the results for the interfacial properties around the respective fitted curves
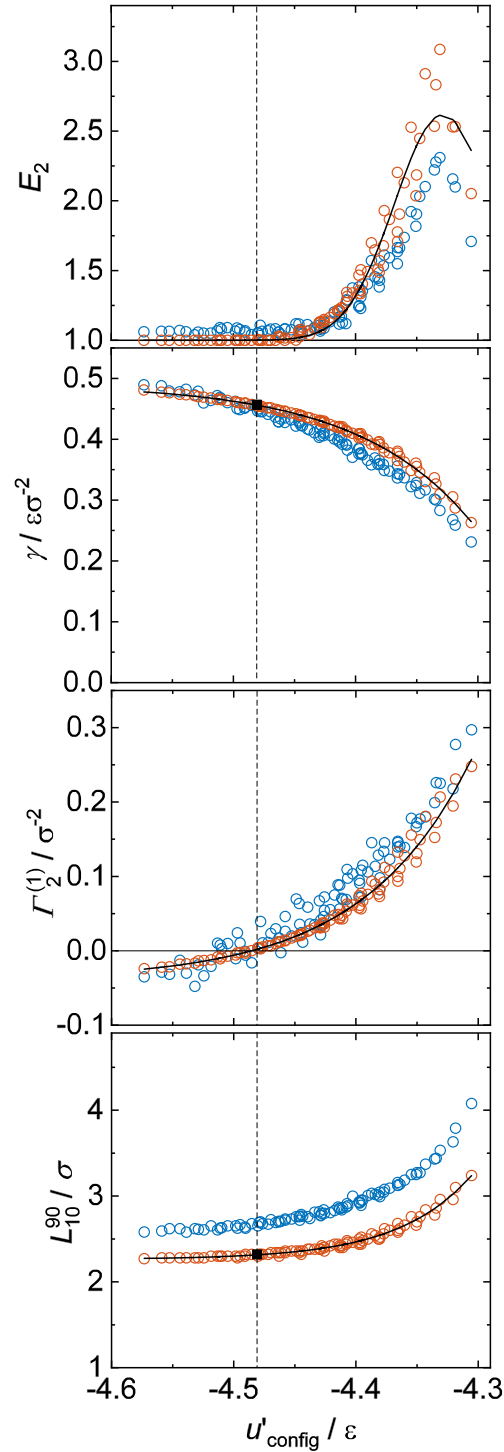
Figure 41: Results for the conformal solution theory applied to the interfacial proper-
ties (enrichment E_2, relative adsorption $\Gamma_2^{(1)}$, surface tension γ, and inter-
facial thickness L_{10}^{90}): the respective interfacial property computed by MD
(blue) and DGT (orange) are shown as a function of the configurational in-
ternal energy of the saturated liquid phase u'_{config} as computed by Eq. (56).
The black solid lines indicate the fitted functions (58) - (59) (fitted to the
DGT results). All results are at $x'_2 = 0.05\,\text{mol}\,\text{mol}^{-1}$ and $T = 0.77\,\varepsilon k_{\text{B}}^{-1}$. The
dashed line indicates u'_{config} of the high-boiling pure component 1 computed
by Eq. (56). Black symbols indicate the values for the pure component 1
obtained from the EOS+DGT.

varies with varying u'_{config}. The scattering is significantly lower for mixtures with large mean dispersive interactions than for those with low mean dispersive interactions, cf. results for $\Gamma_2^{(1)}$, γ, L_{10}^{90} in Fig. 41. Furthermore, the scattering is lower for the surface tension and the interfacial thickness than for the relative adsorption and the enrichment, which indicates that the latter are less dominated by the liquid phase interactions but also influenced by the vapor phase interactions and the anisotropic interactions at the interface. This is supported by the corresponding AADs given in Table 6.

Table 6: Parameters for the correlations (58) - (60).

	$\hat{Y}$	a_1	a_2	a_3	AAD
[c] $H_{2,1}$	$2.32 \cdot 10^{48}$	-	-	25.87506	9.5%
[a] p^s	0.00993	$1.05 \cdot 10^{49}$	-	-0.03718	1.8%
[b] x_2''	0.00823	0.77992	-4.28011	0.08256	3.5%
[b] E_2	1	1.61673	-4.32865	0.03954	3.9%
[a] $\Gamma_2^{(1)}$	-0.03928	$3.19 \cdot 10^{20}$	-	-0.08891	12.8%
[a] γ	0.49078	$-2.03 \cdot 10^{19}$	-	-0.09371	0.6%
[a] L_{10}^{90}	2.26152	$8.42 \cdot 10^{30}$	-	-0.06044	0.7%

[a] uses Eq. (58)

[b] uses Eq. (59)

[c] uses Eq. (60)

High absolute values of u'_{config} are found for mixtures with strong mean liquid phase interactions. Eq. (57) shows that for the conditions that were studied in the present work, the variation of the mean liquid phase interaction stems mainly from the variation of the unlike dispersive interactions between component 1 and 2. The higher the absolute value of u'_{config} is (left side in the diagrams of Figs. 40 and 41), the stronger is the attraction between the components 1 and 2. This explains why high absolute values of u'_{config} lead to low Henry's law constants $H_{2,1}$ (high solubilities of component 2 in component 1), low vapor pressures, and low concentrations of the component 2 in the gas phase, cf. Fig. 40. On the other hand, low absolute values of u'_{config} (weak 1 - 2 attraction) lead to high Henry's law constants $H_{2,1}$ (low solubilities of 2 in 1), high vapor pressures, and high concentrations of the component 2 in the gas phase, cf. Fig. 40.

For mixtures with large mean dispersive interactions, a variation of u'_{config} (which goes in hand with a variation of $\varepsilon_2/\varepsilon_1$ and ξ) has only little influence on the bulk and interfacial properties. Note that $H_{2,1}$ is plotted on an ln-scale. Furthermore, the magnitude of the interfacial properties is small for these mixtures, e.g. small adsorption and enrichment of the low-boiling component.

Eq. (57) shows that the unlike dispersive interactions increase both with ξ (which controls the dispersion energy ε_{12}) and with $\zeta = \varepsilon_2/\varepsilon_1$ (which controls the relative volatility). The unlike dispersive interactions are therefore high in *corner A* and decrease going to *corner B*, cf. Figs. 32, 33 and 35 - 38. This also explains the observed phase behavior, cf. Fig. 31.

For high mean dispersive interactions (left side in the plot shown in Fig. 41), the interfacial thickness L_{10}^{90} is low. For weaker interactions the interfacial thickness L_{10}^{90}

increases, as it might have been expected. Also the dependence of the surface tension γ on the mean dispersive interactions is expected: it decreases with decreasing mean dispersive interactions.

Furthermore, Figs. 40 and 41 show that the developed CST also works in the limit of the pure component. The vapor pressure, surface tension, and interfacial thickness of the pure component 1 computed from DGT+EOS at $T = 0.77\,\varepsilon k_{\mathrm{B}}^{-1}$ are shown as black symbols. Its liquid phase configurational internal energy u'_{config} was computed by Eq. (57). The pure component values agree excellently with mixture values at the same u'_{config}. Hence, the vapor pressure, surface tension, and interfacial thickness of the pure component have the same values as those of mixtures with the same liquid phase mean interactions. Using these observables, a pure component could not be distinguished from these mixtures at the investigated temperature. Also, those mixtures have zero relative adsorption $\Gamma_2^{(1)} = 0$, cf. Fig. 41. This strongly supports the picture of the one-fluid theory and the CST applied in this work.

Interestingly, the dependency of the interfacial properties on the liquid phase mean interactions is not symmetric, i.e. starting at the mixtures with $\Gamma_2^{(1)} = 0$, an increase and decrease of u'_{config} has qualitatively different effects.

The surface tension that is reported here is the number for $x'_2 = 0.05\,\mathrm{mol\,mol^{-1}}$. As the surface tension of the pure component 1 is the same in all cases, a decrease in the reported surface tension goes along with an increase of the gradient of the surface tension with varying x'_2. It therefore follows from the Gibbs adsorption equation that the relative adsorption $\Gamma_2^{(1)}$ must increase, which is in line with the results shown in Fig. 41. High numbers for the relative adsorption of component 2 also go along with an enrichment of that component at the interface E_2, cf. Fig. 41.

The increase of $\Gamma_2^{(1)}$ and E_2 with decreasing u'_{config} can also be understood based on Eq. (57). A decrease in u'_{config} stems either from a decrease in ξ or from a decrease in $\varepsilon_2/\varepsilon_1$. The picture we invoke in the following is that of a dynamic equilibrium. Assume that a particle of component 2 is on the way of entering the liquid phase coming from the gas phase. The liquid phase contains basically only component 1. The chance that the particle 2 will successfully enter the liquid phase decreases with decreasing mixed unlike dispersive interactions 1 - 2 in the liquid phase, i.e. with decreasing ξ and $\varepsilon_2/\varepsilon_1$. Furthermore, low values of $\varepsilon_2/\varepsilon_1$ lead to high concentrations of component 2 in the vapor phase (see Fig. 40), such that there are many particles of component 2 near the interface, which could in principle enter but face difficulties in doing so. This leads to the enrichment E_2 and the positive relative adsorption $\Gamma_2^{(1)}$. In a more colorful picture, the situation resembles that at the door of a disco: there are many people (particles 2) roaming outside and they are attracted by the disco's neon lights (the interface), but there are only few places available in the disco (in the liquid phase). Hence, there will be a crowd at the entrance (enrichment and adsorption).

3.5.3 Conclusions

The relation between the molecular interaction parameters in binary Lennard-Jones mixtures and the bulk and interfacial vapor-liquid equilibrium properties were studied here. All considered bulk and interfacial properties exhibit a regular behavior when they

are considered as a function of the variables $\varepsilon_2/\varepsilon_1$ and ξ, which describe the molecular interactions. A theory was developed which explains this behavior based on a conformal solution theory of the molecular interactions. It is based on the assumption that the behavior of the studied systems is dominated by the liquid phase mean interactions and that the liquid phase can be described with a one-fluid theory. The vapor phase has only a minor influence. The basic finding is a monovariate relationship between the studied VLE properties and the mean liquid phase interactions, i.e. the configurational internal energy. This resembles the physical theory of the so-called entropy-scaling, which uses a monovariate relationship between transport coefficients and the entropy [567]. For the interfacial and bulk VLE properties, different combinations of $\varepsilon_2/\varepsilon_1$ and ξ may lead to different types of phase behavior, but when the internal energy of the liquid phase is the same, the value of the studied properties is the same. The theory also works in the limit of the pure component such that mixtures with the same liquid phase mean interactions as a pure component have the same the vapor pressure, surface tension, and interfacial thickness as that pure component – and zero relative adsorption. The theory also enables predictions outside the range of the parameters $\varepsilon_2/\varepsilon_1$ and ξ that was studied in the present work.

Both large enrichment and large relative adsorption of the low-boiling component are found for mixtures with relatively low mean interactions in the liquid phase, which also goes in hand with low solubilities, i.e. wide-boiling mixtures that tend to form low-boiling azeotropes. Such mixtures also tend to show liquid-liquid phase splits. Systems with liquid-liquid equilibria were, however, not investigated here as this would have overloaded the study. But, such are considered in the following section.

As only data for constant temperature and liquid phase composition were taken in the present work, it would be interesting to extend the applied CST to other temperatures and compositions and test if the monovariate relationship established in this work also holds for those dimensions.

3.6 Relation of Interfacial Properties and the Phase Diagram

Interfacial properties are intrinsically tied to the corresponding phase equilibria. These equilibria are often represented in phase diagrams, which may have complex topologies. Establishing relations between the interfacial properties and the phase diagram requires systematic studies of the different types of equilibria and the corresponding interfaces for a given system. Such work is surprisingly scarce in the literature. Such a study is therefore carried out here for a simple model system: a binary mixture of Lennard-Jones truncated and shifted (LJTS) fluids, and the parameters were chosen such that the phase diagram of the mixture is of type III according to the classification of *van Konyenburg and Scott* [339]. I.e. the mixture has two critical lines and a three-phase line. Hence, the isothermal phase diagram shows vapor-liquid equilibria (VL_1E and VL_2E), liquid-liquid equilibria (L_1L_2E), and a vapor-liquid-liquid equilibrium (VL_1L_2E); furthermore, at very high pressures, also fluid-fluid equilibria (F_1F_2E) exist. For comparison, also mixture A (practically ideal mixture in the sense of Raoult's law) was studied, cf. section 3.3. Mixture A is of type I. Pursuing the labeling of the LJTS mixtures introduced in section 3.3, the type III system is labeled here as 'mixture G'. The phase equilibria and interfacial properties of these two systems were investigated here in a wide range of temperatures and pressures.

The study on different fluid interfacial properties was carried out with both molecular dynamics (MD) simulation and density gradient theory (DGT) in combination with the PeTS equation of state (EOS) – as studies discussed in the previous sections. The following interfacial properties were investigated for all types of interfaces: surface tension, density profiles of the components in the nanoscopic interfacial region, relative adsorption at the interface, interfacial thickness, and the enrichment of the components.

Non-monotonic density profiles of components at interfaces have been reported since the early days of computational work on vapor-liquid interfacial properties of mixtures [91, 192, 361]. The enrichment at vapor-liquid interfaces has attracted much attention in the past decades [32–34, 50, 56, 91, 122, 126, 130, 149, 153, 173, 193, 200, 328, 354, 362, 373, 378, 379, 390, 391, 404, 412, 414, 446, 477, 483, 492, 501–504, 522, 533, 551, 552, 583, 585, 586, 624, 630, 630, 634, 635, 635], also because it is suspected to influence the mass transfer through the interface [199, 328, 488, 634, 635]. Asymmetric mixtures have attracted special interest [56, 173, 354, 373, 391, 483, 501, 504, 583] since a particularly high enrichment is found in these types of mixtures. However, there are only few studies in the literature in which the link between the enrichment at vapor-liquid interfaces and the corresponding bulk phase equilibria was explicitly discussed [173], whereas the link between the relative adsorption, the phase behavior, and the wetting behavior has been studied more systematically for vapor-liquid-liquid equilibria [127, 142, 143, 195, 447, 655, 656].

A further interesting phenomenon observed at fluid interfaces is a non-monotonic behavior of the total density at liquid-liquid interfaces [141, 199, 204, 415, 490, 669]. This has been investigated in only few studies compared to the large body of available work on the enrichment at vapor-liquid interfaces.

We have recently carried out two studies [630, 635] (cf. sections 3.3 and 3.4) in which the influence of molecular interactions on both the phase diagram and interfacial prop-

erties of binary fluid mixtures were investigated systematically for LJTS mixtures. In Ref. [630] (cf. section 3.4) we have demonstrated that the interfacial properties are directly linked to bulk phase equilibrium properties [630] and have established a conformal solution theory for this (cf. section 3.5). The study discussed in this section is complementary to those studies: while in the previous work [630, 635] (cf. sections 3.3 and 3.4) many different mixtures were studied at basically only one condition and only *VLE* were considered, a different approach is taken here: two mixtures are studied in full detail for a wide range of conditions and different types of equilibria are considered. The studied mixtures were selected based on the experience from the previous work [630, 635] in such a way that important interfacial effects, namely a high enrichment, are expected in one of them (mixture G), while the other is an ideal binary mixture that is studied as a reference (mixture A). To the best of our knowledge, this is the first study in which, for a given mixture, interfacial properties of different types of phase equilibria were systematically investigated and characterized regarding the structure of the interface and its properties.

In systematic studies of interfacial properties and phase equilibria, also the temperature must be varied. The present study therefore also extends the knowledge on the temperature dependency of interfacial phenomena, which is known to be important, especially for the enrichment [50, 362, 624].

3.6.1 Specification of LJTS Mixture A and G

Two binary LJTS mixtures were studied in the present work; they are labeled as mixture A and G in the following. Both contain a high-boiling component, denoted as component 1 and a low-boiling component, denoted as 2. The high-boiling component is the same in both mixtures and can be considered as the reference fluid. The low-boiling character of the component 2 is obtained by decreasing its dispersion energy with respect to component 1. The size parameter is not varied and is σ for all components. Also the mass of the LJTS particles M is also the same for both components.

As in the previous sections, the modified Lorentz-Berthelot combination rules are employed [52, 394] for the modeling of the interaction between unlike LJTS particles:

$$\sigma_{ij} = \frac{\sigma_i + \sigma_j}{2},\tag{61}$$

$$\varepsilon_{ij} = \xi\sqrt{\varepsilon_i\varepsilon_j}.\tag{62}$$

Here, indices i and j stand for the interaction of two particles of the same component and ij for the cross interaction between the different components, and ξ is a state-independent interaction parameter.

The studied mixtures are:

- mixture A: ideal mixture with $\varepsilon_2/\varepsilon_1 = 0.9$ and $\xi = 1$ (cf. section 3.3),

- mixture G: asymmetric wide boiling mixture with $\varepsilon_2/\varepsilon_1 = 0.6$ and $\xi = 0.85$.

The two mixtures were selected based on the experience from our previous study [630] (cf. section 3.4). Mixture G is the mixture for which the highest enrichment was found in that study (cf. Fig. 35), which is due to the underlying bulk densities; see the Appendix

for details. The vapor pressure curves of the three pure components are shown in Fig. 42. They were computed with the PeTS EOS [249], which reproduces both stable and metastable states as well as the vapor-liquid equilibrium of the LJTS fluid very well, cf. chapter 2. The binary interaction parameter ξ and the ratio of the dispersion energies $\varepsilon_2/\varepsilon_1$ as specified above were used both in MD and DGT.
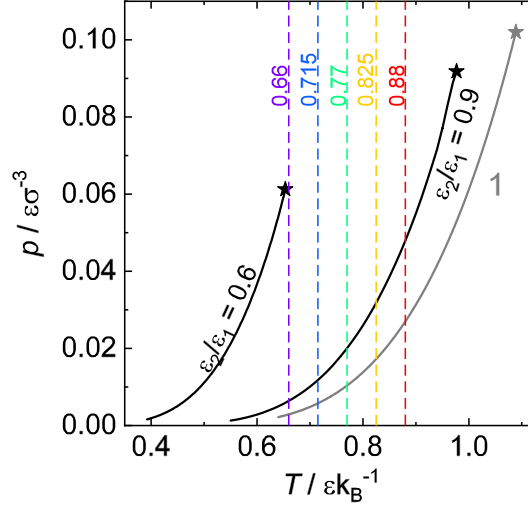
Figure 42: Vapor pressure curves for the three pure LJTS fluids employed in the present work. The high-boiling component 1 is the gray solid curve. The two low-boiling components 2 are the black solid curves. The critical points are indicated as stars. The temperatures that were investigated in the present study are indicated as colored vertical dashed lines.

The fluid interfaces of the binary mixtures A and G were studied in the present work at five temperatures, which are indicated by the vertical dashed lines in Fig. 42: $T/\varepsilon k_{\mathrm{B}}^{-1}$ = 0.66, 0.715, 0.77, 0.825, 0.88. Using the results of *Vrabec et al.* [687] for the critical point of the LJTS fluid with $r_{\mathrm{c}} = 2.5\,\sigma$ ($T_{\mathrm{c}} = 1.0779\,\varepsilon k_{\mathrm{B}}^{-1}$; $\rho_{\mathrm{c}} = 0.319\,\sigma^{-3}$) the reduced temperatures with respect to the critical point of the reference component 1 are approximately: $T_{\mathrm{red}} = T/T_{\mathrm{c},1}$ = 0.6, 0.65, 0.7, 0.75, 0.8. The lowest temperature $T = 0.66\,\varepsilon k_{\mathrm{B}}^{-1}$ is slightly above the triple point temperature ($T_{\mathrm{trip}} = 0.62\,\varepsilon k_{\mathrm{B}}^{-1}$) of the component 1 [442, 667]. The low-boiling component 2 with only slightly decreased dispersion energy ($\varepsilon_2/\varepsilon_1 = 0.9$) is subcritical at all investigated temperatures, whereas the component 2 with $\varepsilon_2/\varepsilon_1 = 0.6$ supercritical at all investigated temperatures.

The focus of this study lies on the highly non-ideal mixture G. Mixture A is used as a reference of a practically ideal mixture. In subsection 3.6.2, the phase diagrams of the mixtures A and G are introduced and the results for bulk phase equilibria are presented. Then, the results for the interfacial properties of mixture A and mixture G are discussed in 3.6.3 and 3.6.4, respectively. For the mixture G, the following subsections report on interfacial properties for different types of phase equilibria: subsection 3.6.4.1 on VL_1 interfaces, subsection 3.6.4.2 contains a discussion of the different types of equilibria adjacent to the three-phase VL_1L_2E, subsection 3.6.4.3 reports on the results for the F_1F_2E and its' interfacial properties. Finally, in subsection 3.6.5 the results for the interfacial properties of the different types of equilibria are summarized and put into context with each other. The results for both the phase equilibria and the interfacial properties are shown graphically here, the corresponding numeric values of the results

are reported in the Appendix.

It was shown in earlier works of our group [630, 635] (cf. section 3.3 and 3.4) that the interfacial density profiles of LJTS mixtures obtained from MD and DGT+PeTS EOS agree very well. Hence, only the DGT density profiles are discussed here for brevity; the corresponding MD results are provided in the Appendix. The good agreement of the results for the interfacial properties derived from the density profiles obtained from MD and DGT affirms this procedure.

3.6.2 Results for the Phase Equilibria of Mixture A and G

Fig. 43 shows the pressure - temperature diagrams with the characteristic curves for the binary mixtures A and G. Besides the vapor pressure curves of the pure components, also the critical lines are shown, and for mixture G the three-phase line. The results were obtained from the PeTS EOS. The phase equilibria were computed with the method and algorithm described in Ref. [137].

Mixture A is almost ideal, cf. section 3.3, and shows a type I phase behavior in the classification of *van Konynenburg and Scott* [339]. The pure component critical points are connected by a single critical line of the binary mixture. Real mixtures that have qualitatively the same phase behavior are for example methane + krypton, krypton + xenon, and krypton + argon. Mixture G is strongly non-ideal and has a type III phase behavior according to Ref. [339]. Real mixtures that have qualitatively the same phase behavior are for example water + carbon dioxide, different alkanes + carbon dioxide, neon + argon, nitrogen + ammonia, and neon + krypton. Mixtures of type III have attracted much attention in the past [139, 173, 354, 553] as they exhibit an interesting and complex phase behavior.

For mixture G, the critical line that starts at the critical point of component 2 ends in an upper critical end point (UCEP), where also the three-phase VL_1L_2E line ends. The critical line that starts at the critical point of component 1 exhibits a temperature minimum, i.e. a bicritical end point (BICEP) in which two critical points merge. The branch of the critical line that is connected to the critical point of component 1 belongs to common binary vapor-liquid phase envelopes. The branch of the critical line that climbs to high pressures belongs to so-called fluid-fluid equilibria [572] (which are sometimes also referred to as 'gas-gas equilibria'). Even though both components are supercritical at such states, a phase split is observed. The fluid-fluid critical line monotonically increases with increasing temperature starting at the BICEP. In the temperature range $T_{UCEP} < T < T_{BICEP}$, the phase envelopes starting at the high-boiling pure component vapor pressure have no critical point. The five temperatures that were studied in the present work were chosen such that the corresponding phase diagrams include all these phenomena, cf. little arrows in Fig. 43.

Fig. 44 shows the isothermal $p - x$ phase diagrams for the mixtures A and G at the five studied temperatures. Results from computer experiments and the EOS are shown.

For mixture G, the low-boiling component 2 is supercritical at all investigated temperatures, whereas the high-boiling component 1 is subcritical at all temperatures. The phase envelope is very wide at low temperatures and gets narrower as the temperature increases. Starting at the critical point of the pure component 1, the critical pressure of
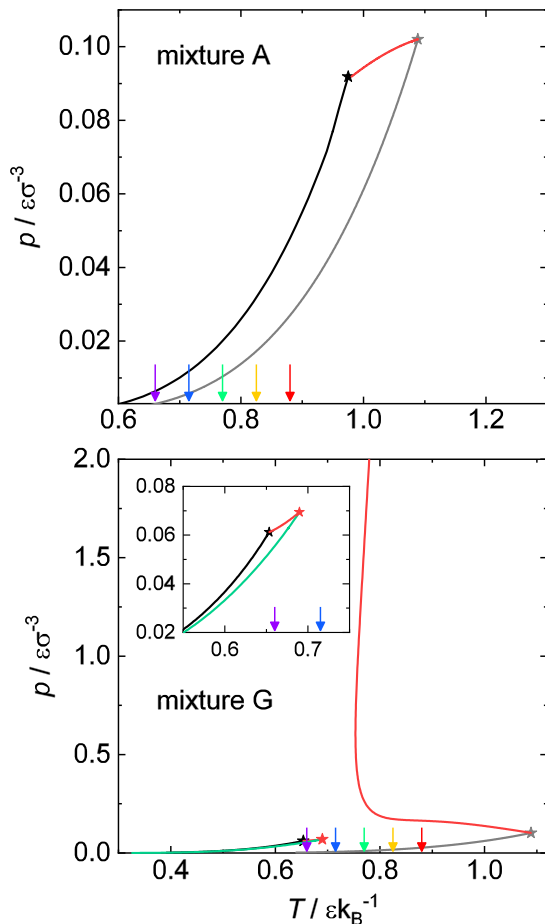
Figure 43: Pressure-temperature diagrams with characteristic curves for the mixtures A and G. Pure component vapor pressure curves and critical points are gray lines and stars (high-boiling component 1) and black lines and stars (low-boiling component 2). Red lines are critical lines of the mixture; the red star is the upper critical end point of mixture G (UCEP). The green line depicts the VL_1L_2E three-phase line of mixture G. Arrows indicate the five temperatures investigated in this work, cf. Fig. 42 for the color coding.

the mixture first increases only slightly with decreasing temperature but then increases dramatically for temperatures below about $T = 0.715\,\varepsilon k_{\mathrm{B}}^{-1}$, which becomes also clear from the critical line depicted in Fig. 43.

Mixture G exhibits a VL_1L_2 three-phase equilibrium at temperatures below $T = 0.689\,\varepsilon k_{\mathrm{B}}^{-1}$, cf. Fig. 43. In the phase diagram, there is a VL_1 equilibrium region below the three-phase line, cf. Fig. 44. Above the three-phase line, there is a small region in which VL_2 equilibria exist and a large L_1L_2 equilibrium region.

The isothermal phase diagram of mixture G at $T = 0.715\,\varepsilon k_{\mathrm{B}}^{-1}$ is special, as in the single two-phase region that is observed at this temperature, at low pressures equilibria are found that can be classified as vapor-liquid equilibria, while at high pressures, the equilibria resemble liquid-liquid equilibria. The density transition between both types is smooth and can be found at pressures lying approximately on an extension of the three-phase line, cf. Fig. 43. This transition occurs at approximately $x_2^{L1} \approx 0.17\,\mathrm{mol\,mol^{-1}}$ for $T = 0.715\,\varepsilon k_{\mathrm{B}}^{-1}$. However, no isopycnic point [553] (both phases have the same density)
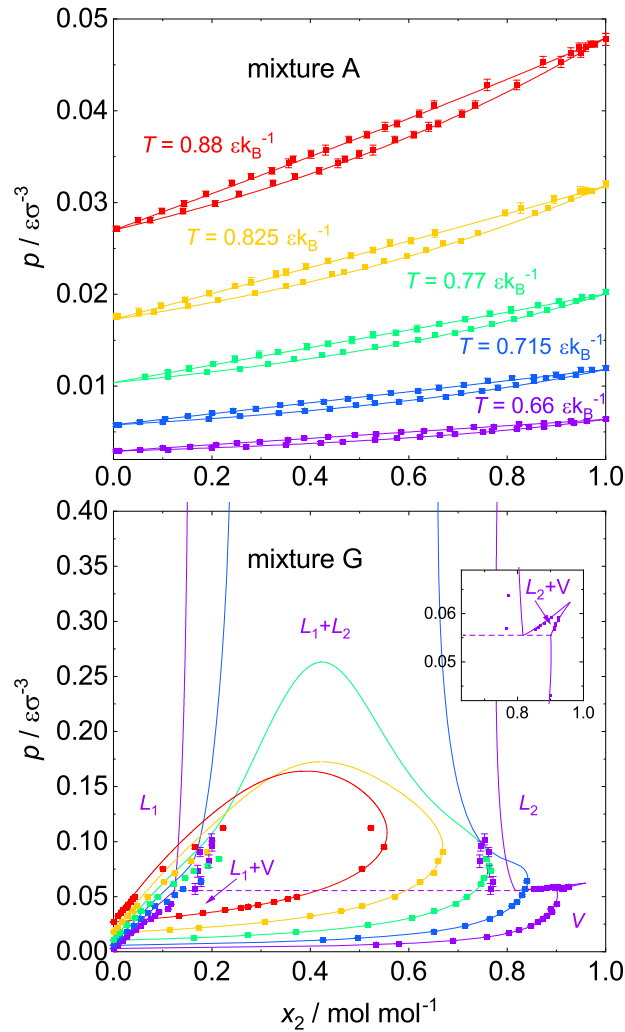
Figure 44: Isothermal $p-x$ phase diagrams for the mixture A and the mixture G at all five investigated temperatures. The temperatures in the top and bottom plot are color-coded using the same scale. Symbols are MD results and lines are the PeTS EOS. The one and two phase regions are labeled only for the lowest temperature $T = 0.66\,\varepsilon k_{\mathrm{B}}^{-1}$. The VL_1L_2 three-phase equilibrium is depicted as dashed line.

is observed in mixture G.

According to the $p-T$ diagram of mixture G (cf. Fig. 43), with increasing pressure the VL_1 region can either terminate at the three-phase line ($T = 0.66\,\varepsilon k_{\mathrm{B}}^{-1}$), be open ($T = 0.715\,\varepsilon k_{\mathrm{B}}^{-1}$), or end in a critical point ($T = 0.77,\ 0.825,\ 0.88\,\varepsilon k_{\mathrm{B}}^{-1}$).

Fig. 44 shows that the agreement between the results from the PeTS EOS and those from the computer experiments is excellent for the ideal mixture A for all temperatures that were studied. Also for the non-ideal mixture G, a good agreement is found in most cases. Exceptions are regions in the vicinity of critical points, and the compositions of the coexisting phases of the L_1L_2 liquid-liquid equilibria, where the EOS yields a miscibility gap which is broader than that obtained from MD. These deviations are probably a result of differences between the force field and the free energy model of the PeTS EOS, which may be due to the simplified expression that is used for the description

of the repulsive interactions in the EOS [66, 249, 639].

3.6.3 Results for the Interfacial Properties of Mixture A

The interfacial properties of mixture A are reported and discussed in this section. The chosen mixture parameters for the mixture A $\xi = 1$ and $\varepsilon_2/\varepsilon_1 = 0.9$ result in a basically ideal mixture in the sense of Raoult's law (cf. Fig. 44 a). The activity coefficients at infinite dilution are in all cases well below 1.1 in the entire temperature range studied here. This ideal behavior holds for the entire investigated temperature range. Both components are subcritical at all chosen temperatures.

Fig. 45 shows the density profiles of both components at the VL interface at $T = 0.66\,\varepsilon k_{\mathrm{B}}^{-1}$. As the density profiles at other temperatures do not provide further insight, they are only shown in the Appendix.
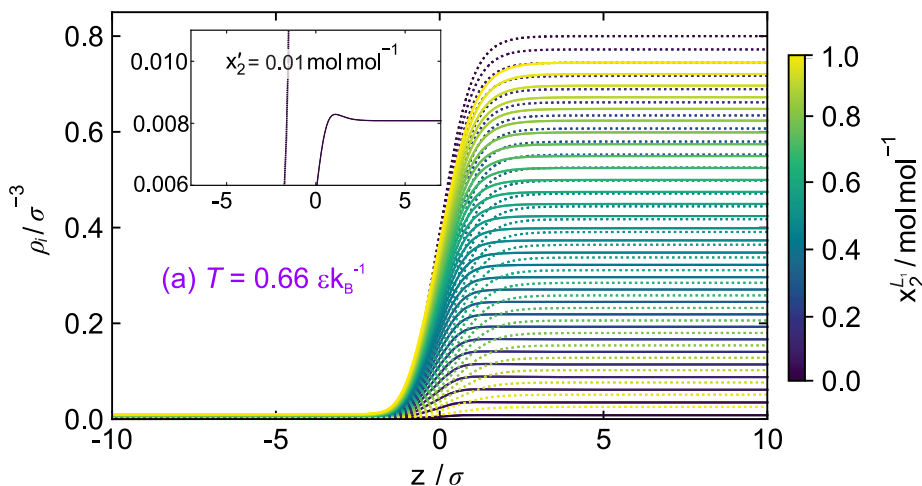
Figure 45: Density profiles of component 1 (dashed lines) and component 2 (full lines) for the mixture A at $T = 0.66\,\varepsilon k_{\mathrm{B}}^{-1}$ obtained by DGT. The color-code indicates the liquid phase composition.

At very low concentrations of component 2, a small but distinct enrichment of component 2 at the interface is found (cf. Fig. 45). This also holds for $T = 0.715\,\varepsilon k_{\mathrm{B}}^{-1}$ and $T = 0.77\,\varepsilon k_{\mathrm{B}}^{-1}$ (see Appendix).

Furthermore, a closer look reveals that the density profiles from component 2 are slightly shifted to $-z$ direction with respect to the density profile of the high-boiling component – at all concentrations but especially at high x_2^L. This is an indication that the component 2 adsorbs at the interface – even though no enrichment is present.

Fig. 46 shows the interfacial properties obtained from MD and DGT for the VL interface of mixture A at all five considered temperatures. Results for the surface tension, relative adsorption, enrichment, and interfacial thickness are shown. The surface tension of mixture A, starting at the pure component 1, decreases almost linearly with increasing x_2^L. This holds for all five investigated temperatures. The surface tension decreases with an increasing temperature, while the slope of the surface tension $\partial\gamma/\partial x_2^L$ does not depend on the temperature.
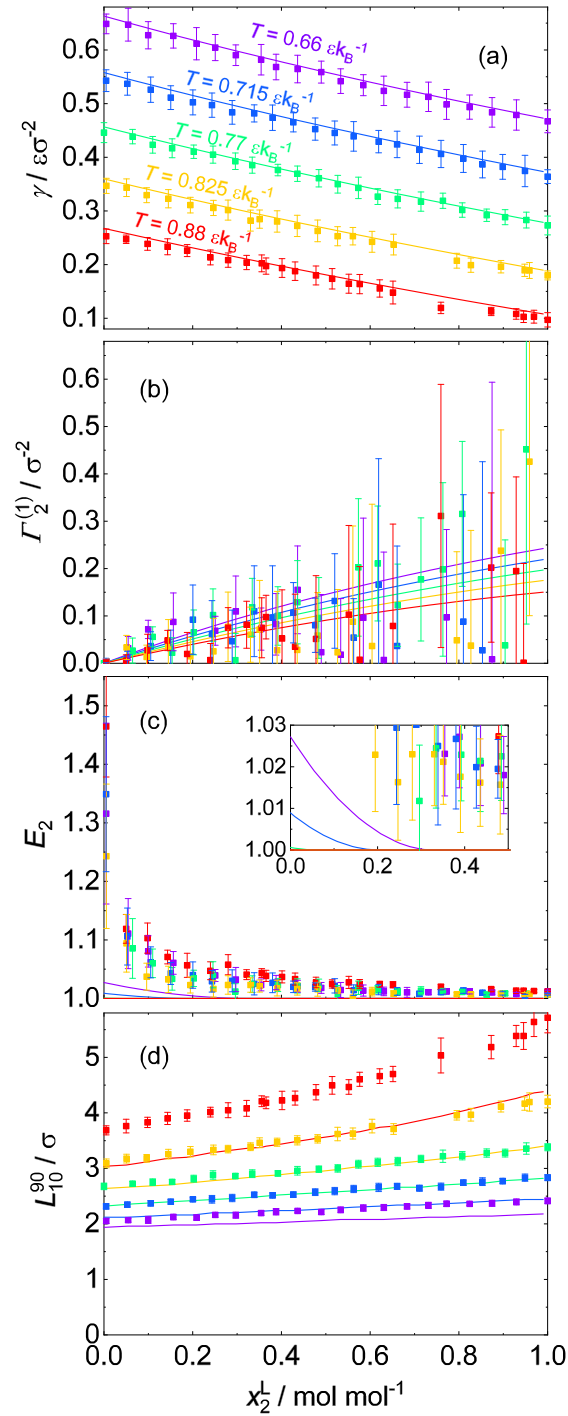
Figure 46: *VL* interfacial properties for mixture A: (a) surface tension γ, (b) relative adsorption of component 2 at the interface $\Gamma_2^{(1)}$, (c) enrichment of component 2 E_2, and (d) interfacial thickness L_{10}^{90}. Symbols are MD simulation results, lines are DGT results. Results for all studied temperatures. The color-code indicates the temperature and is the same for all shown plots.

The adsorption isotherms (Fig. 46 b) for the mixture A are almost linear with a slight concave curvature, which confirms the impressions from the density profiles. Since the relative adsorption and the decay of the surface tension $\partial \gamma / \partial x_2^L$ are linked via the Gibbs adsorption equation, also the temperature dependency of the relative adsorption is faint; the relative adsorption slightly increases with decreasing temperature. This can only be seen in the DGT results, as the scattering of the MD results exceeds this temperature influence on $\Gamma_2^{(1)}$.

For the mixture A the results predicted from DGT lie within the error bars of the MD results, even though the latter scatter intensely and have accordingly large error bars. This is simply due to the fact that the magnitude of the adsorption is relatively small.

As shown in the inset in Fig. 45 also the density profiles of component 2 in mixture A exhibit a slight maximum at the interface, i.e. enrichment $E_2 > 1$. Such an enrichment is only found at low temperatures and low liquid phase concentrations x_2^L, cf. Fig. 46 (c). This is in line with results from a previous study (cf. section 3.4) [630], which showed that the enrichment exhibits a continuous transition upon varying mixture parameters ξ and $\varepsilon_2 / \varepsilon_1$ at constant temperature and x_2^L. Even though MD seems to overestimate the enrichment in ideal mixtures compared to the theory, the present enrichment is probably not an artifact. The systematic overestimation of the enrichment obtained from MD compared to DGT results in the case of an insignificant enrichment has been attributed to the fact that outliers – in the not perfectly smooth density profiles from MD – will have a strong influence at very small values of E_2, cf. section 3.2.5 and Refs. [628, 630, 635] for a detailed discussion. This can also be seen at the strongly increasing error bars of the E_2 results at low liquid phase concentrations x_2^L in mixture A.

The interfacial thickness of mixture A (cf. Fig. 46 d) increases almost linearly between the two pure component values with varying x_2^L, which is similar to the surface tension behavior (cf. Fig. 46 a). However, an important difference can be observed: $\partial \gamma / \partial x_2^L$ does not change with varying temperature, whereas $\partial L_{10}^{90} / \partial x_2^L$ depends on the temperature. This is mainly due to differences in the pure component temperature dependency of the surface tension and the interfacial thickness, cf. chapter 2. As found in previous studies discussed in chapter 2 and sections 3.3 and 3.4, the PeTS+DGT results systematically underestimate the MD results.

3.6.4 Results for the Interfacial Properties of Mixture G

3.6.4.1 VL_1 Interfaces

Fig. 47 shows the VL_1 density profiles of mixture G for all five temperatures that were studied here in the entire composition range. Only DGT results are shown, which agree well in all cases with the MD results (see Appendix).

In contrast to the ideal mixture A, the VL_1 density profiles of component 2 of mixture G exhibit a distinct maximum at all temperatures, i.e. enrichment is observed. This maximum is most prominent at the lowest investigated temperature and decreases with an increasing temperature. The interfacial thickness increases with increasing temperature, which becomes clear from the density profiles of component 1 and the width of the enrichment peak shown in Fig. 47. The density profiles at the three highest studied

Figure 47: VL_1 density profiles of component 1 (dashed lines) and component 2 (full lines) for the mixture G obtained by DGT. Results for all studied temperatures. The color-code indicates the liquid phase composition. Red squares indicate invariant intersection points of density profiles of component 1.
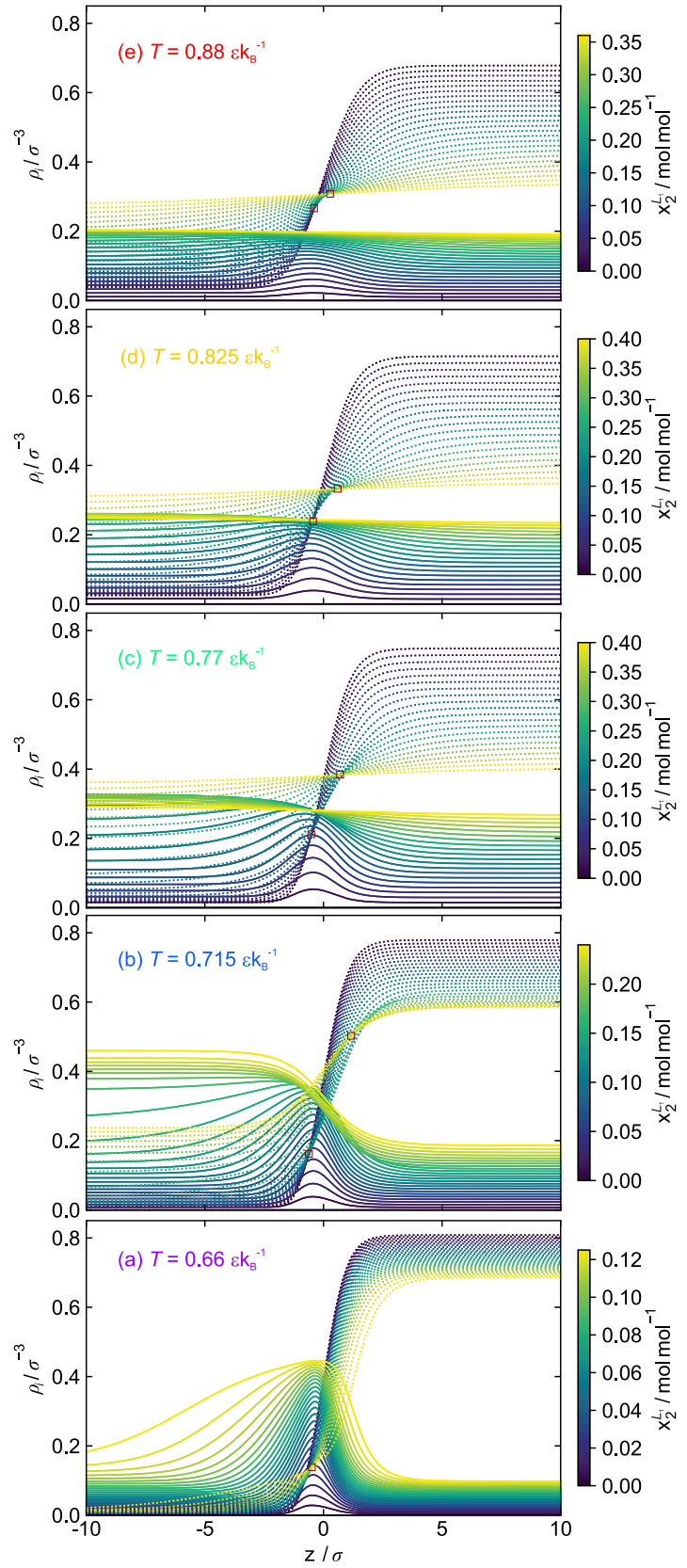
temperatures are similar, those for the two lowest show a distinctly different behavior. This is in line with the differences in the phase diagrams that were obtained for the five temperatures, see Fig. 44 - bottom. For the higher three temperatures, the VL_1E region terminates in a critical point, which is not the case for the lower two temperatures.

For the density profiles at the three higher temperatures ($T = 0.77\,\varepsilon k_{\mathrm{B}}^{-1}$, $0.825\,\varepsilon k_{\mathrm{B}}^{-1}$, and $0.88\,\varepsilon k_{\mathrm{B}}^{-1}$), the enrichment vanishes upon approaching the critical point. Hence, both component density profiles become – as expected at a critical point – horizontally flat. For $T = 0.715\,\varepsilon k_{\mathrm{B}}^{-1}$, the enrichment vanishes as the pressure increases and the vapor phase density increases significantly. For $T = 0.66\,\varepsilon k_{\mathrm{B}}^{-1}$, the enrichment is most prominent and furthermore remains present in the entire composition range up to the VL_1L_2E, cf. Fig. 44. The interfacial structure in the vicinity of the VL_1L_2E is discussed in detail in the next section. The enrichment decreases with increasing temperature but does not fully vanish.

For all five temperatures, the enrichment peak is fairly symmetric at low mole fractions x_2^{L1} of the component 2 in the liquid phase L_1, i.e. for VL_1 equilibria close to the boiling point of the pure component 1. Also, the z-position of the peak does not change for low x_2^{L1}. For high x_2^{L1}, the position of the enrichment peak slightly moves towards the vapor phase. The position of the maximum of the enrichment remains fairly constant upon varying composition and temperature, even when the topology of the phase diagram changes, compare Fig. 47 with Fig. 43. The peak position is approximately at $z(\rho_{\mathrm{max}}) \simeq -\sigma$ in the coordinates that are used here (cf. section 3.2.5). As also reported before, e.g. Refs. [50, 635], no enrichment is found for the high-boiling component in the entire investigated temperature and composition range.

For mixture A, no significant non-monotonic behavior of the density profiles of the two components was found in the entire investigated temperature and composition range. It is noted, however, that at very low temperature and very low concentrations x_2^{L1}, slight maxima in the density profiles $\rho_2(z)$ of component 2 were observed (see above).

For mixture G, some of the density profiles exhibit one or even two invariant common intersection points, which are indicated in Fig. 47. The common intersection points of all examined phase equilibria in this study are discussed in section 3.6.4.4.

Fig. 48 (a) - (d) shows the results that were obtained for the surface tension γ, the relative adsorption $\Gamma_2^{(1)}$, and the enrichment of the low-boiling component E_2, as well as the interfacial thickness of the mixture G in the VL_1E region. Results from both MD and DGT are shown. The results for mixture G are plotted analog to Fig. 46, which shows the results for mixture A.

The surface tension results from DGT lie within the error bars of the MD results for all but one state point for the ideal mixture A (cf. Fig. 46 (a). The agreement is less good for mixture G, cf. Fig. 48 (a), but considering the fact that both methods are independent predictions, the agreement is fair. Deviations increase with decreasing temperature and increasing x_2^{L1}. The DGT results systematically underestimate the molecular simulation surface tensions for such state points. These deviations are likely due to deviations between the PeTS EOS and the LJTS force field since deviations for these state points are also found for the phase behavior, cf. Fig. 44.

Starting at the pure component 1, the VL_1 surface tension γ of the mixture G first decreases linearly with increasing x_2^{L1} at all investigated temperatures. The slope of the
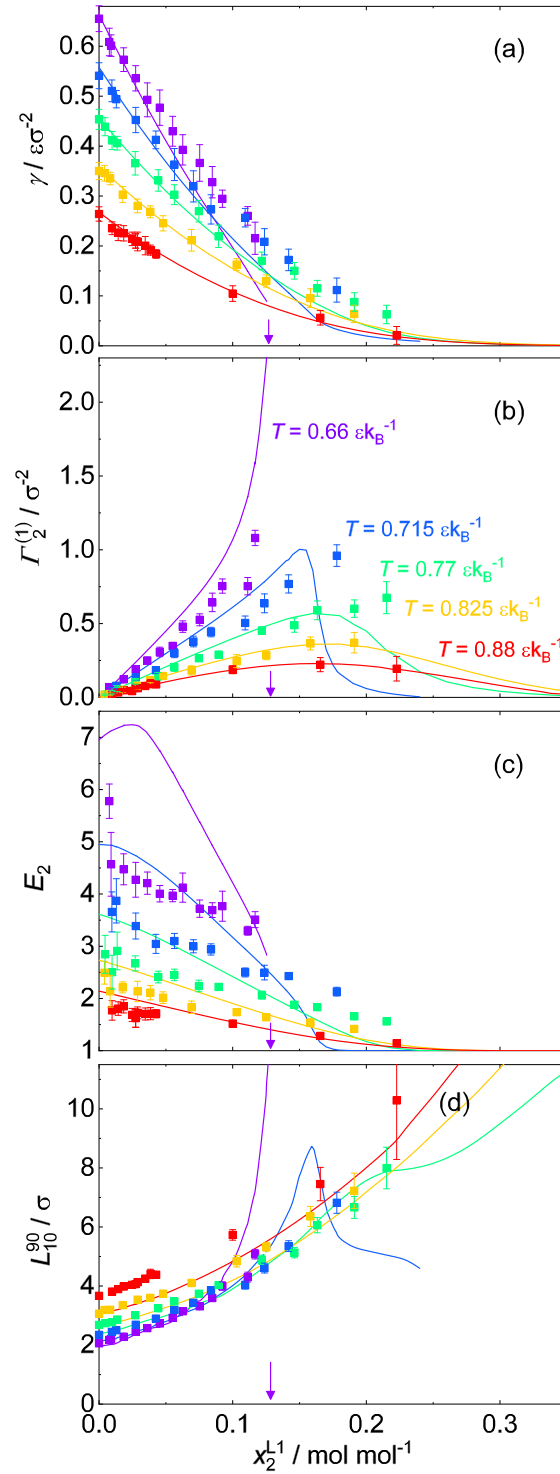
Figure 48: VL_1 interfacial properties for mixture G: (a) surface tension γ, (b) relative adsorption of component 2 at the interface $\Gamma_2^{(1)}$, (c) enrichment of component 2 E_2, and (d) interfacial thickness L_{10}^{90}. Symbols are MD simulation results, lines are DGT results. Results for all studied temperatures are shown. The color-code indicates the temperature and is the same for all plots. The arrow indicates the composition of phase L_1 in the three-phase equilibrium at $T = 0.66\,\varepsilon k_B^{-1}$.

VL_1 surface tension increases with decreasing temperature, which is due to an adsorption of the low-boiling component at the interface following the Gibbs adsorption equation. At $T = 0.66\,\varepsilon k_{\mathrm{B}}^{-1}$, the surface tension decay remains fairly linear until the three-phase equilibrium is reached (small purple arrow). The results for the isotherm $T = 0.715\,\varepsilon k_{\mathrm{B}}^{-1}$ are special, as for that isotherm a transition of the phase equilibria from vapor-liquid-like to liquid-liquid-like occurs, as explained above. For the four higher temperatures, $\gamma(x_2^{L1})$ becomes convex at high x_2^{L1} and falls to zero at the critical point. This is a remainder of the three-phase equilibrium at $T < T_{\mathrm{UCEP}}$ and the fluid-fluid equilibrium at $T > T_{\mathrm{BICEP}}$.

The surface tension of the mixture A has a much simpler behavior: the decay of the surface tension from the pure component 1 to component 2 is practically linear in the entire temperature and composition range (see section 3.6.3).

Fig. 48 (b) shows the adsorption isotherms $\Gamma_2^{(1)}(x_2^{L1})$ for the mixture G in the VL_1E region obtained from MD and DGT. The results from both methods agree qualitatively well in all cases – as found for the mixture A in section 3.6.3. The agreement is excellent for the higher temperatures but less favorable for the lower temperatures. Furthermore, the deviations increase with increasing x_2^{L1}.

All VL_1 adsorption isotherms for the mixture G have in common that, starting at infinite dilution of the component 2, the relative adsorption $\Gamma_2^{(1)}$ first increases with increasing x_2^{L1}. The adsorption isotherms at $T/\varepsilon k_{\mathrm{B}}^{-1} = 0.715$, 0.77, 0.825, 0.88 exhibit a maximum; for the three highest temperatures, the mixtures' phase envelope has a critical point, at which the relative adsorption $\Gamma_2^{(1)}$ vanishes. Such adsorption isotherms are usually found in systems with one supercritical component and a single critical point [16, 33, 50, 116, 624, 635, 692]. The adsorption isotherm for $T = 0.715\,\varepsilon k_{\mathrm{B}}^{-1}$ converges to zero with increasing x_2^{L1} or p, even though the corresponding phase diagram does not possess a critical point, cf. Fig. 43. This is a result of the transition from the vapor-liquid-like behavior to liquid-liquid-like behavior on that isotherm. The adsorption isotherm for $T = 0.66\,\varepsilon k_{\mathrm{B}}^{-1}$ exhibits a pole at the composition in the liquid phase x_2^{L1} that corresponds to the three-phase equilibrium. Hence, component 2 adsorbs ($\Gamma_2^{(1)} > 0$) at the VL_1 interface in the entire temperature and composition range. The adsorption isotherms in mixture G exhibit values approximately an order of magnitude larger than those in mixture A at low temperatures. However, at high temperatures, both mixtures have similar values for $\Gamma_2^{(1)}$, e.g. for the isotherm $T = 0.88\,\varepsilon k_{\mathrm{B}}^{-1}$ the relative adsorption is in both cases in the range of $\Gamma_2^{(1)} = 0\,..\,0.2\,\sigma^{-2}$.

Fig. 48 (c) depicts the enrichment of the low-boiling component E_2 at VL_1 interfaces of mixture G. The enrichment predicted from MD and DGT agrees qualitatively well for both mixtures, but significant deviations are observed. DGT predicts a larger enrichment than MD for mixture A. These differences might be caused by fluctuations that are present in MD but not in DGT [50, 635, 637], but could also be caused by differences between the PeTS EOS and the LJTS force field. The deviations between DGT and MD increase with decreasing temperature (larger E_2). This might be due to the fact that large enrichment at the interface is more sensitive to fluctuations than small enrichment.

For mixture G, values of up to about $E_2 = 7$ are found for the VL_1 interfacial enrichment (cf. Fig. 48 b), which is remarkable considering the fact that it is a simple dispersively

interacting system. We have shown in a previous work [630] that the difference of the component 2 bulk density $\Delta \rho_2 = \rho_2^L - \rho_2^V$ has an important influence on the enrichment E_2 (see the Appendix for more information). For $\Delta \rho_2 = 0$, any adsorption at a vapor-liquid interface – required to satisfy the Gibbs adsorption equation – contributes to the enrichment for geometric reasons, cf. section 3.4. For all state points studied in the present work, $\Delta \rho_2$ was computed and is shown in the Appendix. For mixture G, $|\Delta \rho_2|$ is small, which favors the large enrichment found at the VL_1 interfaces.

A further interesting finding is that at $T = 0.66 \, \varepsilon k_{\mathrm{B}}^{-1}$, the function $E_2(x_2^{L1})$ shows a non-monotonic behavior: starting at low x_2^{L1}, it first increases and then, after passing a maximum, decreases. Such a behavior has to the best of our knowledge not been reported before in the literature. The commonly reported behavior [50, 624, 635] of E_2 is a monotonic decay with increasing x_2^{L1}, as observed for all other temperatures for the mixture G.

Mixture A shows much lower values for the enrichment E_2 than mixture G (see section 3.6.3). The enrichment E_2 that is predicted for mixture A by DGT does not exceed $E_2 = 1.05$; values up to about $E_2 = 1.3$ are predicted by MD, whereas mixture G yields an enrichment up to $E_2 = 7$.

Fig. 48 (d) shows the VL_1 interfacial thickness L_{10}^{90}, cf. Eq. (46), for mixture G. The results from DGT and MD agree qualitatively well, but, as discussed in section 2.3 for the pure LJTS substance and sections 3.3 and 3.4 for binary LJTS mixtures, the interfacial thickness obtained from DGT is systematically smaller than that from MD by about 15%. This has been attributed to fluctuations of the interface present in MD that are not present in DGT [50, 635, 637]; maybe also differences between the PeTS EOS and the LJTS force field play a role [628, 630], cf. chapter 5.

For the upper three temperatures – above the bicritical endpoint – shown in Fig. 48 (d), the interfacial thickness L_{10}^{90} increases monotonously with increasing x_2^{L1}. This increase is expected to continue up to the critical point where L_{10}^{90} diverges. The behavior of L_{10}^{90} that is observed at the lowest temperature $T = 0.66 \, \varepsilon k_{\mathrm{B}}^{-1}$ is highly interesting. Here, L_{10}^{90} diverges upon approaching the VL_1L_2 line, i.e. when x_2^{L1} approaches the composition of the phase L_1 in the three-phase equilibrium. This is discussed and explained in the next section.

Also the maximum of L_{10}^{90} that is observed for $T = 0.715 \, \varepsilon k_{\mathrm{B}}^{-1}$ is directly related to the corresponding phase diagram. The liquid phase composition $x_2^{L1} \approx 0.17 \, \mathrm{mol \, mol^{-1}}$ of the L_{10}^{90} maximum at $T = 0.715 \, \varepsilon k_{\mathrm{B}}^{-1}$ corresponds to the transition of the vapor phase to a 'liquid-like' phase. This goes in hand with a drop of the relative adsorption of component 2 at the interface and a kink in the enrichment $E_2(x_2^{L1})$, cf. Fig. 48 (b). this transition can also be seen in the density profiles, cf. Fig. 47 (b).

3.6.4.2 VL_1, VL_2 and L_1L_2 Interfaces Adjacent to the VL_1L_2E

Below the temperature of the upper critical end point UCEP (cf. Fig. 43), the mixture G exhibits a three-phase VL_1L_2 equilibrium in the phase diagram. Three two-phase equilibrium regions are connected to that VL_1L_2E line: VL_1E, VL_2E, and L_1L_2E (cf. Fig. 44). On the three-phase line, there are three fluid interfaces VL_1, VL_2, and L_1L_2. Their surface tensions determine the wetting behavior of the three-phases, as

discussed in more detail in the literature [127, 132, 447, 573]. The three surface tensions are related by [573]

$$\gamma_{VL1} \leq \gamma_{VL2} + \gamma_{L1L2}, \tag{63}$$

where the equality indicates total wetting (plane layer of phase L_2 between L_1 and V) and the inequality indicates partial wetting of the phase L_2 (droplets of phase L_2 on the phase L_1). While interfacial properties and their relation to the wetting behavior directly on three-phase lines have been reported in the literature [127, 142, 143, 195, 354, 447, 655, 656], only *Falls et al.* [173] discuss features of density profiles in the adjacent two-phase regions. Therefore, we have carried out a systematic study of the transitions of the interfacial properties in the two-phase regions in the vicinity of the three-phase line in mixture G. Together with these results we discuss the VL_2 and L_1L_2 interfaces in general.

The vapor pressure and phase compositions of the three-phase equilibrium of mixture G at $T = 0.66\,\varepsilon k_{\mathrm{B}}^{-1}$ were calculated from the PeTS EOS: $p^s = 0.555\,\varepsilon\sigma^{-3}$, $x_2^{L1} = 0.124\,\mathrm{mol\,mol}^{-1}$, $x_2^{L2} = 0.817\,\mathrm{mol\,mol}^{-1}$, $x_2^{V} = 0.901\,\mathrm{mol\,mol}^{-1}$. The three corresponding total number densities are: $\rho^{L1} = 0.78\,\sigma^{-3}$, $\rho^{L2} = 0.51\,\sigma^{-3}$, and $\rho^{V} = 0.17\,\sigma^{-3}$.

Fig. 49 shows the density profiles at fluid interfaces of VL_1E, VL_2E, and L_1L_2E in the vicinity of the three-phase VL_1L_2 equilibrium at $T = 0.66\,\varepsilon k_{\mathrm{B}}^{-1}$. As discussed above, a large enrichment is found for VL_1 interfaces. Upon approaching the VL_1L_2E, the enrichment peak of the VL_1 interface changes its shape dramatically: while there are only small changes on the L_1 liquid side of the peak, the vapor side V undergoes a transition upon which the peak becomes much broader. This leads to an extremely high adsorption and interfacial thickness in the vicinity of the VL_1L_2E. This transition can be interpreted as a precursor of the second liquid phase L_2. The second liquid phase L_2 starts growing out of the interface before the VL_1L_2E is reached, which can be considered as a wetting transition upon which the adsorption $\Gamma_2^{(1)}$ increases drastically. Furthermore, the density profile of the high-boiling component 1 undergoes a transition (cf. Fig. 49 b), which is in line with the interpretation of a new phase growing at the interface upon approaching the VL_1L_2E.

Interestingly, the enrichment in the VL_1E region is already present at infinite dilution and grows with increasing x_2^{L1} to become eventually the L_2 phase at the three-phase equilibrium. Furthermore, an enrichment in the VL_1E region is also present at temperatures $T > T_{\mathrm{UCEP}}$, where no VL_1L_2E occur.

From the density profiles at $T = 0.66\,\varepsilon k_{\mathrm{B}}^{-1}$ close to the three-phase VL_1L_2E, the density and composition of the enrichment peak can be determined roughly as: $\rho^{\mathrm{peak}} \simeq 0.51\,\sigma^{-3}$ and $x_2^{\mathrm{peak}} \simeq 0.81\,\mathrm{mol\,mol}^{-1}$. This local composition and total number density at the enrichment peak agrees very well with the composition and density of the second liquid phase L_2 in the VL_1L_2E at $T = 0.66\,\varepsilon k_{\mathrm{B}}^{-1}$ (see above). Hence, the enrichment of the component 2 at the interfaces in the VL_1 two-phase region can be considered as the nucleation of the L_2 phase – starting already at infinite dilution of component 2. This interpretation is in line with the picture evoked by *Falls et al.* [173].

The fluid interfaces in the three two-phase regions (VL_1E, VL_2E, and L_1L_2E) have strongly differing features, cf. Fig. 49. The interfaces in the VL_1E region exhibit an enrichment of the low-boiling component, whereas the VL_2E region density profiles of both components show a monotonous transition between the bulk phases. Finally, in
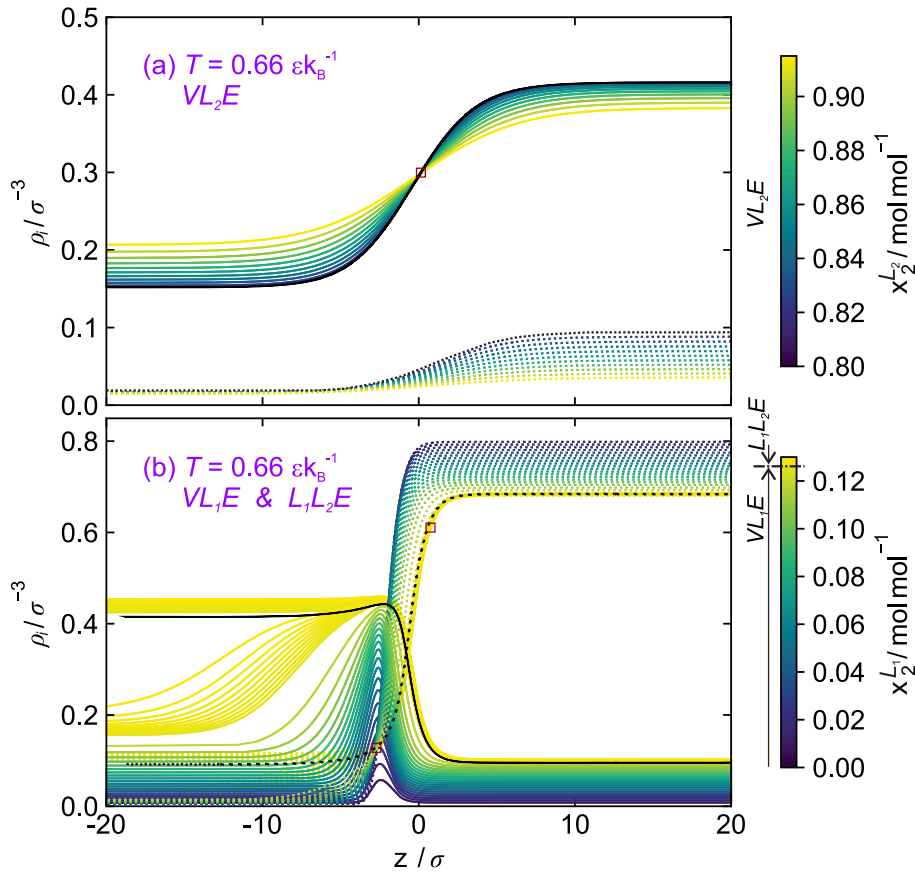
Figure 49: Density profiles of different fluid interfaces for the binary mixture G at $T = 0.66\,\varepsilon k_{\mathrm{B}}^{-1}$ in the vicinity of the three-phase equilibrium. (a) shows the VL_2E two-phase region (V left, L_2 right); (b) the VL_1E (V left, L_1 right) and L_1L_2E (L_2 left, L_1 right) region. Dashed lines stand for the high-boiling component 1 and solid lines for the low-boiling component 2. The color-code represents the liquid phase composition. The black lines indicate the density profiles of the three-phase equilibrium. Red squares indicate invariant intersection points of the density profiles.

the L_1L_2E region, a small enrichment is observed in the vicinity of the three-phase equilibrium, cf. Fig. 49 (b).

Fig. 50 shows the interfacial properties (surface tension, relative adsorption, enrichment, and interfacial thickness) of mixture G at $T = 0.66\,\varepsilon k_{\mathrm{B}}^{-1}$ for the VL_1, VL_2, and L_1L_2 interfaces in the vicinity of the VL_1L_2 three-phase equilibrium. The properties of the VL_1 interfaces have already been discussed above.

The VL_2 interfaces show an unexpected behavior: the surface tension and the relative adsorption are very small, and no enrichment is observed. This may be related to the proximity of the critical point in that small two-phase region. In line with this interpretation, the interfacial thickness is large. As expected, it increases upon approaching the critical point. The predictions of the VL_2 interfacial properties obtained by DGT and MD are in fair agreement.

For the L_1L_2 interfaces, the discrepancies between the predictions of the interfacial
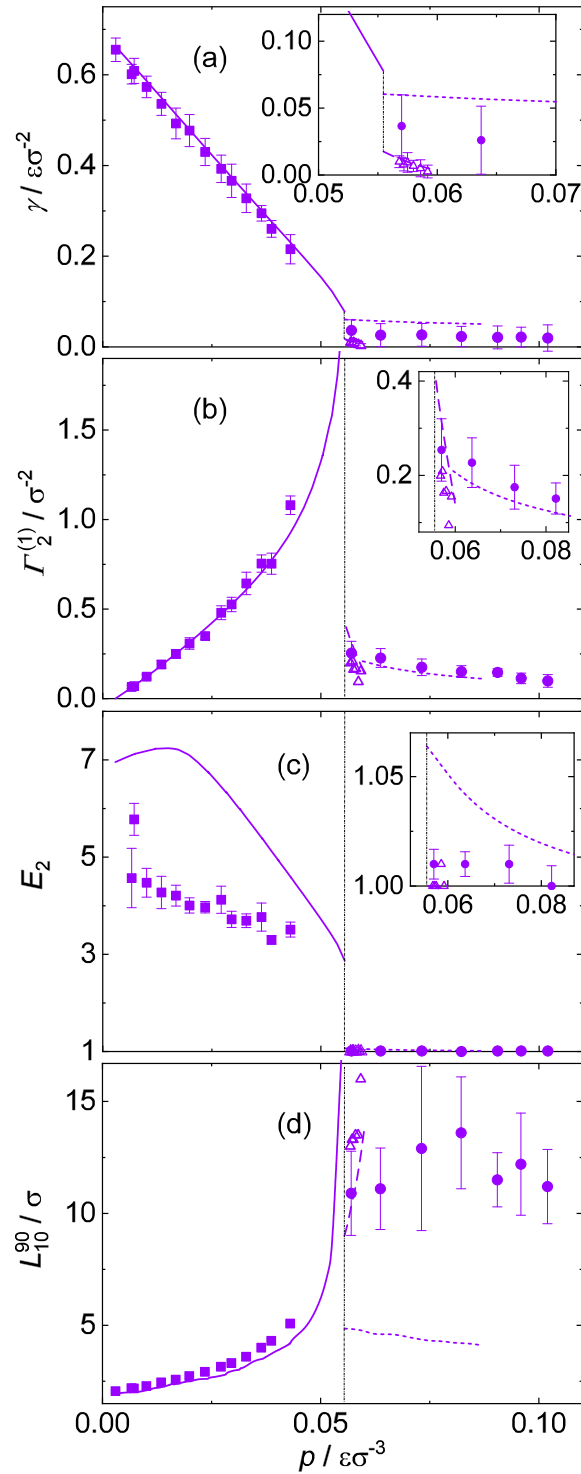
Figure 50: Interfacial properties of the mixture G at $T = 0.66\,\varepsilon k_{\mathrm{B}}^{-1}$ in the vicinity of the three-phase equilibrium as a function of the pressure. Top to bottom are: surface tension, relative adsorption, enrichment of component 2, and interfacial thickness. Symbols are the MD simulation results, lines are DGT results. Solid lines and squares depict the VL_1E region (left side in the diagrams), dotted lines and circles the L_1L_2E region, and dashed lines and triangles the VL_2E region (right side in the diagrams). The black vertical line indicates the VL_1L_2E pressure.

properties obtained from the two methods are larger. This is not astonishing, as there were also discrepancies in the predictions of the bulk phase behavior, cf. Fig. 44. Both methods predict a small surface tension. Again, the enrichment E_2 predicted by DGT is substantially larger than that predicted by MD. However, even for DGT, the maximal enrichment is only about $E_2 = 1.06$. Both methods predict fairly large numbers for the interfacial thickness L_{10}^{90}, but the numbers obtained from MD (about $12\,\sigma$) are again much higher than those obtained from DGT (about $5\,\sigma$). The $L_1 L_2$ surface tension, relative adsorption, and interfacial thickness decrease with increasing pressure.

For all three types of interfaces (VL_1, VL_2, and $L_1 L_2$) in the vicinity of the three-phase equilibrium, the relative adsorption $\Gamma_2^{(1)}$ is highest directly at the three-phase equilibrium and decreases upon moving away from it, cf. Fig. 50 (b). The three surface tensions at the three-phase equilibrium γ_{VL1}, γ_{VL2}, and γ_{L1L2} are directly linked by the wetting behavior of the phases in direct contact [127, 447, 573]. In the case of mixture G, the phase L_2 wets the VL_1 interface, i.e. $\gamma_{VL1} = \gamma_{VL2} + \gamma_{L1L2}$. Hence, a macroscopic layer of the phase L_2 will form between the phases L_1 and V at the three-phase equilibrium at $T = 0.66\,\varepsilon k_B^{-1}$, which is in line with predictions for simple mixtures of that type [127]. This is completely in line with the picture of a wetting transition described above.

As mentioned above, at $T = 0.715\,\varepsilon k_B^{-1}$, there is a transition of the vapor phase upon increasing pressure to a high density liquid-like phase in mixture G. Interestingly, also for this transition, the enrichment acts as a precursor, cf. Fig. 47 (b). Hence, the liquid-like phase starts forming at the interface in the VL_1 region.

3.6.4.3 $F_1 F_2$ Interfaces

Fig. 51 shows the phase behavior of mixture G at temperatures in the vicinity of the bicritical end point (BICEP) and up to very high pressures. At $T > T_{\mathrm{BICEP}}$, the $F_1 F_2$ fluid-fluid equilibrium region is separated from the $VL_1 E$ region. Hence, two critical points are present: the VL_1 equilibrium region has a pressure maximum critical point, the $F_1 F_2$ region a pressure minimum critical point. In the $F_1 F_2 E$ two high-density fluid phases F_1 and F_2 coexist. The $F_1 F_2 E$ is almost symmetric in the phase diagram – especially at high temperatures, cf. Fig. 51.

We have studied the $F_1 F_2$ interface at $T = 0.77\,\varepsilon k_B^{-1}$ and $T = 0.825\,\varepsilon k_B^{-1}$ with DGT. In preliminary MD simulation runs, stability problems due to the extreme pressures were observed in the employed NVT ensemble. Hence, only DGT results are available for the $F_1 F_2$ interfaces.

The obtained density profiles of the $F_1 F_2$ interfaces of both components are shown in Fig. 52. The corresponding results for the interfacial properties (surface tension, relative adsorption, and interfacial thickness) are shown in Fig. 53. The enrichment of both components at the interface is unity in the entire $F_1 F_2 E$ region and is therefore not plotted in Fig. 53. Starting at the $F_1 F_2 E$ critical point, the surface tension is zero and then increases with increasing pressure, cf. Fig. 53 (a). This is opposite to the surface tension dependency in the $L_1 L_2$ equilibrium region, cf. Fig. 50, where the surface tension decreases with increasing pressure. However, the temperature dependency of γ in the $L_1 L_2$ and $F_1 F_2$ equilibrium regions is the same, i.e. the surface tension decreases with increasing temperature. As for the $L_1 L_2 E$, the surface tension γ for the $F_1 F_2 E$ is small and does not exceed $0.06\,\varepsilon\sigma^{-2}$.
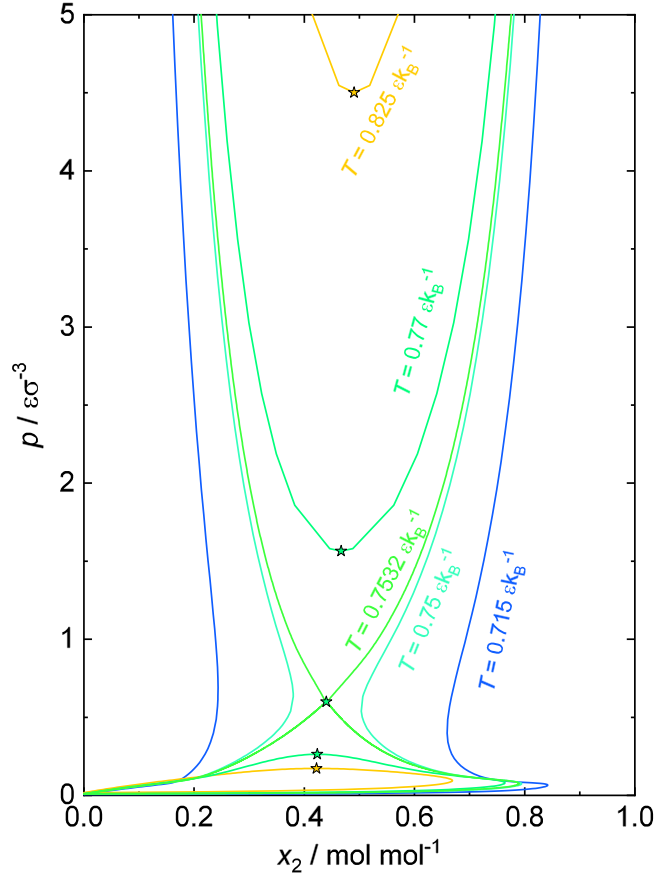
Figure 51: Isothermal $p - x$ phase diagrams for the mixture G at temperatures close to the bicritical endpoint ($T = 0.7532\,\varepsilon k_{\mathrm{B}}^{-1}$) and up to very high pressures. Results from the EOS. Stars indicate critical points.

Interestingly, in contrast to all other types of interfaces that were studied here, the $F_1 F_2$ interfaces are depleted of component 2 (negative values of $\Gamma_2^{(1)}$), cf. Fig. 53 (b). Starting at the $F_1 F_2 E$ critical point, the relative adsorption $\Gamma_2^{(1)}$ is zero and then decreases with increasing pressure. The absolute value of $|\Gamma_2^{(1)}|$ is two orders of magnitude smaller than the relative adsorption at the $L_1 L_2$ and $V L_1$ interfaces. Furthermore, $\Gamma_2^{(1)}(p)$ exhibits an interesting 'S'-shaped behavior, which is related to the particular structure of the $F_1 F_2$ interface that is described in more detail below.

The interfacial thickness of the $F_1 F_2$ interfaces diverges at the critical pressure and decreases with increasing pressure, cf. Fig. 53 (c). At constant pressure, L_{10}^{90} also increases with increasing temperature – as expected. The $F_1 F_2$ and $L_1 L_2$ interfaces have the same qualitative behavior for the relative adsorption and interfacial thickness – both decrease with increasing pressure.

Fig. 54 shows the density profiles at $F_1 F_2$ interfaces at $T = 0.77\,\varepsilon k_{\mathrm{B}}^{-1}$. The top plot shows the density profiles of the mixture at $p = 18.1\,\varepsilon\sigma^{-3}$: besides the profiles of the two individual components, also the total density profile is depicted for a single state point; the bottom plot shows the total density profile for different pressures. The $F_1 F_2$ interfaces are similar to the $L_1 L_2$ interfaces, cf. Fig. 54: Also for the $F_1 F_2$ interfaces, the total density of both bulk phases is high and approximately the same for both phases. The density profiles of both components $\rho_1(z)$ and $\rho_2(z)$ exhibit a monotonous
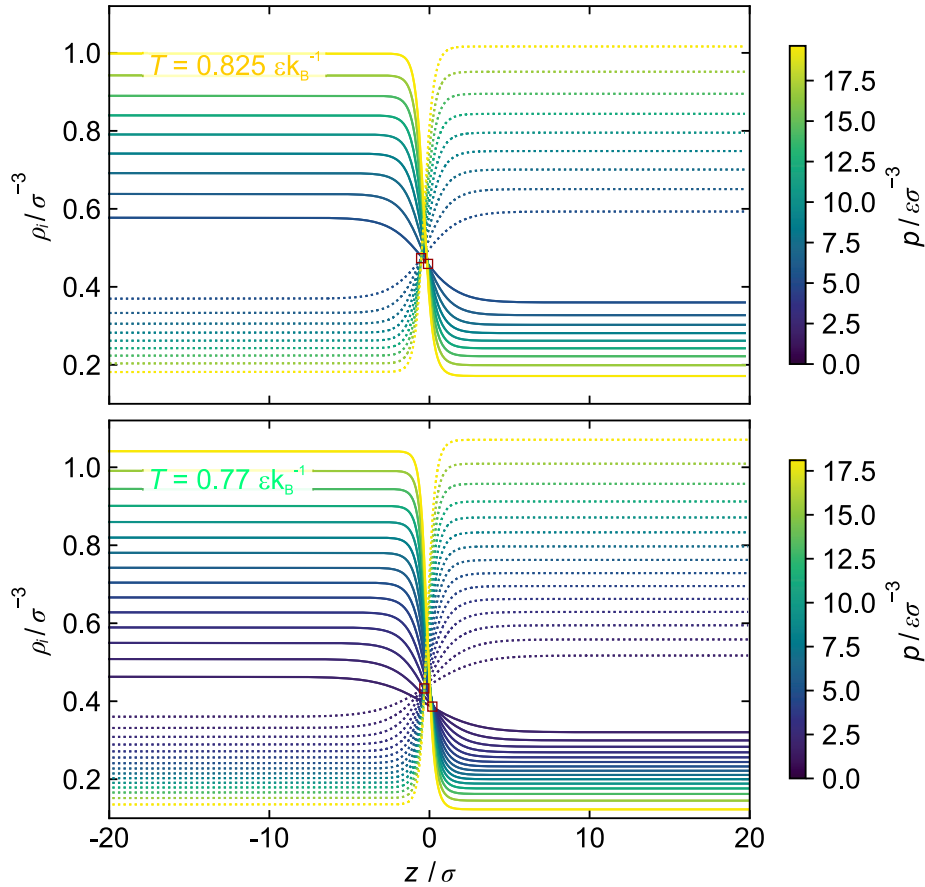
Figure 52: Density profiles of mixture G at $T = 0.77\,\varepsilon k_{\mathrm{B}}^{-1}$ (top) and $T = 0.825\,\varepsilon k_{\mathrm{B}}^{-1}$ (bottom) for the high pressure fluid-fluid $F_1 F_2$ equilibrium obtained from DGT. Dashed lines are the high-boiling component 1 and solid lines are the low-boiling component 2. The color is coded by the pressure. Red squares indicate invariant intersection points of density profiles.

transition between the bulk phases in both cases. This holds for the entire investigated temperature and pressure range. The density profiles of the two components 1 and 2 are almost symmetric, which is analogous to the symmetry of the underlying $p-x$ phase diagram.

However, the $F_1 F_2$ interfaces reveal an interesting phenomenon, which is not present in the other fluid interfaces examined in this study. Usually, the total density changes monotonously between the two bulk phases. This is also the case for the $F_1 F_2$ interfaces for moderate pressures. But for very high pressures, an oscillation is observed in the total density profile, cf. Fig. 54 - bottom. A single minimum in the total density profile has been reported before in the literature [141, 199, 204, 415, 490, 669], but to the best of our knowledge no maximum-minimum structure.

The oscillation structure found at the investigated $F_1 F_2$ interfaces in mixture G formally resembles the oscillatory layering structures [145, 170, 171, 204, 520, 637, 669] of other types of fluid interfaces, cf. section 2.4. But the single oscillation found here at $F_1 F_2$ interfaces is likely a different phenomenon, since DGT was employed for the calculations, which is not able to predict the common oscillatory layering structures [637]. It should be noted that this oscillation might be an artifact of the employed EOS type, which
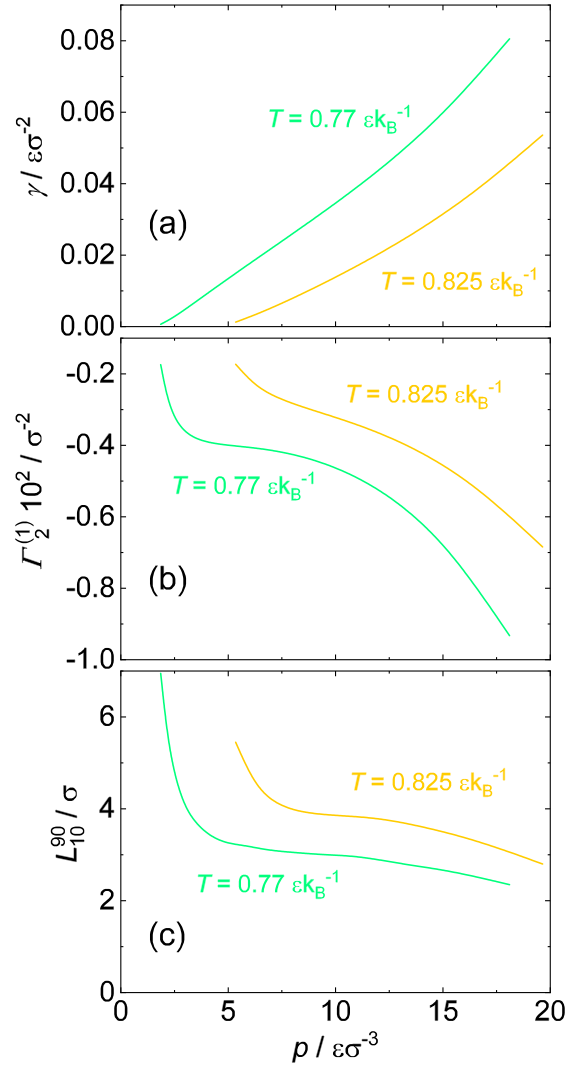
Figure 53: Interfacial properties of the mixture G at $T = 0.77\,\varepsilon k_{\mathrm{B}}^{-1}$ and $T = 0.825\,\varepsilon k_{\mathrm{B}}^{-1}$ for the high pressure fluid-fluid equilibrium $(F_1 F_2 E)$ as a function of the pressure. Top to bottom are: surface tension, relative adsorption, and interfacial thickness. Results from DGT. No enrichment was observed for either of the components, i.e. $E_i = 1$.

is known to exhibit difficulties at extreme pressures due to the simplified repulsive interaction term [66, 249, 639], cf. section 4.3. A detailed investigation of the oscillation observed at the $F_1 F_2$ interfaces would be an interesting topic for future work.
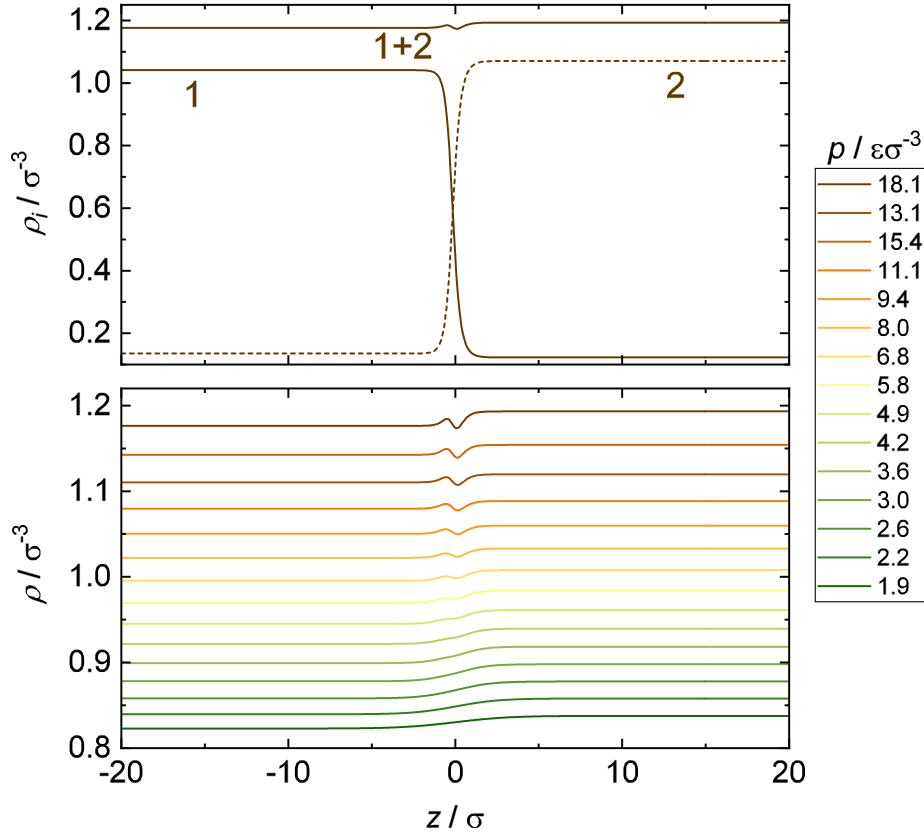
Figure 54: Density profiles of mixture G at $T = 0.77\,\varepsilon k_{\mathrm{B}}^{-1}$ for the high pressure fluid-fluid equilibrium ($F_1 F_2 E$). Results from DGT. The top plot shows the density profiles of component 1, component 2, and the total density $1 + 2$ at $p = 18.1\,\varepsilon\sigma^{-3}$. The bottom plot shows the total density $1 + 2$ at different pressures. The color-code indicates the pressure.

3.6.4.4 Invariant Intersection Points in Density Profiles

Invariant intersection points in the density profiles were observed for many fluid regions studied in this study, cf. Figs. 47, 49 and Fig. 52. The phenomenon of invariant intersection points has already been reported for pure substances [63, 637] and also simple binary model mixtures [635] as well as for real mixtures [624]. In section 2.3.4, an invariant intersection point in the density profiles of the pure LJTS fluid was observed for the results from several theoretical methods. In section 3.3.2, an invariant intersection point was observed for isothermal sets of density profiles of binary LJTS mixtures.

In these invariant intersection points, density profiles $\rho_i(z)$ of a component i intersect. These intersection points have been suspected to be related to critical points [63, 635, 637].

As also noted by *Bongiorno and Davis* [63], the invariant intersection points are not exact, which might be due to computational reasons, i.e. the discretization of the density profiles. Since the MD density profiles furthermore exhibit stochastic fluctuations, the intersection points can only be identified approximately in the respective plots (see Appendix). Their numeric values are not used for the following quantitative evaluation. However, the qualitative features of the invariant intersection points obtained from the

DGT and MD results are in all cases consistent.

Bongiorno and Davis [63] found that the invariant intersection point of the density profiles at different temperatures of the pure van der Waals fluid have the same density as the critical point density. The same was reported for the pure LJTS fluid [637], cf. section 2.3.4. As discussed below in more detail, similar observations are made in the present work for mixture G.

In this study, for VL_1 and L_1L_2 interfaces of mixture G, an intersection point was found for the high-boiling component 1, whereas for VL_2 interfaces, an intersection point was found for the low-boiling component 2. For F_1F_2 interfaces, intersection points were observed for the density profiles of both components. No intersection points were observed in the density profiles obtained for the ideal mixture A. The observations for the intersection points were in all cases consistent among the MD and the DGT results (see Appendix for MD density profiles). These invariant intersection points must have a physical cause, which is, however, presently unknown. Further investigations are needed to elucidate its cause. We limit ourselves to reporting our observations regarding the invariant intersection points and a brief discussion of their relation to the corresponding phase diagram. The discussion presents evidence that the invariant points are not only related to critical points but that some of them also seem to be related to states that can be considered to be an extension of the three-phase line.

Table 7 summarizes the findings on the invariant intersection points of the density profiles for mixture G as obtained from DGT. It also gives reference to the figures in which the corresponding profiles can be found. One or two invariant intersection points were observed in the density profiles of component 1 for the VL_1 and L_1L_2 interfaces. For VL_2 interfaces, one invariant intersection point in the density profile of component 2 was found. For F_1F_2 interfaces, an invariant intersection point was observed in the density profiles of both components. For cases with two invariant intersection points in the set of isothermal density profiles of a component (as observed for the VL_1 interfaces of mixture G at four temperatures (cf. Table 7) that set can can be split into two subsets. One subset going through the first intersection point and a second one going through the second intersection point. In all cases there is one density profile that belongs to both subsets, i.e. it approximately runs through both intersection points and connects them. That density profile is labeled with an asterisk here. There is a certain pressure p^* or liquid phase composition x_2^* associated with that density profile.

Table 7 shows that for phase equilibria in regions that have a critical point at least one of the component density profiles exhibits an invariant intersection point. The component density of that intersection point ρ_i^{IP} is in excellent agreement with the corresponding critical component density $\rho_{\mathrm{c},i} = x_i\rho_\mathrm{c}$ computed from the PeTS EOS, cf. Table 7. Such common intersection points are labeled here as type I. For the VL_1 component 1 density profiles at $T = 0.77\,\varepsilon k_\mathrm{B}^{-1}$, $0.825\,\varepsilon k_\mathrm{B}^{-1}$, and $0.88\,\varepsilon k_\mathrm{B}^{-1}$, the intersection point at $z > 0$ corresponds to the critical density $\rho_{\mathrm{c},1}$, i.e. is of type I. For the VL_2 component 2 density profiles, the invariant intersection point corresponds to the critical density $\rho_{\mathrm{c},2}$, i.e. it is also of type I. For the F_1F_2 interfaces, invariant intersection points are observed in the density profiles of both components and their densities are the same as the corresponding critical densities, $\rho_{\mathrm{c},1}$ and $\rho_{\mathrm{c},2}$, respectively. Also these sintersections points are of type I.

The type I intersection points include the density profile of the critical point. It follows

Table 7: Overview of invariant intersection points and critical point properties in the different fluid regions of mixture G as obtained from DGT and the PeTS EOS. The definitions of the fluid regions are given in the main body of this work, cf. section 3.6.2. The second column refers to the temperature of the respective set of density profiles. The column #IP indicates the number of invariant intersection points and the component profile ρ_i in which they were observed; the following column indicates the corresponding figure. The column #CP indicates the number of critical points present in the given fluid region and for the given T. The column ρ_i^{IP} reports the component density at the invariant intersection points of component i and the last column reports the corresponding critical component density $\rho_{\mathrm{c},i} = x_i \rho_{\mathrm{c}}$ computed from the PeTS EOS. The component-index i in the last two columns corresponds in all cases to the component density indicated in the column #IP.

Fluid region	$T/\varepsilon k_{\mathrm{B}}^{-1}$	#IP	Figure	#CP	$\rho_i^{\mathrm{IP}}/\sigma^{-3}$	$\rho_{\mathrm{c},i}/\sigma^{-3}$
VL_1	0.66	1x ρ_1	47 (a)	-	0.11	-
	0.715	2x ρ_1	47 (b)	-	0.16 & 0.5	-
	0.77	2x ρ_1	47 (c)	1	0.21 & 0.38	0.381
	0.825	2x ρ_1	47 (d)	1	0.24 & 0.33	0.330
	0.88	2x ρ_1	47 (e)	1	0.26 & 0.31	0.307
VL_2	0.66	1x ρ_2	49 (a)	1	0.30	0.299
L_1L_2	0.66	1x ρ_1	49 (b)	-	0.62	-
F_1F_2	0.77	1x ρ_1 & 1x ρ_2	52 (a)	1	0.43 & 0.38	0.433 & 0.380
	0.825	1x ρ_1 & 1x ρ_2	52 (b)	1	0.47 & 0.45	0.471 & 0.454

from this, that the component density at the intersection point of type I must be the critical density. However, nothing can be learnt from this argument about the physical cause for the existence of an intersection point. If this were the sole argument, the component density profiles might as well not intersect in phase equilibrium regions that contain a critical point.

It is noted here that the existence of invariant intersection points is related to the way $z = 0$ is defined for the density profiles, cf. section 3.2.5. The employed definition is based on the averaging of the two bulk densities. This is analogue to the definition of the rectilinear diameter, which is often used to determine the critical point [83, 468, 715, 731]. From this one might infer, that the invariant intersection points of type I that were observed here are related to the so-called 'law of the rectilinear diameter'.

As can be seen from Table 7, there are also intersection points that are not of type I, i.e. they do not contain a critical density profile, and the corresponding component density is not a critical density.

Let us first turn to the component density profiles that contain two invariant points (VL_1 at $T = 0.715\,\varepsilon k_{\mathrm{B}}^{-1}$, $0.77\,\varepsilon k_{\mathrm{B}}^{-1}$, $0.825\,\varepsilon k_{\mathrm{B}}^{-1}$, $0.88\,\varepsilon k_{\mathrm{B}}^{-1}$, cf. Table 7). The invariant point that is not of type I is labeled type II here. The density profiles belonging to the type I intersection point are in all cases those with the higher pressure; those belonging to the type II intersection point are those with the lower pressure. The transition (density profile * going through both points) takes place at the pressure $p^\star$. It is interesting to note that when the pressure $p^\star$ is plotted over the temperature T in the p,T-diagram of mixture G, an extension of the VL_1L_2E line is obtained (see Appendix).

The invariant intersection points of type II are always found at $z < 0$ whereas those of type I are found at $z > 0$. Interestingly, the z-position of the type II points in the density profile of component 1 matches the position of the enrichment peak in the density profile of component 2 very well.

All these findings indicate consistently that a relation may exist between the type II invariant intersection points, the enrichment, and the precursor of the second liquid phase as discussed in the main body of this paper. This leads to the following tentative classification: type I invariant points are related to critical points, type II invariant points are related to interfacial wetting by a precursor of a second liquid phase.

Following this classification, two of the four invariant points that were not discussed so far can also be assigned. There is a single invariant point in the $\rho_1(z)$ set in the VL_1 region of mixture G at $T = 0.66\,\varepsilon k_{\mathrm{B}}^{-1}$ (cf. Table 7). This invariant point is obviously related to the three-phase equilibrium and, hence, of type II. This can also be seen from a continuity argument: the density of the invariant points of type II in the VL_1 equilibrium region can be plotted as a function of temperature. As there is no critical point in the VL_1 equilibrium region at $T = 0.66\,\varepsilon k_{\mathrm{B}}^{-1}$, this invariant point is the only one and all profiles $\rho_1(z)$ go through that point.

Furthermore, there are two invariant intersection points in the $\rho_1(z)$ profiles in the VL_1 equilibrium region of mixture G at $T = 0.715\,\varepsilon k_{\mathrm{B}}^{-1}$. The one with the lower density is of type II, as can be deduced from the same continuity argument as given above. The other invariant point has a high density ρ_1. The state point of the * density profile at $T = 0.715\,\varepsilon k_{\mathrm{B}}^{-1}$ is found to agree well with the transition of the vapor phase to a dense liquid-like phase, cf. Fig. 47 (b) and section 3.6.2 for a discussion.

But as there is no upper critical point in the $T = 0.715\,\varepsilon k_{\mathrm{B}}^{-1}$ phase diagram, the ρ_1 'high density' invariant point cannot be assigned to type I. However, that invariant point resembles the invariant point in the $L_1 L_2$ region at $T = 0.66\,\varepsilon k_{\mathrm{B}}^{-1}$. Also in that fluid region, there is no upper critical point. We assign the latter two invariant points to a type III that, however, has similarities with type I.

3.6.5 Overview of the Findings

This study reports on properties of fluid interfaces of binary mixtures (density profiles, surface tension, relative adsorption, enrichment, and thickness) and their relation to the phase diagram. For this purpose, two Lennard-Jones mixtures were investigated with both molecular dynamics (MD) simulation and density gradient theory (DGT) at five temperatures in the entire range in which fluid phase equilibria exist. The low-boiling component 1 is the same in both mixtures. The high-boiling component 2 and the interaction parameters were chosen such that mixture G is a highly asymmetric non-ideal mixture of type III, in which component 2 is supercritical for all studied temperatures, whereas mixture A is an almost ideal mixture of type I with a subcritical component 2. For mixture A, only vapor-liquid equilibria (VLE) exist, whereas mixture G has a complex phase diagram with a three-phase equilibrium ($VL_1 L_2 E$), two vapor-liquid equilibrium regions ($VL_1 E$ and $VL_2 E$), and regions in which liquid-liquid equilibria ($L_1 L_2 E$), and fluid-fluid equilibria ($F_1 F_2 E$) exist.

The results that were obtained from MD and DGT for the interfaces agree well in most cases. Significant differences were, however, observed for $L_1 L_2$ interfaces and in the vicinity of critical points, which are most likely related to the fact that in these cases also the phase equilibria calculated from MD and from the EOS that was used in DGT show differences.

The ideal mixture A shows the expected behavior: the surface tension γ of the VL interfaces is dominated by the two pure substance values and decreases with increasing temperature; the same holds for the relative adsorption $\Gamma_2^{(1)}$, which is moderate ($\Gamma_2^{(1)} < 0.4\,\sigma^{-2}$). There is no significant enrichment ($E_2 = 1$), i.e. the density profiles in the interfacial regions are monotonous, except very shallow maxima that were observed at the low temperatures. The thickness of the interface L_{10}^{90} increases with increasing temperature and is in the range of 2 to $5\,\sigma$. There is a smooth transition of L_{10}^{90} between the pure component values.

For mixture G, the results that were obtained for the different types of phase equilibria differ significantly and important mixture effects are observed. The complex phase behavior of mixture G causes not only a complex behavior of the surface tension, but also the density profiles at interfaces have complex structures, with wetting transitions, common intersecting points, maxima, and in some cases even minima.

The $VL_1 E$ region in the isothermal phase diagram of mixture G has varying topologies depending on the temperature: at the lowest studied temperature, it connects the boiling point of the pure component 1 with the $VL_1 L_2$ three-phase equilibrium, whereas at high temperatures it ends in a critical point. One intermediate temperature was studied where the phase envelope is open up to extreme pressures and exhibits a smooth transition of the vapor phase V to a high density liquid-like phase, which acts as the

transition between the L_1L_2E at lower temperatures and F_1F_2E at higher temperatures for that type III mixture [553]. All this has important consequences for the interfacial properties.

The phase diagram of mixture G has critical points of three different types. For all critical points, the behavior of the interfacial properties is as expected: the surface tension γ and the relative adsorption $\Gamma_2^{(1)}$ decay to zero, the enrichment E_2 goes to unity, and the thickness L_{10}^{90} goes to infinity upon approaching the critical point.

As for mixture A, also for mixture G typical values of the thickness L_{10}^{90} are between 2 and $5\,\sigma$ for state points that are far away from critical points and VL_1L_2E. This holds for all types of phase equilibria of mixture G.

The fluid-fluid interfaces F_1F_2 of mixture G have small surface tension ($\gamma < 0.1\,\varepsilon\sigma^{-2}$) but a negative relative adsorption ($\Gamma_2^{(1)} < 0$). An interesting phenomenon was observed in the density profiles of the F_1F_2 interfaces: Even though the density profiles of both components 1 and 2 are monotonous (i.e. $E_1 = E_2 = 1$), a non-monotonicity in the total density profile with a minimum and a maximum was observed for several state points. This phenomenon cannot be interpreted as a layering structure of the fluids near surfaces, as it is usually predicted by DFT, as it was found by DGT, which cannot yield these layering structures. Further research is needed to elucidate the cause of this interesting structure.

Also the liquid-liquid interfaces L_1L_2 obtained for mixture G have small surface tension ($\gamma < 0.1\,\varepsilon\sigma^{-2}$), but in contrast to the F_1F_2 interfaces, they have a small positive relative adsorption ($\Gamma_2^{(1)} < 0.3\,\sigma^{-2}$). The enrichment E_2 is in general close to unity, but near the VL_1L_2E, values up to about $E_2 = 1.06$ were found for L_1L_2 interfaces.

There is a small VL_2E region with a critical point in the phase diagram of mixture G, for which the differences in the composition and the density of the coexisting phases are fairly small throughout. This has the expected consequences: the surface tension γ is very small ($\gamma < 0.02\,\varepsilon\sigma^{-2}$), the interfacial thickness is large ($L_{10}^{90} > 10\,\sigma$), and there is no enrichment E_2. The relative adsorption $\Gamma_2^{(1)}$ is small and positive ($\Gamma_2^{(1)} < 0.3\,\sigma^{-2}$).

For VL_1E in mixture G with low mole fractions x_2^{L1}, i.e. near the boiling point of the pure component 1, simple trends are observed: the surface tension is similar to the pure component value ($\gamma < 0.65\,\varepsilon\sigma^{-2}$) and increases with decreasing temperature. The same holds for the relative adsorption, which is positive ($\Gamma_2^{(1)} < 0.5\,\sigma^{-2}$ for $x_2^{L1} < 0.05\,\mathrm{mol\,mol^{-1}}$). The enrichment E_2 is large and increases with decreasing temperature. Values $E_2 > 7$ were found, which is remarkable for a simple dispersive system. In contrast to the common finding that E_2 decreases as x_2^{L1} decreases, $E_2(x_2^{L1})$ has a maximum for the VL_1 interfaces of mixture G at the lowest studied temperature (where the VL_1L_2E exists). Such a feature has not been observed before. As expected, the interfacial thickness L_{10}^{90} increases with increasing temperature for the VL_1 interfaces.

For higher mole fractions x_2^{L1}, the differences between the different topologies of the VL_1E region become important for the interfacial properties: for the cases where the VL_1E region ends in a critical point, the trends are as expected: i.e., the surface tension γ and the relative adsorption $\Gamma_2^{(1)}$ simply decay to zero.

But for the case, in which the VL_1E region ends in the VL_1L_2 three-phase line, interesting phenomena are observed: as the conditions get closer to those of the VL_1L_2

three-phase equilibrium, a precursor of the second liquid phase L_2 forms at the VL_1 interface. This leads to a very strong increase of the relative absorption $\Gamma_2^{(1)}$ and the interfacial thickness L_{10}^{90}. The enrichment E_2 can be considered to be a precursor of the wetting present at the three-phase equilibrium. This interpretation is supported by the fact that the composition at the peak of the enrichment is in very good agreement with that of the second liquid phase L_2 even for conditions that are not close to the VL_1L_2E. Further support comes from the fact that the surface tensions obtained in the three-phase equilibrium are such that the phase L_2 wets the VL_1 interface at the considered temperature.

Some of the features described above for the VL_1E and L_1L_2E region in the phase diagram with a three-phase equilibrium VL_1L_2E are also observed for the isothermal phase diagram for which the VL_1E region is 'open' up to extreme pressures (no critical point) and the vapor phase eventually becomes liquid-like (and no VL_1L_2 three-phase equilibrium exist). Hence, for such temperatures, the relative adsorption $\Gamma_2^{(1)}$ and the interfacial thickness L_{10}^{90} show strong maxima at intermediate pressures. This is interpreted here as a consequence of the fact that the conditions are close to those of the three-phase equilibrium. In principle the observations made for the interfacial properties for 'open' VL_1E phase diagrams can be understood as a transition from what is found for the VL_1 interfaces close to the boiling point of pure component 1 (i.e. at low pressures) to what is found for F_1F_2 interfaces at high pressures. But this transition is not always monotonous. E.g. maxima are observed both for the relative adsorption $\Gamma_2^{(1)}$ and the interfacial thickness L_{10}^{90}, which can be understood as witnesses of the proximity of the VL_1L_2E, that however does not exist any more at those conditions.

The findings for the interfacial properties of mixture G cannot be understood without considering the corresponding phase diagrams. The most interesting observation from the present study is that, as the conditions get closer to those of the three-phase VL_1L_2E, a precursor of the second liquid phase L_2 forms at the VL_1 interface. This leads to a very strong increase of the relative adsorption $\Gamma_2^{(1)}$ and the interfacial thickness L_{10}^{90}. We argue that the strong enrichment that is observed at the VL_1 interface even at conditions that are not close to the three-phase equilibrium can be interpreted as such a precursor of the L_2 phase. These findings and interpretations are in line with those established in the literature for the wetting behavior of the phases in three-phase equilibria [127, 142, 143, 195, 354, 447, 655, 656] and also with the interpretation that *Falls et al.* [173] gave of their observations regarding density profiles in a similar system.

Furthermore, we assume that what was observed here for mixture G regarding the relation of the enrichment at VL_1 interfaces and the three-phase equilibrium can be generalized: our hypothesis is that a similar behavior will be observed in all systems that show three-phase VL_1L_2E; i.e. that high enrichment E_2 will be observed at the VL_1 interfaces in these systems in general. We also argue that generally the enrichment can be understood as a precursor of a second liquid phase L_2 that nucleates under the influence of the gradients at the interface. This does not mean that the existence of a three-phase equilibrium in a given system is a prerequisite for the occurrence of interfacial enrichment; but the presence of a three-phase equilibrium is assumed to strongly favor interfacial enrichment.

3.6.6 Conclusions

Binary Lennard-Jones truncated and shifted mixtures were comprehensively studied in a wide range of interaction parameters as well as thermodynamic conditions. The predictions of the employed theory (DGT+PeTS EOS) was found to be in good agreement with computer experiment results for the phase equilibrium and interfacial properties of binary LJTS mixtures. The focus was on the influence of the interaction parameters on the interfacial structure and the phase equilibrium.

The results from the present work show that the assumption of a temperature-independent influence parameter in DGT works very well even when a broad temperature range is investigated. Also the employed geometric mixing rule for the influence parameter yields excellent results even though the investigated mixture G is highly asymmetric.

An enrichment forming under the influence of the gradients at the interface was observed in many systems for the low-boiling component. Strong enrichment was found at low temperatures, low concentrations of the low-boiling component in the liquid phase, and a wide-boiling phase behavior. No enrichment was observed for the high-boiling component.

The results of the reported studies give insight into the relation between the phase behavior and the interfacial properties in many ways: regarding the critical points, which do not only lead to the well-known effects in their vicinity such as a decrease of the surface tension and the relative adsorption, but are also related to invariant common intersection points that are found in several isothermal sets of density profiles. Further research is needed to reveal the relation of these intersection points and the critical behavior. The results furthermore reinforce a relation of the azeotropic and aneotropic point [133, 184, 194, 195, 435].

For a mixture exhibiting a VLLE, a relationship between the enrichment at vapor-liquid interfaces and the wetting behavior at the three-phase line was established: the enrichment acts as a precursor of the second liquid phase nucleating under the influence of the gradients at vapor-liquid interfaces at conditions that are still far off the three-phase line. As the state point approaches the three-phase line, the enrichment grows into the vapor phase, which results in a strong increase in the interfacial thickness and the relative adsorption in the vicinity of VLLE.

4 Lennard-Jones Fluid: Simulation Data and Equations of State

4.1 Introduction

The Lennard-Jones (12,6) potential [303, 304] has been used extensively as a model of simple fluids with repulsive and dispersive interactions since the early days of computer simulation [15, 238, 431, 451, 555, 566, 677, 717]. It is probably the most frequently investigated monomer model fluid. The Lennard-Jones potential provides, as already stated by *Nicolas et al.* in 1979 [505], "a convenient model for testing liquid theories and for investigating such phenomena as melting, the liquid-vapor surface, nucleation etc.". This has not changed in the past four decades [194, 269, 275, 341, 440, 446, 565, 630, 637, 660, 663, 664]. Also, the Lennard-Jones potential is often used as a starting point for the development of many state-of-the-art force fields for complex molecules [2, 157, 351, 633]. It is often taken as a benchmark for the validation of simulation codes and the test of new simulation techniques. Despite its simplicity, the Lennard-Jones model fluid yields a realistic representation of simple fluids [576, 633]. Due to its importance, it is sometimes even referred to as *Lennard-Jonesium* [98, 104, 452] – suggesting that it is viewed as a chemical element [340].

The Lennard-Jones potential is defined as the pairwise additive and spherically symmetric potential

$$u_{\mathrm{LJ}}(r) = 4\varepsilon\left[\left(\frac{\sigma}{r}\right)^{12} - \left(\frac{\sigma}{r}\right)^{6}\right],\tag{64}$$

where r is the distance between two particles. Its parameters ε and σ characterize the size of the particles and the magnitude of their dispersive attraction, respectively. Simulations are usually performed with a truncated potential in combination with a long-range correction [17].

Different versions of the LJ potential are used in the literature depending on the treatment of the long-range interactions, which has an important influence on the thermodynamic properties [31, 148, 302, 413, 536, 600, 602, 603, 611, 628]. This chapter is limited to the 'full' Lennard-Jones potential, i.e. including long-range correction schemes [17]. The 'full' Lennard-Jones potential is referred to as LJ potential in the following.

Analytical model functions of the LJ fluid for the description of the thermodynamic properties, i.e. equations of state (EOS), are crucial for many applications, e.g. the development of theories for more complex fluids like polymers, electrolyte solutions and associating fluids. LJ EOS have been used successfully as base models for a *reference*

fluid to describe more complex fluids [57, 58, 102, 128, 353]. A large number of equations of state have therefore been proposed for the LJ fluid in the past decades.

This chapter is organized as follows: in section 4.2, computer experiment data for the Lennard-Jones fluid available in the literature is comprehensively assessed and compiled to a consolidated database. To complement the database, new simulations were carried out in fluid regions where only few data were available. This database is used in section 4.3 to assess available LJ EOS regarding their performance on homogeneous states as well as the vapor-liquid equilibrium. A new LJ EOS based on the PC-SAFT monomer model was parametrized (described in detail in the Appendix) and included in the comparison. The development of the new LJ EOS aims at a good description of both the vapor-liquid equilibrium and the homogeneous region and therefore uses elements from multi-criteria optimization. In total, 20 LJ EOS were considered for the comparison. In section 4.4, the studied LJ EOS are furthermore evaluated regarding *Brown's* characteristic curves and the virial coefficients.

4.2 Thermophysical Properties of the Lennard-Jones Fluid: Database and Data Assessment

The assessment of experimental thermophysical property data is a well-established field in chemical engineering [114, 147, 682], especially for phase equilibrium data [310, 311]. For instance, consistency tests based on thermodynamic limits or balance equations are used to evaluate the quality of datasets or data points of a given thermophysical property. However, such approaches are not common in the analysis of thermophysical property data obtained by computer experiments like molecular dynamics (MD) or Monte Carlo (MC) simulations. Also, thermophysical data repositories [1, 381] have so far not addressed molecular simulation data of model fluids like the Lennard-Jones fluid. The present work therefore provides a coherent and consolidated database of thermophysical property data of the Lennard-Jones fluid.

To sample thermophysical properties of the Lennard-Jones fluid, computer experiments are carried out. In general, an obtained simulation result of a given observable x^{sim} will not agree with the true model value x^{mod} [242]. Like in experiments in the laboratory, errors occur also in computer experiments [183, 185, 497, 590] that can cause deviations between the exact true value x^{mod} and the value observed in the simulation x^{sim}. Both stochastic and systematic errors are usually present to some extent in computer experiments. Techniques to assess statistical errors are well established for computer simulations [17, 181, 185]. It is more difficult to assess systematic simulation errors. As in laboratory experiments, round robin studies can be used for doing this, in which the same simulation task is carried out by different groups with different programs. It is known that the results from such studies generally differ by more that the combined statistical uncertainty of the individual data, e.g. the results obtained by repetition usually differ due to varying methods, simulation programs, etc. [590]. Systematic errors may be a consequence of erroneous algorithms [402], user errors, differences due to different simulation methods (for example MD and MC, phase equilibrium simulation methods, techniques for the determination of the chemical potential [333], etc.). Systematic errors may furthermore be caused by finite size effects, erroneous evaluation of long-range interactions, insufficient equilibration or production periods, compilers, parallelization, and hardware architecture [590]. Last but not least, also typographical errors in publications have to be considered as a possible error source. The detection and assessment of outliers in large datasets is a standard task in the field of data science [47, 265, 330] and is widely applied to experimental data [156, 665], but has to the best of our knowledge not yet been applied to thermophysical property data obtained by computer experiments with model fluids. In the present work, we use the terms *accurate* & *precise* as follows: *accurate* simulation results x^{sim} scatter around the true value x^{mod} without trend; *precise* means here that given simulation results x^{sim} are both accurate and exhibit a low scattering.

This work reviews and assesses molecular simulation data of the Lennard-Jones fluid. Approximately 35,000 data points were taken into account, including new simulation data from this work that were taken to complement the available data in regions that were only sparsely investigated in the literature. Vapor-liquid equilibrium (VLE) data and data on state points from the homogeneous regions were considered: for the VLE, the vapor pressure, the saturated densities, the enthalpy of vaporization, and the surface

tension were investigated; for homogeneous state points, the investigated properties are: the pressure, thermal expansion coefficient, isothermal compressibility, thermal pressure coefficient, internal energy, isochoric heat capacity, isobaric heat capacity, Grüneisen parameter, Joule-Thomson coefficient, speed of sound, Helmholtz energy, and chemical potential. Transport properties were not taken into account.

The data were assessed by consistency tests to provide an indication for their accuracy and precision. The entire database was digitalized and is presented in a consistent form as a spreadsheet in the electronic Supplementary Material [640]. The database also contains flags that indicate whether a data point was identified as an outlier.

4.2.1 Molecular Simulation Data of the Lennard-Jones Fluid Available in the Literature

Table 8 gives an overview on the thermophysical property data of the Lennard-Jones fluid from the literature. Only data on homogeneous states and vapor-liquid equilibria were considered in this work. Data on the second and third virial coefficients and the so-called characteristic curves [138, 621] were included in the database, but not further assessed regarding their accuracy. The vast majority of studies in the literature report pvT and internal energy data for homogeneous state points, cf. Table 8. The chemical potential and higher-order derivatives, like speed of sound, heat capacities, or isothermal compressibility were less frequently investigated. Wherever statistical uncertainties were reported in the literature, they were also included in the database, cf. electronic Supplementary Material [640].

Table 8: Computer experiment data of the Lennard-Jones fluid from the literature. The data are sorted chronologically for each property. The # is the number of data points and T the investigated temperature range.

Authors	Year	#	$T \ / \ \varepsilon k_{\mathrm{B}}^{-1}$
pvT data			
Wood and Parker [717]	1957	13	2.74
Fickett and Wood [175]	1960	23	1.92 - 177.95
McDonald and Singer [430]	1967	28	0.72 - 1.24
McDonald and Singer [431]	1967	48	1.45 - 3.53
Verlet and Levesque [678]	1967	7	1.05 - 2.74
Verlet [677]	1967	39	0.59 - 4.63
Wood [716]	1968	41	1.06 - 100
Hansen and Verlet [238]	1969	25	0.75 - 1.15
Levesque and Verlet [370]	1969	25	0.72 - 3.67
McDonald and Singer [432]	1969	28	0.72 - 1.24
Hansen [236]	1970	9	2.74 - 100
McDonald and Woodcock [433]	1970	6	0.75 - 2.33
Toxvaerd and Praestgaard [668]	1970	8	1.35
Weeks et al. [700]	1971	5	0.75 - 1.35
McDonald and Singer [429]	1972	56	0.55 - 1.24

continued on next page

Authors	Year	#	$T\ /\ \varepsilon k_{\mathrm{B}}^{-1}$
Schofield [595]	1973	6	0.73 - 1.1
Street et al. [643]	1974	80	0.75 - 3.05
Adams [5]	1975	12	2 - 4
Adams [6]	1976	16	1 - 1.2
Carley [92]	1977	11	1.35
Adams [7]	1979	31	1.15 - 1.35
Nicolas et al. [505]	1979	108	0.48 - 6.01
Ree [559]	1980	11	0.81 - 2.7
Yao et al. [723]	1982	12	1.15 - 1.25
Powles et al. [537]	1982	37	0.7 - 1.41
Lucas [398]	1986	10	0.79 - 1.83
Shaw [601]	1988	265	0.6 - 136.25
Adachi et al. [4]	1988	328	0.7 - 2.95
Baranyai et al. [40]	1989	12	0.75 - 1.5
Saager and Fischer [577]	1990	38	0.57 - 4
Sowers and Sandler [618]	1991	60	1.35 - 6
Lotfi et al. [395]	1992	19	0.7 - 1.3
Giaquinta et al. [210]	1992	12	0.75 - 1.15
Johnson et al. [302]	1993	199	0.7 - 6
Kolafa et al. [335]	1993	43	0.72 - 4.85
Miyano [460]	1993	112	0.45 - 100
Kolafa and Nezbeda [334]	1994	13	0.81 - 10
Lustig [399]	1994	2	1.18
Mecke et al. [438]	1996	12	1.32 - 1.34
Roccatano et al. [562]	1998	10	1.4 - 10
Meier [443]	2002	351	0.7 - 6
Linhart et al. [380]	2005	108	0.7 - 1.2
Morsali et al. [475]	2007	13	5.01
Baidakov et al. [38]	2008	208	0.35 - 2
Lustig [400]	2011	8	1.02 - 3
May and Mausbach [424]	2012	205	0.69 - 6.17
Yigzawe and Sadus [726, 727]	2012	406	1.3 - 2.62
Mairhofer and Sadus [405, 544]	2013	282	1.36 - 3.05
Thol et al. [661]	2016	197	0.7 - 9
Deiters and Neumaier [138]	2016	255	0.67 - 22.54
Köster et al. [341]	2017	45	1.01 - 30
Köster et al. [341, 543]	2017	65	1.01 - 30
Ustinov [549, 674]	2017	232	0.76 - 1.14
Schultz and Kofke [596]	2018	404	0.68 - 2272
this work	2019	655	0.7 - 90
Internal energy u			
Wood and Parker [717]	1957	13	2.74
McDonald and Singer [430]	1967	27	0.72 - 1.24
McDonald and Singer [431]	1967	48	1.45 - 3.53
Verlet [677]	1967	39	0.59 - 4.63
Verlet and Levesque [678]	1967	7	1.05 - 2.74

Authors	Year	#	$T\ /\ \varepsilon k_{\mathrm{B}}^{-1}$
Wood [716]	1968	41	1.06 - 100
Levesque and Verlet [370]	1969	25	0.72 - 3.67
McDonald and Singer [432]	1969	28	0.72 - 1.24
Hansen [236]	1970	9	2.74 - 100
McDonald and Woodcock [433]	1970	6	0.75 - 2.33
Weeks et al. [700]	1971	5	0.75 - 1.35
McDonald and Singer [429]	1972	56	0.55 - 1.24
Street et al. [643]	1974	80	0.75 - 3.05
Adams [5]	1975	12	2 - 4
Adams [6]	1976	16	1 - 1.2
Torrie and Valleau [666]	1977	7	0.092 - 1.35
Adams [7]	1979	31	1.15 - 1.35
Nicolas et al. [505]	1979	108	0.48 - 6.01
Ree [559]	1980	11	0.81 - 2.7
Yao et al. [723]	1982	12	1.15 - 1.25
Lucas [398]	1986	10	0.79 - 1.83
Shaw [601]	1988	265	0.59 - 136.25
Baranyai et al. [40]	1989	18	0.75 - 1.5
Saager and Fischer [577]	1990	38	0.57 - 4
Sowers and Sandler [618]	1991	54	1.35 - 6
Lotfi et al. [395]	1992	19	0.7 - 1.3
Giaquinta et al. [210]	1992	12	0.75 - 1.15
Johnson et al. [302]	1993	199	0.7 - 6
Kolafa et al. [335]	1993	43	0.72 - 4.85
Miyano [460]	1993	112	0.45 - 100
Kolafa and Nezbeda [334]	1994	13	0.81 - 10
Lustig [399]	1994	2	1.18
Mecke et al. [438]	1996	12	1.32 - 1.34
Roccatano et al. [562]	1998	10	1.4 - 10
Meier [443]	2002	351	0.7 - 6
Baidakov et al. [38]	2008	201	0.35 - 2
May and Mausbach [424]	2012	218	0.68 - 6.17
Yigzawe and Sadus [726, 727]	2012	346	1.31 - 2.62
Mairhofer and Sadus [405, 544]	2013	282	1.36 - 3.05
Thol et al. [661]	2016	197	0.7 - 9
Deiters and Neumaier [138, 540]	2016	255	0.67 - 22.54
Köster et al. [341]	2017	45	1.01 - 30
Köster et al. [341, 543]	2017	65	1.01 - 30
Ustinov [549, 674]	2017	232	0.76 - 1.14
Schultz and Kofke [596]	2018	404	0.68 - 2272
this work	2019	655	0.7 - 90
VLE p^s, ρ', ρ'', Δh_v			
Hansen and Verlet [238] $(p^s, \rho', \rho'', \Delta h_v)$	1969	8	0.75 - 1.15
Lee et al. [363] (ρ', ρ'')	1974	10	0.7 - 1.2
Adams [6] $(p^s, \rho', \rho'', \Delta h_v)$	1976	44	0.6 - 1.1
Chapela et al. [97] (ρ', ρ'')	1977	6	0.7 - 0.84

Authors	Year	#	$T\ /\ \varepsilon k_{\mathrm{B}}^{-1}$
Adams [7] (p^s, ρ', ρ'', Δh_v)	1979	11	1.15 - 1.30
Panagiotopoulos [514] (p^s, ρ', ρ'', Δh_v)	1987	30	0.75 - 1.3
Panagiotopoulos et al. [516] (p^s, ρ', ρ'', Δh_v)	1988	30	0.75 - 1.3
Nijmeijer et al. [507] (ρ', ρ'')	1988	2	0.92
Smit and Frenkel [612] (p^s, ρ', ρ'', Δh_v)	1989	20	1.15 - 1.3
Lotfi et al. [395] (p^s, ρ', ρ'')	1992	52	0.7 - 1.3
Kofke [331] (p^s, ρ', ρ'', Δh_v)	1993	80	0.74 - 1.32
Holcomb et al. [268] (ρ', ρ'')	1993	6	0.72 - 1.13
Agrawal and Kofke [9] (p^s, ρ', ρ'', Δh_v)	1995	52	0.68 - 0.74
Hunter and Reinhardt [283] (ρ', ρ'')	1995	39	1 - 1.35
Sadus and Prausnitz [582] (p^s, ρ', ρ'', Δh_v)	1996	30	1 - 1.25
Mecke et al. [440] (ρ', ρ'')	1997	6	0.7 - 1.1
Plačkov and Sadus [526] (p^s, ρ', ρ'', Δh_v)	1997	55	0.95 - 1.27
Guo et al. [230] (ρ', ρ'')	1997	10	0.75 - 1.25
Guo and Lu [229] (ρ', ρ'')	1997	8	0.75 - 1.15
Martin and Siepmann [410] (p^s, ρ', ρ'')	1998	18	0.75 - 1.18
Trokhymchuk and Alejandre [672] (p^s, ρ', ρ'')	1999	18	0.72 - 1.27
Anisimov et al. [23] (p^s, ρ', ρ'')	1999	18	0.75 - 1
Potoff and Panagiotopoulos [535] (ρ', ρ'')	2000	36	0.95 - 1.31
Baidakov et al. [31] (p^s, ρ', ρ'')	2000	21	0.72 - 1.23
Okumura and Yonezawa [509, 547] (p^s, ρ', ρ'')	2000	39	0.7 - 1.3
Shi and Johnson [603] (ρ', ρ'')	2001	26	1.15 - 1.27
Chen et al. [104] (ρ', ρ'')	2001	6	0.7 - 0.8
Okumura and Yonezawa [510, 548] (p^s, ρ', ρ'')	2001	30	1.25 - 1.32
Baidakov et al. [37] (ρ', ρ'', spinodal)	2002	14	0.72 - 1.23
Kioupis et al. [324] (p^s, ρ', ρ'', Δh_v)	2002	40	1.03 - 1.3
Errington [164] (p^s, ρ', ρ'')	2003	12	0.7 - 1.3
Errington [163, 541] (p^s, ρ', ρ'')	2003	39	0.7 - 1.3
Stoll et al. [642] (p^s, ρ', ρ'', Δh_v)	2003	44	0.73 - 1.26
Baidakov et al. [39] (p^s, ρ', ρ'')	2007	36	0.5 - 1.2
Betancourt-Cárdenas et al. [53] (p^s, ρ', ρ'', Δh_v)	2008	35	0.7 - 1.27
Janeček [297] (p^s, ρ', ρ'', Δh_v)	2009	16	0.72 - 1.25
Galliero et al. [189] (ρ', ρ'')	2009	38	0.7 - 1.3
Sadus [580] (p^s)	2012	14	0.7 - 1.29
Mick et al. [452] (p^s, ρ', ρ'', Δh_v)	2013	36	0.75 - 1.3
Martinez-Ruiz et al. [413] (p^s, ρ', ρ'')	2014	21	0.7 - 1.1
Janeček et al. [298] (p^s, ρ', ρ'', Δh_v)	2017	31	0.7 - 1.25
Janeček et al. [298, 299] (p^s, ρ', ρ'', Δh_v)	2017	24	0.8 - 1.25
Werth et al. [709] (p^s, ρ', ρ'', Δh_v)	2017	36	0.72 - 1.24
this work (p^s, ρ', ρ'') green star in plots	2019	39	0.69 - 1.29
this work (p^s, ρ', ρ'', Δh_v) orange square in plots	2019	124	0.69 - 1.28
Vapor-liquid surface tension γ			
Lee et al. [363]	1974	5	0.7 - 1.2
Miyazaki et al. [461]	1976	1	0.7
Chapela et al. [97]	1977	5	0.7 - 1.27
Nijmeijer et al. [507]	1988	1	0.92

Authors	Year	#	$T\ /\ \varepsilon k_{\mathrm{B}}^{-1}$
Holcomb et al. [268]	1993	3	0.72 - 1.13
Mecke et al. [440]	1997	3	0.7 - 1.1
Guo et al. [230]	1997	5	0.75 - 1.25
Guo and Lu [229]	1997	4	0.75 - 1.15
Trokhymchuk and Alejandre [672]	1999	6	0.72 - 1.27
Anisimov et al. [23]	1999	6	0.75 - 1
Potoff and Panagiotopoulos [535]	2000	18	0.95 - 1.31
Baidakov et al. [31]	2000	7	0.72 - 1.23
Chen et al. [104]	2001	3	0.7 - 0.8
Baidakov et al. [37]	2002	6	0.72 - 1.22
Errington [164]	2003	4	0.7 -1.3
Baidakov et al. [39]	2007	12	0.5 - 1.2
Shen et al. [602]	2007	10	0.7 - 1.1
Janeček et al. [297]	2009	4	0.72 - 1.25
Galliero et al. [189]	2009	13	0.7 - 1.3
Galliero et al. [189]	2009	6	0.7 - 1.2
Werth et al. [706]	2013	7	0.7 - 1.25
Martinez-Ruiz et al. [413]	2014	7	0.7 -1.1
Janeček et al. [298]	2017	8	0.7 - 1.25
Werth et al. [709]	2017	9	0.72 - 1.24
this work	2019	13	0.69 - 1.29
SLE			
Hansen and Verlet [238]	1969	4	0.75 - 2.74
Hansen [236]	1970	6	2.74 - 100
Agrawal and Kofke [9]	1995	37	0.69 - 274
van der Hoef [266]	2000	corr.[A]	0.1 - 2.0
Barroso and Ferreira [48]	2002	18	0.69 - 4.5
Morris and Song [473]	2002	12	0.72 - 2.65
Errington [165]	2004	2	0.75 - 2
McNeil-Watson and Wilding [436]	2006	34	0.72 - 83
Mastny and Pablo [418]	2007	5	1 - 20
Ahmed and Sadus [11, 12]	2009	5	0.8 - 2.74
Sousa et al. [617]	2012	10	0.75 - 5
Köster et al. [341]	2017	8	1.3 - 30
Schultz and Kofke [596]	2018	corr.[A]	0.68 - 2272
Isochoric heat capacity c_v			
Wood and Parker [717]	1957	11	2.74
McDonald and Singer [430]	1967	26	0.72 - 1.24
McDonald and Singer [431]	1967	48	1.45 - 3.53
Adams [5]	1975	12	2 - 4
Adams [7]	1979	31	1.15 - 1.35
Saager et al. [542, 578]	1990	12	1.1 - 1.35
Boda et al. [60]	1996	9	1.31 - 2
Roccatano et al. [562]	1998	10	1.4 - 10
Meier [443, 546]	2002	327	0.7 - 6

Authors	Year	#	$T \, / \, \varepsilon k_\mathrm{B}^{-1}$
Baidakov et al. [38]	2008	208	0.35 - 2
May and Mausbach [424, 545]	2012	218	0.68 - 6.17
Yigzawe and Sadus [726, 727]	2012	406	1.3 - 2.62
Mairhofer and Sadus [405, 544]	2013	282	1.36 - 3.05
Thol et al. [661]	2016	197	0.7 - 9
Köster et al. [341]	2017	45	1.01 - 30
Köster et al. [341, 543]	2017	65	1.01 - 30
this work	2019	515	0.7 - 90
Isobaric heat capacity c_p			
Boda et al. [60]	1996	41	0.65 - 1.9
Lustig [400]	2011	6	1.02 - 3
May and Mausbach [424, 545]	2012	202	0.69 - 6.17
Yigzawe and Sadus [726, 727]	2012	406	1.3 - 2.62
Mairhofer and Sadus [405, 544]	2013	282	1.36 - 3.05
Thol et al. [661]	2016	197	0.7 - 9
Köster et al. [341]	2017	45	1.01 - 30
Köster et al. [341, 543]	2017	65	1.01 - 30
this work	2019	515	0.7 - 90
Grüneisen coefficient Γ			
Emampour et al. [158]	2011	26	1.2 - 1.8
Mausbach and May [422]	2014	212	0.69 - 6.17
Thol et al. [661]	2016	197	0.7 - 9
Mausbach et al. [421]	2016	110	0.72 - 9
Köster et al. [341]	2017	45	1.01 - 30
Köster et al. [341, 543]	2017	65	1.01 - 30
this work	2019	515	0.7 - 90
Thermal expansion coefficient α			
McDonald and Singer [430]	1967	20	0.72 - 1.24
Adams [5]	1975	12	2 - 4
Yigzawe and Sadus [726, 727]	2012	406	1.3 - 2.62
Thol et al. [661]	2016	197	0.7 - 9
Köster et al. [341]	2017	45	1.01 - 30
Köster et al. [341, 543]	2017	65	1.01 - 30
this work	2019	515	0.7 - 90
Isothermal compressibility β			
McDonald and Singer [430]	1967	22	0.72 - 1.24
Adams [5]	1975	12	2 - 4
Adams [7]	1979	31	1.15 - 1.35
Lotfi et al. [395]	1992	19	0.7 - 1.3
Lustig [399]	1994	2	1.18
Morsali et al. [475]	2007	13	3.76
May and Mausbach [424, 545]	2012	205	0.69 - 6.17
Yigzawe and Sadus [726, 727]	2012	406	1.3 - 2.62

Authors	Year	#	$T\ /\ \varepsilon k_{\mathrm{B}}^{-1}$
Mairhofer and Sadus [405, 544]	2013	282	1.36 - 3.05
Thol et al. [661]	2016	197	0.7 - 9
Köster et al. [341]	2017	45	1.01 - 30
Köster et al. [341, 543]	2017	65	1.01 - 30
this work	2019	515	0.7 - 90
Thermal pressure coefficient γ			
McDonald and Singer [430]	1967	20	0.72 - 1.24
Adams [5]	1975	12	2 - 4
Lustig [399]	1994	2	1.18
Meier [443]	2002	326	0.7 - 6
Morsali et al. [475]	2007	13	3.76
May and Mausbach [424, 545]	2012	205	0.69 - 6.17
Yigzawe and Sadus [726, 727]	2012	406	1.3 - 2.62
Mairhofer and Sadus [405, 544]	2013	282	1.36 - 3.05
Thol et al. [661]	2016	197	0.7 - 9
Köster et al. [341]	2017	45	1.01 - 30
Köster et al. [341, 543]	2017	65	1.01 - 30
this work	2019	515	0.7 - 90
Speed of sound w			
Meier [443]	2002	349	0.7 - 6
Lustig [400]	2011	8	1.02 - 3
May and Mausbach [424, 545]	2012	205	0.69 - 6.17
Yigzawe and Sadus [726, 727]	2012	406	1.3 - 2.62
Mairhofer and Sadus [405, 544]	2013	282	1.36 - 3.05
Thol et al. [661]	2016	197	0.7 - 9
Köster et al. [341]	2017	45	1.01 - 30
Köster et al. [341, 543]	2017	65	1.01 - 30
this work	2019	515	0.7 - 90
Joule-Thomson coefficient μ_{JT}			
Lustig [400]	2011	8	1.02 - 3
May and Mausbach [424, 545]	2012	205	0.69 - 6.17
Yigzawe and Sadus [726, 727]	2012	406	1.3 - 2.62
Mairhofer and Sadus [405, 544]	2013	282	1.36 - 3.05
Thol et al. [661]	2016	197	0.7 - 9
Köster et al. [341]	2017	45	1.01 - 30
Köster et al. [341, 543]	2017	65	1.01 - 30
this work	2019	515	0.7 - 90
Entropic properties $a,\ \mu$			
Levesque and Verlet [370] *(a)*	1969	8	1.35
Hansen and Verlet [238] *(a)*	1969	25	0.75 - 1.15
Weeks et al. [700] *(a)*	1971	5	0.75 - 1.35
Weeks et al. [699] *(a)*	1971	27	0.75 - 1.35
Adams [5] *(μ)*	1975	12	2 - 4

Authors	Year	#	$T \ / \ \varepsilon k_{\mathrm{B}}^{-1}$
Torrie and Valleau [666] (*a*)	1977	16	0.75 - 2.74
Adams [7] (*μ*)	1979	31	1.15 - 1.35
Yao et al. [723] (*μ*)	1982	12	1.15 - 1.25
Powles et al. [537] (*μ*)	1982	37	0.7 - 1.41
Panagiotopoulos et al. [516] (*μ*)	1988	18	0.75 - 1.3
Baranyai and Evans [40] (*a*)	1989	6	1.15
Lotfi et al. [395] (*μ*)	1992	19	0.75 - 1.3
Han [235] (*μ*)	1992	3	1.2
Kolafa et al. [335] (*μ*)	1993	7	1.2 - 1.45
Lustig [399] (*μ*)	1994	2	1.18
Cuadros et al. [129] (*a*)	1996	269	0.7 - 2.6
Hong and Jhon [271] (*a*)	1997	36	0.59 - 2.89
Hong and Jang [270] (*a*)	2003	22	0.59 - 2.85
Thol et al. [661] (*a, μ*)	2016	197	0.7 - 9
Köster et al. [341, 543] (*a, μ*)	2017	65	1.01 - 30
Ustinov [549, 674] (*μ*)	2017	232	0.76 - 1.14
this work (*a, μ*)	2019	655	0.7 - 90
Virial coefficients *B, C*			
Bird et al. [55] (*C*)	1950	74	0.7 - 400
Hirschfelder et al. [264] (*B, C*)	1954	156	0.3 - 400
Barker et al. [46] (*B, C*)	1966	66	0.625 - 20
Nicolas et al. [505] (*B*)	1979	33	0.625 - 20
Sun and Teja [646] (*B, C*)	1996	302	0.39 - 6.1
Shaul et al. [600] (*B, C*)	2010	22	0.7 - 2
Wheatley [550, 711] (*B, C*)	2013	100	0.1 - 1000
Ideal curves ID, BL, JTI, JI[B]			
Heyes and Llaguno [260] (JTI)	1992	16	1.15 - 7.1
Colina and Müller [120] (JTI)	1999	24	1.12 - 6.4
Kioupis et al. [324] (JTI)	2002	29	1.3 - 6
Vrabec et al. [688] (JTI)	2005	18	1.2 - 6.3
Yigzawe and Sadus [727] (JTI)	2013	9	1.31 - 2.62
Deiters and Neumaier [138, 540] (ID, BL, JTI, JI)	2016	43	0.01 - 6.4

[A] The authors provided no numerical data, but a correlation that was parametrized to computer experiment data.
[B] ID: Zeno curve, BL: Boyle curve, JTI: Joule-Thomson inversion curve, JI: Joule inversion curve.

The simulation method proposed by *Lustig* [400, 401] provides Helmholtz energy derivatives with respect to the density and the inverse temperature simultaneously from a single simulation run. This technique can be combined with *Widom*'s test particle insertion method [712] for the determination of the Helmholtz energy itself. This approach was applied to the Lennard-Jones fluid by *Thol et al.* [661] and *Köster et al.* [341, 543] in different fluid regions. The simulations of *Thol et al.* [661] were restricted to stable fluid states below $T = 9 \, \varepsilon k_{\mathrm{B}}^{-1}$, while the simulation data of *Köster et al.* [341, 543] focused on the high density region close to the freezing line. These two datasets are complemented

in the present work by data on 655 additional homogeneous state points, cf. Fig. 55, that were also sampled with the *Lustig* formalism. The new data was taken in order to get more information on regions in which literature data was comparatively sparse. For the metastable region, only pressure, chemical potential, and internal energy are reported here. The entity of the simulation results of Refs. [341, 543, 661] and from this work is referred to as the *Lustig* formalism (LF) dataset in the following. All of them were sampled with the simulation program *ms*2 [575] using similar simulation settings. Details on the simulation procedure are given below.
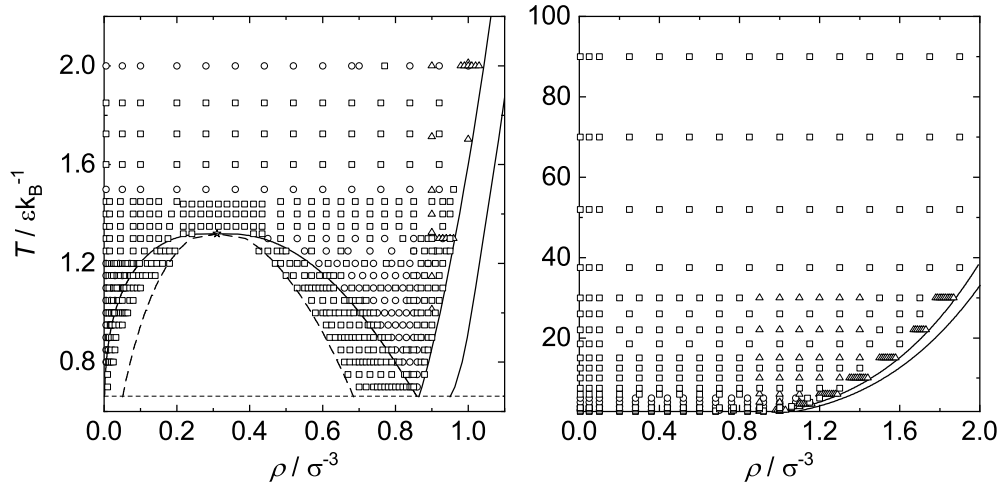
Figure 55: Overview of 963 state points that were studied with the *Lustig* formalism [400, 401] by different authors. Circles: *Thol et al.* [661]; triangles: *Köster et al.* [341, 543]; squares: *this work*. Data for the Helmholtz energy and its density and inverse temperature derivatives up to second-order are available for the stable state points. For the metastable state points, the derivatives are available up to first-order.

Results on VLE properties of the Lennard-Jones fluid have been reported many times in the literature, cf. Table 8. A total of 45 VLE datasets were found in the progress of this work. The simulation methods used in these studies can be separated in two types: simulations in which the liquid and the vapor phase are simulated in two separate volumes that are suitably coupled and simulations in which the liquid and the vapor phase coexist in a single volume that also contains the interface. The first are referred to as *indirect methods* and the latter as *direct methods* in the following. Both VLE simulation types provide in general vapor pressure p^s, saturated densities of the liquid and vapor phase ρ' and ρ'', respectively, and enthalpy of vaporization Δh_v at a given temperature T. However, often only a subset of these properties was reported in the literature, cf. Table 8. Simulation techniques that belong to the indirect type [515] are the Gibbs ensemble method [514, 516], the Grand equilibrium method [685], the NpT+test particle method [470], Gibbs-Duhem integration [332], and the Wang-Landau method [498]. Additional information on interfacial properties can be obtained with the direct method [209, 635]. Data on the surface tension of the Lennard-Jones fluid are also included in the database, cf. Table 8. The Grand equilibrium method was employed in the present work to obtain an extended VLE dataset for the Lennard-Jones fluid. Details are given below.

Data on the triple point [9, 11, 12, 48, 104, 238, 253, 314, 315, 352, 418, 596, 617]

and the critical point [7, 8, 21, 46, 84, 148, 258, 259, 261, 283, 302, 313, 315, 323, 331, 343, 350, 370, 383, 395, 410, 425, 438, 460, 505, 509, 510, 514, 534, 535, 603, 611, 616, 618, 647, 677, 678] of the Lennard-Jones fluid have been reported many times. Numeric values of the critical point are summarized in Table 9. The critical pressure has been less frequently reported than the critical temperature and density. The critical parameters of the Lennard-Jones fluid reported in the literature scatter over a large range – especially regarding the temperature. However, 13 critical temperature and density data points (Refs. [84, 259, 331, 395, 509, 510, 534, 603, 611, 647]) are in fairly good agreement, even though most of them do not agree within their combined statistical uncertainties. The critical temperature reported by Refs. [84, 259, 331, 395, 509, 510, 534, 603, 611, 647] scatters in a range of $T_c = 1.31 .. 1.326 \, \varepsilon k_{\mathrm{B}}^{-1}$; the critical density in a range of $\rho_c = 0.304 .. 0.318 \, \sigma^{-3}$. The reported critical densities obtained from computer experiment reported by Refs. [84, 259, 331, 395, 509, 510, 603, 611, 647] cluster around two different values: $\rho_c = 0.305$ and $0.316 \, \sigma^{-3}$. Other data points were discarded since they significantly deviate from this entity. The critical pressure reported by Refs. [7, 148, 509, 510, 534] scatters in the range $p_c = 0.125 .. 0.135 \, \varepsilon \sigma^{-3}$.

In the following, the critical point of the Lennard-Jones fluid is presumed to be located at $T_c = 1.321 \pm 0.007 \, \varepsilon k_{\mathrm{B}}^{-1}$, $\rho_c = 0.316 \pm 0.005 \, \sigma^{-3}$, and $p_c = 0.129 \pm 0.005 \, \varepsilon \sigma^{-3}$. The stated uncertainties were estimated from the standard deviation of the critical parameters reported by Refs. [84, 259, 331, 395, 509, 510, 603, 611, 647] for the critical temperature and density and Refs. [7, 148, 509, 510, 534] for the critical pressure.

The solid-fluid equilibrium of the Lennard-Jones fluid is used in this study only to delimit the fluid region, as molecular simulation results beyond the freezing line were excluded regarding the assessment. Solid-fluid equilibria have been investigated multiple times, cf. Table 8. The correlation for the freezing line by *Köster et al.* [341] was employed here.

4.2.2 Molecular Simulations of this Work

Homogeneous State Point Simulations

Simulations in the homogeneous state were carried out in the NVT ensemble using Monte Carlo (MC) sampling with an acceptance ratio of 0.5. The simulations contained 1372 particles. The initial conditions were generated as a fcc lattice and subsequently equilibrated for $2.5 \cdot 10^5$ cycles and then sampled for $3 \cdot 10^6$ cycles, where one cycle corresponds to 1372 attempts for a translational move. The cut-off radius was half the edge length of a cubic simulation volume. Statistical uncertainties were estimated by the block averaging method of *Flyvbjerg and Petersen* [181]. Numerical values of the simulation results are reported in the electronic Supplementary Material [640]. Simulations were carried out with the simulation program *ms*2 [575].

VLE Simulations

The vapor-liquid equilibrium of the Lennard-Jones fluid was obtained with the Grand Equilibrium method of *Vrabec and Hasse* [685]. Two simulations were subsequently

Table 9: Critical point data for the Lennard-Jones fluid obtained by computer experiment reported in the literature. The numbers in parentheses indicate the reported uncertainties of the last decimal digits.

Publication	Year	$T_c/\varepsilon k_{\mathrm{B}}^{-1}$	ρ_c/σ^{-3}	$p_c/\varepsilon\sigma^{-3}$
Barker et al. [46]	1966	1.291	0.547	0.249
Verlet & Levesque [678]	1967	1.26	0.316	0.118
Verlet [677]	1967	1.32	0.31	0.12276
Kim et al. [323]	1969	1.35	0.3	0.14
		1.28	0.29	0.13
Levesque & Verlet [370]	1969	1.36(3)	0.36(3)	0.151776
Sung & Chandler [647]	1974	1.348	0.349	0.148
Adams [7]	1979	1.30(2)	0.33(3)	0.13(2)
Panagiotopoulos [514]	1987	<1.35	0.31(2)	
Meroni et al. [450]	1990	1.3317	0.332	
Smit [611]	1992	1.316(6)	0.304(6)	
Lotfi et al. [395]	1992	1.31	0.314	
Kofke [331]	1993	1.321(4)	0.306(1)	
		1.324(12)	0.305(2)	
Valleau [438, 539]	1994	1.328(3)		
Hunter & Reinhardt [283]	1995	1.32		
Mecke et al. [438]	1996	1.328(3)	0.3107	
Mecke et al. [440]	1997	1.32521		
Caillol [84]	1998	1.326(2)	0.316(2)	0.1472(3)
Martin & Siepmann [410]	1998	1.294(9)	0.311(6)	0.1144
		1.311(9)		
Potoff & Panagiotopoulos [534]	1998	1.3120(7)	0.316(1)	0.1279(6)
Potoff & Panagiotopoulos [535]	2000	1.311(2)		
		1.3120(7)	0.316(2)	
Okumura & Yonezawa [509]	2000	1.313(2)	0.304(2)	0.125(1)
Shi & Johnson [603]	2001	1.3241(9)	0.3165(7)	
		1.3145(2)	0.316(1)	
Dunikov et al. [148]	2001	1.350(5)	0.310(5)	0.126(8)
Okumura & Yonezawa [510]	2001	1.3207(4)	0.316(1)	0.1288(5)
Pérez-Pellitero et al. [525]	2006	1.3123(6)	0.3174(6)	
		1.3126(6)	0.3174(6)	
		1.313(1)	0.317(1)	
Betancourt-Cárdenas et al. [53]	2008	1.302(6)	0.311(2)	0.12(3)
Kulinskii [350]	2013	1.333	0.325	0.122
Heyes & Woodcock [261]	2013	1.3365(5)		0.1405(2)
Heyes [259]	2015	1.316(1)	0.309(6)	
Lishchuk & Fischer [383]	2018	1.31766		

carried out to obtain the VLE properties at a given temperature: first, the chemical potential and the molar volume was sampled in an NpT MD liquid phase simulation. Then, the vapor phase was simulated in a pseudo-μVT ensemble using an MC algorithm. The pressure of the liquid state was chosen to be approximately 7% above the vapor pressure, as estimated by the Lennard-Jones EOS from Ref. [639]. 2048 particles were initialized on a fcc lattice for the NpT simulations and then equilibrated for $3 \cdot 10^5$ time steps. The time step was set to $\Delta\tau = 0.001\,\sigma\sqrt{M/\varepsilon}$. Velocity scaling was used to specify the temperature. The chemical potential was sampled with *Widom*'s test particle method [712], inserting 2500 test particles every time step. The chemical potential and its pressure derivative, i.e. the molar volume, were then used during the second simulation to obtain the saturated vapor phase properties. The pseudo-μVT simulation was carried out such that the specified chemical potential was not constant but a function of the actual pressure of the vapor phase. The vapor phase simulations were started with 1000 particles using MC sampling with an acceptance ratio of 0.5. The system was equilibrated for 10^5 time steps and production was carried out for $5 \cdot 10^5$ time steps. The initial vapor density was also estimated with the Lennard-Jones EOS from Ref. [639]. As for the homogeneous state point simulations, the cut-off radius was half the edge length of a cubic simulation volume and the statistical uncertainty was estimated by the block averaging method [181]. The vapor-liquid equilibrium was sampled at 31 temperatures between $T = 0.69$ and $1.28\,\varepsilon k_{\mathrm{B}}^{-1}$. Numerical values of the obtained vapor pressure, saturated densities, and enthalpy of vaporization are reported in the Appendix.

The simulation data from the outlined procedure is depicted by orange squares in the plots. The simulations for the VLE data indicates by the green star (direct VLE simulations) are discussed in chapter 5. The numeric values for both data sets are reported in the Appendix.

4.2.3 Database of Thermophysical Properties

All thermophysical property data (approximately 35,000 data points) considered in this work are summarized in a consistent form in an *.xls* spreadsheet in the electronic Supplementary Material [640]. All data are sorted by thermophysical properties in that spreadsheet. All numerical values are given in a consistent form, i.e. as residual properties with respect to the ideal gas and in the standard 'Lennard-Jones' units. Information on the statistical uncertainties were adopted from publications – wherever such information was reported, which is unfortunately not always the case. The methods for the estimation of statistical uncertainties differ significantly among the publications. Sometimes, statistical uncertainties were reported, but no description on how such were obtained is given. Due to this heterogeneity, statistical uncertainties could unfortunately not be used for the assessment of data points in this work.

The database furthermore contains notes on pitfalls regarding the conversion of the primary literature data to the format used in the database. Furthermore, known misprints in publications from the literature were corrected, e.g. Refs. [543, 546, 661]. A survey of these misprints is also given. Each data point possesses an additional mark, which indicates whether the data point was found to be an outlier or not, according the assessment described in the following.

4.2.4 Assessment of Molecular Simulation Data

4.2.4.1 Assessment of Data on Homogeneous States

Thermophysical property data of the Lennard-Jones fluid reported in the literature (see Table 8) for homogeneous state points were assessed by an equation of state (EOS) consistency test. This consistency test is based on the statistical method proposed by *Rousseeuw and Croux* [571] for the detection of outliers that was adopted and extended for the purposes of the present work. The EOS test evaluates each data point individually by comparing it with the most accurate equations of state of the Lennard-Jones fluid available in the literature and computer experiment data in its vicinity. The EOS test is designed in a way to make a binary decision: either a data point is an outlier or not.

The relative deviation δx of a given data point (DP) $x_{\mathrm{DP}}(T, \rho)$ from a given EOS at the same temperature and density was computed as

$$\delta x = \frac{x_{\mathrm{DP}} - x_{\mathrm{EOS}}}{x_{\mathrm{EOS}}}, \tag{65}$$

where x is one of the following homogeneous bulk phase properties: pressure p, internal energy u, speed of the sound w, thermal pressure coefficient γ, Grüneisen parameter Γ, thermal expansion coefficient α, isothermal compressibility β, Joule-Thomson coefficient μ_{JT}, isochoric heat capacity c_v, isobaric heat capacity c_p, Helmholtz energy divided by the temperature $\tilde{a} = a/T$, or chemical potential μ.

Comprehensive comparisons of EOS for the Lennard-Jones fluid have been carried out recently [639] (see section 4.3 and 4.4). Six of the most accurate EOS were used here: *Johnson et al.* [302], *Kolafa and Nezbeda* [334], *Lafitte et al.* [353], *Mecke et al.* [438, 439], *Stephan et al.* [639], and *Thol et al.* [661] (alphabetically). However, also these EOS have deficiencies, e.g. the EOS of *Thol et al.* [661] exhibits an unrealistic behavior in the two-phase region, that of *Mecke et al.* [438, 439] shows large deviations in the high density region close to the freezing line, that of *Stephan et al.* [639] is less accurate in the high temperature region, the EOS of *Kolafa and Nezbeda* [334] produces distorted characteristic curves [138], and the one of *Lafitte et al.* [353] is less accurate in the low density gas region. The EOS of *Johnson et al.* [302] is overall less precise than the ones mentioned before. To take these deficiencies into account in evaluating an individual data point, only the four EOS were considered that yielded the smallest relative deviation δx_j for a given data point. The four best EOS were identified and selected for each data point individually, to prevent that the mentioned deficiencies of the employed EOS adulterate the assessment.

To take into account that the precision of molecular simulation results varies in different regions, the deviation of each individual state point was put into relation with the average deviation of the data points in its neighborhood in the $T - \rho$ plane. Each data point j has its own neighborhood with $i = 1 .. M$ neighbors, where the number of neighbors is $M = 15 .. 20$. The nearest neighbors were determined using the radial distance $\tilde{\delta} R$ between data points in the $T - \rho$ plane, i.e. $\tilde{\delta} R = (\tilde{\delta} T^2 + \tilde{\delta} \rho^2)^{0.5}$. The choice of the radius and, hence, of M depends on the location of the data point in the $T - \rho$ plane, i.e. in a fluid region where data points are sparse or if a data point is close to

a phase boundary, the radius was chosen large enough such that at least 15 neighbors were allocated to the neighborhood of each data point. The neighbors of each data point j were taken from the entity of all data points N of a given property, i.e. the neighborhood M contains in general data points from different publications.

To decide whether a data point j is an outlier, a measure P_j is introduced. Following the ideas of Refs. [265, 330, 371, 571], P_j was defined as

$$P_j = \frac{|\delta x_j - \text{median}_{i=1}^{M}(\delta x_{ji})|}{\text{MAD}_j} \quad \text{with} \quad i = 1..M \quad \text{and} \quad j = 1..N. \tag{66}$$

In the measure P_j, the deviation of a tested data point j and an EOS are compared to the deviations of the data points from its neighborhood and that EOS. Details on the selection of the EOS are given below. The numerator on the right-hand side of Eq. (66) is the absolute deviation of the data point j and the median [201] of the data points in its neighborhood. The denominator is a measure for the mean absolute deviation (MAD) of the data points in the neighborhood of the given data point [234] j

$$\text{MAD}_j = k \cdot \text{median}_{i=1}^{M}\left(|\delta x_{ij} - \text{median}_{i=1}^{M}(\delta x_{ij})|\right), \tag{67}$$

where $k = 1.4826$. The selection of that number is related to the assumption that the deviation data δx_{ij} is normally distributed in the set of data points [280]. The MAD_j quantifies how strong the data points of the neighborhood M scatter on average from their median, i.e. how precise the data in the neighborhood is on average. The MAD is robust, as the median is less affected by outliers than the mean. Hence, this test takes the accuracy of the EOS and the accuracy of the computer experiment data of a certain thermophysical property in a certain fluid region into account. For brevity, it is called EOS test in the following.

The EOS test requires a sufficiently dense neighborhood of data points, to ensure that the accuracy of the reference, i.e. the EOS, remains fairly constant within the neighborhood. Since the data points for $T > 6\,\varepsilon k_{\text{B}}^{-1}$ are sparsely distributed in the $T - \rho$ plane, the EOS test was only applied to data at $T \leqslant 6\,\varepsilon k_{\text{B}}^{-1}$.

The measure P_j was computed for the four EOS that were selected as described above, and then compared with a parameter $P_{\max}$

$$P_j \geqslant P_{\max}. \tag{68}$$

If this decision criterion was fulfilled for at least two of the four EOS, the data point j was identified as an outlier. The parameter $P_{\max}$ introduces an unavoidable subjective attribute into the method [371, 571] and regulates the severity of the EOS test. A fixed number for $P_{\max}$ is used here for all thermophysical properties, EOS, and fluid regions under consideration, which established a consistent framework. The parameter was set to $P_{\max} = 4$. This results in a confirmation rate of approximately 90% of all homogeneous data. Vise versa, 10% of all homogeneous data points were identified as outliers. This rather conservative choice [371, 571] for $P_{\max}$ was used to prevent a false assessment of data points to be erroneous. A more stringent, but smaller database can be generated easily by increasing $P_{\max}$ and vice versa a larger database, that might however include less precise data, can be generated by decreasing $P_{\max}$. The EOS test enables

a robust assessment of the quality of individual data points based on an assessment of the precision of the data points in its neighborhood.

Fig. 56 summarizes the results of the EOS test for the homogeneous state points for $P_{max} = 4$. About 85% of the pvT data and the data for the internal energy u passed the EOS test. These two thermophysical properties are the most frequently reported: the database contains about five times more pvT and internal energy data than any other thermophysical property. The relatively low confirmation rate of the pvT and internal energy data is a result from significant differences in the precision among different publications that the EOS test used for the detection of the outliers.
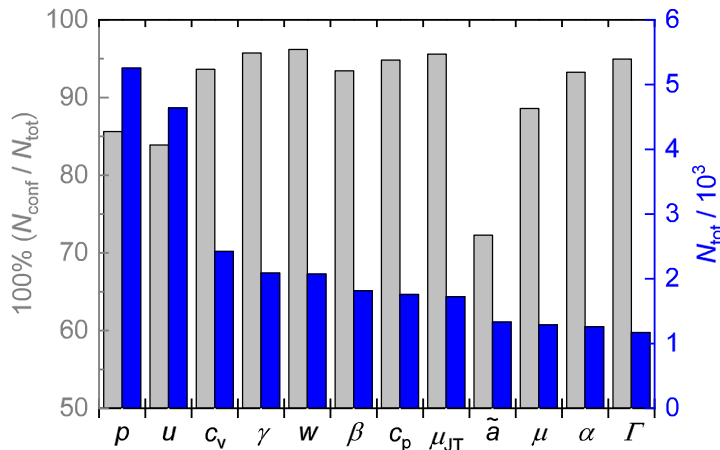
Figure 56: Statistics of the EOS test for homogeneous state points for different thermophysical properties: pressure p, internal energy u, isochoric heat capacity c_v, thermal pressure coefficient γ, speed of sound w, isothermal compressibility β, isobaric heat capacity c_p, Joule-Thomson coefficient μ_{JT}, Helmholtz energy divided by temperature $\tilde{a} = a/T$, chemical potential μ, thermal expansion coefficient α, and Grüneisen parameter Γ. The left ordinate indicates the percentage of confirmed data and the right coordinate the total number of data points available for each thermophysical property.

Confirmation rates of 94 - 96% were obtained for data for the isochoric heat capacity c_v, isobaric heat capacity c_p, speed of sound w, thermal pressure coefficient γ, Joule-Thomson coefficient μ_{JT}, and Grüneisen parameter Γ – which are higher-order temperature and density derivatives of the Helmholtz energy. The confirmation rate for the thermal expansion coefficient α and isothermal compressibility β was 92 - 93%. A confirmation rate of 89% was found for the chemical potential μ, which is particularly challenging to determine by molecular simulation. The lowest confirmation rate of 72% was found for the Helmholtz energy $\tilde{a}$, which is mainly due to particularly low confirmation rates for the results from some publications. Details are given in the electronic Supplementary Material [640].

Also, the numerical values of all data points and the corresponding result of the EOS test, i.e. whether a data point is confirmed or identified as an outlier with $P_{max} = 4$, are provided in the electronic Supplementary Material [640]. Moreover, information on the dependence of the total percentage of confirmed data on the choice of the number for P_{max} is presented there.

4.2.4.2 Assessment of Vapor-Liquid Equilibrium Data

For the vapor-liquid equilibrium, both bulk and interfacial properties were considered: vapor pressure p^s, saturated liquid and vapor density ρ' and ρ'', respectively, and enthalpy of vaporization Δh_v were considered for the bulk properties and the interfacial tension γ as interfacial property, cf. Table 8.

Bulk VLE Data

In contrast to the test on the homogeneous state points, which was assessed for each data point individually, entire VLE bulk property datasets from a given publication were assessed and either confirmed or discarded. Furthermore, the EOS test for homogeneous data is designed to identify gross outliers, whereas the assessment of the VLE data additionally aims at determining the most precise data and to give an estimation of that precision. The estimated *precision* indicates the magnitude that a given dataset scatters around the presumed *true value*. The true value, i.e. exact and correct, of a given property is approximated here by the mean of the most precise and accurate datasets.

VLE bulk data of the Lennard-Jones fluid were assessed by several independent consistency tests. Two of them were taken from the literature: the compressibility factor test proposed by *Nezbeda* [494, 495] and the Clausius-Clapeyron test [395]. Furthermore, as a third test, outliers were determined from a direct comparison of the data points as described below in more detail. For brevity, this test is referred to as *deviation* test in the following. Datasets were discarded, if the majority of data points within a dataset violate one or more consistency tests. For the following discussion, the *vicinity to the critical point* of the VLE region is defined to be above 95% of the critical temperature. Data points in that region were not included in the consistency tests.

To facilitate the assessment, empirical correlation functions for the vapor pressure p^s, saturated liquid and vapor density ρ' and ρ'', respectively, and enthalpy of vaporization Δh_v were used:

$$\ln p^s = n_1 T + \frac{n_2}{T} + \frac{n_3}{T^{n_4}} , \tag{69}$$

$$\left(\frac{\rho'}{\rho_c}\right) = 1 + \sum_{i=1}^{5} n_i \left(1 - \frac{T}{T_c}\right)^{t_i} , \tag{70}$$

$$\ln\left(\frac{\rho''}{\rho_c}\right) = \sum_{i=1}^{5} n_i \left(1 - \frac{T}{T_c}\right)^{t_i} , \tag{71}$$

$$\Delta h_v = \sum_{i=1}^{4} n_i \left(T_c - T\right)^{t_i} . \tag{72}$$

In an initial step, the VLE dataset from this work was used for the parametrization of Eqs. (69) - (72), as it is the most extensive dataset. The absolute average deviation from the correlations (69) - (72) and the respective VLE data from this work is: 0.3% for the vapor pressure, 0.06% for the saturated liquid density, 0.5% for the saturated vapor density, and 0.3% for the enthalpy of vaporization. The numerical values of the parameters n_i and t_i are listed in Table 10. The critical values used in Eqs. (69) - (72)

are $T_c = 1.321\,\varepsilon k_B^{-1}$ and $\rho_c = 0.316\,\sigma^{-3}$. They are called *base correlations* in the following. It will be shown below, that these correlations match the best available guess for the considered properties within their estimated precision.

In the test proposed by *Nezbeda* [494, 495], the compressibility factor of the saturated vapor phase $Z'' = p^s/\rho''T$ is considered. Starting at low temperatures close to the triple point, Z'' must be close to unity. With increasing temperature, Z'' must decrease monotonically until the compressibility factor at the critical point is reached [494, 495].

This simple criterion can be applied for sorting out outliers: $Z'' > 1$ is not acceptable and the slope $\mathrm{d}Z''/\mathrm{d}T$ must be negative. More generally, the slope $\mathrm{d}Z''/\mathrm{d}T$ is sensitive and useful for discriminating data points that deviate from the general trend. Furthermore, the data points were compared to the results for Z'', which was obtained from the base correlations. Data points for which the deviation in Z'' from that correlation is above 1.25% were considered as outliers. The number 1.25% was chosen on the basis of an examination of the scattering of the entire available data. Datasets of which more than 50% of the data points violate at least one of these criteria were discarded. The other datasets are considered as confirmed by the compressibility factor test.

Fig. 57 shows the datasets that were confirmed by the compressibility factor test. These data are in good mutual agreement and in agreement with the base correlation computed from Eqs. (69) and (71). Excellent mutual agreement is found for the datasets from *Agrawal and Kofke* [9], *Errington* [164], *Errington* [163, 541], *Janeček et al.* [298, 299], *Lotfi et al.* [395], *Mick et al.* [452], *Okumura and Yonezawa* [510, 548], and from the present work. Taking these data as the reference, and their scattering as a measure for the precision, with which Z'' is known, that precision is estimated to be approximately ±0.5%, excluding the vicinity of the critical point. Furthermore, the datasets from *Hansen and Verlet* [238], *Janeček* [297], *Kofke* [331], *Martínez-Ruiz et al.* [413], *Okumura and Yonezawa* [509, 547], this work (direct simulations) , *Stoll et al.* [642], and *Werth et al.* [709] also agree well with the data mentioned above, but scatter more. That data were confirmed by the compressibility factor test. The larger scatter of the data of Refs. [413, 628, 709] is probably due to the fact that these data were sampled with the direct simulation method. The datasets from Refs. [163, 164, 509, 541, 547] each contain a single data point that is a clear outlier. These data points are explicitly pointed out in the Appendix. However, apart from the outlier, these datasets are considered as confirmed by the compressibility factor test. Datasets from Refs. [6, 7, 23, 31, 39, 53, 283, 324, 410, 514, 516, 526, 582, 612, 672] were discarded by the compressibility factor test. Details are given in the Appendix.

The second consistency test that was employed for the VLE bulk data is based on the Clausius-Clapeyron equation

$$\frac{\mathrm{d}\ln p^s}{\mathrm{d}(1/T)} = -\frac{T\,\Delta h_v}{p^s\,(1/\rho'' - 1/\rho')}\,. \tag{73}$$

The left-hand side (LHS) and right-hand side (RHS) of Eq. (73) is considered individually for each dataset and compared. The equality of the LHS and RHS within the corresponding statistical uncertainties indicates the thermodynamic consistency by the Clausius-Clapeyron equation. The RHS of Eq. (73) is therefore computed directly from the numerical values of the computer experiments. The statistical uncertainties of the RHS values are determined using the error propagation law. The LHS of Eq. (73)

Table 10: Parameters of correlations (69) - (72) for the vapor pressure p^s, saturated liquid density ρ', saturated vapor density ρ'', and enthalpy of vaporization Δh_v.

	p^s Eq. (69)	ρ' Eq. (70)		ρ'' Eq. (71)		Δh_v Eq. (72)	
	n_i	n_i	t_i	n_i	t_i	n_i	t_i
1	1.156551	1.341700	0.327140	−8.135822	1.651685	6.456728	0.411342
2	−4.431519	2.075332	0.958759	−102.919110	43.469214	2.700099	0.460416
3	−0.423028	−2.123475	1.645654	−3.037979	0.462877	−3.073573	2.350953
4	2.638743	0.328998	17.000001	−44.381841	11.500462	3.149052	5.017010
5	1.386131	1.386131	2.400858	−34.55892948	5.394370		
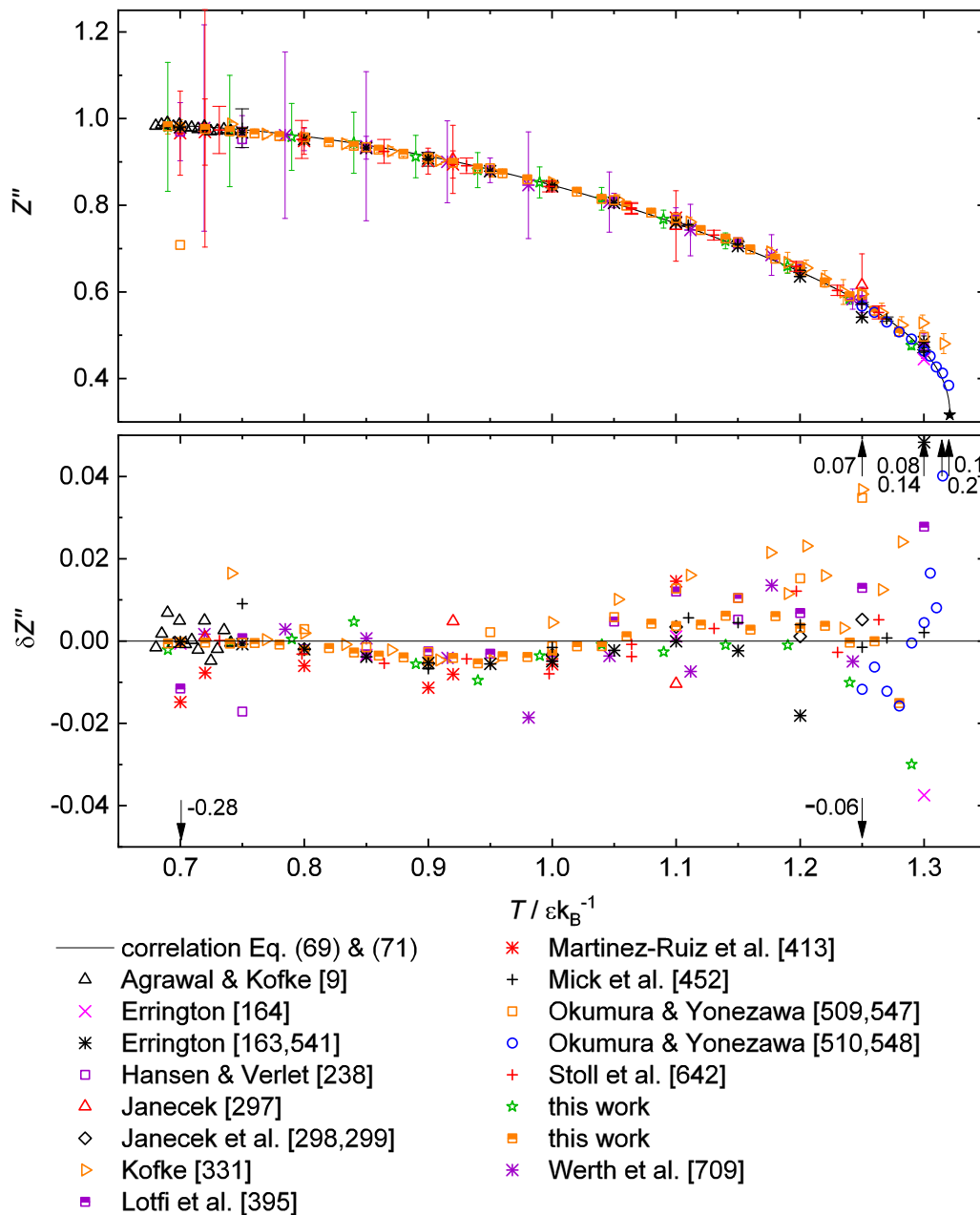
Figure 57: Compressibility factor test for the vapor-liquid equilibrium data of the Lennard-Jones fluid: saturated vapor phase compressibility factor Z'' as function of the temperature T (top) and the relative deviation of Z'' from the base correlations (69) and (71) (bottom). The black filled star indicates the compressibility factor at the critical point according the base correlation. Error bars are omitted in the bottom plot to avoid visual clutter. Only confirmed data is shown.

is calculated with an analytical function for the vapor pressure curve. The Clausius-Clapeyron test is applied here in two ways (Test A and Test B). In Test A, the LHS and RHS of a given dataset are directly compared. This can only be done in a meaningful way for those datasets, that enable the parametrization of a correlation of $p^s(T)$ for the LHS in a sufficiently accurate manner. In Test B, the RHS of remaining datasets are compared with the LHS correlations established in Test A. Data points violate the Clausius-Clapeyron equation in Test A, if the computed RHS of a given data point does not agree within the statistical uncertainty with the corresponding LHS value. In the Test B, data points were considered as outliers, if they deviate 2% or more from the two correlations established in Test A. As for the compressibility factor test, datasets for which more than half of the data points violate the Clausius-Clapeyron test were discarded. The remaining datasets were considered as confirmed by the Clausius-Clapeyron test.

The datasets from *Lotfi et al.* [395] and this work were employed in Test A. Correlations for $p^s(T)$ obtained from the other datasets were not found to be sufficiently accurate for carrying out a meaningful test of type A. For the data from this work, the base correlation for the vapor pressure curve $p^s(T)$ from Eq. (69) was used for the comparison. The statistical uncertainty of the LHS was estimated from the error propagation law. *Lotfi et al.* [395] published a correlation of their own vapor pressure curve data $p^s(T)$ that was used here for computing the LHS of Eq. (73) for the comparison of the corresponding RHS values. The RHS values of Eq. (73) were computed from the VLE data from Refs. [7, 9, 53, 238, 297–299, 324, 331, 395, 452, 514, 516, 526, 582, 612, 642, 709] and Test B was applied accordingly.

Fig. 58 shows the VLE datasets that were confirmed by both the Clausius-Clapeyron test and the compressibility factor test. In the plot, results for the RHS of Eq. (73) that were obtained from the simulation data and are shown as symbols are compared to results for the LHS that were obtained from correlations of the vapor pressure curve and are shown as lines. Two such correlations are depicted: one obtained from the data from the present work and one obtained by *Lotfi et al.* from their data [395]. *Lotfi et al.* [395] compared their results for the Lennard-Jones fluid with results for Ne, Ar, and CH_4 and found very good qualitative agreement, i.e. a parabolic shape of $\mathrm{d}(\ln p^s)/\mathrm{d}(T^{-1})$ as function of the temperature.

Fig. 58 shows that the two correlations of the LHS of Eq. (73) match well. The differences are far below the uncertainties of the data points for the RHS of Eq. (73). The data from the present work and from *Lotfi et al.* [395] agree well with the correlations. There is one outlier in the dataset from the present work. (It was not removed from the dataset to ensure a fair comparison with the literature data, for which almost every dataset was found to have at least one outlier). The LHS and RHS of Eq. (73) agree within the statistical uncertainties for all but this state point, which is likely the result of an overly optimistic error estimation. However, the data of *Lotfi et al.* [395] and this work agree very well throughout, but the data of *Lotfi et al.* [395] show a more pronounced scatter and larger error bars than the data from this work.

The RHS data of *Janeček et al.* [298, 299], *Stoll et al.* [642], *Mick et al.* [452], and *Agrawal and Kofke* [9] are also in excellent agreement with the base correlation of the LHS of Eq. (73). The agreement is also very good for the datasets of *Hansen and Verlet* [238], *Janeček* [297], *Kofke* [331], and *Werth et al.* [709] but their RHS data exhibit considerable scatter, as does the dataset of *Lotfi et al.* [395].
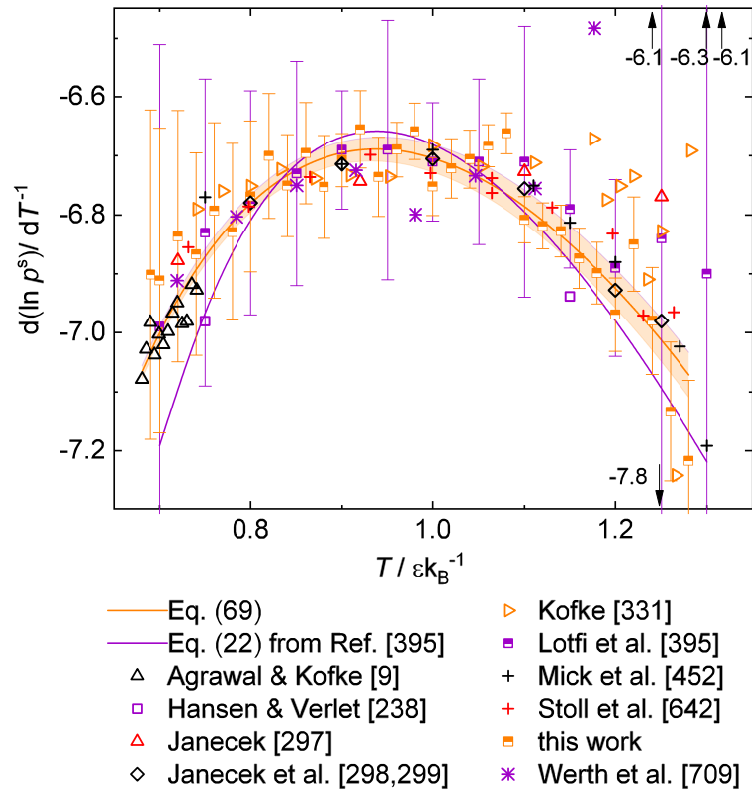
Figure 58: Clausius-Clapeyron test according Eq. (73). Symbols indicate the RHS and the lines the LHS of Eq. (73). The orange shaded area indicates the statistical uncertainty of $\pm 2\%$ computed for the LHS of Eq. (69). The purple line is Eq. (22) from Ref. [395]. Only confirmed data is shown.

The datasets from Refs. [6, 7, 53, 324, 514, 516, 526, 582, 612] were discarded by the Clausius-Clapeyron test. Details are given in the Appendix. The results from the Clausius-Clapeyron test reinforce the findings from the compressibility factor test.

As a third assessment, the deviation plots of each VLE bulk property (p^s, ρ', ρ'', and Δh_v) from the base correlations were used as follows: first, the datasets with the best mutual agreement were identified that were also confirmed by the previous two tests. From these datasets, a confidence interval $\pm X\%$ was estimated for each VLE property ($X = p^s$, ρ', ρ'', and Δh_v) individually that is a measure for the precision of the available information. A data point was considered as an outlier, if its relative deviation to the corresponding base correlation exceeds 2.5 times the number of X of one of the four VLE properties. Again, datasets for which more than half of the data points of a given VLE property violate the criterion were discarded. The remaining datasets were considered as confirmed.

Fig. 59 shows the relative deviation of the VLE data (vapor pressure p^s, enthalpy of vaporization Δh_v, and the saturated densities ρ' and ρ'') from the base correlations. Excellent mutual agreement (and also agreement with the base correlations) was found for the datasets from *Errington* [163, 541], *Errington* [164], *Janeček et al.* [298, 299], *Lotfi et al.* [395], *Mick et al.* [452], *Okumura and Yonezawa* [510, 548], and the dataset from the present work. These seven datasets were also confirmed by the other two tests and comprise a total of 86 state points. Interestingly, the precision, i.e. the scatter,

of each of the seven best datasets (Refs. [163, 164, 298, 299, 395, 452, 510, 541, 548] and this work) is very similar. Only the saturated vapor density and vapor pressure data of *Errington* [163, 541] were found to be significantly more precise than the other datasets. However, the scatter of the saturated liquid density data of *Errington* [163, 541] is significantly larger than the scatter of the other selected best datasets (Refs. [163, 164, 298, 299, 395, 452, 510, 541, 548] and this work).

The mutual agreement of these seven selected best bulk VLE datasets is approximately $\pm 1\%$ for the vapor pressure, $\pm 0.2\%$ for the saturated liquid density, $\pm 1\%$ for the saturated vapor density, and $\pm 0.75\%$ for the enthalpy of vaporization – excluding the region close to the critical point. Five of these seven best datasets contain a single or two clear outliers, which are listed in the Appendix.

The mutual agreement of the seven selected best datasets (Refs. [163, 164, 298, 299, 395, 452, 510, 541, 548] and the dataset from the present work) significantly decreases in the region close to the critical point, i.e. $T \gtrsim 1.25\, \varepsilon k_{\mathrm{B}}^{-1}$. The mutual agreement in the vicinity of the critical point is better for the vapor pressure and the saturated liquid density than for the enthalpy of vaporization and the saturated vapor density.

The following datasets agree well but scatter strongly (however, within the confidence interval and are thereby considered as confirmed by the deviation test): *Betancourt-Cárdenas et al.* [53], *Chen et al.* [104], *Hansen and Verlet* [238], *Martínez-Ruiz et al.* [413], *Okumura and Yonezawa* [509, 547], *Stoll et al.* [642], this work (direct simulations), and *Werth et al.* [709]. The datasets from Refs. [6, 7, 9, 23, 31, 37, 39, 97, 189, 229, 230, 268, 283, 297, 298, 324, 331, 363, 410, 440, 507, 514, 516, 526, 534, 580, 582, 612, 672] were discarded because more than 50% of the respective data points exceed the confidence interval of one of the bulk VLE properties.

The seven datasets from Refs. [163, 164, 298, 299, 395, 452, 510, 541, 548] and from the present work were confirmed by all applicable tests and were found to be in excellent mutual agreement and are therefore recommended as a reference. The datasets from Refs. [238, 413, 509, 547, 628, 642, 709] were also confirmed by all applicable tests, but exhibit a significantly larger scattering compared to these seven most precise datasets. The datasets from Refs. [9, 37, 104, 189, 229, 230, 268, 283, 363, 507, 535, 603] were discarded by a single consistency test, the datasets from Refs. [23, 31, 39, 331, 410, 672] were discarded by two tests, and the the datasets from Refs. [7, 53, 324, 514, 516, 612] by three tests. Note that, for most datasets only a selection of tests could be applied due to missing properties that were not reported in these publications. For all but one VLE dataset, the results of the three applicable tests reinforce each other. The only exception is the dataset of *Agrawal and Kofke* [9]: the dataset was confirmed by the compressibility factor test and the Clausius-Clapeyron test, but discarded by the deviation test.

For many of the investigated datasets, the data points do not agree with the seven selected best datasets within the reported statistical uncertainties. Therefore, systematic simulation errors [590] are hold responsible for these deviations.

Fitting the combined data of the seven best datasets (Refs. [163, 164, 298, 299, 395, 452, 510, 541, 548] and the dataset from the present work) with the correlations presented in Eqs. (69) - (72) yields a fit that is essentially the same as the one presented in Table 10. For all studied properties, the differences between both fits are well below
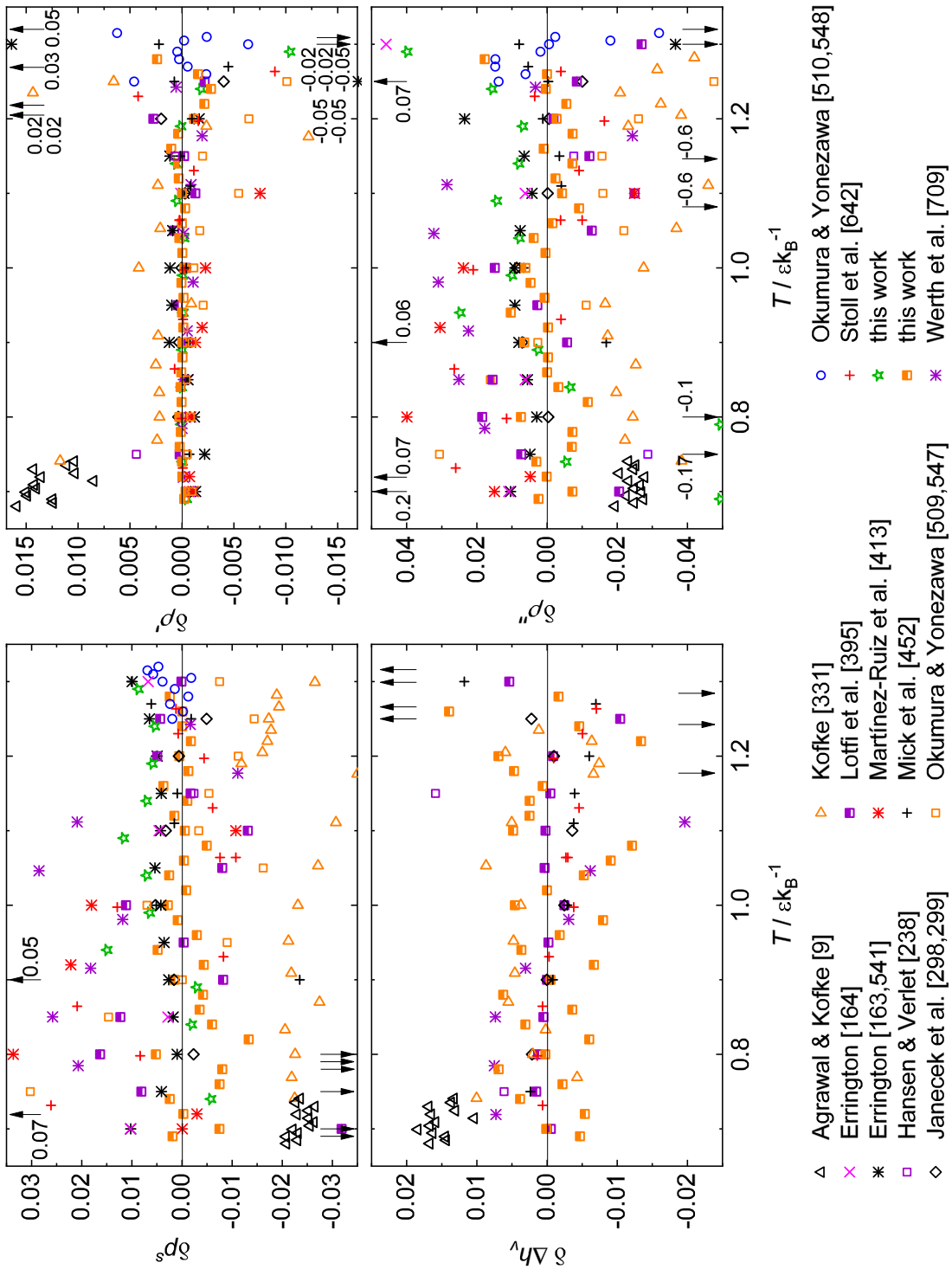
Figure 59: Relative deviations of the vapor-liquid equilibrium data for the vapor pressure p^s, saturated liquid density ρ', saturated vapor density ρ'', and enthalpy of vaporization Δh_v from correlations (69) - (72) as a function of the temperature T. Error bars were omitted to avoid visual clutter. For clarity, numerical values for out-of-range data points with negative deviation for the vapor pressure, the enthalpy of vaporization, and the saturated vapor density ρ'' are omitted in the respective plot; they lie in the range of $\delta p^s = -0.05 .. -0.16$, $\delta \Delta h_v = -0.15 .. 0.45$, and $\delta \rho'' = -0.08 .. -0.2$.

the differences among the data from the seven datasets. Hence, we simply recommend using the correlations from Table 10.

Interfacial VLE Data

As for the bulk VLE properties, the computer experiment data for the surface tension were assessed with respect to their mutual agreement. To facilitate this assessment, a base correlation function was also used for the temperature dependence of the surface tension

$$\gamma / \varepsilon \sigma^{-2} = a \Big(1 - \frac{T}{T_c} \Big)^b \, , \tag{74}$$

where a and b are parameters. $T_c = 1.321 \, \varepsilon k_{\mathrm{B}}^{-1}$ was specified for the critical temperature in Eq. (74). In an initial step, the surface tension data from Refs. [628, 706] were used for the parametrization of Eq. (74). The obtained values for the parameters are: $a = 3.03327$ and $b = 1.27748$. The absolute average deviation between correlation (74) and the data used for the parametrization is 1.2%. It will be shown below, that Eq. (74) matches the best available guess for the surface tension within its estimated precision.

The surface tension data was also assessed with the deviation test: first, the datasets with the best mutual agreement were identified. From these datasets, a confidence interval $\pm X\%$ was estimated as measure for the precision that the surface tension is known. For the assessment, a data point was considered as an outlier, if its relative deviation to the base correlation (74) exceeds 2.5 times the number of $\pm X\%$. Again, datasets for which more than half of the data points violate the criterion were discarded. The remaining datasets were considered as confirmed.

Fig. 60 shows the surface tension data as a function of the temperature. Overall, the agreement is significantly poorer than for the bulk VLE properties. The best mutual agreement is found for the datasets of *Chen et al.* [104], *Janeček et al.* [298], *Janeček* [297], *Werth et al.* [706], *Werth et al.* [709], *Lee et al.* [363], *Martinez-Ruiz et al.* [413], *Mecke et al.* [437], *Nijmeijer et al.* [507], this work (direct simulations), *Shen et al.* [602]. These datasets agree approximately within $\pm 4\%$ – excluding the region close to the critical point.

The following datasets agree well, i.e. are considered as confirmed, but exhibit a more pronounced scatter or systematic deviations from the aforementioned datasets: *Trokhymchuk and Alejandre* [672], *Potoff and Panagiotopoulos* [535], *Miyazaki et al.* [461], *Galliero et al.* [189], *Errington* [164], *Baidakov et al.* [39], and *Baidakov et al.* [37]. The datasets of Refs. [23, 31, 97, 229, 230, 268] were discarded since more than 50% of the respective data points exceed the confidence interval. Details are given in the Appendix.
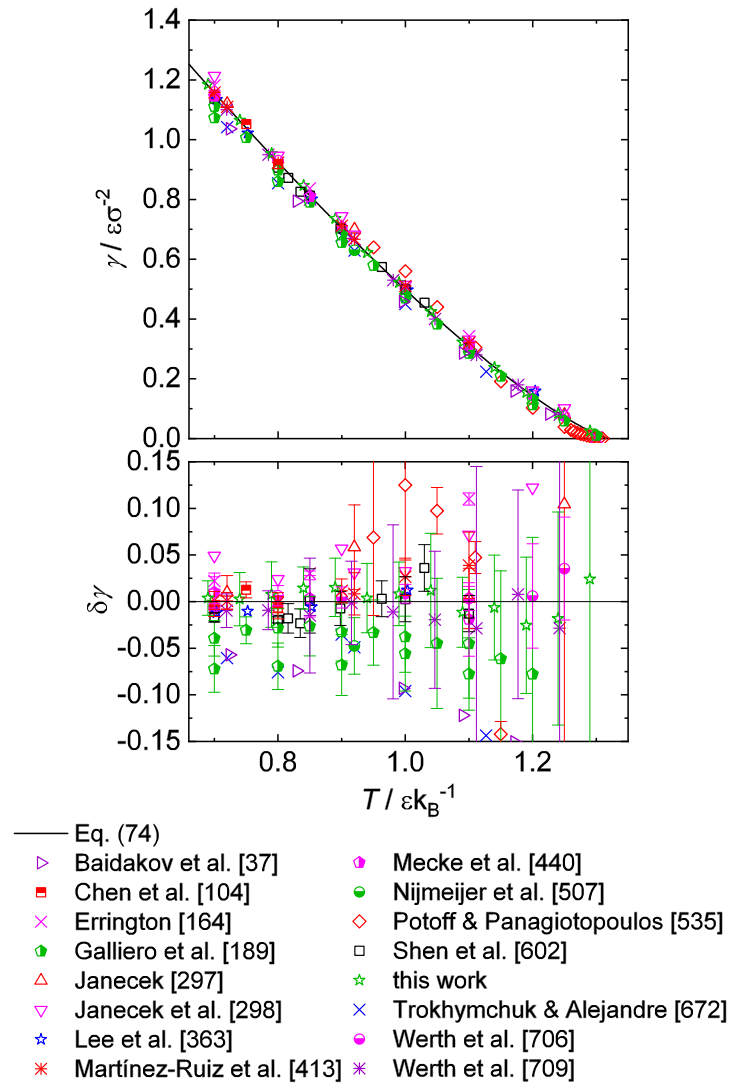
Figure 60: Surface tension of the Lennard-Jones fluid as a function of the temperature (top) and the corresponding relative deviation plot (bottom). The black line (top) and baseline (bottom) indicates Eq. (74). Symbols indicate computer experiment data. For clarity, numerical values for out-of-range data points in the vicinity of the critical temperature are omitted in the deviation plot.

4.2.5 Conclusions

This work reviews and assesses thermophysical property data for the Lennard-Jones fluid. Literature data (approximately 35,000 data points) were digitalized, evaluated, and provided in the electronic Supplementary Material [640] as a consistent database. For the homogeneous state points, approximately 10% of the data were identified to be gross outliers by an EOS test. The lack of information on the statistical uncertainties in some studies is unfortunate.

Three independent consistency tests were employed for the evaluation of the VLE data: the compressibility factor test considers only the vapor pressure and the saturated vapor density, whereas the Clausius-Clapeyron test also considers the saturated liquid density and the enthalpy of vaporization. The third test evaluates the mutual agreement of datasets for each VLE property individually. The VLE datasets of *Errington* [163, 541], *Errington* [164], *Janeček et al.* [298, 299], *Lotfi et al.* [395], *Mick et al.* [452], *Okumura and Yonezawa* [510, 548], and this work were confirmed by all tests and found to be the most precise. The precision with which the VLE of the Lennard-Jones fluid is known is thereby estimated to be ±1% for the vapor pressure, ±0.2% for the saturated liquid density, ±1% for the saturated vapor density, and ±0.75% for the enthalpy of vaporization – excluding the region close to the critical point. Since almost every VLE dataset – even the most precise – contain individual outliers, we recommend to use the combination of the above listed datasets as reference. Furthermore, the datasets of *Hansen and Verlet* [238], *Martínez-Ruiz et al.* [413], *Okumura and Yonezawa* [509, 547], this work (direct simulations), *Stoll et al.* [642], and *Werth et al.* [709] were found to be accurate, but not as precise. The precision of the surface tension is estimated to be ±4%, i.e. significantly larger than the VLE bulk properties.

The EOS test presented here can be adopted easily to other applications in thermodynamics. A test based on the ideas described here could for example be used for testing VLE data of a given mixture based on models of the Gibbs excess energy G^{E}.

Future simulation work should focus on the region in the direct vicinity of the critical point, where the available VLE data and accordingly the location of the critical point agree less well.

The consolidated data base that is presented here is used in sections 4.3 and 4.4 to investigate the performance of equations of state for the Lennard-Jones fluid.

4.3 Equations of State for the Lennard-Jones Fluid

A large number of equations of state of the Lennard-Jones (LJ) fluid have been proposed in the literature of which Table 11 gives a survey. To the best of our knowledge, the different LJ EOS from the literature have never been compared systematically. We have therefore compared 20 of the most widely used LJ EOS using a consistent approach and consolidated reference data. The LJ EOS that were included in the present study are marked with abbreviations in Table 11. The focus of this study is on the LJ EOS developed in the past 30 years. However, some older yet still frequently used LJ EOS were also included in the comparison [4, 128, 505, 559].

There are about 35,000 data points on thermophysical properties of the LJ fluid in the literature, which were critically assessed and screened for outliers, cf. section 4.2 [640]. This consolidated database still contains about 32,000 entries and was used here as basis for the assessment of the LJ EOS.

The following physical properties were considered in the present study:

- the vapor-liquid equilibrium (for given T: vapor pressure p^s, saturated liquid and vapor densities ρ' and ρ'', respectively, and enthalpy of vaporization Δh_v).

- the critical point (critical temperature T_c, critical density ρ_c, and critical pressure p_c).

- homogeneous states (for given temperature T and density ρ: pressure p, thermal expansion coefficient α, isothermal compressibility β, thermal pressure coefficient γ, internal energy u, isochoric heat capacity c_v, isobaric heat capacity c_p, Grüneisen parameter Γ, Joule-Thomson coefficient μ_{JT}, speed of sound w, Helmholtz energy a, and chemical potential μ) in the different fluid regions such as: gas, liquid, supercritical, etc. (details are given below). Also, second and third thermal virial coefficients B and C are considered.

- the qualitative behavior of $p(\rho)$ isotherms in the metastable and unstable region and the spinodal curve.

LJ EOS can be broadly classified into *empirical* EOS and *theoretically-based* EOS. This is only a crude classification and used here in the following sense [135]: empirical EOS are data-driven and aim at correlating the data well. This is usually accomplished by a flexible mathematical form with a large number of parameters. In contrast, the mathematical form of theoretically-based EOS is derived from theoretical considerations. They usually have a smaller number of adjustable parameters than the empirical EOS. Obviously, the border between these two types of EOS is blurred. Most LJ EOS have some physically motivated features and some empirical features, see *Deiters and de Reuck* [135] for a detailed discussion. LJ EOS that could not be clearly assigned to either of the two categories are labeled as *semi-empirical* LJ EOS here.

Table 11: Overview of Lennard-Jones equations of state from the literature – sorted chronologically. # indicates the number of parameters of the LJ EOS. LJ EOS indicated with an abbreviation were included in the comparison in the present work.

Authors	Abbr.	EOS-type	Year	#
Levesque and Verlet [370]		BH perturbation theory; pressure explicit	1969	10
Toxvaerd and Praestgaard [668]		BH perturbation theory; pressure explicit	1970	10
McDonald and Singer [429]		empirical; Helmholtz energy explicit	1972	20
Nicolas et al. [505]	Ni	empirical (MBWR); pressure explicit	1979	33
Ree [559]	Re	empirical; pressure explicit	1980	21
Sýs and Malijevský [649]		empirical + 2nd and 3rd virial coefficient; pressure explicit	1980	21
Cotterman et al. [128]	Co	BH perturbation theory + virial; Helmholtz energy explicit	1986	15
Adachi et al. [4]	Ad	empirical (MBWR); pressure explicit	1988	33
Song and Mason [616]		modified van der Waals equation + virial; pressure explicit	1989	0
Nezbeda and Aim [496]		empirical; pressure explicit	1989	5
Sowers and Sandler [618]		BH perturbation theory; pressure explicit	1991	6
Koutras et al. [343]	Kou	modified HS equation; pressure explicit	1992	15
Miyano [460]	Mi	empirical (MBWR); pressure explicit	1993	33
Johnson et al. [302]	Jo	empirical (MBWR); pressure explicit	1993	33
Kolafa and Nezbeda [334]	Ko	HS + virial + empirical; Helmholtz energy explicit	1994	32

Authors	Abbr.	EOS-type	Year	#
Mecke et al. [438, 439]	Me	HS + empirical; Helmholtz energy explicit	1996	38
Sun and Teja [646]	Su	empirical (MBWR); pressure explicit	1996	33
Cuadros et al. [129]		WCA perturbation theory; Helmholtz energy explicit	1996	5
Amadei et al. [21]		quasi Gaussian entropy theory; Helmholtz energy explicit	1999	11
Hess [258]	He	WCA reference + virial; pressure explicit	1999	0
Boltachev and Baidakov [62]	Bo	empirical + virial; pressure explicit	2003	39
Paricaud [519]	Pa	BH perturbation theory; Helmholtz energy explicit	2006	34
Betancourt-Cardenas et al. [53]		BH perturbation theory; Helmholtz energy explicit	2008	10
Quiñones-Cisneros et al. [554]	Qui	empirical; pressure explicit	2009	16
May and Mausbach [423, 425]	Ma	empirical (MBWR); pressure explicit	2012	33
Lafitte et al. [353]	La	BH perturbation theory; Helmholtz energy explicit	2013	62
Thol et al. [661]	Th	empirical; Helmholtz energy explicit	2016	89
van Westen and Gross [710]	vWe	BH perturbation theory; Helmholtz energy explicit	2017	43
Gottschalk [217]	Go	empirical + virial coefficients	2019	167
this work	th	BH perturbation theory; Helmholtz energy explicit	2020	18

It is widely accepted that both types of EOS have strengths and weaknesses that are often characterized as follows [135, 137, 619]: empirical EOS are strong regarding the accurate description of available data, but weak regarding extrapolations into regions where no data was used for the training of the EOS; for theoretically-based EOS it is the other way around: they are expected to be strong regarding extrapolations but typically less accurate in the description of existing data. Furthermore, empirical EOS are prone to yield unphysical behavior such as crossing isotherms [10, 527, 725] or several van der Waals loops in the vapor-liquid coexistence region [249, 619, 661].

Lennard-Jones equations of state are often used as a base model for building models of more complex fluids [57, 58, 102, 128, 353]. Among the theoretically-based EOS, those of the SAFT-type are particularly successful and have been widely used for describing complex fluids [100, 102, 155, 226, 353, 482]. Most of them were developed starting from an LJ EOS for describing the monomer unit [57, 58, 99, 106, 206–208, 345, 479, 482, 650]. Different LJ EOS are used in different SAFT EOS. The monomer equations of the following SAFT EOS were included in the present study: the Lennard-Jones extended SAFT [206, 207], LJ-SAFT [345, 479], LJ-based SAFT [106], soft-SAFT [57, 58], and SAFT-VR Mie [353, 518]; the corresponding LJ EOS considered in the present work are those from Refs. [302, 334, 353, 505]. Another important SAFT EOS is PC-SAFT [223, 224]. The monomer term of PC-SAFT was not developed to give a good description of the LJ fluid. In the present work, the monomer term of PC-SAFT was re-parametrized in order to get good results for the LJ fluid and enable direct comparisons with the monomer terms in other versions of SAFT EOS. The parametrization, which aims at a good description of both the vapor-liquid equilibrium and the homogeneous region, uses elements from multi-criteria optimization and is described in the Appendix. The results that were obtained with the new LJ EOS give insights in strengths and weaknesses of the functional form of the monomer term that is used in PC-SAFT, which is put into relation to the results from other LJ EOS.

The outline of this study is as follows: first, an overview of the LJ EOS from the literature that were considered in this work is given. The second and main part comprises the evaluation and comparison of LJ EOS. Finally, conclusions are drawn.

The present work is limited to the fluid regions of the Lennard-Jones fluid, i.e. no solid phases are considered. This includes the two-phase regions in which solids occur. The term *two-phase region* refers therefore exclusively to the vapor-liquid coexistence region here.

4.3.1 Overview of Lennard-Jones EOS

Table 11 gives an overview of LJ EOS from the literature. Equations of state that are only defined piecewise are not considered in Table 11, since their derivatives can be discontinuous. The 20 LJ EOS for which an abbreviation is given in Table 11 were considered for the comparison in the present work. As only some of the LJ EOS are available in executable form or as source code, such a comparison requires programming and validation of the considered EOS. Besides the 20 LJ EOS studied here, two more LJ EOS [53, 129] were implemented in the course of this work, but the results reported in the respective publications could not be reproduced using the given equations and

numerical values of the parameters. Hence, they were not considered for the comparison in this work.

Furthermore, in the course of the present work, misprints were identified in Refs. [710] and [554]. The corrections are reported in the Appendix. Using these corrections, our implementations of the LJ EOS from Refs. [554, 710] yield results that are consistent with data reported in the respective publications.

All LJ EOS listed in Table 11 are either formulated explicitly in the pressure or the Helmholtz energy. The number of parameters that were adjusted to obtain a good fit of data from computer experiments varies between 0 and 177. The LJ EOS that were considered in the present work are classified as follows: theoretically-based: Refs. [128, 353, 519, 710] and the LJ EOS from the present work; empirical: Refs. [4, 217, 302, 423, 425, 460, 505, 554, 559, 646, 661]; and semi-empirical: Refs. [62, 258, 334, 343, 438, 439].

The most popular LJ EOS are those of *Johnson et al.* [302], *Nicolas et al.* [505], *Kolafa and Nezbeda* [334], *Cotterman et al.* [128], *Lafitte et al.* [353], *Ree* [559], and *Mecke et al.* [438, 439] (sorted by their the number of citations; for more information, see the Appendix).

The first LJ EOS were published soon after molecular simulations became feasible by *'computing machines'* [15, 451, 566, 717]. The oldest LJ EOS considered in the present work is that of *Nicolas et al.* [505] from 1979, which is a modified *Benedict-Webb-Rubin* (MBWR) type EOS [51, 294]. That LJ EOS has been re-parametrized several times, e.g. from *Adachi et al.* [4], *Miyano* [460], *Johnson et al.* [302], *Sun and Teja* [646], and *May and Mausbach* [423, 425], of which the parametrization of *Johnson et al.* [302] is by far the most frequently used. The oldest LJ EOS of the 'theoretical' type considered here is that of *Cotterman et al.* [128] from 1986. Both *Kolafa and Nezbeda* [334] and *Mecke et al.* [438, 439] proposed semi-empirical LJ EOS in the 90s that became popular. Several theoretically-based LJ EOS have been developed in the recent years, e.g. those of *Paricaud* [519], *Lafitte et al.* [353], and *van Westen and Gross* [710]. But also new empirical LJ EOS have become available recently, e.g. those of *Thol et al.* [661] and *Gottschalk* [217]. Further empirical and semi-empirical LJ EOS that are considered in the present work are those of *Boltachev and Baidakov* [62], *Quiñones-Cisneros et al.* [554], *Ree* [559], *Koutras et al.* [343], and *Hess* [258].

Theoretically-based LJ EOS are usually either built on the perturbation theory of *Barker and Henderson* [42, 43] (BH) or that of *Weeks-Chandler-Andersen* [699] (WCA). The LJ EOS of *Song and Mason* [616] is of the WCA type, those of *Cotterman et al.* [128], *Paricaud* [519], *Lafitte et al.* [353], *van Westen and Gross* [710], and the PC-SAFT monomer are of the BH type. *Van Westen and Gross* [710] also proposed a WCA type LJ EOS and found it equally precise as their BH type LJ EOS. Only the latter is employed here for comparison. Perturbation theory is expected to be a good approximation for state points for which the influence of the attractive forces is not particularly strong, i.e. high temperatures [43, 44].

The theoretically-based LJ EOS apply different formulations for the hard sphere reference term, e.g. the LJ EOS of *Cotterman et al.* [128], *Paricaud* [519], *van Westen and Gross* [710], and *Lafitte et al.* [353] use the hard sphere equation of *Carnahan and Starling* [93], whereas the PC-SAFT monomer uses that of *Boublík* [67] and *Mansoori et al.* [407]. Also the semi-empirical LJ EOS of *Mecke et al.* [438, 439] employs the *Carnahan*

and Starling [93] equation as a description of the hard sphere Helmholtz energy. The semi-empirical LJ EOS of *Kolafa and Nezbeda* [334] employs a slightly modified version of the *Carnahan and Starling* [93] equation. The LJ EOS of *Koutras et al.* [343] is based on an empirically modified version of the *Carnahan and Starling* [93] equation.

The BH type LJ EOS of *Cotterman et al.* [128], *Paricaud* [519], *Lafitte et al.* [353], and *van Westen and Gross* [710] as well as the PC-SAFT monomer use slightly differing formulations for the temperature-dependent diameter for the modeling of the softness of the repulsive interactions [43, 44]. The PC-SAFT monomer model, which was re-parametrized in the present work, uses a simplified version of the temperature-dependent diameter, cf. Eq. (145) in the Appendix.

The theoretically-based LJ EOS of *Cotterman et al.* [128], *Paricaud* [519], and the PC-SAFT monomer model are developed up to the second-order perturbation term. The LJ EOS of *Lafitte et al.* [353] and *van Westen and Gross* [710] are formulated up to third and fourth-order perturbation terms, respectively.

Also the perturbation terms are designed differently in the considered theoretically-based LJ EOS: the LJ EOS of *Cotterman et al.* [128] and the PC-SAFT monomer model are simplified and developed in a series expansion in the packing fraction, whereas the LJ EOS *Paricaud* [519], *Lafitte et al.* [353], and *van Westen and Gross* [710] use an analytic function for the radial distribution function of the hard sphere system.

All LJ EOS considered here were fitted to computer experiment data (except that of *Hess* [258], which has no adjustable parameter). However, the data that was used generally differs. Furthermore, in many cases the training dataset, the objective functions, and weights were not disclosed in the publications. Most LJ EOS were parametrized using pvT data and eventually internal energy data. In some cases also data on the thermal virial coefficients were used for the parametrization – mainly for empirical LJ EOS. The LJ EOS of *Thol et al.* [661], which is explicit in the Helmholtz energy a, was parametrized directly using computer experiment data of a and its density and inverse temperature derivatives. Most theoretically-based LJ EOS [128, 353, 710] are directly parametrized using computer experiment data of the perturbation term. The data type used for the parametrization of each LJ EOS is summarized in the Appendix.

In some publications in which new LJ EOS are proposed (cf. Table 11), an estimated range of validity of the LJ EOS is reported (which is usually given for the density and temperature). Since this range of validity is mostly based only on estimates and in some cases only described ambiguously, we compare all LJ EOS to the same computer experiment database (cf. section 4.2), disregarding the eventual statements on the range of validity to ensure a fair comparison. We find that the reported range of validity of many LJ EOS is either far too optimistic or pessimistic. Information on the reported range of validity of each LJ EOS is given in the Appendix.

4.3.2 Evaluation of Lennard-Jones EOS

Table 8 summarizes the reference database used for comparison, which contains approximately 35,000 data points. These data are also available electronically in the electronic Supplementary Material [640], such that the tests of the different LJ EOS that were

carried out in the present work can easily be reproduced and the approach can be extended to the evaluation of new LJ EOS. Data points that were identified as outliers in Ref. [640] were discarded for the comparison in the present work. The reference data was not differentiated here regarding the source of the data points. However, also that information can be retrieved from the electronic Supplementary Material [640].

As the results from computer simulations are subject to both systematic and statistical errors [242, 590, 640], the true value of a given property of the LJ fluid at a given state point is only known with some uncertainty. That uncertainty depends on the property that is investigated as well as on the state point. Furthermore, the uncertainty can only be estimated and, depending on the way this estimate is carried out, different numbers for the uncertainty are obtained. We do not re-enter into the discussion of the quality of the reference data and simply refer to Ref. [242, 590, 640]. The goal of any description of properties of the LJ fluid by an EOS must be to describe the primary data within their uncertainty. Ideally, this should be fulfilled for all properties of interest in the entire fluid region.

The systematic approach for the comparison of the LJ EOS that was applied in the present study is briefly described in the following. The performance of each LJ EOS i was examined for different thermophysical properties j, and fluid regions k regarding data points l from computer experiments.

The relative deviation δY_{ijkl} of a result Y_{ijkl} from an LJ EOS i from the corresponding computer experiment value $Y_{\mathrm{ref},jkl}$ for a given property j in a given fluid region k is defined as

$$\delta Y_{ijkl} = \frac{Y_{ijkl} - Y_{\mathrm{ref},jkl}}{Y_{\mathrm{ref},jkl}} \ . \tag{75}$$

The complete set of numeric values Y_{ijkl} computed for each data point l from the database [640] for each LJ EOS i is provided in the electronic Supplementary Material [639] together with the corresponding reference value $Y_{\mathrm{ref},jkl}$. Where available, also the statistical uncertainties from the computer experiment data is given.

The absolute average deviation AAD_{ijk} of a given LJ EOS i for a thermophysical property j in a fluid region k is defined as

$$\mathrm{AAD}_{ijk} = 1/N_{jk} \sum_{l=1}^{N_{jk}} |\delta Y_{ijkl}| , \tag{76}$$

where N_{jk} is the number of reference data points for the respective property j in the fluid region k. Hence, the AAD_{ijk} quantifies the performance of an LJ EOS for a certain property j in a certain fluid region k. The overall performance of an LJ EOS i for a given property j was evaluated using

$$\mathrm{AAD}_{ij} = 1/N_{\mathrm{tot}} \sum_{l=1}^{N_{\mathrm{tot}}} |\delta Y_{ijl}| , \tag{77}$$

where N_{tot} is the number of data points available for a given property j. For clarity and simplicity we sometimes refer to AAD_{ij} for a given property j simply as $\mathrm{AAD}_{j,\mathrm{total}}$ in the following text, when it is clear which LJ EOS i is meant.

The classification into different fluid regions k is only used for homogeneous state data

points specified as $Y = Y(T, \rho)$. Fig. 61 shows the eight fluid regions that were used in the present work for the classification of $Y = Y(T, \rho)$ data.
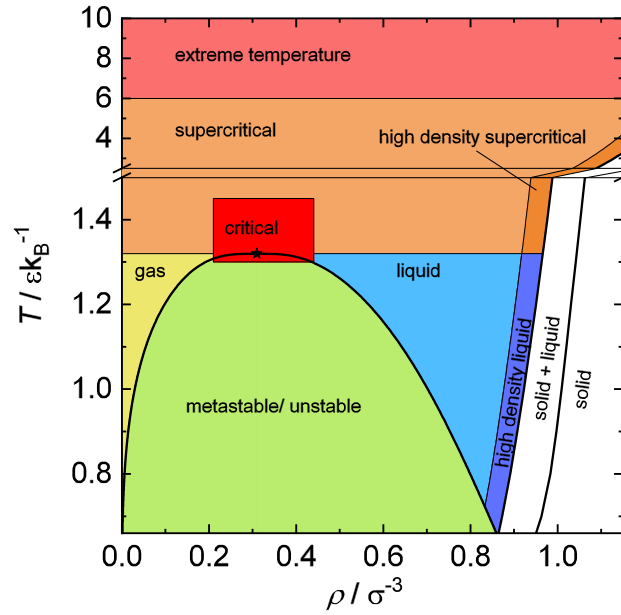
Figure 61: Definition of characteristic fluid regions (colored) of the LJ fluid used for the evaluation and comparison of LJ EOS in the present work: metastable/ unstable (MU), gas (G), liquid (L), critical (C), supercritical (Su), high density liquid (HD-L), high density supercritical (HD-Su), and extreme temperature (Ex-T). Details on the boundaries of the regions are given in Table 12. Solid states and the melting region were not considered in the present study.

Table 12 summarizes the conditions for each region. The binodal was adopted from an analytic correlation of *Stephan et al.* [640] (cf. section 4.2.4.2) and the freezing line from *Köster et al.* [341]. The line separating data in the high density liquid and high density supercritical region was chosen as 95% of the density of the freezing line reported by *Köster et al.* [341]. Since only very few computer experiment data has been reported for the unstable region [460, 537, 640] obtained from specialized techniques and the location of the spinodal is only known with large uncertainty (see below), the metastable and unstable region were combined for the comparison to a single region enclosed by the binodal. An eighth characteristic region was defined at extreme temperatures $T > 6\,\varepsilon k_{\mathrm{B}}^{-1}$, i.e. the supercritical and high density supercritical region end at $T = 6\,\varepsilon k_{\mathrm{B}}^{-1}$. All data points from the database compiled in section 4.2 of the type $Y = Y(T, \rho)$ were assigned to one of these eight regions. The allocation of each data point is reported in the electronic Supplementary Material [639]. Data points that are specified as $Y = Y(T)$, namely VLE properties, virial coefficients, and spinodal data, belong to individual fluid regions.

For each LJ EOS i, the obtained AAD_{ijk} for each property j and each region k and AAD_{ij} are reported in Tables 13 - 15 and are discussed in the following sections.

Table 12: Definition of characteristic fluid regions, cf. Fig. 61. The correlations for the bubble line $\rho'(T)$, the dew line $\rho''(T)$, and the freezing line $\rho'''(T)$ were adopted from section 4.2.4.2 and Refs. [341], respectively. The employed critical parameters are $T_c = 1.321\,\varepsilon k_\mathrm{B}^{-1}$ and $\rho_c = 0.316$.

Name	Abbr.	$T_\mathrm{min}\,/\,\varepsilon k_\mathrm{B}^{-1}$	$T_\mathrm{max}\,/\,\varepsilon k_\mathrm{B}^{-1}$	$\rho_\mathrm{min}\,/\,\sigma^{-3}$	$\rho_\mathrm{max}\,/\,\sigma^{-3}$
gas[a]	G	≤ 0.66	< 1.321	-	$< \rho''$
liquid[a]	L	≤ 0.66	< 1.321	$> \rho'$	$< 0.95\rho'''$
high density liquid	HD-L	≤ 0.66	< 1.321	$> 0.95\rho'''$	$< \rho'''$
critical	C	≤ 1.3	< 1.45	> 0.21	< 0.44
metastable & unstable[a]	MU	≤ 0.66	< 1.321	$> \rho''$	$< \rho'$
supercritical[a]	Su	≤ 1.321	≥ 6	-	$< 0.95\rho'''$
high density supercritical	HD-Su	≤ 1.321	≥ 6	$> 0.95\rho'''$	$< \rho'''$
extreme temperature	Ex-T	> 6	-	-	-

[a] excluding critical region C

4.3.2.1 Vapor-Liquid Equilibrium

The vapor-liquid equilibrium of the LJ fluid has been investigated numerous times [6, 7, 9, 23, 31, 37, 39, 53, 97, 104, 163, 164, 189, 229, 230, 238, 268, 283, 297, 298, 298, 324, 331, 363, 395, 410, 413, 440, 452, 507, 509, 510, 514, 516, 526, 535, 580, 582, 603, 612, 628, 640, 642, 672, 709]. Seven of these 45 datasets were found to be significantly more precise and accurate than the remaining, cf. section 4.2.4.2. Only these seven best datasets were used here for the comparison. However, also these seven datasets contain 8 clear outliers [640] that were discarded for the present investigation. The mutual agreement of these seven datasets was estimated to be ±1% for the vapor pressure, ±0.2% for the saturated liquid density, ±1% for the saturated vapor density, and ±0.75% for the enthalpy of vaporization – excluding the region close to the critical point ($T > 1.26\,\varepsilon k_{\mathrm{B}}^{-1}$) [640]. Furthermore, empirical correlations of these 7 best datasets for p^s, Δh_{v}, ρ', and ρ'' have been proposed in section 4.2.4.2. The relative deviations of the VLE properties are shown in Fig. 62 (vapor pressure p^s and the enthalpy of vaporization Δh_{v}) and in Fig. 63 (saturated liquid and vapor density ρ' and ρ'', respectively). The baselines are the empirical correlations from section 4.2.4.2, other lines are the LJ EOS, and symbols indicate reference data from the computer experiments. Table 13 lists the $\mathrm{AAD}_{j,\mathrm{total}}$ as defined by Eq. (77) obtained from the reference VLE data and each of the 20 considered LJ EOS for $j = \rho'$, ρ'', p^s, Δh_{v}. The VLE computed from each of the considered LJ EOS are reported in the electronic Supplementary Material [639].

The LJ EOS of *Thol et al.* [661], *Mecke et al.* [438, 439], *Kolafa and Nezbeda* [334], *Gottschalk* [217], and from the present work show the best agreement with the VLE simulation results. Nevertheless, the LJ EOS of *Thol et al.* [661], *Mecke et al.* [438, 439], *Gottschalk* [217], and the LJ EOS from the present work exhibit minor systematic deviations from the simulation results in the saturated liquid density at $T > 1\,\varepsilon k_{\mathrm{B}}^{-1}$. Only the LJ EOS of *Kolafa and Nezbeda* [334] captures this trend correctly.

The LJ EOS of *Johnson et al.* [302], *May and Mausbach* [423, 425], *Sun & Teja* [646], *Lafitte et al.* [353], and *van Westen and Gross* [710] also give a good description of the VLE properties of the LJ fluid. However, the LJ EOS of *Lafitte et al.* [353], *van Westen and Gross* [710], and *Johnson et al.* [302] exhibit distinct systematic deviations from the reference data of the vapor pressure and the saturated densities. The LJ EOS of *May and Mausbach* [423, 425] exhibits noticeable deviations regarding the saturated liquid density at $T > 1\,\varepsilon k_{\mathrm{B}}^{-1}$.

Particularly large deviations from the computer experiment VLE data are found for the LJ EOS of *Nicolas et al.* [505], *Miyano* [460], *Boltachev and Baidakov* [62], *Adachi et al.* [4], *Cotterman et al.* [128], *Paricaud* [519], *Hess* [258], *Koutras et al.* [343], *Ree* [559], and *Quiñones-Cisneros et al.* [554].

All considered LJ EOS are fully analytic and thereby exhibit classical scaling behavior, e.g. quadratic convergence of the saturated densities near the critical point [178, 326, 599]. This, and the fact that the investigated LJ EOS have significantly differing critical temperatures (see following section), leads to the diverging deviations of the VLE properties in Figs. 62 and 63 in the vicinity of the critical point. Also, the scattering of the computer experiment VLE data significantly increases in the vicinity of the critical point and, accordingly, only very few consistent data points are available in that region [640].
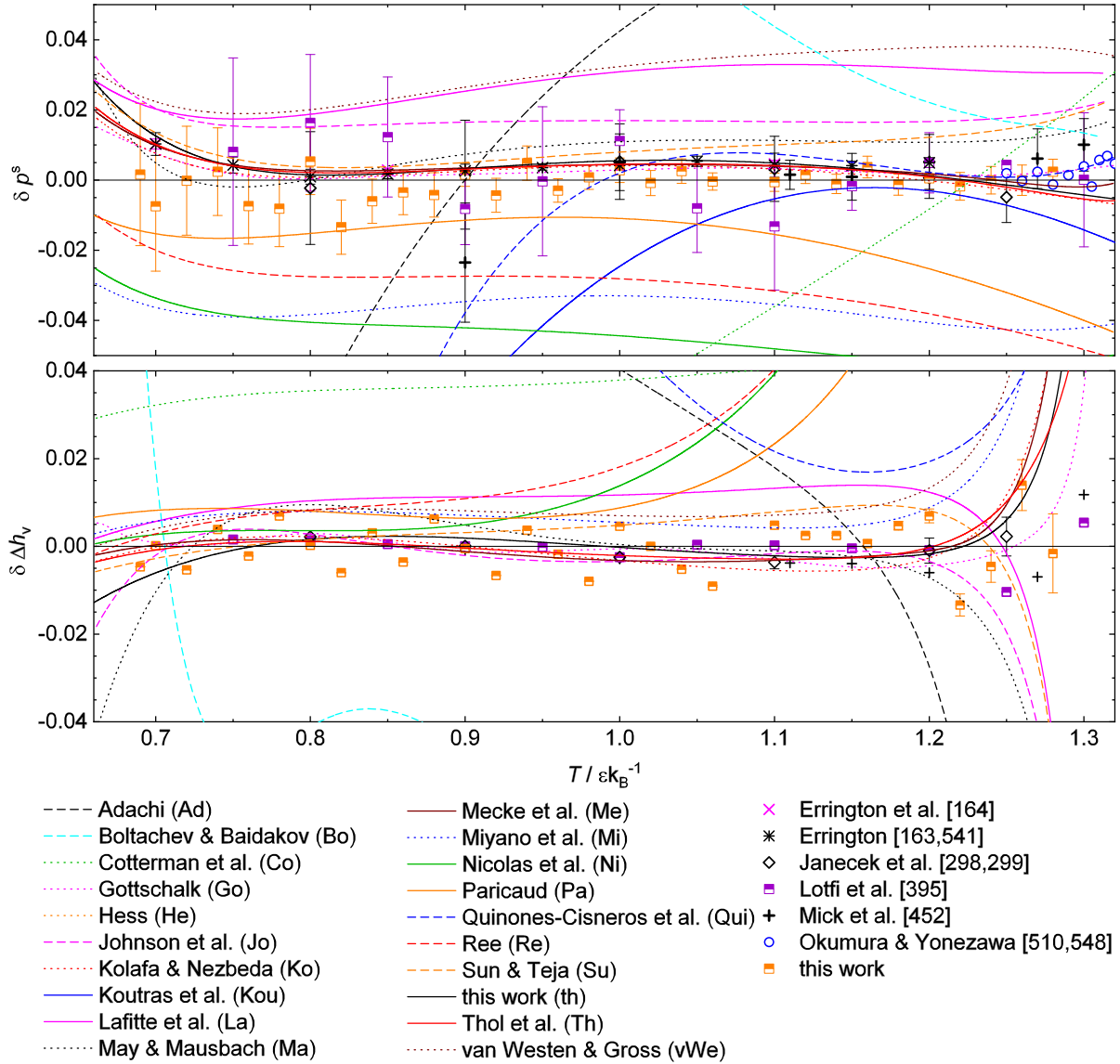
Figure 62: Comparison of the results from 20 LJ EOS with reference data: relative deviation of the vapor pressure (top) and enthalpy of vaporization (bottom). The base line indicates the respective correlation of computer experiment data from section 4.2.4.2. The other lines are results from the LJ EOS; symbols are data from computer experiment.
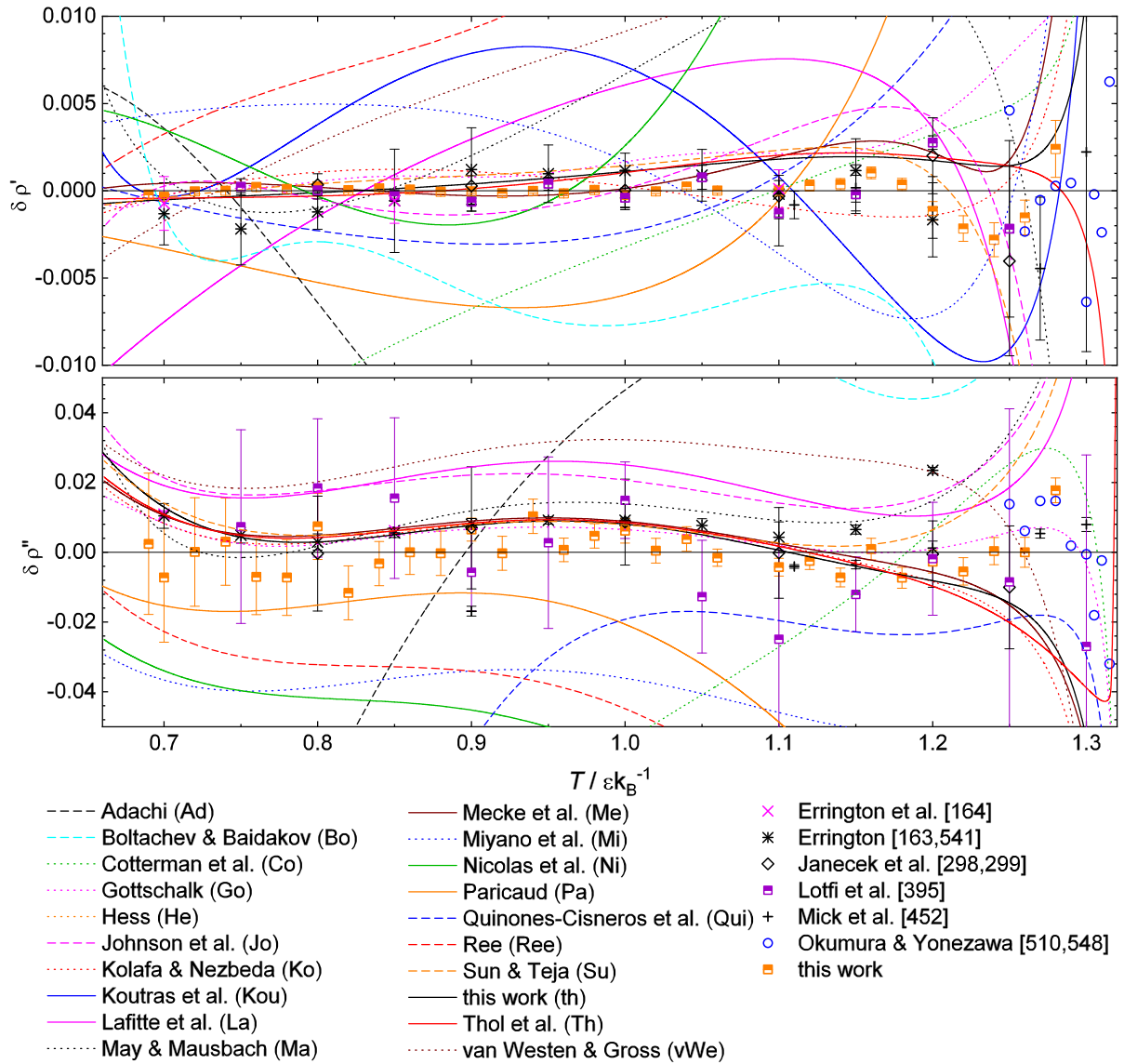
Figure 63: Comparison of the results from 20 LJ EOS with reference data: relative deviation of the saturated densities: liquid density (top) and vapor density (bottom). The base line indicates the correlation of computer experiment data from section 4.2.4.2. The other lines are results from the LJ EOS; symbols are data from computer experiment.

Table 13: Comparison of results from 20 LJ EOS i with reference data from Refs. [163, 164, 298, 299, 395, 452, 510, 541, 548] and the dataset from the present work: absolute average deviations AAD_{ijk} (cf. Eq. 76) for the vapor-liquid equilibrium region k with the properties j = vapor pressure p^s, saturated liquid and vapor densities ρ' and ρ'', and the corresponding spinodal properties ρ' and ρ'', enthalpy of vaporization Δh_v, and the corresponding spinodal properties (from Refs. [37, 380]). # indicates the number of data points available. The LJ EOS of *Gottschalk* [217] and *Thol et al.* [661] yield unphysical results in the two-phase region and were therefore not applied for the computation of the spinodal (see Appendix for details). The lines 'total' states the mean AAD_{ij} for all binodal and spinodal VLE data according Eq. (77).

	#	Cotterman et al. [128]	Paricaud [519]	Lafitte et al. [353]	van Westen & Gross [710]	this work	Koutras et al. [343]	Kolafa & Nezbeda [334]	Mecke et al. [438, 439]	Hess [258]	Boltachev et al. [62]	Gottschalk [217]	Quiñones-Cisneros et al. [554]	Nicolas et al. [505]	Adachi et al. [4]	Miyano [460]	Johnson et al. [302]	Sun & Teja [646]	May & Mausbach [423, 425]	Ree [559]	Thol et al. [661]
binodal																					
ρ'	77	0.7	1.5	0.7	1.3	0.2	0.5	0.2	0.2	4.7	1.2	0.3	0.6	2.6	6.7	0.5	0.3	0.3	0.6	3.4	0.2
ρ''	77	6.3	6.1	2.2	2.7	1.3	10.9	1.4	1.4	47.4	10.4	1.0	8.6	8.4	13.5	4.8	2.4	1.4	1.8	8.1	1.4
p^s	77	6.4	2.2	3.0	3.3	0.8	5.5	0.8	0.8	40.9	8.3	0.7	6.9	4.7	10.8	3.9	1.9	1.2	1.2	3.4	0.8
Δh_v	57	4.0	4.2	1.4	1.5	0.7	10.4	0.7	0.7	40.6	6.3	0.6	11.1	5.2	9.1	1.2	0.8	0.9	1.1	5.9	0.6
total	288	**4.3**	**3.4**	**1.8**	**2.2**	**0.7**	**6.6**	**0.8**	**0.8**	**32.9**	**6.5**	**0.7**	**6.5**	**5.2**	**10.1**	**2.7**	**1.4**	**1.0**	**1.2**	**5.2**	**0.8**
spinodal																					
ρ' spin	3	2.3	3.3	1.0	0.7	0.9	4.3	0.5	0.7	2.3	0.7	-	2.3	3.3	3.4	2.5	1.1	1.7	2.2	2.2	-
ρ'' spin	9	8.6	17.0	12.1	12.4	9.0	14.7	4.8	4.0	11.8	5.6	-	9.3	10.6	8.3	7.0	5.7	9.6	6.3	24.1	-
p^s spin	7	6.2	20.6	16.8	16.3	10.8	23.0	5.2	4.2	6.3	5.7	-	15.0	12.8	11.8	7.6	6.4	11.7	7.2	30.4	-
total	19	**6.7**	**16.1**	**12.1**	**12.0**	**8.4**	**16.1**	**4.3**	**3.5**	**8.3**	**4.9**	-	**10.3**	**10.3**	**8.8**	**6.5**	**5.2**	**9.1**	**6.0**	**23.0**	-

For each VLE property j, the lowest absolute average deviation AAD_{ij} among the considered LJ EOS i in Table 13 is in good agreement with the stated mutual agreement of the best computer experiment data, which indicates that the lowest absolute average deviation values are in fact good guesses for the accuracy of the reference data.

4.3.2.2 Critical Point

Critical data derived from computer experiment data of the LJ fluid have been reported numerous times in the literature [7, 46, 53, 84, 148, 259, 261, 283, 323, 332, 350, 370, 383, 395, 410, 450, 509, 510, 514, 534, 535, 559, 603, 611, 618, 647, 677, 678]. They were summarized and assessed in section 4.2. The critical data of the LJ fluid were thereby estimated to be $T_c = 1.321 \pm 0.007\,\varepsilon k_{\mathrm{B}}^{-1}$ and $\rho_c = 0.316 \pm 0.005\,\sigma^{-3}$ and $p_c = 0.129 \pm 0.005\,\varepsilon\sigma^{-3}$. These values are referred to as 'computer experiment' critical data in the following.

The numeric values of the critical data computed from the LJ EOS are reported in the Appendix. Fig. 64 shows the comparison of the critical data obtained from the LJ EOS and the computer experiment values with their uncertainties. The critical data from the LJ EOS scatter in a large range compared to the uncertainty of the critical data from the computer experiments. Six LJ EOS (Refs. [258, 343, 460, 505, 519, 710]) have particularly large deviations from the computer experiment critical point. Many LJ EOS show fair agreement with the critical density from the computer experiments, but a significant overestimation of the critical temperature and pressure is found in most cases, which is due to the scaling behavior of the EOS [178, 326, 599]. The critical pressure obtained from the vast majority of LJ EOS lies within a narrow band in the $p - T$ diagram. The width of that band is similar to the estimated uncertainty of the critical pressure from the computer experiments $\delta p_c = \pm 0.005\,\varepsilon\sigma^{-3}$. Hence, the deviation of the critical point computed from the LJ EOS is mainly a result of the mismatching critical temperature – as expected from the scaling behavior.

The critical parameters obtained from the LJ EOS of *Johnson et al.* [302], *Lafitte et al.* [353], *May and Mausbach* [423, 425], and *Thol et al.* [661] are in excellent agreement with the computer experiment, which is surprising considering the fact that they are analytic EOS and therefore should not be accurate in the vicinity of the critical point. *Lafitte et al.* [353] assume that the applied third-order perturbation term is responsible for the relatively low critical temperature of their LJ EOS. However, the LJ EOS of *van Westen and Gross* [710] significantly overestimates the critical temperature of the computer experiment, but also includes higher-order perturbation terms. Despite its good results for the critical data, the LJ EOS of *Thol et al.* [661] has a relatively poor performance for state points in the vicinity of the critical point – even crossing isotherms are observed (see below).

The critical parameters obtained from the LJ EOS of *Cotterman et al.* [128], *Kolafa and Nezbeda* [334], *Mecke et al.* [438, 439], *Sun and Teja* [646], *Quiñones-Cisneros et al.* [554], *Gottschalk* [217], and the LJ EOS from the present work are generally in reasonable agreement with critical data from the computer simulations, but they overestimate the critical temperature T_c by about $0.01 \dots 0.02\,\varepsilon k_{\mathrm{B}}^{-1}$. The LJ EOS of *Paricaud* [519], *Hess* [258], and *Ree* [559] overestimate the critical temperature by about $0.06 \dots 0.09\,\varepsilon k_{\mathrm{B}}^{-1}$.
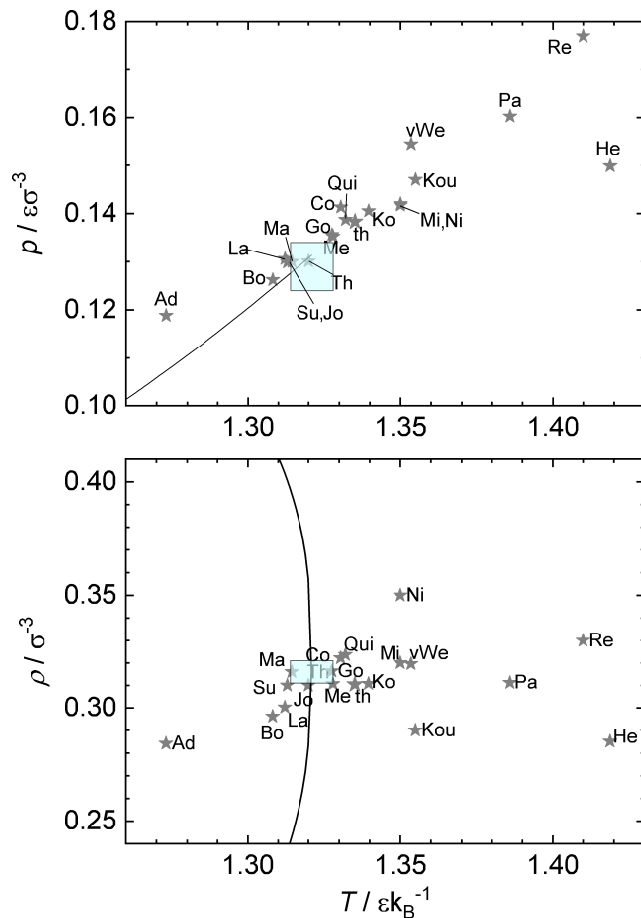
Figure 64: Critical point of the LJ fluid. Top: critical pressure over temperature. Bottom: critical density over temperature. Each combination of a star & abbreviation indicates the critical parameters from an LJ EOS. The abbreviations are the same as those in Table 11. The blue shaded area indicates the critical parameters from computer experiments and their uncertainties [640]. The solid lines indicate the correlations of the VLE properties from *Stephan et al.* [640]. The numeric values of the critical parameters obtained from the LJ EOS are reported in the Supplementary Material.

4.3.2.3 Isotherms in the Two-Phase Region and Spinodal

Equations of state should exhibit only a single van der Waals loop in the vapor-liquid two-phase region. Multiple oscillations of isotherms are prohibitive for calculating interfacial properties, e.g. with density gradient theory [167, 168, 573]. Furthermore, isotherms in the two-phase region can show artificial undulations around the general course of the van der Waals loop, which have a smaller amplitude than that of the van der Waals loop. Another problem that can occur are crossing isotherms (multiplicity).

In this section, the behavior of the LJ EOS is characterized regarding the behavior of isotherms in the two-phase region in the $p - \rho$ diagram and the spinodal. The results from the quantitative comparison of the LJ EOS with computer experiment data of the type $Y = Y(T, \rho)$ for state points between the binodals with LJ EOS are discussed in the subsequent section.

The isotherms in the $p-\rho$ diagram of all 20 considered LJ EOS were examined in the temperature range $T = 0.5\ldots 1.32\,\varepsilon k_\mathrm{B}^{-1}$ regarding the following features in the two-phase region: the number of zero crossings of $\mathrm{d}p/\mathrm{d}\rho = 0$ and $\mathrm{d}^2p/\mathrm{d}\rho^2 = 0$; the results are summarized in Fig. 65. The numeric values for four isotherms in the two-phase region are reported in the electronic Supplementary Material [639].
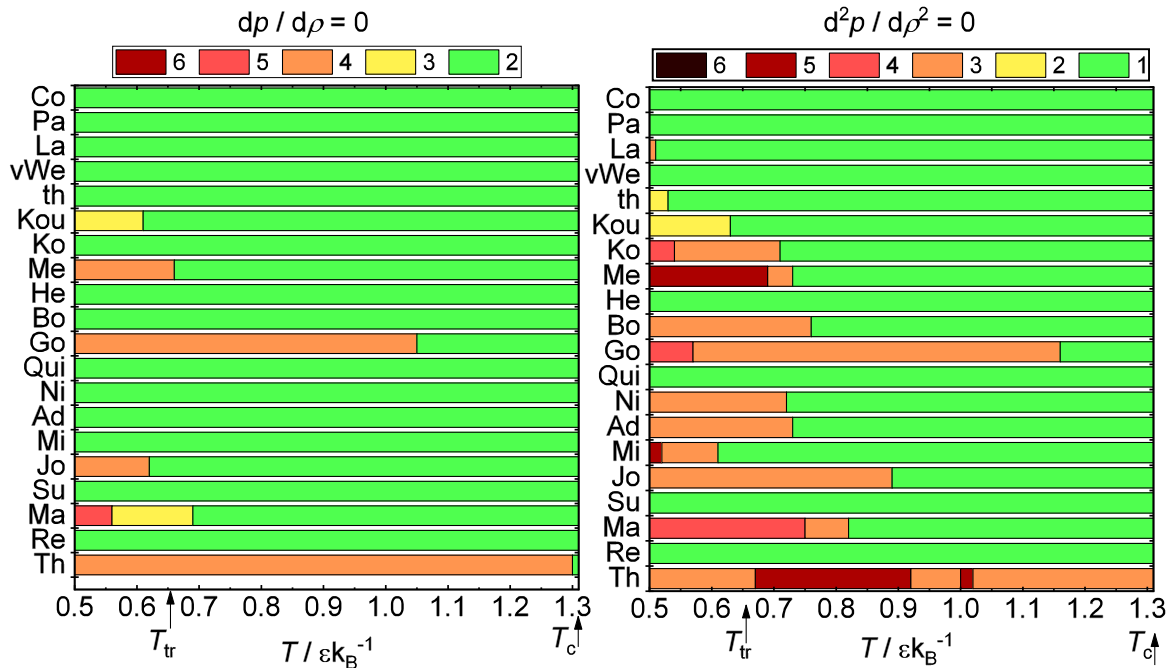
Figure 65: Number of zero crossings of the first and second derivative of the $p-\rho$ isotherms ($\mathrm{d}p/\mathrm{d}\rho = 0$ and $\mathrm{d}^2p/\mathrm{d}\rho^2 = 0$) in the two-phase region as a function of the temperature for all 20 considered LJ EOS. The left panel indicates the number of $\mathrm{d}p/\mathrm{d}\rho = 0$ at a given temperature; the right panel indicates the number of $\mathrm{d}^2p/\mathrm{d}\rho^2 = 0$. The desired values are: 2 for the left panel and 1 for the right and are indicated in green. The abbreviations for the LJ EOS are the same as in Table 11.

Most theoretically-based LJ EOS show none of the problems mentioned above in the two-phase region, whereas most empirical and semi-empirical LJ EOS show at least some artifacts in the two-phase region. The LJ EOS of *Gottschalk* [217] and *Thol et al.* [661] exhibit multiple minima and maxima in a wide temperature range, cf. Fig. 65. The LJ EOS of *Thol et al.* [661] exhibits artificial oscillations up to extreme negative and positive pressures, which results in a crossing of isotherms [10, 527, 725] not only in the two-phase region but also the supercritical region (details are given in the Appendix). The LJ EOS of Refs. [302, 423, 425, 438, 439] exhibit multiple extrema only in the vicinity or below of the triple point temperature. For the LJ EOS of *Boltachev and Baidakov* [62], isotherms exhibit a second (unphysical) maximum in the homogeneous high density region, which yields large deviations from reference data in that region (see following section).

Several LJ EOS also exhibit undulations of the isotherms between the binodals in the $p-\rho$ diagram. This leads to the fact that the isotherms in the $p-\rho$ diagram of the LJ EOS of *Johnson et al.* [302], *May and Mausbach* [423, 425], *Nicolas et al.* [505], *Mecke et al.* [438, 439], *Boltachev and Baidakov* [62], *Kolafa and Nezbeda* [334], and

Adachi et al. [4] exhibit a single van der Waals loop, but multiple turning points. The isotherms of the LJ EOS of *Miyano* [460], *Lafitte et al.* [353], *Koutras et al.* [343], and the LJ EOS from the present work exhibit such turning points only below the triple point temperature, cf. Fig. 65 - right.

For most of the investigated LJ EOS, the undulations of the isotherms in the two-phase region decrease with increasing temperature and vanish upon approaching the critical point (see the electronic Supplementary Material [639]). The only exception is the LJ EOS of *Thol et al.* [661], which exhibits large oscillations up to the critical temperature.

LJ EOS with isotherms with a single and smooth van der Waals loop in the entire considered temperature range (cf. Fig. 65) are those of *Cotterman et al.* [128], *Paricaud* [519], *Quiñones-Cisneros et al.* [554], *Hess* [258], *Ree* [559], and *van Westen and Gross* [710]. The isotherms of the LJ EOS of *Sun and Teja* [646], *Lafitte et al.* [353], and the LJ EOS from the present work exhibit very small undulations between the binodals above the triple point – without producing a second turning point in the isotherms (see electronic Supplementary Material).

Recently, *Alsaifi* [19] carried out a study on the behavior of six empirical and semi-empirical LJ EOS [302, 334, 423, 425, 438, 439, 505, 661] regarding possible artificial phenomena. The findings for these six LJ EOS are in line with the results from the present work.

Data derived from computer experiments for the spinodal of the LJ fluid have been reported by *Baidakov et al.* [37] and *Linhart et al.* [380]. This data was compared with the spinodals computed from the 20 LJ EOS that were considered here. The bottom section of Table 13 reports the obtained absolute average deviations. In the assessment of the deviations, it must be considered that only few reference data points are available that are also subject to strong scattering (see Appendix).

The LJ EOS of *Mecke et al.* [438, 439], *Kolafa and Nezbeda* [334], *Boltachev and Baidakov* [62], and *Johnson et al.* [302] yield the best agreement with the spinodal reference data. Due to the artificial oscillatory behavior of the isotherms from the LJ EOS of *Gottschalk* [217] and *Thol et al.* [661], no meaningful spinodal could be computed for those LJ EOS.

4.3.2.4 Homogeneous Fluid States

In the present section, the performance of the LJ EOS for describing thermodynamic properties of homogeneous fluid state points is discussed, which are calculated as $Y = Y(T, \rho)$. The considered states are grouped in the fluid regions k shown in Fig. 61. Computer experiment data points that were identified as outliers in section 4.2.4.1 were discarded for the evaluation of the LJ EOS here. The reference data of each property j of that type (cf. Table 8) was compared with the corresponding results of each of the LJ EOS i. The obtained numbers for AAD_{ijk} and AAD_{ij}, cf. Eq. (76) and (77), are reported in Tables 14 - 15. Since several LJ EOS have extremely large deviations from the reference data (many orders of magnitude) in the extreme temperature region $k = \text{Ex-T}$, which would lead to a meaningless total AAD_{ij}, the Ex-T results were not comprised in the AAD_{ij} calculation but are reported separately in Table 15 instead.

For all considered LJ EOS, the thermodynamic properties were computed from their relations to the reduced Helmholtz energy $\tilde{a} = a/T$ and its derivatives with respect to the density and the inverse temperature using the following notation:

$$\tilde{a}_{nm} = \tilde{a}_{nm}^{\mathrm{id}} + \tilde{a}_{nm}^{\mathrm{res}} = (1/T)^n \rho^m \frac{\partial^{n+m}(\tilde{a}^{\mathrm{id}} + \tilde{a}^{\mathrm{res}})}{\partial(1/T)^n \partial\rho^m} \ , \tag{78}$$

where 'id' and 'res' indicate the ideal gas contribution and the residual contribution to the Helmholtz energy, respectively. Only, data for $n, m = 0, 1, 2$ were considered here. This formalism was also applied to pressure-explicit LJ EOS, cf. Table 11. As the Lennard-Jones fluid is a monoatomic gas, its ideal gas heat capacity is a priori known. The following thermodynamic properties were studied here [619, 661]:

thermal properties

pressure
$$p = -\left(\frac{\partial a}{\partial v}\right)_T = \rho T \left(1 + \tilde{a}_{01}^{\mathrm{res}}\right) \tag{79}$$

caloric properties

residual internal energy
$$u^{\mathrm{res}} = a^{\mathrm{res}} + T s^{\mathrm{res}} = T\tilde{a}_{10}^{\mathrm{res}} \tag{80}$$

isobaric heat capacity
$$c_p = \left(\frac{\partial h}{\partial T}\right)_p = -(\tilde{a}_{20}^{\mathrm{id}} + \tilde{a}_{20}^{\mathrm{res}}) + \frac{(1 + \tilde{a}_{01}^{\mathrm{res}} - \tilde{a}_{11}^{\mathrm{res}})^2}{1 + 2\tilde{a}_{01}^{\mathrm{res}} + \tilde{a}_{02}^{\mathrm{res}}} \tag{81}$$

isochoric heat capacity
$$c_v = \left(\frac{\partial u}{\partial T}\right)_v = -(\tilde{a}_{20}^{\mathrm{id}} + \tilde{a}_{20}^{\mathrm{res}}) \tag{82}$$

entropic properties

residual chemical potential
$$\mu^{\mathrm{res}} = h^{\mathrm{res}} - T s^{\mathrm{res}} = T\left(1 + \tilde{a}_{00}^{\mathrm{res}} + \tilde{a}_{01}^{\mathrm{res}}\right) \tag{83}$$

2nd-order thermodynamic derivatives

thermal pressure coefficient
$$\gamma = \left(\frac{\partial p}{\partial T}\right)_\rho = \rho\left(1 + \tilde{a}_{01}^{\mathrm{res}} - \tilde{a}_{11}^{\mathrm{res}}\right) \tag{84}$$

isothermal compressibility
$$\beta = \left(\rho \frac{\partial p}{\partial \rho}\right)_T^{-1} = \frac{1}{\rho T(1 + 2\tilde{a}_{01}^{\mathrm{res}} + \tilde{a}_{02}^{\mathrm{res}})} \tag{85}$$

thermal expansion coefficient
$$\alpha = \beta\gamma = \frac{\left(\frac{\partial p}{\partial T}\right)_\rho}{\rho\left(\frac{\partial p}{\partial \rho}\right)_T} = \frac{1 + \tilde{a}_{01}^{\mathrm{res}} - \tilde{a}_{11}^{\mathrm{res}}}{T(1 + 2\tilde{a}_{01}^{\mathrm{res}} + \tilde{a}_{02}^{\mathrm{res}})} \tag{86}$$

speed of sound
$$w = \sqrt{\left(\frac{\partial p}{\partial \rho}\right)_s} =$$
(87)

$$= \left(T\left((1 + 2a_{01}^{\mathrm{res}} + a_{02}^{\mathrm{res}}) - \frac{(1 + a_{01}^{\mathrm{res}} - a_{11}^{\mathrm{res}})^2}{a_{20}^{\mathrm{id}} + a_{20}^{\mathrm{res}}}\right)\right)^{0.5}$$

Joule-Thomson coefficient
$$\mu_{\mathrm{JT}} = \left(\frac{\partial T}{\partial p}\right)_h =$$
(88)

$$= \rho^{-1} \frac{-(\tilde{a}_{01}^{\mathrm{res}} + \tilde{a}_{02}^{\mathrm{res}} + \tilde{a}_{11}^{\mathrm{res}})}{(1 + \tilde{a}_{01}^{\mathrm{res}} - \tilde{a}_{11}^{\mathrm{res}})^2 - (\tilde{a}_{20}^{\mathrm{id}} + \tilde{a}_{20}^{\mathrm{res}})(1 + 2\tilde{a}_{01}^{\mathrm{res}} + \tilde{a}_{02}^{\mathrm{res}})}$$

Grüneisen parameter
$$\Gamma = \frac{\left(\frac{\partial p}{\partial T}\right)_\rho}{\rho\, c_v} = \frac{1 + \tilde{a}_{01}^{\mathrm{res}} - \tilde{a}_{11}^{\mathrm{res}}}{-\tilde{a}_{20}^{\mathrm{id}} - \tilde{a}_{20}^{\mathrm{res}}}$$
(89)

Thermal Properties

The AAD_{ijk} computed according Eq. (76) for the pressure data $j = p$ is given in Table 14 for all considered LJ EOS i and all regions k, except for the extreme temperature region $k = $ Ex-T, for which the corresponding results are presented in Table 15. Table 14 furthermore reports the absolute average deviations from the (exact) values for the second and third virial coefficient $k = B, C$, which were taken from the literature [46, 264, 505, 640, 711].

The overall best description of the pvT data is found for the LJ EOS of *Gottschalk* [217], *Thol et al.* [661], *Mecke et al.* [438, 439], and *Kolafa and Nezbeda* [334]. However, the LJ EOS of *Thol et al.* [661] and *Gottschalk* [217] exhibit extreme deviations in the metastable/ unstable region (see above). The LJ EOS from the present work describes the pvT data in the gas, liquid, and critical region as good as the best LJ EOS in those regions. In the high density liquid, and metastable/ unstable region, the LJ EOS from the present work has slightly larger mean deviations than the best LJ EOS in those regions.

Table 14: Comparison of the results from 20 LJ EOS i with reference data, cf. Table 8 (outliers identified in the dataset as discussed in section 4.2.4.1 were discarded): absolute average deviations AAD_{ijk} (cf. Eq. 76) for different thermodynamic properties j for homogeneous state points in different regions k. The last line 'total' of each section gives the mean absolute average deviation (cf. Eq. 77). # is the number of data points.

	#	Cotterman et al. [128]	Paricaud [519]	Lafitte et al. [353]	van Westen & Gross [710]	this work	Koutras et al. [343]	Kolafa & Nezbeda [334]	Mecke et al. [438, 439]	Hess [258]	Boltachev et al. [62]	Gottschalk [217]	Quiñones-Cisneros et al. [554]	Nicolas et al. [505]	Adachi et al. [4]	Miyano [460]	Johnson et al. [302]	Sun & Teja [646]	May & Mausbach [423, 425]	Ree [559]	Thol et al. [661]
pvT data																					
G	169	1.2	1.0	0.9	0.8	0.1	2.4	0.1	0.1	0.8	0.1	0.1	1.0	0.6	0.9	0.6	0.2	0.2	0.1	1.2	0.1
L	537	15.2	9.5	6.4	8.1	2.8	11.6	3.4	3.0	65.8	16.4	2.9	5.0	8.6	21.0	8.2	3.6	5.0	5.1	16.9	2.9
HD-L	233	32.0	5.6	18.6	10.6	3.9	6.8	3.4	3.1	87.7	40.8	3.2	3.5	6.8	7.3	6.9	3.1	5.0	6.2	5.4	3.2
MU	495	14.9	23.5	13.9	20.7	7.8	21.7	7.1	6.1	89.5	14.5	167.3	15.4	28.7	35.8	11.1	7.5	8.1	14.4	51.9	528.7
C	225	4.6	6.5	5.0	4.0	2.1	3.1	2.1	2.1	27.4	4.1	2.1	2.3	4.5	13.5	3.7	3.7	4.2	3.1	9.0	2.3
Su	1715	2.7	2.1	2.0	2.3	1.5	10.5	0.5	0.5	4.2	3·10³	0.5	1.1	1.9	3.6	1.3	0.7	1.5	0.6	1.9	0.5
HD-Su	152	4.4	9.6	10.4	12.8	5.6	20.4	0.2	0.2	4.3	3·10⁴	0.1	3.9	0.3	1.1	0.2	0.2	1.2	0.2	1.3	0.2
total	**3526**	**8.4**	**7.0**	**5.9**	**6.8**	**2.9**	**11.6**	**2.1**	**1.9**	**32.4**	**3·10³**	**24.5**	**4.1**	**7.1**	**11.4**	**4.2**	**2.4**	**3.3**	**3.7**	**11.8**	**75.3**
2nd and 3rd virial coefficient																					
B	359	12.6	0.6	5.4	4.1	13.2	56.8	0.4	1.0	0.0	0.6	0.0	146.7	9.3	1.4	0.6	1.4	3.4	1.4	41.9	1.1
C	393	317.5	299.0	115.4	100.0	110.8	159.3	53.2	46.6	50.0	22.6	25.9	170.9	253.4	254.2	74.5	123.8	134.0	103.9	338.7	7.7
total	**752**	**171.9**	**156.5**	**62.9**	**54.2**	**64.2**	**110.4**	**28.0**	**24.8**	**26.1**	**12.1**	**13.5**	**159.4**	**136.9**	**133.5**	**39.2**	**65.4**	**71.6**	**55.0**	**197.0**	**4.6**

	#	Cottermann et al. [128]	Paricaud [519]	Lafitte et al. [353]	van Westen & Gross [710]	this work	Koutras et al. [343]	Kolafa & Nezbeda [334]	Mecke et al. [438, 439]	Hess [258]	Boltachev et al. [62]	Gottschalk [217]	Quiñones-Cisneros et al. [554]	Nicolas et al. [505]	Adachi et al. [4]	Miyano [460]	Johnson et al. [302]	Sun & Teja [646]	May & Mausbach [423, 425]	Ree [559]	Thol et al. [661]
Internal energy u^{res}																					
G	174	13.3	5.1	9.7	6.7	1.5	$2\cdot10^4$	0.5	0.4	0.8	0.3	0.3	29.7	5.3	2.5	1.2	0.9	3.6	1.1	18.7	0.3
L	438	4.5	0.8	0.4	0.4	0.3	623.3	0.1	0.1	24.1	6.7	0.1	6.2	0.2	5.2	0.2	0.1	0.2	0.5	0.8	0.1
HD-L	212	3.3	1.1	0.6	0.5	0.5	$2\cdot10^3$	0.3	0.3	33.6	15.8	0.3	14.2	0.4	8.1	0.5	0.4	0.4	0.9	0.3	0.3
MU	307	6.6	4.6	6.3	5.0	2.5	$2\cdot10^4$	0.6	0.6	21.6	3.6	0.3	18.3	3.5	7.2	1.9	1.3	3.1	2.1	11.7	0.5
C	185	4.9	4.6	3.9	5.1	1.6	484.4	1.0	1.1	10.0	1.9	0.8	12.9	2.7	1.2	2.0	0.9	1.9	1.2	10.8	1.0
Su	1492	5.4	2.8	2.2	2.3	6.8	$4\cdot10^3$	0.3	0.3	4.6	$1\cdot10^4$	0.3	7.7	1.1	3.6	1.1	0.7	1.3	0.6	3.0	0.2
HD-Su	139	10.2	13.3	20.6	22.3	36.0	$2\cdot10^3$	0.9	0.7	9.0	$2\cdot10^5$	0.5	9.4	1.8	13.9	0.8	2.2	4.8	3.0	1.2	0.3
total	**2947**	**5.9**	**3.3**	**3.7**	**3.5**	**5.7**	$\mathbf{5\cdot10^3}$	**0.4**	**0.3**	**11.7**	$\mathbf{2\cdot10^4}$	**0.3**	**10.8**	**1.5**	**4.8**	**1.1**	**0.8**	**1.6**	**0.9**	**4.7**	**0.3**
Isochoric heat capacity c_v																					
G	151	2.4	4.7	6.0	5.0	4.4	$1\cdot10^4$	1.1	0.9	2.5	2.0	0.5	4.2	3.4	2.5	3.3	1.7	4.1	2.3	10.5	0.4
L	205	3.9	3.3	4.3	1.8	5.3	$1\cdot10^4$	0.4	0.4	121.8	208.1	2.4	99.0	2.5	41.2	1.8	2.5	1.6	6.8	3.5	0.4
HD-L	57	9.5	2.9	5.3	1.6	9.6	$3\cdot10^4$	0.7	0.7	212.5	730.5	4.9	235.1	1.8	51.3	1.1	10.2	3.1	28.8	0.9	0.5
MU	113	10.7	9.8	11.6	9.4	10.1	$4\cdot10^4$	4.6	3.7	103.5	65.5	10.6	135.9	6.7	32.6	7.0	7.9	8.4	15.6	16.2	16.6
C	152	18.1	20.3	18.4	20.2	17.5	$3\cdot10^3$	10.1	8.1	9.6	30.7	3.2	16.0	14.5	7.7	19.1	9.1	19.6	14.8	30.5	42.9
Su	1160	3.9	2.9	1.7	2.0	4.2	$3\cdot10^3$	0.4	0.3	12.6	$2\cdot10^3$	0.5	9.7	1.6	6.6	2.0	1.2	2.3	2.0	5.6	0.4
HD-Su	53	4.8	4.8	1.0	1.1	16.4	$2\cdot10^3$	0.6	0.3	20.6	$2\cdot10^4$	0.5	6.0	1.3	14.9	0.7	2.9	2.7	3.5	0.7	0.3
total	**1891**	**5.5**	**5.0**	**4.4**	**4.1**	**6.3**	$\mathbf{7\cdot10^3}$	**1.5**	**1.2**	**35.1**	$\mathbf{2\cdot10^3}$	**1.7**	**33.7**	**3.2**	**13.3**	**3.7**	**2.7**	**4.2**	**5.3**	**8.1**	**4.8**
Isobaric heat capacity c_p																					
G	92	1.9	4.7	5.3	4.3	2.4	$8\cdot10^3$	0.5	0.4	0.9	0.8	0.2	5.4	3.3	2.6	1.3	1.1	2.9	1.3	9.8	0.3
L	156	4.7	2.9	3.5	2.9	3.7	$6\cdot10^3$	1.4	1.5	77.0	187.8	2.5	51.1	3.5	22.8	2.4	2.6	2.4	4.8	2.2	1.4
HD-L	45	7.1	4.6	4.1	2.5	8.1	$1\cdot10^4$	0.7	0.8	130.8	$2\cdot10^3$	2.8	112.6	2.1	35.0	1.4	6.2	2.7	18.7	2.0	0.9
MU	6	15.8	95.9	29.4	14.0	27.2	$2\cdot10^4$	29.2	30.7	77.6	26.5	30.5	48.8	109.4	23.7	22.3	26.9	23.1	24.2	45.8	68.7
C	101	26.4	332.9	28.5	82.2	26.6	432.4	29.9	30.6	977.1	30.7	25.2	29.0	$1\cdot10^3$	36.4	101.1	35.8	28.2	27.5	839.4	30.2
Su	934	4.4	3.8	3.0	2.9	3.7	$1\cdot10^3$	2.0	2.0	14.6	$4\cdot10^3$	2.0	6.3	3.3	5.5	2.7	2.3	2.7	2.5	5.3	2.0
HD-Su	43	6.6	4.5	5.1	3.2	10.9	$2\cdot10^3$	1.2	0.9	15.2	$4\cdot10^4$	1.0	4.9	1.4	11.9	1.6	2.6	2.6	3.1	1.6	0.6
total	**1377**	**6.1**	**28.3**	**5.3**	**8.8**	**5.8**	$\mathbf{3\cdot10^3}$	**4.0**	**4.0**	**95.4**	$\mathbf{4\cdot10^3}$	**3.8**	**16.6**	**81.1**	**10.8**	**9.8**	**4.9**	**4.6**	**5.1**	**66.4**	**4.1**

	#	Cotterman et al. [128]	Paricaud [519]	Lafitte et al. [353]	van Westen & Gross [710]	this work	Koutras et al. [343]	Kolafa & Nezbeda [334]	Mecke et al. [438, 439]	Hess [258]	Boltachev et al. [62]	Gottschalk [217]	Quiñones-Cisneros et al. [554]	Nicolas et al. [505]	Adachi et al. [4]	Miyano [460]	Johnson et al. [302]	Sun & Teja [646]	May & Mausbach [423, 425]	Ree [559]	Thol et al. [661]
Helmholtz energy $\tilde{a}^{\mathrm{res}}$																					
G	95.0	11.4	2.2	5.1	3.0	0.2	$4 \cdot 10^4$	0.1	0.1	0.5	0.1	0.1	18.7	1.9	1.8	0.8	0.7	0.8	0.4	2.8	0.1
L	136.0	2.4	0.3	1.4	1.3	0.3	$2 \cdot 10^3$	0.3	0.3	15.2	1.9	0.3	1.4	1.9	3.6	1.8	0.5	0.4	0.3	1.4	0.3
HD-L	49.0	2.6	0.9	1.7	1.7	0.8	$2 \cdot 10^3$	0.8	0.8	23.0	5.4	0.8	3.1	2.2	4.1	2.0	0.8	1.0	0.8	1.5	0.8
MU	155.0	5.2	1.6	2.8	2.2	0.3	$7 \cdot 10^3$	0.2	0.2	12.9	1.6	0.2	6.8	1.8	2.6	1.3	0.7	0.7	0.5	2.4	0.8
C	34.0	2.1	2.1	2.3	2.8	0.3	$4 \cdot 10^3$	0.1	0.1	7.1	0.2	0.1	0.8	0.5	4.4	3.4	0.9	0.2	0.2	1.0	0.1
Su	224.0	8.3	1.6	3.4	3.3	4.2	$5 \cdot 10^4$	0.7	0.6	7.8	$1 \cdot 10^3$	0.6	15.1	5.2	8.7	6.6	1.9	2.0	0.5	10.6	0.5
HD-Su	25.0	5.2	6.5	6.5	8.8	4.1	$3 \cdot 10^3$	2.1	2.1	15.9	$2 \cdot 10^4$	2.2	3.7	4.9	8.9	4.4	1.6	3.1	2.1	3.3	2.1
total	**718.0**	**6.1**	**1.6**	**3.0**	**2.7**	**1.7**	$\mathbf{2 \cdot 10^4}$	**0.5**	**0.4**	**10.6**	$\mathbf{1 \cdot 10^3}$	**0.4**	**9.3**	**3.0**	**5.0**	**3.2**	**1.1**	**1.2**	**0.5**	**4.7**	**0.5**
Chemical potential μ^{res}																					
G	105	10.0	3.0	5.0	3.2	0.2	$2 \cdot 10^4$	0.2	0.2	1.1	0.1	0.0	13.9	2.3	2.4	1.3	0.7	0.8	0.4	3.6	0.1
L	205	4.2	3.4	8.0	9.3	1.5	$3 \cdot 10^3$	1.5	1.4	59.3	71.7	1.7	3.5	7.0	12.4	5.3	2.2	6.9	2.0	3.3	1.4
HD-L	103	14.6	3.5	25.3	25.6	6.6	$3 \cdot 10^3$	2.9	2.6	116.5	194.3	2.9	4.7	11.3	7.0	7.7	3.3	12.7	5.7	3.3	2.7
MU	153	3.8	2.9	2.9	2.5	0.7	$4 \cdot 10^3$	0.3	0.3	13.2	1.5	0.2	5.3	2.6	3.0	2.9	0.8	1.1	1.0	5.4	0.4
C	39	0.6	1.3	2.2	2.4	0.4	$2 \cdot 10^3$	0.3	0.1	10.1	0.7	0.1	0.4	1.2	5.3	2.9	0.9	0.7	0.3	2.1	0.2
Su	206	7.0	2.8	3.5	4.1	3.8	$3 \cdot 10^4$	0.3	0.3	9.3	$4 \cdot 10^3$	0.3	10.3	5.0	9.3	4.9	1.5	2.8	0.5	7.8	0.2
HD-Su	26	6.2	12.0	11.8	14.9	7.4	$3 \cdot 10^2$	0.3	0.4	6.1	$4 \cdot 10^4$	0.3	5.3	0.5	2.0	0.6	0.5	1.7	0.3	1.1	0.4
total	**837**	**6.7**	**3.3**	**7.6**	**7.9**	**2.5**	$\mathbf{1 \cdot 10^4}$	**0.9**	**0.8**	**34.4**	$\mathbf{2 \cdot 10^3}$	**0.9**	**6.8**	**5.2**	**7.4**	**4.0**	**1.6**	**4.3**	**1.6**	**4.7**	**0.8**

	#	Cotterman et al. [128]	Paricaud [519]	Laffite et al. [353]	van Westen & Gross [710]	this work	Koutras et al. [343]	Kolafa & Nezbeda [334]	Mecke et al. [438, 439]	Hess [258]	Boltachev et al. [62]	Gottschalk [217]	Quiñones-Cisneros et al. [554]	Nicolas et al. [505]	Adachi et al. [4]	Miyano [460]	Johnson et al. [302]	Sun & Teja [646]	May & Mausbach [423, 425]	Ree [559]	Thol et al. [661]
Thermal expansion coefficient α																					
G	86	2.5	4.0	4.0	3.1	1.1	8.1	0.3	0.3	0.8	0.3	0.2	5.7	3.0	2.5	0.5	0.9	1.9	0.8	6.9	0.3
L	126	8.2	4.2	6.2	4.5	3.0	8.8	2.2	2.3	22.0	251.3	2.3	2.5	4.5	9.3	3.3	2.6	2.7	4.0	2.2	2.2
HD-L	44	16.1	5.4	13.4	9.5	8.5	3.5	1.3	1.4	32.1	926.2	3.1	2.2	3.7	12.1	1.7	2.8	1.3	18.0	3.9	1.7
MU	7	25.1	30.6	30.6	32.8	32.6	20.3	34.5	36.6	92.6	38.1	37.9	37.0	39.0	42.4	39.4	38.3	33.8	25.5	34.5	34.0
C	84	28.3	346.1	31.0	95.6	29.6	164.2	33.6	34.6	866.0	33.2	28.2	30.5	$1 \cdot 10^3$	40.6	122.2	39.4	29.9	29.1	976.6	35.8
Su	525	5.2	5.4	5.3	4.8	3.8	8.8	3.1	3.0	12.9	46.8	3.0	4.1	4.9	6.6	3.7	3.1	4.1	3.2	7.5	3.1
HD-Su	28	11.5	5.8	18.0	17.9	3.2	26.0	1.8	1.4	11.0	218.5	1.4	6.9	1.2	3.0	2.8	1.8	3.2	1.4	2.6	1.1
total	**900**	**8.4**	**37.1**	**8.7**	**14.0**	**6.3**	**23.6**	**5.7**	**5.8**	**94.2**	**118.0**	**5.2**	**6.8**	**130.0**	**10.2**	**14.6**	**6.4**	**6.2**	**6.3**	**97.0**	**5.9**
Isothermal compressibility β																					
G	92	2.0	2.7	2.1	2.0	0.4	4.8	0.2	0.2	2.6	0.3	0.2	1.9	1.8	2.0	1.1	0.6	0.7	0.4	3.4	0.3
L	159	4.9	4.7	5.4	5.5	2.8	7.2	2.6	2.5	13.8	204.8	2.4	2.6	5.6	7.5	4.4	2.6	4.5	3.9	4.5	2.3
HD-L	46	8.0	3.6	11.7	11.5	5.4	6.7	0.8	0.7	16.2	322.1	1.6	1.3	2.5	5.9	1.0	1.3	2.0	12.4	4.7	1.0
MU	23	12.6	13.1	11.5	14.0	11.3	15.9	12.7	12.0	50.3	12.8	11.8	11.0	14.5	27.6	14.4	12.0	11.4	11.9	14.5	18.2
C	108	42.1	379.9	40.2	84.5	36.0	137.6	38.1	41.2	869.5	37.9	44.2	46.1	$1 \cdot 10^3$	44.6	107.6	42.3	35.6	33.8	779.9	44.8
Su	935	5.7	5.3	5.0	5.1	4.0	12.0	2.6	2.6	10.5	482.8	2.5	3.3	4.6	5.3	3.3	2.6	3.8	2.6	5.6	2.6
HD-Su	43	11.5	14.2	18.8	20.7	9.5	18.9	1.0	1.0	6.1	91.0	0.7	9.1	1.0	0.5	1.3	1.0	0.7	1.0	2.5	1.1
total	**1406**	**8.5**	**34.2**	**8.3**	**11.9**	**6.4**	**20.7**	**5.2**	**5.4**	**77.1**	**360.7**	**5.6**	**6.7**	**92.4**	**8.6**	**11.3**	**5.6**	**6.1**	**5.4**	**64.8**	**5.8**
Thermal pressure coefficient γ																					
G	113	0.8	1.8	2.0	1.6	0.8	3.8	0.2	0.2	0.4	0.3	0.1	4.1	1.5	0.7	1.0	0.4	1.3	0.5	4.4	0.1
L	177	5.0	1.9	1.6	3.0	1.2	9.0	0.6	0.5	8.1	67.3	0.8	0.9	1.5	3.7	1.1	0.7	2.3	1.9	4.2	0.5
HD-L	52	8.9	3.6	2.3	2.0	3.7	4.5	0.6	0.6	12.6	234.8	2.1	1.0	1.3	5.5	1.3	1.5	2.5	6.6	1.1	0.6
MU	50	4.0	5.3	5.3	5.7	4.0	9.6	2.0	1.7	9.9	3.9	1.3	6.1	3.8	4.0	3.7	2.2	4.7	4.3	9.5	3.9
C	131	6.8	4.6	3.2	3.4	1.9	11.1	1.6	1.4	14.1	3.3	0.7	3.2	1.6	5.3	3.2	1.1	3.2	1.2	4.9	2.8
Su	1111	3.4	2.3	1.1	1.8	2.7	16.4	0.4	0.4	3.8	$8 \cdot 10^3$	0.4	1.6	0.9	1.4	1.2	0.6	1.3	0.6	1.8	0.4
HD-Su	54	7.3	14.2	2.3	5.7	14.1	49.8	1.2	0.5	5.1	$1 \cdot 10^5$	0.9	5.7	0.9	3.0	1.7	1.5	2.7	0.9	0.6	0.4
total	**1688**	**3.9**	**2.9**	**1.6**	**2.3**	**2.8**	**14.8**	**0.6**	**0.5**	**5.3**	**$9 \cdot 10^3$**	**0.5**	**2.1**	**1.1**	**2.2**	**1.5**	**0.7**	**1.7**	**1.0**	**2.6**	**0.7**

	#	Cotterman et al. [128]	Paricaud [519]	Lafitte et al. [353]	van Westen & Gross [710]	this work	Koutras et al. [343]	Kolafa & Nezbeda [334]	Mecke et al. [438, 439]	Hess [258]	Boltachev et al. [62]	Gottschalk [217]	Quiñones-Cisneros et al. [554]	Nicolas et al. [505]	Adachi et al. [4]	Miyano [460]	Johnson et al. [302]	Sun & Teja [646]	May & Mausbach [423, 425]	Rée [559]	Thol et al. [661]
Speed of sound w																					
G	117	0.4	0.5	0.8	0.6	0.6	28.8	0.1	0.1	0.1	0.2	0.1	1.4	0.2	0.6	0.1	0.3	0.3	0.2	0.8	0.1
L	182	2.5	1.5	1.3	2.8	1.3	32.6	0.4	0.3	15.7	52.2	0.7	11.8	1.4	6.9	1.1	0.6	1.9	2.0	4.2	0.3
HD-L	50	1.8	2.1	2.5	4.4	0.7	22.8	0.2	0.1	15.9	72.0	0.8	11.5	0.3	6.2	0.5	1.5	1.0	6.3	1.8	0.1
MU	49	2.9	3.1	3.2	3.7	2.9	36.8	1.4	1.1	4.8	6.0	1.3	6.1	1.8	3.8	1.7	1.8	2.6	5.9	5.8	1.5
C	131	17.5	12.8	13.9	12.4	9.3	69.3	5.5	4.5	8.4	23.0	1.8	9.4	7.3	10.0	10.1	6.2	14.5	8.0	17.4	8.9
Su	1111	2.6	2.3	2.0	2.3	2.4	30.3	0.4	0.4	3.5	84.8	0.4	3.0	0.8	1.4	0.9	0.6	1.8	0.7	2.3	0.4
HD-Su	43	4.1	8.7	8.1	9.7	5.7	12.2	0.3	0.1	4.5	100.0	0.1	4.5	0.3	1.3	0.3	0.4	0.6	0.5	0.8	0.2
total	**1683**	**3.6**	**3.1**	**3.0**	**3.3**	**2.7**	**33.0**	**0.8**	**0.7**	**5.4**	**68.3**	**0.5**	**4.7**	**1.3**	**2.8**	**1.6**	**1.1**	**2.7**	**1.7**	**3.6**	**1.1**
Joule–Thomson coefficient μ_{JT}																					
G	100	8.2	5.3	6.2	4.3	1.2	100.2	0.6	0.5	3.4	0.9	0.4	13.9	4.5	3.5	2.3	1.0	2.3	1.1	10.1	0.5
L	138	11.5	8.5	7.6	5.8	5.0	99.0	3.3	3.2	50.7	49.0	3.8	27.6	9.1	25.2	6.7	4.5	4.4	6.4	3.2	2.8
HD-L	45	13.9	6.0	9.3	6.0	9.2	97.7	1.1	1.2	55.8	140.1	3.2	42.0	3.2	28.5	1.8	8.0	3.2	26.1	3.5	1.3
MU	7	15.0	9.2	12.2	8.7	4.4	165.6	4.5	1.8	21.2	6.4	1.0	14.5	11.7	11.5	9.0	5.5	7.2	3.2	12.7	90.3
C	126	8.1	9.3	7.6	5.7	5.9	161.1	5.5	5.0	11.9	6.8	4.6	5.7	7.5	14.9	6.8	5.8	7.2	5.2	14.7	7.0
Su	898	11.2	6.1	7.1	5.8	7.1	236.8	4.5	4.6	10.5	163.5	4.6	7.9	7.9	11.9	6.6	5.0	6.2	5.3	7.3	4.5
HD-Su	44	8.9	4.4	9.0	6.8	12.0	101.2	1.6	1.2	14.7	100.0	1.4	6.3	1.6	11.7	2.2	2.9	3.1	3.6	2.3	0.9
total	**1358**	**10.8**	**6.5**	**7.3**	**5.7**	**6.5**	**196.3**	**4.0**	**3.9**	**15.9**	**121.7**	**4.0**	**11.3**	**7.4**	**13.5**	**6.0**	**4.7**	**5.6**	**5.7**	**7.5**	**4.5**
Grüneisen coefficient Γ																					
G	90	0.9	1.5	2.9	2.3	2.6	101.0	0.5	0.3	1.3	0.8	0.1	3.3	1.0	1.1	1.2	0.8	1.5	1.0	4.6	0.1
L	154	7.9	3.2	4.9	2.2	4.5	99.7	0.7	0.6	51.2	127.6	2.4	44.8	3.3	27.5	1.7	2.4	2.3	6.6	6.6	0.5
HD-L	43	11.8	3.4	5.4	1.1	6.0	98.3	0.4	0.4	55.7	114.5	1.9	48.1	1.1	25.9	0.9	2.3	2.3	13.5	1.3	0.4
MU	15	16.6	11.4	12.1	10.7	10.6	100.6	5.4	3.8	41.6	50.9	9.3	49.1	6.2	26.4	6.8	14.0	11.6	45.1	20.0	7.0
C	39	24.7	24.6	20.8	22.3	15.9	96.3	8.0	6.0	10.5	47.2	1.3	15.9	13.8	7.2	18.7	7.3	22.5	13.0	40.3	4.4
Su	419	2.9	4.5	1.8	2.5	9.3	100.2	0.4	0.3	11.3	448.3	0.5	7.7	1.4	6.6	1.3	1.4	2.3	2.1	4.5	0.3
HD-Su	36	5.6	14.2	2.8	5.0	39.4	101.9	0.9	0.4	17.0	404.5	0.4	12.8	1.0	10.1	1.3	3.2	3.2	3.0	0.4	0.3
total	**796**	**5.6**	**5.4**	**3.9**	**3.6**	**9.2**	**100.0**	**0.9**	**0.7**	**21.1**	**288.5**	**1.1**	**18.0**	**2.4**	**11.6**	**2.3**	**2.3**	**3.4**	**4.8**	**6.6**	**0.7**

Also the LJ EOS of *Johnson et al.* [302] gives a good description of the pvT data (cf. Table 14); however, it is somewhat less precise than the three aforementioned LJ EOS. The LJ EOS of *Sun and Teja* [646], *May and Mausbach* [423, 425], *Quiñones-Cisneros et al.* [554], and *Miyano* [460] are in turn slightly less precise than the LJ EOS of *Johnson et al.* [302]. The theoretically-based LJ EOS of *Cotterman et al.* [128], *Lafitte et al.* [353], *Paricaud* [519], and *van Westen and Gross* [710] overall yield an absolute average deviation two to three times larger than the most precise LJ EOS, cf. Table 14. In general no fluid region is represented significantly better or worse than the others by the theoretically-based LJ EOS. The performance of the LJ EOS from *Cotterman et al.* [128], *Lafitte et al.* [353], *Paricaud* [519], and *van Westen and Gross* [710] regarding the pvT behavior is overall similar. Also the LJ EOS of *Nicolas et al.* [505] has a similar performance regarding the pvT data as the theoretically-based LJ EOS from Refs. [128, 353, 519, 710], which is surprising considering the fact that the LJ EOS of *Nicolas et al.* [505] is one of the oldest LJ EOS considered here. The LJ EOS from the present work performs significantly better than the other theoretically-based LJ EOS, which is likely due to the parametrization procedure (see Appendix). The LJ EOS of *Koutras et al.* [343], *Hess* [258], *Ree* [559], *Boltachev and Baidakov* [62], and *Adachi et al.* [4] exhibit large deviations in all fluid regions ($\mathrm{AAD}_{i,j=p} > 10\%$).

The isotherms obtained from the LJ EOS of *Boltachev et al.* [62] exhibit an artificial maximum in the supercritical region, which results in gross deviations in the high density liquid, the supercritical and the high density supercritical region. This also holds for properties discussed in the following. The LJ EOS of *Boltachev et al.* [62] is therefore discarded from the following discussions.

For the second and third virial coefficients B and C, the obtained absolute average deviations are reported in the bottom section of Table 14. The second virial coefficient B is exactly described by the LJ EOS of *Gottschalk* [217] and *Hess* [258], which comprise the corresponding expression in their mathematical form. Good results are also obtained for the LJ EOS of *Paricaud* [519], *Kolafa and Nezbeda* [334], *Mecke et al.* [438, 439], *Boltachev and Baidakov* [62], *Miyano* [460], and *Thol et al.* [661]. The third virial coefficient C is described best by the LJ EOS of *Thol et al.* [661]. Also the LJ EOS of *Gottschalk* [217] yields an excellent description of C in a wide temperature range, but a wrong limit at low temperatures yields an overall large absolute average deviation. A detailed discussion on the performance of LJ EOS on the virial coefficients and their relation to the characteristic curves can be found in section 4.4 [625].

Caloric Properties

Also the absolute average deviations AAD_{ijk} for the residual internal energy $j = u^{\mathrm{res}}$ (for brevity, the addition 'residual' is omitted in the following) in the different fluid regions k are reported in Table 14 for all studied LJ EOS i. As for the pvT data, the LJ EOS from *Mecke et al.* [438, 439], *Gottschalk* [217], *Thol et al.* [661], and *Kolafa and Nezbeda* [334] give the best descriptions of the internal energy data. The LJ EOS from the present work performs well in most fluid regions, i.e. only slightly exceeds the absolute average deviations from the best LJ EOS, but becomes unreliable in the supercritical and high density supercritical region. This is likely due to the simplifications of the temperature-dependent diameter, cf. Eq. (145) in the Appendix, and hence an inadequate description

of the soft repulsive interactions [66] of the PC-SAFT monomer equation in that fluid region (details are given in the Appendix).

The LJ EOS of *Johnson et al.* [302], *May and Mausbach* [423, 425], *Nicolas et al.* [505], *Sun and Teja* [646], and *Miyano* [460] exhibit total deviations $\mathrm{AAD}_{i,j=u^{\mathrm{res}}}$ for the internal energy of about $1..2\%$, cf. Table 14, and are thereby less precise than the aforementioned LJ EOS [217, 334, 438, 439, 661] – in agreement with what was observed for the pvT data.

The $\mathrm{AAD}_{i,j=u^{\mathrm{res}}}$ obtained for the theoretically-based LJ EOS of *Cotterman et al.* [128], *Lafitte et al.* [353], *Paricaud* [519], *van Westen and Gross* [710], and the LJ EOS from the present work is about an order of magnitude larger than the most precise LJ EOS (Refs. [217, 334, 438, 439, 661]). The deviations of the theoretically-based LJ EOS are particularly large in the gas and high density supercritical region. Nevertheless, the theoretically-based LJ EOS of *Lafitte et al.* [353], *Paricaud* [519], and *van Westen and Gross* [710], and from the present work show a good performance in the liquid and high density liquid region, where the deviations are not significantly higher than those of the empirical LJ EOS, cf. Table 14.

The empirical LJ EOS of *Ree* [559] and *Adachi et al.* [4] perform not better than the considered theoretically-based LJ EOS for the internal energy. The LJ EOS of *Koutras et al.* [343], *Hess* [258], *Quiñones-Cisneros et al.* [554], and *Boltachev and Baidakov* [62] exhibit mean deviations $\mathrm{AAD}_{i,j=u^{\mathrm{res}}} > 10\%$.

Interestingly, most LJ EOS show a better performance for the internal energy u^{res} than for the pressure p, i.e. $\mathrm{AAD}_{i,j=p} > \mathrm{AAD}_{i,j=u^{\mathrm{res}}}$. This does not hold for the LJ EOS from the present work, which is based on the PC-SAFT monomer equation. The mean deviation for the internal energy data $\mathrm{AAD}_{i,j=u^{\mathrm{res}}}$ is more than three times larger than the corresponding value for the pvT data $\mathrm{AAD}_{i,j=p}$, which is likely due to the mathematical form of the underlying model, namely on the chosen simplification for describing the temperature-dependent diameter and the perturbation terms (see Appendix for details). These simplifications have also been attributed to shortcomings of PC-SAFT regarding its description of the soft repulsion, see *Boshkova and Deiters* [66]. The simplifications in describing the soft repulsion in the PC-SAFT EOS may also explain its poorer performance for caloric properties at supercritical states that was reported in the literature [140, 376, 530, 531].

The absolute average deviations AAD_{ijk} of the isochoric and isobaric heat capacity $j = c_v$ and $j = c_p$, respectively, found for the different LJ EOS i in the different fluid regions k are also reported in Table 14. The four LJ EOS from *Thol et al.* [661], *Gottschalk* [217], *Mecke et al.* [438, 439], and *Kolafa and Nezbeda* [334] give the best description of the computer experiment data for the heat capacities, which is in line with the findings for the internal energy u^{res} and the pvT data. The LJ EOS of *Thol et al.* [661] has large deviations in the critical and metastable/ unstable region, but performs slightly better than the LJ EOS of *Mecke et al.* [438, 439] and *Kolafa and Nezbeda* [334] in the gas and in both the high density liquid and high density supercritical region. While the LJ EOS of *Gottschalk* [217] gives a slightly better description of the pvT data than that of *Thol et al.* [661], this is reversed for the caloric properties in most fluid regions except the critical and metastable/ unstable region.

For the isochoric and isobaric heat capacity, the LJ EOS of *Johnson et al.* [302] and *Sun and Teja* [646] have slightly increased absolute average deviations in most fluid regions

compared to the four best LJ EOS. The theoretically-based LJ EOS of *Cotterman et al.* [128], *Lafitte et al.* [353], *Paricaud* [519], *van Westen and Gross* [710], and the LJ EOS from the present work are less precise than the best empirical ones for the isochoric and isobaric heat capacity, but the difference is only about a factor of two to four instead an order of magnitude as found for the internal energy data.

The LJ EOS of *Nicolas et al.* [505] and *Paricaud* [519] exhibit large relative deviations of the isobaric heat capacity data in the critical region, which is due to the significantly overestimated critical temperature of these LJ EOS. The large deviations found for both isochoric and isobaric heat capacity data for the LJ EOS of *Thol et al.* [661] in the critical and metastable/ unstable region are probably a result of the multiple van der Waals loops and the crossing of the isotherms in the critical region. However, it should be noted, that the critical temperature of the LJ EOS of *Thol et al.* [661] is in excellent agreement with the presumed true value (see above).

The LJ EOS of *Koutras et al.* [343], *Hess* [258], *Ree* [559], *Adachi et al.* [4], *Boltachev and Baidakov* [62], and *Quiñones-Cisneros et al.* [554] exhibit for both $j = c_v$ and $j = c_p$ mean deviations $\text{AAD}_{i,j} \gtrsim 10\%$.

Entropic Properties

The results obtained for performance of the considered LJ EOS i on entropic properties j = (residual reduced Helmholtz energy $\tilde{a}^{\text{res}} = a^{\text{res}}/T$ and chemical potential μ^{res} – mentioning 'residual' is again omitted for brevity in the following) in the different fluid regions k are also given in Table 14. The LJ EOS of *Thol et al.* [661], *Gottschalk* [217], *Mecke et al.* [438, 439], and *Kolafa and Nezbeda* [334] give a generally similar precise description of the entropic properties, cf. Table 14. The relative deviation of the LJ EOS of *Johnson et al.* [302] is approximately twice as large as those of the four best LJ EOS [217, 334, 438, 439, 661] for both the Helmholtz energy and the chemical potential. The absolute average deviation for the entropic properties obtained for the theoretically-based LJ EOS of *Cotterman et al.* [128], *Lafitte et al.* [353], *Paricaud* [519], and *van Westen and Gross* [710], and the LJ EOS from the present work significantly exceed those from the most precise LJ EOS. Large deviations for the entropic properties are found for all theoretically-based LJ EOS in the high density supercritical region. Furthermore, high deviations are found for the LJ EOS of *Cotterman et al.* [128] and *Lafitte et al.* [353] in the gas region for both the Helmholtz energy and the chemical potential. The LJ EOS of *Boltachev and Baidakov* [62], *Koutras et al.* [343], and *Hess* [258] exhibit $\text{AAD}_{ij} > 10\%$ for both considered entropic properties $j = \tilde{a}^{\text{res}}$ and $j = \mu^{\text{res}}$.

Overall, the results for the entropic properties support the findings from the caloric and thermal properties discussed above. This also indicates that the reference data compiled and assessed in section 4.2 for these properties has overall a similar quality and outliers were equally well detected.

Second-Order Derivatives of the Helmholtz energy

The Helmholtz energy is considered here as a function of the inverse temperature and the density, cf. Eq. (78). Accordingly, the second derivatives are $\tilde{a}_{20}$, $\tilde{a}_{11}$, and $\tilde{a}_{02}$. Six

more thermodynamic properties were studied here that contain at least one of these derivatives: the thermal pressure coefficient γ, the isothermal compressibility β, the thermal expansion coefficient α, the speed of sound w, the Joule-Thomson coefficient μ_{JT}, and the Grüneisen parameter Γ, cf. Eqs. (84) - (89). The AAD_{ijk} results for the considered LJ EOS i for $j = \alpha$, β, γ, w, μ_{JT}, Γ in the different fluid regions k are given in Table 14.

The thermal pressure coefficient γ, isothermal compressibility β, and thermal expansion coefficient α is best and overall equally well described by the LJ EOS of *Kolafa and Nezbeda* [334], *Mecke et al.* [438, 439], *Gottschalk* [217], and *Thol et al.* [661] – as it was also found for the thermal, caloric, and entropic properties discussed above.

The LJ EOS of *Johnson et al.* [302], *May and Mausbach* [423, 425], and *Sun and Teja* [646] exhibit slightly larger mean deviations for α, β, and γ than the aforementioned LJ EOS, cf. Table 14. Also the LJ EOS of *Lafitte et al.* [353], *Cotterman et al.* [128], *Quiñones-Cisneros et al.* [554], and the LJ EOS from the present work give a reasonably precise description of the α, β, and γ computer experiment data. Mean deviations $\mathrm{AAD}_{ij} > 10\%$ for either $j = \alpha$, β, or γ were obtained for the LJ EOS of *Miyano* [460], *Adachi et al.* [4], *Ree* [559], *Nicolas et al.* [505], *Hess* [258], *Paricaud* [519], *van Westen and Gross* [710], *Koutras et al.* [343], and *Boltachev and Baidakov* [62]. For the latter two LJ EOS mean deviations $\mathrm{AAD}_{ij} > 10\%$ are found for all three properties $j = \alpha$, β, and γ, cf. Table 14.

All five theoretically-based LJ EOS (*Cotterman et al.* [128], *Lafitte et al.* [353], *Paricaud* [519], and *van Westen and Gross* [710], and the LJ EOS present work) exhibit high relative deviations for α, β, and γ in the high density supercritical and high density liquid region compared to other fluid regions. Furthermore, the theoretically-based LJ EOS of *Lafitte et al.* [353] and *Paricaud* [519] are considerably less precise in the gas region for $j = \alpha$, β, and γ than the other theoretically-based LJ EOS, cf. Table 14.

The LJ EOS of *Nicolas et al.* [505], *Hess* [258], *Ree* [559], and *Paricaud* [519] exhibit large relative deviations for the α and β computer experiment data in the critical region, similar to the findings for the heat capacity. This is attributed to the significantly overestimated critical temperature by these LJ EOS (see above).

The findings for $j = w$, μ_{JT}, and Γ are in line with the findings for the properties discussed above: the three LJ EOS of *Kolafa and Nezbeda* [334], *Mecke et al.* [438, 439], *Gottschalk* [217], and *Thol et al.* [661] give similarly precise descriptions, followed by that of *Johnson et al.* [302]. The theoretically-based LJ EOS are significantly less precise.

Distinct performance features for w, μ_{JT}, and Γ are: the LJ EOS of *Thol et al.* [661] exhibits large deviations in the metastable/ unstable region for the Joule-Thomson coefficient and the LJ EOS from the present work is significantly less precise than other LJ EOS for the Grüneisen parameter in the supercritical and high density supercritical region. The latter is again attributed to the simplified temperature-dependent diameter (see Appendix).

Extreme Temperature Region

The performance of the investigated LJ EOS i in the extreme temperature region, i.e. $T > 6\,\varepsilon k_{\mathrm{B}}^{-1}$, is summarized in Table 15 by reporting the corresponding absolute average deviations AAD_{ijk} with k = Ex-T for all considered homogeneous state properties j. Since the reference data in the extreme temperature region covers a large range of states [640], high absolute average deviations obtained for a given LJ EOS are in some cases a result of a poor performance in only a sub-region of states, cf. electronic Supplementary Material.

The LJ EOS of *Quiñones-Cisneros et al.* [554], *Boltachev and Baidakov* [62], and *Koutras et al.* [343] give an erratic description of the extreme temperature region. The empirical LJ EOS of *Thol et al.* [661] and *Ree* [559] give an astonishingly accurate description of thermodynamic properties at extreme temperatures considering the fact that they were parametrized exclusively using data at moderate temperatures. On the contrary, the theoretically-based LJ EOS exhibit large deviations for most properties, especially for the pressure and the internal energy. This is surprising, considering the fact that the studied theoretically-based LJ EOS are based on perturbation theory, which is expected to perform well at high temperatures, where the attractive forces, i.e. the perturbation contribution of the temperature expansion, plays a minor role.

The LJ EOS of *Mecke et al.* [438, 439] and *Gottschalk* [217], which are generally precise (see above), exhibit large deviations for the pressure and the internal energy at extreme temperatures – the LJ EOS of *Mecke et al.* [438, 439] also for other properties. A detailed examination of the data (see the electronic Supplementary Material [639]) shows that these large deviations mainly stem from the region $T > 50\,\varepsilon k_{\mathrm{B}}^{-1}$ and $\rho > 2\,\sigma^{-3}$ (for the LJ EOS of *Gottschalk* [217], very few reference data points entail these large deviations). The LJ EOS of *Johnson et al.* [302], *Sun and Teja* [646], *May and Mausbach* [423, 425], *Nicolas et al.* [505], *Adachi et al.* [4], *Hess* [258], and *Kolafa and Nezbeda* [334] give a reasonable description of the extreme temperature region – except the internal energy data in some cases.

Table 15: Comparison of the results from 20 LJ EOS i with reference data, cf. Table 8 (outliers identified in the dataset as discussed in section 4.2.4.1 were discarded): absolute average deviations AAD_{ijk} (cf. Eq. 76) for different thermodynamic properties j for homogeneous state points in the extreme temperature (k = Ex-T) region. The last line 'total' gives the mean AAD_i for all extreme temperature data in a given column. # is the number of data points.

	#	Cotterman et al. [128]	Paricaud [519]	Laffitte et al. [353]	van Westen & Gross [710]	this work	Koutras et al. [343]	Kolafa & Nezbeda [334]	Mecke et al. [438, 439]	Hess [258]	Boltachev et al. [62]	Gottschalk [217]	Quiñones-Cisneros et al. [554]	Nicolas et al. [505]	Adachi et al. [4]	Miyano [460]	Johnson et al. [302]	Sun & Teja [646]	May & Mausbach [423, 425]	Ree [559]	Thol et al. [661]
pvT	643	$2 \cdot 10^{3}$	173.8	$2 \cdot 10^{5}$	$1 \cdot 10^{4}$	$1 \cdot 10^{3}$	$1 \cdot 10^{7}$	37.6	$1 \cdot 10^{7}$	38.9	$1 \cdot 10^{7}$	$3 \cdot 10^{4}$	$3 \cdot 10^{297}$	14.2	14.2	183.9	15.3	12.1	14.3	7.5	9.2
u^{res}	626	$2 \cdot 10^{3}$	165.6	$2 \cdot 10^{5}$	$9 \cdot 10^{3}$	307.3	$9 \cdot 10^{5}$	30.5	$5 \cdot 10^{6}$	39.2	$3 \cdot 10^{6}$	$3 \cdot 10^{4}$	$2 \cdot 10^{298}$	118.5	110.0	44.3	90.1	71.2	87.8	28.7	7.7
c_v	298	17.3	8.0	1.7	2.4	23.5	$7 \cdot 10^{4}$	2.3	516.3	3.0	$1 \cdot 10^{5}$	1.4	$2 \cdot 10^{294}$	6.3	13.0	1.3	11.4	8.4	11.2	0.2	0.4
c_p	273	8.2	7.3	4.5	5.6	23.8	$2 \cdot 10^{5}$	4.0	449.9	6.3	$4 \cdot 10^{5}$	2.3	$7 \cdot 10^{143}$	3.8	6.2	6.6	5.7	4.7	5.5	0.5	0.8
$\tilde{a}^{\mathrm{res}}$	236	10.9	7.3	4.0	5.7	58.0	$2 \cdot 10^{5}$	1.3	97.9	2.6	$3 \cdot 10^{5}$	0.5	$9 \cdot 10^{294}$	9.0	10.3	4.0	8.7	5.8	7.3	1.9	0.9
μ^{res}	236	14.5	16.2	8.7	13.6	182.3	$2 \cdot 10^{7}$	2.9	384.1	4.4	$7 \cdot 10^{5}$	0.4	$6 \cdot 10^{297}$	9.1	10.2	9.3	9.6	6.2	7.9	1.5	1.6
α	262	36.4	19.1	17.5	20.4	6.9	972.3	9.1	63.2	13.7	47.1	3.3	199.0	9.4	13.6	23.6	6.4	10.9	7.1	0.9	3.0
β	273	17.7	19.6	13.5	18.1	34.5	334.3	10.5	64.6	9.4	90.5	1.3	58.3	4.7	5.1	97.0	7.4	3.9	5.7	0.8	4.1
γ	294	30.9	7.7	7.6	7.8	303.3	$6 \cdot 10^{7}$	6.8	$2 \cdot 10^{3}$	8.2	$1 \cdot 10^{6}$	2.2	$2 \cdot 10^{301}$	13.8	18.2	20.1	14.1	12.6	13.0	0.5	1.3
w	294	9.4	12.3	6.9	10.3	117.5	$1 \cdot 10^{5}$	3.4	63.4	3.6	$1 \cdot 10^{4}$	0.4	$1 \cdot 10^{71}$	7.0	10.5	10.9	9.6	6.2	8.5	0.3	1.6
μ_{JT}	273	14.9	12.5	9.9	18.6	14.6	104.2	7.8	105.5	11.7	304.0	3.1	57.3	7.1	8.7	20.6	8.5	8.4	7.7	3.1	1.7
Γ	299	44.7	9.1	10.0	23.0	605.7	$4 \cdot 10^{3}$	7.0	69.7	5.7	$5 \cdot 10^{3}$	1.4	72.8	23.4	40.6	21.3	33.0	25.1	31.4	0.2	1.5
total	**4007**	**679.7**	**61.8**	$6 \cdot 10^{4}$	$3 \cdot 10^{3}$	**357.1**	$7 \cdot 10^{6}$	**14.6**	$3 \cdot 10^{6}$	**17.1**	$3 \cdot 10^{6}$	$9 \cdot 10^{3}$	$2 \cdot 10^{300}$	**27.3**	**29.0**	**51.2**	**24.6**	**19.5**	**23.4**	**6.3**	**3.8**

4.3.3 Overview of the Performance of Lennard-Jones EOS

To enable a systematic comparison of the performance of the considered LJ EOS, we define the performance index PI_{ij} of a given LJ EOS i for a given property j by setting its absolute average deviation in a given region k AAD_{ijk} in relation to the lowest absolute average deviation obtained from all considered LJ EOS for that property and region $\mathrm{AAD}_{i=\mathrm{best},jk}$ and summing up the result over all regions:

$$\mathrm{PI}_{ij} = 1/N_{\mathrm{reg}} \sum_{k=1}^{N_{\mathrm{reg}}} \frac{\mathrm{AAD}_{ijk}}{\mathrm{AAD}_{i=\mathrm{best},jk}} \,, \tag{90}$$

where N_{reg} indicates the number of fluid regions. Here, $N_{\mathrm{reg}} = 7$, as the extreme temperature region was excluded. The $\mathrm{AAD}_{i=\mathrm{best},jk}$ is the smallest value in a row in Table 13 and 14 for a given property k, i.e.

$$\mathrm{AAD}_{i=\mathrm{best},jk} = \min_i (\mathrm{AAD}_{ijk}) \,. \tag{91}$$

The formalism of Eq. (90) and (91) implies that all fluid regions are equally important and sufficiently densely occupied by reference data points to enable a reasonable evaluation. The value $\mathrm{AAD}_{i=\mathrm{best},jk}$ describes how accurate a given property can be currently described in a given fluid region by the considered LJ EOS.

Low values of the performance index PI_{ij} are desired. A $\mathrm{PI}_{ij} = 1$ would imply that the LJ EOS i is the best for a given property j in all studied fluid regions. High values of PI_{ij} imply that the LJ EOS is bad compared to the best competitors. Furthermore, the $\mathrm{AAD}_{i=\mathrm{best},jk}$ can be considered as an upper limit for the uncertainty, i.e. the scattering of the reference data $Y_{\mathrm{ref},jkl}$. The ratios of the number of reference data points available for a given property j in the different fluid regions k does not influence the PI_{ij} value. Eq. (90) was applied to all properties discussed in Table 14 ($j = p$, B, C, u^{res}, c_v, c_p, $\tilde{a}^{\mathrm{res}}$, μ^{res}, α, β, γ, w, μ_{JT}, Γ) as well as the VLE properties discussed in Table 13 ($j = \rho'$, ρ'', p^s, Δh_{v}). Since the VLE properties stem all from the same region, no summation has to be carried out in the evaluation of Eq. (90).

Following the differential approach for the extreme temperature region $k = $ ex-T in Table 15, this region was not comprised in the calculation of the PI_{ij} values in Eq. (90). Instead, a separate performance index was defined for the comparison of the ex-T region performance of the LJ EOS on the homogeneous state properties:

$$\mathrm{PI}_i^{\mathrm{ex\text{-}T}} = 1/N_{\mathrm{prop}} \sum_{j=1}^{N_{\mathrm{prop}}} \frac{\mathrm{AAD}_{ij,k=\mathrm{ex\text{-}T}}}{\mathrm{AAD}_{i=\mathrm{best},j,k=\mathrm{ex\text{-}T}}} \,, \tag{92}$$

where $N_{\mathrm{prop}} = 12$ indicates the number of properties ($j = p$, B, C, u^{res}, c_v, c_p, $\tilde{a}^{\mathrm{res}}$, μ^{res}, α, β, γ, w, μ_{JT}, Γ) for which data are available in that region and the denominator $\mathrm{AAD}_{i=\mathrm{best},j,k=\mathrm{ex\text{-}T}}$ indicates the absolute average deviation of the best performing LJ EOS for a given property j in the region $k = $ ex-T (smallest value in a line in Table 15).

Table 16 summarizes the performance of the investigated LJ EOS regarding the VLE and homogeneous state properties by reporting the PI_{ij} and $\mathrm{PI}_i^{\mathrm{ex\text{-}T}}$ values according Eqs. (90) and (92), respectively. Additionally, it summarizes the maximum number of points with $\mathrm{d}p/\mathrm{d}\rho = 0$ and $\mathrm{d}^2p/\mathrm{d}\rho^2 = 0$ found in $p - \rho$ isotherms in the two-phase region

(cf. Fig. 65).

The LJ EOS of *Kolafa and Nezbeda* [334], *Mecke et al.* [438, 439], *Gottschalk* [217], and *Thol et al.* [661] yield an overall similar performance. However, their performance on individual properties differs significantly: the LJ EOS of *Mecke et al.* [438, 439] and *Gottschalk* [217] exhibit large deviations in the extreme-temperature region; the LJ EOS of *Thol et al.* [661] and *Gottschalk* [217] exhibit multiple van der Waals loops, which yields large PI_{ij} values for the pvT data. Overall, the LJ EOS of *Kolafa and Nezbeda* [334] is found to give the most favorable and robust performance of those four most precise LJ EOS, i.e. for the majority of properties its performance index values are in the range $1.2 < PI_{ij} < 1.9$.

The LJ EOS of *Johnson et al.* [302] and the LJ EOS from the present work (re-parametrized PC-SAFT monomer) also give a good description of the LJ fluid.

In the group of the MBWR type LJ EOS [4, 302, 423, 425, 460, 505, 646] (cf. Table 11), that of *Johnson et al.* [302] yields overall the best performance. Comparing the PI_{ij} values among the MBWR type LJ EOS yields: the LJ EOS of *Johnson et al.* [302] has eight lowest performance index values, that of *May and Mausbach* [423, 425] has four lowest values, and both those of *Miyano* [460] and *Sun and Teja* [646] have two lowest values.

Comparing the LJ EOS of *Johnson et al.* [302] and *Kolafa and Nezbeda* [334] (two of the most popular ones; see Appendix for details), the latter has better performance index values for all properties that were considered here. This is surprising, considering the fact that the LJ EOS of *Johnson et al.* [302] has approximately four times more citations. This also holds comparing their performance on practically all considered properties in the individual fluid regions, cf. Table 13 - 15.

The theoretically-based LJ EOS yield PI_{ij} values between about 2 and 10 for the majority of studied properties j. Surprisingly, they show a poor performance when used for extrapolations into the extreme temperature region, where they perform worse than some empirical and semi-empirical LJ EOS. However, the theoretically-based LJ EOS show a good performance in the two-phase region, throughout, i.e. no undulations of the isotherms at most temperatures. Among the studied theoretically-based LJ EOS, the one from the present work shows the best performance as measured by the PI_{ij} values: for 11 properties it has the best PI_{ij} value in that group, which is probably due to the parametrization procedure that considers both bulk and VLE properties. However, for the caloric properties, it performs only poorly, which is attributed here to the unfavorable choice of the temperature-dependent diameter term, see Appendix. The other four theoretically-based LJ EOS (Refs. [128, 353, 519, 710]) show overall a similar good performance – with strengths and weaknesses in different properties.

Table 16: Summary of the performance of all 20 considered LJ EOS using the performance index PI, cf. Eq. (90) and (92). The columns '$\#_{dp/d\rho=0}$' and '$\#_{d^2p/d\rho^2=0}$' indicate the highest number of maxima and minima and the highest number of turning points observed for $p-\rho$ isotherms in the two-phase region, respectively, cf. Fig. 65.

EOS	abbr.	p_s	Δh_v	p'	p''	$\#_{dp/d\rho=0}$	$\#_{d^2p/d\rho^2=0}$	$p_\rho T$	n_{res}	c_v	c_p	a_{res}	h_{res}	α	β	γ	w	μ_{JT}	T	ext-T
Cotterman et al. [128]	Co	8.9	6.7	4.1	6.4	2	1	12.5	32.3	10.8	5.3	34.1	46.3	6.1	7.2	10.3	12.3	9.3	16.9	88.7
Paricaud [519]	Pa	3.0	7.1	9.2	6.2	2	1	17.3	15.6	9.0	8.2	10.6	22.9	6.6	8.8	11.1	17.7	5.5	18.5	24.9
Lafitte et al. [353]	La	4.1	2.4	4.3	2.2	2	1	18.1	20.2	7.9	6.2	18.5	33.2	7.5	10.0	5.9	17.9	7.3	16.4	$4\cdot10^3$
van Westen and Gross [710]	vWe	4.6	2.5	8.1	2.8	2	1	20.7	19.0	5.7	4.9	15.1	29.0	6.7	10.6	7.3	22.7	5.2	13.9	$2\cdot10^2$
this work	th	1.1	1.1	1.1	1.4	2	1	8.4	22.5	18.5	6.8	3.0	8.6	2.8	4.7	9.2	12.0	4.9	36.5	$3.8\cdot10^2$
Koutras et al. [343]	Kou	7.7	17.6	3.1	11.1	2	3	37.0	$2\cdot10^4$	$2\cdot10^4$	$9\cdot10^3$	$1\cdot10^5$	$9\cdot10^4$	11.2	11.7	35.8	$1\cdot10^2$	$1\cdot10^2$	$5\cdot10^2$	$1.4\cdot10^7$
Kolafa and Nezbeda [334]	Ko	1.1	1.2	1.1	1.4	2	1	1.2	1.6	1.9	1.5	1.3	2.2	1.3	1.2	1.7	1.9	1.7	3.4	10.1
Mecke et al. [438, 439]	Me	1.1	1.1	1.4	1.4	2	5	1.1	1.4	1.5	1.4	1.2	1.7	1.3	1.2	1.3	1.3	1.2	2.2	$2\cdot10^5$
Hess [258]	He	57.0	68.7	29.2	48.4	2	1	20.3	99.5	$1\cdot10^2$	46.8	39.2	56.1	12.6	12.5	13.1	36.6	17.0	56.4	11.8
Boltachev and Baidakov [62]	Bo	11.6	10.6	7.5	10.6	2	3	$3\cdot10^4$	$1\cdot10^5$	$1\cdot10^4$	$1\cdot10^4$	$2\cdot10^3$	$2\cdot10^4$	$1\cdot10^2$	$1\cdot10^2$	$4\cdot10^4$	$3\cdot10^2$	44.0	$5\cdot10^2$	$7\cdot10^5$
Gottschalk [217]	Go	1.0	1.0	2.0	1.0	4	4	4.8	1.2	3.6	1.8	1.1	1.1	1.4	1.3	1.6	2.1	1.4	2.5	$6\cdot10^2$
QuiñonesoCisneros et al. [554]	Qui	9.6	18.8	3.6	8.8	2	2	8.8	58.7	$1\cdot10^2$	34.3	48.9	61.3	5.9	4.8	9.5	32.1	15.1	53.9	$4\cdot10^{300}$
Nicolas et al. [505]	Ni	6.6	8.8	16.4	8.6	2	3	4.3	7.1	5.0	10.4	9.1	17.2	10.3	7.7	4.0	3.2	4.8	7.1	22.2
Adachi et al. [4]	Ad	15.0	15.4	42.0	13.8	2	3	7.9	30.8	45.1	14.9	18.9	29.7	4.9	4.0	6.4	16.0	10.6	30.7	33.7
Miyano [460]	Mi	5.4	2.1	3.1	4.9	2	3	3.4	3.7	4.6	2.7	11.8	15.4	2.2	2.4	3.9	3.2	3.4	7.8	34.3
Johnson et al. [302]	Jo	2.7	1.4	2.1	2.4	2	3	1.8	3.1	7.5	3.5	4.4	6.5	1.9	1.6	2.2	4.3	3.2	8.1	28.3
Sun and Teja [646]	Su	1.7	1.6	2.2	1.4	2	1	3.5	7.3	6.7	3.7	3.7	9.0	2.6	1.9	5.4	5.8	3.3	11.4	21.7
May and Mausbach [423, 425]	Ma	1.7	1.8	4.0	1.8	3	4	1.8	5.3	16.2	6.5	2.1	3.8	3.4	3.7	4.0	11.9	5.5	15.5	26.3
Ree [559]	Re	4.7	10.0	21.4	8.3	2	1	8.2	22.1	10.1	12.4	13.3	27.2	11.2	8.0	9.7	10.2	6.8	22.7	1.8
Thol et al. [661]	Th	1.1	1.1	1.0	1.4	4	5	13.4	1.2	3.3	1.6	1.6	1.8	1.2	1.5	1.7	1.8	13.4	1.5	3.0

4.3.4 Conclusions

In this study, Lennard-Jones equations of state were reviewed and evaluated by comparing their results to an extensive consolidated database of molecular simulation results [640]. Different types of LJ EOS were considered; they are classified here as: empirical EOS, semi-empirical EOS, and theoretically-based EOS. In total, 20 LJ EOS were considered in the present work. The performance of these LJ EOS was investigated and compared for a large number of properties. The numeric values computed from each LJ EOS for each reference data point are reported in the electronic Supplementary Material [639], which makes the employed test procedure fully transparent and reproducible and enables an extension of the present study to new LJ EOS that may be developed in future work.

Despite the simplicity of the Lennard-Jones fluid and the underlying intermolecular potential and the fact that for more than 50 years LJ EOS have been proposed, no LJ EOS gives a satisfactory description of the LJ fluid, in a sense that it a) represent the available reference data well for most of the properties, i.e. the deviations between the results of the EOS and the computer simulation data are of the same order of magnitude as the uncertainties of the simulation data, b) it shows no unphysical behavior in the two-phase region, and c) it is well-behaved when used for extrapolations to regions in which extreme conditions prevail. Some LJ EOS meet the criterion a) well, namely the LJ EOS of *Mecke et al.* [438, 439], *Gottschalk* [217], and *Thol et al.* [661], but they fail to meet the other criteria in one or several ways. Only the LJ EOS of *Kolafa and Nezbeda* [334] is found to meet all criteria reasonably well, but is, regarding criterion a) slightly less precise than the three aforementioned LJ EOS. The four LJ EOS of *Kolafa and Nezbeda* [334], *Mecke et al.* [438, 439], *Gottschalk* [217], and *Thol et al.* [661] were found to give an overall similarly good description of the Lennard-Jones fluid. However, their performance was found to differ significantly in different fluid regions and thermodynamic properties. The LJ EOS of *Kolafa and Nezbeda* [334] is found to be the most robust LJ EOS, cf. Table 16. The LJ EOS of *Thol et al.* [661] and *Gottschalk* [217] exhibit multiple van der Waals loops and the LJ EOS of *Mecke et al.* [438, 439] and *Gottschalk* [217] exhibit large deviations at extreme temperature and density.

The LJ EOS of *Johnson et al.* [302] has been used extensively in the literature, but is found to be significantly less precise than either of the four aforementioned. Nevertheless, among the MBWR type LJ EOS [4, 302, 423, 425, 460, 505, 646], that of *Johnson et al.* [302] is found to be the best.

The four overall most precise LJ EOS [217, 334, 438, 439, 661] are empirical or semi-empirical LJ EOS; the theoretically-based LJ EOS are found to be overall significantly less precise (for most properties they are about an order of magnitude less precise than the best LJ EOS). Very surprisingly, the theoretically-based LJ EOS were found to give a poor performance upon extrapolating to extreme temperatures and densities compared to the best empirical LJ EOS. This is particularly striking since the considered LJ EOS are based on *Barker and Henderson*'s perturbation theory, which is expected to perform well at high temperatures, where the attractive forces play a minor role. Hence, the systematic deviations are probably due to the modeling of the soft repulsion in the theory around the hard sphere reference system.

The theoretically-based LJ EOS of *Cotterman et al.* [128], *Paricaud* [519], *Lafitte et al.* [353], and *van Westen and Gross* [710] are found to give a good representation

of most thermodynamic properties, but are overall significantly less precise than the best empirical and semi-empirical LJ EOS. Despite the large differences of the year of publication which varies between 1986 and 2017 and differences of the underlying models, the performance of the four theoretically-based LJ EOS of Refs. [128, 353, 519, 710] is overall similar.

SAFT type EOS have become very popular in the last 30 years and many variants of these EOS exist. Several of them use monomer terms that were developed to match data of the Lennard-Jones fluid, i.e. the monomer terms are LJ EOS. Four of them were included in the present study [302, 334, 353, 505]. However, the monomer term of PC-SAFT – a particularly important version of SAFT – could not be included directly in the present study, as it was not developed to describe the Lennard-Jones fluid. Therefore, in the present work, the PC-SAFT monomer term was re-parameterized using data of the LJ fluid. The resulting LJ EOS is found to be more precise than the theoretically-based LJ EOS of Refs. [128, 353, 519, 710], which is probably due to the employed parametrization strategy that takes both VLE and homogeneous data into account. However, the present work reveals also shortcomings of the PC-SAFT monomer term: it exhibits important systematic deviations in the supercritical region – especially for caloric properties. This is attributed to the simplified form of the temperature-dependent diameter, which is used for the modeling of the soft repulsive interactions in the PC-SAFT monomer term. This supports findings from *Boshkova and Deiters* [66].

The comparison and evaluation of LJ EOS employed in this study is based on a systematic strategy: an extensive and consolidated database is used as reference data that comprises a broad variety of properties; each EOS is tested on that reference data; the fluid region is divided into characteristic sub-regions, e.g. in the $T - \rho$ space; each property is studied in each region separately before the results are combined to achieve an overall assessment. This strategy could also be useful for testing other pure component EOS and be applied as a benchmark test for new Lennard-Jones equations of state.

4.4 Characteristic Curves and Virial Coefficients of the Lennard-Jones Fluid

In section 4.3, 20 LJ EOS (cf. Table 11) were systematically reviewed and compared with available computer experiment data of the Lennard-Jones fluid for homogeneous state points and the vapor-liquid equilibrium. This section pursues this comparison and gives a detailed discussion of the virial coefficients, important characteristic states that depend on these, and *Brown*'s characteristic curves [73]. This comparison is of particular interest, since the virial coefficients of the LJ fluid can be computed exactly from their definitions in statistical mechanics, while reference data obtained from computer simulations are subject to errors and uncertainties [242, 590, 640]. *Brown*'s characteristic curves and the virial coefficients are directly linked in the limit of the ideal gas and are therefore corporately investigated in the present work. *Brown* proposed the *characteristic curves* for the assessment of equations of state for a simple fluid with repulsive and dispersive interactions [73]. The Lennard-Jones fluid is evidently an excellent candidate for such an assessment.

From *Brown*'s characteristic curves, the Amagat curve exhibits the largest pressure and temperature. For most gases, the Amagat curve is therefore not relevant for technical applications. Nevertheless, for particularly light-boiling gases, like neon, helium, and hydrogen, the pressure and temperature range of the Amagat curve is often relevant for technical applications. Furthermore, thermodynamic conditions in the range of the Amagat curve are relevant for fluids in geological applications as well as lubrication gaps in tribological applications. Only equations of state that produce reasonable Amagat curves are appropriate for such applications.

4.4.1 Theory

Brown's characteristic curves are defined as curves on which the compressibility factor $Z = \frac{pv}{T}$ or its derivatives match the values of an ideal gas at the same temperature and density [73]. Since EOS are usually fitted to reference data at moderate conditions, the evaluation of its characteristic curves is often referred to as 'testing the extrapolation behavior' of EOS [138, 491, 621, 661]. The testing of these characteristic curves has also been included in the IUPAC guidelines for publishing equations of state [136]. In this section, the definitions of *Brown*'s characteristic curves along with the description of the their general features are briefly outlined. Also their relation to the second and third virial coefficients B and C, respectively, is discussed.

Brown's characteristic curves are defined as the loci of state points at which a certain thermodynamic property of the fluid matches that of an ideal gas [66, 73, 138, 621]. *Brown* defined four main characteristic curves: one 0th-order (named Zeno curve) and three 1st-order curves (named Amagat, Boyle, and Charles curve) [73] based on the compressibility factor itself and its derivatives with respect to the temperature and pressure. For a real fluid, Z and its derivatives can match the values of the ideal gas for special T, v combinations only [73, 138], as a result of Gibbs' phase rule. These state points collectively constitute a characteristic curve.

The characteristic curves are also known under other names: the Zeno curve as 'ideal curve', the Amagat curve as 'Joule inversion curve', and the Charles curve as 'Joule-Thomson inversion curve'. Here, we adopt the original naming introduced by *Brown* [73]. The characteristic curves are usually plotted in a double-logarithmic $p-T$ diagram; this convention is also adopted here. In such a diagram the characteristic curves exhibit a typical concave dome shape, i.e. they have a negative curvature.

The Zeno, Amagat, Boyle, and Charles curve are required to have a negative curvature throughout and a single maximum in a double logarithmic pressure–temperature diagram [73, 138]. Furthermore, *Brown* postulated that all four characteristic curves end in the limit of $p \to 0$ with an infinite slope in a double logarithmic $p-T$ diagram [73]. *Brown* furthermore deduced that the four characteristic curves of 0th and 1st-order may only contact each other at three distinct points [73, 138]: (1) the Zeno curve converges against the Amagat curve on the hypothetical extension of the vapor pressure curve; (2) the Zeno curve converges against the Boyle curve in their common limit of $p \to 0$ at $T = T_{\text{Boyle}}$ (the zero crossing temperature of the second virial coefficient), and (3) the Zeno curve intersects the Charles curve at the point of maximum pressure of the Zeno curve. Usually, the Amagat and Zeno curve are truncated at low temperatures by the solid-fluid equilibrium. Finally, the Amagat, Boyle, and Charles curve must not cross, but enclose each other in a $p-T$ diagram [73]: the Amagat curve surrounding the Charles curve surrounding the Boyle curve.

The characteristic curves can be computed from the Helmholtz energy per particle a and its derivatives. The following notation is used for the derivatives of the Helmholtz energy with respect to the inverse temperature and density

$$\tilde{a}_{nm} = \tilde{a}_{nm}^{\text{id}} + \tilde{a}_{nm}^{\text{res}} = (1/T)^n \, \rho^m \, \frac{\partial^{n+m}(\tilde{a}^{\text{id}} + \tilde{a}^{\text{res}})}{\partial(1/T)^n \, \partial\rho^m}, \tag{93}$$

with $n, m = 0, 1, 2$ and the tilde indicating $\tilde{a} = a/T$. In Eq. (93), 'id' indicates the ideal gas contribution and 'res' the configurational contribution.

The Zeno curve ($\mathcal{Z}$) is defined as the locus of state points that satisfy $Z = \frac{pv}{T} \equiv 1$ and can be computed from the Helmholtz energy as [621]

$$\tilde{a}_{01}^{\text{res}} = 0 \,. \tag{94}$$

Furthermore, state points on the Zeno curve have $u^{\text{res}} = 0$. The Zeno and Boyle curve end at the Boyle temperature T_{Boyle} in the zero pressure limit $p \to 0$, which corresponds to the condition for the second virial coefficient $B(T_{\text{Boyle}}) = 0$.

The Amagat curve ($\mathcal{A}$) is defined as the locus of state points that satisfy $\left(\frac{\partial Z}{\partial T}\right)_v \equiv 0$ and can be computed from the Helmholtz energy as [621]

$$\tilde{a}_{11}^{\text{res}} = 0 \,. \tag{95}$$

The Amagat curve originates on the vapor pressure curve at low temperatures (if crystallization is disregarded). It ends at the Amagat temperature T_{Amagat} in the zero pressure limit $p \to 0$, which corresponds to the maximum of the second virial coefficient with $\mathrm{d}B/\mathrm{d}T = 0$. Equations of state that do not exhibit a maximum in the second virial coefficient $B(T)$ have a distorted Amagat curve in the limit $p \to 0$ [73, 138].

The Boyle curve ($\mathcal{B}$) is defined as the locus of state points that satisfy $\left(\frac{\partial Z}{\partial p}\right)_T \equiv 0$ and can be computed from the Helmholtz energy as [621]

$$\tilde{a}_{01}^{\mathrm{res}} + \rho \cdot \tilde{a}_{02}^{\mathrm{res}} = 0 \,. \tag{96}$$

The Boyle curve originates on the vapor pressure curve close to the critical point, runs through a pressure maximum and ends with the Zeno curve at the Boyle temperature in the limit $p \to 0$.

The Charles curve ($\mathcal{C}$) is defined as the locus of state points that satisfy $\left(\frac{\partial Z}{\partial T}\right)_p \equiv 0$ and can be computed from the Helmholtz energy as [621]

$$\tilde{a}_{01}^{\mathrm{res}} + \rho \cdot \tilde{a}_{02}^{\mathrm{res}} + 1/T \cdot \tilde{a}_{11}^{\mathrm{res}} = 0 \,. \tag{97}$$

The Charles curve – also known as Joule-Thomson inversion curve – is of fundamental technical importance as it determines the transition locus from heating to cooling upon isenthalpic throttling, i.e. $\left(\frac{\partial T}{\partial p}\right)_h = 0$ also holds on the Charles curve. The Charles curve originates on the vapor pressure curve. The Charles curve ends at the Charles temperature T_{Charles} in the zero pressure limit $p \to 0$, which corresponds to the condition for the second virial coefficient $\mathrm{d}B/\mathrm{d}T = B/T$ (the secant of the second virial coefficient at $B(T_{\mathrm{Charles}})$ is a line through the origin) [135].

Details and alternative thermodynamic definitions for the characteristic curves can be found in Refs. [66, 73, 135, 138, 621].

The second and third virial coefficient B and C, respectively, of a fluid can be directly computed from the pairwise additive intermolecular potential, e.g. the LJ potential u_{LJ} [263, 416]. Using the *Mayer* function

$$f_{ij} = \exp\left(-u_{\mathrm{LJ}}(r_{ij})/k_{\mathrm{B}}T\right) - 1 \,, \tag{98}$$

where r_{ij} indicates the distance between two interacting particles, the second and third virial coefficient can be written as [263]

$$B = -\frac{1}{2V} \iint f_{12} \, \mathrm{d}\mathbf{r}_1 \mathrm{d}\mathbf{r}_2 \,, \tag{99}$$

$$C = -\frac{1}{3V} \iiint f_{12} \, f_{23} \, f_{13} \, \mathrm{d}\mathbf{r}_1 \mathrm{d}\mathbf{r}_2 \mathrm{d}\mathbf{r}_3 \,, \tag{100}$$

where $\mathrm{d}\mathbf{r}$ indicates a finite volume element in which the particle is located. Eq. (99) can be integrated in a trivial way, cf. Ref. [263]. The integrals in Eq. (100) were solved in this work using the method proposed by *Hutem and Boonchui* [284]. Eq. (99) and (100) were implemented and numerically integrated to obtain exact results for B and C as well as their characteristic points using the Lennard-Jones potential, cf. Eq. (64).

Furthermore, the second and third viral coefficient were computed from the considered LJ EOS, cf. Table 11. Eq. (101) and (102) give the thermodynamic definitions for the calculation of the second and third virial coefficient B and C from the Helmholtz

energy:

$$B = \lim_{\rho \to 0} \left(\frac{\partial(p/\rho T)}{\partial \rho} \right)_T = \rho^{-1} \lim_{\rho \to 0} (\tilde{a}_{01}^{\rm res}/\rho) \,, \tag{101}$$

$$C = 1/2 \cdot \lim_{\rho \to 0} \left(\frac{\partial^2(p/\rho T)}{\partial \rho^2} \right)_T = \rho^{-2} \lim_{\rho \to 0} (\tilde{a}_{02}^{\rm res}/\rho^2) \,. \tag{102}$$

4.4.2 Results for the Virial Coefficients

The second and third virial coefficient computed from the 20 considered LJ EOS are compared in Fig. 66 with exact data obtained from statistical mechanics [262] published in the literature [46, 264, 600, 640, 646, 711]. Numbers from our implementation perfectly agree with that literature data. The literature values are plotted for reproducibility reasons. The numeric values for the second and third virial coefficient computed from the 20 considered LJ EOS is reported in the electronic Supplementary Material [625].

Qualitatively, the second virial coefficient B of the LJ fluid is captured well by all considered LJ EOS, cf. Fig. 66 - top, except that of *Koutras et al.* [343]. All other LJ EOS have a single zero crossing at the Boyle temperature $T_{\rm Boyle}$ (defined as $B(T_{\rm Boyle}) = 0$). The exact value of the Boyle temperature obtained from numerical integration is $T_{\rm Boyle} = 3.417927982 \, \varepsilon k_{\rm B}^{-1}$. However, significant deviations from the exact second virial coefficient data are found for most LJ EOS at low temperatures (below the triple point temperature, which is approximately $T_{\rm tr} = 0.68 \pm 0.02 \, \varepsilon k_{\rm B}^{-1}$ [9, 11, 12, 238, 352, 418, 596, 617]) and at high temperatures ($T > 10 \, \varepsilon k_{\rm B}^{-1}$), cf. Fig. 66 - middle. Excluding the direct vicinity of the Boyle temperature, all LJ EOS except that of *Paricaud* [519], *Gottschalk* [217], and *Hess* [258] show relative deviations from the exact values for the second virial coefficient of at least 20% in some temperature range. The LJ EOS of Refs. [217, 258, 519] comprise the statistical mechanical formulation for the second virial coefficient in their mathematical formulation, which consequently leads to an excellent agreement for B. However, minor deviations for B are observed for the results obtained from our implementation of the LJ EOS of *Paricaud* [519] at low temperatures.

The LJ EOS of *Quiñones-Cisneros et al.* [554], *Nicolas et al.* [505], *Cotterman et al.* [128], *Sun and Teja* [646], *Koutras et al.* [343], and from this work (see Appendix) deviate by more than 20% from the exact values in the range $T < T_{\rm tr}$ and $T > 6 \, \varepsilon k_{\rm B}^{-1}$. The LJ EOS of *van Westen and Gross* [710], *Lafitte et al.* [353], *Thol et al.* [661], *Adachi et al.* [4], *May and Mausbach* [423, 425], *Johnson et al.* [302], *Kolafa and Nezbeda* [334], *Boltachev and Baidakov* [62], *Ree* [559], and *Miyano* [460] deviate by more than 20% from the exact values at $T < T_{\rm tr}$, too, but perform better at high temperatures. Excluding the vicinity of the Boyle temperature and extreme temperature conditions at $T < T_{\rm tr}$ and $T > 6 \, \varepsilon k_{\rm B}^{-1}$, the LJ EOS of *Mecke et al.* [438, 439], *Johnson et al.* [302], *Boltachev and Baidakov* [62], *Miyano* [460], and *Kolafa and Nezbeda* [334] describe the exact second virial coefficient data within $\delta B = \pm 2\%$.

The agreement of the LJ EOS and exact values for the third virial coefficient C is overall significantly less good than for the second virial coefficient. Only the LJ EOS of *Johnson et al.* [302], *Kolafa and Nezbeda* [334], *Lafitte et al.* [353], *Mecke et al.* [438, 439], *May*
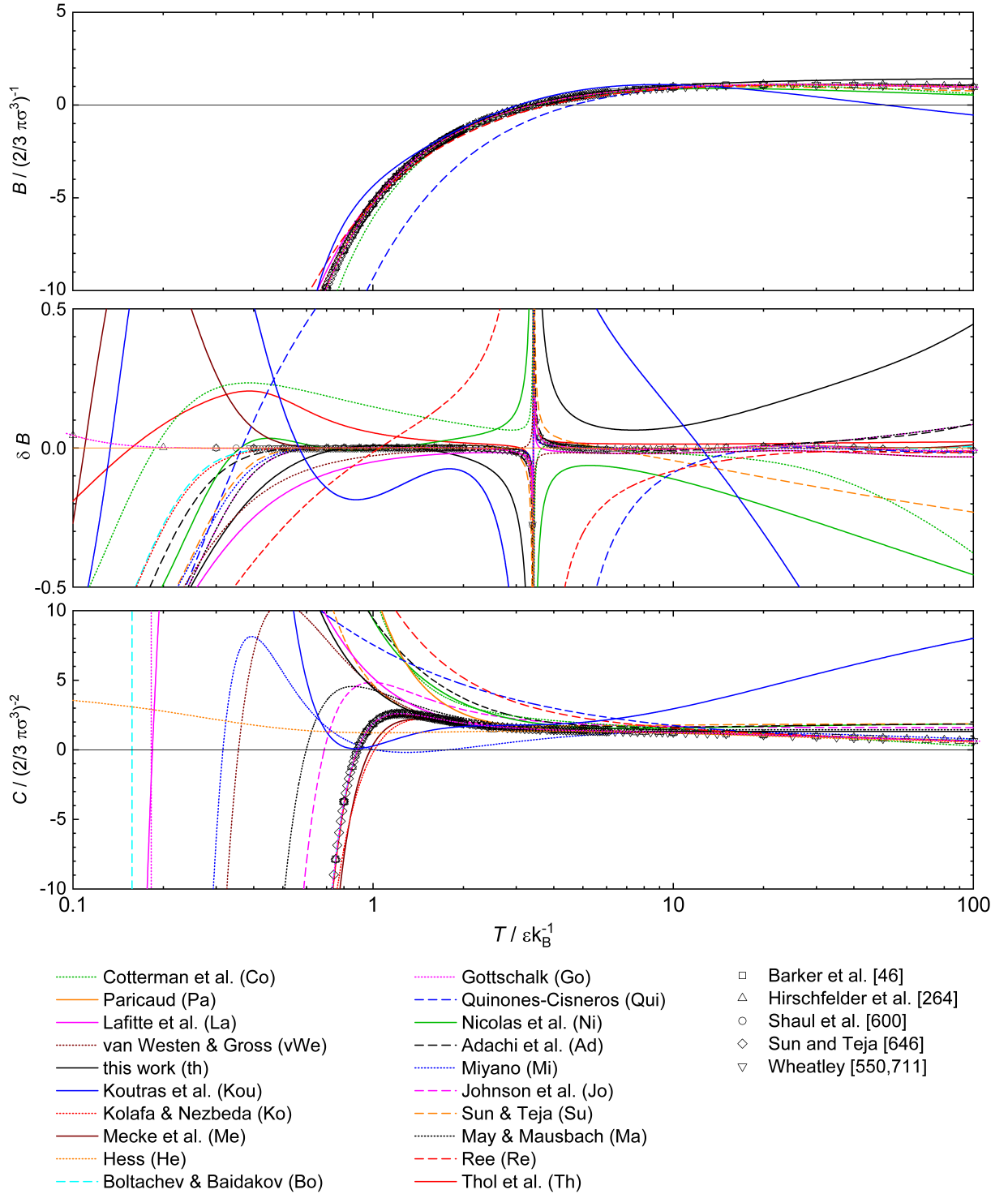
Figure 66: Second (top and middle) and third (bottom) virial coefficient as a function of the temperature. The top and bottom plot show the virial coefficients them self; the middle plot shows the relative deviation of the second virial coefficient from the LJ EOS of *Paricaud* [519]. For all three plots: lines are LJ-EOS and exact values from Refs. [46, 55, 264, 600, 646, 711] are symbols.

and Mausbach [423, 425], *Thol et al.* [661], and *van Westen and Gross* [710] qualitatively describe the trend of the third virial coefficient accurately. The LJ EOS of *Kolafa and Nezbeda* [334], *Mecke et al.* [438, 439], and *Thol et al.* [661] describe the third virial coefficient qualitatively well up to $T = 100\,\varepsilon k_{\mathrm{B}}^{-1}$. The absolute average deviations from these three LJ EOS and the exact values for C from the literature are $\mathrm{AAD}^{\mathrm{Me}} = 47\%$, $\mathrm{AAD}^{\mathrm{Ko}} = 53\%$, and $\mathrm{AAD}^{\mathrm{Th}} = 8\%$, i.e. that of *Thol et al.* [661] is the most accurate regarding the description of C, cf. Table 14.

Other considered LJ EOS either exhibit no maximum or two maxima or a wrong limit at low temperatures. Even though the LJ EOS of Refs. [217, 258, 519] were found to be the most precise LJ EOS to describe the second virial coefficient, these LJ EOS produce a qualitatively wrong trend for the third virial coefficient.

Castro-Marcano et al. [94] showed that theoretically based EOS, such as soft-SAFT [57, 58], SAFT-VR [353, 518], and PC-SAFT [223, 224] do not adequately describe third virial coefficients of real substances in a sense that they do not exhibit a maximum at moderate temperatures and wrong limits at low temperatures. Our results indicate that for the PC-SAFT equation, this deficiency is already inherent in the corresponding monomer term (the LJ EOS from this work, see Appendix), whereas the soft-SAFT and SAFT-VR Mie equation show a physically correct behavior for monomers.

4.4.3 Results for the Characteristic Curves

Several computer experiment datasets for the characteristic curves of the LJ fluid are available in the literature [120, 138, 260, 324, 689, 727]. The Charles curve (also known as Joule-Thomson inversion curve) of the LJ fluid has been investigated several times in the literature by molecular simulations [120, 138, 260, 324, 689, 727]. The Amagat, Boyle, and Zeno curve of the LJ fluid have only investigated by computer experiment by *Deiters and Neumaier* [138]. The numeric values of these computer experiment data were summarized in Ref. [640] and are taken here as reference.

The computer experiment data available for the characteristic curves is compared in Fig. 67 with the results obtained from the LJ EOS of *Lafitte et al.* [353], which gives the best description of the reference data (discussed in detail below). The Charles curve computer experiment data points of Refs. [120, 138, 324, 689, 727] are in good mutual agreement. For the Charles curve, the computer experiment data reported by *Heyes and Llaguno* [260] is found to deviate significantly from the data of Refs. [120, 138, 324, 689, 727]. To avoid visual clutter, only the data of *Deiters and Neumaier* [138] is used in the following for the evaluation of the LJ EOS. Fig. 67 also shows the solid-fluid transition reported by *Agrawal and Kofke* [9].

It turns out that some of the simulation data of *Deiters and Neumaier* [138] for the Amagat and Charles curves lie probably beyond the freezing line. It is well known, however, that small simulation ensembles in cubic boxes with periodic boundary conditions tend to subcool. *Deiters and Neumaier* [138] used a moderate ensemble size of $N = 1000$ particles, they always started their simulations from random configurations, and they monitored the simulation runs for signs of crystallization. One can therefore conclude that the reported simulation states beyond the freezing line represent subcooled fluid states.
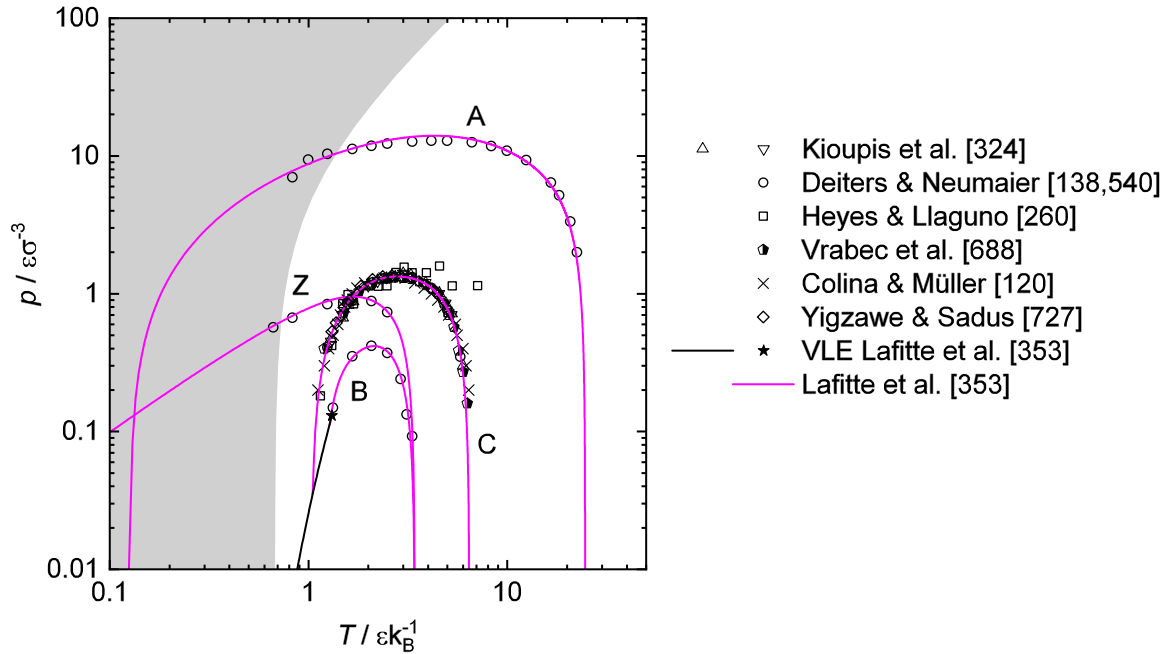
Figure 67: *Brown*'s characteristic curves: lines are the LJ EOS of *Lafitte et al.* [353]; symbols are molecular simulations results from the literature [120, 138, 260, 324, 689, 727]. The black solid line and star indicate the VLE and critical point. The gray shaded region indicates the solid phase of the LJ potential as reported by *Agrawal and Kofke* [9].

Fig. 67 shows that the four characteristic curves computed from the LJ EOS of *Lafitte et al.* [353] satisfies all requirements postulated by *Brown* [73], i.e. starting points on the vapor pressure curve, limits at $p \to 0$, and intersection points, except the termination point of the Zeno and Amagat curve. *Brown* deduced from rational thermodynamic arguments that the Zeno and Amagat curve converge into each other in the zero temperature and zero pressure limit with infinite slope. However, it is interesting to note that the LJ EOS of *Lafitte et al.* [353] yields a crossing of the Zeno and Amagat curve at approximately the critical pressure. Furthermore, the Zeno curve of the LJ EOS of *Lafitte et al.* [353] does not exhibit an infinite slope in the zero pressure limit as postulated by *Brown* [73].

Brown's [73] assumption for an infinite slope of the Zeno curve in the zero pressure limit at low T is probably incorrect. The compressibility factor on the Zeno curve is by definition $Z = 1$, which yields $\ln p = \ln T + \ln \rho$. The last term converges approximately to a constant value at low p for $T \to 0$. Hence, the Zeno curve has a constant slope of unity at $T \to 0$ in a double logarithmic $p - T$ diagram – as predicted by the LJ EOS of *Lafitte et al.* [353] and others (see below). Nonetheless, for the Lennard-Jones model, that region lies in the solid region.

The characteristic curve computer experiment data of *Deiters and Neumaier* [138] are compared in Fig. 68 individually with the results obtained from the 20 investigated LJ EOS. The LJ EOS are ordered roughly according their types, i.e. starting from the theoretically-based LJ EOS, to the semi-empirical and fully empirical LJ EOS.

None except the LJ EOS of *Lafitte et al.* [353] satisfies all requirements for the characteristic curves. Most LJ EOS yield reasonable Zeno, Boyle, and Charles curves, but fail
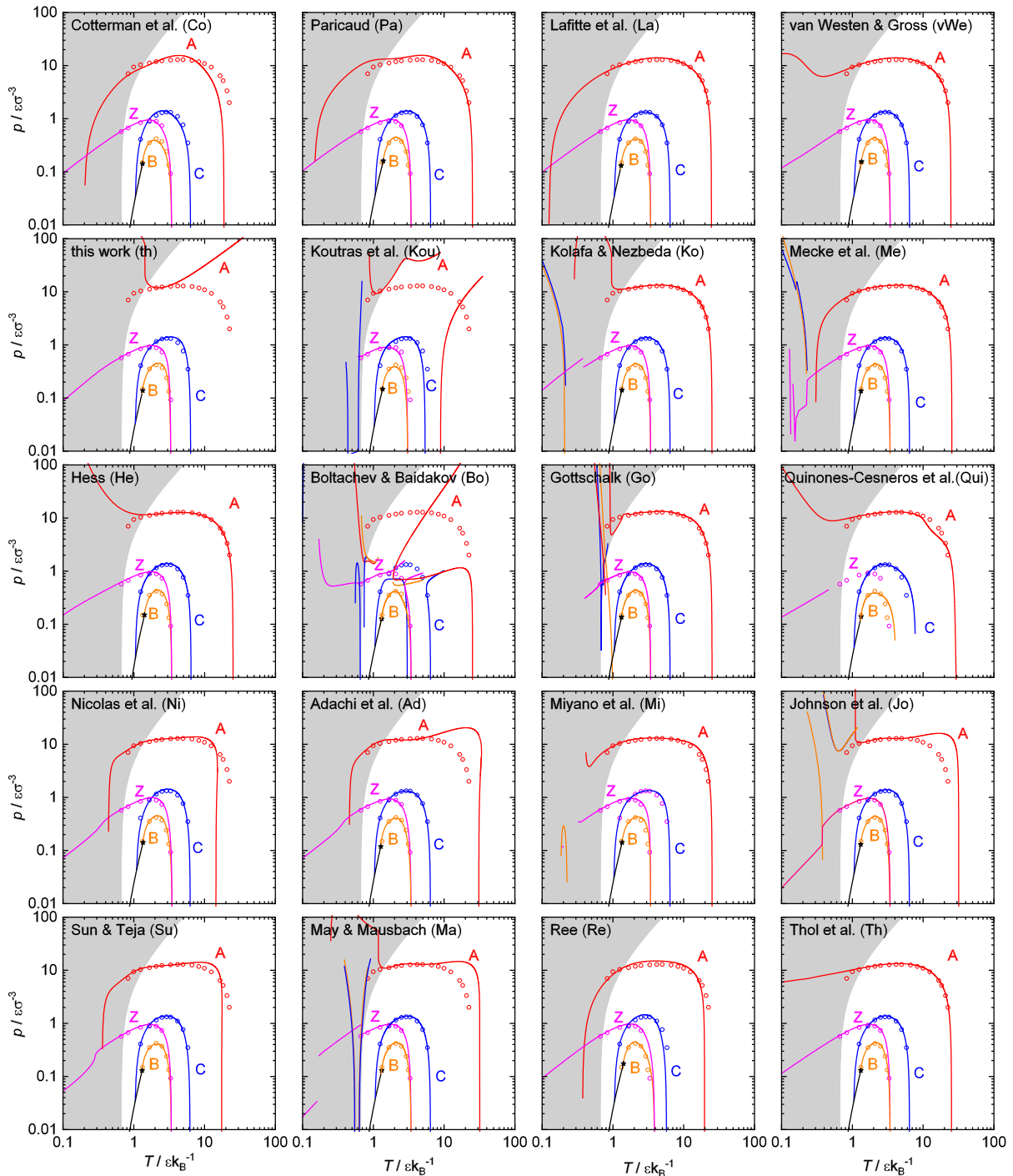
Figure 68: Comparison of *Brown*'s characteristic curves obtained from different LJ EOS (colored lines) with the molecular simulations results (symbols) of *Deiters and Neumaier* [138]. The black solid line and star indicate the VLE and critical point obtained from the respective LJ EOS. The gray shaded region indicates the solid phase of the LJ potential as reported by *Agrawal and Kofke* [9].

for the Amagat curve. In the case of inaccurate Zeno, Boyle, and Charles curves, they are mostly distorted at low temperatures. Several LJ EOS [217, 258, 334, 460, 661, 710] produce reasonable Amagat curves over a wide temperature range, but yield distortions in the vicinity of the solid-fluid equilibrium. There are also some LJ EOS that produce Amagat curves exhibiting minor oscillations at high pressures [4, 128, 302, 423, 425, 505, 519, 554, 646], i.e. a wrong curvature.

The four characteristic curves studied here evidently represent challenges of different severity, i.e. the Charles curve is predicted qualitatively correct by most LJ EOS, while the Amagat curve is predicted qualitatively correct and in good agreement with reference data in the entire temperature range by merely one LJ EOS. There is a tendency among the four characteristic curves to be predicted qualitatively correct (Charles → Boyle → Zeno → Amagat).

Boshkova and Deiters [66] reported that many theoretically-based EOS fail to yield accurate Amagat curves due to simplifications in the modeling of the repulsive interactions. However, we find that the theoretically-based LJ EOS of *Lafitte et al.* [353], *Cotterman et al.* [128], and *Paricaud* [519] yield reasonable Amagat curves in a wide temperature range – the LJ EOS of *Lafitte et al.* [353] is even quantitatively in good agreement with computer experiment results.

The LJ EOS from this work based on the PC-SAFT monomer model yields qualitatively accurate Zeno, Boyle, and Charles curves, but a completely distorted Amagat curve. This type of behavior was also reported by *Boshkova and Deiters* [66] for the original PC-SAFT parametrization. They showed that this is a result of the simplified temperature-dependent diameter of the PC-SAFT approach, which gives a poor description of the soft repulsion of the Lennard-Jones potential [66]. This is supported by the results from section 4.3, which showed that the LJ EOS from this work (re-parametrized PC-SAFT monomer term) yields large deviations at high temperatures and densities for most homogeneous state point properties, where the softness of the repulsive interactions becomes more important.

The LJ EOS of the MBWR type (Refs. [4, 302, 423, 425, 460, 505, 646]) have in common that they yield Zeno curves with a kink at low temperatures. Some of them also exhibit a distorted Boyle curve (LJ EOS of Refs. [302, 423, 425, 460]). All LJ EOS of the MBWR type yield distorted Amagat curves, but most of them yield accurate Charles curves. For some MBWR type LJ EOS [4, 505, 646], the Amagat curve has a positive curvature at high temperature.

The LJ EOS of *Cotterman et al.* [128], *Paricaud* [519], *Thol et al.* [661], and *van Westen and Gross* [710] produce qualitatively accurate Zeno, Boyle, and Charles curves, but wrong Amagat curves. The LJ EOS of *Ree* [559], *Koutras et al.* [343], and *Hess* [258] yield unrealistic results for at least two characteristic curves. The LJ EOS of *Boltachev and Baidakov* [62] and *Quiñones-Cisneros et al.* [554] show a distorted shape for all four characteristic curves. For the LJ EOS of *Quiñones-Cisneros et al.* [554], the Zeno curve at moderate temperatures lies below $p = 0.01\,\varepsilon\sigma^{-3}$, i.e. out of the range of the depicted plot. The characteristic curves obtained from the LJ EOS of *Gottschalk* [217] are in good agreement with the reference data in a wide temperature and pressure range of the fluid region, but all four curves yield unrealistic solutions at low temperatures.

The characteristic curves obtained from the LJ EOS of *Mecke et al.* [438, 439] are in excellent agreement with the available computer experiment data, but show unphysical

features in the low temperature limit. *Deiters and Neumaier* [138] reported that the LJ EOS of *Mecke et al.* [438, 439] gives a realistic description of all characteristic curves, which is found differently in the present work. An additional (physically unrealistic [66, 73]) branch is found for all four characteristic curves. Likewise, an unrealistic behavior is found for the Charles, Boyle, Zeno, and Amagat curve of the LJ EOS of *Kolafa and Nezbeda* [334] at low temperature.

The Amagat curve of the LJ EOS of *Thol et al.* [661] is distorted at lower temperatures – as also pointed out by *Thol et al.* [661] and *Deiters and Neumaier* [138]. However, we find a significantly different Amagat curve as reported by *Thol et al.* [661] for their LJ EOS. The Amagat curve computed from our implementation is in good agreement with the computer experiment results reported by *Deiters and Neumaier* [138] for most temperatures. We suspect a misprint in the publication of *Thol et al.* [661].

4.4.4 Results for the Characteristic State Points

The thermodynamic behavior of a pure substance contains multiple uniquely defined state points, of which the critical point is the most prominent one. Such state points can be favorably used to characterize the quality of equations of state, since they comprise a condensed description of the thermodynamic behavior in a single state point. The critical point obtained from different LJ EOS in comparison to computer experiment data has been discussed in detail in section 4.3.2.2. Here, characteristic state points related to the virial coefficients and *Brown*'s characteristic curves are discussed. In particular, exact values for a given interaction potential can be obtained for some characteristic points from statistical mechanics.

Characteristic state points considered in the present work are:

- the state points of the four characteristic curves in the zero density limit, labeled as $\mathcal{Z}(\rho \to 0)$, $\mathcal{A}(\rho \to 0)$, $\mathcal{B}(\rho \to 0)$, and $\mathcal{C}(\rho \to 0)$ (which can also be computed from the virial coefficients – see above),

- the zero crossing of the third virial coefficient $C(T) = 0$, and the maximum of the third virial coefficient $\max(C(T))$,

- the intersection of the Boyle and Charles curve with the vapor pressure curve labeled as VLE $\cap$ $\mathcal{B}$ and VLE $\cap$ $\mathcal{C}$,

- the intersection point of the Zeno and Charles curve labeled as $\mathcal{Z} \cap \mathcal{C}$,

- the maxima of the four characteristic curves in the $p-T$ plane labeled as $\max(\mathcal{A})$, $\max(\mathcal{B})$, $\max(\mathcal{C})$, and $\max(\mathcal{Z})$.

Exact values from numerical integration of the virial coefficients can be obtained for the temperature at $\mathcal{Z}(\rho \to 0)$, $\mathcal{A}(\rho \to 0)$, $\mathcal{B}(\rho \to 0)$ (from the second virial coefficient), the zero crossing of the third virial coefficient $C(T) = 0$, and the maximum of the third virial coefficient $\max(C(T))$ as indicated in Table 17. Those reported values in Table 17 were obtained in this work and were – where available – compared and found to be in excellent agreement with results from the literature [581].

Furthermore, the above defined characteristic state points were computed for each of the considered LJ EOS. For the maxima and intersection points of the characteristic curves,

an iterative solver was used to find the state point satisfying the respective conditions. For the intersection points of the characteristic curves with the phase envelope, both the VLE and the characteristic curves were iteratively computed by means of a given LJ EOS to find the intersection point. The zero density limit state points of the characteristic curves were computed directly from the definition of the respective curve at $\rho \to 0$. To validate the consistency of the LJ EOS implementations used in the present work, these state points were also computed by the LJ EOS from the corresponding definition from the second virial coefficient (see above) for comparison. The results obtained from the two thermodynamic definitions were found in all cases to be in excellent agreement.

Table 17 lists the temperatures of the characteristic state points. The temperature, pressure, and density of each state point are reported in the electronic Supplementary Material [625]. The numeric values therein are reported with more decimal places than in Table 17. Blanks in Table 17 indicate cases where the shape of a characteristic curve or the third virial coefficient is distorted in a way that a maximum or crossing point could not be evaluated in a meaningful way.

For the zero density limit state points of the characteristic curves the temperature $T_{\mathcal{Z}(\rho \to 0)}$, $T_{\mathcal{B}(\rho \to 0)}$, $T_{\mathcal{C}(\rho \to 0)}$, and $T_{\mathcal{A}(\rho \to 0)}$ can be compared with exact values obtained via the virial coefficient route by numerical integration of the Lennard-Jones potential, cf. Table 17. Excellent agreement is found for many LJ EOS except the LJ EOS of Refs. [343, 505, 554, 559, 639, 646, 710] which yield significantly deviating $T_{\mathcal{Z}(\rho \to 0)}$ and $T_{\mathcal{B}(\rho \to 0)}$; the LJ EOS of Refs. [4, 128, 302, 343, 423, 425, 505, 554, 559, 639, 646] yield significantly deviating $T_{\mathcal{A}(\rho \to 0)}$ (or even no solution).

The zero density limits $T_{\mathcal{Z}(\rho \to 0)}$, $T_{\mathcal{B}(\rho \to 0)}$, $T_{\mathcal{C}(\rho \to 0)}$, and $T_{\mathcal{A}(\rho \to 0)}$ obtained from the LJ EOS of *Gottschalk* [217] and *Hess* [258] agree with the exact values within the computer precision employed for the calculations since those are integrated in the respective equation. For the LJ EOS of *Paricaud* [519] small deviations for the values of $T_{\mathcal{Z}(\rho \to 0)}$, $T_{\mathcal{B}(\rho \to 0)}$, $T_{\mathcal{C}(\rho \to 0)}$, and $T_{\mathcal{A}(\rho \to 0)}$ in comparison to the exact data are found, which is in line with the small deviations observed for the second virial coefficient itself. Also the LJ EOS of *Kolafa & Nezbeda* [334] has a second virial coefficient term and therefore gives an excellent description of the zero density limits of the characteristic curves. Also the empirical LJ EOS of *Thol et al.* [661] yields accurate results for $T_{\mathcal{Z}(\rho \to 0)}$, $T_{\mathcal{B}(\rho \to 0)}$, $T_{\mathcal{C}(\rho \to 0)}$, and $T_{\mathcal{A}(\rho \to 0)}$ (deviations below 2%).

Exact values were also obtained in the present work for the temperature of the zero crossing and maximum of the third virial coefficient $T_{C=0}$ and $T_{\max(C)}$, respectively, from numerical integration, cf. Table 17. Only results from the LJ EOS of Refs. [334, 438, 439, 661] are found to be in good agreement with exact values for $T_{C=0}$ and $T_{\max(C)}$; reasonable agreement is found for the LJ EOS of Refs. [302, 423, 425]. The best results for $T_{C=0}$ and $T_{\max(C)}$ are obtained from the LJ EOS of *Thol et al.* [661].

The temperature of the Zeno curve maximum $T_{\max(\mathcal{Z})}$ obtained from the 20 investigated LJ EOS are in good agreement. They lie in the range $T_{\max(\mathcal{Z})} = 1.74 \pm 0.06 \, \varepsilon k_{\mathrm{B}}^{-1}$. The temperature of the Boyle curve maximum obtained from the 20 LJ EOS scatters slightly more in the range $T_{\max(\mathcal{B})} = 2.12 \pm 0.09 \, \varepsilon k_{\mathrm{B}}^{-1}$. Only the LJ EOS of *Koutras et al.* [343] yields a significantly lower $T_{\max(\mathcal{Z})}$ and $T_{\max(\mathcal{B})}$ compared to all other investigated LJ EOS. The scattering is significantly larger for the temperature of the Charles curve maximum obtained from the different LJ EOS as $T_{\max(\mathcal{C})} = 2.92 \pm 0.5 \, \varepsilon k_{\mathrm{B}}^{-1}$. For the temperature of the Amagat curve maximum, 11 LJ EOS scatter around $T_{\max(\mathcal{A})} = 4.5 \pm 1.5 \, \varepsilon k_{\mathrm{B}}^{-1}$. The

Table 17: Temperatures of characteristic state points calculated from different LJ EOS. The columns are from left to right: the maxima of the four characteristic curves, the intersection point of the Boyle and Charles curve with the VLE phase boundary, the intersection point of the Zeno and Charles curve, the zero density limit of the four characteristic curves, the zero crossing of the third virial coefficient, and the maximum of the third virial coefficient. The full specifications of the state points are reported in the electronic Supplementary Material [625]. All temperature values are given in εk_B^{-1}. (A) Exact values obtained from the virial coefficient route Eq. (99) and (100).

	$T_{\max(Z)}$	$T_{\max(B)}$	$T_{\max(C)}$	$T_{\max(A)}$	$T_{VLE\cap B}$	$T_{VLE\cap C}$	$T_{Z\cap C}$	$T_{Z(\rho\to0)}$	$T_{B(\rho\to0)}$	$T_{C(\rho\to0)}$	$T_{A(\rho\to0)}$	$T_{C=0}$	$T_{\max(C)}$
Cotterman et al. [128]	1.6310	1.9335	2.5495	4.3358	1.3005	1.0572	1.6310	3.4321	3.4321	6.3469	18.7773	-	-
Paricaud [519]	1.7642	2.0918	2.9776	4.7771	1.3469	1.0651	1.7642	3.4248	3.4248	6.4571	25.1718	-	-
Lafitte et al. [353]	1.6711	2.1382	2.7890	4.2976	1.2838	1.0525	1.6711	3.4220	3.4220	6.4379	24.6615	0.1838	0.2704
van Westen & Gross [710]	1.7026	2.0406	2.8827	4.0655	1.2029	1.0579	1.7026	3.4280	3.4280	6.4444	24.6640	0.3559	0.4994
this work	1.7884	2.2171	3.3279	-	1.3008	1.0505	1.7884	3.3172	3.3172	6.3423	-	-	-
Koutras et al. [343]	1.5278	1.9851	2.8420	-	1.3187	1.0343	1.5278	3.0549	3.0549	5.3955	8.8877	-	-
Kolafa & Nezbeda [334]	1.7437	2.1305	2.9641	4.5240	1.3037	1.0448	1.7437	3.4176	3.4176	6.4303	25.1215	1.0110	1.5316
Mecke et al. [438, 439]	1.7326	2.1531	2.8817	4.4880	1.3058	1.0535	1.7326	3.4181	3.4181	6.4315	25.4520	0.9791	1.4068
Hess [258]	1.7466	2.1710	2.9804	4.6380	1.3789	1.0526	1.7466	3.4179	3.4179	6.4308	25.1526	-	-
Boltachev & Baidakov [62]	-	2.0292	-	-	1.1894	1.0538	1.8050	3.4183	3.4183	6.4339	25.2259	-	-
Gottschalk [217]	1.7392	2.1185	2.9255	4.6550	1.2959	1.0497	1.7393	3.4179	3.4179	6.4308	25.1526	-	-
Quiñones-Cisneros et al. [554]	1.7456	2.0612	2.8011	4.1177	1.3029	1.0570	1.7456				38.0169	-	-
Nicolas et al. [505]	1.8031	2.1744	3.0167	7.3349	1.3281	1.0998	1.8031	3.4748	3.4748	6.2763	14.4852	-	-
Adachi et al. [4]	1.6818	2.0867	2.8610	20.3570	1.2570	1.0373	1.6818	3.4148	3.4148	6.4090	30.9385	-	-
Miyano [460]	1.7547	2.2564	3.2542	3.6436	1.3165	1.0349	1.7547	3.4151	3.4151	6.4166	25.1903	0.3159	0.3938
Johnson et al. [302]	1.7321	2.1165	3.0488	16.6742	1.2838	1.0567	1.7321	3.4150	3.4150	6.4147	31.8491	0.6878	0.9906
Sun & Teja [646]	1.6831	2.1198	2.8851	8.6988	1.2858	1.0506	1.6831	3.4004	3.4004	6.2288	17.4236	-	-
May & Mausbach [423, 425]	1.7267	2.1387	3.0118	15.9232	1.2859	1.0617	1.7267	3.4150	3.4150	6.4147	31.8491	0.5986	0.8588
Ree [559]	1.7771	2.0370	2.9266	3.8508	1.3725	1.0894	1.7771	3.8746	3.8746	7.3462	28.5118	-	-
Thol et al. [661]	1.7424	2.1760	2.9211	4.4841	1.2943	1.0512	1.7424	3.4168	3.4168	6.4253	25.1728	0.8884	1.2139

(A) Exact values obtained from numerical integration are: $T_{C=0}=0.886917868\,\varepsilon k_B^{-1}$, $T_{\max(C)}=1.229875759\,\varepsilon k_B^{-1}$, $T_{B(\rho\to0)}=3.417927982\,\varepsilon k_B^{-1}$, $T_{C(\rho\to0)}=6.430798418\,\varepsilon k_B^{-1}$, $T_{A(\rho\to0)}=25.15242837\,\varepsilon k_B^{-1}$.

LJ EOS of Refs. [4, 62, 128, 302, 423, 425, 646] show significantly shifted $T_{\max(\mathcal{A})}$ which is due to the distorted Amagat curves produced by these LJ EOS.

The differences in the intersection points of the Charles and Boyle curve with the VLE are dominated by differences in the VLE obtained from the different LJ EOS – especially close to the critical point. The temperature of the Zeno and Charles curve intersection point (corresponding to $\max(\mathcal{Z})$) obtained from the considered LJ EOS agrees within $T_{\mathcal{Z} \cap \mathcal{C}} = 1.74 \pm 0.06 \, \varepsilon k_\mathrm{B}^{-1}$, excluding the LJ EOS of Ref. [62].

Sadus [581] recently reported values for the Boyle temperature and the maximum of the second virial coefficient computed from the LJ EOS *Koutras et al.* [343], which significantly deviate from the values obtained from our implementation for that LJ EOS. However, we compared $B(T)$ obtained from our implementation with results originally reported by *Koutras et al.* [343] and found excellent agreement.

4.4.5 Conclusions

This study revisits *Brown*'s characteristic curves and virial coefficients of the Lennard-Jones fluid. They were computed from a large number of LJ EOS and from rigorous statistical mechanics (where accessible). For most LJ EOS, these properties have not been examined yet – especially the theoretically-based ones.

The second virial coefficient is predicted qualitatively correctly by all but one LJ EOS. However, significant quantitative deviations are observed for most considered LJ EOS. For the third virial coefficient, only few LJ EOS produce qualitatively correct results.

Brown's characteristic curves [73] predicted from the different LJ EOS were compared with computer experiment data of *Deiters and Neumaier* [138] and with exact values in the ideal gas limit. The theoretically-based LJ EOS are found to give an overall better description of the characteristic curves – especially at low temperature and high pressure. Most LJ EOS produce distorted Amagat curves. Only the LJ EOS of *Lafitte et al.* [353] yields realistic results for all characteristic curves.

We showed that *Brown*'s assumption that the Amagat and Zeno curve should converge with an infinite slope in the zero pressure limit at low temperatures (in the double logarithmic pressure–temperature diagram) is probably inaccurate. The Zeno curve exhibits a limiting slope of unity. Hence, the required intersection point of the Amagat and Zeno curve is not found in the zero pressure limit.

Brown's characteristic curves are found to be sensitive properties, in a sense that they clearly reveal unphysical behavior of an equation of state, which holds in particular for the Amagat and Zeno curve. The Boyle and Charles curve are found to be predicted accurately by most LJ EOS and are therefore less sensitive indicators. Nevertheless, the application of the characteristic curves to investigate 'the extrapolation behavior of EOS' [621] should be carried out with caution. For example, the characteristic curves from the LJ EOS of *Mecke et al.* [438, 439] and *Lafitte et al.* [353] are in good agreement with corresponding computer experiment data in a wide temperature range, but both LJ EOS exhibit large deviations from pressure and internal energy reference data at extreme temperature and density (beyond the Amagat curve), cf. section 4.3.2.4. Vice versa, the LJ EOS of *Kolafa and Nezbeda* [334] and *Thol et al.* [661] exhibit distorted Amagat

curves, but both LJ EOS give an accurate and fairly precise description of pressure and internal energy reference data also at extreme conditions, cf. section 4.3.2.4. Hence, for these LJ EOS, the findings for the performance on the characteristic curves could not be transferred to conditions significantly above the pressure and temperature range of the characteristic curves. Instead, it is emphasized that the characteristic curves are a necessary requirement for an EOS to be accurate, but not a sufficient one.

Among the molecular model fluids, the Lennard-Jones fluid has a similar role as water has among real fluids: it is the fluid that has been studied most extensively and most thoroughly. This work summarizes the present state of these studies. The accuracy with which the properties of the Lennard-Jones fluid are known is assessed here. It can be assumed that it is a lower limit to the accuracy with which properties of fluids can presently be determined with molecular simulations and accordingly described by theoretically-based equations of state. Moreover, the Lennard-Jones potential is also a point of departure for developing models of complex fluids. Most SAFT-type equations of state are built on EOS for the LJ fluid for the modeling the soft repulsive and dispersive interactions of monomers [482]. Hence, the study also enables an assessment of their performance in the limit of a simple dispersively interacting monomer fluid. The monomer terms of several SAFT EOS were included in the present study, e.g. SAFT-VR Mie [353], soft SAFT [57, 58], LJ-SAFT [345, 479], and PC-SAFT [223].

5 Influence of Dispersive Long-Range Interactions on Phase Equilibria and Interfacial Properties of Simple Mixtures

5.1 Introduction

The influence of dispersive long-range interactions on properties of vapor-liquid equilibria and interfaces of six binary Lennard-Jones mixtures is studied by molecular dynamics (MD) simulations and density gradient theory (DGT). The mixtures were investigated at a constant temperature, at which the low-boiling component, which is the same in all mixtures, is subcritical. The molecular interaction parameters of the six mixtures are adopted from section 3.3: two different high-boiling components were considered: one is subcritical, the other is supercritical at the studied temperature. Furthermore, the unlike dispersive interaction was varied such that mixtures with three different types of phase behavior were obtained: ideal, low-boiling azeotrope, and high-boiling azeotrope. To assess the influence of the long-range interactions, the results for the Lennard-Jones truncated and shifted (LJTS) mixtures (cf. section 3.3) are compared here with results from the full Lennard-Jones (LJ) potential. Hence, the six binary mixtures A - F were additionally studied here using the full Lennard-Jones potential using both MD and DGT+EOS. The results from the LJTS mixtures and the LJ mixtures are compared applying the corresponding states principle.

In molecular simulations of classical force fields, in which interactions are computed from pair-potentials [17, 410, 633], this is done explicitly only up to a certain distance of the interacting sites. If no correction is applied, this causes a deviation of the simulation results from what would be obtained with the full potential. Different corrections schemes have been developed to account for the influence of the long-range interactions in simulations [17, 505, 537]. They are based on simplifying assumptions regarding the structure of the fluid. For simple cases, such as in studies of the equilibrium of homogeneous fluids, simple correction terms yield excellent results. In other cases, such as in studies of inhomogeneous fluids with different phases, accounting for the long-range interactions is more tedious [296, 383, 707], and it is not uncommon to simply truncate the potential in these cases and to neglect the long-range terms [391, 447, 483]. More generally, the ways in which long-range interactions are treated in molecular simulations vary largely and it is interesting to evaluate which influence they have on the simulation results.

This has been studied in great detail for the Lennard-Jones (LJ) 12-6 pair potential [31, 31, 59, 148, 148, 169, 170, 229, 230, 268, 296, 296, 298, 302, 383, 395, 413, 507, 536, 536, 537, 600, 600, 602, 603, 603, 611, 611, 672, 706, 706, 707]. In these studies, the full LJ potential (as approximated by using a large value of the cut-off radius r_c and suitable long-range corrections) is typically compared to either a truncated LJ potential (LJT potential; with some given r_c and without applying long-range corrections), or to the so-called LJ truncated and shifted potential (LJTS potential, which is a LJT potential that is shifted in such way that the potential energy becomes zero at r_c [148, 536, 603, 611]). In homogeneous systems, the intermolecular forces that are calculated from the LJT and the LJTS potential are the same, if the same r_c is used in both cases, whereas the energy and the pressure are affected by the shifting.

Different observables show different sensitivities to long-range interactions: the influence of the truncation has been studied for virial coefficients [600], the vapor-liquid equilibrium (VLE) [148, 395, 611], and vapor-liquid interfacial properties [31, 706]. The influence of the long-range interactions on phase equilibria and properties of inhomogeneous systems has been of particular interest [31, 59, 169, 170, 209, 220, 229, 230, 230, 286, 397, 413, 440, 507, 672, 676, 706].

To the best of our knowledge, all previous studies regarding the influence of the long-range interactions refer to pure fluids only, and no study has been performed yet on the influence of the long-range interactions for mixtures. We have therefore carried out an investigation of the influence of these interactions on binary vapor-liquid interfacial properties and the corresponding phase equilibria of binary fluid mixtures by comparing results of the LJ and LJTS potential.

Vapor-liquid interfaces of mixtures are important in many fields of science and engineering. They have recently received particular attention as in many systems an enrichment of components at this interface occurs, which is thought to have an influence on the mass transfer [50, 194, 328, 361, 634, 635]. Vapor-liquid interfacial properties of Lennard-Jones mixtures have been investigated many times in the literature by molecular simulations, density gradient theory (DGT) or density functional theory [79, 194, 195, 200, 362, 446, 551, 552, 635]. Reports on studies of the influence of the size and energy parameters of the pure components as well as the influence of the cross interactions on binary interfacial properties are available [551, 552, 635]. Also results on the composition- and temperature-dependency of the enrichment of components at these interfaces have been published [194, 195, 362, 635].

In this study, the influence of the dispersive long-range interactions on VLE properties (isothermal phase envelopes and Henry's law constants) and interfacial properties (surface tension, interfacial thickness, relative adsorption, and enrichment) of binary Lennard-Jones mixtures were investigated. Therefore, results from LJTS mixtures are compared with those from LJ mixtures. The results for the interfacial properties of the LJTS mixtures were taken from an earlier work of our group [635], cf. section 3.3. The computer experiments were accompanied by calculations with equations of state (EOS) and density gradient theory. The equation of state for the LJ fluid [639] developed in section 4.3 and the LJTS fluid [249] (PeTS EOS) were used for the DGT and for the computation of phase equilibria.

5.2 Modeling and Simulation

The Lennard-Jones (LJ) potential is defined as the pairwise-additive and spherically symmetric potential

$$u_{\mathrm{LJ}}(r) = 4\varepsilon \left[\left(\frac{\sigma}{r} \right)^{12} - \left(\frac{\sigma}{r} \right)^6 \right],$$

(103)

where r is the distance between two particles. The parameters σ and ε characterize the diameter of the particles and the strength of the attractive interaction, respectively. Simulations of the LJ potential were performed with a truncated potential in combination with a correction of long-range interactions [17, 640]. The interactions were explicitly computed to a cut-off radius of 5σ in the present work and long-range interactions beyond were considered with an implicit correction scheme, taking into account inhomogeneities in simulations of two-phase systems as described in more detail below. The corresponding results are referred to as 'results of the LJ potential' in the following.

For comparison, the Lennard-Jones truncated and shifted potential (LJTS) is used, cf. chapter 3. The truncation radius of the LJTS potential is 2.5σ throughout the present work:

$$u_{\mathrm{LJTS}}(r) = \begin{cases} u_{\mathrm{LJ}}(r) - u_{\mathrm{LJ}}(r_{\mathrm{c}}) & r \leq 2.5\sigma \\ 0 & r > 2.5\sigma. \end{cases}$$

(104)

The corresponding results are referred to as 'results of the LJTS potential'.

The interaction parameters ε and σ were chosen to be the same for the binary mixtures modeled by the LJ and the LJTS potential. The cross interactions of the mixtures were described by the modified Lorentz-Berthelot combination rules [52, 394]:

$$\sigma_{12} = \frac{\sigma_1 + \sigma_2}{2},$$

(105)

$$\varepsilon_{12} = \xi_{12}\sqrt{\varepsilon_1 \varepsilon_2},$$

(106)

where ξ_{12} is a state-independent binary interaction parameter.

Analogue to the study discussed in section 3.3, properties of the six binary mixtures (A - F) were investigated, cf. Fig. 69. For all binary mixtures, the high-boiling component is labeled as '1' and the low-boiling component as '2'. Each mixture was investigated using the LJ potential and the LJTS potential. The temperatures in this pair of simulations was chosen such that the reduced temperature with respect to the critical temperature of the high-boiling component $T_{\mathrm{red}} = T/T_{\mathrm{c},1}$ was the same for both LJ and LJTS potential. This results in $T = 0.92\,\varepsilon k_{\mathrm{B}}^{-1}$ for the LJ mixtures and $T = 0.77\,\varepsilon k_{\mathrm{B}}^{-1}$ for the LJTS mixtures, which corresponds in both cases to approximately $T/T_{\mathrm{c},1} = 0.7$. The critical temperature of the pure LJ and LJTS fluid has been reported numerous times in the literature, cf. sections 2.3 and 4.2 for reviews of such data. Note, that the reported values show significant scattering and thus are only known within a certain confidence interval. Table 18 summarizes critical and triple point data of the LJ and LJTS fluid that are used in this study with the estimated uncertainties.

The size parameter and the mass of both components are the same for all six mixtures A - F, i.e. $\sigma_1 = \sigma_2$ and $M_1 = M_2$, respectively. The vapor pressure of the low-boiling component 2 was decreased by decreasing the dispersion energy compared to component 1.

Table 18: Critical point properties (top) and triple point properties (bottom) of the LJ and LJTS fluid. The stated computer experiment (CE) values were estimated from a large collective of reported literature values [637, 640, 662]: the stated CE value is the mean average value and the corresponding uncertainty is estimated from their standard deviation. ρ_{tr}' and ρ_{tr}'' indicate the liquid and vapor density at the triple point.

	$T_c \ / \ \varepsilon k_B^{-1}$	$\rho_c \ / \ \sigma^{-3}$	$p_c \ / \ \varepsilon\sigma^{-3}$
LJ-CE	1.321 ± 0.007	0.316 ± 0.005	0.129 ± 0.005
LJ-EOS [639]	1.335	0.311	0.138
LJTS-CE	1.078 ± 0.017	0.319 ± 0.004	0.098 ± 0.007
LJTS-EOS [249]	1.089	0.309	0.102

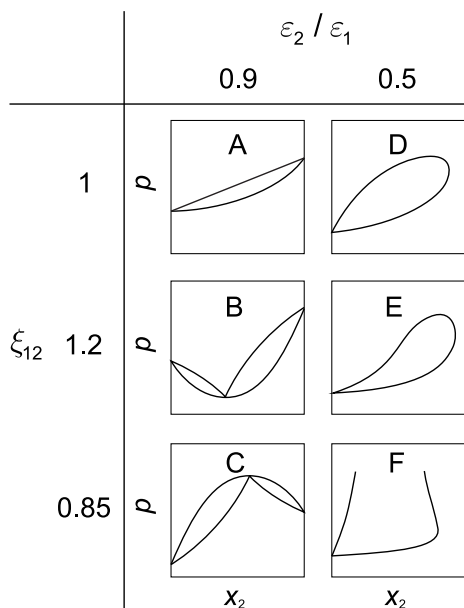|	$T_{tr} \ / \ \varepsilon k_B^{-1}$	$\rho_{tr}' \ / \ \sigma^{-3}$	$\rho_{tr}'' \ / \ \sigma^{-3}$	$p_{tr} \ / \ \varepsilon\sigma^{-3}$
LJ-CE	0.66 ± 0.024	0.845 ± 0.023	0.019 ± 0.0004	0.0015 ± 0.0008
LJTS-CE	0.597 ± 0.066	-	-	0.0027

Figure 69: Sketches of the isothermal phase diagrams of the studied binary mixtures
1 + 2. The different choices of the ratio of the dispersion energies $\varepsilon_2/\varepsilon_1$
and the binary interaction parameter ξ_{12} lead to six different types of phase
behavior (A - F).

Two different low-boiling components were considered: for the first, the ratio of dispersion energies was $\varepsilon_2/\varepsilon_1$ = 0.9; for the second it was $\varepsilon_2/\varepsilon_1$ = 0.5. Also the binary interaction parameter was varied. Three values were chosen ξ_{12} = 1, 1.2, and 0.85. These variations result in six mixtures (A - F) that were investigated. Their phase behavior is shown qualitatively in Fig. 69. Depending on the choice of $\varepsilon_2/\varepsilon_1$, component 2 is either subcritical (mixtures A - C) or supercritical (mixtures D - F). For ξ_{12} = 1 the mixture is almost ideal in the sense of Raoult's law, the value of ξ_{12} = 1.2 causes a negative deviation from Raoult's law and ξ_{12} = 0.85 causes positive deviation from Raoult's law. This leads to a high-boiling azeotrope for mixture B and a low-boiling azeotrope for the mixture C.

5.2.1 Molecular Dynamics Simulations

Direct Vapor-Liquid Equilibrium Simulations

The simulations for the coexisting vapor and liquid phase were carried out in the NVT ensemble with 16,000 particles using the MD code *ls1 mardyn* [506]. A liquid film was positioned in a rectangular box such that two planar vapor-liquid interfaces were oriented perpendicular to the z-axis. The time step was $\Delta\tau$ = 0.001 $\sigma\sqrt{M/\varepsilon}$. The equilibration was executed for 2,000,000 time steps. For the initialization, the saturated densities and the bulk phase compositions of the mixtures were estimated with the EOS. The production was carried out for 6,000,000 time steps. Density and pressure profiles were calculated in block averages of 500,000 time steps during the production phase. The statistical uncertainty was estimated to be three times the standard deviation of all block averages. The elongation of the simulation box normal to the interface was

$80\,\sigma$ and the thickness of the liquid film in the center of the simulation box was $40\,\sigma$. The elongation in the directions parallel to the interface was at least $20\,\sigma$. The pressure and density profiles were calculated in z-direction at 1200 bins. A slab-based long-range correction scheme based on the approach of *Janeček* [296, 707] was used for the LJ potential simulations.

The saturated densities ρ' and ρ'', the vapor pressure p, and the saturated vapor and liquid phase composition x_i' and x_i'' were calculated as an average over the respective phases excluding the area close to the interface. Also the density profiles along the z-axis were obtained as averages over all sampled block averages.

The interfacial tension was calculated via the mechanical route, i.e. from the deviation between the normal and the tangential diagonal components of the overall pressure tensor [325, 695]

$$\gamma = \frac{1}{2} \int_{-\infty}^{\infty} (p_{\mathrm{N}} - p_{\mathrm{T}}) \, \mathrm{d}z \,. \tag{107}$$

The applied simulation procedure is described in detail in Ref. [635].

Henry's Law Constant Simulations

Henry's law constants $H_{2,1}$ of the low-boiling component 2 in component 1 were sampled in the NpT ensemble with 1372 solvent particles using the MD code *ms*2 [575]. The Henry's law constants were obtained from the residual chemical potential of the solute at infinite dilution from the relation [607]

$$H_{2,1} = \rho' k_{\mathrm{B}} T \, \exp(\mu_2^{\infty}/k_{\mathrm{B}}T) \,, \tag{108}$$

where ρ' is the saturated liquid density of the solvent and T is the temperature. The residual chemical potential at infinite dilution μ_2^{∞} was computed using *Widom*'s test particle method [712]. The equilibration was carried out for 300,000 time steps and the production for 1,000,000 time steps. The time step was $\Delta\tau = 0.001\,\sigma\sqrt{M/\varepsilon}$. The statistical uncertainty of the Henry's law constant was estimated to be three times the standard deviation of ten block averages, each sampling 100,000 time steps.

5.2.2 Density Gradient Theory and Equation of State

Density Gradient Theory

Density gradient theory is applied here to binary systems with a planar interface, such that there is only a dependence on one spatial coordinate, which is labeled z here, cf. Eq. (39). As in chapter 3, the cross interaction influence parameter was computed as the geometric mean of the pure substance influence parameters [91, 458, 635], i.e. $\kappa_{ij} = \sqrt{\kappa_i \kappa_j}$. The stabilized DGT (sDGT) algorithm proposed by *Mu et al.* [477] was applied for solving Eq. (39) between the bulk phases and the computation of the surface tension. The domain length was in all cases set to $20\,\sigma$ with a spatial discretization of $0.02\,\sigma$.

EOS for the LJ and LJTS Fluid

The LJTS and LJ EOS discussed in section 2.2 and section 4.3, respectively, [249, 639] were employed for computing phase equilibria and interfacial properties with DGT. For the LJTS fluid, the PeTS EOS [249] was used; for the LJ fluid, the LJ EOS from this work was used (see Appendix). The DGT influence parameters κ_i for the LJ EOS and the LJTS EOS were parametrized to surface tension data from molecular simulation [249, 639].

The VLE computed from the LJ and LJTS EOS are compared in Fig. 70 with corresponding computer experiment data from the literature. Both EOS describe the VLE of the pure components very well. Details on the performance of both EOS can be found in sections 2.2 and 4.3 [249, 639]. Also, the critical points from both EOS are in good agreement with those obtained from molecular simulations, cf. Table 18.

The long-range interactions applied for the LJ fluid significantly increase the critical temperature and pressure compared to the LJTS fluid but hardly affect the critical density [148, 536, 603, 611]. Furthermore, the critical parameters are influenced more strongly by the long-range interactions than the triple point parameters. The vapor pressure and the enthalpy of vaporization are influenced more strongly by the long-range interactions than the saturated densities.

5.2.3 Interfacial Properties Derived from Density Profiles

The direct VLE MD simulations as well as the DGT calculations yield density profiles of both components $\rho_1(z)$ and $\rho_2(z)$ at the planar interface. The relative adsorption $\Gamma_2^{(1)}$ and enrichment E_2 of the low-boiling component 2 and the interfacial thickness L_{10}^{90} are used to characterize the vapor-liquid interfaces. This follows the evaluation of the fluid interfaces of LJTS mixtures in chapter 4. Hence, the definitions for the computation of $\Gamma_2^{(1)}$, E_2, and L_{10}^{90} from the density profiles used in this study are given in section 3.3.2.2; Eq. (44) - (46). Also the computation of the statistical uncertainties of the interfacial properties performed here is described in section 3.3.2.2.

5.3 Results for the Interfacial Properties of Pure Substances

First, the interfacial properties obtained for the pure fluids described by the LJ potential and LJTS potential are compared. Subsequently, the results for the phase equilibria and interfacial properties of the mixtures obtained from both potentials are compared. The numerical values of the results for the phase equilibria and the interfacial properties obtained in this study are presented in the Appendix.

Results from the present work for the surface tension and the interfacial thickness of the pure LJ fluid and the pure LJTS fluid are compared in Fig. 71. Besides the results from molecular simulation, also results from EOS+DGT are shown, that were obtained after an adjustment of a state-independent number for κ to simulation data of the surface tension resulting in $\kappa_{\mathrm{LJ}} = 5.10911$ and $\kappa_{\mathrm{LJTS}} = 2.7334$ [249].
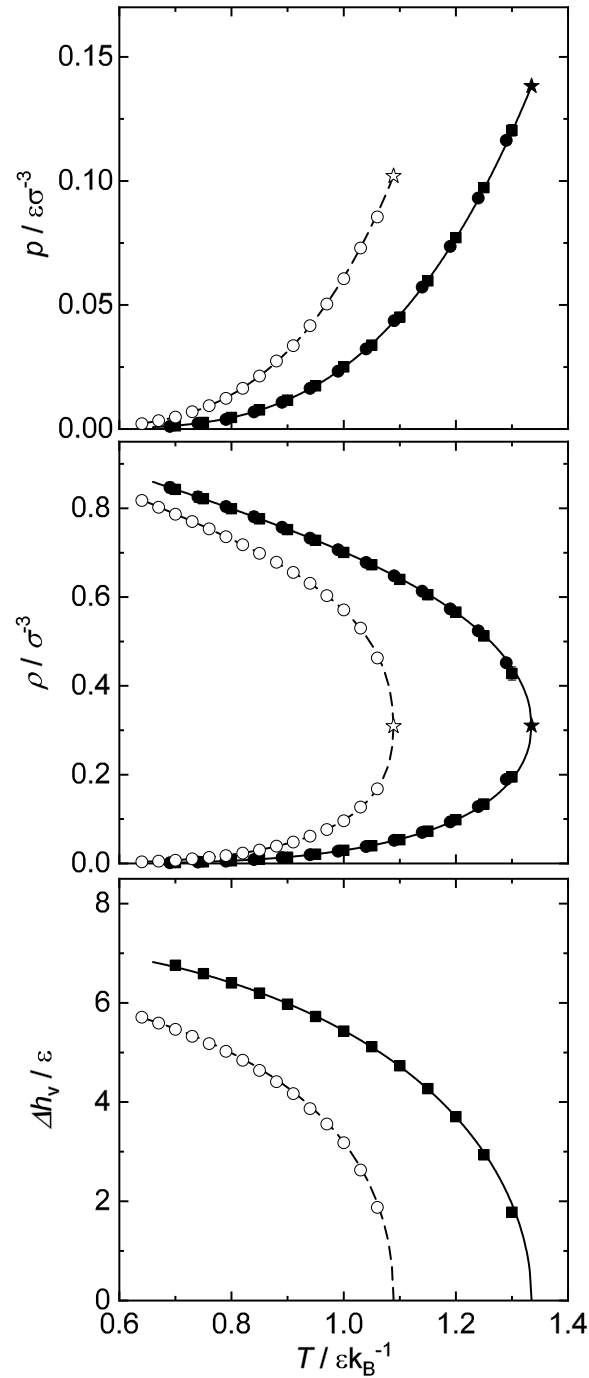
Figure 70: Vapor-liquid equilibrium of the LJ and LJTS fluid: vapor pressure (top), saturated densities (middle), and enthalpy of vaporization (bottom). Black lines and black symbols indicate the LJ fluid; dashed lines and open symbols indicate the LJTS fluid. Lines indicate the corresponding EOS (cf. sections 2.2 and 4.3) [249, 639]; stars indicate the critical point computed from the EOS. All other symbols are MD: • this work; ■ *Lotfi et al.* [395]; ○ *Vrabec et al.* [687].
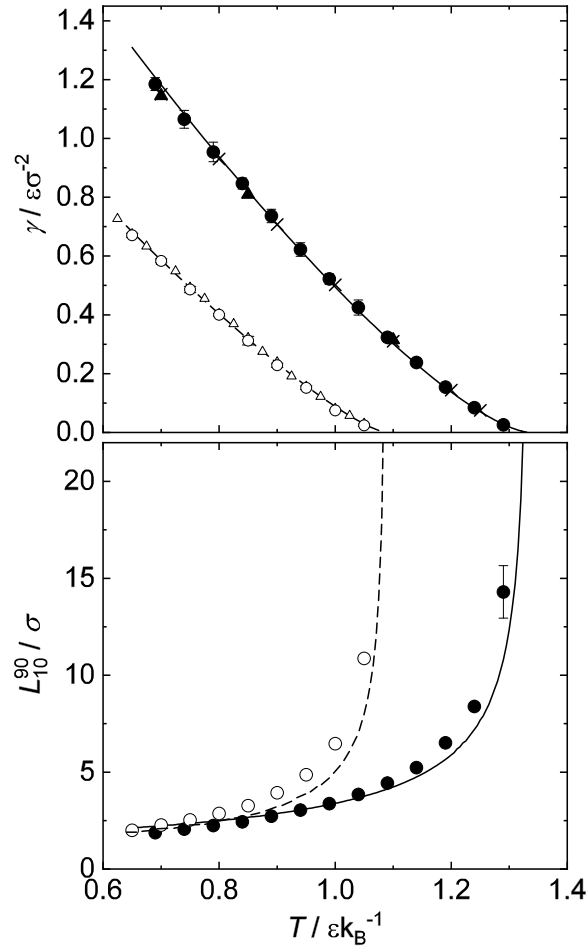
Figure 71: Vapor-liquid interfacial properties of the LJ and LJTS fluid: surface tension (top), interfacial thickness (bottom). Lines are EOS+DGT results: solid lines indicate the LJ fluid; dashed lines indicate the LJTS fluid. Symbols are MD results. LJ fluid: ● this work; ▲ *Mecke et al.* [440]; ×*Werth et al.* [706]. LJTS fluid: ○ this work; △ *Vrabec et al.* [687].

The surface tension of both components decreases monotonically from the triple point temperature to the critical temperature. Starting at the triple point temperature, the interfacial thickness increases only slightly with increasing temperature but exhibits a strong convex trend and a pole at the critical temperature.

For both the LJ potential and the LJTS potential, computer experiment data for the surface tension from the literature are shown for comparison. In a recent study (cf. section 4.2) [640], surface tension data of the LJ fluid was reviewed and assessed. The results of *Mecke et al.* [440] and *Werth et al.* [706] were found to be precise and accurate and are used as reference here. The LJ surface tension results from the present work are in excellent agreement with those of Refs. [440, 706]. The LJTS surface tension results from the present work are in good agreement with those reported by *Vrabec et al.* [687], who found their data to be in excellent agreement with other reliable literature data.

At the same reduced temperature, the LJ fluid has a larger surface tension and interfacial thickness than the LJTS fluid. The long-range interactions have no significant influence on the shape of $\gamma(T)$ and $L_{10}^{90}(T)$, except the shifted critical point. This is in line with the results reported by *Dunikov et al.* [148] and *Baidakov et al.* [31]. The long-range

interactions have a stronger influence on the surface tension than on the interfacial thickness – especially at lower temperatures. At the same reduced temperature, the surface tension of the LJ fluid is up to about 40% higher than that of the LJTS fluid, indicating a strong influence of the long-range interactions on this property. Evidently, these differences vanish at the critical point $T/T_{c,1} = 1$. Also the interfacial thickness of the LJ fluid is larger than that of the LJTS fluid, but only by about 15%. Also this increase is expected as a consequence of the long-range interactions [148].

For both the LJ potential and the LJTS potential, the EOS+DGT results are in good agreement with the results from the corresponding computer experiments. The agreement is better for the surface tension than it is for the interfacial thickness, as γ was used for the fitting of the DGT influence parameter [249, 637], while the EOS+DGT results for the interfacial thickness are predictions. For L_{10}^{90}, the agreement of computer experiment and EOS+DGT is slightly better for the LJ fluid compared to the LJTS fluid. The deviations between the MD results and those from EOS+DGT are likely due to fluctuations at the interface which are present in MD but not in DGT.

5.4 Results for the Phase Equilibria of Binary Mixtures

Fig. 72 shows the results for the Henry's law constants $H_{2,1}$ of the supercritical component 2 in the solvent 1 for the mixtures D - F. Results for the LJ potential and LJTS potential are compared. Both MD simulation results and results from the corresponding EOS are shown. Results for the entire temperature range between the triple point and the critical point of the solvent 1 are shown. The results for the three systems differ strongly. This is a consequence of the differences in the binary interaction parameter ξ_{12}, that controls the strength of the unlike attractive interactions 1 - 2, which are highly important for the gas solubility: the stronger the attraction 1 - 2 (the higher ξ_{12}), the better the solubility (the lower $H_{2,1}$). The variation of ξ_{12} between 0.85 (mixture F) and 1.2 (mixture E) leads to differences in $H_{2,1}$ of almost an order of magnitude. Not only the numbers of $H_{2,1}$ are strongly affected by ξ_{12}, but also the temperature dependence $H_{2,1}(T)$, which is related to the enthalpy of absorption of the solute 2 in the solvent 1. Strong unlike attractive interactions lead to exothermal absorption and a positive slope of $H_{2,1}(T)$ (mixture E), weak unlike attractive interactions lead to endothermal absorption and a negative slope of $H_{2,1}(T)$ (mixture F). In the ideal mixture, a maximum of $H_{2,1}(T)$ is found. All these observations hold both for the results from the LJ potential and those from the LJTS potential.

Fig. 72 gives also insights on the influence of the long-range interactions on the Henry's law constants $H_{2,1}$. This influence depends strongly on ξ_{12}. For strong unlike attractive interactions ($\xi_{12} = 1.2$, mixture E) neglecting the long-range part leads to a decrease of the solubility (increase of $H_{2,1}$), as might be expected. The inverse trend is observed for mixture F. This is astonishing, but can be understood by the fact that not only the solute–solvent interactions 1 - 2 are subject to the truncation but also the solvent–solvent interactions 1 - 1. Neglecting the long-range interactions 1 - 1 facilitates the insertion of 2 and increases the solubility (decreases $H_{2,1}$). Both effects compete in the ideal mixture D.
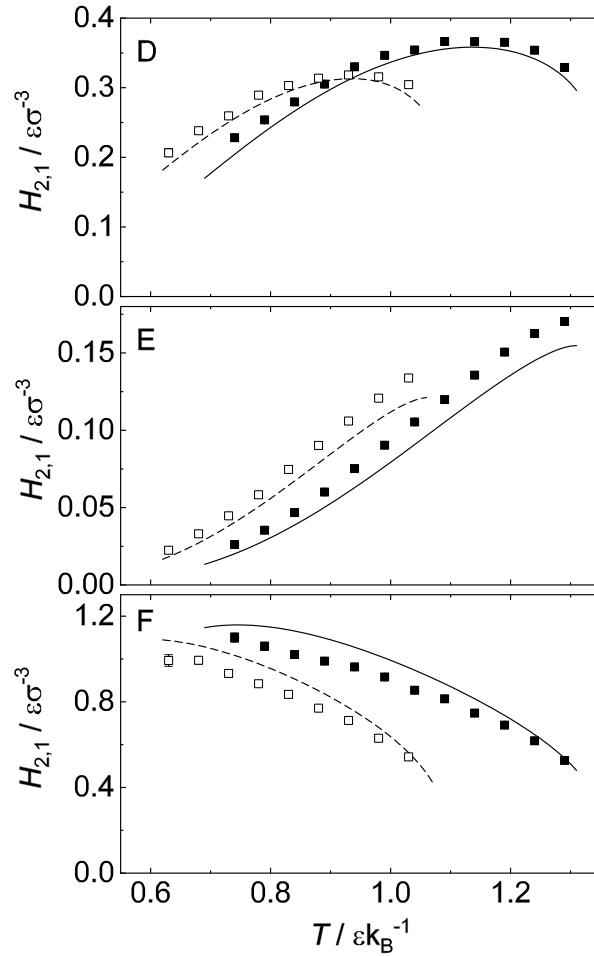
Figure 72: Henry's law constants of the binary mixtures D, E, and F between the triple and critical temperature. Symbols are MD results; lines are EOS results. Black lines and black symbols indicate the LJ potential; dashed lines and open symbols indicate the LJTS potential.

The results from the EOS and those from the computer experiments agree overall well. The best agreement is observed for mixture D, while for the mixtures E and F deviations up to 10% are found. The EOS underestimate the results from the computer experiment for mixture E but overestimate them for mixture F. These findings hold for both the results of the LJ fluid and the LJTS fluid, which may be related to the fact that both EOS have the same functional form [249, 639].

Fig. 73, panels A - F, show the binary phase diagrams obtained from the LJ potential and LJTS potential at the same reduced temperature and pressure. The influence of the interaction parameters $\varepsilon_2/\varepsilon_1$ and ξ_{12} on the phase behavior of Lennard-Jones mixtures has already been discussed in section 3.3.

Fig. 73 reveals that the long-range interactions have practically no influence on the type of phase behavior of mixtures. As the weakening of the attractive interactions by cutting off the long-range interactions affects all interactions that occur in the mixture (those between the same partners as well as those between unlike partners), the qualitative phase behavior is not influenced, e.g. the position of the azeotropic points in the systems B and C is almost the same for the LJ potential and LJTS potential. As for the Henry's

Figure 73: Vapor-liquid equilibria of the binary mixtures A, B, C, D, E, and F at $T/T_{c,1}$ = 0.7, where $T_{c,1}$ is the critical temperature of the high-boiling component 1. The pressure axis is reduced by the critical pressure of the respective high-boiling component ($p_{c,1}$ = 0.129 $\varepsilon\sigma^{-3}$ in the case of the LJ potential and $p_{c,1}$ = 0.098 $\varepsilon\sigma^{-3}$ in the case of the LJTS potential). Symbols are MD results; lines are EOS results. Black lines and black symbols indicate the LJ potential; dashed lines and open symbols indicate the LJTS potential.

law constants, the results from the EOS and the computer experiments are in good agreement. This holds for both the LJ and the LJTS potential.

For the mixture A and B, the results obtained for the LJ potential and LJTS potential agree almost perfectly when reduced variables are used, as in Fig. 73. For the mixtures C - F, the MD results obtained for the LJ potential and LJTS potential show small deviations – mainly for the bubble line. The EOS results for the mixtures D - F for the LJ potential and LJTS potential show distinct deviations close to the critical point, which is mainly due to the fact that all results were reduced with the computer experiment critical pressure and temperature of the respective potential.

Fig. 74, panels A - F, show the binary saturated density phase diagrams obtained from the LJ potential and LJTS potential at $T/T_{c,1} = 0.7$. The saturated liquid density ρ' and the saturated vapor density ρ'' are shown as a function of the pressure. The results obtained from the LJ and the LJTS potential show only little differences, as expected from the pure substance properties, cf. Fig. 70. Hence, the long-range interactions have no significant influence on the saturated densities of the mixtures. The results obtained from both the LJ and LJTS EOS agree very well with the corresponding computer experiments.

For the mixture A (ideal mixture), the saturated densities show a monotonous and almost linear transition between the two pure component density values. For the mixture B and C on the other hand, the saturated densities show a more complex behavior. For the mixture B (high-boiling azeotrope), starting at the pure component 1, the difference of the two densities $\Delta\rho = \rho' - \rho''$ first increases with increasing pressure until the azeotropic point and then decreases with further increasing pressure until the pure component 2 value is reached; vice versa for the mixture C. Hence, the difference of the two densities $\Delta\rho = \rho' - \rho''$ exhibits a minimum as a function of the pressure in the mixture C and a maximum in the mixture B.
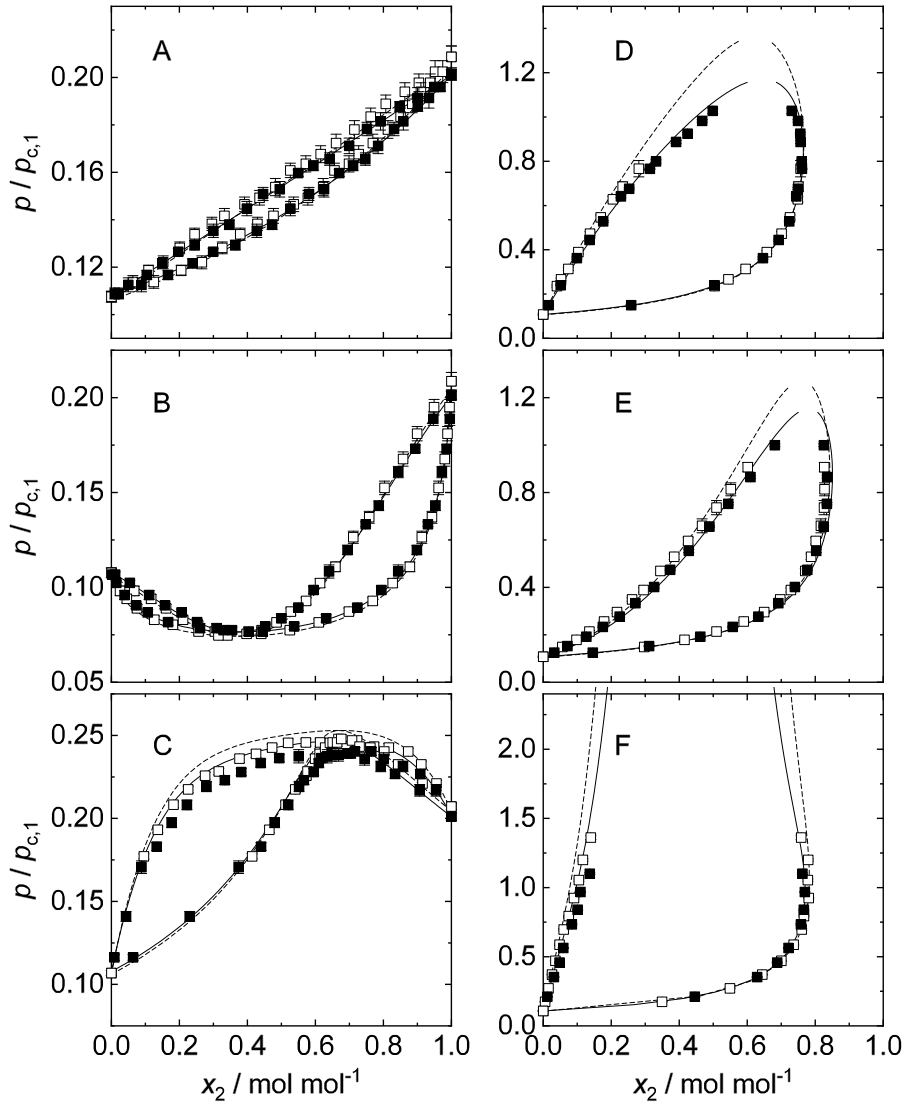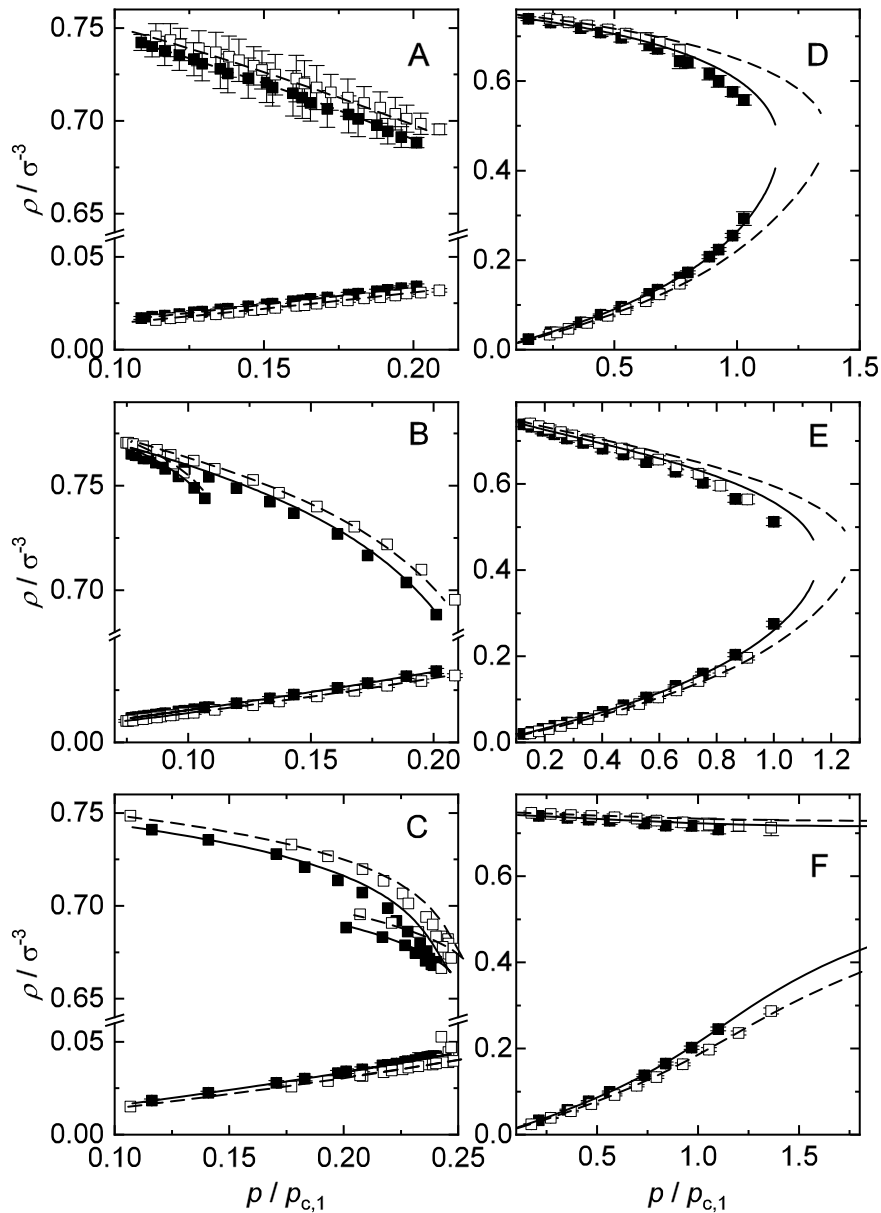
Figure 74: Saturated densities as a function of the pressure of the binary mixtures A,
B, C, D, E, and F at $T/T_{c,1} = 0.7$, where $T_{c,1}$ is the critical temperature
of the high-boiling component 1. Symbols are MD results; lines are EOS
results. Black lines and black symbols indicate the LJ potential; dashed
lines and open symbols indicate the LJTS potential. For the mixtures B
and C, the MD error bars for the liquid density were omitted to avoid visual
clutter.

5.5 Results for the Interfacial Properties of Binary Mixtures

The influence of the mixture type A - F on vapor-liquid interfacial properties has been studied before, cf. section 3.3 [635]. The following discussion therefore focuses exclusively on the influence of the long-range interactions on the interfacial properties of the binary mixtures.

Fig. 75, panels A - F, show the results for the surface tension obtained from the LJ potential and LJTS potential. The EOS+DGT and the simulation results agree almost always within the MD error bars. Slight deviations are found for the mixtures B, E, and F. Overall, the EOS+DGT results describe the results of the computer experiment for the surface tension similarly well for both the LJ potential and LJTS potential.

Figure 75: Surface tension γ of the binary mixtures A, B, C, D, E, and F at $T/T_{c,1} = 0.7$ as a function of the liquid phase composition x_2'. Symbols are MD results; lines are EOS+DGT results. Black lines and black symbols indicate the LJ potential; dashed lines and open symbols indicate the LJTS potential.

As for the pure substance surface tension, the long-range interactions have an important influence on the surface tension of binary mixtures. The long-range interactions present in the LJ simulations increase the surface tension for all six investigated mixtures compared to the LJTS results. The surface tension obtained from the LJ potential exceeds that from the LJTS potential by 40 - 50%. Nevertheless, the shape of $\gamma(x_2')$ is hardly affected by the long-range interactions. Also the aneotropic composition (minimum and maximum of $\gamma(x_2')$) [133, 434, 435] is only slightly affected by the long-range interactions.

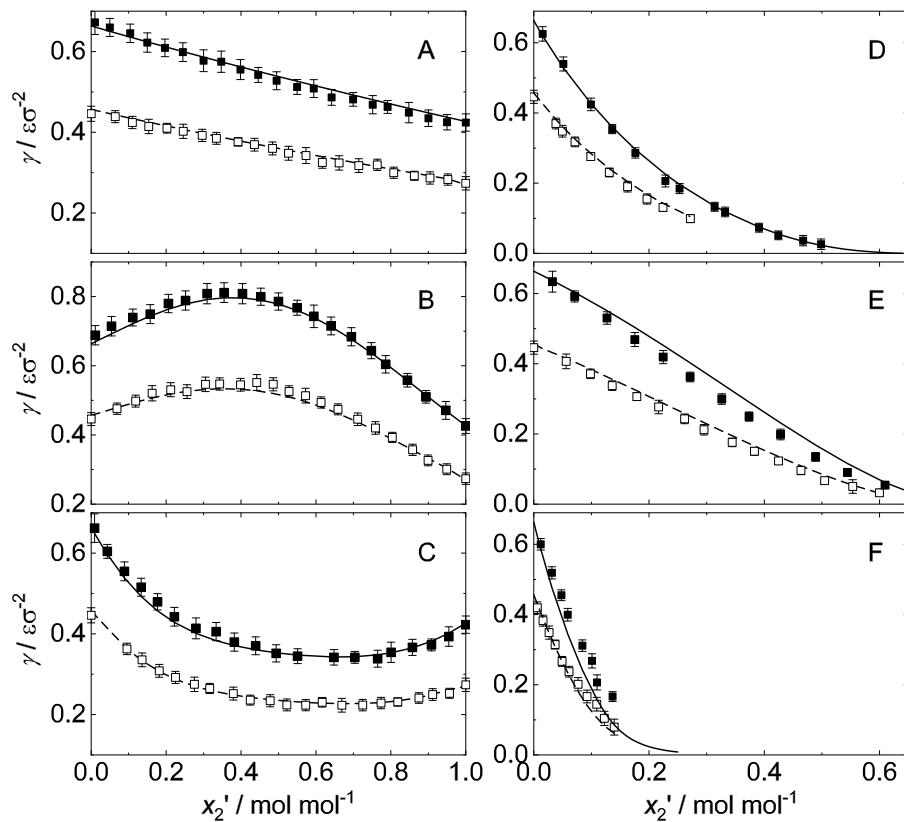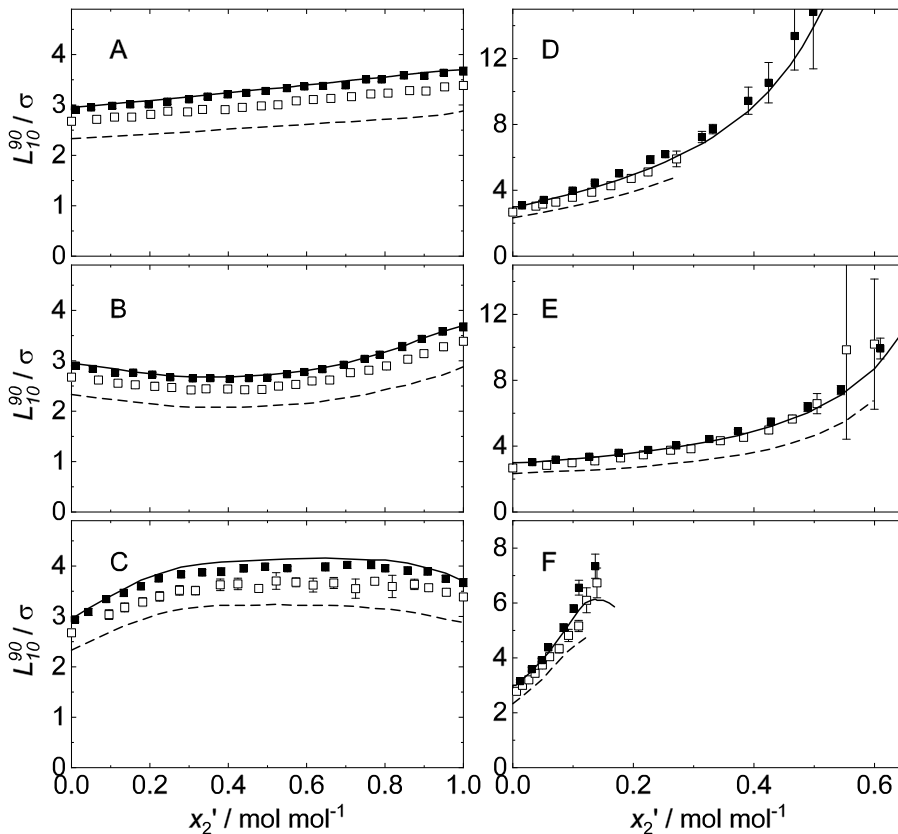**Figure 76:** Interfacial thickness L_{10}^{90} of the binary mixtures A, B, C, D, E, and F at $T/T_{c,1} = 0.7$ as a function of the liquid phase composition x_2'. Symbols are MD results; lines are EOS+DGT results. Black lines and black symbols indicate LJ potential; dashed lines and open symbols indicate LJTS potential.

Fig. 76, panels A - F, show the results for the interfacial thickness obtained from the LJ potential and LJTS potential. As for the pure substances (cf. Fig. 71), the interfacial thickness of the LJ mixtures exceed those of the LJTS mixtures. The average difference of the LJ and LJTS computer experiment results for the interfacial thickness is approximately 10%. As for the surface tension, these differences between the LJ and the LJTS fluid are practically composition-independent. The shape of $L_{10}^{90}(x_2')$ for the LJ potential and LJTS potential are similar.

The $L_{10}^{90}(x_2')$ results from MD and EOS+DGT agree very well for the case of the LJ potential. In contrast, for the results of the LJTS potential, the MD simulations are generally underestimated by the EOS+DGT. This indicates a weakness of the EOS that was used for describing the LJTS fluid. A major difference of that EOS as compared to the one used for describing the LJ fluid is that in the parametrization of the latter, also homogeneous bulk properties were used, cf. section 4.3 [635]. On the other hand, the employed LJTS EOS was exclusively parametrized to VLE data [249].

Fig. 77, panels A - F, show the results for the relative adsorption $\Gamma_2^{(1)}$ of the low-boiling component at the vapor-liquid interface (cf. Eq. (44)). The long-range interactions only have a minor influence on the relative adsorption of the investigated Lennard-Jones mixtures. This is due to the fact that the relative adsorption $\Gamma_2^{(1)}$ is closely linked
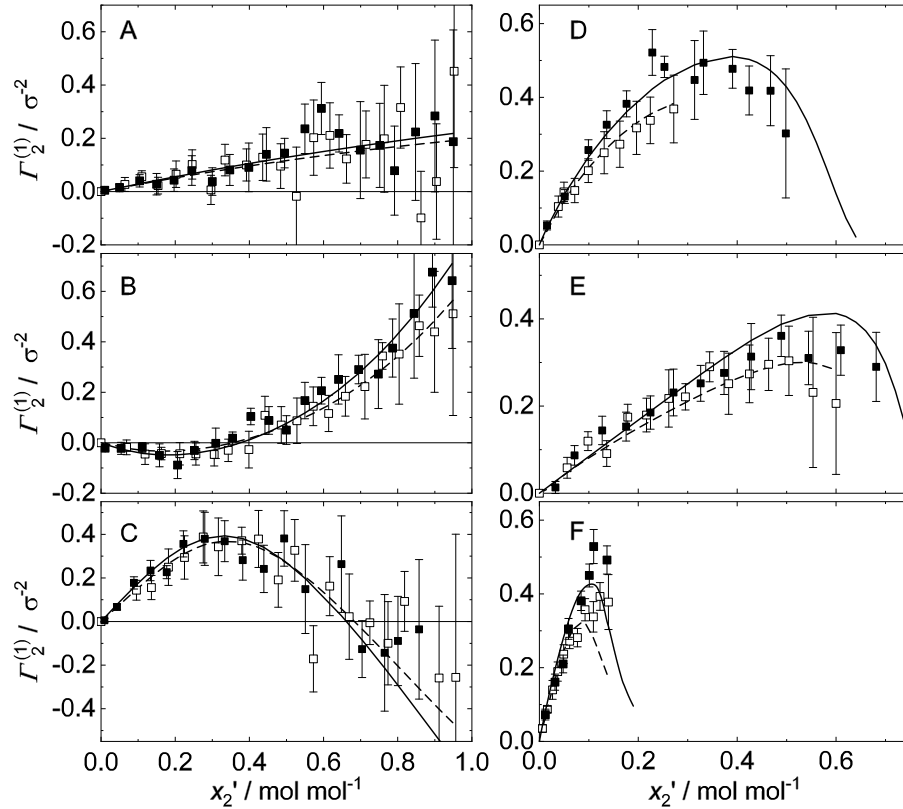
Figure 77: Relative adsorption $\Gamma_2^{(1)}$ of the low-boiling component of the binary mixtures A, B, C, D, E, and F at $T/T_{c,1} = 0.7$ as a function of the liquid phase composition x_2'. Symbols are MD results; lines are EOS+DGT results. Black lines and black symbols indicate the LJ potential; dashed lines and open symbols indicate the LJTS potential.

to the slope of the surface tension $\gamma(x_2')$ via the Gibbs adsorption equation and the composition dependency of $\gamma(x_2')$ is hardy affected by the long-range interactions, cf. Fig. 75. The MD results for $\Gamma_2^{(1)}$ of the mixtures A - F obtained from the LJ potential and LJTS potential agree within their statistical uncertainties. Nevertheless, $\Gamma_2^{(1)}$ from the LJ potential is in most cases slightly higher than the corresponding LJTS results. The EOS+DGT results support this tendency.

For the mixtures A and D - F, the relative adsorption is always positive $\Gamma_2^{(1)} > 0$, i.e. the low-boiling component adsorbs at the interface in the entire investigate composition range. For the mixtures B and C, the relative adsorption exhibits a range of positive and a range of negative adsorption connected by a zero crossing $\Gamma_2^{(1)} = 0$, which is a result of the aneotropic behavior. For all mixtures and compositions where $\Gamma_2^{(1)} > 0$, the relative adsorption obtained by the LJ potential slightly exceeds that obtained by the LJTS potential: $\Gamma_{2,\mathrm{LJ}}^{(1)} > \Gamma_{2,\mathrm{LJTS}}^{(1)}$. For the composition range of the mixture B and C where $\Gamma_2^{(1)} < 0$, results obtained for the LJ potential yield a stronger desorption of the low-boiling component at the interface than the corresponding results for the LJTS potential.

The long-range interactions have no significant influence on the slope of $\Gamma_2^{(1)}(x_2')$. As for the surface tension results (cf. Fig. 75), the EOS+DGT results of $\Gamma_2^{(1)}(x_2')$ agree
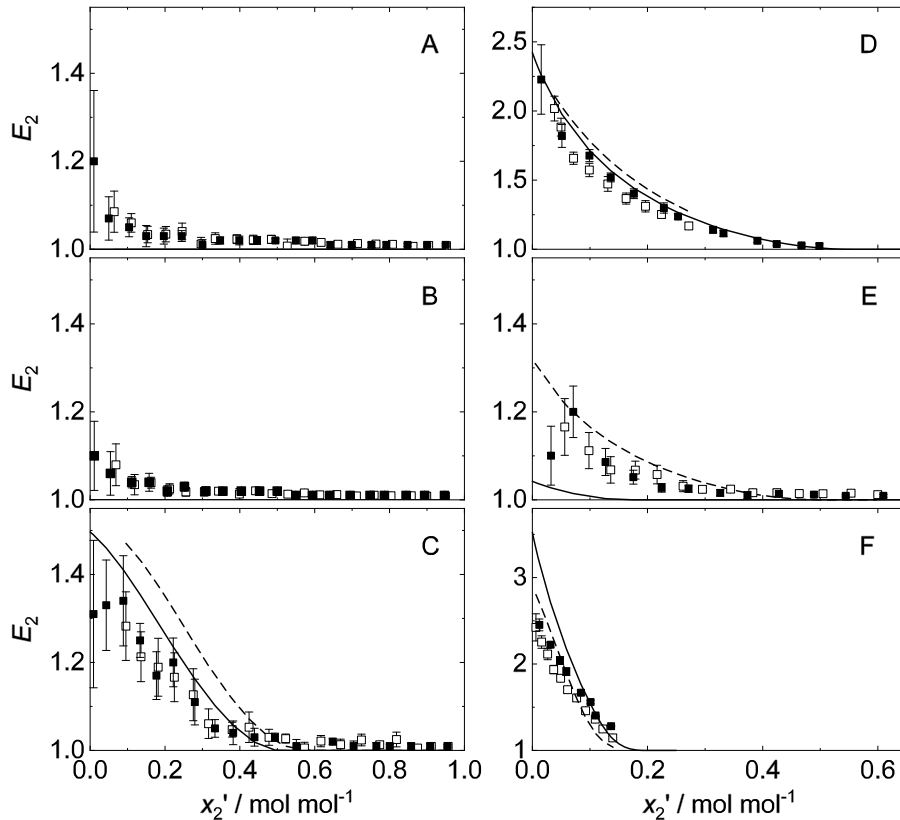
Figure 78: Enrichment of the low-boiling component E_2 at the interface of the binary mixtures A, B, C, D, E, and F at $T/T_{c,1} = 0.7$ as a function of the liquid phase composition x_2'. Symbols are MD results; lines are EOS+DGT results. Black lines and black symbols indicate the LJ potential; dashed lines and open symbols indicate the LJTS potential. In mixture A and B the enrichment obtained from EOS+DGT is $E_2 = 1.0$.

well with the corresponding MD results.

Fig. 78, panels A - F, show the results for the enrichment E_2 of the low-boiling component at the vapor-liquid interface (cf. Eq. (45)) in the six studied mixtures. Large enrichment is only found in the mixtures D and F. The influence of the long-range interactions on the enrichment of the low-boiling component at the interface is marginal. The results from the computer experiments for E_2 obtained from the LJ potential and LJTS potential agree within their statistical uncertainties for most mixtures. Nonetheless, there is a trend that the results obtained from the LJ potential are slightly higher than those obtained from the LJTS potential. This is not unexpected as the enrichment is important at low x_2' where the interactions 1 - 2 are dominant, which are weaker when the potential is truncated.

While the results from EOS+DGT agree very well with the computer experiment for the other interfacial properties discussed above, this does not hold for the enrichment E_2. The results agree only qualitatively. As already discussed in Refs. [50, 634, 635], partially significant differences between results from EOS+DGT and computer experiments are observed (cf. chapter 9 for a detailed discussion). For the EOS+DGT, the LJ and LJTS results show the same trends but partially significant deviations from the MD data are observed. Furthermore, there are also significant differences between the

EOS+DGT results obtained for the LJ potential and the LJTS potential in some mixtures, whereas such differences are not found in the MD results. As discussed above, the differences in the qualities of the EOS might also play a role here. The agreement for the enrichment obtained by the EOS+DGT and computer experiments is slightly better for the LJ potential than the LJTS potential (cf. Fig. 78 - panels C and D). The enrichment is the most sensitive of the investigated properties – regarding the agreement of the theory and computer experiments.

5.6 Conclusions

In this study, the influence of dispersive long-range interactions on thermophysical properties of mixtures was systematically investigated for the first time. For that purpose, six binary Lennard-Jones mixtures were studied with the LJ potential and the LJTS potential. The comparison was carried out at the same reduced temperature of the high-boiling component 1. Different low-boiling components 2 (subcritical and supercritical) were used. Also the strength of the unlike interactions was varied, such that six different types of phase behaviors were obtained.

The truncation and shifting of the potential in the LJTS fluid weakens the attractive interactions compared to the LJ fluid. This affects pure component properties in ways that are well-known from previous studies, e.g. the vapor pressure of the LJ fluid is lower than that of the LJTS fluid at the same temperature [31, 148, 600, 603, 611]. In binary mixtures, the reduced attractive interactions in the LJTS potential compared to the full LJ potential affect all interactions in the same way, the like ones as well as the unlike ones. Hence, it is expected that the qualitative behavior of the LJ mixtures and the corresponding LJTS mixtures should be similar. This is confirmed in the present study for different mixture types and all bulk and interfacial properties that were investigated: the concentration-dependence that is observed for the different properties is always similar for the LJ and the LJTS mixtures. The sign of the offset between the results depends on the studied property and can generally be explained by the weaker attractive interactions in the LJTS fluid. As for the pure fluids, the surface tension in mixtures that is obtained from the LJ potential is always higher than the corresponding number obtained from the LJTS potential, whereas the interfacial thickness is only slightly increased. In contrast to the surface tension γ, the relative adsorption $\Gamma_2^{(1)}$, which is related to the slope of $\gamma(x_2')$, is almost the same for the LJ fluid and the LJTS fluid. Furthermore, no significant influence of the long-range interactions on the enrichment at interfaces was observed.

Henry's law constants obtained for LJ and LJTS mixtures differ in general. The differences may have different signs, depending on the strength of the unlike interactions, that was varied here using the parameter ξ_{12}.

All comparisons in this study were carried out not only with MD simulations but also using EOS for the LJ and the LJTS fluid – for the interfacial properties in connection with DGT. The EOS and EOS+DGT calculations confirm the findings from the MD simulations.

6 Mass Transfer Through Vapor-Liquid Interfaces: A New Molecular Simulation Method

6.1 Introduction

The present chapter presents a new quasi-stationary molecular simulation method for studying mass transfer through vapor-liquid interfaces of mixtures driven by gradients of the chemical potential. The new simulation method is applied to two binary LJTS mixtures that were examined regarding their equilibrium properties in chapter 3. In the first mixture, a strong enrichment of the low-boiling component at the vapor-liquid interface is observed, whereas practically no enrichment is present in the second mixture. This comparison enables an evaluation of the influence of the enrichment on the mass transfer through vapor-liquid interfaces.

To the best of our knowledge, no molecular simulation method has been described in the literature for studying a stationary mass transfer of components through vapor-liquid interfaces driven by gradients of the chemical potential. However, some related simulation methods have been described previously in the literature. The heat and mass transfer through vapor-liquid interfaces during evaporation and condensation has been studied extensively in the literature using molecular simulation [54, 103, 110, 202, 203, 232, 233, 250, 251, 289, 327, 337, 348, 396, 419, 568, 569, 609, 673] or mesoscopic models such as density functional theory [54, 202, 213, 233, 289, 300, 301, 329]. Most of these studies consider a temperature gradient as the driving force of the heat and mass transfer. Furthermore, in most of these studies only pure components are considered.

Diffusion near vapor-liquid interfaces is known to be anisotropic. The available studies on this subject deal mostly with self-diffusion [111–113, 150]. Interestingly, the diffusion parallel to the interface has been investigated more often than the diffusion perpendicular [71, 150, 385] to the interface, which is relevant for the mass transfer in fluid separation techniques.

Nagl et al. [488] recently reported on a combined theoretical–experimental investigation of the mass transfer through liquid-liquid interfaces. Also *Braga et al.* [70] investigated diffusion at liquid-liquid interfaces. The free energy barrier of particles crossing a vapor-liquid interface has been studied by *Braga et al.* [71] and *Garrett et al.* [197]. The build up of the interfacial excess at vapor-liquid interfaces of binary mixtures in a relaxation process has been studied recently by *Baidakov et al.* [35, 36].

The simulation method developed in the present work is inspired by simulations of diffusion in crystals, membranes, and pores, in which the so-called *dual control volume* method was applied [26, 243, 382, 403, 411, 528, 529, 645]. In this method, the chemical potential in two sub-sections of the simulation volume is prescribed by a Monte Carlo algorithm. Particles are then inserted in one sub-section and removed from the other, causing a mass flux. We adapt the basic idea of the dual control volume method [243, 245–247, 403] to induce a mass flux through vapor-liquid interfaces driven by a gradient of the chemical potential. This approach was applied in the present work on a rectangular simulation volume in which there is a liquid slab in the middle with a vapor slab on each side. In each of the vapor domains, there is a control volume near the outer boundary of the simulation volume. The chemical potential is prescribed such that there is a mass transfer through the two vapor-liquid interfaces. The developed simulation scenario is tested using simple Lennard-Jones model mixtures. In the tests, we address a current topic: the influence of the enrichment of components at the vapor-liquid interface on the mass transfer.

Results from equilibrium molecular thermodynamics show an enrichment of low-boiling components at vapor-liquid interfaces for many mixtures [50, 89, 95, 121, 159, 173, 184, 198, 372, 389, 445, 501, 504, 624, 628–630, 634, 635], cf. chapter 9 for a survey. This enrichment is predicted consistently by molecular simulations, i.e. Monte Carlo or molecular dynamics simulations, as well as density gradient theory [50, 446, 459, 483, 624, 635]. Since the enrichment is a nanoscopic effect at fluctuating fluid interfaces, currently no experimental methods are available to study it directly. The enrichment of components at fluid interfaces of mixtures is believed to influence the mass transfer through fluid interfaces [159, 194, 199, 312, 328, 361, 488, 634, 635], but a proof is still lacking.

The new simulation scenario is applied on the two binary Lennard-Jones mixtures A and G, cf. section 3.6. Hence, the equilibrium interfacial and bulk properties of the mixtures used in the present study have been studied systematically beforehand. For the mixture G, the low-boiling component exhibits a strong enrichment at the interface; for the mixture A, the low-boiling component exhibits no enrichment at the interface. Mass transfer simulations with both mixtures are performed at four temperatures in this study.

This chapter is organized as follows: first, the simulation method is introduced. Then, the two mixtures are defined and described. The simulation results for the two mixtures are subsequently presented and compared; finally conclusions are drawn.

6.2 Molecular Simulations

6.2.1 Overview of the Simulation Method

In the present section, the new molecular simulation method for studying the mass transfer through vapor-liquid interfaces driven by a gradient in the chemical potential is described in a general way. The actual settings that were used for the simulations in the present work are reported below.

The simulation scenario is schematically shown in Fig. 79. It contains a liquid domain in the middle and two vapor domains on each side. Each of the vapor domains contains a control volume (labeled CV+ and CV-), in which the chemical potential is prescribed such that the chemical potential difference causes a mass flux in $+z$-direction, which passes through both vapor-liquid interfaces. This mass flux is the most important observable in the simulation. Periodic boundary conditions are applied in x- and y-direction perpendicular to the interfaces. In z-direction, the simulation volume is confined by soft repulsive walls.
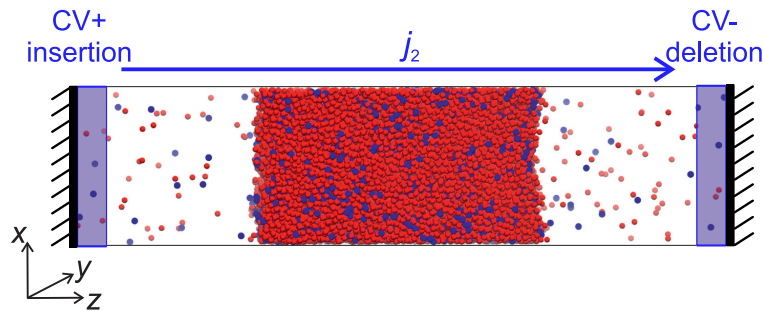
Figure 79: Scheme of the simulation set-up used in the present work for studying the mass transfer through vapor-liquid interfaces in binary mixtures. Red spheres indicate the high-boiling component 1 and blue spheres the low-boiling component 2. A liquid domain in the middle is surrounded by two vapor domains. The simulation box has periodic boundaries in x- and y-direction and soft repulsive walls in z-direction. The chemical potential of component 2 is adjusted to prescribed values in the control volumes CV+ and CV- (shaded blue) by a Monte Carlo algorithm. The resulting flux j_2 of component 2 is measured.

As described in more detail in the following section, binary Lennard-Jones mixtures were studied in the present work for testing the simulation scenario. The high-boiling component is component 1, the low-boiling component is component 2. The chemical potential difference was only set for component 2. No action on component 1 was taken in the control volumes. As a consequence of the chosen boundary conditions, the flux of component 1 j_1 is zero. The flux j_2 of component 2 is defined here as the mean number of particles per time passing through a plane perpendicular to the z-axis. All fluxes are reported in the fixed laboratory frame.

Quasi-stationary conditions were established before the sampling was started. The magnitude of the chemical potential difference of component 2 was chosen such that the

resulting flux of component 2 was low, but still reasonably measurable. The resulting response is described well by linear theory.

The simulation was specified as follows: the temperature T was prescribed in the entire simulation volume using velocity-scaling. As the particle velocity from the Brownian movements is much larger than the averaged component velocity that causes the flux, the thermostat was simply applied to the actual velocities of all particles without subtracting the average component velocity. The error induced by this simplification is negligible. The total volume of the simulation box V was constant. Due to the boundary conditions, the number of particles of component 1 N_1 was also constant. Particles of component 2 were inserted into the control volume CV+ and removed from the control volume CV- by prescribing the number for the chemical potential of component 2 in the two control volumes μ_2^{CV+} and μ_2^{CV-}. This was achieved by a grand canonical Monte Carlo algorithm [245–247].

The simulation was carried out as follows: the initialization and an equilibration were carried out in the NVT ensemble – as it is done in direct vapor-liquid equilibrium simulations (cf. chapter 2 - 3). After that, the control volumes, which are placed next to the soft repulsive walls, were switched on. With all settings active, the simulation was run until the mass flux of component 2 through the simulation box was stationary; then, the sampling was started.

The primary measured observable during the production phase is the flux of component 2 j_2. It is measured by monitoring the number of particles of component 2 that are inserted in the control volume CV+ and those that are deleted in the control volume CV-; details are given in the Appendix. These numbers are equal – within their fluctuation bandwidth – in the stationary sampling phase. The area that is used for calculating the flux is the geometric cross section of the simulation box perpendicular to the z-direction. Besides the flux j_2, also profiles of different variables depending on the z-position in the simulation box were sampled. For that purpose, the box was divided into bins in z-direction, in which the number densities of both components $\rho_1(z)$ and $\rho_2(z)$ and the diagonal components of the pressure tensor were measured.

The pressure in the bulk domains in the simulation box is not constant in z-direction. This can be understood as a consequence of prescribing the temperature and imposing a chemical potential gradient that controls the concentration profiles. The pressure gradient and the flux of the particles of component 2 act in such a way that the momentum balance is practically fulfilled in any sub-volume in the simulation box, i.e. no measures had to be taken to stabilize the position of the liquid slab in the center of the simulation volume.

The simulations with the new method pose several challenges. Unfavorable choices for the difference of the chemical potential between both control volumes can yield nucleation of droplets in the vapor domain, separation of the liquid film, movements of the liquid film during simulations, and exceedingly long simulation times to reach a quasi-stationary state. However, by choosing suitable settings, these problems can be circumvented. Further details on the simulation method are given in the Appendix.

6.2.2 Studied Lennard-Jones Mixtures

The simulation method introduced in the present work was used to study binary Lennard-Jones mixtures. The Lennard-Jones fluid is one of the most frequently studied model fluids as it is computationally relatively inexpensive but still yields a realistic description of simple fluids. It is therefore often used to test new methods in molecular simulations and fluid state theory [144, 154, 273, 359, 446, 626, 637]. In the present study, the Lennard-Jones truncated and shifted (LJTS) potential with a cut-off radius of $2.5\,\sigma$ is used:

$$u_{\mathrm{LJ}}(r) = 4\varepsilon\left[\left(\frac{\sigma}{r}\right)^{12} - \left(\frac{\sigma}{r}\right)^{6}\right] \quad \text{and} \tag{109}$$

$$u_{\mathrm{LJTS}}(r) = \begin{cases} u_{\mathrm{LJ}}(r) - u_{\mathrm{LJ}}(r_{\mathrm{c}}) & r \leq r_{\mathrm{c}} \\ 0 & r > r_{\mathrm{c}}, \end{cases} \tag{110}$$

where u_{LJ} is the full Lennard-Jones potential, ε and σ are the energy and size parameter, respectively. The distance between two particles is r. The truncation radius r_{c} of the potential is $2.5\,\sigma$ throughout the present study. No long-range corrections are required in the simulations.

Two binary LJTS systems (named mixture A and G in the following) were used for testing the new simulation method; they are the same as the systems studied in section 3.6. Hence, the high-boiling component 1 is the same in both mixtures. The low-boiling character of component 2 was obtained by decreasing its dispersion energy ε_2 with respect to ε_1 of component 1. The size parameter and the mass of the components 1 and 2 are the same for both mixtures, i.e. $\sigma_1 = \sigma_2$ and $M_1 = M_2$.

The cross-interactions between unlike particles were modeled using the modified Lorentz-Berthelot combination rules [52, 394]

$$\sigma_{ij} = \frac{\sigma_i + \sigma_j}{2}, \tag{111}$$

$$\varepsilon_{ij} = \xi\sqrt{\varepsilon_i\varepsilon_j}, \tag{112}$$

where the single indices i and j stand for the interaction of two particles of the same component and the double index ij for the cross interaction between different components.

The two binary LJTS mixtures investigated here are:

- mixture A (ideal mixture): $\varepsilon_2/\varepsilon_1 = 0.9$ and $\xi = 1$,

- mixture G (asymmetric wide-boiling mixture): $\varepsilon_2/\varepsilon_1 = 0.6$ and $\xi = 0.85$.

Both bulk and interfacial equilibrium properties of these two mixtures have been investigated systematically in previous works of our group [628–630, 635], cf. chapter 3. Mixture A is essentially an ideal mixture in the sense of Raoult's law, whereas mixture G is highly asymmetric and strongly non-ideal. It exhibits a vapor-liquid-liquid equilibrium at low temperatures, cf. section 3.6. In mixture A, the low-boiling component 2 exhibits practically no enrichment at the vapor-liquid interface in the entire composition and temperature range, whereas in mixture G component 2 exhibits a large enrichment,

cf. section 3.6. This enrichment was found to increase with decreasing temperature and decreasing mole fraction of the low-boiling component. There is no enrichment of the high-boiling component 1 at the vapor-liquid interface, neither for mixture A nor for mixture G, cf. section 3.6. Since we want to study the influence of the enrichment on the mass transfer, the focus is on mixture G and mixture A is taken as a reference – analogue to section 3.6.

The mass transfer through the vapor-liquid interfaces was studied with the new simulation method for both mixture A and G at four temperatures: $T/\varepsilon k_{\mathrm{B}}^{-1} = 0.66, 0.715, 0.77, 0.825$. For mixture G, the component 2 is supercritical at all investigated temperatures, while for mixture A, the component 2 is subcritical at all investigated temperatures.

6.2.3 Simulation Details

We will first explain the principles and then discuss their realization. Let us start by considering an equilibrium situation (or, equivalently, assume that only a negligible gradient in the chemical potential of component 2 were applied). Then, after the equilibration, a vapor-liquid equilibrium would be established in the simulation. Let us first consider this vapor-liquid equilibrium in intensive variables. In our simulations, it is specified by the temperature T and the chemical potential of component 2 μ_2. Furthermore, the number of particles of component 1 N_1 as well as the simulation volume V are set (N_2 is not set and will adjust itself to meet the specification of μ_2). Hence, such a simulation can be characterized as a N_1, V, T, μ_2-simulation. These settings fully determine the vapor-liquid equilibrium in the simulation box, including the amounts of the vapor and the liquid phase and the corresponding compositions. Starting from this equilibrium, the finite gradient of the chemical potential of component 2 μ_2 is imposed by increasing μ_2 in one control volume CV+ by $\delta\mu_2$ and decreasing it by the same amount in the other control volume CV-. The resulting steady state is then sampled in the simulation, which is near the equilibrium state described above for small $\delta\mu_2$. The new simulation scenario is based on these principles; but the realization involves additional considerations, that are discussed now.

The rectangular simulation volume V has a quadratic cross section in x- and y-direction with a side length a. The length of the simulation volume in z-direction was always $b = 170\,\sigma$. The length a was $21.1\,\sigma$ in the simulations with mixture G and $22\,\sigma$ in the simulations with mixture A. The settings were chosen such that the thickness of the liquid domain (in z-direction) was about $40\,\sigma$ and the thickness of the vapor domain was $55\,\sigma$ each, cf. Fig. 80. The maximal range of the soft repulsive wall potential was $5\,\sigma$ and the thickness of the control volumes was $10\,\sigma$, such that each of the two undisturbed bulk vapor domains has a thickness of approximately $40\,\sigma$, when these regions are excluded. The total particle number $N_1 + N_2$ was about 16,000 in all simulations. The selection of the actual choices for the initial densities and compositions was supported by preliminary calculations of the phase equilibrium using the PeTS EOS [249, 635].

The soft repulsion of the walls acts on both components 1 and 2 and was modeled by half a harmonic potential which starts to become effective at a distance of $5\,\sigma$ from the end of the simulation box, as indicated in Fig. 80. At closer distances, a repulsive force acts on the particle that rises linearly with a force constant of $k = 20\,\varepsilon\sigma^{-2}$.
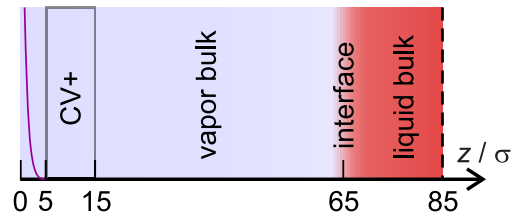
Figure 80: Geometric parameters of the scenario used in the present simulations. Only one half of the geometrically symmetric simulation box is shown; the symmetry plane is indicated by the dashed line. The cross section of the simulation box in the x, y-plane was quadratic (edge length was $21.1\,\sigma$ for mixture G simulations and $22\,\sigma$ for the mixture A simulations). The purple parable indicates the soft repulsive wall. The control volume is the gray line.

In the left control volume CV+ (cf. Fig. 79) particles of component 2 were inserted; and in the right control volume CV- particles of component 2 were removed from the simulation box. The choice of the chemical potentials of component 2 μ_2 in the control volumes is not trivial. Basically, μ_2, as determined in the NVT equilibrium simulations was increased by $\delta\mu_2$ in the control volume CV+ and decreased by the same $\delta\mu_2$ in the control volume CV-. The difference of the chemical potentials between the two control volumes was the same in all simulations and was $\Delta\mu_2 = 0.5\,\varepsilon$. Preliminary simulations showed that this is sufficient to ensure a reliable determination of the flux of component 2, but still well in the linear regime. It turns out that this value – chosen based on computational considerations – lies in the same range as the chemical potential differences that are common in chemical engineering mass transfer problems [658]. However, the chemical potential gradient, that results from this choice, is much larger than that in common chemical engineering problems, as the distance of the control volumes is of the order of 10^{-7} m whereas the boundary layers in chemical engineering mass transfer problems are of the order of 10^{-4} m [658]. The corresponding difference of 3 - 4 orders of magnitude is also found for the fluxes between engineering mass transfer problems and the fluxes obtained from the mass transfer simulations of the present work (see results section below).

The simulations were carried out as follows: the first phase of the simulation is a pre-run in the NVT ensemble. It is used to establish an equilibrium with a liquid slab in the middle and the two surrounding vapor domains, see Figs. 79 and 80. The initial positions and velocities were chosen as it is common in direct simulations of phase equilibria; the description given in Ref. [630] applies also here, correspondingly. The time step was $\Delta\tau = 0.001\,\sigma\sqrt{M/\varepsilon}$ in all simulations. The NVT simulations were carried out for 50,000 time steps. Subsequently, the control volumes in the vapor domains were switched on to evoke the mass flux j_2 in z-direction through the simulation box. The simulations were then run for at least 3,000,000 further time steps, until a stationary mass flux was established. The settings for the MC algorithm that was used for this purpose in the control volumes were: 50 Monte Carlo insertion/ removal trials every 40 MD time steps. The insertion and removal is steered by a grand canonical Monte Carlo algorithm, cf. Refs. [245–247] for details.

After a steady state was achieved, the sampling was started and carried out for at

least 5,000,000 time steps. The simulation box was divided in 1200 equal bins by a discretization in the z-direction. The pressure profile and the component density profiles were sampled in these bins. Density and pressure profiles were computed in block averages of 200,000 time steps during the production phase. During the entire simulation time, the box was temperature-controlled by velocity scaling, as discussed above. The velocity associated with the flux of the particles of component 2 was two to three orders of magnitude smaller then the mean thermal motion velocity. The flux j_2 of component 2 was measured by counting the insertions and deletions of particles of component 2 in the control volumes in the production phase. A detailed discussion of the sampling and the computation of the statistical uncertainties is given in the Appendix.

An inspection of the profiles (see below) shows that the gradients of the pressure and the component densities in the bulk domains are moderate. For the discussion, it is helpful to consider the average properties over the three bulk domains, which are labeled here V_{left} (vapor left), L (liquid), and V_{right} (vapor right). The density ρ, the pressure p, and the composition x_i were calculated as an average over the respective bulk domain excluding the area close to the interface and close to the control volumes, i.e. keeping a distance of at least $10\,\sigma$ to the control volume and to the center of the interface. The corresponding statistical uncertainties were computed from the standard deviation of the individual bin values.

Furthermore, the enrichment E_2 of the low-boiling component at the interfaces [50] was computed from each density profile from the production phase as

$$E_2 = \frac{\max\big(\rho_2(z)\big)}{\max\big(\rho_2^{L}, \rho_2^{V}\big)}\,. \tag{113}$$

Here, ρ_2^{L} and ρ_2^{V} are the values of densities in the adjoining bulk domains. For each simulation and interface, E_2 and its uncertainty was computed as the mean value from the block averages and three times their standard deviation, respectively.

The mass transfer simulations were carried out using the molecular dynamics code *ls1 mardyn* [506].

6.3 Results and Discussion

Table 19 reports the numeric values for the mass flux j_2 in the mass transfer simulations of both mixtures for all considered temperatures. The numeric values of the average bulk domain state points and the interface positions are reported in the Appendix.

Also the results for the bulk diffusion coefficients of the two mixtures [638] are compared in the Appendix. Those homogeneous bulk phase diffusion coefficients were determined for both mixtures at the studied temperatures using Green-Kubo simulations for the liquid phase and the Chapman-Enskog theory for the vapor phase [638].

In the following, the results of the mass transfer simulations are discussed, starting with a detailed consideration of a single temperature, before also the results for other temperatures are presented and discussed.

6.3.1 Temperature $T = 0.715\,\varepsilon k_{\mathrm{B}}^{-1}$

For the simulations at $T = 0.715\,\varepsilon k_{\mathrm{B}}^{-1}$, the mass flux sampled in the production phase was $j_2 = 0.26\cdot10^{-3}\,\sigma^{-3}(\mathrm{M}/\varepsilon)^{-0.5}$ for mixture A and $j_2 = 0.11\cdot10^{-3}\,\sigma^{-3}(\mathrm{M}/\varepsilon)^{-0.5}$ for mixture G (the unit of j_2 corresponds to the dimension of number of particles per area and time). Hence, the obtained mass flux in mixture G is smaller than that for the mixture A by more than a factor of two, even though the chemical potential gradient and the bulk phase transport diffusion coefficient of both mixtures are approximately the same – see Appendix for details.

Fig. 81 - left and middle shows the density and pressure profiles obtained from the mass transfer simulations for mixture G and A at $T = 0.715\,\varepsilon k_{\mathrm{B}}^{-1}$ during the production phase. The density profiles in Fig. 81 show that the density of the low-boiling component exhibits a gradient $\frac{\partial\rho_2}{\partial z}$ in the bulk domains as a response to the gradient of the chemical potential, whereas the total density exhibits no gradient in the bulk domains. Since the diffusion coefficient is lower in the liquid phase than in the vapor phase (see Appendix), the gradient $\frac{\partial\rho_2}{\partial z}$ is larger in the liquid bulk domain than in the vapor bulk. This holds for both mixtures.

For mixture G, the low-boiling component exhibits a large enrichment at the interface, which is not observed for the mixture A. To the best of our knowledge, this is the first time that the enrichment is studied under the influence of a mass transfer. The observations for the enrichment in Fig. 81 are in line with results from equilibrium simulations for these mixtures, cf. section 3.6. The numeric values for the enrichment in mixture G at the left and right interface are compared in Table 20 with equilibrium results from section 3.6 at the same liquid phase composition. Two values are reported for the enrichment at the right interface. The evaluation of Eq. (113) requires the computation of the larger value of the density of component 2 in the adjoining bulk domains as reference in the denominator. In equilibrium simulations, the choice poses no problem as the bulk phase is equilibrated. In mass transfer simulations, however, gradients occur. This introduces an ambiguity in the choice of the bulk value: it could be chosen as the average value of the domain, or be selected as values at the foot of the peak. For the left peak, this makes no difference; the reference is always the vapor domain and there is no substantial difference between the average vapor density and that at the foot of the peak. For the right peak, this is different. When the average bulk densities are used for the evaluation of Eq. (113), the reference is the liquid density; when the values at the foot of the peak are used, the reference is the vapor density (for which the value at the foot of the peak is again basically the same as the average value). Hence, we report two values for the right peak.

As a reference, we have also included results for the enrichment obtained from for the same mixture in vapor-liquid equilibrium simulations at the same temperature and the same composition of the liquid bulk domain in Table 20. The results are also illustrated in Fig. 82, from which it can be seen that the results for the left interface that were obtained in the mass transfer simulations agree very well with those of the equilibrium simulations. For the right interface, depending on the choice of the reference, the results lie below or above the corresponding equilibrium values. Overall, it can be concluded that the values for the enrichment E_2 do not change strongly when mass transfer occurs, at least for moderate gradients of the chemical potential, as they were applied here.
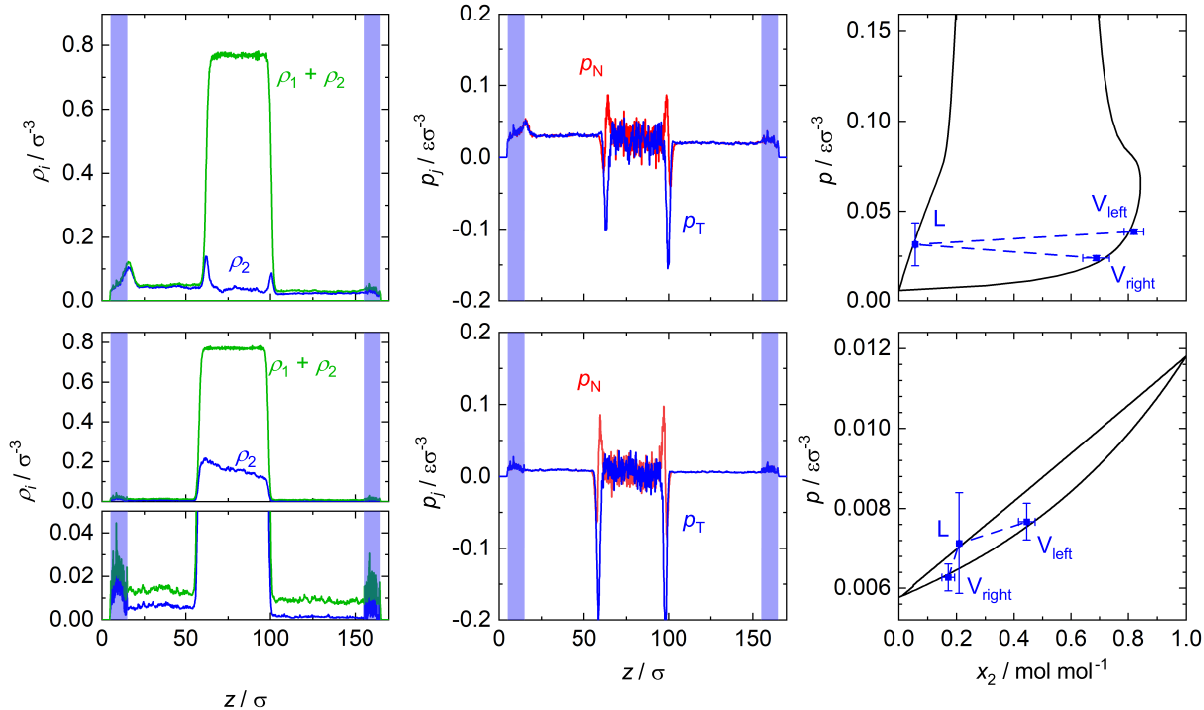
Figure 81: Density profiles (left), pressure profiles (middle), and averaged thermodynamic state points in the bulk domains (right) for the mixtures G (top) and A (bottom) obtained in the mass transfer simulations at $T = 0.715\,\varepsilon k_B^{-1}$. The lower part of the split plot is just an expansion of the upper part. The blue shaded area indicates the control volumes. For the pressure profiles, the indices $j = N, T$ indicate the normal and tangential component of the pressure tensor, respectively. The thermodynamic state points indicated as symbols in the right plots were sampled in the three bulk domains during the production phase of the simulations. They are compared to results for the vapor-liquid equilibrium computed with the LJTS EOS [249, 635] (lines). The density and pressure profiles are from one block average during the production phase; the state points depicted in the $p-x$ diagrams (right) are the average of all blocks.

No enrichment is found for mixture A, i.e. $E_2 = 1$ within the numeric uncertainty in all simulations, cf. the corresponding component density profiles in the Appendix. This finding is in line with the findings from the equilibrium simulations, cf. section 3.6.

For both mixtures G and A, the average state points computed for the three bulk domains V_{left}, L, and V_{right} are compared with the corresponding phase equilibrium obtained from the PeTS EOS [249, 635] in the right panels of Fig. 81. The averaged state points sampled in the bulk domains agree astonishingly well with the isothermal phase envelope from the EOS. The individual state points in each bin for a bulk domain show an elliptic scattering around the averaged value, cf. Fig. A.18 in the Appendix. The average pressure in the three bulk domains decreases from left to right with the gradient of the chemical potential, as expected.

Table 19: Numeric values of the mass flux j_2, the prescribed residual chemical potential in the inserting and deleting control volume μ_2^{CV+} and μ_2^{CV-}, respectively, and the number of component 1 particles N_1 in the performed mass transfer simulations for both mixtures G and A at all four investigated temperatures. The box size was $170\,\sigma$ in z-direction in all cases; the xy-cross section was a square with the edge length $21.1\,\sigma$ for the simulations with mixture G and $22\,\sigma$ for the simulations with mixture A.

$T\ /\ \varepsilon k_{\mathrm{B}}^{-1}$	$j_2\ /\ 10^3\,\sigma^{-3}(M/\varepsilon)^{-0.5}$		$\mu_2^{CV+}\ /\ \varepsilon$		$\mu_2^{CV-}\ /\ \varepsilon$		N_1	
	G	A	G	A	G	A	G	A
0.66	0.06(5)	0.23(1)	-0.75	-2.22	-0.25	-1.72	12705	12447
0.715	0.11(5)	0.26(1)	-0.8	-2.4	-0.3	-1.9	12703	12344
0.77	0.10(4)	0.21(1)	-0.95	-2.6	-0.45	-2.1	12642	12344
0.825	0.19(3)	0.24(1)	-1.1	-2.6	-0.6	-2.1	12689	12347

Table 20: Numeric values of the enrichment of the low-boiling component at the interface for mixture G at all four investigated temperatures. The column x_2^{L} indicates the mole fraction of component 2 in the liquid bulk domain L sampled during the mass transfer simulations. The columns E_2^{left} and E_2^{right} indicate the enrichment at the left and right interface, respectively. For the right interface, V and L indicate the evaluation of Eq. (113) using the vapor or liquid domain as reference, respectively (details are given in the text). E_2^{eq} indicates the equilibrium enrichment at the corresponding temperature and liquid phase composition taken from Ref. [629].

$T\ /\ \varepsilon k_{\mathrm{B}}^{-1}$	$x_2^{\mathrm{L}}\ /\ \mathrm{mol\ mol^{-1}}$	E_2^{left}	$E_2^{\mathrm{right,L}}$	$E_2^{\mathrm{right,V}}$	E_2^{eq}
0.66	0.057(5)	4.4(2)	3.2(3)	5.4(4)	4.0(3)
0.715	0.056(3)	3.2(2)	2.6(2)	3.7(4)	3.1(1)
0.77	0.058(4)	2.5(1)	1.9(2)	2.9(2)	2.5(1)
0.825	0.055(3)	2.1(1)	1.6(2)	2.2(2)	1.9(1)

6.3.2 Influence of the Temperature

The influence of the temperature on the mass transfer in the two mixtures G and A was studied by performing additional simulations at three further temperatures ($T/\varepsilon k_{\mathrm{B}}^{-1} = 0.66,\ 0.77,\ 0.825$). The numeric values obtained for the mass fluxes and the non-equilibrium enrichment are reported in Table 19 and 20, respectively.

Density profiles and isothermal $p-x$ diagrams obtained during the quasi-stationary production phase for mixture G at $T/\varepsilon k_{\mathrm{B}}^{-1} = 0.66,\ 0.77,\ 0.825$ are shown in Fig. 83. The corresponding plots for mixture A are presented in the Appendix. For all four investigated temperatures (see above), the difference of the chemical potential applied between the two control volumes was the same for mixture G and mixture A. The density profiles obtained for mixture G (cf. Fig. 83) show in all cases a gradient of the low-boiling component $\frac{\partial \rho_2}{\partial z}$, i.e. ρ_2 decreases from the left to the right side in each bulk domain. An enrichment of component 2 is observed in all cases for mixture G, but
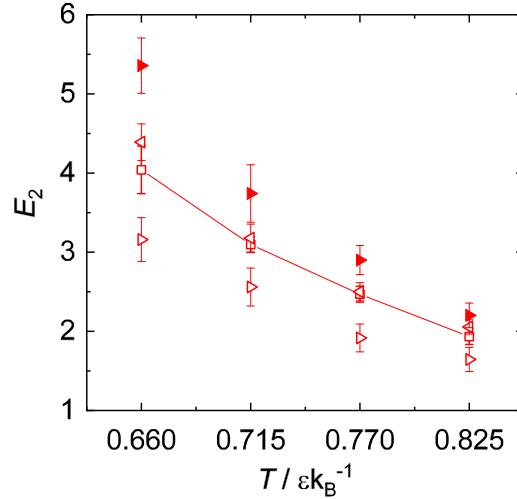
Figure 82: Enrichment of component 2 E_2 at the interface at different temperatures
during the mass transfer simulations (triangles) in comparison to the en-
richment at equilibrium states (squares; adapted from section 3.6) at the
same liquid phase composition. Left triangles and right triangles indicate
the enrichment obtained for the left and right interface in the mass trans-
fer simulations, respectively. The filled and empty right triangles indicate
the enrichment using the vapor or liquid domain as reference, respectively
(details are given in the text). Lines are a guide for the eye.

its height decreases with increasing temperature, which is in line with corresponding
equilibrium results, cf. section 3.6.

The enrichment computed from Eq. (113) for the left and right interface is depicted
in Fig. 82 for all temperatures. As a reference, also the equilibrium enrichment at
the corresponding temperature and liquid phase composition are shown. As discussed
above, the enrichment of the right interface was evaluated in two different ways: using
the averaged bulk liquid density (open triangles right) and using the vapor density (filled
triangles right) for the evaluation of the denominator in Eq. (113). For all temperatures,
the enrichment at the left interface is in fair agreement with the enrichment obtained
from equilibrium simulations (cf. section 3.6). For the right interface, the evaluation
based on the average liquid bulk density as reference yields consistently lower enrichment
than the equilibrium results. Vice versa, the evaluation based on the vapor bulk density
reference yields larger enrichment. The differences between the enrichment obtained
for the left and the right interface are likely due to the fact that interfacial properties
strongly depend on the liquid bulk composition adjoined to the interface (cf. section
3.5), which varies for the left and right interface in the mass transfer simulations. A
comprehensive comparison of equilibrium and non-equilibrium interfacial properties is
out of the scope of this work but is an interesting topic for future work.

In some of the density profiles shown in Fig. 81 and 83, small peaks of the total density
in the vicinity of the control volumes indicate the presence of a small droplet. This is
due to the fact that the perturbations of the control volume act as nucleation precursor.
Hence, in some cases, small nucleus form in the saturated vapor domains attached to the
control volume. This also produces more pronounced fluctuations for the insertion rate
than the removal rate of component 2 particles in the control volumes, cf. Appendix.
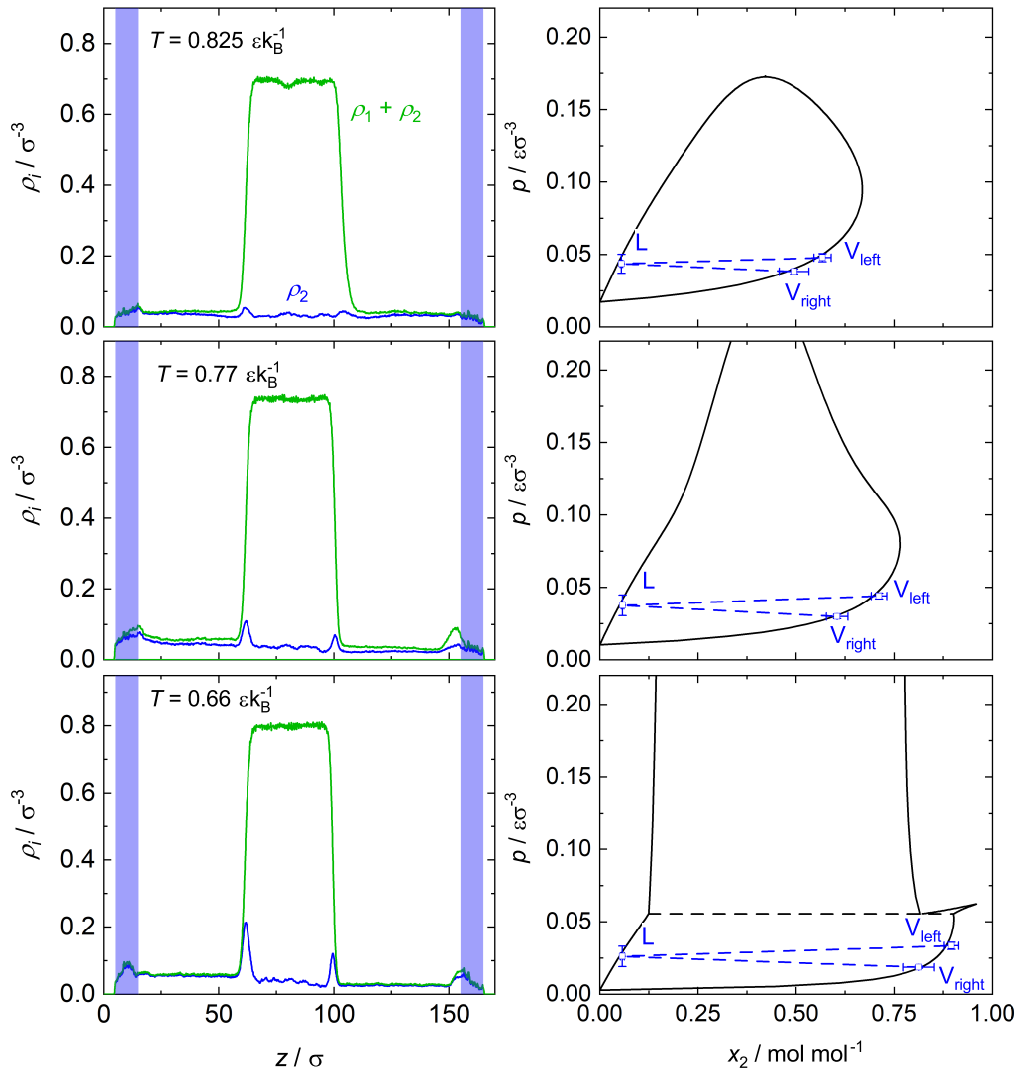
Figure 83: Density profiles (left panels) and isothermal $p - x$ diagrams (right panels) sampled during the production phase of the simulations of mixture G at different temperatures. The blue shaded area indicates the elongation of the control volumes in z-direction.

For all temperatures, the average state point computed for the three bulk domains V_{left}, L, and V_{left} for mixture G are in excellent agreement with the corresponding phase equilibrium, cf. Fig. 83 - right. The same holds for mixture A, see Appendix. Also, the composition difference between the left and right bulk vapor domain is similar for the results from the different temperatures.

Fig. 84 shows the stationary mass flux j_2 sampled during the production phase as a function of the temperature for mixture G and A. For all studied temperatures, the ideal mixture A yields a significantly larger mass flux j_2 – especially at low temperatures. The mass flux obtained for mixture A exceeds that obtained for mixture G by a factor of two to four. This is astonishing as the diffusivities of both components are similar for both mixtures [638], both in the gas and liquid phase (see Appendix), the chemical potential gradient was the same, and also the geometric parameters almost identical. The major difference is that mixture G shows a high enrichment while mixture A shows almost no enrichment. Hence, the present finding might point to an influence of the enrichment on
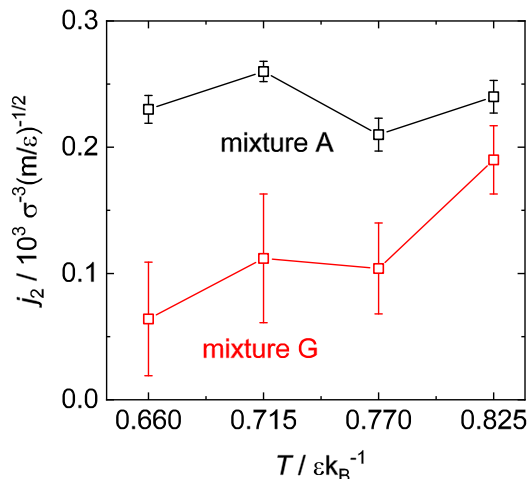
Figure 84: Mass flux j_2 sampled during the mass transfer simulations in mixture G and mixture A at different temperatures. Lines are a guide for the eye. The unit of j_2 corresponds to the dimension of number of particles per area and time

the mass transfer. A further investigation of this hypothesis would require carrying out accompanying continuum simulations, which was not in the scope of the present work.

6.4 Conclusions

A new method for studying mass transfer in mixtures driven by a chemical potential difference across vapor-liquid interfaces by molecular simulation was developed and tested. It is based on a simulation scenario in which two vapor domains encase a liquid domain. Different values of the chemical potential of a selected component are prescribed in two control volumes in the two vapor domains and evoke a flux of that component that passes through two vapor-liquid interfaces; the other component is stagnant due to the chosen boundary conditions. In isothermal simulations, the profiles of the component densities, the pressure tensor, and the flux of the selected component is measured. To the best of our knowledge, this is the first report on a molecular simulation method for studying mass transfer through vapor-liquid interfaces driven by chemical potential gradients. This is astonishing, as mass transfer through vapor-liquid interfaces is very important in technical and natural processes. The new method opens the way for detailed studies of these processes on the molecular level. In particular, the new method can be used for systematic studies of the influence of mass transfer on interfacial properties, which are presently still lacking.

The new simulation method was applied to study the influence of the enrichment of components at the vapor-liquid interface on the mass transfer. Two Lennard-Jones mixtures were examined, of which the phase equilibrium including the interfacial equilibrium properties were systematically studied in chapter 3. Mixture G exhibits a large enrichment of the low-boiling component at the interface, whereas mixture A exhibits no enrichment. We find that, even though both mixtures have similar bulk diffusivities and the same chemical potential gradient was applied, the mass flux observed in both systems differs significantly. These differences might be related to the presence

of an enrichment at the interface in one of the mixtures. Hence, the results support the assumption [194, 199, 328, 361, 488, 634, 635] that the enrichment influences the mass transfer through fluid interfaces. Further studies are, however, needed to prove or refute this hypothesis. The new scenario is a valuable tool for this. Such studies should include also simulations with continuum methods, that can be compared to the results from the molecular dynamics simulations.

7 Vapor-Liquid Interfacial Properties of the System Cyclohexane + CO$_2$: Experiments, Molecular Simulation and Density Gradient Theory

7.1 Introduction

There are basically two approaches for developing a better understanding of the phenomena at fluid interfaces. On the one side, studies on simple model systems can be carried out. We have recently systematically studied binary mixtures of Lennard-Jones fluids and have examined the influence of the variation of parameters, which describe the molecular interactions on the interfacial properties (cf. chapter 3 and 5) [628, 630, 634, 635]. Similar studies have also been carried out by multiple other groups, e.g. Refs. [149, 192–195, 200, 361, 362, 412, 441, 446, 551, 552, 585, 586]. The second approach is to study real systems, both by experiments and simulation. Unfortunately, only the surface tension is directly accessible by experiments and the relative adsorption indirectly [211, 417, 573], while other properties, like the enrichment and interfacial thickness, are not as readily accessible. However, the composition and orientation of molecules at fluid interfaces can be examined by radiation scattering methods, cf. [22, 216, 292, 584, 608].

The models used in both MD and DGT can be calibrated using experimental data to predict the density profiles at vapor-liquid interfaces. The models should not only represent the interfacial properties well, but also the bulk VLE properties. Theoretical studies on nanoscopic interfacial properties of real mixtures have been for example reported in Refs. [50, 89, 121, 159, 173, 305, 328, 354, 374, 404, 444, 453, 456, 458, 459, 483, 501, 504, 533, 705].

In the present work we have followed the second route and studied the mixture of cyclohexane + CO$_2$. As in Refs. [50, 445], the present study was carried out using several methods: pendant drop experiments, molecular dynamics (MD) simulation, and density gradient theory (DGT) calculations in combination with the PCP-SAFT equation of state [100–102, 221, 223]. We report surface tension and relative adsorption data obtained from all three methods, whereas nanoscopic density profiles at the interface, the enrichment of CO$_2$ at the interface, and the interfacial thickness were only investigated by MD and DGT. The experiments were carried out at temperatures between 303 K and 373 K in intervals of 10 K. MD and DGT calculations were carried out at 303 K,

333 K, and 363 K. The employed methods are described in section 7.2 and the results are reported and discussed in section 7.3. Conclusions are drawn in section 7.4.

In this study, different interfacial properties of the binary system cyclohexane + CO$_2$ were studied both by experiments and simulations. Also some data on the pure substances are reported. Table 21 gives an overview of the available experimental data on the surface tension of pure cyclohexane and pure CO$_2$ as well as their binary mixture. To the best of our knowledge, no information on the nanoscopic properties at the vapor-liquid interface of the system cyclohexane + CO$_2$ is available in the literature. Data on the surface tension of the mixture is still scarce.

Table 21: Literature overview of experimental data of the system cyclohexane + carbon dioxide as well as the pure components.

Author	T / K	p / MPa
cyclohexane + carbon dioxide		
VLE		
Al-Sahhaf et al. [14]	333.15	1.08 - 8.17
Dymond [151]	304.23	0.1
Esmelindro et al. [166]	303, 333	4.59 - 9.81
Kaminishi et al. [309]	303.15	1.09 - 5.81
Mukhopadhyay & Srinivas [481]	366	10.2 - 11.97
Shibata & Sandler [606]	366.5 - 410.9	1.75 - 12.8
Yang et al. [721]	333.15	3.46 - 8.6
Zhang & Zheng [730]	303.15	0.97 - 6.66
Nagarajan & Robinson [487]	344.26	6.8 - 11
Krichevskii & Sorina [346]	473.15 - 483.15	1.3 - 13
Surface tension		
Nagarajan & Robinson [487]	344.3	6.87 - 10.96
Yang et al. [722]	308.15, 323.15, 333.15	3.6 - 9.6
cyclohexane		
VLE		
correlation of experimental data from *Span and Wagner* [622]		
Surface tension		
Azizian & Bashavard [29]	293.15 - 323.15	
Azizian et al. [30]	293.15 - 313.15	
Campbell & Anand [85]	298.15 - 323.15	
Clever and Chase [118]	298.15 - 308.15	
Gómez-Díaz et al. [214]	298.15 - 323.15	
Grafe [218]	295.15 - 306.15	
Hückel & Harder [282]	279.55 - 349.95	
Hennaut-Roland & Lek [254]	288.15 - 303.15	

Author	T / K	p / MPa
Jain & Singh [295]	298.16 - 308.16	
Kahl et al. [308]	287.81 - 327.88	
Kahl et al. [307]	279.33 - 337.93	
Kaur et al. [316]	298.15 - 308.15	
Konobeev & Lyapin [338]	293.15 - 353.85	
Lakomy & Lehar [355]	298.15	
Lam & Benson [356]	293.15 - 303.15	
Mc Lure et al. [427]	303.2	
Moll [469]	293.15	
Ramakrishna & Patel [556]	308.15	
Romero et al. [564]	283.15 - 313.15	
Rusanov et al. [574]	293.15 - 323.15	
Siskova & Secova [610]	293.15 - 313.15	
Suri & Ramakrishna [648]	293.15 - 303.15	
Trieschmann [670]	295.15	
Villares et al. [680]	298.15 - 313.15	
Vogel [681]	293.95 - 316.75	
Wang et al. [696]	288.15 - 328.15	
Wright & Akhtar [719]	303.15	
Wright & Akhtar [718]	303.15	
Zvereva & Smirnova [733]	303.15	
carbon dioxide		
VLE		
correlation of experimental data from *Span and Wagner* [620]		
Surface tension		
Muratov & Skripov [485]	216.55 - 302	
Anonymous [24]	298.15	
Rathjien & Straub [557]	273.15 - 304.14	

The mixture was furthermore chosen for two reasons: first, a significant enrichment of the CO_2 at the interface was to be expected according to the experiences from studies of similar systems [121, 173, 635, 705]. Second, for both pure substances cyclohexane and CO_2 and their mixture, accurate and validated force field and PCP-SAFT EOS models for the description of the vapor-liquid equilibrium are available in the literature [221, 223, 448, 449, 633], such that the main focus of the present work could be laid on the interfacial properties.

While interfaces are treated as two-dimensional objects on a macroscopic level, it is found that the density changes continuously at the interface on an atomistic scale. There are presently no experimental methods that yield information on such density profiles across

fluid interfaces and thereby on the arrangement of the surface excess and the interfacial thickness. However, such data can be obtained from molecular simulations based on classical force fields on the one side and density gradient theory (DGT) combined with an equation of state (EOS) or density functional theory (DFT) on the other side [168, 573].

Interesting phenomena have been observed in the nanoscopic interfacial region of binary and multicomponent mixtures, such as maxima in the density profiles of the low-boiling component at the interface [194, 195, 362, 630]. The density of low-boiling components at such maxima can be several times higher than the bulk densities. This phenomenon is referred to as *enrichment* and is closely related to the relative adsorption. The enrichment of components at the vapor-liquid interface of mixtures has recently received particular attention as it is suspected to influence the mass transfer across the interface [328, 488, 634, 635, 705], which is of fundamental importance for fluid separation processes. Also, the relation between the relative adsorption and the enrichment (both describe the surface excess) and their relation to the molecular interactions is not yet fully understood [50, 635].

7.2 Methods

7.2.1 Pendant Drop Experiments

7.2.1.1 Measurements and Experimental Setup

Details of all materials (CAS Number, supplier, purity) used for the experiments are listed in Table 22. Carbon dioxide was used without further purification. Cyclohexane was degassed by vacuum distillation. The samples of the mixture were prepared as described by *Becker et al.* [50].

Table 22: Chemicals that were used in the present work.

	CAS number	Supplier	Purity / $\mathrm{mol\,mol^{-1}}$
cyclohexane (C_6H_{12})	110-82-7	Merck KGaA, Germany	0.998
carbon dioxide (CO_2)	124-38-9	Air Liquide, France	0.99995

The pendant drop method [146, 240, 615] was used for the determination of the surface tension of pure cyclohexane and its binary mixture with CO_2. Due to the low critical temperature of CO_2, no measurements with pure CO_2 were carried out. The method is based on the mechanical equilibrium of a drop pending at a capillary tube, which is governed by gravitational forces and the surface tension. The surface tension γ is determined from

$$\gamma = \frac{\Delta\rho g z}{A},\tag{114}$$

where $\Delta\rho = \rho' - \rho''$ is the density difference between the liquid and the vapor phase, g is the gravitational constant, z is the height coordinate of the drop as measured from the apex, and A is a geometric factor characterizing the shape of the drop [146, 615]. The latter was obtained from a photographic examination of the pending droplet.

The pendant drop measurements were carried out with a custom-built apparatus as introduced in a previous publication of our group [50]. The procedure was the same as described therein. The measurements yield data on the surface tension as a function of temperature and pressure [50]. The mole fraction of CO_2 in the liquid phase x'_{CO_2} at a given temperature and pressure was subsequently determined with the PCP-SAFT EOS, such that the experimental data can be related to the liquid phase composition. It is shown in the results section 7.3.2.4 that the PCP-SAFT EOS gives a good description of the bulk properties of the mixture cyclohexane + CO_2.

As discussed in Ref. [50], the main contribution to the uncertainty of the surface tension determined from Eq. (114) stems from the density difference $\Delta\rho$. Any error in $\Delta\rho$ will result in a similar error in γ, cf. Eq. (114). In the present work, $\Delta\rho$ was calculated from the PCP-SAFT EOS. It is shown in section 7.3.2.4 that the numbers for $\Delta\rho$ obtained in this way are in good agreement with available experimental data. Nevertheless, the resulting uncertainty of the surface tension that stems from the uncertainty in $\Delta\rho$ is up to 3%, cf. section 7.3.2.4. The random uncertainty of the measurement method was estimated from repeated measurements of the surface tension of pure cyclohexane. Hence, the statistical error was computed from three times the standard deviation of

five independent data points. This random uncertainty of the measurement method is less than 1.1% and the total uncertainty in the experimental data on the surface tension of the binary mixture is better than 4.1%.

7.2.1.2 Determination of the Relative Adsorption from the Experimental Data on the Surface Tension

The relative adsorption $\Gamma_2^{(1)}$ of a component 2 with reference to a component 1 in a binary mixture can be obtained from the Gibbs adsorption equation [211], which yields for the relative adsorption of CO$_2$ at the vapor-liquid interface $\Gamma_{\mathrm{CO}_2}^{(\mathrm{C_6H_{12}})}$ in a mixture of CO$_2$ with cyclohexane (C$_6$H$_{12}$)

$$\Gamma_{\mathrm{CO}_2}^{(\mathrm{C_6H_{12}})} = -\left(\frac{\partial \gamma}{\partial \mu_{\mathrm{CO}_2}}\right)_T , \tag{115}$$

where μ_{CO_2} is the chemical potential of CO$_2$ in the equilibrated phases.

Different ways have been established in the literature to describe the chemical potential in Eq. (115) to obtain the relative adsorption, e.g. with activity coefficient models [307, 308], equations of state [50], or an ideal gas phase assumption [417, 445]. The PCP-SAFT EOS is used here for the determination of the chemical potential. The chemical potential of CO$_2$ μ_{CO_2} was therefor computed from the PCP-SAFT EOS at every state point (characterized by (T, p)) at which the surface tension was measured. A value of the chemical potential μ_{CO_2} was subsequently assigned to each value of the surface tension obtained from the pendant drop experiment. For each isotherm, a polynomial curve was fitted to the data points $(\gamma, \mu_{\mathrm{CO}_2})$, which is then used to compute the derivative in Eq. (115). The adsorption data $\Gamma_{\mathrm{CO}_2}^{(\mathrm{C_6H_{12}})}$ obtained in this way are referred to as experimental data in the following.

7.2.2 Molecular Models and Simulation Method

Molecular dynamics simulations were carried out with the program *ls1 mardyn* [506], the force fields were taken from the MolMod database [633]. The molecular model for CO$_2$ was that from *Merker et al.* [448]. It consists of three Lennard-Jones sites, representing each atom and a point quadrupole in the center of mass representing the polarity of the molecule. The cyclohexane model was taken from *Merker et al.* [449] and consists of six Lennard-Jones sites (one for each methylene group). The molecular models of both substances are rigid. It has been shown that thermodynamic properties of low molecular weight molecules can be described well by rigid models, cf. Refs. [13, 88, 162].

The potential energy of the molecular models is given by

$$\begin{aligned}
U = \sum_{i=1}^{N-1} \sum_{j=i+1}^{N} \Bigg\{ &\sum_{a=1}^{n_i^{\mathrm{LJ}}} \sum_{b=1}^{n_j^{\mathrm{LJ}}} 4\varepsilon_{ijab} \left[\left(\frac{\sigma_{ijab}}{r_{ijab}}\right)^{12} - \left(\frac{\sigma_{ijab}}{r_{ijab}}\right)^{6}\right] \\
&+ \sum_{c=1}^{n_i^e} \sum_{d=1}^{n_j^e} \frac{1}{4\pi\varepsilon_0}\left[\frac{Q_{ic}Q_{jd}}{r_{ijcd}^5} \cdot f(\omega_i, \omega_j)\right] \Bigg\} ,
\end{aligned} \tag{116}$$

where ε_{ijab} and σ_{ijab} are the Lennard-Jones energy and size parameter, r_{ijab} and r_{ijcd} are site-site distances, Q_{ic} and Q_{jd} are the magnitude of the electrostatic interactions, i.e. the point quadrupole moments, and $f(\omega_i, \omega_j)$ are dimensionless angle-dependent expressions representing the orientation ω_i, ω_j of the point multipoles [80]. The indices i and j indicate the molecules, the indices a, b, c, d the interaction sites of a molecule.

The modified Lorentz-Berthelot combination rules [52, 394] were employed for describing the dispersive/ repulsive interactions between unlike particles:

$$\sigma_{ij} = \frac{\sigma_{ii} + \sigma_{jj}}{2} \,, \tag{117}$$

$$\varepsilon_{ij} = \xi_{ij} \sqrt{\varepsilon_{ii}\varepsilon_{jj}} \,, \tag{118}$$

where the index ii and jj indicate the interaction of two particles of the same type and the index ij the cross interaction between different particle types. Eq. (117) and (118) were also employed for the modeling of the cross interactions using the PCP-SAFT EOS; see the following section for details. The binary interaction parameter $\xi_{\mathrm{CO_2,C_6H_{12}}}^{\mathrm{MD}} = 0.95$ was used in the present work for the MD simulations. It was fitted by *Merker et al.* [449] to experimental data of the Henry's law constant of the mixture cyclohexane + CO_2.

The molecular force field models of the pure components which were employed in the present work were parametrized to reproduce the saturated liquid density, the vapor pressure, and the enthalpy of vaporization [448, 449]. The absolute average deviations between the calculated values by the molecular simulation and experimental data are 0.3%, 3.7%, and 0.9% for cyclohexane [449] and 0.4%, 1.8%, and 8.1% for carbon dioxide [448]. The surface tension was not considered in the parametrization of the molecular models. For other pure fluid force field models developed with a similar parametrization strategy the surface tension agrees with experimental data within 20%, whereat the MD results often overestimate the experimental data [27, 28, 50, 153, 209, 640, 701, 705, 732].

In the molecular simulations of the vapor-liquid interfaces, systems were studied in which a liquid phase is arranged as a slab in the middle of the simulation volume with a vapor phase on each side. Periodic boundary conditions were applied in all directions. The coordinate z is perpendicular to the interfaces. The elongation of the simulation box normal to the interface was 30 nm and the thickness of the liquid slab in the middle of the simulation box was 15 nm. The elongation in the directions parallel to the interfaces was at least 6 nm. The simulations were performed in the NVT ensemble with $N = 32{,}000$ particles. The equation of motion was solved by a leapfrog integrator [176] with a time step of $\Delta\tau = 2$ fs. The initial densities and compositions in the simulations were taken from the PCP-SAFT EOS to ensure fast equilibration.

For all simulations carried out in the present work, the cut-off radius was set to 17.5 Å with a center-of-mass cut-off scheme. A slab-based long-range correction scheme was employed to incorporate the long-range Lennard-Jones interactions [296, 707].

The equilibration was executed for 750,000 time steps. The production was conducted for 4,000,000 time steps for the pure substances, and 8,000,000 for the mixture. Density and pressure profiles were computed in block averages of 500,000 time steps during the production phase. From each block average, the vapor pressure p, the saturated liquid and vapor density ρ' and ρ'', respectively, and the saturated vapor and liquid phase mole

fractions x'_i and x''_i were calculated as an average in the respective phase – excluding the area close to the interface, where the first derivative of the density with respect to the z-coordinate significantly deviates from zero.

The surface tension in the MD simulations was calculated from the deviation between the normal and the tangential diagonal components of the pressure tensor [325, 695] in the pressure profiles, i.e. by the mechanical route

$$\gamma = \frac{1}{2} \int_{-\infty}^{\infty} \left(p_{\mathrm{N}} - p_{\mathrm{T}} \right) \mathrm{d}z \,, \tag{119}$$

where p_{N} is the normal pressure given by the z-component of the diagonal of the pressure tensor and p_{T} is the tangential pressure, which was determined by averaging over the x- and y-components of the diagonal of the pressure tensor. The statistical uncertainties of the surface tension γ and the bulk VLE properties (p, ρ', ρ'', x'_i, x''_i) were estimated to be three times the standard deviation of all sampled block averages.

7.2.3 Density Gradient Theory + PCP-SAFT EOS

7.2.3.1 Density Gradient Theory

Density gradient theory [81, 82] is a widely used method for computing the surface tension of both pure substances [89, 121, 455, 532] and mixtures [78, 90, 159, 305, 404, 456, 458, 477, 533]. Also, nanoscopic interfacial properties can be obtained from DGT, namely the density profiles across the interface. To model fluid interfaces, DGT requires a model of the Helmholtz energy of the bulk fluid and the so-called influence parameter κ that describes the influence of the density gradient on the Helmholtz energy. For a comprehensive introduction of DGT we refer the reader to Refs. [125, 455, 573].

The cross-interaction influence parameter was assumed here to be the geometric mean of the pure substance influence parameters [91, 458]

$$\kappa_{ij} = \sqrt{\kappa_i \kappa_j} \,. \tag{120}$$

In a previous work of our group, it was shown that this assumption leads to almost perfect agreement between results from DGT and computer experiment for different Lennard-Jones mixtures with various types of phase behavior in the entire composition range, cf. chapter 3. The influence parameters of the pure components cyclohexane and carbon dioxide were adopted from the literature [500, 503], cf. Table 23.

Table 23: Pure component parameters used in the present work in the PCP-SAFT + DGT calculations.

Component	m	σ / Å	$\varepsilon/k_{\mathrm{B}}$ / K	Q / DÅ	$10^{20}\,\kappa_{\mathrm{DGT}}$ / Jm^5 mol^{-2}
cyclohexane	2.5303	3.8499	278.11	-	34.07
carbon dioxide	1.5131	3.1869	163.33	4.4	2.327

The stabilized DGT algorithm proposed by *Mu et al.* [477] was employed to obtain the equilibrium density profiles $\rho_i(z)$ of both components connecting the bulk phases, which

is numerically robust and avoids choosing a reference component, which has numerical pitfalls [378]. The domain length was set to 12 nm with a spatial discretization of 0.02 nm.

The surface tension γ was calculated from

$$\gamma = \int \sum_{i=1}^{2} \sum_{j=1}^{2} \kappa_{ij} \nabla \rho_i \nabla \rho_j \; \mathrm{d}z \,. \tag{121}$$

7.2.3.2 PCP-SAFT Equation of State

The PCP–SAFT equation of state [221, 223], which is an extension of the original SAFT EOS of *Chapman et al.* [100–102], was used in this work for describing the Helmholtz energy in DGT. It was also used for the computation of phase equilibria of the studied systems, the density differences $\Delta\rho$ used in the pendant drop method (cf. Eq. (114)), and the calculation of the chemical potential of CO_2 in the mixture (cf. Eq. (115)). The details of the EOS are described elsewhere [221, 223].

For non-associating components, as the ones that are studied here, the PCP-SAFT EOS has four pure component parameters: the segment number m, the segment diameter σ, the segment dispersion energy ε, and the quadrupole moment Q. The pure component parameters for cyclohexane and CO_2 were taken from the literature [221, 223] and are summarized in Table 23. Carbon dioxide was modeled as a component with a quadrupole moment. Cyclohexane was described with the dispersion and chain term, cf. Table 23. The pure component models were adjusted in Refs. [221, 223] such as to yield a good description of the saturated liquid density and the vapor pressure [221, 223].

The modified combination rules of Lorentz and Berthelot presented in Eq. (117) and (118) were also used in the PCP-SAFT equation of state. The binary interaction parameter $\xi_{CO_2,C_6H_{12}}^{\mathrm{EOS}} = 0.945$ was fitted in the present work to experimental data [14, 166, 721] of the vapor-liquid equilibrium at $T = 333.15\,\mathrm{K}$.

The molecular models employed for the molecular dynamics simulations and those employed for the PCP-SAFT and DGT calculations are summarized in Table 24.

7.2.4 Interfacial Properties Derived from Density Profiles

Molecular simulations and density gradient theory yield the component density profiles $\rho_i(z)$ across the vapor-liquid interface on a nanoscopic scale. On the basis of the density profiles of both pure components, the relative adsorption $\Gamma_{CO_2}^{(C_6H_{12})}$ and enrichment E_{CO_2} of CO_2 at the interface as well as the interfacial thickness L_{10}^{90} were computed. The equations are reported in section section 3.3.2.2; Eq. (44) - (46). Also the computation of the corresponding statistical uncertainties performed in this study is described in section 3.3.2.2. Section 3.3.2.2 also comprises a brief discussion on the relation of the relative adsorption and enrichment and computational aspects.

For both MD and DGT, the origin on the z-axis of the interfacial profiles was chosen here such that $\rho_{\mathrm{tot}}(z) = 0$ at $\rho_{\mathrm{tot}} = \rho_{\mathrm{tot}}'' + 0.5\,(\rho_{\mathrm{tot}}' - \rho_{\mathrm{tot}}'')$.

Table 24: Overview of models used in the present work. The column MD indicates the employed force fields, the column PCP-SAFT the respective EOS models. The column κ_{DGT} reports the DGT influence parameter used. The first and second lines give the pure component models, the third line the cross interaction.

	Force field	PCP-SAFT	DGT influence parameter κ
cyclohexane	*Merker et al.* [449]	*Gross & Sadowski* [223]	*Niño-Amézquita* [503]
CO2	*Merker et al.* [448]	*Gross* [221]	*Niño-Amézquita* [500]
cyclohexane + CO2	*Merker et al.* [449]	this work	Eq. (120)

7.3 Results and Discussion

First, the results for the pure components are discussed (vapor-liquid equilibrium and interfacial properties) and subsequently the results for the binary mixture. The numeric values of all results from this work (pendant drop experiment, MD, and DGT) are reported in the Appendix.

7.3.1 Results for the Pure Substances

7.3.1.1 Bulk Properties

Fig. 85 shows the vapor-liquid equilibrium of the two pure substances cyclohexane and carbon dioxide. Both the vapor pressure and the saturated densities from both components are shown. The results from the molecular models (MD force field and PCP-SAFT model) are compared with correlations of experimental data from *Span and Wagner* [620, 622]. These correlations are reported to agree with experimental data within the following range [620, 622]: the absolute average deviation for cyclohexane is at least 0.2% for the vapor pressure and 0.3% for the saturated liquid density [622]; and for carbon dioxide 0.006% for the vapor pressure, 0.01% for the saturated liquid density, and 0.01% for the saturated vapor density [620]. It is known that the critical pressure is not represented well by the reference EOS of cyclohexane [622], cf. Fig. 85.

The results obtained from the MD force fields and the PCP-SAFT models agree excellently with the reference correlations. The absolute average deviations of the PCP-SAFT models and experimental data are: for cyclohexane: 0.5% for the vapor pressure and 3.1% for the saturated liquid density [223]; and for carbon dioxide: 0.3% for the vapor pressure and 1.3% for the saturated liquid density [221], excluding the region in the vicinity of the critical point.

The molecular simulation results from this work are in excellent agreement with results reported in the literature for the same force fields [448, 449, 704, 708], i.e. the results agree within their statistical uncertainties. The agreement of the results obtained with the force fields for the two pure substances with experimental data has been studied before: for carbon dioxide, the deviations were reported to be below 1.8% for the vapor pressure and 0.4% for the saturated liquid density [448], for cyclohexane the corresponding numbers are 3% for the vapor pressure and 0.4% for the saturated liquid density [449]. This is confirmed by the results from the present work.

The three dashed lines in the plot of Fig. 85 - top indicate the three temperatures that were investigated by all three methods (experiment, MD, and DGT) for the binary mixture of cyclohexane + CO_2: 303.15 K, 333.15 K, and 363.15 K. The experimental value of the critical temperature of cyclohexane is $T_c^{C_6H_{12}}$ = 553.8 K [131]. Hence, the temperatures of the binary mixture investigated with all three methods correspond to reduced temperatures of approximately $T/T_c^{C_6H_{12}}$ = 0.55, 0.6, 0.65.

The experimental critical temperature of CO_2 is 304.2 K [1]. The lowest investigated temperature 303.15 K is thereby slightly below the critical temperature of CO_2. The critical temperature of the molecular force field model was estimated to be 304 K [448]; for the PCP-SAFT model [221] that number is 304.99 K.
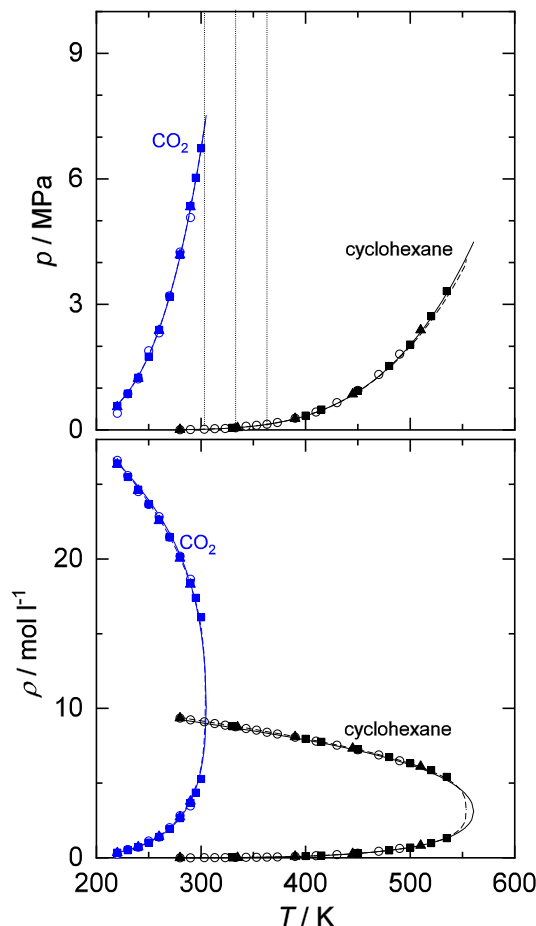
Figure 85: Vapor pressure curves (top) and saturated densities (bottom) of the pure substances cyclohexane (black) and carbon dioxide (blue). The solid lines are the results from the PCP-SAFT EOS. The dashed lines are the correlations of the experimental data [620, 622]. All symbols are MD results: open symbols represent data from this work, filled squares data from *Merker et al.* [449], and filled triangles data from *Werth et al.* [704, 708]. The vertical dashed lines in the upper plot indicate the three temperatures (303.15 K, 333.15 K, and 363.15 K) for which data of the binary mixture was taken with all three methods (experiments, MD, and DGT) in the present work.

7.3.1.2 Interfacial Properties

Fig. 86 shows the surface tension (top) and interfacial thickness (bottom) of the vapor-liquid interface of the pure substances cyclohexane and CO$_2$. For the surface tension, data from experiment, MD, and DGT are compared, whereas for the thickness only results from the theoretical methods MD and DGT can be compared. As explained above, no experimental data for the surface tension of pure carbon dioxide was taken in the present work. The surface tension from both cyclohexane and CO$_2$ decreases with increasing temperature and becomes zero at the critical point. The interfacial thickness, on the other hand, increases monotonously and has a pole at the critical point.

The experimental results for the surface tension of cyclohexane from the present work agree with corresponding results from the literature (cf. Table 22) within their scattering.
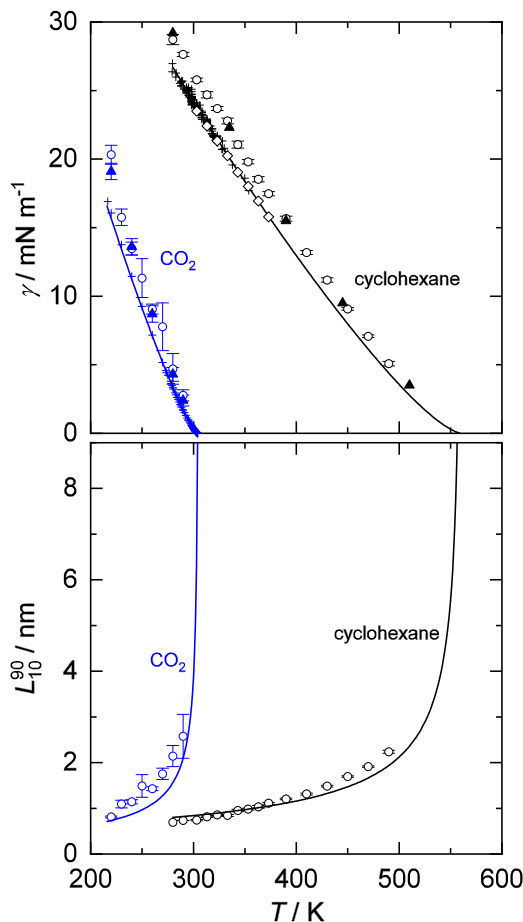
Figure 86: Surface tension (top) and interfacial thickness (bottom) of the pure substances cyclohexane (black) and carbon dioxide (blue). Crosses are experimental data from the literature: Refs. [29, 30, 85, 118, 214, 218, 254, 282, 295, 307, 308, 316, 338, 355, 356, 427, 469, 556, 564, 574, 610, 648, 670, 680, 681, 696, 718, 719, 733] for cyclohexane and Refs. [24, 485, 557] for CO_2. The solid lines are the results from DGT (this work). Open symbols are results from this work: open diamonds are results from the pendant drop experiment which were only carried out for cyclohexane; open circles are MD results. Filled triangles are results from *Werth et al.* [704, 705, 708].

The surface tension obtained from DGT agrees excellently with experimental data, for both cyclohexane and CO_2, since such data was used for the parametrization of the DGT influence parameter κ [500, 503]. For both substances, the molecular dynamics simulation results systematically overestimate the surface tension, which has already been reported by *Werth et al.* [704, 705, 708] for both employed force fields. These deviations might be related to the parameterization strategy employed for the force field development (see section 7.2.2), i.e. the surface tension was not considered during the parametrization. However, the results for the surface tension obtained in the present work agree very well with MD results from the literature [704, 705, 708].

For the interfacial thickness, the results obtained from MD and DGT agree qualitatively well. Nevertheless, for most temperatures, the MD results exceed those from DGT, which is likely due to the fluctuations, which are present in MD but not in DGT [637].

7.3.2 Results for the Mixture Cyclohexane + CO$_2$

7.3.2.1 Bulk Properties

Fig. 87 shows isothermal $p - x$ phase diagrams of the binary mixture cyclohexane + CO$_2$ at 303.15 K, 333.15 K, and 363.15 K. Experimental data from the literature (cf. Table 21) are compared with molecular simulation data from this work and the PCP-SAFT EOS. As discussed above, CO$_2$ is still subcritical at $T = 303.15$ K, which is described correctly by the EOS.
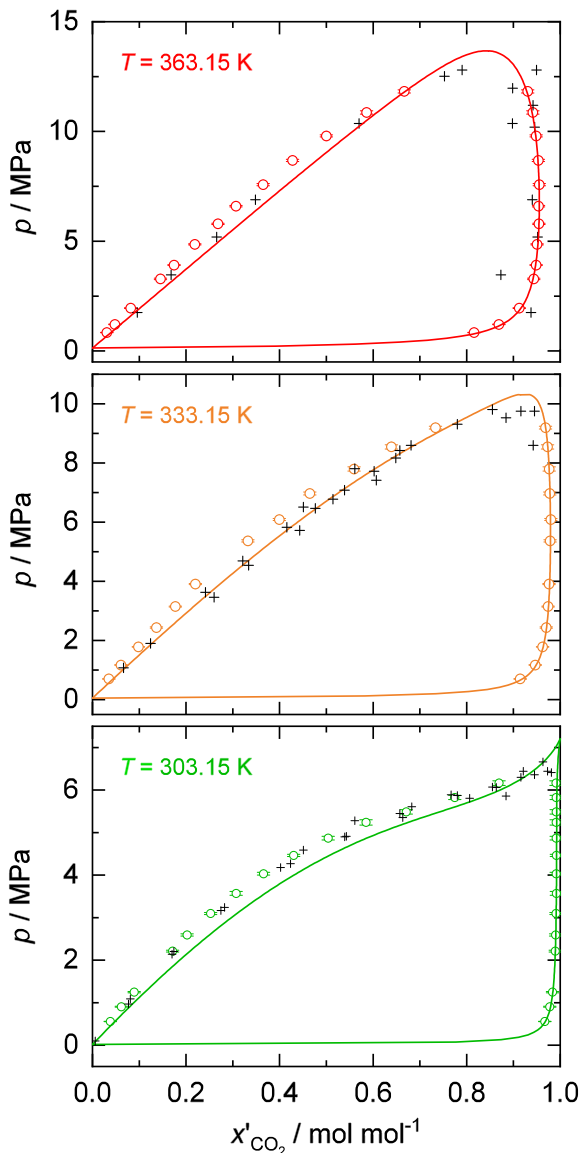
Figure 87: Vapor-liquid equilibrium of the system cyclohexane + CO$_2$ at three temperatures. The solid lines are PCP-SAFT results and the open circles are MD simulation results obtained in this work; the crosses indicate experimental data from the literature: 303.15 K (Refs. [151, 166, 309, 730]), 333.15 K (Refs. [14, 166, 721]), and 363.15 K (Refs. [481, 605]).

Overall, EOS and MD results agree well with the experimental data. For both theoretical methods, the agreement with the experimental data is better for the dew line than

for the bubble line. At 303.15 K, the molecular simulation results agree excellently with the experimental bubble line data while the PCP-SAFT EOS results show some deviations, whereas at 333.15 K, these trends are inversed: the EOS agrees very well with experimental bubble line data while the MD simulation results show some deviations. The good agreement of the results from the EOS model with the experimental data at 333.15 K is due to the fact that it was used for the fitting of $\xi^{\text{EOS}}_{\text{CO}_2,\text{C}_6\text{H}_{12}}$. For both temperatures where CO_2 is supercritical, the PCP-SAFT EOS overestimates the critical pressure, as it is usually observed for classical EOS. The PCP-SAFT EOS yields an absolute average deviation for the equilibrium pressure from the available experimental data at the three studied temperatures of 5.2%.

7.3.2.2 Surface Tension

The surface tension for the binary system cyclohexane + CO_2 was determined with the pendant drop method at eight temperatures between 303.15 K and 373.15 K in intervals of 10 K and pressures up to 6 MPa. The numeric values of all experimental data is reported in the Appendix. DGT and MD calculations were only carried out at three temperatures (303.15 K, 333.15 K, and 363.15 K), cf. Fig. 85.
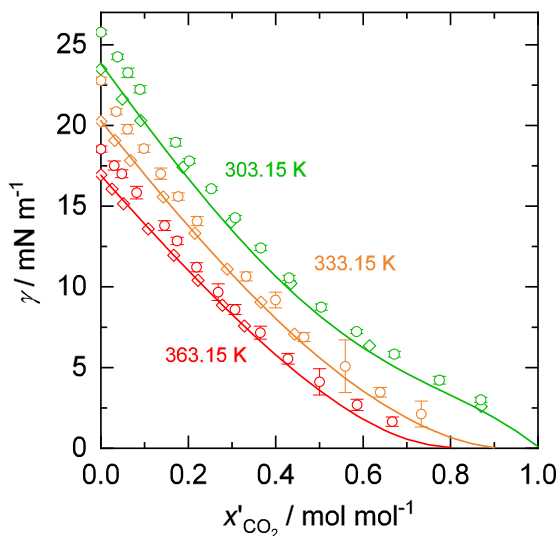
Figure 88: Surface tension of the system cyclohexane + CO_2 as a function of the liquid phase mole fraction of carbon dioxide x'_{CO_2} at three temperatures (indicated by the color). The lines are DGT results, circles are MD results, and diamonds are results from the pendant drop experiments. For T = 303.15 K and $x'_{\text{CO}_2} = 1\,\text{mol}\,\text{mol}^{-1}$, the DGT yields $\gamma_{\text{DGT}} = 0.0983\,\text{mN}\,\text{m}^{-1}$.

Fig. 88 shows results for the surface tension obtained in this work for the temperatures 303.15 K, 333.15 K, and 363.15 K. Results from all three employed methods (pendant drop experiment, MD, and DGT) are shown. Experimental data on the surface tension in the system cyclohexane + CO_2 has been reported previously by *Nagarajan & Robinson* [487] and *Yang et al.* [722]. Their data is compared to results from the present work in section 7.3.2.4. The data from *Nagarajan & Robinson* [487] is found to be in good agreement with our results, whereas the data of *Yang et al.* [722] systematically deviates from our results.

The surface tension of the binary mixture decreases with increasing liquid phase mole fraction of carbon dioxide x'_{CO_2} and with increasing temperature. For high concentrations of CO$_2$, the surface tension of the binary mixture exhibits an interesting feature: above the critical temperature of CO$_2$, the surface tension isotherms have a convex shape close to the critical point, as it is observed in many systems of the type solvent + supercritical solute. However, for the subcritical isotherm at 303.15 K, the surface tension of the mixture exhibits a concave shape at high CO$_2$ concentrations x'_{CO_2}. This behavior is described well by both molecular simulations and DGT.

The DGT surface tension results agree very well with the experimental data from the present work. The absolute average deviation is approximately 1.8% for the data shown in Fig. 88, which confirms the assumption of using a geometric mixing for the influence parameter, cf. Eq. (120). The molecular simulation results systematically overestimate the surface tension of the binary mixture obtained from DGT by approximately 13% in the entire temperature and composition range, which is due to the deviations already present in the pure substances surface tension, cf. Fig. 86.

7.3.2.3 Nanoscopic Interfacial Properties

Nanoscopic interfacial properties were studied with MD and DGT. Fig. 89 shows the density profiles in the vapor-liquid interface obtained from MD and DGT at three state points at high CO$_2$ concentrations and temperature of 303.15 K, 333.15 K, and 363.15 K. In all cases, starting in the bulk vapor phase, the component density of cyclohexane $\rho_{C_6H_{12}}(z)$ increases monotonously towards the liquid bulk phase, whereas the component density of carbon dioxide $\rho_{CO_2}(z)$ exhibits a distinct maximum in the interfacial region, i.e. there is an enrichment. Such an enrichment of low-boiling components at vapor-liquid interfaces has been reported many times in the literature, e.g. [56, 57, 91, 122, 126, 130, 173, 184, 192–195, 305, 361, 362, 372, 373, 379, 390, 391, 412, 446, 483, 492, 522, 533, 551, 552, 583, 604]. A review of enrichment data at vapor-liquid interfaces available in the literature is given in chapter 9.

Overall, the results from MD and DGT show excellent agreement. However, small differences may be pointed out. Since the liquid phase composition was prescribed for the calculations shown in Fig. 89, the densities from MD and DGT + PCP-SAFT match very well in the liquid bulk phase. The minor differences for the gas phase simply stem from differences in the description of the bulk VLE data (cf. Fig. 87).

The MD simulations predict a slightly larger interfacial width compared to the results from DGT. This is due to the fluctuations of the interface, which are present in MD, whereas in DGT the surface is always perfectly flat – as already discussed for the pure substances, cf. Fig. 86. Considering the fact that both methods are independent predictions for the mixture, the density profiles obtained from both methods agree remarkably well.

The adsorption of carbon dioxide increases with decreasing temperature, which agrees well with findings for similar systems, cf. section 3.6 and Refs. [50, 362, 705]. The interfacial thickness, on the other hand, decreases with decreasing temperature.

It has been shown in a recent work of our group that the difference of the bulk density of the low-boiling component $\Delta\rho_{CO_2} = \rho'_{CO_2} - \rho''_{CO_2}$ has an important influence on the
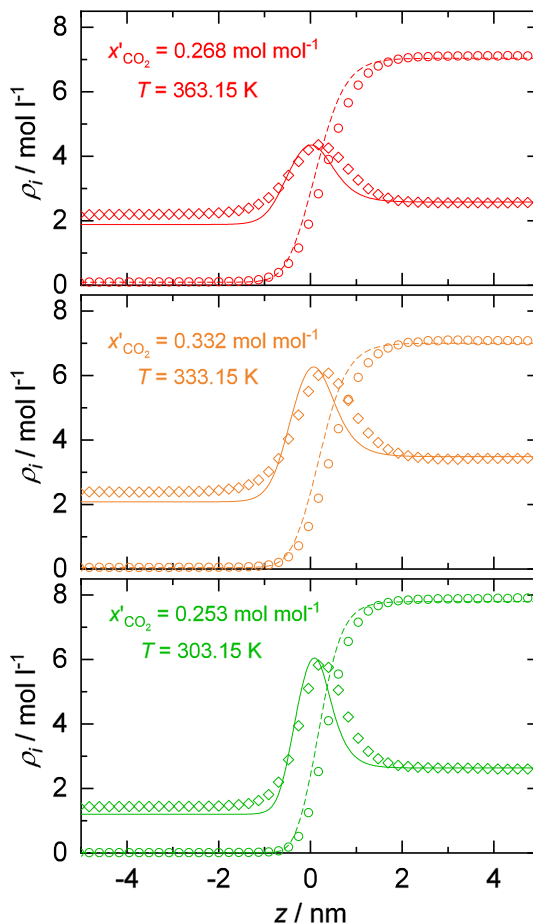
Figure 89: Component density profiles of cyclohexane and CO_2 at the vapor-liquid interface of their binary mixture. Each plot shows one state point. Symbols are MD simulation results, lines are DGT results. Diamonds and solid lines represent CO_2; circles and dashed lines are cyclohexane.

enrichment, cf. section 3.4 [630]. According to that, $\Delta\rho_{CO_2} \approx 0$ favors an enrichment, since the relative adsorption (cf. Eq. (44)) must always result in an enrichment in that case. For the binary mixture cyclohexane + CO_2 investigated in the present work, $\Delta\rho_{CO_2} > 0$ holds in the entire considered temperature range.

Fig. 90 shows the density profiles obtained from DGT in the entire composition range at the three temperatures 303.15 K, 333.15 K, and 363.15 K. The corresponding plots for the MD results are shown in the Supplementary Material. The state points depicted in Fig. 90 are the same as for the MD results in the Appendix. For all state points, the agreement between the MD and the DGT results is similar to that found for the examples shown in Fig. 89.

For all state points, the high-boiling component cyclohexane exhibits a monotonous transition from the vapor to the liquid bulk phase and the low-boiling component CO_2 exhibits a maximum at the interface. The interfacial width increases with increasing mole fraction x'_{CO_2} and with increasing temperature. The adsorption of CO_2 increases with x'_{CO_2} but decreases with increasing temperature.

The position of the density maximum z_{max} exhibits an interesting behavior with varying x'_{CO_2}: at T = 363.15 K, the position of the maximum in the CO_2 density profile is
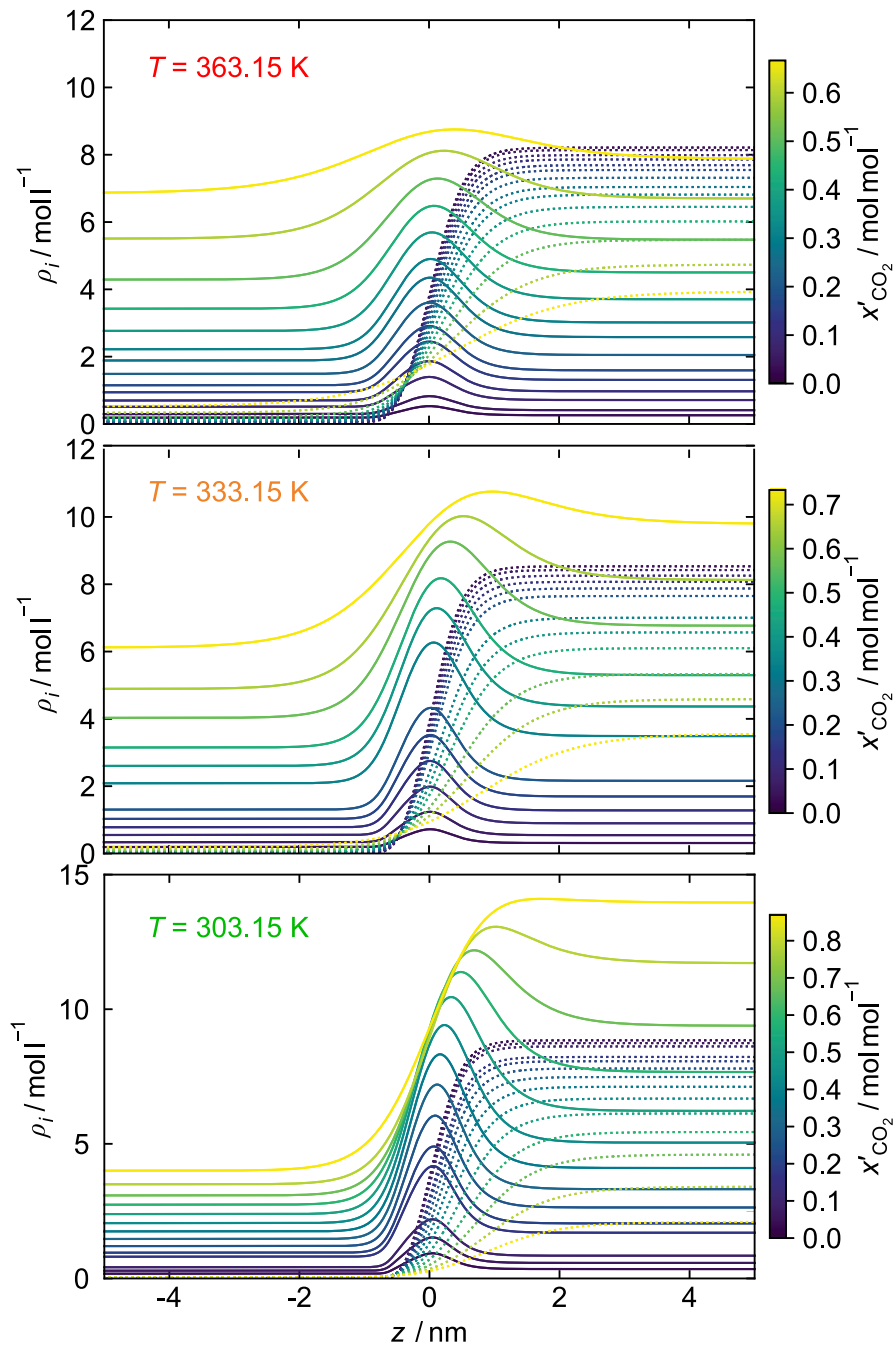
Figure 90: Density profiles of cyclohexane and CO_2 at the vapor-liquid interface of binary mixtures of these components for three temperatures: 303.15 K (bottom), 333.15 K (middle), and 363.15 K (top) and different compositions of the bulk liquid phase (indicated by the colors). Results from DGT. Dashed lines are cyclohexane; solid lines are CO_2.

found at approximately $z_{\max} = 0$ for all studied x'_{CO_2}. On the contrary, at 333.15 K and 303.15 K, starting at low concentrations of CO_2, the maximum moves towards the liquid bulk phase, i.e. $z_{\max} > 0$, with increasing x'_{CO_2}. This is an indication for a decreasing adsorption with increasing x'_{CO_2}. Evidently, this finding is linked to our choice of the definition of $z = 0$, cf. section 7.2.4.

Fig. 91 - top shows results for the relative adsorption of CO_2 at the vapor-liquid interface $\Gamma_{CO_2}^{(C_6H_{12})}$. The relative adsorption $\Gamma_{CO_2}^{(C_6H_{12})}$ computed from the nanoscopic density profiles (MD and DGT) via the symmetric interface segregation presented in Eq. (44) is compared to the results obtained from the macroscopic relation given by the Gibbs adsorption equation (115). The latter are referred to as 'experimental results'.

Overall, the results obtained from both routes (nanoscopic and macroscopic) agree very well – both qualitatively and quantitatively. The relative adsorption of CO_2 at the vapor-liquid interface is found to be up to 12 $\mu mol\,m^{-2}$, which is in the range of results reported in the literature for similar systems [50, 445, 692].

Starting at infinite dilution of CO_2 in the liquid phase, $\Gamma_{CO_2}^{(C_6H_{12})}$ first increases linearly with increasing x'_{CO_2}, passes through a maximum and drops down to zero towards the critical point. The relative adsorption of CO_2 at the interface increases with decreasing temperature, as discussed for the density profiles in Fig. 90.

As the density profiles obtained from MD and DGT agree very well (cf. Fig. 89), the relative adsorption computed by the integral in Eq. (44) agree also well. However, the MD results are slightly above those from DGT in the linear regime of $\Gamma_{CO_2}^{(C_6H_{12})}(x'_{CO_2})$, whereas they are below those from DGT in the concave regime. However, there is a high statistical uncertainty of the MD results at high x'_{CO_2}. The DGT and the experimental results agree excellently, especially for moderate values of x'_{CO_2}.

The enrichment of CO_2 at the vapor-liquid interface of the binary mixture as obtained from MD and DGT is shown in Fig. 91 - middle. The enrichment of CO_2 is highest at infinite dilution and decreases to unity with increasing x'_{CO_2}. Furthermore, the enrichment decreases with increasing temperature.

The results for the enrichment obtained from MD and DGT agree very well, especially at low x'_{CO_2}. At high x'_{CO_2}, the enrichment predicted by DGT exceeds that predicted by MD.

The fact that the behavior of $E_{CO_2}(T, x'_{CO_2})$ resembles that of the surface tension, cf. Fig. 88, may well be a coincidence, since differing behavior of $E_{CO_2}(T, x'_{CO_2})$ and $\gamma(T, x'_{CO_2})$ has been reported for other mixture types, cf. [184, 635].

The surface excess of CO_2 at the interface is characterized here by the relative adsorption $\Gamma_{CO_2}^{(C_6H_{12})}$ and the enrichment E_{CO_2}. The temperature dependency of $\Gamma_{CO_2}^{(C_6H_{12})}$ and E_{CO_2} are similar: both decrease with increasing temperature. However, the composition dependency of $\Gamma_{CO_2}^{(C_6H_{12})}$ and E_{CO_2} differs strongly: at infinite dilution, the relative adsorption is $\Gamma_{CO_2}^{(C_6H_{12})} = 0$ by definition, whereas the enrichment E_{CO_2} is highest at infinite dilution of CO_2. With increasing x'_{CO_2}, $\Gamma_{CO_2}^{(C_6H_{12})}$ increases until a maximum is reached and then decreases, whereas E_{CO_2} decreases monotonously. This supports the findings from previous work [50, 635], that $\Gamma_{CO_2}^{(C_6H_{12})}$ and E_{CO_2} contain different information even though both describe the surface excess of the low-boiling component.
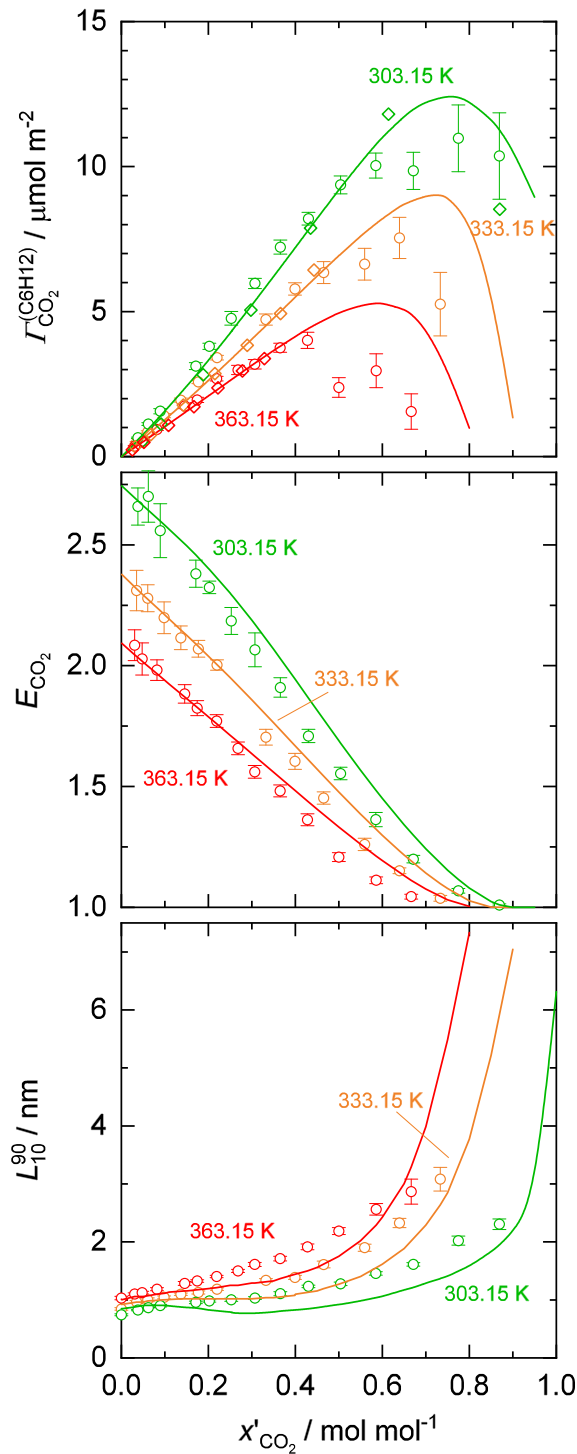
Figure 91: Relative adsorption (top) and enrichment (middle) of CO_2 at the vapor-liquid interface and it's thickness (bottom) as a function of the liquid phase mole fraction x'_{CO_2} in the system cyclohexane + CO_2. Results for three temperatures (indicated by the color). The lines are DGT results, circles are MD results, and diamonds are results from the pendant drop experiment (only available for $\Gamma^{(C_6H_{12})}_{CO_2}$). The MD and DGT results were calculated from the density profiles via Eq. (44); the experimental results were calculated from the macroscopic definition Eq. (115).

The results for the interfacial thickness L_{10}^{90} of the vapor-liquid interface as defined by Eq. (46) are shown in Fig. 91 - bottom. As for the enrichment, results are only available from the theoretical methods MD and DGT.

Adding CO_2 to cyclohexane at constant temperature first leads to a moderate increase of the interfacial thickness, followed by a steep increase as the critical point is approached. Hence, the composition dependency of L_{10}^{90} for the binary mixture is similar to the temperature dependency of L_{10}^{90} of the pure components. The interfacial thickness of the binary mixture also increases with increasing temperature.

For the lowest investigated temperature 303.15 K, the interfacial thickness obtained from DGT shows an unexpected anomaly that is, however, not found in the results from MD: the curve $L_{10}^{90}(x'_{CO_2})$ has a wiggle in the region of low x'_{CO_2} before the continuous increase of L_{10}^{90} sets in. These calculations were confirmed using the reference density DGT method. The maximum/ minimum of the interfacial thickness might be due to the specific phase behavior at 303.15 K (CO_2 is subcritical and cyclohexane is close to it's triple point temperature). The mathematical form of the PCP-SAFT equation is known to yield artifacts in the metastable and unstable region at low temperatures, cf. chapter 4 [639]. This might be related to the anomaly that was observed here in the DGT results. Apart from this difference, the results from MD and DGT agree qualitatively well, but the molecular simulations yield a larger interfacial thickness for most state points as discussed already for the pure substances.

7.3.2.4 Comparison with Experimental Data from the Literature

Saturated Densities in the Binary Mixture of Cyclohexane + CO_2

The density difference of the saturated phases $\Delta\rho = \rho' - \rho''$ of the binary mixture cyclo-hexane + CO_2 is shown in Fig. 92. Results from the PCP-SAFT EOS are compared with experimental data from the literature (cf. Table 21). Experimental data is available in Refs. [346, 487, 606] for five temperatures. The results obtained from the PCP-SAFT EOS agree very well with the experimental data from *Nagarajan & Robinson* [487] and *Shibata & Sandler* [606] – except in the vicinity of the critical point. The data from *Krichevskii & Sorina* [346] deviates significantly from the PCP-SAFT results in the entire composition range. The absolute average deviation from the results of Refs. [487, 606] and the PCP-SAFT EOS are better than 3% – when the direct vicinity of the critical point is excluded.
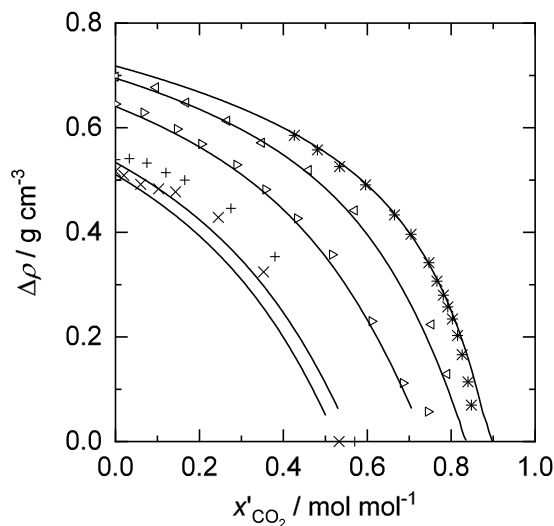
Figure 92: Difference between the saturated liquid and vapor density $\Delta\rho = \rho' - \rho''$ of the binary mixture cyclohexane + CO_2. Experimental data from the literature (symbols) is compared with results obtained from the PCP-SAFT EOS (lines). Experimental data are from *Nagarajan & Robinson* [487] ($*$ 344.3 K), *Shibata & Sandler* [606] (◁ 366.5 K and ▷ 410.9 K), and *Krichevskii & Sorina* [346] (+ 473.15 K and × 483.15 K).

Surface Tension in the Binary Mixture of Cyclohexane + CO_2

The surface tension results obtained in the present work for the mixture cyclohexane + CO_2 are compared to the available data from the literature in Fig. 93. Surface tension data of mixtures of cyclohexane and CO_2 is available at four temperatures in the literature [487, 722], cf. the four plots in Fig. 93. At three of those four temperatures experiments were also carried out in the present work. The surface tension at all four temperatures was computed by DGT as described in section 7.2.3 and compared with the literature data.

For $T \cong 344\,K$, the surface tension results from the present work and the data of *Nagarajan & Robinson* [487] agree well. The surface tension data reported by *Yang et al.* [722] shows significant systematic deviations from the results obtained in the present work.
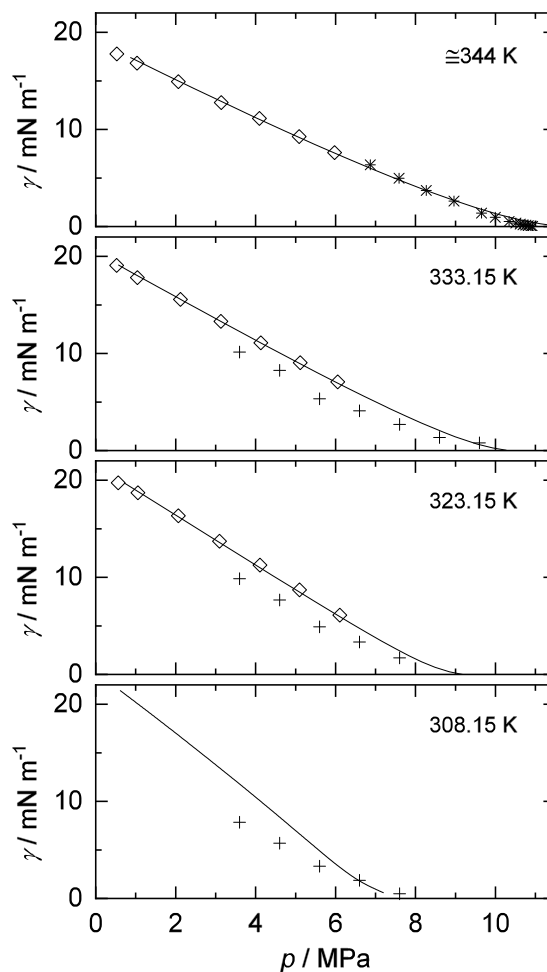
Figure 93: Comparison of experimental data for the surface tension of the system cyclohexane + CO_2 from the literature with results from the present work. All available literature data are shown: ($*$) *Nagarajan & Robinson* [487] and (+) *Yang et al.* [722]. The lines are results from DGT obtained in the present work, ($\diamond$) are experimental results from the present work. In the upper panel, the temperatures are: 343.15 K for ($\diamond$); and 344.23 K for both ($*$) and DGT.

7.4 Conclusions

Interfacial properties of the mixture cyclohexane + CO$_2$ were studied by experiment, molecular dynamics simulations, and density gradient theory in combination with the PCP-SAFT equation of state. Properties that can be determined in experiments were investigated with all three methods (surface tension and relative adsorption). Furthermore, using MD and DGT, the density profiles of the components at the interface were determined and used for calculating the enrichment and the interfacial thickness, which cannot be measured experimentally. The experimental surface tension data obtained from the pendant drop method agrees well with experimental data from the literature for pure cyclohexane. For mixtures of cyclohexane with CO$_2$, two sets of data were available, which, however, do not agree. The present data confirms that of *Nagarajan & Robinson* [487]. The results for the surface tension of the mixture obtained from DGT + PCP-SAFT agrees very well with the experimental data. The model was adjusted to bulk VLE data of the mixture as well as to pure component data, which included surface tension data. The molecular models of cyclohexane and carbon dioxide that were used for the MD simulations describe the VLE data of the pure components and the mixture (to which they were adjusted) well. The results for the surface tension, which was not used in the adjustment, are systematically too high by about 10 - 15% for both the pure components and the mixture. Similar findings have been reported before by *Werth et al.* [701, 704] for a large number of systems. However, the temperature and composition dependency of the surface tension is predicted well by the MD simulations.

The surface excess of carbon dioxide at the vapor-liquid interface was quantified using the relative adsorption $\Gamma_{\text{CO}_2}^{(\text{C}_6\text{H}_{12})}$ and the enrichment E_{CO_2}. The experimental data for the relative adsorption was obtained from the experimental data for the surface tension in the Gibbs adsorption equation and the chemical potential from the PCP-SAFT EOS, whereas the data for the relative adsorption from MD and DGT were determined from the nanoscopic density profiles at the vapor-liquid interface. The results for the relative adsorption of CO$_2$ obtained from the macroscopic and nanoscopic route agree very well.

As the enrichment of CO$_2$ at the interface is not accessible by experiment, it was determined by MD and DGT only. The predictions of the enrichment from both methods are in excellent agreement. Even though $\Gamma_{\text{CO}_2}^{(\text{C}_6\text{H}_{12})}$ and E_{CO_2} characterize the surface excess of the low-boiling component, both properties show important differences: starting at infinite dilution of CO$_2$ in cyclohexane, the relative adsorption $\Gamma_{\text{CO}_2}^{(\text{C}_6\text{H}_{12})}$ increases with increasing mole fraction of CO$_2$ in the liquid phase x'_{CO_2}, passes through a maximum and decreases to zero at the critical point. The enrichment E_{CO_2}, on the other hand, is highest at infinite dilution of CO$_2$ and monotonously decreases with increasing x'_{CO_2}.

The detailed study of the system cyclohexane and CO$_2$ that was carried out here shows that interfacial properties of mixtures can be predicted well both by MD and DGT if models are used that are suitably parameterized using pure component data and bulk VLE mixture data. However, no mixture data on interfacial properties was needed for the parameterization.

The results from this study support the findings from the chapters 3 and 5 on binary Lennard-Jones model mixtures regarding the interfacial enrichment: the enrichment decreases with increasing temperature and liquid phase concentration of the enriching

component. Furthermore, the considered system cyclohexane + CO_2 exhibits a wide-boiling phase behavior and has a relatively large enrichment – as found for the dispersively interacting model fluids. The behavior of the enrichment in solvent + supercritical solvent systems is further discussed in chapter 9.

8 Enrichment of Components at Vapor-Liquid Interfaces in the Systems Toluene + CO$_2$ and Ethanol + CO$_2$

8.1 Introduction

In fluid separation processes, not only thermodynamic bulk but also interfacial properties play a crucial role. In separation technology, mass transport between phases is a key factor for apparatus design. This transport is accounted for by models like the two-film theory, assuming that the transport resistance in the interface is negligible. If, however, low-boiling components like inert gases are present in the mixture, enrichment of these components at the interface can occur. It is known that surfactants, which also show enrichment at the interface, can reduce mass transfer rates [107, 109, 215, 579]. The same might hold for the enrichment of other chemicals, provided that this enrichment is high enough, cf. section 6. The present work compares results from different systems of the type solvent + supercritical solute.

The enrichment of a component i at the interface is defined as

$$E_i = \frac{\max(\rho_i(z))}{\max\left(\rho_i', \rho_i''\right)} \; , \tag{122}$$

where z is the spatial coordinate perpendicular to the interface, $\max(\rho_i(z))$ is the maximum density of the low-boiling component in the density profile $\rho_i(z)$ and $\max\left(\rho_i', \rho_i''\right)$ the higher of the two bulk densities.

Recent studies from our group on the vapor-liquid interface of several real mixtures and model fluids using theoretical methods (MD and DGT + EOS) yield consistent results and reveal an important enrichment in some cases [50, 624, 635, 705]. Strong enrichment is found at vapor-liquid interfaces in the systems in which one of the components is supercritical. These results indicate that mixtures, which are typical for absorption processes usually show an important enrichment, whereas this is not the case for mixtures that are typically separated by distillation.

In the present study, the enrichment obtained from molecular simulation and DGT + EOS for different systems of the type solvent + supercritical solute are compared. Two real mixtures and a model fluid mixture are considered:

  I) toluene + carbon dioxide,

 II) ethanol + carbon dioxide,

III) binary mixture of Lennard-Jones truncated and shifted (LJTS) fluids.

For describing the real fluids in the molecular simulations, force fields from previous work of our group were used [278, 448, 593, 633]. In the density gradient theory approach, the Perturbed-Chain Statistical Associating Fluid Theory (PC-SAFT) equation of state [223] was used to model the real fluids and the PeTS (Perturbed truncated and shifted) equation of state was used for describing the LJTS fluid [249, 635].

8.2 Modeling and Simulation

8.2.1 Molecular Simulations

Molecular dynamics simulations (MD) of equilibrated systems in which a vapor and a liquid phase are in direct contact were carried out in the NVT ensemble with $N = 16,000$ particles. The *ls1 mardyn* code [506] was used for the simulations, where the equations of motion were solved with the leapfrog integrator with a time step of 1 fs. After an equilibration of at least 500,000 time steps, production ran for at least 2,500,000 time steps. Periodic boundary conditions were used. The simulation box contains a liquid slab in the middle surrounded by two vapor phases on either sides. The temperature was kept constant by velocity-scaling. The numbers of particles of the two components was chosen in such a way that mole fraction of the low-boiling component in the liquid phase varies between about $x_2 = 0.05$ and $x_2 = 0.85 \, \mathrm{mol \, mol^{-1}}$ to investigate the composition dependence of the enrichment. The cut-off radius was 17.5 Å for the real fluids in I) and II), while it was 2.5 σ for the LJTS fluids in III), cf. Refs. [50, 635, 705] for details.

The molecular models consist of Lennard-Jones sites (describing the dispersion and repulsion between the particles) and eventually point multipoles (describing the polarity of the molecule and hydrogen bonding between molecules). Unlike electrostatic interactions, e.g. between charges and quadrupoles, were treated in a physically straightforward way, using the laws of electrostatics. The molecular model of ethanol, carbon dioxide, and toluene were taken from Refs. [278, 448, 593, 633].

The size parameters of the two components in the LJTS model mixture were the same, i.e. $\sigma_{11} = \sigma_{22}$, the ratio of the energy parameters was $\varepsilon_{22}/\varepsilon_{11} = 0.5$, such that component 2 was the low-boiling component. The cut-off radius of the LJTS fluids was $r_\mathrm{c} = 2.5 \, \sigma$. For the representation of the results for the LJTS fluids, reduced variables are used that are based on the size parameter σ and the energy parameter ε of the model [17].

For modeling interactions between unlike Lennard-Jones sites, the modified Lorentz-

Berthelot combining rules were used:

$$\sigma_{ij} = \frac{\sigma_{ii} + \sigma_{jj}}{2} \,, \tag{123}$$

$$\varepsilon_{ij} = \xi_{ij}\sqrt{\varepsilon_{ii}\varepsilon_{jj}} \,. \tag{124}$$

The state-independent binary interaction parameter ξ_{ij} has been adjusted to a single experimental vapor pressure for the systems I) and II) resulting in $\xi_{\text{EtOH,CO2}} = 1.08$ [705] and $\xi_{\text{tolouene,CO2}} = 0.95$ [50]. The binary interaction parameter for the LJTS mixture was set to $\xi_{\text{LJTS}}^{\text{MD}} = 1.0$.

8.2.2 Density Gradient Theory

Density gradient theory describes the continuous change of density in inhomogeneous systems, for example at vapor-liquid interfaces, see e.g. Refs. [82, 124]. Applying density gradient theory requires an equation of state for the Helmholtz free energy A. The so-called influence parameter κ_{ij} describes the influence of the density gradients on the thermodynamic properties, cf. Eq. (125). The basic idea of DGT is the development of the free energy of an inhomogeneous system around the homogeneous equilibrium state in the spatial derivative of the density, cf. Eq. (125). Usually, the series is truncated after the square gradient term [456], which results in

$$A[\underline{\rho}(z)] = S \int_{-\infty}^{\infty} \left[\hat{a}_0(\underline{\rho}(z)) + \frac{1}{2}\sum_j\sum_i \kappa_{ij}\left(\frac{\mathrm{d}\rho_i}{\mathrm{d}z}\right)\left(\frac{\mathrm{d}\rho_j}{\mathrm{d}z}\right) \right]\mathrm{d}z \,, \tag{125}$$

for an inhomogeneous system with a planar interface. Eq. (125) expresses the free energy as a functional of the density profiles $\rho_i(z)$. Here, S is the surface area, $\hat{a}_0$ is the local free energy per volume, and ρ_i is the molar density of component i. The interfacial profiles were determined using the method of Ref. [456]. The pure component influence parameter κ_{ii} is usually fit to experimental surface tension data, e.g. Refs. [502, 503], while a geometric mixing rule is applied for the binary influence parameters:

$$\kappa_{ij} = \sqrt{\kappa_{ii}\kappa_{jj}} \,. \tag{126}$$

The PC-SAFT equation of state [223] was used in the present work for the calculation of the Helmholtz free energy of the real substances and the PeTS EOS for the truncated and shifted Lennard-Jones fluids [249, 635]. The pure component parameters for PC-SAFT were taken from [223] for toluene and carbon dioxide and from Ref. [224] for ethanol. The parameters for the unlike interaction energy ξ_{ij}^{EOS} in the PC-SAFT EOS were taken from Ref. [705] for the toluene + carbon dioxide mixture and from Ref. [50] for the ethanol + carbon dioxide mixture. The unlike energy interaction parameters in the PeTS EOS for the LJTS mixtures have the same value as the one used in the mixing rule of the molecular model, i.e. $\xi_{ij}^{\text{EOS}} = \xi_{ij}^{\text{MD}}$. The influence parameters κ_{ii} for carbon dioxide, ethanol, toluene, and the LJTS fluid were taken from Refs. [50, 160, 705], and Ref. [249], respectively.

8.3 Results and Discussion

Figs. 94, 95, and 96 show results for the binary mixtures toluene + carbon dioxide [705], ethanol + carbon dioxide [50], and the binary LJTS mixture [635]. Results for several further isotherms for the systems toluene + carbon dioxide (as well as toluene + nitrogen) are provided in the electronic Supplementary Material [627, 632].

In Figs. 94, 95, and 96, panel (a) shows the phase behavior, an exemplary density profile is shown in panel (b), and the enrichment of the low-boiling component is depicted as a function of the liquid phase mole fraction of that component in panel (c). Figs. 94 and 95 show that the molecular simulation results are in excellent agreement with the experimental data for the vapor-liquid equilibrium (panels a). The same holds for the PC-SAFT EOS except for the data near the critical point. Fig. 96 (a) shows that the vapor-liquid equilibrium of the LJTS mixture is described very well by the PeTS EOS, although no adjustment of the binary interaction parameter was carried out (as described above, that parameter was simply adopted from the molecular model).

The density profiles in Figs. 94 - 96 (b) reveal that a significant enrichment of the low-boiling component occurs at the interface in all three mixtures. The density profiles predicted by MD and DGT are in good agreement. This is remarkable, as the methods are completely independent. The fact that the peak in the density of the low-boiling component in the interfacial region is slightly broader for MD than for DGT is due to the fluctuations that are present in MD but not in DGT. The composition dependence of the enrichment of the low-boiling component is shown in Figs. 94 - 96 (c). In all systems, the highest enrichment is observed for low concentrations of the low-boiling component. It is about 2.5 for all systems. The results from MD and DGT agree well, although DGT slightly overestimates the enrichment predicted by MD, which is probably again due to the absence of fluctuations in DGT.
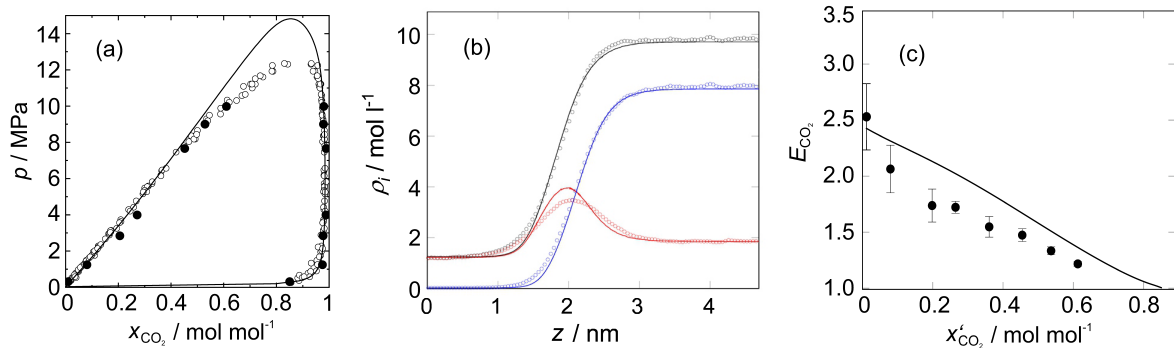
Figure 94: Results for the system toluene + carbon dioxide at 353 K: (a) Phase behavior; empty symbols are experimental data [321, 474, 480, 489, 694] full symbols are molecular simulation results [705], and the solid line is obtained from PC-SAFT. (b) Density profiles for $x'_{CO_2} = 0.2\,\mathrm{mol\,mol^{-1}}$: solid lines are obtained from DGT, symbols are MD results [705]. The black color corresponds to the total density, blue to the toluene density, and red to the carbon dioxide density. (c) Enrichment of carbon dioxide at the interface; solid line corresponds to DGT and symbols to MD results.
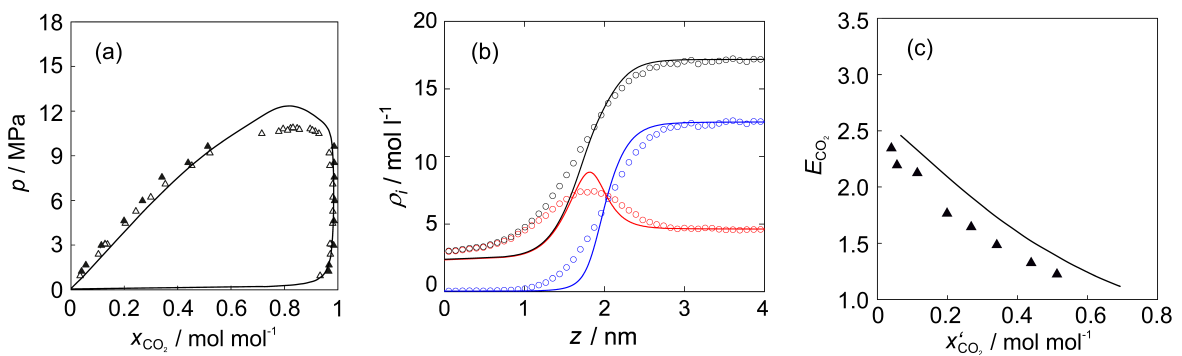
Figure 95: Results for the system ethanol + carbon dioxide at 333 K: (a) Phase behavior; empty symbols are experimental data [597], full symbols are molecular simulation results [50], and the solid line is obtained from PC-SAFT [50]. (b) Density profiles for $x'_{CO_2} = 0.3\,\mathrm{mol\,mol^{-1}}$: solid lines are obtained from DGT, symbols are MD results [50]. The black color corresponds to the total density, blue to the ethanol density, and red to the carbon dioxide density. (c) Enrichment of carbon dioxide at the interface; solid line corresponds to DGT and symbols to MD results.
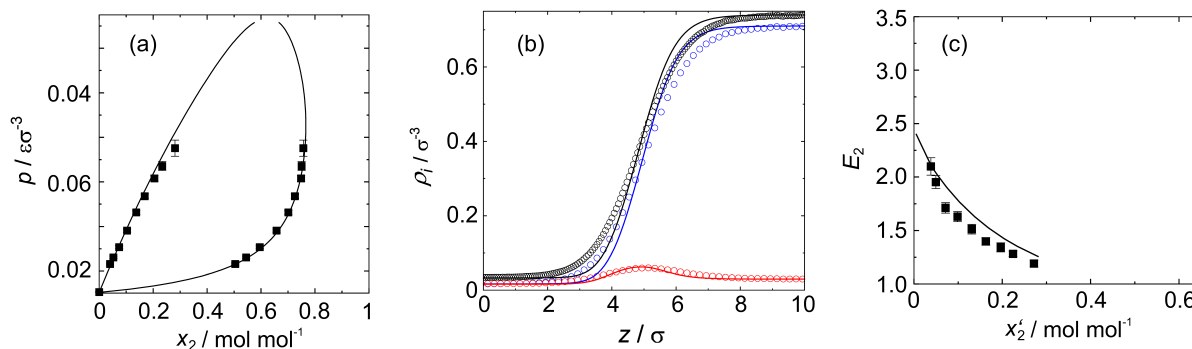
Figure 96: Results for the binary LJTS mixture at $T = 0.7\,T_{\text{c},1}$: (a) Phase behavior; full symbols are molecular simulation results [635], and the solid line is obtained from the PeTS EOS. (b) Density profiles for $x_2' = 0.04\,\text{mol}\,\text{mol}^{-1}$: solid lines are obtained from DGT, symbols are MD results [635]. The black color corresponds to the total density, blue to the component 1 density, and red to the component 2 density. (c) Enrichment of component 2 at the interface; solid line corresponds to DGT and symbols to MD results.

8.4 Conclusions

The observation made for model mixtures in chapter 3 and 5 also hold for real substance mixtures: significant enrichment is found in different systems of the type solvent + supercritical solute. The results show that enrichment is always observed for the low-boiling component but not for the high-boiling component. Interestingly, the behavior of the enrichment in the three discussed systems is very similar – despite the fact that the molecular interactions in the three systems differ significantly: system I) consists of a dispersively interacting aromatic hydrocarbon as solvent and a quadrupolar solute; system II) consists of an associating small solvent molecule and a quadrupolar solvent; and system III) consists of a purely dispersively interacting solvent and solute. Nevertheless, all three mixtures likewise yield an enrichment in the range $1 < E_2 < 2.5$. Furthermore, in all three cases, the enrichment decreases with increasing mole fraction of the low-boiling component in the liquid phase.

Molecular simulation and density gradient theory lead to consistent results for phase equilibria and interfacial behavior. The enrichment predicted by MD and DGT agrees well for all three investigated mixtures. The results show that enrichment of low-boiling components is important at low concentrations of that component in the liquid phase, i.e. for conditions that are typically encountered in absorption fluid separation processes. It is a hypothesis for future work, that this influences mass transfer in absorption and should be accounted for explicitly.

The observations from this study are generalized in chapter 9 by establishing a short-cut method to estimate the enrichment based on phase equilibrium data solely.

9 Enrichment at Vapor-Liquid Interfaces of Mixtures: Establishing a Link between Nanoscopic and Macroscopic Properties

9.1 Introduction

Predictions of the enrichment with theoretical methods is a complex task: for molecular simulations, suitable force fields must be available and time-consuming direct simulations of the interface must be carried out; similarly DGT requires a suitable equation of state together with a parametrization of the gradient term and a DGT code, which is presently not standard in process simulators. Hence, a reliable short-cut method for the estimation of the enrichment would be desirable.

In this study, we review the available literature data on component density profiles at vapor-liquid interfaces, give an account on central points of the existing knowledge on the enrichment, and propose a simple model for the prediction of the enrichment from vapor-liquid equilibrium properties. The literature data is evaluated and the available data on the enrichment is collected in a database that is provided in an electronic form in the Supplementary Material [627]. A comprehensive dataset on the enrichment at vapor-liquid interfaces in simple model mixtures (cf. chapter 3 [629, 630, 635]) was used for the training of the model, which is then tested on all available enrichment data. The predictions from that model are practically within the uncertainties of the computations using molecular thermodynamics, which provides a short-cut method to reliably estimate the enrichment from macroscopic properties instead of using complex theoretical methods such as molecular simulations or DGT.

The present work is limited to the investigation of vapor-liquid interfaces of binary mixtures of molecular fluids. Related work on electrolyte solutions and ionic liquids [96, 287, 290–292, 499, 523, 524], on the behavior of surfactants at interfaces [239, 322, 387, 388, 464, 465], as well as on the enrichment of components at liquid-liquid interfaces [79, 115, 161, 196, 347, 349, 488, 629] is not covered. Since theoretical methods for the prediction of component density profiles, namely molecular simulation, DGT, and DFT have been reviewed in detail elsewhere [167, 168, 209, 357, 573] their description is not subject of this work.

This study is organized as follows: as different terminologies are used in the literature, first, the studied properties are defined. Then, the literature data on the enrichment

of components at vapor-liquid interfaces in binary mixtures is reviewed and discussed. Subsequently, the development and parametrization of the empirical model for the prediction of the enrichment from macroscopic properties is presented, including a brief discussion of the choice of descriptors. Then, the empirical model is tested on available enrichment data from the literature. Finally, conclusions are drawn and options for future developments in the field are discussed.

9.2 Nanoscopic Interfacial Properties: Enrichment and Relative Adsorption

To quantify the non-monotonicity of component density profiles, *Becker et al.* [50] introduced the enrichment $E_i = \frac{\max(\rho_i(z))}{\max(\rho_i', \rho_i'')}$ of a component i at the interface, where $\rho_i(z)$ are the component number density profiles across the vapor-liquid interface, z indicates the direction normal to a (nanoscopically) planar interface, and ρ_i' and ρ_i'' indicate the saturated liquid and vapor densities of component i, respectively. Hence, the enrichment E_i is a dimensionless property and can be therefore favorably used to study both model fluid mixtures as well as real substance mixtures.

The focus of this study is on the investigation of the non-monotonicity of component density profiles $\rho_i(z)$ at vapor-liquid interfaces of mixtures. Two similar effects are not covered: the oscillatory layering structure at fluid interfaces (a structural effect which is also observed for pure components, cf. section 2.4) [169, 170, 204, 637] and the non-monotonic behavior of the total density which is sometimes observed at liquid-liquid and fluid-fluid interfaces [74, 141, 199, 204, 415, 490, 629, 669] (cf. section 3.6). The amplitude of the enrichment, i.e. the peak height of component density profiles $\rho_i(z)$ at vapor-liquid interfaces, is usually significantly larger than the amplitude of the peaks in the aforementioned phenomena. But, it should be noted that the enrichment and the two aforementioned phenomena may be present simultaneously in some situations, cf. Ref. [714].

In this study, vapor-liquid interfaces of binary mixtures are discussed; the low-boiling component is denoted by '2' and the high-boiling component by '1'. By definition, cf. Eq. (122), the enrichment E_i has values equal to or larger than unity. In binary mixtures, an enrichment $E_i > 1$ is only observed for the low-boiling component 2, cf. sections 3.3, 3.4, 3.6, 5.5, 7.3, and 8.3. At least, no contrary evidence has been reported yet to the best of our knowledge. In the case of multicomponent mixtures, a simultaneous enrichment has been reported for several low-boiling components [78, 256, 404, 466, 467, 560, 705].

Fig. 97 shows snapshots of two exemplary mixtures with the corresponding density profiles of component 2: the mixture that is depicted in the top panel of Fig. 97 exhibits an enrichment of the low-boiling component at the vapor-liquid interface, while no enrichment is observed for the mixture shown in the lower panel.

Besides the enrichment E_2, also the relative adsorption $\Gamma_2^{(1)}$ of a low-boiling component 2 with respect to component 1 (blue shaded area in Fig. 97) characterizes the surface excess. $\Gamma_2^{(1)}$ quantifies the number of adsorbed molecules per unit area at the interface, as described in more detail in section 3.2.5 and 7.2. The relative adsorption $\Gamma_2^{(1)}$ can be calculated from macroscopic properties and the nanoscopic density profiles $\rho_i(z)$ [193].
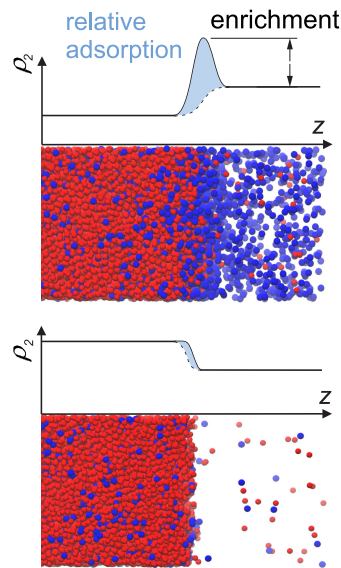
Figure 97: Schemes of vapor-liquid interfaces of two exemplary mixtures. The particles of the high-boiling component 1 are shown in red, those of the low-boiling component 2 in blue. Top: component 2 exhibits an enrichment $E_2 > 1$ and a relative adsorption $\Gamma_2^{(1)} > 0$; Bottom: component 2 exhibits no enrichment $E_2 = 1$ but a relative adsorption $\Gamma_2^{(1)} > 0$. The scheme is based on simulation screenshots from the simulation data from mixture G and A, respectively, cf. section 3.6. For the visualization, the distance of the particles from the image plane is indicated by their transparency.

The relative adsorption $\Gamma_2^{(1)}$ can be determined experimentally – at least indirectly [133, 573]: the Gibbs adsorption equation provides a direct link between macroscopic properties and the relative adsorption, cf. chapter 7. The relative adsorption obtained from that macroscopic route and from its nanoscopic definition, i.e. the integral under the density profiles (cf. Fig. 97), are usually found to be in good agreement [16, 25, 33, 34, 50, 116, 354, 361, 441, 445, 483, 522, 624, 659, 692]. This indicates that the underlying density profiles (including the contribution of the enrichment to $\Gamma_2^{(1)}$, cf. Fig. 97 - top) predicted from theoretical methods are in agreement with the reality.

Comparing the enrichment E_2 and the relative adsorption $\Gamma_2^{(1)}$, it should be noted that only the latter is thermodynamically rigorously defined, in a sense that it can be derived from thermodynamic potentials (see section 7.2), whereas the enrichment was introduced as a simple geometric measure to characterize the surface excess regarding the non-monotonicity of the density profiles.

Even though both $\Gamma_2^{(1)}$ and E_2 characterize the surface excess of the low-boiling component at vapor-liquid interfaces, both properties show important differences, cf. sections 3.3, 3.4, and 7.3. For example for systems solvent 1 + supercritical gas 2: starting at infinite dilution of component 2, the relative adsorption $\Gamma_2^{(1)}$ increases with increasing mole fraction of component 2 in the liquid phase x_2', passes through a maximum and decreases to zero at the critical point of the mixture. The enrichment E_2 in such mixtures, on the other hand, is highest at infinite dilution of component 2 and decreases monotonously with increasing x_2'.

Furthermore, it is not unusual that mixtures exhibit a positive relative adsorption $\Gamma_2^{(1)} > 0$ but no enrichment, i.e. $E_2 = 1$, cf. the results from section 3.3 and 3.6 [629, 635]. Such a case is visualized in Fig. 97 - bottom. Both component density profiles exhibit a monotonic transition across the interface, but the profiles are slightly shifted with regard to one another in z-direction, which causes a positive relative adsorption $\Gamma_2^{(1)} > 0$ – without an enrichment. However, an enrichment $E_2 > 1$ usually favors high relative adsorption $\Gamma_2^{(1)} > 0$, cf. Fig. 97 - top. Hence, both the relative adsorption $\Gamma_2^{(1)}$ and the enrichment E_2 characterize the surface excess and are closely linked, but do not express the same information.

9.3 Review of Literature Data on the Enrichment at Vapor-Liquid Interfaces and Database

There is a large body of studies in the literature (approximately 100 publications) reporting on component density profiles $\rho_i(z)$ at vapor-liquid interfaces of binary mixtures, of which Table 25 gives an overview. The density profiles $\rho_i(z)$ were obtained in these studies from different theoretical methods (molecular simulations, DGT, DFT or a combination of those). Since data on ternary and multicomponent mixtures have been reported relatively scarcely in the literature [78, 190, 196, 255, 256, 312, 342, 384, 404, 456, 457, 466, 467, 560, 728], they are not listed in Table 25.

Studies on the prediction of interfacial properties of mixtures by theoretical methods mostly focus on the prediction of the surface tension, but also often report density profiles and the relative adsorption $\Gamma_2^{(1)}$. In most cases, a qualitative description and discussion of the observations regarding the monotonicity of the component density profiles $\rho_i(z)$ is given in the publications. But those findings are rarely put into relation with other works and to the phase behavior of the considered mixture.

In most publications on vapor-liquid interfacial properties, cf. Table 25, the density profiles are unfortunately only reported for a small subset of the performed simulations (the surface tension is the main observable of interest). Hence, a large number of primary data remained unpublished in this field. The vast majority of studies (cf. Table 25) report the density profiles $\rho_i(z)$ only graphically. The enrichment E_2 according Eq. (122) was rarely computed and reported. For the density profiles, unfortunately no consistent form for plotting the data was established, i.e. sometimes only one of the component density profiles was reported and sometimes all. Electronic data of density profiles was practically never reported.

From the density profiles $\rho_2(z)$ reported in the literature, cf. Table 25, the enrichment E_2 was calculated in the present work. If, as in most cases, $\rho_2(z)$ was only reported graphically in the publication, the data were digitalized [563] and the maximum of the low-boiling component's density profile as well as the larger bulk density were metered from the plots which introduces a considerable uncertainty. To estimate the uncertainty of this 'measuring' process, the digitalization and evaluation was repeated five times and the standard deviation was taken as a measure of the uncertainty due to the digitalization procedure. The average uncertainty of the results for E_2 is approximately $\delta E_2 = \pm 0.1$. The digitalized data $E_2(T, x_2', \Delta\rho_2)$ is reported in an electronic spread sheet in the Supplementary Material [627] where also more details on the procedure are given.

Table 25: Overview of literature data on density profiles at vapor-liquid interfaces of binary mixtures. The vast majority of publications report density profiles only graphically. The density profiles were evaluated in the present work to obtain data on the enrichment E_2. # indicates the number of E_2 data points that could be retrieved from the respective publication. For density profiles from DGT, also the equation of state that was used is specified.

Authors	Year	#	Method	System
Algaba et al. [16]	2019	12	MD	tetrahydrofuran C_4H_8O + methane CH_4
Almeida & Telo da Gama [18]	1989	6	DFT	ethane C_2H_6 + krypton Kr
				ethene C_2H_4 + krypton Kr
				ethane C_2H_6 + ethene C_2H_4
Aracil et al. [25]	1989	10	DFT	carbon disulfide CS_2 + carbon tetrachloride CCl_4
				carbon disulfide CS_2 + dichloromethane CH_2Cl_2
Baidakov & Khotienkova [33]	2016	6	DGT+VDW	methane CH_4 + nitrogen N_2
Baidakov & Protsenko [34]	2008	1	MD	argon Ar + neon Ne
Becker et al. [50]	2016	148	MD & DGT+PC-SAFT	ethanol C_2H_6O + carbon dioxide CO_2
Biscay [56]	2009	2	MC	water H_2O + carbon dioxide CO_2
				water H_2O + hydrogensulfide H_2S
Breure & Peters [72]	2012	7	DGT+PC-SAFT	n-heptane C_7H_{16} + ethylene C_2H_4
				n-pentane C_5H_{12} + methane CH_4
				n-heptane C_7H_{16} + methane CH_4
				n-hexane C_6H_{14} + nitrogen N_2
				n-decane $C_{10}H_{22}$ + nitrogen N_2
Bühl et al. [77]	2016	6	DGT+PC-SAFT	sulfur dioxide SO_2 + carbon dioxide CO_2
				hydrogen sulfide H_2S + carbon dioxide CO_2

Authors	Year	#	Method	System
Cao et al. [86]	2016	1	MD	n-decane $C_{10}H_{22}$ + carbon dioxide CO_2
Carey et al. [89, 91]	1980	1	DGT+PR	isooctane C_8H_{18} + cyclohexane C_6H_{12}
Chang & Dang [95]	2005	3	MD	water H_2O + methanol CH_4O
Chen et al. [105]	2019	1	MD	water H_2O + carbon dioxide CO_2
Choudhary et al. [116]	2019	12	MD & DGT+PR	n-decane $C_{10}H_{22}$ + methane CH_4
				n-decane $C_{10}H_{22}$ + carbon dioxide CO_2
Chow et al. [117]	2016	5	DGT+SAFT-VR Mie	water H_2O + carbon dioxide CO_2
				water H_2O + argon Ar
Cornelisse et al. [122, 123]	1993	7	DGT+PR	n-decan $C_{10}H_{22}$ + carbon dioxide CO_2
Cornelisse [121]	1997	2	DGT+PR	water H_2O + ethanol C_2H_6O
				n-hexane C_6H_{14} + ethanol C_2H_6O
Eckelsbach et al. [152]	2014	3	MD	acetone C_3H_6O + nitrogen N_2
Eckelsback & Vrabec [153]	2015	2	MD	acetone C_3H_6O + oxygen O_2
				acetone C_3H_6O + nitrogen N_2
Enders & Kahl [159]	2008	4	DGT+SAFT	water H_2O + ethanol C_2H_6O
				water H_2O + butanol $C_4H_{10}O$
Fabian et al. [172]	2014	4	MD	water H_2O + hydrogen cyanid HCN
Falls et al. [173]	1983	5	DGT+PR	n-decane $C_{10}H_{22}$ + carbon dioxide CO_2
Fouad and Vega [184]	2017	3	DGT+PC-SAFT	propane C_3H_8 + difluoromethane CH_2F_2
Fu et al. [187]	2011	6	DGT+PC-SAFT	ethanol C_2H_6O + carbon dioxide CO_2
				methanol CH_4O + carbon dioxide CO_2
Garrido et al. [198]	2017	8	MD & DGT+SAFT-VR Mie	n-hexane C_6H_{14} + nitrogen N_2
				n-octane C_8H_{18} + nitrogen N_2
Greberg et al. [219]	2001	2	DGT	krypton Kr + argon Ar

Authors	Year	#	Method	System
Ghobadi & Elliot [205]	2014	4	MD & DFT+SAFT-γ	heptane C_7H_{16} + ethane C_2H_6
Horváth et al. [276]	2019	7	MD	water H_2O + methylamine CH_3N_2
Ibarra-Tandi et al. [285]	2013	1	MD	Morse fluid + Morse fluid
Kahl & Enders [305]	2002	3	DGT+SAFT	n-hexane C_6H_{14} + methanol CH_4O
Kahl et al. [306]	2005	1	DFT	methane CH_4 + argon Ar
Khosharay et al. [317]	2014	4	DGT+sPC-SAFT	water H_2O + carbon dioxide CO_2 water H_2O + hydrogen sulfide H_2S
Khosharay et al. [318]	2014	2	DGT+PR	dufluoroethane $C_2H_4F_2$ + propane C_3H_8 dufluoroethane $C_2H_4F_2$ + pentafluorethan C_2HF_5
Khosharay et al. [320]	2014	2	DGT+CK-SAFT	water H_2O + carbon dioxide CO_2 water H_2O + methane CH_4
Khosharay et al. [319]	2016	2	DGT+PR	propane C_3H_8 + methane CH_4 heptane C_7H_{16} + methane CH_4
Klink & Gross [328]	2014	5	DFT+PC-SAFT	methane CH_4 + carbon monoxide CO
Koller et al. [336]	2019	4	MD	n-hexane C_6H_{14} + carbon dioxide CO_2 n-decane $C_{10}H_{22}$ + carbon dioxide CO_2 1-hexanol $1\text{-}C_6H_{14}O$ + carbon dioxide CO_2
Kou et al. [342]	2015	3	DGT+PR	n-decane $C_{10}H_{22}$ + methane CH_4
Lafitte et al. [354]	2010	2	DGT+SAFT-VR Mie	water H_2O + carbon dioxide CO_2
Lee et al. [361]	1984	12	MD & DFT	krypton Kr + argon Ar
Lee et al. [362]	1985	33	MD	Lennard-Jones + Lennard-Jones
Li et al. [373]	2008	4	DGT+PC-SAFT	water H_2O + carbon dioxide CO_2
Li & Jin [372]	2019	11	MD	water H_2O + methane CH_4 water H_2O + ethane C_2H_6

Authors	Year	#	Method	System
Li et al. [374]	2019	2	MD	water H_2O + propane C_3H_8 isobutane C_4H_{10} + 2,3,3,3-tetrafluoropropene $C_3H_2F_4$ isobutane C_4H_{10} + 1,3,3,3-tetrafluoropropene $C_3H_2F_4$
Lin et al. [379]	2007	8	DGT+PR & DGT+SRK	1,1,1,2-tetrafluoroethane $C_2H_2F_4$ + difluoromethane CH_2F_2 difluoromethane CH_2F_2 + R227ea C_3HF_7 krypton Kr + methane CH_4 n-decane $C_{10}H_{22}$ + carbon dioxide CO_2
Liu et al. [386]	2009	3	DGT+PC-SAFT	n-pentane C_5H_{12} + nitrogen N_2
Llovell et al. [390]	2010	13	DFT+SAFT-VR	square well monomer + square well chain propane C_3H_8 + methane CH_4 n-decane $C_{10}H_{22}$ + methane CH_4
Llovell et al. [389]	2012	5	DFT+SAFT-VR	n-pentane C_5H_{12} + methane CH_4 n-heptane C_7H_{16} + methane CH_4 n-butane C_4H_{10} + carbon dioxide CO_2 n-decane $C_{10}H_{22}$ + carbon dioxide CO_2 n-tetradecane $C_{14}H_{30}$ + carbon dioxide CO_2
Lobanova et al. [391]	2016	5	MD	water H_2O + carbon dioxide CO_2 water H_2O + n-hexane C_6H_{14} n-pentadecane $C_{15}H_{32}$ + carbon dioxide CO_2
Mairhofer & Gross [404]	2017	2	DFT & DGT+PCP-SAFT	ethanol C_2H_6O + n-hexane C_6H_{14}
Martínez-Ruiz & Blas [412]	2016	27	MC	square well + square well
Matsumoto [419]	1996	3	MD	water H_2O + carbon dioxide CO_2 water H_2O + sulfur dioxide SO_2 water H_2O + methanol CH_4O

Authors	Year	#	Method	System
Mecke et al. [441]	1999	1	MD	krypton Kr + argon Ar
Mejía et al. [446]	2005	14	MD & DGT+soft SAFT	Lennard-Jones + Lennard-Jones
Mejía et al. [445]	2014	8	MD & DGT+SAFT-VR Mie	n-decane $C_{10}H_{22}$ + carbon dioxide CO_2
				n-eicosane $C_{20}H_{42}$ + carbon dioxide CO_2
Míguez et al. [453]	2014	9	MC & DGT+SAFT-γ Mie	water H_2O + carbon dioxide CO_2
Miqueu et al. [459]	2011	6	MC & DGT+SAFT-VR Mie	water H_2O + methane CH_4
Miqueu et al. [458]	2004	4	DGT+PR	n-decane $C_{10}H_{22}$ + methane CH_4
Morita [471, 472]	2003	1	MD	water H_2O + methanol CH_4O
Mu et al. [477]	2017	2	DGT+PC-SAFT	propane C_3H_8 + methane CH_4
Mucha et al. [478]	2003	3	MD	krypton Kr + argon Ar
Müller & Mejía [483]	2009	18	MD & DGT+SAFT	n-decane $C_{10}H_{22}$ + cyclohexane C_6H_{12}
				n-decane $C_{10}H_{22}$ + carbon dioxide CO_2
				n-eicosane $C_{20}H_{42}$ + ethane C_2H_6
Müller & Mejía [484]	2014	1	MD	water H_2O + carbon dioxide CO_2
Naeiji et al. [486]	2019	3	MD	water H_2O + methane CH_4
Neyt et al. [493]	2012	4	MC	n-butane C_4H_{10} + carbon dioxide CO_2
				n-decane $C_{10}H_{22}$ + carbon dioxide CO_2
Neyt et al. [492]	2013	2	MD	water H_2O + methane CH_4
				water H_2O + nitrogen N_2
Niño-Amézquita et al. [502]	2010	4	DGT+PR	n-heptane C_7H_{16} + carbon dioxide CO_2
Niño-Amézquita et al. [504]	2012	3	DGT+PC-SAFT	water H_2O + carbon dioxide CO_2
Niño-Amézquita et al. [503]	2010	4	DGT+PC-SAFT	n-heptane C_7H_{16} + methane CH_4
Niño-Amézquita & Enders [501]	2016	3	DGT+PC-SAFT	water H_2O + methane CH_4
Niño-Amézquita [508]	2013	1	DGT+PC-SAFT	n-heptane C_7H_{16} + nitrogen N_2

Authors	Year	#	Method	System
Panayiotou [517]	2003	1	DGT+QCHB	1-propanol C_3H_8O + n-hexane C_6H_{14}
Pereira et al. [522]	2016	9	DGT+PR	n-decane $C_{10}H_{22}$ + methane CH_4
				n-decane $C_{10}H_{22}$ + carbon dioxide CO_2
				n-decane $C_{10}H_{22}$ + nitrogen N_2
Poser & Sanchez [533]	1981	1	DGT+LFT	benzene C_6H_6 + n-hexane C_6H_{14}
Protsenko & Baidakov [551]	2016	20	MD	Lennard-Jones + Lennard-Jones
Protsenko et al. [552]	2016	6	MD	Lennard-Jones + Lennard-Jones
Sahimi & Taylor [583]	1991	2	DGT+PR	n-butane C_4H_{10} + carbon dioxide CO_2
				n-decane $C_{10}H_{22}$ + carbon dioxide CO_2
Salomons & Mareschal [585]	1991	4	MC	Lennard-Jones + Lennard-Jones
Salomons & Mareschal [586]	1991	3	MC	Lennard-Jones + Lennard-Jones
Schäfer et al. [589]	2014	2	DGT+PC-SAFT	N,N-dimethylformamid DMF + n-heptane C_7H_{16}
				N,N-dimethylformamid DMF + n-dodecane $C_{12}H_{26}$
Schenk et al. [591]	2019	3	MD	carbon dioxide CO_2 + methane CH_4
Shi etl a. [604]	2015	3	MD	polydimethylsiloxane C_2H_6SiO + carbon dioxide CO_2
Stephan et al. [632]	2020	296	MD & DGT+PCP-SAFT	toluene C_7H_8 + carbon dioxide CO_2
				toluene C_7H_8 + nitrogen N_2
Stephan et al. [624]	2020	135	MD & DGT+PCP-SAFT	cyclohexane C_6H_{12} + carbon dioxide CO_2
Stephan et al. [637]	2019	186	MD & DGT+PeTS	Lennard-Jones + Lennard-Jones (six systems)
Stephan & Hasse [628]	2019	142	MD & DGT+LJ EOS	Lennard-Jones + Lennard-Jones (six systems)
Stephan & Hasse [630]	2020	180	MD & DGT+PeTS	Lennard-Jones + Lennard-Jones (90 systems)
Stephan & Hasse [629]	2020	330	MD & DGT+PeTS	Lennard-Jones + Lennard-Jones (two systems)
Stephan [631]	2020	381	MD	LJ + LJD (15 systems)
				LJ + LJQ (7 systems)

Authors	Year	#	Method	System
Sullivan [644]	1982	5	DGT+VDW	LJD + LJD (4 systems) LJQ + LJQ (4 systems) LJD + LJQ (3 systems) vdW fluid + vdW fluid
Teixeira et al. [659]	1992	20	DFT	acetonitrile CH_3CN + carbon tetrachloride CCl_4 methyl iodide CH_3I + carbon tetrachloride CCl_4
Tardon et al. [657]	2012	4	MD & DGT+LJ EOS	Lennard-Jones + Lennard-Jones
Telo da Gama [192]	1980	4	SGA	krypton Kr + argon Ar
Telo da Gama & Evans [194]	1983	5	SGA	Lennard-Jones + Lennard-Jones
Telo da Gama & Evans [195]	1983	9	SGA	Lennard-Jones + Lennard-Jones
Vilaseca et al. [679]	2010	3	DGT+soft SAFT	difluoroethane $C_2H_4F_2$ + propane C_3H_8
Wadewitz & Winkelmann [692]	1996	20	DFT	argon Ar + nitrogen N_2
Werth et al. [705]	2016	159	MD & DGT+PC-SAFT	toluene C_7H_8 + n-heptane C_7H_{16} toluene C_7H_8 + carbon dioxide CO_2 toluene C_7H_8 + hydrogen chloride HCl
Winkelmann [714]	2001	6	MD	methane CH_4 + argon Ar
Zeng & Oxtoby [729]	1991	2	DFT	krypton Kr + argon Ar

Abbreviations used in Table 25:

DFT	density functional theory
DGT	density gradient theory
EOS	equation of state
LFT	lattice fluid theory [587]
LJ	Lennard-Jones fluid EOS [302–304, 368, 639]
MC	Monte Carlo simulation [17, 451]
MD	molecular dynamics simulation [17]
PC-SAFT	perturbed-chain statistical associating fluid theory EOS [223, 224]
PCP-SAFT	perturbed-chain polar statistical associating fluid theory EOS [221, 225, 684]
PeTS	perturbed truncated shifted EOS [249, 635]
PR	Peng-Robinson EOS [521]
QCHB	quasi-chemical hydrogen bonding [517]
SAFT	statistical associating fluid theory EOS [100–102]
CK-SAFT	Chen-Kreglewski SAFT EOS [277, 724]
SAFT-VR Mie EOS	SAFT variable range Mie potential EOS [353]
SAFT-γ Mie	group contribution SAFT-VR Mie EOS version [518]
SAFT VR	SAFT variable range EOS [188, 212]
soft SAFT	soft SAFT EOS [57, 58]
SRK	Soave-Redlich-Kwong EOS [558, 614]
VDW	van der Waals EOS

Studies reporting vapor-liquid interfacial properties focus on a large variety of different systems and applications, such as enhanced oil recovery [116, 198, 386, 389, 445, 483, 500, 508, 583], natural gas [77, 319, 372, 391, 453, 459, 486], CO_2 absorption and carbon-capture and storage (CCS) [56, 105, 117, 354, 373, 391, 445, 493, 504], refrigerants [184, 318, 374, 679], evaporation and nucleation [328, 729], environmental science [172, 276, 478], process and chemical engineering [16, 50, 153, 187, 336, 373, 589, 624, 634], polymers [533, 604], fundamental physics [191, 192, 362, 484, 630, 714], and the development of computational methods and algorithms [36, 72, 86, 91, 205, 328, 342, 441, 477]. Hence, they were published in a large variety of different journals. Due to this heterogeneity of applications and motivations, there is no dense citation network present in this field. It was one goal of this study to establish the corresponding links.

Strong enrichment at vapor-liquid interfaces is usually found in systems in which one of the components is supercritical. Furthermore, strong enrichment is usually found at low temperatures and low concentrations of the low-boiling component. These results indicate that mixtures that are typical for absorption processes for fluid separation usually show an important enrichment, whereas the enrichment is less important for mixtures that are typically separated by distillation. It is well-known that absorption and distillation processes are generally designed differently, even though the columns that are used in both processes are similar: while rate-based models are preferred for absorption, equilibrium stage models are the standard choice for distillation. These differences might be related to the presence of the enrichment in the absorption systems. Rate-based models do not account explicitly for the influence of the enrichment, but they can do this indirectly as a result of their parametrization. Also, important enrichment effects are observed at many interfaces of mixtures that are important in environmental

science, like water + CO_2 and water + acid gas systems [56, 78, 172, 276, 354, 419, 478].

Density profiles at vapor-liquid interfaces have been investigated for both model fluids [149, 192–195, 200, 361, 362, 412, 441, 446, 551, 552, 585, 586, 630, 635] (very often the Lennard-Jones fluid) and models of real substances [50, 89, 121, 159, 173, 305, 328, 354, 404, 444, 453, 456, 458, 459, 483, 501, 504, 533]. These groups differ mainly in the way the molecular model is used: model fluids are usually used to study the effect of a variation of a molecular parameter on a given observable (cf. chapter 3), whereby a generic information is obtained, whereas models of real substances are used to study properties of a given mixture (cf. chapter 7), which causes the findings to be restricted to that case.

The influence of the molecular parameters on density profiles and other interfacial properties has been studied several times in the literature. Results are available for the influence of the size and energy parameters of the pure components [79, 194, 195, 200, 362, 446, 551, 552, 628–630, 635, 635], the cross interactions [194, 195, 200, 362, 446, 628–630, 635, 635], and the chain length of the components [149, 328, 390, 390, 391, 414, 483, 583]. Some studies also investigated the influence of associating components [50, 56, 354, 504] on vapor-liquid interfacial properties. Asymmetric mixtures have caused special interest [56, 173, 354, 373, 391, 483, 501, 504, 583] since a particularly large enrichment is found in such cases.

The most frequently studied systems are (H_2O + CO_2), (H_2O + alcohols), as well as (CO_2 or N_2 + alkanes), and Lennard-Jones mixtures (cf. Table 25). The latter were mostly used for systematic studies of the influence of molecular parameters on different interfacial and bulk properties. Also, most of the early simulation studies on interfacial properties [192, 194, 195, 361, 362] were performed with Lennard-Jones fluids. Mixtures of simple fluids (argon, neon, krypton, methane etc.) can be modeled reasonably well as Lennard-Jones mixtures. Hence, such data can be considered real substance data or model fluid data. Table 25 reports such data as it is referred to in the respective publication.

Also the influence of the temperature [50, 362, 624, 629] and the composition [634, 635] on the interfacial enrichment has been investigated systematically in the literature. Overall, it was found that an enrichment is favored by asymmetric molecular interactions, large differences in the volatility of the pure components (i.e. wide-boiling phase behavior), low concentrations of the low-boiling components, and low temperatures [50, 56, 379, 459, 483, 492, 504, 583, 630, 634, 635]. In most cases, starting at infinite dilution of component 2, the enrichment E_2 was found to decrease monotonically with increasing concentration of the low-boiling component 2 at constant temperature to converge to unity either at a critical point, an azeotropic point, or the high-boiling pure component vapor pressure (depending on the phase behavior).

Furthermore, two types of enrichment behavior have been reported for wide-boiling mixtures (cf. section 3.3 and 3.4) [630, 635] depending on the sign of the density difference of component 2 $\Delta\rho_2 = \rho_2' - \rho_2''$: mixtures with $\Delta\rho_2 > 0$ usually yield large enrichment, whereas mixtures with $\Delta\rho_2 < 0$ usually yield small enrichment. For example solvent + nitrogen systems usually yield $\Delta\rho_2 < 0$, which goes in hand with small enrichment, whereas solvent + carbon dioxide or solvent + methane systems usually have $\Delta\rho_2 > 0$, which goes in hand with large enrichment. This differentiation has also been confirmed for different types of Lennard-Jones model mixtures, cf. section 3.4 [630].

The results for the enrichment obtained from the literature data lie almost exclusively in the range of $1 < E_2 < 10$, whereat the vast majority of data lies in the range $1 < E_2 < 3$. On the other hand, enrichment data in the range $6 < E_2 < 10$ is rare. Fig. 98 shows a corresponding histogram.
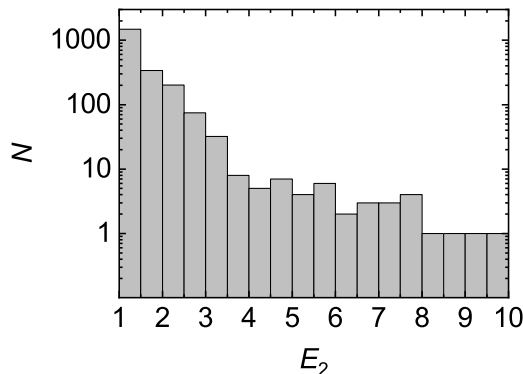
Figure 98: Histogram of the data on the enrichment E_2 obtained from the literature, cf. Table 25. N is the number of data points in the indicated E_2 interval. A logarithmic scale is used for N.

Particularly large enrichment is often observed for mixtures that exhibit a three-phase vapor-liquid-liquid-equilibrium (VLLE). The enrichment at (two-phase) vapor-liquid interfaces is related to a wetting transition in the vicinity of a three-phase VLLE (cf. section 3.6): approaching the VLLE line through a VL two-phase region, the enrichment increases and can be understood as a precursor of the second liquid phase. The enrichment at two-phase vapor-liquid interfaces approaching a VLL three-phase equilibrium line forms a layer that can be considered as a pre-wetting layer. This layer has similar thermodynamic properties as the second liquid phase L2 that appears at the three-phase line. Nevertheless, enrichment $E_2 > 1$ at vapor-liquid interfaces in such systems is also found at thermodynamic conditions (temperature and pressure) far away from the three-phase line. Furthermore, an enrichment has also been reported for many mixtures that do not exhibit a miscibility gap and a VLLE line.

It has been shown, that the enrichment exhibits a continuous transition between different types of systems at constant reduced temperature and liquid phase composition. Systematic studies on Lennard-Jones model mixtures (cf. chapter 3) [630, 635] recently showed that ideal mixtures (in the sense of Raoult's law) and high-boiling azeotropic mixtures exhibit no enrichment, whereas for low-boiling azeotropic mixtures, a significant enrichment is found. This is in line with findings for real substance mixtures reported in the literature [159, 194, 589, 635]. Furthermore, it was found that the enriching component changes at the azeotropic point [589]. Hence, in each azeotropic branch, the respective low-boiling component exhibits an enrichment at the interface. Nevertheless, enrichment data on azeotropic mixtures is relatively scarce in the literature.

The number of theoretical studies of vapor-liquid interfaces has grown significantly in the last decade, which is probably due to the fact that MD and MC studies of direct VLE simulations, where the vapor and the liquid phase coexist in a simulation box, became computationally readily affordable. Approximately 60% of the available studies

reporting vapor-liquid density profile data of binary mixtures have been published in the last ten years, cf. Table 25.

Most studies on density profiles of vapor-liquid interfaces employ either molecular simulations, i.e. molecular dynamics or Monte Carlo simulations using classical force fields [157, 633], or DGT in combination with an EOS. Approximately half of the studies reporting vapor-liquid interfacial density profiles employ density gradient theory in combination with an equation of state. Not all EOS are suited for such studies. An essential prerequisite is that they exhibit only a single van der Waals loop in the two-phase region [572], like cubic EOS or SAFT type EOS [100, 226, 249, 482, 619, 623]. Density functional theory (DFT) was only applied in few cases, cf. Table 25. As in the present work (cf. chapters 3, 5, 7, and 8), in some studies from the literature two methods were employed for a given mixture – usually molecular simulations and DGT. Even though both methods were found to yield good qualitative agreement for the predicted enrichment in practically all cases, significant quantitative differences have been reported many times [50, 116, 198, 445, 446, 453, 459, 483, 624, 628, 635, 657, 705]. For a given mixture, the reported absolute deviation for the predicted enrichment among different methods mostly lies in the range $\delta E_2 = 0.1 .. 1$.

Systematic deviations between molecular simulations and DGT results for the enrichment have been observed several times: for low E_2 values, molecular simulations typically yield larger enrichment than DGT, whereas for high E_2 values, the DGT results mostly overestimate the MD results for the enrichment [50, 116, 205, 361, 362, 445, 446, 453, 459, 483, 624, 629, 705].

Assessing these deviations between the results from molecular simulations and DGT, several sources of error and uncertainties should be considered: leaving aside the problem of the topic of the reproducibility of molecular simulations results [3, 228, 392, 590, 640], the underlying pure substance models (EOS and force field) have to be parametrized adequately to yield conformal representations of the VLE, which is not trivial even for the most simple fluids, cf. chapter 3 [639]. Furthermore, molecular simulations and DGT have some fundamental differences, e.g. fluctuations are present in the MD density profiles $\rho_i(z)$ but not in the corresponding DGT results, cf. chapters 2 - 5 for a detailed discussion.

For the sake of completeness, we briefly point out further interesting aspects related to the enrichment that have been studied in the literature: the peak position and the shape of the peak was found to depend on the system and varies with temperature and composition such that the position of the peak can either be on the liquid or the vapor side of the interface [624, 629, 635] (with respect to the center of the interface defined as $\rho^{\mathrm{centre}} = 0.5\left(\rho' + \rho''\right)$). Furthermore, the interfacial thickness, the enrichment, and the relative adsorption have been examined simultaneously in some cases as these three properties comprehensively characterize the structure of an interface [624, 629]. Long-range interactions were found to have a minor influence on the enrichment in simple fluid mixtures [628]. Also the pressure tensor across vapor-liquid interfaces of mixtures was measured by several authors [56, 152, 173, 361, 412, 478, 492]. The pressure profiles do not exhibit additional oscillations in cases of high E_2 compared to cases with low E_2. Moreover, the orientation of enriching species at the interface [172, 276, 292, 523] and the details on the distribution of functional groups at the interface [205, 523, 524, 584] has been investigated. In several cases, a preferential orientation of low-boiling components

with respect to the interface was observed [172, 276, 584], compared to a stochastic orientation in the bulk phases.

9.4 Enrichment Model and Parametrization

9.4.1 Dataset Used for the Parametrization

The enrichment database compiled from literature data in the present work (cf. Table 25) was split into two datasets: one for the training of the empirical model and one for the testing. For the training of the empirical enrichment model, the comprehensive dataset on binary Lennard-Jones mixtures (cf. chapter 3) was used [629, 630, 635]. The test-dataset comprises the remaining enrichment data from the literature, cf. Table 25.

The training-dataset comprises a large variety of mixture types and thermodynamic conditions (temperature and liquid phase composition). An overview of the Lennard-Jones mixtures comprised in the training-dataset [629, 630, 635] is given in Fig. 99, in which the molecular interaction parameters are depicted. For all mixtures, the high-boiling component 1 was the same and both components have the same size parameter σ and mass M. The mixtures differ in the dispersion energy of the low-boiling component ε_2 and the parameter ξ that is used in the modified Berthelot combination rule for describing the cross interaction dispersion energy $\varepsilon_{12} = \xi\sqrt{\varepsilon_1\varepsilon_2}$. Values of $\xi > 1$ indicate an increased cross affinity of the two components and $\xi < 1$ a decreased cross affinity. A selection of the resulting isothermal phase diagrams is given in Fig. 31.

Fig. 100 shows the results for the enrichment obtained in these systematic studies [629, 630, 635]. The obtained enrichment is plotted as a function of the liquid phase concentration for the data from Refs. [629, 635] (panels a) - d) and as a function of the partition coefficient for the data from Ref. [630] (panel e).

The training-dataset thereby contains enrichment data of 90 Lennard-Jones systems at only one temperature and liquid phase composition ($x_2' = 0.05\,\mathrm{mol\,mol^{-1}}$), six systems at one temperature but the entire composition range, and two systems at five temperatures in the entire composition range. All three studies (cf. chapter 3) [629, 630, 635] were carried out using both MD and DGT. For the parametrization of the enrichment model, only the MD results reported in chapter 3 were used. The training-dataset covers a wide range of types of phase behavior. Furthermore, it contains data for a selection of mixtures in the temperature range between the triple point temperature and the critical temperature of the high-boiling component and the entire concentration range where vapor-liquid equilibria exist in these systems. In total, the training-dataset consists of 338 data points.

For all studied mixtures in the training-dataset, the enrichment E_2 predicted by MD is largest at infinite dilution of the low-boiling component and monotonically decreases with increasing x_2'. The enrichment increases with decreasing temperature, cf. Fig. 100 c) and d). The enrichment data at constant temperature and liquid phase concentration ($x_2' = 0.05\,\mathrm{mol\,mol^{-1}}$) plotted as a function of the partition coefficient $K_2 = x_2''/x_2'$ (Fig. 100 e) shows an interesting behavior: all data points collapse to a single curve for values of K_2 of up to about 12. This is not completely surprising, as in section 3.5, a
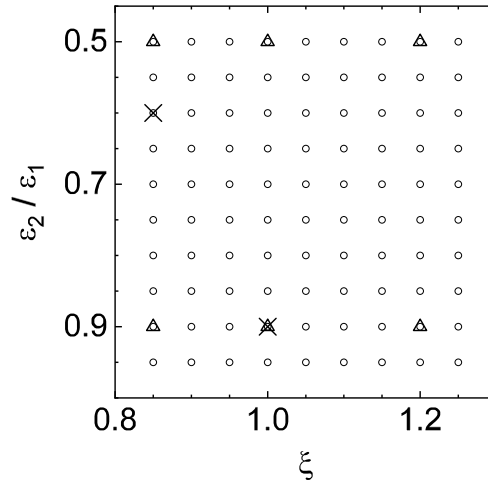
Figure 99: Overview of the binary Lennard-Jones mixtures that were used for the training of the empirical enrichment model (cf. chapter 3). Component 1 was the same for all mixtures. $\varepsilon_2/\varepsilon_1$ denotes the ratio of the two components' dispersion energy and ξ the cross interaction parameter used in the modified Berthelot combination rule. The particle size σ was the same for both components in all cases. Mixtures that are indicated by circles were studied at $x'_2 = 0.05\,\mathrm{mol\,mol^{-1}}$ and $T/T_{c,1} = 0.7$, cf. section 3.4 [630]. Mixtures indicated by triangles were studied in the entire composition range at $T/T_{c,1} = 0.7$, cf. section 3.3 [635]. Mixtures indicated by crosses were studied in the entire composition range and at the temperatures $T/T_{c,1} = 0.6$, 0.65, 0.7, 0.75, 0.8, cf. section 3.6 [629].

general monovariate dependency of the interfacial properties on the internal energy of the liquid phase was found. However, at $K_2 \approx 12$ a second branch appears in the plot shown in Fig. 100 e). The existence of this second branch is related to the difference of the partial densities of component 2 in the two phases $\Delta\rho_2 = \rho''_2 - \rho'_2$. For most systems, the partial density difference $\Delta\rho_2$ is positive, i.e. ρ_2 in the liquid phase is larger than ρ_2 in the vapor phase (which is related to the gas solubility, cf. section 3.4 [630]). However, for some systems, the inverse is true, i.e. $\Delta\rho_2$ is negative. Both types of systems show large values of K_2 (the limit is about $K_2 = 12$). As shown in section 3.4 [630], the sign of $\Delta\rho_2$ has important influence on the enrichment. As a consequence, for $K_2 > 12$ a distinction is necessary between systems with $\Delta\rho_2 > 0$ and systems with $\Delta\rho_2 < 0$. The branch found for $\Delta\rho_2 > 0$ in this range of K_2 is a simple extension of the curve found for lower K_2, whereas on the other branch ($\Delta\rho_2 < 0$), distinctly smaller values of E_2 are found. While the database is dense for low K_2, not as many data points are currently available at high K_2 in the training-dataset, cf. Fig. 100.

9.4.2 Empirical Enrichment Model

As described above, the enrichment E_2 is considered here as a function of T and x'_2 for a given mixture. The aim was to establish a correlation of E_2 with readily available macroscopic data on the VLE of the mixture. Correlations in dimensionless variables are preferred. Many options are available for establishing such correlations and we have tested a number of them in preliminary work. For brevity, we will not describe all these
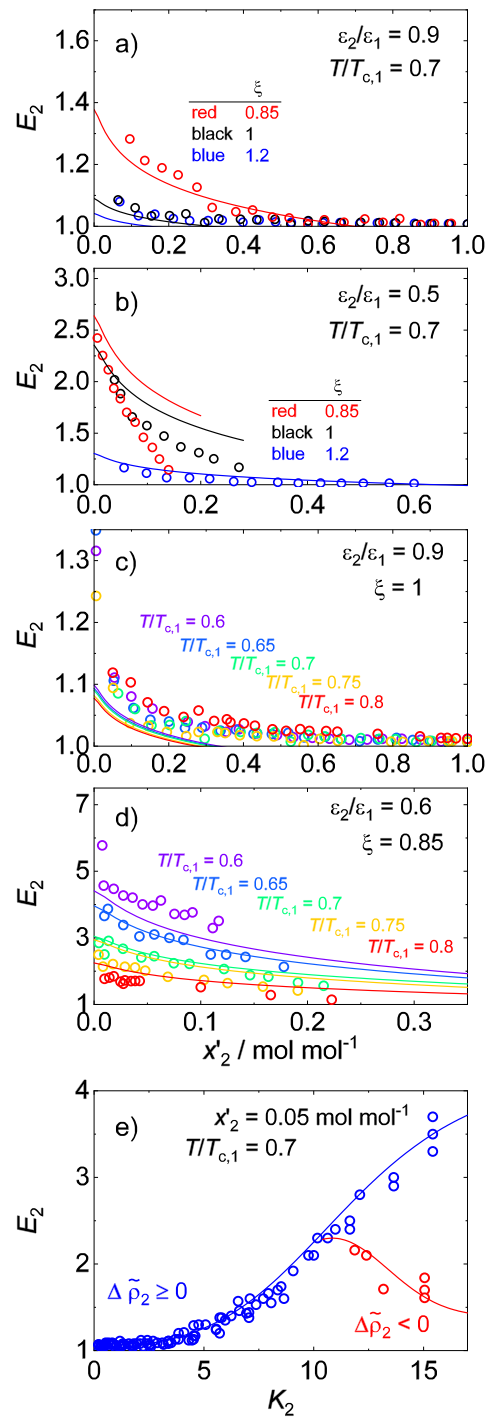
Figure 100: Data on the enrichment obtained from molecular simulations of Lennard-Jones mixtures (cf. chapter 3) [629, 630, 635] (symbols) that was used for training of the empirical model (lines). The plots (a) and (b) show the enrichment observed in six different Lennard-Jones mixtures at $T/T_{c,1} = 0.7$ as a function of the liquid phase concentration; (c) and (d) show the enrichment observed in two Lennard-Jones mixtures at five temperatures as a function of the liquid phase concentration; (e) shows the enrichment observed in 96 different Lennard-Jones mixtures at $T/T_{c,1} = 0.7$ and $x_2' = 0.05 \, \mathrm{mol \, mol^{-1}}$ as a function of the partition coefficient $K_2 = x_2''/x_2'$. For all mixtures, both particles have the same size $\sigma_1 = \sigma_2$.

tests and present here only the final result. Our only claim is the usefulness of the correlation, i.e. a good description of the available E_2 data, not any kind of optimality. A clear indication of the usefulness is the fact that the simple correlation presented here describes the available data on E_2 in most cases within the uncertainty of the prediction of E_2 from different methods.

The proposed correlation describes E_2 as a product of two terms:

$$E_2 = \alpha_0 + f_a(x_2') \, f_b(\text{VLE}) \ , \tag{127}$$

and an empirical offset parameter α_0. The term f_a describes the concentration dependence of E_2 in a generalized way, the term f_b includes the information on the VLE of the considered binary system. Preliminary tests showed that it is not necessary to introduce a universal function of the temperature. The influence of temperature is accounted for in the term f_b. In the following, empirical parameters employed in the functions f_a and f_b are labeled as α_i.

Following the findings shown in Figure 100 e), the VLE of a mixture is characterized here by the partition coefficient of component 2, i.e. $K_2 = x_2''/x_2'$. This is convenient, as in all studies of interfacial properties in the literature, the partition coefficient K_2 can be calculated easily from the available data. Furthermore, the required data on x_2'' and x_2' is readily available in databases for a large number of mixtures of practical relevance.

The partition coefficient K_2 depends both on the temperature and composition. For characterizing the studied systems, the partition coefficient at infinite dilution would have been a convenient choice, since E_2 was found in all cases to be largest at infinite dilution and monotonically decrease with increasing x_2' (see chapter 3 for a detailed discussion). But since MD simulations can only be carried out at finite concentrations and based on an analysis of the available data and preliminary tests, it was decided to use the partition coefficient at the liquid phase concentration of $x_2' = 0.05 \, \text{mol} \, \text{mol}^{-1}$

$$K_2^{5\%} = \frac{x_2''}{x_2' \equiv 0.05 \, \text{mol} \, \text{mol}^{-1}} \ . \tag{128}$$

For a given mixture, the value of $K_2^{5\%}$ depends on the temperature. This is how the temperature is accounted for in the model.

The dependency of the enrichment on the liquid phase concentration is described by a simple monotonically decaying universal function

$$f_a(x_2') = \alpha_1 + \ln\left(\frac{1}{x_2' + \alpha_2}\right) - \frac{\alpha_2}{x_2' + \alpha_2} \ . \tag{129}$$

The function f_a has a finite value at $x_2' = 0$ and monotonically decreases with a convex curvature to zero at $x_2' = 0$. The outlined model does not explicitly take three-phase VLLE and critical points into account as termination points for E_2 isotherms, cf. chapter 3. It would be desirable to consider these end points in the model, but there is presently not enough data to do this in a meaningful way. If more data were available, this is expected to lead to further improvements of the model.

As discussed above, for mixtures with large K_2, the influence of the density difference of the low-boiling component $\Delta\rho_2 = \rho_2' - \rho_2''$ must be taken into account. This is incorporated

in the empirical model by defining

$$f_b = \alpha_3 \, g_I\big(K_2^{5\%}\big) \, \delta(\Delta\tilde{\rho}_2) + \alpha_4 \, g_{II}\big(K_2^{5\%}\big) \, (1 - \delta(\Delta\tilde{\rho}_2)) \,, \tag{130}$$

where δ is a smoothed step function taking values between 0 and 1 of the form

$$\delta\,(\Delta\tilde{\rho}_2) = \frac{\tanh\,(100 \cdot \Delta\tilde{\rho}_2) + 1}{2} \,. \tag{131}$$

In Eq. (131), $\Delta\tilde{\rho}_2$ is the reduced density difference with respect to the critical density of the high-boiling component, i.e. $\Delta\tilde{\rho}_2 = \Delta\rho_2/\rho_{c,1}$. Hence, also $\Delta\tilde{\rho}_2$ is a dimensionless variable. The reduced density difference $\Delta\tilde{\rho}_2$ is only used for the decision function $\delta(\Delta\tilde{\rho}_2)$ to navigate between the terms $g_I(K_2^{5\%})$ and $g_{II}(K_2^{5\%})$ depending on the sign of $\Delta\tilde{\rho}_2$. The value of $\Delta\tilde{\rho}_2$ can easily be obtained from saturated density and concentrations data, which is readily available for a large number of systems [1, 381].

The two functions for the modeling of the enrichment dependency on the partition coefficient g_I and g_{II} are defined as

$$g_I(K_2^{5\%}) = \Big(\exp\big(\tanh\big(\alpha_5 \cdot K_2^{5\%} - \alpha_6\big)\big) \Big)^{\alpha_7} \,, \tag{132}$$

$$g_{II}(K_2^{5\%}) = \alpha_8 + \exp\left(\alpha_9 \cdot \left(\frac{K_2^{5\%} - \alpha_{10}}{\alpha_{11}} \right)^2 \right) \,. \tag{133}$$

The equations (127) - (133) define an empirical enrichment model as a function

$$E_2 = E_2(x_2', \, K_2^{5\%}, \Delta\tilde{\rho}_2) \,. \tag{134}$$

All three variables are dimensionless macroscopic VLE properties that are easily accessible by experiment and available in databases for a large number of systems [1, 381]. The values for $K_2^{5\%}$ and $\Delta\tilde{\rho}_2$ can be determined conveniently for both the training-dataset and the test-dataset. For the training-dataset, all required numeric values were reported in the respective publications. The determination of $K_2^{5\%}$ and $\Delta\tilde{\rho}_2$ for the test-dataset is discussed in the next section.

The empirical enrichment model has 12 adjustable parameters α_i with $i = 0$ - 11, which were fitted to the training-dataset, i.e. the MD Lennard-Jones mixture data from chapter 3 [629, 630, 635]. The parametrization was carried out by minimizing the absolute average deviation

$$\mathrm{AAD}_{E_2} = 1/N \sum_{j=1}^{N} \frac{|\Delta E_{2,j}|}{E_{2,j}^{\mathrm{ref}}} \,, \tag{135}$$

where N is the number of enrichment data points in the training-dataset, $E_{2,j}^{\mathrm{ref}}$ is the reference enrichment from the training-dataset [629, 630, 635], and ΔE_2 is the absolute deviation between the reference value and the value predicted by the empirical enrichment model $\Delta E_{2,j} = E_{2,j}^{\mathrm{ref}} - E_{2,j}^{\mathrm{model}}$. Table 26 reports the obtained values for the parameters α_i.

The model described above is empirical. Experience tells us that the limits of applicability of such models are related to the range of states covered by the training-dataset. In our case the considered VLE regions ended always in the boiling point of the high-boiling component 1, i.e. infinite dilution of component 2, and the temperatures were

Table 26: Parameters of the empirical enrichment model Eq. (127).

i	α_i	i	α_i
0	0.9594	6	0.5521
1	0.0199	7	2.7099
2	0.01	8	0.4706
3	0.0811	9	-0.05
4	0.3414	10	10.85
5	0.1345	11	0.8

between the triple point temperature and the critical temperature of the high-boiling component 1. The upper limit of the concentration of the low-boiling component 2 was determined by the occurrence of a critical point or a three-phase line. For more details see section 3.6. Furthermore, reference data was available for $0 < K_2^{5\%} < 15$. It is noted that neither the training-dataset nor the test-dataset contain data points with $\Delta\tilde{\rho}_2 < 0$ and $K_2^{5\%} < 12$. Hence, the empirical enrichment model is not valid in that region. We therefore assume that, if such data exist at all, they are rare. But should they exist, the model would probably not describe them well.

Fig. 101 depicts the enrichment determined from the empirical model as a function of the liquid phase concentration x_2' and the partition coefficient $K_2^{5\%}$ – also extrapolating into the region $K_2^{5\%} > 15$.
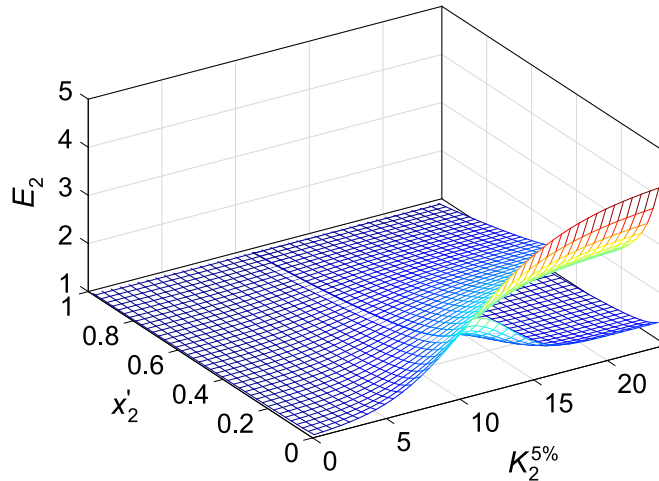
Figure 101: Results of the empirical enrichment model $E_2 = E_2(x_2', K_2^{5\%})$. Results are shown for $\Delta\tilde{\rho}_2 = 0.1$ and -0.1. The color coding references to the magnitude of E_2. The branches of the graph for $K_2^{5\%} > 12$ correspond to $\Delta\tilde{\rho}_2 < 0$ (low E_2) and $\Delta\tilde{\rho}_2 > 0$ (high E_2), cf. Eq. (130).

The plot shown in Fig. 101 was obtained for $\Delta\tilde{\rho}_2 = 0.1$ or $\Delta\tilde{\rho}_2 = -0.1$, respectively. Due to the character of the Eq. (127) - (133), other choices of $\Delta\tilde{\rho}_2$ yield similar results as long as the sign of $\Delta\tilde{\rho}_2$ is the same. Only for $\Delta\tilde{\rho}_2$ values with a very small absolute value $|\Delta\tilde{\rho}_2| < 0.01$, there is a smooth transition between the branches, which is numerically convenient.

For $K_2^{5\%} < 12$ and $\Delta\tilde{\rho}_2 > 0$ (the region where only a single branch exists), the model converges to unity with decreasing $K_2^{5\%}$ at infinite dilution of component 2. For the composition dependency, the model decreases monotonically to approximately unity for all $K_2^{5\%}$ and $\Delta\tilde{\rho}_2$ with increasing x_2'. At infinite dilution of component 2, the enrichment model yields $E_2 = 4.3$ at $K_2^{5\%} = 15$ and $\Delta\tilde{\rho}_2 > 0$ (upper branch depicted in Fig. 101). At infinite dilution of component 2 at $\Delta\tilde{\rho}_2 < 0$ (bottom branch in Fig. 101), the enrichment model converges to $E_2 = 1.4$ with increasing $K_2^{5\%}$.

The empirical enrichment model is compared to the training-dataset in Fig. 100. The enrichment model generally describes the influence of the composition, the temperature, and the partition coefficient on E_2 well. However, Fig. 100 b) shows deviations for the composition dependency for isotherms that exhibit a critical point. Figs. 100 c) and d) show that the temperature dependency is captured reasonably well by the model. Fig. 100 e) shows the enrichment as a function of the partition coefficient $K_2^{5\%}$, i.e. the performance of the term $f_b(K_2^{5\%})$ in Eq. (127). Deviations are observed for data points $K_2^{5\%} > 12$, which is mainly due to the fact that the training data was sparsely populated in that region. Figs. 100 a) - e) contain data points from a large range of temperatures and large variety of mixture types, which are described well by the empirical enrichment model. Hence, the implicit temperature dependency of the model via $K_2^{5\%}(T)$ is found to perform astonishingly well, considering the fact that both the influence of the temperature and the mixture type is taken into account only by $K_2^{5\%}$.

Fig. 102 shows the deviation plots for the performance of the empirical enrichment model on the training data. The fit yields an absolute average deviation of $\text{AAD}_{E_2} = 6.5\%$. Fig. 102 a) shows the absolute deviation ΔE_2 as a function of the partition coefficient $K_2^{5\%}$ (for different T and x_2'); Fig. 102 b) shows ΔE_2 as a function of the liquid phase concentration x_2' (for different T and $K_2^{5\%}$); and Fig. 102 c) shows the absolute deviation ΔE_2 as a function of the enrichment E_2 itself (for different T, x_2', and $K_2^{5\%}$).

The model captures generally the enrichment behavior well. The largest absolute deviations are observed for high values of E_2 and high values $K_2^{5\%}$ and are about 0.75. The model slightly underestimates the training data in the range $E_2 = 1.2..2.5$ and slightly overestimates the training data for $E_2 > 2.5$.

Assessing the performance of the empirical model, it should be kept in mind that the MD data that were used here as training data, deviate also from the corresponding data obtained by DGT by up to $|E_2^{\text{MD}} - E_2^{\text{DGT}}| = 1$ [629, 630, 635] (indicated by the dashed lines in Fig. 102) which is more than the largest deviations of the empirical model to the training data. Furthermore, the MD results exhibit statistical uncertainties from the simulation sampling of up to $\delta E_2 = \pm 0.1$.

Fig. 103 depicts the histogram of the absolute deviations of the enrichment obtained from the empirical model E_2^{model} and the corresponding training-dataset values E_2^{ref}. 97.3% of the data points of the training-dataset are described with an absolute deviation below $|\Delta E_2| = 0.5$. For the majority of the data points with $|\Delta E_2| > 0.5$, the empirical model slightly underestimates the training data.
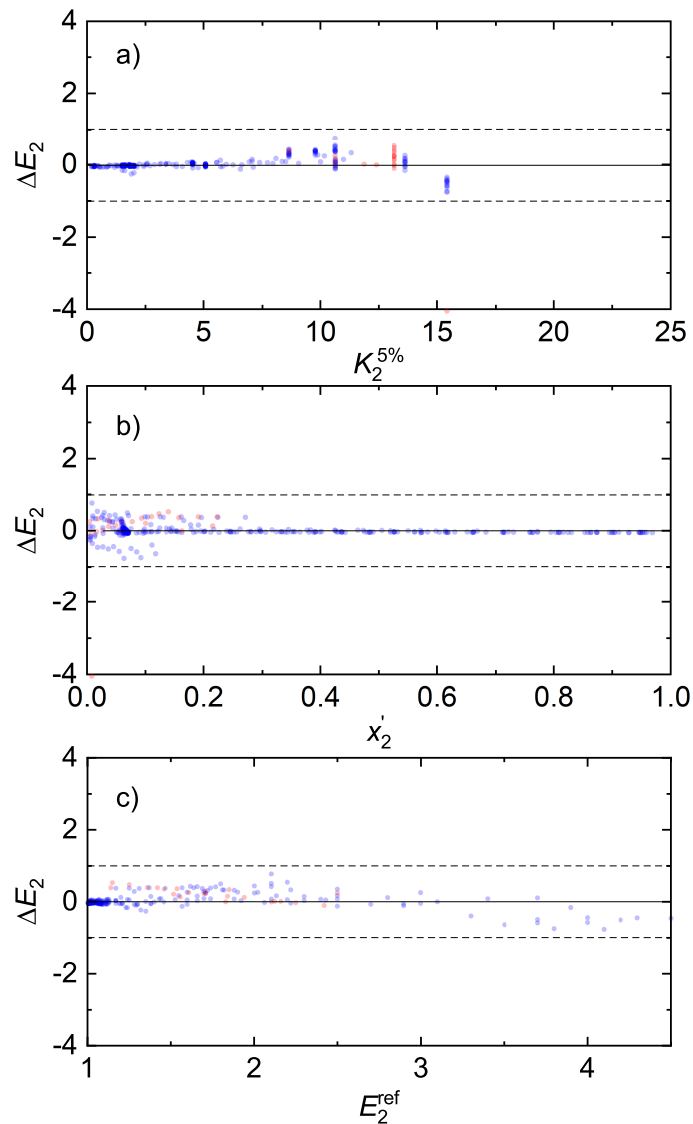
Figure 102: Deviation plots of the enrichment data from the training-dataset (MD data from chapter 3 [629, 630, 635]) and the predictions from the empirical model: a) shows the absolute deviation ΔE_2 as a function of the partition coefficient $K_2^{5\%}$; b) shows ΔE_2 as a function of the liquid phase concentration x_2'; c) shows ΔE_2 as a function of the enrichment E_2 itself. Red indicates data points with $\Delta \tilde{\rho}_2 < 0$ and blue data points with $\Delta \tilde{\rho}_2 > 0$. The dashed lines indicate $\delta E_2 = \pm 1$, which corresponds to the uncertainty of the data.
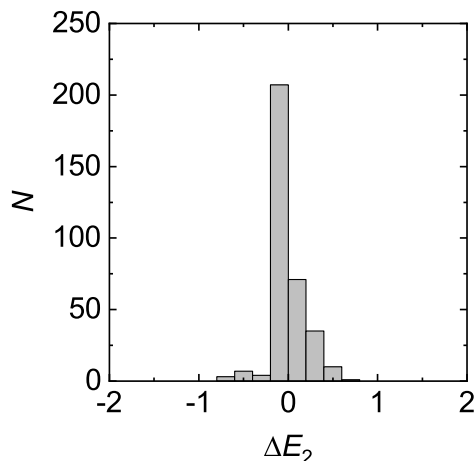
Figure 103: Histogram of the absolute deviations $\Delta E_2 = E_2^{\mathrm{ref}} - E_2^{\mathrm{model}}$ of the empirical enrichment model from the training-dataset. The bin width is 0.2.

9.5 Testing the Model Predictions

The empirical enrichment model was tested on available enrichment data for binary mixtures from the literature, cf. Table 25 – excluding the training-dataset from chapter 3 [629, 630, 635].

The test-dataset comprises data on real mixtures as well as on model mixtures, e.g. LJ mixtures. For applying the enrichment model, VLE data on the mixtures is needed. For the real mixtures, the VLE data was taken from thermophysical property databases [1, 381]; for the model mixtures, the vast majority of publications reporting vapor-liquid density profiles also report the corresponding T, x', x''-data, which was employed here. 2% of the enrichment data points of the test-dataset (cf. Table 25) could not be used for the testing of the empirical model, as no T, x', x''-data for the calculation of $K_2^{5\%}(T)$ was available. In many cases, the VLE data – required for the computation of the partition coefficient – was not available at exactly $x_2' = 0.05\,\mathrm{mol\,mol}^{-1}$ and the required temperature. The required input was estimated from the available data as described in more detail in the Appendix.

Fig. 104 shows the histogram of the absolute deviations of the enrichment predicted from the empirical model E_2^{model} and the reference values E_2^{ref} from the test-dataset. The absolute average deviation is $\mathrm{AAD}_{E_2} = 16.1\%$, which is astonishingly low considering the fact that the empirical model was trained to an MD dataset based on purely dispersively interacting fluids, whereas the test-dataset contains a large variety of molecular interactions, mixture types, and employed methods. 84% of the data points are described within an absolute deviation of $\Delta E_2 = \pm 0.5$ by the empirical model. Hence, the empirical model predicts the enrichment of a low-boiling component E_2 practically within the uncertainty of the determination of E_2 with different theoretical methods. However, as found for the performance on the training-dataset, the empirical model shows a trend to slightly overestimate the enrichment.

The performance of the model predictions are analyzed in more detail in Fig. 105, which shows the deviation plots for E_2 predicted by the empirical model and the values from the test-dataset. Its layout is analogue to that of Fig. 102. Fig. 105 a) shows
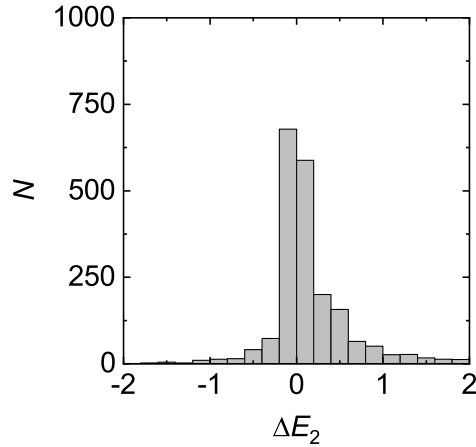
Figure 104: Histogram of the absolute deviations $\Delta E_2 = E_2^{\mathrm{ref}} - E_2^{\mathrm{model}}$ of the predictions of the empirical enrichment model to the data from the test-dataset (cf. Table 25). The bin width is 0.2.

the absolute deviation ΔE_2 as a function of the partition coefficient $K_2^{5\%}$; Fig. 105 b) shows ΔE_2 as a function of the liquid phase concentration x_2'; and Fig. 105 c) shows the absolute deviation ΔE_2 as a function of the enrichment E_2 itself. Absolute deviations $\Delta E_2 > 1$ are mainly found for large partition coefficients $K_2^{5\%}$, low x_2', and large E_2, which is attributed to simplifications in the term f_b in the empirical model. This is likely due to the fact that the training-dataset has only a relatively small amount of data points at large $K_2^{5\%} > 12$ and the fact that the model was applied to predict data points with $K_2^{5\%} > 15$. For mixtures with low $K_2^{5\%}$, the model performs very well.

From Figs. 105 a) - c), it becomes clear that the empirical model slightly overestimates the enrichment for most data points – especially data points with $\Delta \tilde{\rho}_2 < 0$, whereas data points with $\Delta \tilde{\rho}_2 > 0$ are mostly slightly underestimated. Some of the few outliers that can be seen in Fig. 105 might be due to the digitalization, see the Appendix for details.

The lined-up data points in Fig. 105 c) correspond to enrichment isotherms obtained from DGT from Refs. [50, 624, 632, 705]. In most cases, they are predicted well by the empirical model in a large composition range, but deviations are observed for high E_2. For low E_2 values, the empirical model correctly predicts the vast majority of reference values within an absolute deviation of $\Delta E_2 = \pm 0.3$, which is surprisingly good since even the deviations between the DGT and MD data usually exceed that range.
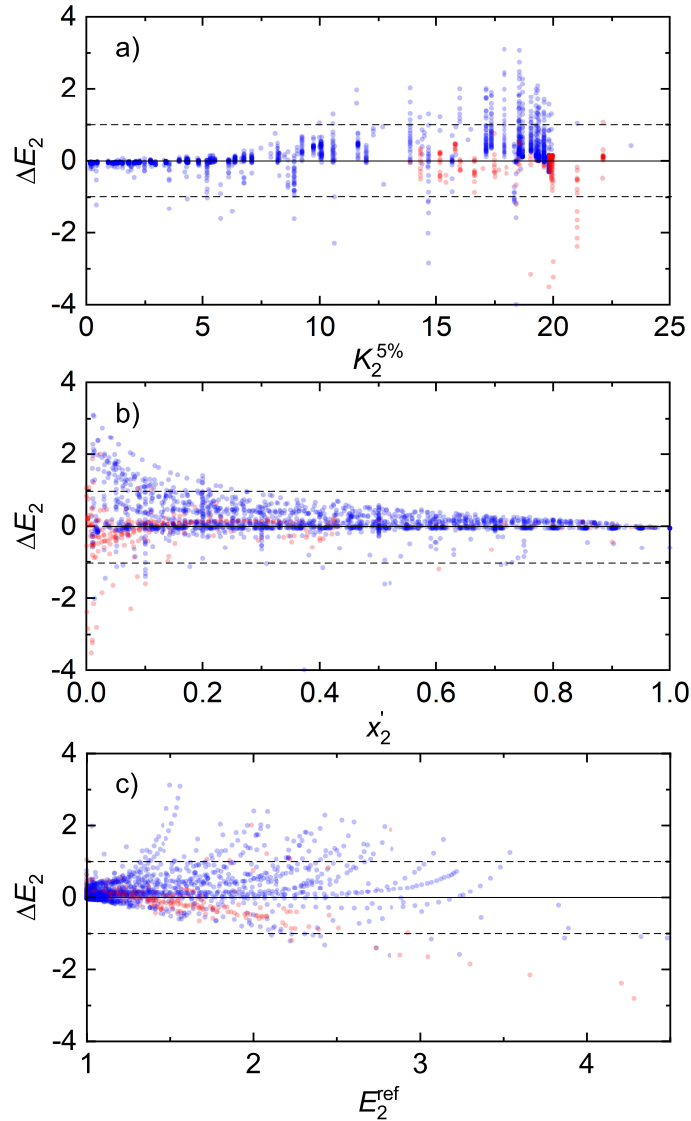
Figure 105: Deviation plots of the enrichment data from the test-dataset (cf. Table 25) and the predictions from the empirical model: a) shows the absolute deviation ΔE_2 as a function of the partition coefficient $K_2^{5\%}$; b) shows $\Delta E_2 = E_2^{\text{ref}} - E_2^{\text{model}}$ as a function of the liquid phase concentration x_2'; c) shows ΔE_2 as a function of the enrichment E_2 itself. Data that was used for the training of the empirical model [629, 630, 635] is not shown. Red indicates data points with $\Delta\tilde{\rho}_2 < 0$ and blue data points with $\Delta\tilde{\rho}_2 > 0$. The dashed lines indicate $\delta E_2 = \pm 1$, which corresponds to the uncertainty of the reference data.

9.6 Conclusions

The starting point of this study was a review of the enrichment of components at vapor-liquid interfaces and data available in the literature. The enrichment is defined quantitatively and is a measure for the non-monotonicity of the component density profile in the interfacial region. The enrichment is a highly interesting property as it is believed to influence the mass transfer across interfaces [159, 194, 199, 312, 328, 361, 488, 634, 635]. We have digitalized component density profiles from more than 100 publications and have used the profiles to determine the enrichment for about 2,300 data points. The established database is supplied in the electronic Supplementary Material [627]. The enrichment predicted from independent theoretical methods usually agrees within $\delta E_2 \pm 1$. The values of the enrichment lie mostly in the range $1 < E_2 < 10$.

The determination of the enrichment for a given system is presently tedious as it can only be achieved by complex theoretical methods. Therefore, an empirical short-cut method was developed in the present work to estimate the enrichment, a nanoscopic property, solely from macroscopic vapor-liquid equilibrium data for a given mixture. The database on the enrichment established in the present work was therefore split into a training-set and a test-set. The training-set (approximately 300 data points) consists of data from comprehensive studies on binary Lennard-Jones mixtures (cf. chapter 3) [629, 630, 635]. The test-set contains all remaining data on the enrichment available in the literature (approximately 2,000 data points). The empirical model describes the enrichment of the training-dataset with an AAD of 6.5%. The vast majority of data points is described by the empirical model with an error of $\Delta E_2 \pm 0.5$, which is well below the uncertainty of the reference data. Applying the empirical model on the test-dataset yields an AAD of 16.1%, whereat 84% of the data points are described within $\Delta E_2 \pm 0.5$. This is remarkable considering the fact that the enrichment model characterizes a mixture only by its partition coefficient at $x_2' = 0.05\,\mathrm{mol\,mol^{-1}}$ $K_2^{5\%}$ and the density difference in the bulk phases $\Delta\rho_2 = \rho_2' - \rho_2''$ of the low-boiling component 2. Moreover, for $\Delta\rho_2$, basically only the sign has to be known. As further input for the model, only the liquid phase concentration x_2' is needed. The model gets its information on the temperature only indirectly by the specification of $K_2^{5\%}$, which depends on the temperature. Hence, the model is designed in a way that the enrichment can be computed from the bulk compositions and densities solely, which is available in thermophysical property databases for a large number of systems.

For future work, it would be interesting to extend the dataset employed for the training of the model to systems with $K_2^{5\%} > 15$, i.e. particularly wide-boiling phase behavior, comprising mixtures with $\Delta\rho_2 > 0$ and $\Delta\rho_2 < 0$ as well as azeotropic systems. Furthermore, the performance of the model could probably be further improved by extending the model such that information on the critical composition or the three-phase equilibrium (if present) are incorporated. However, this would have the drawback that such data is not as readily available for most mixtures.

Finally, we would like to emphasize that it would be desirable that data on density profiles or profiles of other thermodynamic properties in interfacial regions, which is obtained by costly simulations, should be reported electronically. This has not been the case in the past such that the vast majority of the corresponding data that has been obtained in previous studies by expensive simulations is now lost for the community.

Based on the developed enrichment model, it was shown, that the nanoscopic enrichment is closely linked to the macroscopic phase behavior. This knowledge can be used for the screening of systems to identify mixtures with large enrichment.

10 Conclusions

The present work contributes to the general understanding of the physics of vapor-liquid interfaces. Both macroscopic and nanoscopic properties of vapor-liquid interfaces were studied, with a focus on mixtures. Two independent theoretical methods were employed: molecular dynamics (MD) simulations based on classical force fields and density gradient theory (DGT) in combination with theoretically-based equations of state (EOS). Furthermore, complementary laboratory experiments were performed for validation.

Different aspects of vapor-liquid interfaces of fluids were studied. Special attention was given to the density profiles of the components in the interfacial region and their dependence on the thermodynamic conditions as well as on the molecular interaction parameters and the resulting macroscopic phase behavior. As the nanoscopic structure of fluid interfaces is not accessible by experiment, it was studied here by MD and DGT. The vapor-liquid interfaces were thereby characterized by the surface tension, the relative adsorption, the interfacial thickness, and the enrichment of components.

While density profiles at vapor-liquid interfaces have been studied many times in the literature, no systematic evaluation on the characteristics of the surface excess in mixtures has been reported yet. The well-known relative Gibbs adsorption $\Gamma_i^{(j)}$ quantifies the number of adsorbed molecules of component i per unit area at the interface and can be calculated from both macroscopic properties (via the Gibbs adsorption equation) as well as from the nanoscopic density profiles $\rho_i(z)$. The enrichment E_i simply quantifies the relative peak hight of the non-monotonicity of the density profile of component i and is therefore dimensionless. The relative adsorption $\Gamma_i^{(j)}$ obtained from the nanoscopic and macroscopic routes were found in the present work to be in good agreement for an exemplary mixture, which confirms the consistency of the two routes [33, 50, 354, 361, 445, 483, 522, 692] and indicates that the underlying density profiles – including the enrichment – predicted from molecular thermodynamics are in agreement with the reality. This is supported by the fact that the enrichment in the density profiles is consistently predicted from MD and DGT for all systems considered in the present work. It is furthermore shown in the present work that the two properties $\Gamma_i^{(j)}$ and E_i show important differences upon characterizing the surface excess: starting at infinite dilution of component i, $\Gamma_i^{(j)}$ is zero and increases with increasing mole fraction in the liquid phase x_i' at constant temperature. The enrichment E_i, on the other hand, is mostly found to be highest at infinite dilution and monotonously decreases with increasing x_i'. However, both the enrichment E_i and the relative adsorption $\Gamma_i^{(j)}$ increase with decreasing temperature.

Even though the non-monotonicity of density profiles has been discussed in the literature before, no framework has been established yet elucidating the dependency of the

enrichment on the molecular interaction parameters as well as on the thermodynamic conditions and the corresponding phase behavior. By studying a large number of mixtures of model fluids, the present work, for the first time, establishes a general picture of the enrichment at vapor-liquid interfaces: enrichment is only found for the respective low-boiling component. Large enrichment is found for wide-boiling mixtures. The enrichment decreases with increasing temperature and increasing concentration of the of the low-boiling component in the liquid phase. Furthermore, strong enrichment is favored by similar number densities of the enriching component i in the bulk phases. For the case $\rho_i' = \rho_i''$, the relative adsorption has to result in an enrichment at the interface for geometric reasons.

In addition, it was shown in the present work that the enrichment can be understood as a precursor of a second liquid phase that nucleates under the influence of the gradients at the interface. Upon approaching a vapor-liquid-liquid three-phase line from a vapor-liquid two-phase region, the enrichment peak eventually exhibits the same density and composition as the second liquid phase. In the direct vicinity of the three-phase equilibrium, the enrichment peak broadens and a macroscopic phase evolves, which wets the vapor-liquid interface. Hence, the enrichment is strongly linked to the wetting behavior of the phases in vapor-liquid-liquid equilibria. This connection has not been described previously. The actual existence of a three-phase equilibrium is, however, not a necessary condition for an enrichment.

Conformal solution theory has been applied for a long time to explain the bulk behavior of mixtures. In the present work, a conformal solution theory of fluid interfaces was developed and tested: it was thereby shown that the properties of vapor-liquid interfaces are directly linked to the mean interactions of the liquid phase and can therefore be described as a simple function of the configurational internal energy. By comparing results that were obtained in the present work for a large number of different mixtures of simple fluids, it was shown that mixtures with the same configurational internal energy exhibit the same interfacial properties. This theory was found to be also valid in the limit of the pure component such that mixtures with the same configurational internal energy as a pure component have the same surface tension and interfacial thickness as that pure component – and zero relative adsorption. The monovariate relationship between vapor-liquid interfacial properties and the internal energy resembles the relationship between transport coefficients and the entropy [567]. It would be interesting to test the theory on real substance mixtures in a future work.

Based on these findings, a short-cut method was developed in the present work to establish a direct link between bulk vapor-liquid equilibrium properties and the nanoscopic enrichment at the interface. The comprehensive enrichment dataset on binary Lennard-Jones mixtures established in this work was used for the parametrization of that model. The model was tested on all available enrichment data from the literature, which comprises a large variety of binary mixtures. The good performance in that rigorous test reinforces the findings described above regarding an intimate relation between the bulk and interfacial VLE properties. The new short-cut method can be used in future work for the design of laboratory experiments to elucidate the influence of the enrichment on the mass transfer through interfaces.

These findings from the present work may have consequences for mixtures of practical relevance: no enrichment is expected for systems that exhibit an ideal behavior or high-

boiling azeotropic behavior. Large enrichment, on the other hand, is expected in wide-boiling systems, e.g. of the type solute + supercritical solvent or low-boiling azeotropic mixtures. Particularly large enrichment is expected in the vicinity of vapor-liquid-liquid equilibria and at low temperatures in general. Furthermore, high enrichment is expected at low concentrations of the low-boiling component. These results consistently indicate that mixtures, which are typical for absorption fluid separation processes usually show an important enrichment, whereas this is not the case for mixtures that are typically separated by distillation. This might explain the necessity for different approaches in the corresponding process design.

Non-equilibrium molecular simulation results from the present work furthermore indicate that the enrichment influences the mass transfer through fluid interfaces, which might have important consequences for fluid separation processes in chemical engineering as well as processes in nature. A new molecular simulation method for corresponding investigations was developed in this work and applied to Lennard-Jones mixtures that were studied prior to this regarding their equilibrium properties. Even though the two studied mixtures exhibit very similar bulk diffusivities, the mass fluxes through vapor-liquid interfaces in a system exhibiting an enrichment is found to be two to four times lower than in a reference system that does not exhibit an enrichment. This difference may indicate a hindrance caused by the enrichment at the interface. However, further studies are needed to prove or refute this hypothesis.

In the course of the present work, several other interesting results were obtained: isothermal sets of density profiles in vapor-liquid interfaces of mixtures may show common intersection points. They are clearly related to critical points – similar to the rectilinear diameter, which supports previous statements of *Bongiorno and Davis* [63]. Furthermore, the dispersive long-range interactions were found to have a significant influence on the surface tension and the interfacial thickness of Lennard-Jones mixtures, whereas the relative adsorption and the enrichment are hardly affected. The long-range interactions have practically no influence on the composition dependency of the investigated mixture properties. Moreover, using a new method for the examination of the oscillatory layering structure at vapor-liquid interfaces (as it is well-known from adsorption at solid-fluid interfaces) shows that density oscillations, as predicted by DFT [637], are also present in the molecular simulations density profiles, however, with a lower amplitude. The decay of the amplitude of the oscillatory layering structure with increasing temperature was found to be in good agreement with results from the literature [145].

Conformal representations of the VLE properties of the pure substance models (EOS and force field) are a prerequisite for a rigorous comparison of results from MD and DGT. The Lennard-Jones fluid was therefore comprehensively reviewed in the present work regarding two aspects: first, available simulation data was collated (35,000 data points), complemented by new simulations in in regions where previously only sparse data were available, and assessed. For the assessment different thermodynamic tests were applied: a new test was developed for homogeneous state points using data from their respective vicinity in combination with equations of state. For the VLE data assessment, the Clausius-Clapeyron equation and the compressibility factor of the vapor phase were used. The consolidated database was subsequently used for a systematic evaluation of 20 LJ EOS. A consolidated database for the simulation data and the corresponding results from the considered equations of state is provided in the electronic Supplementary Material [639, 640]. Hence, the developed test procedure can be used in future work as

benchmark test.

Furthermore, the PC-SAFT monomer term was re-parametrized in this work using Lennard-Jones molecular simulation data with the objective to describe both VLE and homogeneous state properties well. The evaluation and comparison with other LJ EOS reveals shortcomings for the description of caloric properties and supercritical states in general. This is probably a result of the simplified form of the temperature-dependent diameter used for the modeling of the soft repulsion in the EOS. This supports findings from *Boshkova and Deiters* [66] regarding PC-SAFT.

Nevertheless, the new LJ EOS yields an excellent description of the VLE properties and shows a reasonable behavior in the vapor-liquid two-phase region, i.e. a single van der Waals loop. It is therefore a good candidate for studies of interfacial properties using density gradient theory. Furthermore, the functional form of the new LJ EOS is consistent with that of the PeTS EOS [249], which enables a meaningful comparison of the DGT results for LJ and LJTS mixtures, as it was performed in this work to study the influence of dispersive long-range interactions (see above).

Interfacial properties are a direct result of the large gradients of the profiles of thermodynamic properties across the interface. These profiles connect the bulk values of the properties. It is therefore obvious that the interfacial properties are closely related to the respective bulk phase properties. The success of the conformal solution theory developed in the present work shows that properties of vapor-liquid interfaces are dominated by the properties of the respective liquid phase. Furthermore, the profiles of thermodynamic properties in the interfacial region often show invariant intersection points, when several of these profiles, obtained by changing only a single parameter, are plotted together. Also this surprising feature is closely related to bulk properties, e.g. the results from the present work clearly show that the invariant points of sets of density profiles are linked to critical points in the corresponding phase diagram. Moreover, the oscillatory layering structure at vapor-liquid interfaces is a consequence of the corresponding radial distribution function of the liquid bulk phase. Last not least, the enrichment at vapor-liquid interfaces can be interpreted as a precursor of a second liquid phase that is eventually found in the phase diagram of the studied system. Hence, a picture evolves in which the properties of the interfacial region mirror bulk properties of the system, albeit in the way of a fun-house mirror in which the bulk behavior is distorted by the strong gradients.

Literature

[1] Dortmund data bank (accessed january 2020), www.ddbst.com, 2020.

[2] J.L.F. Abascal, C. Vega: A general purpose model for the condensed phases of water: TIP4P/2005, The Journal of Chemical Physics 123 (2005) 234505. doi:`10.1063/1.2121687`.

[3] M. Abraham, R. Apostolov, J. Barnoud, P. Bauer, C. Blau, A.M. Bonvin, M. Chavent, J. Chodera, K. Condic-Jurkic, L. Delemotte, H. Grubmueller, R.J. Howard, E.J. Jordan, E. Lindahl, O.H.S. Ollila, J. Selent, D.G.A. Smith, P.J. Stansfeld, J.K. Tiemann, M. Trellet, C. Woods, A. Zhmurov: Sharing data from molecular simulations, Journal of Chemical Information and Modeling 59 (2019) 4093–4099. doi:`10.1021/acs.jcim.9b00665`.

[4] Y. Adachi, I. Fijihara, M. Takamiya, K. Nakanishi: Generalized equation of state for Lennard-Jones fluids – I. pure fluids and simple mixtures, Fluid Phase Equilibria 39 (1988) 1–38. doi:`10.1016/0378-3812(88)80001-3`.

[5] D.J. Adams: Grand canonical ensemble Monte Carlo for a Lennard-Jones fluid, Molecular Physics 29 (1975) 307–311. doi:`10.1080/00268977500100221`.

[6] D.J. Adams: Calculating the low temperature vapour line by Monte Carlo, Molecular Physics 32 (1976) 647–657. doi:`10.1080/00268977600102101`.

[7] D.J. Adams: Calculating the high-temperature vapour line by Monte Carlo, Molecular Physics 37 (1979) 211–221. doi:`10.1080/00268977900100171`.

[8] D.J. Adams, E.M. Adams, G.J. Hills: The computer simulation of polar liquids, Molecular Physics 38 (1979) 387–400. doi:`10.1080/00268977900101751`.

[9] R. Agrawal, D.A. Kofke: Thermodynamic and structural properties of model systems at solid-fluid coexistence, Molecular Physics 85 (1995) 43–59. doi:`10.1080/00268979500100921`.

[10] J. Ahlers, J. Gmehling: Development of an universal group contribution equation of state: I. prediction of liquid densities for pure compounds with a volume translated Peng-Robinson equation of state, Fluid Phase Equilibria 191 (2001) 177–188. doi:`10.1016/S0378-3812(01)00626-4`.

[11] A. Ahmed, R.J. Sadus: Solid-liquid equilibria and triple points of n-6 Lennard-Jones fluids, The Journal of Chemical Physics 131 (2009) 174504. doi:`10.1063/1.3253686`.

[12] A. Ahmed, R.J. Sadus: Erratum: Solid-liquid equilibria and triple points of n-6 Lennard-Jones fluids [J. Chem. Phys. 131, 174504 (2009)], The Journal of Chemical Physics 133 (2010) 229902. doi:10.1063/1.3512996.

[13] C.G. Aimoli, E.J. Maginn, C.R.A. Abreu: Transport properties of carbon dioxide and methane from molecular dynamics simulations, The Journal of Chemical Physics 141 (2014) 134101. doi:10.1063/1.4896538.

[14] T.A. Al-Sahhaf, R.S. Al-Ameeri, S.E. Hamam: Bubble point measurements for the ternary system: Carbon dioxide, cyclohexane and naphthalene, Fluid Phase Equilibria 53 (1989) 31–37. doi:10.1016/0378-3812(89)80070-6.

[15] B.J. Alder, T.E. Wainwright: Studies in molecular dynamics. I. general method, The Journal of Chemical Physics 31 (1959) 459–466. doi:10.1063/1.1730376.

[16] J. Algaba, M. Cartes, M. A., J.M. Miguez, F.J. Blas: Phase equilibria and interfacial properties of the tetrahydrofuran + methane binary mixture from experiment and computer simulation, The Journal of Physical Chemistry C 123 (2019) 20960–20970. doi:10.1021/acs.jpcc.9b05412.

[17] M.P. Allen, D.J. Tildesley: Computer Simulation of Liquids, Oxford University Press, Oxford, 1989.

[18] B.S. Almeida, M.M. Telo da Gama: Surface tension of simple mixtures: comparison between theory and experiment, The Journal of Physical Chemistry 93 (1989) 4132–4138. doi:10.1021/j100347a051.

[19] N.M. Alsaifi: Simulation-based equations of state for the Lennard-Jones fluid: Apparent success and hidden failure, AIChE Journal (2020) e16244. doi:10.1002/aic.16244.

[20] F. Alsmeyer, H. Koß, W. Marquardt: Indirect spectral hard modeling for the analysis of reactive and interacting mixtures, Applied Spectroscopy 58 (2004) 975–985. doi:10.1366/0003702041655368.

[21] A. Amadei, M.E.F. Apol, G. Chillemi, H.J.C. Berendsen, A. Di Nola: Derivation of a general fluid equation of state based on the quasi-Gaussian entropy theory: Application to the Lennard-Jones fluid, Molecular Physics 96 (1999) 1469–1490. doi:10.1080/00268979909483091.

[22] G. Andersson, T. Krebs, H. Morgner: Activity of surface active substances determined from their surface excess, Physical Chemistry Chemical Physics 7 (2005) 136. doi:10.1039/b412375a.

[23] S.I. Anisimov, D.O. Dunikov, V.V. Zhakhovskii, S.P. Malyshenko: Properties of a liquid-gas interface at high-rate evaporation, The Journal of Chemical Physics 110 (1999) 8722–8729. doi:10.1063/1.478779.

[24] Anonymous: Surface tension of carbon dioxide, Confident. Comp. Res. Rep.; cf. Ref. [1] Nr. 20568 (1972) 1.

[25] J. Aracil, G. Luengo, B.S. Almeida, M.M. Telo da Gama, R.G. Rubio, M. Diaz Pena: Surface properties of mixtures of molecular fluids: an experimental and theoretical study of carbon disulfide + dichloromethane and carbon disulfide + carbon tetrachloride, The Journal of Physical Chemistry 93 (1989) 3210–3218. doi:10.1021/j100345a065.

[26] G. Arya, H.C. Chang, E.J. Maginn: A critical comparison of equilibrium, non-equilibrium and boundary-driven molecular dynamics techniques for studying transport in microporous materials, The Journal of Chemical Physics 115 (2001) 8112–8124. doi:10.1063/1.1407002.

[27] C. Avendaño, T. Lafitte, C. Adjiman, A. Galindo, E. Müller, G. Jackson: Saft–γ force field for the simulation of molecular fluids: 2. coarse-grained models of greenhouse gases, refrigerants, and long alkanes, The Journal of Physical Chemistry B 117 (2013) 2717–2733. doi:10.1021/jp306442b.

[28] C. Avendaño, T. Lafitte, A. Galindo, C. Adjiman, G. Jackson, E. Müller: Saft–γ force field for the simulation of molecular fluids. 1. a single-site coarse grained model of carbon dioxide, The Journal of Physical Chemistry B 115 (2011) 11154–11169. doi:10.1021/jp204908d.

[29] S. Azizian, N. Bashavard: Surface tension of dilute solutions of alkanes in cyclohexanol at different temperatures, Journal of Chemical & Engineering Data 53 (2008) 2422–2425. doi:10.1021/je8004112.

[30] S. Azizian, N. Bashavard, B. Yahyaei: Surface properties of dilute solutions of alkanes in benzyl alcohol, Journal of Chemical & Engineering Data 51 (2006) 56–59. doi:10.1021/je050159x.

[31] V. Baidakov, G. Chernykh, S. Protsenko: Effect of the cut-off radius of the intermolecular potential on phase equilibrium and surface tension in Lennard-Jones systems, Chemical Physics Letters 321 (2000) 315–320. doi:10.1016/S0009-2614(00)00217-7.

[32] V.G. Baidakov, A.M. Kaverin, M.N. Khotienkova: Surface tension of ethane-methane solutions: 1. experiment and thermodynamic analysis of the results, Fluid Phase Equilibria 356 (2013) 90–95. doi:10.1016/j.fluid.2013.07.008.

[33] V.G. Baidakov, M.N. Khotienkova: Surface tension of methane-nitrogen solutions: 2. description in the framework of the van der Waals gradient theory, Fluid Phase Equilibria 425 (2016) 402–410. doi:10.1016/j.fluid.2016.06.038.

[34] V.G. Baidakov, S.P. Protsenko: Molecular-dynamics investigation of phase equilibrium and surface tension in argon-neon system, The Journal of Physical Chemistry C 112 (2008) 17231–17234. doi:10.1021/jp805566g.

[35] V.G. Baidakov, S.P. Protsenko: Molecular-dynamics simulation of relaxation processes at liquid–gas interfaces in single- and two-component lennard-jones systems, Colloid Journal 81 (2019) 491–500. doi:10.1134/S1061933X19040021.

[36] V.G. Baidakov, S.P. Protsenko, V.M. Bryukhanov: Relaxation processes at liquid-gas interfaces in one- and two-component Lennard-Jones systems: Molecular dynamics simulation, Fluid Phase Equilibria 481 (2019) 1–14. doi:10.1016/j.fluid.2018.10.012.

[37] V.G. Baidakov, S.P. Protsenko, G.G. Chernykh, G.S. Boltachev: Statistical substantiation of the van der Waals theory of inhomogeneous fluids, Physical Review E 65 (2002) 041601. doi:10.1103/PhysRevE.65.041601.

[38] V.G. Baidakov, S.P. Protsenko, Z.R. Kozlova: Thermal and caloric equations of state for stable and metastable Lennard-Jones fluids: I. molecular-dynamics simulations, Fluid Phase Equilibria 263 (2008) 55–63. doi:10.1016/j.fluid.2007.09.019.

[39] V.G. Baidakov, S.P. Protsenko, Z.R. Kozlova, G.G. Chernykh: Metastable extension of the liquid-vapor phase equilibrium curve and surface tension, The Journal of Chemical Physics 126 (2007) 214505. doi:10.1063/1.2734964.

[40] A. Baranyai, D.J. Evans: Direct entropy calculation from computer simulation of liquids, Physical Review A 40 (1989) 3817–3822. doi:10.1103/PhysRevA.40.3817.

[41] J.A. Barker, D. Henderson: Perturbation theory and equation of state for fluids. II. a successful theory of liquids, The Journal of Chemical Physics 47 (1967) 4714. doi:10.1063/1.1701689.

[42] J.A. Barker, D. Henderson: Perturbation theory and equation of state for fluids: The square-well potential, The Journal of Chemical Physics 47 (1967) 2856–2861. doi:10.1063/1.1712308.

[43] J.A. Barker, D. Henderson: Theories of liquids, Annual Review of Physical Chemistry 23 (1972) 439–484. doi:10.1146/annurev.pc.23.100172.002255.

[44] J.A. Barker, D. Henderson: What is "liquid"? understanding the states of matter, Review of modern physics 48 (1976) 587–671. doi:10.1103/RevModPhys.48.587.

[45] J.A. Barker, J.R. Henderson: Generalized van der Waals theories and the asymptotic form of the density profile of a liquid-vapor interface, The Journal of Chemical Physics 76 (1982) 6303–6307. doi:10.1063/1.443033.

[46] J.A. Barker, P.J. Leonard, A. Pompe: Fifth virial coefficients, The Journal of Chemical Physics 44 (1966) 4206–4211. doi:10.1063/1.1726606.

[47] V. Barnett, T. Lewis: Outliers in Statistical Data, Wiley, Chichester, 1978.

[48] M.A. Barroso, A.L. Ferreira: Solid-fluid coexistence of the Lennard-Jones system from absolute free energy calculations, The Journal of Chemical Physics 116 (2002) 7145–7150. doi:10.1063/1.1464828.

[49] S. Becker, H.M. Urbassek, M. Horsch, H. Hasse: Contact angle of sessile drops in Lennard-Jones systems, Langmuir 30 (2014) 13606. doi:10.1021/la503974z.

[50] S. Becker, S. Werth, M. Horsch, K. Langenbach, H. Hasse: Interfacial tension and adsorption in the binary system ethanol and carbon dioxide: Experiments, molecular simulation and density gradient theory, Fluid Phase Equilibria 427 (2016) 476. doi:`10.1016/j.fluid.2016.08.007`.

[51] M. Benedict, G.B. Webb, L.C. Rubin: An empirical equation for thermodynamic properties of light hydrocarbons and their mixtures i. methane, ethane, propane and n-butane, The Journal of Chemical Physics 8 (1940) 334–345. doi:`10.1063/1.1750658`.

[52] D. Berthelot: Sur le mélange des gaz, Comptes rendus hebdomadaires des séances de l'Académie des Sciences 126 (1898) 1703–1706.

[53] F. Betancourt-Cardenas, L. Galicia-Luna, S. Sandler: Equation of state for the Lennard-Jones fluid based on the perturbation theory, Fluid Phase Equilibria 264 (2008) 174–183. doi:`10.1016/j.fluid.2007.11.015`.

[54] E. Bird, Z. Liang: Transport phenomena in the Knudsen layer near an evaporating surface, Physical Review E 100 (2019) 043108. doi:`10.1103/PhysRevE.100.043108`.

[55] R.B. Bird, E.L. Spotz, J.O. Hirschfelder: The third virial coefficient for non-polar gases, The Journal of Chemical Physics 18 (1950) 1395–1402. doi:`10.1063/1.1747484`.

[56] F. Biscay, A. Ghoufi, V. Lachet, P. Malfreyt: Monte Carlo simulations of the pressure dependence of the water-acid gas interfacial tensions, The Journal of Physical Chemistry B 113 (2009) 14277–14290. doi:`10.1021/jp906953a`.

[57] F.J. Blas, L.F. Vega: Thermodynamic behaviour of homonuclear and heteronuclear Lennard-Jones chains with association sites from simulation and theory, Molecular Physics 92 (1997) 135–150. doi:`10.1080/002689797170707`.

[58] F.J. Blas, L.F. Vega: Prediction of binary and ternary diagrams using the statistical associating fluid theory (SAFT) equation of state, Industrial & Engineering Chemistry Research 37 (1998) 660–674. doi:`10.1021/ie970449+`.

[59] E. Blokhuis, D. Bedeaux, C. Holcomb, J. Zollweg: Tail corrections to the surface tension of a Lennard-Jones liquid-vapour interface, Molecular Physics 85 (1995) 665–669. doi:`10.1080/00268979500101371`.

[60] D. Boda, T. Lukács, J. Liszi, I. Szalai: The isochoric-, isobaric- and saturation-heat capacities of the Lennard-Jones fluid from equations of state and Monte Carlo simulations, Fluid Phase Equilibria 119 (1996) 1–16. doi:`10.1016/0378-3812(96)02998-6`.

[61] P.G. Bolhuis, D. Chandler: Transition path sampling of cavitation between molecular scale solvophobic surfaces, The Journal of Chemical Physics 113 (2000) 8154–8160. doi:`10.1063/1.1315997`.

[62] G.S. Boltachev, V.G. Baidakov: Equation of state for Lennard-Jones fluid, High Temperature 41 (2003) 270–272. doi:`10.1023/A:1023394122000`.

[63] V. Bongiorno, H.T. Davis: Modified van der Waals theory of fluid interfaces, Physical Review A 12 (1975) 2213–2224. doi:`10.1103/PhysRevA.12.2213`.

[64] M. Bortz, J. Burger, N. Asprion, S. Blagov, R. Böttcher, U. Nowak, A. Scheithauer, R. Welke, K.H. Küfer, H. Hasse: Multi-criteria optimization in chemical process design and decision support by navigation on pareto sets, Computers & Chemical Engineering 60 (2014) 354–363. doi:`10.1016/j.compchemeng.2013.09.015`.

[65] M. Bortz, V. Maag, J. Schwientek, R. Benfer, R. Böttcher, J. Burger, E. von Harbou, N. Asprion, K.H. Küfer, H. Hasse: Decision support by multicriteria optimization in process development: An integrated approach for robust planning and design of plant experiments, in: K.V. Gernaey, J.K. Huusom, R. Gani (Eds.), 12th International Symposium on Process Systems Engineering and 25th European Symposium on Computer Aided Process Engineering, volume 37 of *Computer Aided Chemical Engineering*, 2015, pp. 2063–2068. doi:`10.1016/B978-0-444-63576-1.50038-8`.

[66] O.L. Boshkova, U.K. Deiters: Soft repulsion and the behavior of equations of state at high pressures, International Journal of Thermophysics 31 (2010) 227–252. doi:`10.1007/s10765-010-0727-7`.

[67] T. Boublík: Hard sphere equation of state, The Journal of Chemical Physics 53 (1970) 471. doi:`10.1063/1.1673824`.

[68] R. Bracewell: The Fourier Tranform and its Applications, 2nd ed., McGraw-Hill, New York, 1978.

[69] J. Brader, R. Evans, M. Schmidt: Statistical mechanics of inhomogeneous model colloid-polymer mixtures, Molecular Physics 101 (2003) 3349–3384. doi:`10.1080/00268970320000174263`.

[70] C. Braga, A. Galindo, E.A. Müller: Nonequilibrium molecular dynamics simulation of diffusion at the liquid-liquid interface, The Journal of Chemical Physics 141 (2014) 154101. doi:`10.1063/1.4897159`.

[71] C. Braga, J. Muscatello, G. Lau, E.A. Müller, G. Jackson: Nonequilibrium study of the intrinsic free-energy profile across a liquid-vapour interface, The Journal of Chemical Physics 144 (2016) 044703. doi:`10.1063/1.4940137`.

[72] B. Breure, C. Peters: Modeling of the surface tension of pure components and mixtures using the density gradient theory combined with a theoretically derived influence parameter correlation, Fluid Phase Equilibria 334 (2012) 189–196. doi:`10.1016/j.fluid.2012.08.010`.

[73] E.H. Brown: On the thermodynamic properties of fluids, Bulletin de l'Institut International du Froid Annexe 1960-1 (1960) 169–178.

[74] J.R. Brown, Y. Seo, T.A.D. Maula, L.M. Hall: Fluids density functional theory and initializing molecular dynamics simulations of block copolymers, The Journal of Chemical Physics 144 (2016) 124904. doi:`10.1063/1.4943982`.

[75] W.E. Brown: The Fisher-Widom line for a hard core attractive Yukawa fluid, Molecular Physics 88 (1996) 579–584. doi:`10.1080/002689979650026541`.

[76] F.P. Buff, R.A. Lovett, F.H. Stillinger: Interfacial density profile for fluids in the critical region, Physical Review Letters 15 (1965) 621–623. doi:`10.1103/PhysRevLett.15.621`.

[77] C. Bühl, A. Danzer, S. Enders: Prediction of surface properties of binary, sulfur containing mixtures, Fluid Phase Equilibria 416 (2016) 94–103. doi:`10.1016/j.fluid.2015.08.026`.

[78] C. Bühl, S. Enders: Prediction of interfacial properties of ternary, sulfur-containing mixtures, Journal of Chemical & Engineering Data 61 (2016) 4261–4269. doi:`10.1021/acs.jced.6b00637`.

[79] J.B. Buhn, P.A. Bopp, M.J. Hampe: A molecular dynamics study of a liquid-liquid interface: Structure and dynamics, Fluid Phase Equilibria 224 (2004) 221–230. doi:`10.1016/j.fluid.2004.02.012`.

[80] C. G. Gray, K. E. Gubbins: Theory of Molecular Fluids, Vol. 1: Fundamentals, Clarendon Press, Oxford, 1984.

[81] J.W. Cahn: Free energy of a nonuniform system. II. thermodynamic basis, The Journal of Chemical Physics 30 (1959) 1121. doi:`10.1063/1.1730145`.

[82] J.W. Cahn, J.E. Hilliard: Free energy of a nonuniform system. I. interfacial free energy, The Journal of Chemical Physics 28 (1958) 258. doi:`10.1063/1.1744102`.

[83] Cailletet, L., Mathias, E.: Recherches sur les densités des gaz liquéfiés et de leurs vapeurs saturées, J. Phys. Theor. Appl. 5 (1886) 549–564. doi:`10.1051/jphystap:018860050054900`.

[84] J.M. Caillol: Critical-point of the Lennard-Jones fluid: A finite-size scaling study, The Journal of Chemical Physics 109 (1998) 4885–4893. doi:`10.1063/1.477099`.

[85] A.N. Campbell, S.C. Anand: Densities, excess volumes, surface tensions, viscosities, and dielectric constants of the systems: Methanol-cyclohexane, acetone-methanol, acetone-cyclohexane, and methanol-cyclohexane-acetone, Canadian Journal of Chemistry 50 (1972) 1109–1114. doi:`10.1139/v72-176`.

[86] F. Cao, J.D. Deetz, H. Sun: Free energy-based coarse-grained force field for binary mixtures of hydrocarbons, nitrogen, oxygen, and carbon dioxide, Journal of Chemical Information and Modeling 57 (2016) 50–59. doi:`10.1021/acs.jcim.6b00685`.

[87] H. Cardenas, A. Mejía: Phase behaviour and interfacial properties of ternary system CO_2 + n-butane + n-decane: Coarse-grained theoretical modelling and molecular simulations, Molecular Physics 114 (2016) 2627–2640. doi:`10.1080/00268976.2016.1170221`.

[88] G. Cardini: A comparison between the rigid and flexible model of cyclohexane in the plastic phase by molecular dynamic simulations, Chemical Physics 193 (1995) 101–108. doi:`10.1016/0301-0104(94)00396-R`.

[89] B. Carey: The Gradient Theory of Fluid Interfaces, Ph.D. thesis, University of Minnesota, Minneapolis, 1979.

[90] B.S. Carey, L.E. Scriven, H.T. Davis: On gradient theories of fluid interfacial stress and structure, The Journal of Chemical Physics 69 (1978) 5040–5049. doi:`10.1063/1.436494`.

[91] B.S. Carey, L.E. Scriven, H.T. Davis: Semiempirical theory of surface tension of binary systems, AIChE Journal 26 (1980) 705–711. doi:`10.1002/aic.690260502`.

[92] D.D. Carley: Integral equation and perturbation method for equations of state for a low temperature Lennard-Jones gas, The Journal of Chemical Physics 67 (1977) 4812–4818. doi:`10.1063/1.434684`.

[93] N.F. Carnahan, K.E. Starling: Equation of state for nonattracting rigid spheres, The Journal of Chemical Physics 51 (1969) 635–636. doi:`10.1063/1.1672048`.

[94] F. Castro-Marcano, C.G. Olivera-Fuentes, C.M. Colina: Joule-Thomson inversion curves and third virial coefficients for pure fluids from molecular-based models, Industrial & Engineering Chemistry Research 47 (2008) 8894–8905. doi:`10.1021/ie800651q`.

[95] T.M. Chang, L.X. Dang: Liquid-vapor interface of methanol-water mixtures: A molecular dynamics study, The Journal of Physical Chemistry B 109 (2005) 5759–5765. doi:`10.1021/jp045649v`.

[96] T.M. Chang, K.A. Peterson, L.X. Dang: Molecular dynamics simulations of liquid, interface, and ionic solvation of polarizable carbon tetrachloride, The Journal of Chemical Physics 103 (1995) 7502–7513. doi:`10.1063/1.470319`.

[97] G.A. Chapela, G. Saville, S.M. Thompson, J.S. Rowlinson: Computer simulation of a gas-liquid surface. part 1, Journal of The Chemical Society, Faraday Transactions 2 73 (1977) 1133–1144. doi:`10.1039/F29777301133`.

[98] G.A. Chapela, L.E. Scriven, H.T. Davis: Molecular dynamics for discontinuous potential. IV. Lennard-Jonesium, The Journal of Chemical Physics 91 (1989) 4307–4313. doi:`10.1063/1.456811`.

[99] W.G. Chapman: Prediction of the thermodynamic properties of associating Lennard-Jones fluids: Theory and simulation, The Journal of Chemical Physics 93 (1990) 4299–4304. doi:`10.1063/1.458711`.

[100] W.G. Chapman, K.E. Gubbins, G. Jackson, M. Radosz: SAFT: Equation-of-state solution model for associating fluids, Fluid Phase Equilibria 52 (1989) 31–38. doi:`10.1016/0378-3812(89)80308-5`.

[101] W.G. Chapman, G. Jackson, K.E. Gubbins: Phase equilibira of associating fluids. Chain molecules with multiple bonding sites, Molecular Physics 65 (1988) 1057–1079.

[102] W.G. Chapman, G. Jackson, K.E. Gubbins, M. Radosz: New reference equation of state for associating liquids, Industrial & Engineering Chemistry Research 29 (1990) 1709.

[103] R.S. Chatwell, M. Heinen, J. Vrabec: Diffusion limited evaporation of a binary liquid film, International Journal of Heat and Mass Transfer 132 (2019) 1296–1305. doi:10.1016/j.ijheatmasstransfer.2018.12.030.

[104] B. Chen, J.I. Siepmann, M.L. Klein: Direct Gibbs Ensemble Monte Carlo simulations for solid-vapor phase equilibria: Applications to Lennard-Jonesium and carbon dioxide, The Journal of Physical Chemistry B 105 (2001) 9840–9848. doi:10.1021/jp011950p.

[105] C. Chen, W. Hu, W. Li, Y. Song: Model comparison of the CH4/CO2/water system in predicting dynamic and interfacial properties, Journal of Chemical Engineering Data 64 (2019) 2464–2474. doi:10.1021/acs.jced.9b00006.

[106] C.k. Chen, M. Banaszak, M. Radosz: Statistical associating fluid theory equation of state with Lennard-Jones reference applied to pure and binary n-alkane systems, The Journal of Physical Chemistry B 102 (1998) 2427–2431. doi:10.1021/jp9731819.

[107] L.H. Chen, Y.L. Lee: Adsorption behavior of surfactants and mass transfer in single-drop extraction, AIChE Journal 46 (2000) 160–168. doi:10.1002/aic.690460118.

[108] S.S. Chen, A. Kreglewski: Applications of the augmented van der Waals theory of fluids.: I. pure fluids, Berichte der Bunsengesellschaft für physikalische Chemie 81 (1977) 1048. doi:10.1002/bbpc.19770811037.

[109] X. Chen, G.h. Liu, H. Fan, M. Li, T. Luo, L. Qi, H. Wang: Effects of surfactant contamination on oxygen mass transfer in fine bubble aeration process, Korean Journal of Chemical Engineering 30 (2013) 1741–1746.

[110] S. Cheng, J.B. Lechman, S.J. Plimpton, G.S. Grest: Evaporation of Lennard-Jones fluids, The Journal of Chemical Physics 134 (2011) 224704. doi:10.1063/1.3595260.

[111] H.K. Chilukoti, G. Kikugawa, T. Ohara: A molecular dynamics study on transport properties and structure at the liquid-vapor interfaces of alkanes, International Journal of Heat and Mass Transfer 59 (2013) 144–154. doi:10.1016/j.ijheatmasstransfer.2012.12.015.

[112] H.K. Chilukoti, G. Kikugawa, T. Ohara: Self-diffusion coefficient and structure of binary n-alkane mixtures at the liquid-vapor interfaces, The Journal of Physical Chemistry B 119 (2015) 13177–13184. doi:10.1021/acs.jpcb.5b07189.

[113] H.K. Chilukoti, G. Kikugawa, T. Ohara: Structure and mass transport characteristics at the intrinsic liquid-vapor interfaces of alkanes, The Journal of Physical Chemistry B 120 (2016) 7207–7216. doi:`10.1021/acs.jpcb.6b05332`.

[114] R.D. Chirico, M. Frenkel, J.W. Magee, V. Diky, C.D. Muzny, A.F. Kazakov, K. Kroenlein, I. Abdulagatov, G.R. Hardin, W.E. Acree, J.F. Brenneke, P.L. Brown, P.T. Cummings, T.W. de Loos, D.G. Friend, A.R.H. Goodwin, L.D. Hansen, W.M. Haynes, N. Koga, A. Mandelis, K.N. Marsh, P.M. Mathias, C. McCabe, J.P. O'Connell, A. Pádua, V. Rives, C. Schick, J.P.M. Trusler, S. Vyazovkin, R.D. Weir, J. Wu: Improvement of quality in publication of experimental thermophysical property data: Challenges, assessment tools, global implementation, and online support, Journal of Chemical & Engineering Data 58 (2013) 2699–2716. doi:`10.1021/je400569s`.

[115] J.S. Choi, Y.C. Bae: Phase equilibrium and interfacial tension of binary and ternary polymer solutions, Journal of Chemical & Engineering Data 61 (2016) 4157–4163. doi:`10.1021/acs.jced.6b00573`.

[116] N. Choudhary, A.K.N. Nair, M.F.A.C. Ruslan, S. Sun: Bulk and interfacial properties of decane in the presence of carbon dioxide, methane, and their mixture, Scientific Reports 9 (2019) 1–10. doi:`10.1038/s41598-019-56378-y`.

[117] Y.T.F. Chow, D.K. Eriksen, A. Galindo, A.J. Haslam, G. Jackson, G.C. Maitland, J.P. Trusler: Interfacial tensions of systems comprising water, carbon dioxide and diluent gases at high pressures: Experimental measurements and modelling with SAFT-VR Mie and square-gradient theory, Fluid Phase Equilibria 407 (2016) 159–176. doi:`10.1016/j.fluid.2015.07.026`.

[118] H.L. Clever, W.E. Chase: Thermodynamics of liquid surfaces., Journal of Chemical & Engineering Data 8 (1963) 291–292. doi:`10.1021/je60018a004`.

[119] B.D. Coleman, W. Noll: The thermodynamics of elastic materials with heat conduction and viscosity, Archive for Rational Mechanics and Analysis 13 (1963) 167–178. doi:`10.1007/BF01262690`.

[120] C.M. Colina, E.A. Müller: Molecular simulation of Joule-Thomson inversion curves, International Journal of Thermophysics 20 (1999) 229–235. doi:`10.1023/A:1021402902877`.

[121] P.M. Cornelisse: The Square Gradient Theory Applied Simultaneous Modelling of Interfacial Tension and Phase Behaviour, Ph.D. thesis, Technische Universiteit Delft, 1997.

[122] P.M. Cornelisse, C.J. Peters, J. de Swaan Arons: Application of the Peng-Robinson equation of state to calculate interfacial tensions and profiles at vapour-liquid interfaces, Fluid Phase Equilibria 82 (1993) 119–129. doi:`10.1016/0378-3812(93)87135-N`.

[123] P.M. Cornelisse, C.J. Peters, J. de Swaan Arons: Simultaneous prediction of phase equilibria, interfacial tension and concentration profiles, Molecular Physics 80 (1993) 941–955. doi:`10.1080/00268979300102781`.

[124] P.M. Cornelisse, C.J. Peters, J. de Swaan Arons: Non-classical interfacial tension and fluid phase behaviour, Fluid Phase Equilibria 117 (1996) 312–319. doi:`10.1016/0378-3812(95)02968-0`.

[125] P.M. Cornelisse, C.J. Peters, J. de Swaan Arons: On the fundamentals of the gradient theory of van der Waals, The Journal of Chemical Physics 106 (1997) 9820–9834. doi:`10.1063/1.473872`.

[126] P.M. Cornelisse, C.J. Peters, J. de Swaan Arons: Interfacial phase transitions at solid-fluid and liquid-vapor interfaces, International Journal of Thermophysics 19 (1998) 1501–1509. doi:`10.1007/BF03344902`.

[127] M.E. Costas, C. Varea, A. Robledo: Global phase diagram for the wetting transition at interfaces in fluid mixtures, Physical Review Letters 51 (1983) 2394–2397. doi:`10.1103/PhysRevLett.51.2394`.

[128] R.L. Cotterman, B.J. Schwarz, J.M. Prausnitz: Molecular thermodynamics for fluids at low and high densities. Part I: Pure fluids containing small or large molecules, AIChE Journal 32 (1986) 1787–1798. doi:`10.1002/aic.690321104`.

[129] F. Cuadros, A. Mulero, W. Ahumada: An extensive study of the Helmholtz free energy of Lennard-Jones fluids using WCA theory, Thermochimica Acta 277 (1996) 85–105. doi:`10.1016/0040-6031(95)02757-2`.

[130] C. Cumicheo, M. Cartes, H. Segura, E.A. Müller, A. Mejía: High-pressure densities and interfacial tensions of binary systems containing carbon dioxide + n-alkanes: (n-dodecane, n-tridecane, n-tetradecane), Fluid Phase Equilibria 380 (2014) 82. doi:`10.1016/j.fluid.2014.07.039`.

[131] T.E. Daubert: Vapor-liquid critical properties of elements and compounds. 5. branched alkanes and cycloalkanes, Journal of Chemical & Engineering Data 41 (1996) 365–372. doi:`10.1021/je9501548`.

[132] P.G. De Gennes, F. Brochard-Wyart, D. Quéré: Capillarity and wetting phenomena: drops, bubbles, pearls, waves, Springer Science & Business Media, New York, 2013.

[133] R. Defay, I. Prigogine, A. Bellmans, D.H. Everett: Surface Tension and Adsorption, Longmans, London, 1966.

[134] U.K. Deiters: A modular program system for the calculation of thermodynamic properties of fluids, Chemical Engineering & Technology 23 (2000) 581–584.

[135] U.K. Deiters, K.M. De Reuck: Guidelines for publication of equations of state – I. pure fluids, Chemical Engineering Journal 69 (1998) 69–81. doi:`10.1016/S1385-8947(97)00070-3`.

[136] U.K. Deiters, K.M. De Reuck: Guidelines for publication of equations of state – I. pure fluids, Pure and Applied Chemistry 69 (1998) 1237–1250. doi:`10.1351/pac199769061237`.

[137] U.K. Deiters, T. Kraska: High-Pressure Fluid Phase Equilibria – Phenomenology and Computation, Elsevier, Amsterdam, 2012.

[138] U.K. Deiters, A. Neumaier: Computer simulation of the characteristic curves of pure fluids, Journal of Chemical & Engineering Data 61 (2016) 2720–2728. doi:`10.1021/acs.jced.6b00133`.

[139] U.K. Deiters, I.L. Pegg: Systematic investigation of the phase behavior in binary fluid mixtures. I. calculations based on the Redlich-Kwong equation of state, The Journal of Chemical Physics 90 (1989) 6632–6641. doi:`10.1063/1.456280`.

[140] N.I. Diamantonis, I.G. Economou: Evaluation of statistical associating fluid theory (saft) and perturbed chain-saft equations of state for the calculation of thermodynamic derivative properties of fluids related to carbon capture and sequestration, Energy & Fuels 25 (2011) 3334–3343. doi:`10.1021/ef200387p`.

[141] E. Díaz-Herrera, J. Alejandre, G. Ramírez-Santiago, F. Forstmann: Interfacial tension behavior of binary and ternary mixtures of partially miscible Lennard-Jones fluids: A molecular dynamics simulation, The Journal of Chemical Physics 110 (1999) 8084–8089. doi:`10.1063/1.478710`.

[142] E. Díaz-Herrera, J.A. Moreno-Razo, G. Ramírez-Santiago: Wetting phenomenon in the liquid-vapor phase coexistence of a partially miscible Lennard-Jones binary mixture, Physical Review E 70 (2004) 051601. doi:`10.1103/PhysRevE.70.051601`.

[143] E. Díaz-Herrera, G. Ramírez-Santiago, J.A. Moreno-Razo: Phase and interfacial behavior of partially miscible symmetric Lennard-Jones binary mixtures, The Journal of Chemical Physics 123 (2005) 184507. doi:`10.1063/1.2102787`.

[144] F. Diewald, M. Lautenschlaeger, S. Stephan, K. Langenbach, C. Kuhn, S. Seckler, H.J. Bungartz, H. Hasse, R. Müller: Molecular dynamics and phase field simulations of droplets on surfaces with wettability gradient, Computer Methods in Applied Mechanics and Engineering 361 (2020) 112773. doi:`10.1016/j.cma.2019.112773`.

[145] M. Dijkstra, R. Evans: A simulation study of the decay of the pair correlation function in simple fluids, The Journal of Chemical Physics 112 (2000) 1449–1456. doi:`10.1063/1.480598`.

[146] D. Dittmar, A. Fredenhagen, S. Oei, R. Eggers: Interfacial tensions of ethanol–carbon dioxide and ethanol–nitrogen. dependence of the interfacial tension on the fluid density – prerequisites and physical reasoning, Chemical Engineering Science 58 (2003) 1223–1233. doi:`10.1016/S0009-2509(02)00626-7`.

[147] Q. Dong, X. Yan, R.C. Wilhoit, X. Hong, R.D. Chirico, V.V. Diky, M. Frenkel: Data quality assurance for thermophysical property databases: Applications to the TRC SOURCE data system, Journal of Chemical Information and Computer Sciences 42 (2002) 473–480. doi:`10.1021/ci010118e`.

[148] D.O. Dunikov, S.P. Malyshenko, V.V. Zhakhovskii: Corresponding states law and molecular dynamics simulations of the Lennard-Jones fluid, The Journal of Chemical Physics 115 (2001) 6623–6631. doi:`10.1063/1.1396674`.

[149] D. Duque, J.C. Pamies, L.F. Vega: Interfacial properties of Lennard-Jones chains by direct simulation and density gradient theory, The Journal of Chemical Physics 121 (2004) 11395–11401. doi:`10.1063/1.1818679`.

[150] D. Duque, P. Tarazona, E. Chacon: Diffusion at the liquid-vapor interface, The Journal of Chemical Physics 128 (2008) 134704. doi:`10.1063/1.2841128`.

[151] J.H. Dymond: Solubility of a series of gases in cyclohexane and dimethylsul-foxide, The Journal of Physical Chemistry 71 (1967) 1829–1831. doi:`10.1021/j100865a043`.

[152] S. Eckelsbach, T. Janzen, A. Köster, S. Miroshnichenko, Y.M. Muñoz-Muñoz, J. Vrabec: Molecular models for cyclic alkanes and ethyl acetate as well as surface tension data from molecular simulation, in: W.E. Nagel, D.H. Kröner, M.M. Resch (Eds.), High Performance Computing in Science and Engineering '14, Springer International Publishing, 2014, pp. 645–659. doi:`10.1007/978-3-319-10810-0_42`.

[153] S. Eckelsbach, J. Vrabec: Fluid phase interface properties of acetone, oxygen, nitrogen and their binary mixtures by molecular simulation, Physical Chemistry Chemical Physics 17 (2015) 27195–27203. doi:`10.1039/C5CP03415A`.

[154] W. Eckhardt, A. Heinecke, R. Bader, M. Brehm, N. Hammer, H. Huber, H.G. Kleinhenz, J. Vrabec, H. Hasse, M. Horsch, M. Bernreuther, C.W. Glass, C. Niethammer, A. Bode, H.J. Bungartz: 591 tflops multi-trillion particles simulation on SuperMUC, in: Supercomputing, Springer, Berlin, Heidelberg, 2013, pp. 1–12. doi:`10.1007/978-3-642-38750-0_1`.

[155] I.G. Economou: Statistical associating fluid theory: A successful model for the calculation of thermodynamic and phase equilibrium properties of complex fluid mixtures, Industrial & Engineering Chemistry Research 41 (2002) 953–962. doi:`10.1021/ie0102201`.

[156] W.J. Egan, S.L. Morgan: Outlier detection in multivariate analytical chemical data, Analytical Chemistry 70 (1998) 2372–2379. doi:`10.1021/ac970763d`.

[157] B.L. Eggimann, A.J. Sunnarborg, H.D. Stern, A.P. Bliss, J.I. Siepmann: An online parameter and property database for the TraPPE force field, Molecular Simulation 40 (2014) 101–105. doi:`10.1080/08927022.2013.842994`.

[158] J.S. Emampour, A. Morsali, S.A. Beyramabadi, M.R. Bozorgmehr, K. Khakzadan: The pseudo Grüneisen parameter in dense fluids from distribution functions, International Journal of The Physical Sciences 6 (2011) 5731–5737. doi:`10.5897/IJPS`.

[159] S. Enders, H. Kahl: Interfacial properties of water + alcohol mixtures, Fluid Phase Equilibria 263 (2008) 160–167. doi:`10.1016/j.fluid.2007.10.006`.

[160] S. Enders, H. Kahl, J. Winkelmann: Interfacial properties of polystyrene in contact with carbon dioxide, Fluid Phase Equilibria 228-229 (2005) 511–522. doi:`10.1016/j.fluid.2004.10.001`.

[161] S. Enders, K. Quitzsch: Calculation of interfacial properties of demixed fluids using density gradient theory, Langmuir 14 (1998) 4606–4614. doi:`10.1021/la9712707`.

[162] C. Engin, T. Merker, J. Vrabec, H. Hasse: Flexible or rigid molecular models? a study on vapour–liquid equilibrium properties of ammonia, Molecular Physics 109 (2011) 619–624. doi:`10.1080/00268976.2010.542894`.

[163] J.R. Errington: Direct calculation of liquid-vapor phase equilibria from transition matrix Monte Carlo simulation, The Journal of Chemical Physics 118 (2003) 9915–9925. doi:`10.1063/1.1572463`.

[164] J.R. Errington: Evaluating surface tension using grand-canonical transition-matrix Monte Carlo simulation and finite-size scaling, Physical Review E 67 (2003) 012102. doi:`10.1103/PhysRevE.67.012102`.

[165] J.R. Errington: Solid-liquid phase coexistence of the Lennard-Jones system through phase-switch Monte Carlo simulation, The Journal of Chemical Physics 120 (2004) 3130–3141. doi:`10.1063/1.1642591`.

[166] M.C. Esmelindro, O.A.C. Antunes, E. Franceschi, G.R. Borges, M.L. Corazza, J.V. Oliveira, W. Linhares, C. Dariva: Phase behavior of the reactant and products of cyclohexane oxidation in compressed CO2, Journal of Chemical & Engineering Data 53 (2008) 2050–2055. doi:`10.1021/je800109s`.

[167] R. Evans: The nature of the liquid-vapour interface and other topics in the statistical mechanics of non-uniform, classical fluids, Advances in Physics 28 (1979) 143–200. doi:`10.1080/00018737900101365`.

[168] R. Evans: Fundamentals of Inhomogeneous Fluids, Marcel Dekker, New York, 1992.

[169] R. Evans: Oscillatory behaviour of density profiles: Relevance for fluid interfacial phenomena, Berichte der Bunsengesellschaft für physikalische Chemie 98 (1994) 345–352. doi:`10.1002/bbpc.19940980312`.

[170] R. Evans, J.R. Henderson, D.C. Hoyle, A.O. Parry, Z.A. Sabeur: Asymptotic decay of liquid structure: Oscillatory liquid-vapour density profiles and the Fisher-Widom line, Molecular Physics 80 (1993) 755–775. doi:`10.1080/00268979300102621`.

[171] R. Evans, R.J.F. Leote de Carvalho, J.R. Henderson, D.C. Hoyle: Asymptotic decay of correlations in liquids and their mixtures, The Journal of Chemical Physics 100 (1994) 591–603. doi:`10.1063/1.466920`.

[172] B. Fábián, M. Szőri, P. Jedlovszky: Floating patches of HCN at the surface of their aqueous solutions – can they make "HCN world" plausible?, The Journal of Physical Chemistry C 118 (2014) 21469–21482. doi:`10.1021/jp505978p`.

[173] A.H. Falls, L.E. Scriven, H.T. Davis: Adsorption, structure, and stress in binary interfaces, The Journal of Chemical Physics 78 (1983) 7300–7317. doi:`10.1063/1.444720`.

[174] E.M. Fernández, E. Chacón, P. Tarazona, A.O. Parry, C. Rascón: Intrinsic fluid interfaces and nonlocality, Physical Review Letters 111 (2013) 096104. doi:`10.1103/PhysRevLett.111.096104`.

[175] W. Fickett, W.W. Wood: Shock Hugoniots for liquid argon, Physics of Fluids 3 (1960) 204–209. doi:`10.1063/1.1706018`.

[176] D. Fincham: Leapfrog rotational algorithms, Molecular Simulation 8 (1992) 165–178. doi:`10.1080/08927029208022474`.

[177] G.D. Fisher, T.W. Leland: Corresponding states principle using shape factors, Industrial & Engineering Chemistry Fundamentals 9 (1970) 537–544. doi:`10.1021/i160036a003`.

[178] M.E. Fisher: Renormalization group theory: Its basis and formulation in statistical physics, Reviews of Modern Physics 70 (1998) 653–681. doi:`10.1103/RevModPhys.70.653`.

[179] M.E. Fisher, B. Widom: Decay of correlations in linear systems, The Journal of Chemical Physics 50 (1969) 3756–3772. doi:`10.1063/1.1671624`.

[180] S. Fisk, B. Widom: Structure and free energy of the interface between fluid phases in equilibrium near the critical point, The Journal of Chemical Physics 50 (1969) 3219–3227. doi:`10.1063/1.1671544`.

[181] H. Flyvbjerg, H.G. Petersen: Error estimates on averages of correlated data, The Journal of Chemical Physics 91 (1989) 461–466. doi:`10.1063/1.457480`.

[182] E. Forte, J. Burger, K. Langenbach, H. Hasse, M. Bortz: Multi-criteria optimization for parameterization of SAFT-type equations of state for water, AIChE Journal 64 (2018) 226–237. doi:`10.1002/aic.15857`.

[183] E. Forte, F. Jirasek, M. Bortz, J. Burger, J. Vrabec, H. Hasse: Digitalization in thermodynamics, Chemie Ingenieur Technik 91 (2019) 201–214. doi:`10.1002/cite.201800056`.

[184] W.A. Fouad, L.F. Vega: The phase and interfacial properties of azeotropic refrigerants: the prediction of aneotropes from molecular theory, Physical Chemistry Chemical Physics 19 (2017) 8977–8988. doi:`10.1039/C6CP08031F`.

[185] D. Frenkel: Simulations: The dark side, The European Physical Journal Plus 128 (2013) 10. doi:`10.1140/epjp/i2013-13010-8`.

[186] D. Frenkel, B. Smit: Understanding Molecular Simulation: From Algorithms to Applications, 2nd ed., Academic Press, Orlando, FL, USA, 2002.

[187] D. Fu, X. Hua, Y. Xu: Cross-association model for the phase equilibria and surface tensions of CO2-methanol and CO2-ethanol mixtures, The Journal of Physical Chemistry C 115 (2011) 3340–3345. doi:`10.1021/jp108400z`.

[188] A. Galindo, L.A. Davies, A. Gil-Villgeas, G. Jackson: The thermodynamics of mixtures and the corresponding mixing rules in the SAFT-VR approach for potentials of variable range, Molecular Physics 93 (1998) 241–252. doi:`10.1080/002689798169249`.

[189] G. Galliero, M.M. Piñeiro, B. Mendiboure, C. Miqueu, T. Lafitte, D. Bessières: Interfacial properties of the Mie-6 fluid: Molecular simulations and gradient theory results, The Journal of Chemical Physics 130 (2009) 104704. doi:`10.1063/1.3085716`.

[190] M.M. Telo da Gama: Phase equilibria and interfacial properties of model ternary mixtures, Molecular Physics 62 (1987) 585–604. doi:`10.1080/00268978700102421`.

[191] M.M. Telo da Gama, R. Evans: The density profile and surface tension of a Lennard-Jones fluid from a generalized van der Waals theory, Molecular Physics 38 (1979) 367–375. doi:`10.1080/00268977900101731`.

[192] M.M. Telo da Gama, R. Evans: Theory of the liquid-vapour interface of a binary mixture of Lennard-Jones fluids, Molecular Physics 41 (1980) 1091–1112. doi:`10.1080/00268978000103811`.

[193] M.M. Telo da Gama, R. Evans: Surface segregation and surface tension at the liquid-vapour interface of a binary mixture of Lennard-Jones fluids, Faraday Symposia of The Chemical Society 16 (1981) 45–58. doi:`10.1039/FS9811600045`.

[194] M.M. Telo da Gama, R. Evans: The structure and surface tension of the liquid-vapour interface near the upper critical end point of a binary mixture of Lennard-Jones fluids I. the two phase region, Molecular Physics 48 (1983) 229–250. doi:`10.1080/00268978300100181`.

[195] M.M. Telo da Gama, R. Evans: The structure and surface tension of the liquid-vapour interface near the upper critical end point of a binary mixture of Lennard-Jones fluids II. the three phase region and the Cahn wetting transition, Molecular Physics 48 (1983) 251–266. doi:`10.1080/00268978300100191`.

[196] M.M. Telo da Gama, J.H. Thurtell: Interfacial phase transitions in molecular fluids and multicomponent mixtures, J. Chem. Soc., Faraday Trans. 2 82 (1986) 1721–1737. doi:`10.1039/F29868201721`.

[197] B.C. Garrett, G.K. Schenter, A. Morita: Molecular simulations of the transport of molecules across the liquid/vapor interface of water, Chemical Reviews 106 (2006) 1355–1374. doi:`10.1021/cr040370w`.

[198] J.M. Garrido, M. Cartes, A. Mejía: Coarse-grained theoretical modeling and molecular simulations of nitrogen + n-alkanes: (n-pentane, n-hexane, n-heptane, n-octane), The Journal of Supercritical Fluids 129 (2017) 83–90. doi:`10.1016/j.supflu.2017.01.001`.

[199] J.M. Garrido, M.M. Piñeiro, A. Mejía, F.J. Blas: Understanding the interfacial behavior in isopycnic Lennard-Jones mixtures by computer simulations, Physical Chemistry Chemical Physics 18 (2016) 1114–1124. doi:`10.1039/C5CP06562C`.

[200] J.M. Garrido, H. Quinteros-Lama, M.M. Piñeiro, A. Mejía, H. Segura: On the phase and interface behavior along the three-phase line of ternary Lennard-Jones mixtures: A collaborative approach based on square gradient theory and molecular dynamics simulations, The Journal of Chemical Physics 141 (2014) 014503. doi:`10.1063/1.4885348`.

[201] C. Gauss: Bestimmung der Genauigkeit der Beobachtungen, Zeitschrift für Astronomie und verwandte Wissenschaften 1 (1816) 185.

[202] J. Ge, D. Bedeaux, J. Simon, S. Kjelstrup: Integral relations, a simplified method to find interfacial resistivities for heat and mass transfer, Physica A: Statistical Mechanics and its Applications 385 (2007) 421–432. doi:`10.1016/j.physa.2007.07.033`.

[203] J. Ge, S. Kjelstrup, D. Bedeaux, J.M. Simon, B. Rousseau: Transfer coefficients for evaporation of a system with a Lennard-Jones long-range spline potential, Physical Review E 75 (2007) 061604. doi:`10.1103/PhysRevE.75.061604`.

[204] P. Geysermans, N. Elyeznasni, V. Russier: Layered interfaces between immiscible liquids studied by density-functional theory and molecular-dynamics simulations, The Journal of Chemical Physics 123 (2005) 204711. doi:`10.1063/1.2126592`.

[205] A.F. Ghobadi, J.R. Elliott: Adapting SAFT-γ perturbation theory to site-based molecular dynamics simulation. II. confined fluids and vapor-liquid interfaces, The Journal of Chemical Physics 141 (2014) 024708. doi:`10.1063/1.4886398`.

[206] D. Ghonasgi, W. Chapman: Prediction of the properties of model polymer solutions and blends, AICHE Journal 40 (1994) 878. doi:`10.1002/aic.690400514`.

[207] D. Ghonasgi, W.G. Chapman: Theory and simulation for associating chain fluids, Molecular Physics 80 (1993) 161–176. doi:`10.1080/00268979300102151`.

[208] D. Ghonasgi, W.G. Chapman: Theory and simulation for associating fluids with four bonding sites, Molecular Physics 79 (1993) 291–311. doi:`10.1080/00268979300101221`.

[209] A. Ghoufi, P. Malfreyt, D.J. Tildesley: Computer modelling of the surface tension of the gas-liquid and liquid-liquid interface, Chemical Society Reviews 45 (2016) 1387–1409. doi:`10.1039/C5CS00736D`.

[210] P.V. Giaquinta, G. Giunta, S. Prestipino Giarritta: Entropy and the freezing of simple liquids, Physical Review A 45 (1992) R6966–R6968. doi:`10.1103/PhysRevA.45.R6966`.

[211] J.W. Gibbs: The Scientific Papers of J. W. Gibbs, Dover Publications, 1961.

[212] A. Gil-Villegas, A. Galindo, P.J. Whitehead, S.J. Mills, G. Jackson, A.N. Burgess: Statistical associating fluid theory for chain molecules with attractive potentials of variable range, The Journal of Chemical Physics 106 (1997) 4168.

[213] K. Glavatskiy, D. Bedeaux: Transport of heat and mass in a two-phase mixture: From a continuous to a discontinuous description, The Journal of Chemical Physics 133 (2010) 144709. doi:`10.1063/1.3486555`.

[214] D. Gómez-Díaz, J.C. Mejuto, J.M. Navaza: Physicochemical properties of liquid mixtures. 1. viscosity, density, surface tension and refractive index of cyclohexane + 2,2,4-trimethylpentane binary liquid systems from 25°C to 50°C, Journal of Chemical & Engineering Data 46 (2001) 720–724. doi:`10.1021/je000310x`.

[215] D. Gómez-Díaz, J.M. Navaza, B. Sanjurjo: Mass-transfer enhancement or reduction by surfactant presence at a gas-liquid interface, Industrial & Engineering Chemistry Research 48 (2009) 2671–2677. doi:`10.1021/ie8009523`.

[216] S. Gopalakrishnan, D. Liu, H.C. Allen, M. Kuo, M.J. Shultz: Vibrational spectroscopic studies of aqueous interfaces: Salts, acids, bases, and nanodrops, Chemical Reviews 106 (2006) 1155–1175. doi:`10.1021/cr040361n`.

[217] M. Gottschalk: An EOS for the Lennard-Jones fluid: A virial expansion approach, AIP Advances 9 (2019) 125206. doi:`10.1063/1.5119761`.

[218] R. Grafe: Über Oberflächenenergie und Koordinationszahl. Ein Beitrag zur Morphologie der Flüssigkeiten, Nova Acta Leopoldina 12 (1942) 141–194.

[219] H. Greberg, G.V. Paolini, J. Satherley, R. Penfold, S. Nordholm: Generalized van der Waals theory of interfaces in simple fluid mixtures, Journal of Colloid and Interface Science 235 (2001) 334–343. doi:`10.1006/jcis.2000.7314`.

[220] P. Grosfils, J.F. Lutsko: Dependence of the liquid-vapor surface tension on the range of interaction: A test of the law of corresponding states, The Journal of Chemical Physics 130 (2009) 054703. doi:`10.1063/1.3072156`.

[221] J. Gross: An equation-of-state contribution for polar components: Quadrupolar molecules, AIChE Journal 51 (2005) 2556–2568. doi:`10.1002/aic.10502`.

[222] J. Gross, G. Sadowski: Application of perturbation theory to a hard-chain reference fluid: an equation of state for square-well chains, Fluid Phase Equilibria 168 (2000) 183. doi:`10.1016/S0378-3812(00)00302-2`.

[223] J. Gross, G. Sadowski: Perturbed-Chain SAFT: An equation of state based on a perturbation theory for chain molecules, Industrial & Engineering Chemistry Research 40 (2001) 1244. doi:`10.1021/ie0003887`.

[224] J. Gross, G. Sadowski: Application of the perturbed-chain SAFT equation of state to associating systems, Industrial & Engineering Chemistry Research 41 (2002) 5510–5515. doi:`10.1021/ie010954d`.

[225] J. Gross, J. Vrabec: An equation-of-state contribution for polar components: Dipolar molecules, AIChE Journal 52 (2006) 1194–1204. doi:`10.1002/aic.10683`.

[226] K.E. Gubbins: Perturbation theories of the thermodynamics of polar and associating liquids: A historical perspective, Fluid Phase Equilibria 416 (2016) 3–17. doi:`10.1016/j.fluid.2015.12.043`.

[227] H. Guérin: Simple analytic equations of state for the generalized hard-core mie(α, β) and mie(α, β) fluids from perturbation theory, Journal of Molecular Liquids 164 (2011) 162–170. doi:`10.1016/j.molliq.2011.09.003`.

[228] W.F. van Gunsteren, A.E. Mark: Validation of molecular dynamics simulation, The Journal of Chemical Physics 108 (1998) 6109–6116. doi:`10.1063/1.476021`.

[229] M. Guo, B.C.Y. Lu: Long range corrections to thermodynamic properties of inhomogeneous systems with planar interfaces, The Journal of Chemical Physics 106 (1997) 3688–3695. doi:`10.1063/1.473463`.

[230] M. Guo, D.Y. Peng, B. C.-Y.Lu: On the long-range corrections to computer simulation results for the Lennard-Jones vapor-liquid interface, Fluid Phase Equilibria 130 (1997) 19–30. doi:`10.1016/S0378-3812(96)03206-2`.

[231] M. Gurtin, E. Fried, L. Anand: The Mechanics and Thermodynamics of Continua, 1st ed., Cambridge Univ. Press, Cambridge, 2010.

[232] B. Hafskjold, T. Ikeshoji: Non equilibrium molecular dynamics simulation of coupled heat- and mass transport across a liquid/vapor interface, Molecular Simulation 16 (1996) 139–150. doi:`10.1080/08927029608024068`.

[233] L. van der Ham, R. Bock, S. Kjelstrup: Modelling the coupled transfer of mass and thermal energy in the vapour-liquid region of a nitrogen-oxygen mixture, Chemical Engineering Science 65 (2010) 2236–2248. doi:`10.1016/j.ces.2009.12.021`.

[234] F.R. Hampel: The influence curve and its role in robust estimation, Journal of The American Statistical Association 69 (1974) 383–393. doi:`10.1080/01621459.1974.10482962`.

[235] K.K. Han: A new Monte Carlo method for estimating free energy and chemical potential, Physics Letters A 165 (1992) 28–32. doi:`10.1016/0375-9601(92)91048-V`.

[236] J.P. Hansen: Phase transition of the Lennard-Jones system. II. high-temperature limit, Physical Review A 2 (1970) 221–230. doi:`10.1103/PhysRevA.2.221`.

[237] J.P. Hansen, I. McDonald: Theory of Simple Liquids, 4th ed., Academic Press, 2013.

[238] J.P. Hansen, L. Verlet: Phase transitions of the Lennard-Jones system, Physical Review 184 (1969) 151–161. doi:`10.1103/PhysRev.184.151`.

[239] G. Hantal, L.B. Pártay, I. Varga, P. Jedlovszky, T. Gilányi: Counterion and surface density dependence of the adsorption layer of ionic surfactants at the vapor-aqueous solution interface: A computer simulation study, The Journal of Physical Chemistry B 111 (2007) 1769–1774. doi:`10.1021/jp066969c`.

[240] S. Hartland, R. Hartley: Axisymmetric Fluid-Liquid Interfaces, Elsevier, Amsterdam, 1976.

[241] R. Hartley, A. Zisserman: Multiple View Geometry in Computer Vision, 2nd ed., Cambridge University Press, 2004. doi:`10.1017/CBO9780511811685`.

[242] H. Hasse, J. Lenhard: Boon and bane: On the role of adjustable parameters in simulation models, in: J. Lenhard, M. Carrier (Eds.), Mathematics as a Tool: Tracing New Roles of Mathematics in the Sciences, Springer International Publishing, 2017, pp. 93–115. doi:`10.1007/978-3-319-54469-4_6`.

[243] Z.Ható, D. Boda, T. Kristóf: Simulation of steady-state diffusion: Driving force ensured by dual control volumes or local equilibrium Monte Carlo, The Journal of Chemical Physics 137 (2012) 054109. doi:10.1063/1.4739255.

[244] M.J. Haye, C. Bruin: Molecular dynamics study of the curvature correction to the surface tension, The Journal of Chemical Physics 100 (1994) 556–559. doi:10.1063/1.466972.

[245] G.S. Heffelfinger, D. Ford: Massively parallel dual control volume grand canonical molecular dynamics with LADERA II. gradient driven diffusion through polymers, Molecular Physics 94 (1998) 673–683. doi:10.1080/0026897981678368.

[246] G.S. Heffelfinger, D.M. Ford: Massively parallel dual control volume grand canonical molecular dynamics with LADERA I. gradient driven diffusion in Lennard-Jones fluids, Molecular Physics 94 (1998) 659–671. doi:10.1080/0026897981678827.

[247] G.S. Heffelfinger, F. van Swol: Diffusion in Lennard-Jones fluids using dual control volume grand canonical molecular dynamics simulation (DCV-GCMD), The Journal of Chemical Physics 100 (1994) 7548–7552. doi:10.1063/1.466849.

[248] M. Heida, J. Malek: On compressible Korteweg fluid-like materials, International Journal of Engineering Science 48 (2010) 1313–1324. doi:10.1016/j.ijengsci.2010.06.031.

[249] M. Heier, S. Stephan, J. Liu, W.G. Chapman, H. Hasse, K. Langenbach: Equation of state for the Lennard-Jones truncated and shifted fluid with a cut-off radius of 2.5σ based on perturbation theory and its applications to interfacial thermodynamics, Molecular Physics 116 (2018) 2083–2094. doi:10.1080/00268976.2018.1447153.

[250] M. Heinen, J. Vrabec: Evaporation sampled by stationary molecular dynamics simulation, The Journal of Chemical Physics 151 (2019) 044704. doi:10.1063/1.5111759.

[251] M. Heinen, J. Vrabec, J. Fischer: Communication: Evaporation: Influence of heat transport in the liquid on the interface temperature and the particle flux, The Journal of Chemical Physics 145 (2016) 081101. doi:10.1063/1.4961542.

[252] D. Henderson, J. Barker: Physical Chemistry – An Advanced Treatise: Volume VIIIA / Liquid State, Academic Press, New York, 1971.

[253] V.R. Heng, M. Nayhouse, M. Crose, A. Tran, G. Orkoulas: Communication: Direct determination of triple-point coexistence through cell model simulation, The Journal of Chemical Physics 137 (2012) 141101. doi:10.1063/1.4758698.

[254] L. Hennaut-Roland, M. Lek: Methods and equipment used at the bureau of physico-chem. standards. IV. Surface tension of a series of org. substances, Bulletin Des Societes Chimiques Belges 40 (1931) 177–188.

[255] C. Herdes, A. Ervik, A. Mejía, E.A. Müller: Prediction of the water/oil interfacial tension from molecular simulations using the coarse-grained SAFT-γ Mie force field, Fluid Phase Equilibria 476 (2018) 9–15. doi:`10.1016/j.fluid.2017.06.016`.

[256] C. Herdes, T.S. Totton, E.A. Müller: Coarse grained force filed for the molecular simulation of natural gases and condensates, Fluid Phase Equilibria 406 (2015) 91–100. doi:`10.1016/j.fluid.2015.07.014`.

[257] J. Hernández-Muñoz, E. Chacón, P. Tarazona: Capillary waves and the decay of density correlations at liquid surfaces, Physical Review E 94 (2016) 062802. doi:`10.1103/PhysRevE.94.062802`.

[258] S. Hess: Augmented van der Waals equation of state for the Lennard-Jones fluid, Physica A 267 (1999) 58–70. doi:`10.1016/S0378-4371(98)00670-0`.

[259] D.M. Heyes: The Lennard-Jones fluid in the liquid-vapour critical region, Computational Methods in Science and Technology 21 (2015) 169. doi:`10.12921/cmst.2015.21.04.001`.

[260] D.M. Heyes, C.T. Llaguno: Computer simulation and equation of state study of the Boyle and inversion temperature of simple fluids, Chemical Physics 168 (1992) 61–68. doi:`10.1016/0301-0104(92)80109-9`.

[261] D.M. Heyes, L.V. Woodcock: Critical and supercritical properties of Lennard-Jones fluids, Fluid Phase Equilibria 356 (2013) 301–308. doi:`10.1016/j.fluid.2013.07.056`.

[262] T.L. Hill: Statistical Mechanics, McGraw-Hill Book, New York, 1956.

[263] T.L. Hill: An Introduction to Statistical Thermodynamics, Dover Publications, New York, 1986.

[264] J.O. Hirschfelder, C.F. Curtiss, R.B. Bird: Molecular Theory of Gases and Liquids, Wiley, New York, 1954.

[265] V. Hodge, J. Austin: A survey of outlier detection methodologies, Artificial Intelligence Review 22 (2004) 85–126. doi:`10.1023/B:AIRE.0000045502.10941.a9`.

[266] M.A. van der Hoef: Free energy of the Lennard-Jones solid, The Journal of Chemical Physics 113 (2000) 8142–8148. doi:`10.1063/1.1314342`.

[267] Höfling, F., Dietrich, S.: Enhanced wavelength-dependent surface tension of liquid-vapour interfaces, Europhysics Letters 109 (2015) 46002. doi:`10.1209/0295-5075/109/46002`.

[268] C.D. Holcomb, P. Clancy, J.A. Zollweg: A critical study of the simulation of the liquid-vapour interface of a Lennard-Jones fluid, Molecular Physics 78 (1993) 437–459. doi:`10.1080/00268979300100321`.

[269] J.D. Honeycutt, H.C. Andersen: Molecular dynamics study of melting and freezing of small Lennard-Jones clusters, The Journal of Physical Chemistry 91 (1987) 4950–4963. doi:10.1021/j100303a014.

[270] S.D. Hong, D.J. Jang: Direct calculation of the free energy using reduced Boltzmann factors: Application to Lennard-Jones fluids and square-well fluids, Bulletin of The Korean Chemical Society 24 (2003) 1351–1353.

[271] S.D. Hong, M.S. Jhon: Calculation of excess free energy from the averaged effective acceptance ratio for the Lennard-Jones fluid and the inverse twelve fluid, Chemical Physics Letters 273 (1997) 79–82. doi:10.1016/S0009-2614(97)00581-2.

[272] M. Horsch, H. Hasse: Molecular simulation of nano-dispersed fluid phases, Chemical Engineering Science 107 (2014) 235. doi:10.1016/j.ces.2013.12.026.

[273] M. Horsch, H. Hasse, A.K. Shchekin, A. Agarwal, S. Eckelsbach, J. Vrabec, E.A. Müller, G. Jackson: Excess equimolar radius of liquid drops, Physical Review E 85 (2012) 031605. doi:10.1103/PhysRevE.85.031605.

[274] M. Horsch, S. Miroshnichenko, J. Vrabec: Steady-state molecular dynamics simulation of vapour to liquid nucleation with McDonald's daemon, Journal of Physical Studies 13 (2009) 4004.

[275] M. Horsch, J. Vrabec, H. Hasse: Modification of the classical nucleation theory based on molecular simulation data for surface tension, critical nucleus size, and nucleation rate, Physical Review E 78 (2008) 011603. doi:10.1103/PhysRevE.78.011603.

[276] R.A. Horváth, B. Fábián, M. Szőri, P. Jedlovszky: Investigation of the liquid-vapour interface of aqueous methylamine solutions by computer simulation methods, Journal of Molecular Liquids 288 (2019) 110978. doi:10.1016/j.molliq.2019.110978.

[277] S.H. Huang, M. Radosz: Equation of state for small, large, polydisperse, and associating molecules, Industrial & Engineering Chemistry Research 29 (1990) 2284–2294. doi:10.1021/ie00107a014.

[278] Y.L. Huang, M. Heilig, H. Hasse, J. Vrabec: Vapor-liquid equilibria of hydrogen chloride, phosgene, benzene, chlorobenzene, ortho-dichlorobenzene, and toluene by molecular simulation, AIChE Journal 57 (2011) 1043–1060. doi:10.1002/aic.12329.

[279] M.L. Huber, J.F. Ely: Properties of Lennard-Jones Mixtures at Various Temperatures and Energy Ratios with a Size Ratio of Two, technical note 1331, NIST, 1989.

[280] P. Huber: Robust Statistics, John Wiley, New York, 1981.

[281] P.J. Huber: Robust estimation of a location parameter, Ann. Math. Statist. 35 (1964) 73–101. doi:10.1214/aoms/1177703732.

[282] W. Hückel, H. Harder: Die Oberflächenspannung einiger alicyclischer Kohlenwasserstoffe, Chemische Berichte 80 (1947) 357–361.

[283] J.E. Hunter, W.P. Reinhardt: Finite-size scaling behavior of the free energy barrier between coexisting phases: Determination of the critical temperature and interfacial tension of the Lennard-Jones fluid, The Journal of Chemical Physics 103 (1995) 8627–8637. doi:10.1063/1.470121.

[284] A. Hutem, S. Boonchui: Numerical evaluation of second and third virial coefficients of some inert gases via classical cluster expansion, Journal of Mathematical Chemistry 50 (2012) 1262–1276. doi:10.1007/s10910-011-9966-5.

[285] B. Ibarra-Tandi, A. Lira, J. Lopez-Lemus: Effect of softness on relative adsorption for binary mixtures of simple fluids, Journal of Molecular Liquids 185 (2013) 62–69. doi:10.1016/j.molliq.2012.12.004.

[286] C. Ibergay, A. Ghoufi, F. Goujon, P. Ungerer, A. Boutin, B. Rousseau, P. Malfreyt: Molecular simulations of the n-alkane liquid-vapor interface: Interfacial properties and their long range corrections, Physical Review E 75 (2007) 051602. doi:10.1103/PhysRevE.75.051602.

[287] T. Imamura, Y. Mizukoshi, T. Ishiyama, A. Morita: Surface structures of NaF and Na2SO4 aqueous solutions: Specific effects of hard ions on surface vibrational spectra, The Journal of Physical Chemistry C 116 (2012) 11082–11090. doi:10.1021/jp3019777.

[288] A.R. Imre, G. Mayer, G. Házi, R. Rozas, T. Kraska: Estimation of the liquid-vapor spinodal from interfacial properties obtained from molecular dynamics and lattice boltzmann simulations, The Journal of Chemical Physics 128 (2008) 114708. doi:10.1063/1.2837805.

[289] I. Inzoli, S. Kjelstrup, D. Bedeaux, J. Simon: Transfer coefficients for the liquid-vapor interface of a two-component mixture, Chemical Engineering Science 66 (2011) 4533–4548. doi:10.1016/j.ces.2011.06.011.

[290] T. Ishiyama, A. Morita: Molecular dynamics analysis of interfacial structures and sum frequency generation spectra of aqueous hydrogen halide solutions, The Journal of Physical Chemistry A 111 (2007) 9277–9285. doi:10.1021/jp072997z.

[291] T. Ishiyama, A. Morita: Molecular dynamics study of gas-liquid aqueous sodium halide interfaces. I. flexible and polarizable molecular modeling and interfacial properties, The Journal of Physical Chemistry C 111 (2007) 721–737. doi:10.1021/jp065191s.

[292] T. Ishiyama, A. Morita, T. Miyamae: Surface structure of sulfuric acid solution relevant to sulfate aerosol: Molecular dynamics simulation combined with sum frequency generation measurement, Physical Chemistry Chemical Physics 13 (2011) 20965. doi:10.1039/c1cp21920k.

[293] A.E. Ismail, G.S. Grest, M.J. Stevens: Capillary waves at the liquid-vapor interface and the surface tension of water, The Journal of Chemical Physics 125 (2006) 014702. doi:10.1063/1.2209240.

[294] R.T. Jacobsen, R.B. Stewart: Thermodynamic properties of nitrogen including liquid and vapor phases from 63K to 2000K with pressures to 10,000 bar, Journal of Physical and Chemical Reference Data 2 (1973) 757–922. doi:10.1063/1.3253132.

[295] D. Jain, S. Singh: Thermodynamics of binary mixtures: Excess gibbs energies & surface tension of binary mixtures of cyclohexane with o-xylene, m-xylene, p-xylene & ethylbenzene in surface phase, Indian Journal of Chemistry 12 (1974) 714–717.

[296] J. Janeček: Long range corrections in inhomogeneous simulations, The Journal of Physical Chemistry B 110 (2006) 6264–6269. doi:10.1021/jp056344z.

[297] J. Janeček: Effect of the interfacial area on the equilibrium properties of Lennard-Jones fluid, The Journal of Chemical Physics 131 (2009) 124513. doi:10.1063/1.3238550.

[298] J. Janeček, O. Said-Aizpuru, P. Paricaud: Long range corrections for inhomogeneous simulations of Mie n-m potential, Journal of Chemical Theory and Computation 13 (2017) 4482–4491. doi:10.1021/acs.jctc.7b00212.

[299] J. Janeček, O. Said-Aizpuru, P. Paricaud: Long range corrections for inhomogeneous simulations of Mie n-m potential, Journal of Chemical Theory and Computation 13 (2017) 4482–4491. (GEMC results from private communication with Janeček, 2019).

[300] E. Johannessen, D. Bedeaux: Integral relations for the heat and mass transfer resistivities of the liquid-vapor interface, Physica A: Statistical Mechanics and its Applications 370 (2006) 258–274. doi:10.1016/j.physa.2006.02.047.

[301] E. Johannessen, J. Gross, D. Bedeaux: Nonequilibrium thermodynamics of interfaces using classical density functional theory, The Journal of Chemical Physics 129 (2008) 184703. doi:10.1063/1.3009182.

[302] J.K. Johnson, J.A. Zollweg, K.E. Gubbins: The Lennard-Jones equation of state revisited, Molecular Physics 78 (1993) 591. doi:10.1080/00268979300100411.

[303] J. Jones: On the determination of molecular fields. I. from the variation of the viscosity of a gas with temperature, Proc. R. Soc. London Ser. A 106 (1924) 441–462. doi:10.1098/rspa.1924.0081.

[304] J. Jones: On the determination of molecular fields. II. from the equation of state of a gas, Proc. R. Soc. London Ser. A 106 (1924) 463–477. doi:10.1098/rspa.1924.0082.

[305] H. Kahl, S. Enders: Interfacial properties of binary mixtures, Physical Chemistry Chemical Physics 4 (2002) 931–936. doi:10.1039/B108535M.

[306] H. Kahl, M. Mecke, J. Winkelmann: Prediction of internal structure and properties in fluid model interfaces of binary and ternary liquid mixtures, Fluid Phase Equilibria 228-229 (2005) 293–302. doi:10.1016/j.fluid.2004.09.032.

[307] H. Kahl, T. Wadewitz, J. Winkelmann: Surface tension and interfacial tension of binary organic liquid mixtures, Journal of Chemical & Engineering Data 48 (2003) 1500–1507. doi:10.1021/je034062r.

[308] H. Kahl, T. Wadewitz, J. Winkelmann: Surface tension of pure liquids and binary liquid mixtures, Journal of Chemical & Engineering Data 48 (2003) 580–586. doi:10.1021/je0201323.

[309] G.I. Kaminishi, C. Yokoyama, T. Shinji: Vapor pressures of binary mixtures of carbon dioxide with benzene, n-hexane and cyclohexane up to 7 MPa, Fluid Phase Equilibria 34 (1987) 83–99. doi:10.1016/0378-3812(87)85052-5.

[310] J.W. Kang, V. Diky, R.D. Chirico, J.W. Magee, C.D. Muzny, I. Abdulagatov, A.F. Kazakov, M. Frenkel: Quality assessment algorithm for vapor-liquid equilibrium data, Journal of Chemical & Engineering Data 55 (2010) 3631–3640. doi:10.1021/je1002169.

[311] J.W. Kang, V. Diky, R.D. Chirico, J.W. Magee, C.D. Muzny, A.F. Kazakov, K. Kroenlein, M. Frenkel: Algorithmic framework for quality assessment of phase equilibrium data, Journal of Chemical & Engineering Data 59 (2014) 2283–2293. doi:10.1021/je500327k.

[312] B. Karlsson, R. Friedman: Dilution of whisky – the molecular perspective, Scientific Reports 7 (2017) 1–9. doi:10.1038/s41598-017-06423-5.

[313] Y. Kataoka: Extension of a van der Waals equation of state to the solid-liquid-vapor phases of a Lennard-Jones system, Journal of Computer Chemistry, Japan 4 (2018). doi:10.2477/jccjie.2017-0043.

[314] Y. Kataoka, Y. Yamada: Phase diagram for a Lennard-Jones system obtained through constant-pressure molecular dynamics simulations, Journal of Computer Chemistry, Japan 13 (2014) 257–262. doi:10.2477/jccj.2014-0016.

[315] Y. Kataoka, Y. Yamada: Thermodynamics and molecular dynamic simulations of three-phase equilibrium in argon (v8), Journal of Computer Chemistry, Japan 13 (2014) 130–138. doi:10.2477/jccj.2014-0002.

[316] S. Kaur, B.S. Lark, S.K. Aggarwal, S. Singh: Surface tension and surface excess heats of mixing of n-butyric acid with various solvents, Indian Journal of Chemistry 35 (1996) 832–835.

[317] S. Khosharay, M. Abolala, F. Varaminian: Modeling the surface tension and surface properties of CO_2+H_2O and H_2S+H_2O with gradient theory in combination with sPC-SAFT EOS and a new proposed influence parameter, Journal of Molecular Liquids 198 (2014) 292–298. doi:10.1016/j.molliq.2014.07.017.

[318] S. Khosharay, M.S. Mazraeno, F. Varaminian, A. Bagheri: A proposed combination model for predicting surface tension and surface properties of binary refrigerant mixtures, International Journal of Refrigeration 40 (2014) 347–361. doi:10.1016/j.ijrefrig.2013.12.001.

[319] S. Khosharay, N. Rezakhani: Using a new proposed influence parameter of gradient theory for CH4/n-alkane binary systems: What advances can be achieved?, Periodica Polytechnica Chemical Engineering 60 (2016) 282–289. doi:`10.3311/PPch.9061`.

[320] S. Khosharay, F. Varaminian: Experimental and modeling investigation on surface tension and surface properties of (CH4 + H2O), (C2H6 + H2O), (CO2 + H2O) and (C3H8 + H2O) from 284.15 K to 312.15 K and pressures up to 60 bar, International Journal of Refrigeration 47 (2014) 26–35. doi:`10.1016/j.ijrefrig.2014.08.003`.

[321] C.H. Kim, P. Vimalchand, M.D. Donohue: Vapor-liquid equilibria for binary mixtures of carbon dioxide with benzene, toluene and p-xylene, Fluid Phase Equilibria 31 (1986) 299–311. doi:`10.1016/0378-3812(86)87014-5`.

[322] H.Y. Kim, K.A. Fichthorn: Molecular dynamics simulation of amphiphilic dimers at a liquid-vapor interface, The Journal of Chemical Physics 122 (2005) 034704. doi:`10.1063/1.1839171`.

[323] S. Kim, D. Henderson, J.A. Barker: Perturbation theory of fluids and deviations from classical behavior, Canadian Journal of Physics 47 (1969) 99–102. doi:`10.1139/p69-012`.

[324] L.I. Kioupis, G. Arya, E.J. Maginn: Pressure-enthalpy driven molecular dynamics for thermodynamic property calculation II: Applications, Fluid Phase Equilibria 200 (2002) 93–110. doi:`10.1016/S0378-3812(02)00015-8`.

[325] J.G. Kirkwood, F.P. Buff: The statistical mechanical theory of surface tension, The Journal of Chemical Physics 17 (1949) 338–343. doi:`10.1063/1.1747248`.

[326] S.B. Kiselev, J.F. Ely: Crossover SAFT equation of state: Application for normal alkanes, Industrial & Engineering Chemistry Research 38 (1999) 4993–5004. doi:`10.1021/ie990387i`.

[327] S. Kjelstrup, B. Hafskjold: Nonequilibrium molecular dynamics simulations of steady-state heat and mass transport in distillation, Industrial & Engineering Chemistry Research 35 (1996) 4203–4213. doi:`10.1021/ie960199h`.

[328] C. Klink, J. Gross: A density functional theory for vapor-liquid interfaces of mixtures using the perturbed-chain polar statistical associating fluid theory equation of state, Industrial & Engineering Chemistry Research 53 (2014) 6169. doi:`10.1021/ie4029895`.

[329] C. Klink, C. Waibel, J. Gross: Analysis of interfacial transport resistivities of pure components and mixtures based on density functional theory, Industrial & Engineering Chemistry Research 54 (2015) 11483–11492. doi:`10.1021/acs.iecr.5b03270`.

[330] E.M. Knorr, R.T. Ng, V. Tucakov: Distance-based outliers: Algorithms and applications, VLDB Journal 8 (2000) 237–253. doi:`10.1007/s007780050006`.

[331] D.A. Kofke: Direct evaluation of phase coexistence by molecular simulation via integration along the saturation line, The Journal of Chemical Physics 98 (1993) 4149–4162. doi:`10.1063/1.465023`.

[332] D.A. Kofke: Gibbs-Duhem integration: A new method for direct evaluation of phase coexistence by molecular simulation, Molecular Physics 78 (1993) 1331–1336. doi:`10.1080/00268979300100881`.

[333] D.A. Kofke, P.T. Cummings: Quantitative comparison and optimization of methods for evaluating the chemical potential by molecular simulation, Molecular Physics 92 (1997) 973–996. doi:`10.1080/0026897971696600`.

[334] J. Kolafa, I. Nezbeda: The Lennard-Jones fluid: an accurate analytic and theoretically-based equation of state, Fluid Phase Equilibria 100 (1994) 1–34. doi:`10.1016/0378-3812(94)80001-4`.

[335] J. Kolafa, H.L. Vörtler, K. Aim, I. Nezbeda: The Lennard-Jones fluid revisited: Computer simulation results, Molecular Simulation 11 (1993) 305–319. doi:`10.1080/08927029308022515`.

[336] T.M. Koller, S. Yan, C. Steininger, T. Klein, A.P. Fröba: Interfacial tension and liquid viscosity of binary mixtures of n-hexane, n-decane, or 1-hexanol with carbon dioxide by molecular dynamics simulations and surface light scattering, International Journal of Thermophysics 40 (2019). doi:`10.1007/s10765-019-2544-y`.

[337] M. Kon, K. Kobayashi, M. Watanabe: Kinetic boundary condition in vapor-liquid two-phase system during unsteady net evaporation/condensation, European Journal of Mechanics - B/Fluids 64 (2017) 81 – 92. doi:`10.1016/j.euromechflu.2016.12.001`.

[338] B. Konobeev, V. Lyapin: J. Appl. Chem. USSR (Engl. Transl.) 43 (1970) 803–811.

[339] P.H. van Konynenburg, R.L. Scott: Critical lines and phase equilibria in binary van der Waals mixtures, Philosophical Transactions of the Royal Society of London A 298 (1980) 495–540. doi:`10.1098/rsta.1980.0266`.

[340] W. Koppenol, J. Corish, J. Garcia-Martinez, J. Meija, J. Reedijk: How to name new chemical elements (IUPAC recommendations 2016), Pure and Applied Chemistry 88 (2016) 401–405. doi:`10.1515/pac-2015-0802`.

[341] A. Köster, P. Mausbach, J. Vrabec: Premelting, solid-fluid equilibria, and thermodynamic properties in the high density region based on the Lennard-Jones potential, The Journal of Chemical Physics 147 (2017) 144502. doi:`10.1063/1.4990667`.

[342] J. Kou, S. Sun, X. Wang: Efficient numerical methods for simulating surface tension of multi-component mixtures with the gradient theory of fluid interfaces, Computer Methods in Applied Mechanics and Engineering 292 (2015) 92–106. doi:`10.1016/j.cma.2014.10.023`.

[343] N. Koutras, V. Harismiadis, D. Tassios: A simple equation of state for the Lennard-Jones fluid: A new reference term for equations of state and perturbation theories, Fluid Phase Equilibria 77 (1992) 13–38. doi:`10.1016/0378-3812(92)85097-R`.

[344] T. Kraska, U.K. Deiters: Systematic investigation of the phase behavior in binary fluid mixtures. II. calculations based on the Carnahan-Starling-Redlich-Kwong equation of state, The Journal of Chemical Physics 96 (1992) 539–547. doi:`10.1063/1.462490`.

[345] T. Kraska, K.E. Gubbins: Phase equilibria calculations with a modified SAFT equation of state. 1. pure alkanes, alkanols, and water, Industrial & Engineering Chemistry Research 35 (1996) 4727.

[346] I. Krichevskii, G. Sorina: Liquid-gas phase equilibria in the cyclohexane-carbon dioxide and cyclohexane-nitrous oxide systems, Russian Journal of Physical Chemistry 34 (1960) 679–681.

[347] K.F. Kruber, M. Krapoth, T. Zeiner: Interfacial mass transfer in ternary liquid-liquid systems, Fluid Phase Equilibria 440 (2017) 54–63. doi:`10.1016/j.fluid.2017.02.013`.

[348] A. Kryukov, V. Levashov: About evaporation-condensation coefficients on the vapor-liquid interface of high thermal conductivity matters, International Journal of Heat and Mass Transfer 54 (2011) 3042 – 3048. doi:`10.1016/j.ijheatmasstransfer.2011.02.042`.

[349] A. Kulaguin-Chicaroux, T. Zeiner: Interfacial behavior of aqueous two-phase systems based on linear and hyperbranched polymers, Journal of Chemical & Engineering Data 63 (2018) 2467–2476. doi:`10.1021/acs.jced.7b01001`.

[350] V.L. Kulinskii: The critical compressibility factor of fluids from the global isomorphism approach, The Journal of Chemical Physics 139 (2013) 184119. doi:`10.1063/1.4829837`.

[351] A. Kulkarni, E.J. Garcia, A. Damone, M. Schappals, S. Stephan, M. Kohns, H. Hasse: A force field for poly(oxymethylene) dimethyl ethers (OMEn), Journal of Chemical Theory and Computation 16 (2020) 2517–2528. doi:`10.1021/acs.jctc.9b01106`.

[352] A. Ladd, L. Woodcock: Interfacial and co-existence properties of the Lennard-Jones system at the triple point, Molecular Physics 36 (1978) 611–619. doi:`10.1080/00268977800101791`.

[353] T. Lafitte, A. Apostolakou, C. Avendano, A. Galindo, C.S. Adjiman, E.A. Müller, G. Jackson: Accurate statistical associating fluid theory for chain molecules formed from Mie segments, The Journal of Chemical Physics 139 (2013) 154504. doi:`10.1063/1.4819786`.

[354] T. Lafitte, B. Mendiboure, M.M. Piñeiro, D. Bessières, C. Miqueu: Interfacial properties of water/CO_2: A comprehensive description through a gradient theory SAFT-VR Mie approach, The Journal of Physical Chemistry B 114 (2010) 11110–11116. doi:`10.1021/jp103292e`.

[355] J. Lakomy, L. Lehar: Measurement of the surface tension of chorosilanes using the maximum bubble pressure method. (cz), Chemicke Listy Pro Vedu A Prumysl 59 (1965) 985–992.

[356] V.T. Lam, G.C. Benson: Surface tensions of binary liquid systems. I. mixtures of nonelectrolytes, Canadian Journal of Chemistry 48 (1970) 3773–3781. doi:`10.1139/v70-637`.

[357] A. Lamorgese, R. Mauri, L. Sagis: Modeling soft interface dominated systems: A comparison of phase field and Gibbs dividing surface models, Physics Reports 675 (2017) 1–54. doi:`10.1016/j.physrep.2017.01.002`.

[358] K. Langenbach: Co-oriented fluid functional equation for electrostatic interactions (COFFEE), Chemical Engineering Science 174 (2017) 40 – 55. doi:`https://doi.org/10.1016/j.ces.2017.08.025`.

[359] M. Lautenschlaeger, S. Stephan, M. Horsch, B. Kirsch, J. Aurich, H. Hasse: Effects of lubrication on the friction and heat transfer in machining processes on the nanoscale: A molecular dynamics approach, Procedia CRIP 67 (2018) 296–301. doi:`10.1016/j.procir.2017.12.216`.

[360] M. Lautenschlaeger, S. Stephan, H.M. Urbassek, B. Kirsch, J.C. Aurich, M. Horsch, H. Hasse: Effects of lubrication on the friction in nanometric machining processes: A molecular dynamics approach, Applied Mechanics and Materials 869 (2017) 85–93. doi:`10.4028/www.scientific.net/AMM.869.85`.

[361] D.J. Lee, M.M. Telo da Gama, K.E. Gubbins: The vapour-liquid interface for a Lennard-Jones model of argon-krypton mixtures, Molecular Physics 53 (1984) 1113–1130. doi:`10.1080/00268978400102891`.

[362] D.J. Lee, M.M. Telo da Gama, K.E. Gubbins: Adsorption and surface tension reduction at the vapor-liquid interface, The Journal of Physical Chemistry 89 (1985) 1514–1519. doi:`10.1021/j100254a041`.

[363] J.K. Lee, J.A. Barker, G.M. Pound: Surface structure and surface tension: Perturbation theory and Monte Carlo calculation, The Journal of Chemical Physics 60 (1974) 1976–1980. doi:`10.1063/1.1681303`.

[364] L.L. Lee, H.M. Hulburt: Correlation functions of classical fluids. I. the radial distribution functions of mixtures of Kihara molecules in the Percus-Yevick approximation and their thermodynamic functions, The Journal of Chemical Physics 58 (1973) 44–60. doi:`10.1063/1.1678952`.

[365] J. Lekner, J.R. Henderson: Surface tension and energy of a classical liquid-vapour interface, Molecular Physics 34 (1977) 333–359. doi:`10.1080/00268977700101771`.

[366] T.W. Leland, J.S. Rowlinson, G.A. Sather: Statistical thermodynamics of mixtures of molecules of different sizes, Transactions of the Faraday Society 64 (1968) 1447–1460. doi:`10.1039/TF9686401447`.

[367] T.W. Leland, J.S. Rowlinson, G.A. Sather, I.D. Watson: Statistical thermodynamics of two-fluid models of mixtures, Transactions of the Faraday Society 65 (1969) 2034–2043. doi:`10.1039/TF9696502034`.

[368] J.E. Lennard-Jones: Cohesion, Proceedings of the Physical Society 43 (1931) 461–482. doi:`10.1088/0959-5309/43/5/301`.

[369] R.J.F. Leote de Carvalho, R. Evans, D.C. Hoyle, J.R. Henderson: The decay of the pair correlation function in simple fluids: Long- versus short-ranged potentials, Journal of Physics: Condensed Matter 6 (1994) 9275.

[370] D. Levesque, L. Verlet: Perturbation theory and equation of state for fluids, Physical Review 182 (1969) 307–316. doi:`10.1103/PhysRev.182.307`.

[371] C. Leys, C. Ley, O. Klein, P. Bernard, L. Licata: Detecting outliers: Do not use standard deviation around the mean, use absolute deviation around the median, Journal of Experimental Social Psychology 49 (2013) 764–766. doi:`10.1016/j.jesp.2013.03.013`.

[372] W. Li, Z. Jin: Molecular dynamics simulation of natural gas-water interfacial tensions over wide range of pressures, Fuel 236 (2019) 480–492. doi:`10.1016/j.fuel.2018.09.040`.

[373] X.S. Li, J.M. Liu, D. Fu: Investigation of interfacial tensions for carbon dioxide aqueous solutions by perturbed-chain statistical associating fluid theory combined with density-gradient theory, Industrial & Engineering Chemistry Research 47 (2008) 8911–8917. doi:`10.1021/ie800959h`.

[374] Y. Li, W.A. Fouad, L.F. Vega: Interfacial anomaly in low global warming potential refrigerant blends as predicted by molecular dynamics simulations, Physical Chemistry Chemical Physics 21 (2019) 22092–22102. doi:`10.1039/c9cp03231b`.

[375] X. Liang, G.M. Kontogeorgis: New variant of the universal constants in the perturbed chain-statistical associating fluid theory equation of state, Industrial & Engineering Chemistry Research 54 (2015) 1373–1384. doi:`10.1021/ie503925h`.

[376] X. Liang, B. Maribo-Mogensen, K. Thomsen, W. Yan, G.M. Kontogeorgis: Approach to improve speed of sound calculation within PC-SAFT framework, Industrial & Engineering Chemistry Research 51 (2012) 14903–14914. doi:`10.1021/ie3018127`.

[377] X. Liang, M.L. Michelsen, G.M. Kontogeorgis: A density gradient theory based method for surface tension calculations, Fluid Phase Equilibria 428 (2016) 153–163. doi:`10.1016/j.fluid.2016.06.017`.

[378] X. Liang, M.L. Michelsen, G.M. Kontogeorgis: Pitfalls of using the geometric-mean combining rule in the density gradient theory, Fluid Phase Equilibria 415 (2016) 75–83. doi:`10.1016/j.fluid.2016.01.047`.

[379] H. Lin, Y.Y. Duan, Q. Min: Gradient theory modeling of surface tension for pure fluids and binary mixtures, Fluid Phase Equilibria 254 (2007) 75. doi:`10.1016/j.fluid.2007.02.013`.

[380] A. Linhart, C.C. Chen, J. Vrabec, H. Hasse: Thermal properties of the metastable supersaturated vapor of the Lennard-Jones fluid, The Journal of Chemical Physics 122 (2005) 144506. doi:`10.1063/1.1872774`.

[381] P. Linstrom, W. Mallard: NIST Chemistry WebBook, NIST standard reference database number 69, website, 2019. National Institute of Standards and Technology, Gaithersburg MD (retrieved january 2020).

[382] M. Lísal, J.K. Brennan, W.R. Smith, F.R. Siperstein: Dual control cell reaction ensemble molecular dynamics: A method for simulations of reactions and adsorption in porous materials, The Journal of Chemical Physics 121 (2004) 4901–4912. doi:`10.1063/1.1782031`.

[383] S.V. Lishchuk, J. Fischer: Communication: Long range corrections in liquid-vapor interface simulations, The Journal of Chemical Physics 149 (2018) 091102. doi:`10.1063/1.5048925`.

[384] B. Liu, J. Shi, M. Wang, J. Zhang, B. Sun, Y. Shen, X. Sun: Reduction in interfacial tension of water–oil interface by supercritical CO2 in enhanced oil recovery processes studied with molecular dynamics simulation, The Journal of Supercritical Fluids 111 (2016) 171–178. doi:`10.1016/j.supflu.2015.11.001`.

[385] P. Liu, E. Harder, B.J. Berne: On the calculation of diffusion coefficients in confined fluids and interfaces with an application to the liquid-vapor interface of water, The Journal of Physical Chemistry B 108 (2004) 6595–6602. doi:`10.1021/jp0375057`.

[386] S.T. Liu, D. Fu, J.Y. Lu: Investigation of bulk and interfacial properties for nitrogen and light hydrocarbon binary mixtures by perturbed-chain statistical associating fluid theory combined with density-gradient theory, Industrial & Engineering Chemistry Research 48 (2009) 10734–10739. doi:`10.1021/ie9007437`.

[387] Z.Y. Liu, C. Wang, H. Zhou, Y. Wang, L. Zhang, L. Zhang, S. Zhao: Characterizing the impact of surfactant structure on interfacial tension: a molecular dynamics study, Journal of Molecular Modeling 23 (2017) 112. doi:`10.1007/s00894-017-3285-0`.

[388] Z.Y. Liu, N. Wei, C. Wang, H. Zhou, L. Zhang, Q. Liao, L. Zhang: Interfacial assignment of branched-alkyl benzene sulfonates: A molecular simulation, AIP Advances 5 (2015) 117203. doi:`10.1063/1.4935339`.

[389] F. Llovell, N.M. Dowell, F.J. Blas, A. Galindo, G. Jackson: Application of the SAFT-VR density functional theory to the prediction of the interfacial properties of mixtures of relevance to reservoir engineering, Fluid Phase Equilibria 336 (2012) 137–150. doi:`10.1016/j.fluid.2012.07.033`.

[390] F. Llovell, A. Galindo, F.J. Blas, G. Jackson: Classical density functional theory for the prediction of the surface tension and interfacial properties of fluids mixtures of chain molecules based on the statistical associating fluid theory for potentials of variable range, The Journal of Chemical Physics 133 (2010) 024704. doi:`10.1063/1.3449143`.

[391] O. Lobanova, A. Mejía, G. Jackson, E.A. Müller: SAFT-γ force field for the simula-
tion of molecular fluids 6: Binary and ternary mixtures comprising water, carbon
dioxide, and n-alkanes, The Journal of Chemical Thermodynamics 93 (2016) 320–
336. doi:`10.1016/j.jct.2015.10.011`.

[392] H.H. Loeffler, S. Bosisio, G. Duarte Ramos Matos, D. Suh, B. Roux, D.L. Mobley,
J. Michel: Reproducibility of free energy calculations across different molecular
simulation software packages, Journal of Chemical Theory and Computation 14
(2018) 5567–5582. doi:`10.1021/acs.jctc.8b00544`.

[393] H. Longuet-Higgins: The statistical thermodynamics of multicomponent systems,
Proceedings of the Royal Society of London A 205 (1951) 247–269. doi:`10.1098/`
`rspa.1951.0028`.

[394] H.A. Lorentz: Über die Anwendung des Satzes vom Virial in der kinetischen
Theorie der Gase, Annalen Der Physik 248 (1881) 127–136. doi:`10.1002/andp.`
`18812480110`.

[395] A. Lotfi, J. Vrabec, J. Fischer: Vapour liquid equilibria of the Lennard-Jones fluid
from the NpT plus test particle method, Molecular Physics 76 (1992) 1319–1333.
doi:`10.1080/00268979200102111`.

[396] A. Lotfi, J. Vrabec, J. Fischer: Evaporation from a free liquid surface, Inter-
national Journal of Heat and Mass Transfer 73 (2014) 303. doi:`10.1016/j.`
`ijheatmasstransfer.2014.02.010`.

[397] B.Q. Lu, R. Evans, M.M. Telo da Gama: The form of the density profile at
a liquid-gas interface, Molecular Physics 55 (1985) 1319–1338. doi:`10.1080/`
`00268978500102041`.

[398] K. Lucas: Angewandte Statistische Thermodynamik, 1st ed., Springer Verlag,
Berlin, 1986. doi:`10.1007/978-3-662-05751-3`.

[399] R. Lustig: Statistical thermodynamics in the classical molecular dynamics ensem-
ble. III. numerical results, The Journal of Chemical Physics 100 (1994) 3068–3078.
doi:`10.1063/1.466448`.

[400] R. Lustig: Direct molecular NVT simulation of the isobaric heat capacity, speed
of sound and Joule-Thomson coefficient, Molecular Simulation 37 (2011) 457–465.
doi:`10.1080/08927022.2011.552244`.

[401] R. Lustig: Statistical analogues for fundamental equation of state deriva-
tives, Molecular Physics 110 (2012) 3041–3052. doi:`10.1080/00268976.2012.`
`695032`.

[402] M.R. Lyu (Ed.): Handbood of Software Reliability Engineering, McGraw-Hill,
New York, 1996.

[403] J.M.D. MacElroy: Nonequilibrium molecular dynamics simulation of diffusion and
flow in thin microporous membranes, The Journal of Chemical Physics 101 (1994)
5274–5280. doi:`10.1063/1.467381`.

[404] J. Mairhofer, J. Gross: Modeling of interfacial properties of multicomponent systems using density dradient theory and PCP-SAFT, Fluid Phase Equilibria 439 (2017) 31. doi:10.1016/j.fluid.2017.02.009.

[405] J. Mairhofer, R.J. Sadus: Thermodynamic properties of supercritical n-m Lennard-Jones fluids and isochoric and isobaric heat capacity maxima and minima, The Journal of Chemical Physics 139 (2013) 154503. doi:10.1063/1.4824626.

[406] G.A. Mansoori: Radial distribution functions and their role in modeling of mixtures behavior, Fluid Phase Equilibria 87 (1993) 1–22. doi:10.1016/0378-3812(93)85015-E.

[407] G.A. Mansoori, N.F. Carnahan, K.E. Starling, T.W. Leland: Equilibrium thermodynamic properties of the mixture of hard spheres, The Journal of Chemical Physics 54 (1971) 1523. doi:10.1063/1.1675048.

[408] G.A. Mansoori, T.W. Leland: Statistical thermodynamics of mixtures. a new version for the theory of conformal solution, Journal of the Chemical Society, Faraday Transactions 2: 68 (1972) 320–344. doi:10.1039/F29726800320.

[409] M. Mareschal, M. Baus, R. Lovett: The local pressure in a cylindrical liquid-vapor interface: A simulation study, The Journal of Chemical Physics 106 (1997) 645–654. doi:10.1063/1.473402.

[410] M.G. Martin, J.I. Siepmann: Transferable potentials for phase equilibria. 1. United-atom description of n-alkanes, The Journal of Physical Chemistry B 102 (1998) 2569–2577. doi:10.1021/jp972543+.

[411] M.G. Martin, A.P. Thompson, T.M. Nenoff: Effect of pressure, membrane thickness, and placement of control volumes on the flux of methane through thin silicalite membranes: A dual control volume grand canonical molecular dynamics study, The Journal of Chemical Physics 114 (2001) 7174–7181. doi:10.1063/1.1360256.

[412] F.J. Martinez-Ruiz, F.J. Blas: Interfacial properties of binary mixtures of square-well molecules from Monte Carlo simulation, The Journal of Chemical Physics 144 (2016) 154705. doi:10.1063/1.4947017.

[413] F.J. Martinez-Ruiz, F.J. Blas, B. Mendiboure, A.I. Moreno-Ventas Bravo: Effect of dispersive long-range corrections to the pressure tensor: The vapour-liquid interfacial properties of the Lennard-Jones system revisited, The Journal of Chemical Physics 141 (2014) 184701. doi:10.1063/1.4900773.

[414] F.J. Martinez-Ruiz, F.J. Blas, A.I. Moreno-Ventas Bravo, J.M. Miguez, L.G. MacDowell: Vapour-liquid interfacial properties of square-well chains from density functional theory and Monte Carlo simulation, Physical Chemistry Chemical Physics 19 (2017) 12296–12309. doi:10.1039/C7CP01182B.

[415] F.J. Martinez-Ruiz, A.I. Moreno-Ventas Bravo, F.J. Blas: Liquid-liquid interfacial properties of a symmetrical Lennard-Jones binary mixture, The Journal of Chemical Physics 143 (2015) 104706. doi:10.1063/1.4930276.

[416] E. Mason, T. Spurling: The Virial Equation of State, Pergamon Press, Oxford, 1969.

[417] W.L. Masterton, J. Bianchi, E.J. Slowinski: Surface tension and adsorption in gas-liquid systems at moderate pressures, The Journal of Physical Chemistry 67 (1963) 615–618. doi:`10.1021/j100797a018`.

[418] E.A. Mastny, J.J. de Pablo: Melting line of the Lennard-Jones system, infinite size, and full potential, The Journal of Chemical Physics 127 (2007) 104504. doi:`10.1063/1.2753149`.

[419] M. Matsumoto: Molecular dynamics simulation of interphase transport at liquid surfaces, Fluid Phase Equilibria 125 (1996) 195–203. doi:`10.1016/S0378-3812(96)03123-8`.

[420] E. Matteoli, G.A. Mansoori: A simple expression for radial distribution functions of pure fluids and mixtures, The Journal of Chemical Physics 103 (1995) 4672–4677. doi:`10.1063/1.470654`.

[421] P. Mausbach, A. Köster, G. Rutkai, M. Thol, J. Vrabec: Comparative study of the Grüneisen parameter for 28 pure fluids, The Journal of Chemical Physics 144 (2016) 244505. doi:`10.1063/1.4954282`.

[422] P. Mausbach, H.O. May: Direct molecular simulation of the Grüneisen parameter and density scaling exponent in fluid systems, Fluid Phase Equilibria 366 (2014) 108–116. doi:`10.1016/j.fluid.2014.01.015`.

[423] H.O. May, P. Mausbach: Erratum: Riemannian geometry study of vapor-liquid phase equilibria and supercritical behavior of the Lennard-Jones fluid [Phys. Rev. E 85, 031201 (2012)], Physical Review E 86 (2012) 059905. doi:`10.1103/PhysRevE.86.059905`.

[424] H.O. May, P. Mausbach: Fluid properties from equations of state compared with direct molecular simulations for the Lennard-Jones system, AIP Conf. Proc. 1501 (2012) 954–960. doi:`10.1063/1.4769645`.

[425] H.O. May, P. Mausbach: Riemannian geometry study of vapor-liquid phase equilibria and supercritical behavior of the Lennard-Jones fluid, Physical Review E 85 (2012) 031201. doi:`10.1103/PhysRevE.85.031201`.

[426] V. Mazur, L. Boshkov, V. Murakhovsky: Global phase behaviour of binary mixtures of Lennard-Jones molecules, Physics Letters A 104 (1984) 415–418. doi:`10.1016/0375-9601(84)90746-1`.

[427] I.A. Mc Lure, B. Edmonds, M. Lal: The surface tension of hexafluorobenzene and its binary mixtures with benzene, cyclohexene, and cyclohexane, Journal of Colloid and Interface Science 91 (1983) 361–367. doi:`10.1016/0021-9797(83)90348-X`.

[428] B.F. McCoy, H.T. Davis: Free-energy theory of inhomogeneous fluids, Physical Review A 20 (1979) 1201–1207. doi:`10.1103/PhysRevA.20.1201`.

[429] I. McDonald, K. Singer: An equation of state for simple liquids, Molecular Physics 23 (1972) 29–40. doi:`10.1080/00268977200100021`.

[430] I.R. McDonald, K. Singer: Calculation of thermodynamic properties of liquid argon from Lennard-Jones parameters by a Monte Carlo method, Discussions of The Faraday Society 43 (1967) 40–49. doi:`10.1039/DF9674300040`.

[431] I.R. McDonald, K. Singer: Machine calculation of thermodynamic properties of a simple fluid at supercritical temperatures, The Journal of Chemical Physics 47 (1967) 4766–4772. doi:`10.1063/1.1701695`.

[432] I.R. McDonald, K. Singer: Examination of the adequacy of the 12-6 potential for liquid argon by means of Monte Carlo calculations, The Journal of Chemical Physics 50 (1969) 2308–2315. doi:`10.1063/1.1671381`.

[433] I.R. McDonald, L.V. Woodcock: Triple-dipole dispersion forces in dense fluids, Journal of Physics C 3 (1970) 722. doi:`10.1088/0022-3719/3/3/028`.

[434] I.A. McLure, B. Edmonds, M. Lal: Extremes in surface tension of fluorocarbon + hydrocarbon mixtures, Nature Physical Science 241 (1973) 71–71. doi:`10.1038/physci241071a0`.

[435] I.A. McLure, V.A.M. Soares, A.M. Williamson: Total surface segregation. a fresh look at the Gibbs adsorption isotherm for binary liquid mixtures., Langmuir 9 (1993) 2190–2201. doi:`10.1021/la00032a048`.

[436] G.C. McNeil-Watson, N.B. Wilding: Freezing line of the Lennard-Jones fluid: A phase switch Monte Carlo study, The Journal of Chemical Physics 124 (2006) 064504. doi:`10.1063/1.2166395`.

[437] M. Mecke, A. Müller, J. Winkelmann, J. Fischer: An equation of state for two-center Lennard-Jones fluids, International Journal of Thermophysics 18 (1997) 683–698. doi:`10.1007/bf02575128`.

[438] M. Mecke, A. Müller, J. Winkelmann, J. Vrabec, J. Fischer, R. Span, W. Wagner: An accurate van der Waals-type equation of state for the Lennard-Jones fluid, International Journal of Thermophysics 17 (1996) 391–404. doi:`10.1007/BF01443399`.

[439] M. Mecke, A. Müller, J. Winkelmann, J. Vrabec, J. Fischer, R. Span, W. Wagner: Erratum – an accurate van der Waals-type equation of state for the Lennard-Jones fluid, International Journal of Thermophysics 19 (1998) 1493–1498. doi:`10.1023/A:1021995905315`.

[440] M. Mecke, J. Winkelmann, J. Fischer: Molecular dynamics simulation of the liquid-vapor interface: The Lennard-Jones fluid, The Journal of Chemical Physics 107 (1997) 9264–9270. doi:`10.1063/1.475217`.

[441] M. Mecke, J. Winkelmann, J. Fischer: Molecular dynamics simulation of the liquid-vapor interface: Binary mixtures of Lennard-Jones fluids, The Journal of Chemical Physics 110 (1999) 1188–1194. doi:`10.1063/1.478160`.

[442] J.A. van Meel, A.J. Page, R.P. Sear, D. Frenkel: Two-step vapor-crystal nucleation close below triple point, The Journal of Chemical Physics 129 (2008) 204505. doi:`10.1063/1.3026364`.

[443] K. Meier: Computer Simulation and Interpretation of the Transport Coefficients of the Lennard-Jones Model Fluid, Dissertation, University of the Federal Armed Forces Hamburg, 2002.

[444] A. Mejía, M. Cartes, H. Segura: Interfacial tensions of binary mixtures of ethanol with octane, decane, dodecane, and tetradecane, The Journal of Chemical Thermodynamics 43 (2011) 1395–1400. doi:`10.1016/j.jct.2011.04.005`.

[445] A. Mejía, M. Cartes, H. Segura, E.A. Müller: Use of equations of state and coarse grained simulations to complement experiments: Describing the interfacial properties of carbon dioxide + decane and carbon dioxide + eicosane mixtures, Journal of Chemical & Engineering Data 59 (2014) 2928. doi:`10.1021/je5000764`.

[446] A. Mejía, J.C. Pàmies, D. Duque, H. Segura, L.F. Vega: Phase and interface behaviors in type-I and type-V Lennard-Jones mixtures: Theory and simulations, The Journal of Chemical Physics 123 (2005) 034505. doi:`10.1063/1.1955529`.

[447] A. Mejía, L.F. Vega: Perfect wetting along a three-phase line: Theory and molecular dynamics simulations, The Journal of Chemical Physics 124 (2006) 244505. doi:`10.1063/1.2206772`.

[448] T. Merker, C. Engin, J. Vrabec, H. Hasse: Molecular model for carbon dioxide optimized to vapor-liquid equilibria, The Journal of Chemical Physics 132 (2010) 234512. doi:`10.1063/1.3434530`.

[449] T. Merker, J. Vrabec, H. Hasse: Molecular simulation study on the solubility of carbon dioxide in mixtures of cyclohexane+ cyclohexanone, Fluid Phase Equilibria 315 (2012) 77–83.

[450] A. Meroni, A. Parola, L. Reatto: Differential approach to the theory of fluids, Physical Review A 42 (1990) 6104–6115. doi:`10.1103/PhysRevA.42.6104`.

[451] N. Metropolis, A.W. Rosenbluth, M.N. Rosenbluth, A.H. Teller, E. Teller: Equation of state calculations by fast computing machines, The Journal of Chemical Physics 21 (1953) 1087–1092. doi:`10.1063/1.1699114`.

[452] J. Mick, E. Hailat, V. Russo, K. Rushaidat, L. Schwiebert, J. Potoff: GPU-accelerated Gibbs ensemble Monte Carlo simulations of Lennard-Jonesium, Computer Physics Communications 184 (2013) 2662–2669. doi:`10.1016/j.cpc.2013.06.020`.

[453] J.M. Míguez, J.M. Garrido, F.J. Blas, H. Segura, A. Mejía, M.M. Piñeiro: Comprehensive characterization of interfacial behavior for the mixture CO2 + H2O + CH4: Comparison between atomistic and coarse grained molecular simulation models and density gradient theory, The Journal of Physical Chemistry C 118 (2014) 24504–24519. doi:`10.1021/jp507107a`.

[454] L. Mikheev, A. Chernov: Structure of surface layers and thin films of a dense simple liquid: Weak-ordering region, Sov. Phys. JETP 65 (1987) 971.

[455] C. Miqueu, B. Mendiboure, A. Graciaa, J. Lachaise: Modelling of the surface tension of pure components with the gradient theory of fluid interfaces: a simple and accurate expression for the influence parameters, Fluid Phase Equilibria 207 (2003) 225. doi:`10.1016/S0378-3812(03)00028-1`.

[456] C. Miqueu, B. Mendiboure, A. Graciaa, J. Lachaise: Modeling of the surface tension of multicomponent mixtures with the gradient theory of fluid interfaces, Industrial & Engineering Chemistry Research 44 (2005) 3321–3329. doi:`10.1021/ie049086l`.

[457] C. Miqueu, B. Mendiboure, A. Graciaa, J. Lachaise: Petroleum mixtures: An efficient predictive method for surface tension estimations at reservoir conditions, Fuel 87 (2008) 612–621. doi:`10.1016/j.fuel.2007.05.049`.

[458] C. Miqueu, B. Mendiboure, C. Graciaa, J. Lachaise: Modelling of the surface tension of binary and ternary mixtures with the gradient theory of fluid interfaces, Fluid Phase Equilibria 218 (2004) 189–203. doi:`10.1016/j.fluid.2003.12.008`.

[459] C. Miqueu, J.M. Miguez, M.M. Piñeiro, T. Lafitte, B. Mendiboure: Simultaneous application of the gradient theory and Monte Carlo molecular simulation for the investigation of methane/water interfacial properties, The Journal of Physical Chemistry B 115 (2011) 9618–9625. doi:`10.1021/jp202276k`.

[460] Y. Miyano: An equation of state for Lennard-Jones pure fluids applicable over a very wide temperature range, Fluid Phase Equilibria 85 (1993) 71–80. doi:`10.1016/0378-3812(93)80005-8`.

[461] J. Miyazaki, J.A. Barker, G.M. Pound: A new Monte Carlo method for calculating surface tension, The Journal of Chemical Physics 64 (1976) 3364–3369. doi:`10.1063/1.432627`.

[462] K.C. Mo, K.E. Gubbins: Conformal solution theory for viscosity and thermal conductivity of mixtures, Molecular Physics 31 (1976) 825–847. doi:`10.1080/00268977600100631`.

[463] K.C. Mo, K.E. Gubbins, G. Jacucci, I.R. McDonald: The radial distribution function in fluid mixtures: Conformal solution theory and molecular dynamics results, Molecular Physics 27 (1974) 1173–1183. doi:`10.1080/00268977400101041`.

[464] A. Moghimikheirabadi, P. Ilg, L.M.C. Sagis, M. Kröger: Surface rheology and structure of model triblock copolymers at a liquid-vapor interface: A molecular dynamics study, Macromolecules 53 (2020) 1245–1257. doi:`10.1021/acs.macromol.9b01995`.

[465] A. Moghimikheirabadi, L.M.C. Sagis, M. Kröger, P. Ilg: Gas-liquid phase equilibrium of a model langmuir monolayer captured by a multiscale approach, Physical Chemistry Chemical Physics 21 (2019) 2295–2306. doi:`10.1039/c8cp05447a`.

[466] S. Mohammed, G. Mansoori: Effect of CO2 on the interfacial and transport properties of water/binary and asphaltenic oils: Insights from molecular dynamics, Energy & Fuels 32 (2018) 5409–5417. doi:`10.1021/acs.energyfuels.8b00488`.

[467] S. Mohammed, G.A. Mansoori: Molecular insights on the interfacial and transport properties of supercritical CO2/brine/crude oil ternary system, Jorunal of Molecular Liquids 218 (2018) 268–273. doi:`10.1016/j.molliq.2018.05.009`.

[468] M.R. Moldover, J.S. Gallagher: Critical points of mixtures: An analogy with pure fluids, AIChE Journal 24 (1978) 267–278. doi:`10.1002/aic.690240216`.

[469] W.L.H. Moll: Dielektrische Untersuchungen über die Einwirkung organischer Lösungsmittel auf hochmolekulare Stoffe, Kolloid-Beihefte 49 (1939) 1–74. doi:`10.1007/BF02557807`.

[470] D. Möller, J. Fischer: Vapour liquid equilibrium of a pure fluid from test particle method in combination with NpT molecular dynamics simulations, Molecular Physics 69 (1990) 463–473. doi:`10.1080/00268979000100341`.

[471] A. Morita: Molecular dynamics study of mass accommodation of methanol at liquid-vapor interfaces of methanol/water binary solutions of various concentrations, Chemical Physics Letters 375 (2003) 1–8. doi:`10.1016/S0009-2614(03)00746-2`.

[472] A. Morita, B.C. Garrett: Molecular theory of mass transfer kinetics and dynamics at gas-water interface, Fluid Dynamics Research 40 (2008) 459–473. doi:`10.1016/j.fluiddyn.2007.12.003`.

[473] J.R. Morris, X. Song: The melting lines of model systems calculated from coexistence simulations, The Journal of Chemical Physics 116 (2002) 9352–9358. doi:`10.1063/1.1474581`.

[474] W.O. Morris, M.D. Donohue: Vapor-liquid equilibria in mixtures containing carbon dioxide, toluene, and 1-methylnaphthalene, Journal of Chemical & Engineering Data 30 (1985) 259–263. doi:`10.1021/je00041a007`.

[475] A. Morsali, S.A. Beyramabadi, M.R. Bozorgmehr: Evaluation of p–v–t differential properties of the Lennard-Jones fluid using radial distribution functions and molecular dynamics, Chemical Physics 335 (2007) 194–200. doi:`10.1016/j.chemphys.2007.04.019`.

[476] A. Morsali, E.K. Goharshadi, A.G. Mansoori, M. Abbaspour: An accurate expression for radial distribution function of the Lennard-Jones fluid, Chemical Physics 310 (2005) 11–15. doi:`10.1016/j.chemphys.2004.09.027`.

[477] X. Mu, F. Frank, F.O. Alpak, W.G. Chapman: Stabilized density gradient theory algorithm for modeling interfacial properties of pure and mixed systems, Fluid Phase Equilibria 435 (2017) 118–130. doi:`10.1016/j.fluid.2016.11.024`.

[478] M. Mucha, T. Hrobárik, P. Jungwirth: Surface tension from molecular dynamics simulation: Adsorption at the gas-liquid interface, Israel Journal of Chemistry 43 (2003) 393–397. doi:`10.1560/ww15-pbew-m3w4-uagn`.

[479] E.A. Müeller, K.E. Gubbins: An equation of state for water from a simplified intermolecular potential, Industrial & Engineering Chemistry Research 34 (1995) 3662–3673. doi:10.1021/ie00037a055.

[480] A. Muhlbauer, J. Raal: Measurement and thermodynamic interpretation of high-pressure vapour-liquid equilibria in the toluene+CO2 system, Fluid Phase Equilibria 64 (1991) 213–236. doi:10.1016/0378-3812(91)90015-Y.

[481] M. Mukhopadhyay, P. Srinivas: Multicomponent solubilities of reactants and products of cyclohexane oxidation in supercritical carbon dioxide, Industrial & Engineering Chemistry Research 35 (1996) 4713–4717. doi:10.1021/ie9601155.

[482] E.A. Müller, K.E. Gubbins: Molecular-based equations of state for associating fluids: A review of SAFT and related approaches, Industrial & Engineering Chemistry Research 40 (2001) 2193–2211. doi:10.1021/ie000773w.

[483] E.A. Müller, A. Mejía: Interfacial properties of selected binary mixtures containing n-alkanes, Fluid Phase Equilibria 282 (2009) 68–81. doi:10.1016/j.fluid.2009.04.022.

[484] E.A. Müller, A. Mejía: Resolving discrepancies in the measurements of the interfacial tension for the CO2 + H2O mixture by computer simulation, The Journal of Physical Chemistry 5 (2014) 1267–1271. doi:10.1021/jz500417w.

[485] G. Muratov, V. Skripov: Surface tension of carbon dioxide (in russian), Teplofiz. Vys. Temp. 20 (1982) 596–598.

[486] P. Naeiji, T. Woo, S. Alavi, F. Varaminian, R. Ohmura: Interfacial properties of hydrocarbon/water systems predicted by molecular dynamic simulations, Journal of Chemical Physics 150 (2019) 114703. doi:10.1063/1.5078739.

[487] N. Nagarajan, R.L. Robinson: Equilibrium phase compositions, phase densities, and interfacial tensions for carbon dioxide + hydrocarbon systems. 3. CO2 + cyclohexane. 4. CO2 + benzene, Journal of Chemical & Engineering Data 32 (1987) 369–371. doi:10.1021/je00049a025.

[488] R. Nagl, P. Zimmermann, T. Zeiner: Interfacial mass transfer in water-toluene systems, Journal of Chemical & Engineering Data 65 (2020) 328–336. doi:10.1021/acs.jced.9b00672.

[489] P. Naidoo, D. Ramjugernath, J.D. Raal: A new high-pressure vapour-liquid equilibrium apparatus, Fluid Phase Equilibria 269 (2008) 104–112. doi:10.1016/j.fluid.2008.05.002.

[490] I. Napari, A. Laaksonen, V. Talanquer, D.W. Oxtoby: A density functional study of liquid-liquid interfaces in partially miscible systems, The Journal of Chemical Physics 110 (1999) 5906–5912. doi:10.1063/1.478490.

[491] A. Neumaier, U.K. Deiters: The characteristic curves of water, International Journal of Thermophysics 37 (2016) 96. doi:10.1007/s10765-016-2098-1.

[492] J.C. Neyt, A. Wender, V. Lachet, A. Ghoufi, P. Malfreyt: Molecular modeling of the liquid-vapor interfaces of a multi-component mixture: Prediction of the coexisting densities and surface tensions at different pressures and gas compositions, The Journal of Chemical Physics 139 (2013) 024701. doi:10.1063/1.4811679.

[493] J.C. Neyt, A. Wender, V. Lachet, P. Malfreyt: Modeling the pressure dependence of acid gas + n-alkane interfacial tensions using atomistic Monte Carlo simulations, Journal of Physical Chemistry 116 (2012) 10563–10572. doi:10.1021/jp212004c.

[494] I. Nezbeda: Simulations of vapor-liquid equilibria: Routine versus thoroughness, Journal of Chemical & Engineering Data 61 (2016) 3964–3969. doi:10.1021/acs.jced.6b00539.

[495] I. Nezbeda: Vapour-liquid equilibria from molecular simulations: Some issues affecting reliability and reproducibility, Molecular Physics 117 (2019) 2814–2821. doi:10.1080/00268976.2018.1562125.

[496] I. Nezbeda, K. Aim: On the way from theoretical calculations to practical equations of state for real fluids, Fluid Phase Equilibria 52 (1989) 39–46. doi:10.1016/0378-3812(89)80309-7.

[497] I. Nezbeda, J. Kolafa: The use of control quantities in computer simulation experiments: Application to the exp-6 potential fluid, Molecular Simulation 14 (1995) 153–163. doi:10.1080/08927029508022013.

[498] K.N. Ngale, C. Desgranges, J. Delhommelle: Wang-Landau configurational bias Monte Carlo simulations: Vapour-liquid equilibria of alkenes, Molecular Simulation 38 (2012) 653–658. doi:10.1080/08927022.2012.694432.

[499] C.V. Nguyen, H. Nakahara, O. Shibata, C.M. Phan: Adsorption of sodium iodine at air/water interface, Journal of Molecular Liquids 298 (2020) 112076. doi:10.1016/j.molliq.2019.112076.

[500] O.G. Niño-Amézquita, S. Enders: Prediction of interfacial tension of binary mixtures, in: S. Pierucci, G.B. Ferraris (Eds.), 20th European Symposium on Computer Aided Process Engineering, volume 28 of *Computer Aided Chemical Engineering*, Elsevier, 2010, pp. 85–90. doi:10.1016/S1570-7946(10)28015-X.

[501] O.G. Niño-Amézquita, S. Enders: Phase equilibrium and interfacial properties of water+methane mixtures, Fluid Phase Equilibria 407 (2016) 143–151. doi:10.1016/j.fluid.2015.05.005.

[502] O.G. Niño-Amézquita, S. Enders, P.T. Jaeger, R. Eggers: Interfacial properties of mixtures containing supercritical gases, The Journal of Supercritical Fluids 55 (2010) 724. doi:10.1016/j.supflu.2010.09.040.

[503] O.G. Niño-Amézquita, S. Enders, P.T. Jaeger, R. Eggers: Measurement and prediction of interfacial tension of binary mixtures, Industrial & Engineering Chemistry Research 49 (2010) 592–601. doi:10.1021/ie901209z.

[504] O.G. Niño-Amézquita, D. van Putten, S. Enders: Phase equilibrium and interfacial properties of water+CO_2 mixtures, Fluid Phase Equilibria 332 (2012) 40. doi:`10.1016/j.fluid.2012.06.018`.

[505] J.J. Nicolas, K.E. Gubbins, W.B. Streett, D.J. Tildesley: Equation of state for the Lennard-Jones fluid, Molecular Physics 37 (1979) 1429. doi:`10.1080/00268977900101051`.

[506] C. Niethammer, S. Becker, M. Bernreuther, M. Buchholz, W. Eckhardt, A. Heinecke, S. Werth, H.J. Bungartz, C.W. Glass, H. Hasse, J. Vrabec, M. Horsch: ls1 mardyn: The massively parallel molecular dynamics code for large systems, Journal of Chemical Theory Computation 10 (2014) 4455. doi:`10.1021/ct500169q`.

[507] M.J.P. Nijmeijer, A.F. Bakker, C. Bruin, J.H. Sikkenk: A molecular dynamics simulation of the Lennard-Jones liquid-vapor interface, The Journal of Chemical Physics 89 (1988) 3789–3792. doi:`10.1063/1.454902`.

[508] O.G. Niño-Amézquita: Interfacial Properties and Phase Equilibria for Mixtures relevant in the Oil Industry, Ph.D. thesis, TU Berlin, 2013. URL: `https://depositonce.tu-berlin.de/bitstream/11303/4321/1/nino%20amezquita_oscar%20gabriel.pdf`.

[509] H. Okumura, F. Yonezawa: Liquid-vapor coexistence curves of several interatomic model potentials, The Journal of Chemical Physics 113 (2000) 9162–9168. doi:`10.1063/1.1320828`.

[510] H. Okumura, F. Yonezawa: Reliable determination of the liquid-vapor critical point by the NVT plus test particle method, Journal of The Physical Society of Japan 70 (2001) 1990–1994. doi:`10.1143/JPSJ.70.1990`.

[511] A. Onuki: Dynamic van der Waals theory, Physical Review E 75 (2007) 036304. doi:`10.1103/PhysRevE.75.036304`.

[512] M.J. Osborne, D.J. Lacks: Surface segregation in liquid mixtures with strong interspecies attraction, Physical Review E 70 (2004) 010501. doi:`10.1103/PhysRevE.70.010501`.

[513] S. Paliwal, V. Prymidis, L. Filion, M. Dijkstra: Non-equilibrium surface tension of the vapour-liquid interface of active Lennard-Jones particles, The Journal of Chemical Physics 147 (2017) 084902. doi:`10.1063/1.4989764`.

[514] A.Z. Panagiotopoulos: Direct determination of phase coexistence properties of fluids by Monte Carlo simulation in a new ensemble, Molecular Physics 61 (1987) 813–826. doi:`10.1080/00268978700101491`.

[515] A.Z. Panagiotopoulos: Monte Carlo methods for phase equilibria of fluids, Journal of Physics: Condensed Matter 12 (1999) R25–R52. doi:`10.1088/0953-8984/12/3/201`.

[516] A.Z. Panagiotopoulos, N. Quirke, M. Stapleton, D.J. Tildesley: Phase equilibria by simulation in the Gibbs ensemble, Molecular Physics 63 (1988) 527–545. doi:`10.1080/00268978800100361`.

[517] C. Panayiotou: Interfacial tension and interfacial profiles: an equation-of-state approach, Journal of Colloid and Interface Science 267 (2003) 418–428. doi:`10.1016/j.jcis.2003.07.023`.

[518] V. Papaioannou, T. Lafitte, C. Avendano, C.S. Adjiman, G. Jackson, E.A. Müller, A. Galindo: Group contribution methodology based on the statistical associating fluid theory for heteronuclear molecules formed from Mie segments, The Journal of Chemical Physics 140 (2014) 054107. doi:`10.1063/1.4851455`.

[519] P. Paricaud: A general perturbation approach for equation of state development: Applications to simple fluids, ab initio potentials, and fullerenes, The Journal of Chemical Physics 124 (2006) 154505. doi:`10.1063/1.2181979`.

[520] A.O. Parry, C. Rascon, R. Evans: The local structure factor near an interface; beyond extended capillary-wave models, Journal of Physics: Condensed Matter 28 (2016) 244013.

[521] D.Y. Peng, D.B. Robinson: A new two-constant equation of state, Industrial & Engineering Chemistry Fundamentals 15 (1976) 59–64. doi:`10.1021/i160057a011`.

[522] L.M. Pereira, A. Chapoy, R. Burgass, B. Tohidi: Measurement and modelling of high pressure density and interfacial tension of (gas + n-alkane) binary mixtures, The Journal of Chemical Thermodynamics 97 (2016) 55–69. doi:`10.1016/j.jct.2015.12.036`.

[523] M.E. Perez-Blanco, E.J. Maginn: Molecular dynamics simulations of CO2 at an ionic liquid interface: Adsorption, ordering, and interfacial crossing, The Journal of Physical Chemistry B 114 (2010) 11827–11837. doi:`10.1021/jp103862v`.

[524] M.E. Perez-Blanco, E.J. Maginn: Molecular dynamics simulations of carbon dioxide and water at an ionic liquid interface, The Journal of Physical Chemistry B 115 (2011) 10488–10499. doi:`10.1021/jp203838j`.

[525] J. Pérez-Pellitero, P. Ungerer, G. Orkoulas, A.D. Mackie: Critical point estimation of the Lennard-Jones pure fluid and binary mixtures, The Journal of Chemical Physics 125 (2006) 054515. doi:`10.1063/1.2434954`.

[526] D. Plačkov, R.J. Sadus: Molecular simulation of intermolecular attraction and repulsion in coexisting liquid and vapour phases, Fluid Phase Equilibria 134 (1997) 77–85. doi:`10.1016/S0378-3812(97)00047-2`.

[527] O. Pohl: Correspondence – evaluation of an improved volume translation for the prediction of hydrocarbon volumetric properties, Fluid Phase Equilibria 163 (1999) 157–159. doi:`10.1016/S0378-3812(99)00199-5`.

[528] P. Pohl, G.S. Heffelfinger, D.M. Smith: Molecular dynamics computer simulation of gas permeation in thin silicalite membranes, Molecular Physics 89 (1996) 1725–1731. doi:`10.1080/002689796173048`.

[529] P.I. Pohl, G.S. Heffelfinger: Massively parallel molecular dynamics simulation of gas permeation across porous silica membranes, Journal of Membrane Science 155 (1999) 1–7. doi:`10.1016/S0376-7388(98)00283-X`.

[530] I. Polishuk: Implementation of SAFT + cubic, PC-SAFT, and soave-benedict-webb-rubin equations of state for comprehensive description of thermodynamic properties in binary and ternary mixtures of CH4, CO2, and n-C16H34, Industrial & Engineering Chemistry Research 50 (2011) 14175–14185. doi:`10.1021/ie201952n`.

[531] I. Polishuk: Implementation of SAFT+cubic and PC-SAFT for comprehensive description of thermodynamic properties of n-octane and its mixtures, The Journal of Supercritical Fluids 62 (2012) 47–54. doi:`10.1016/j.supflu.2011.11.009`.

[532] C.I. Poser, I.C. Sanchez: Surface tension theory of pure liquids and polymer melts, Journal of Colloid and Interface Science 69 (1979) 539–548. doi:`10.1016/0021-9797(79)90142-5`.

[533] C.I. Poser, I.C. Sanchez: Interfacial tension theory of low and high molecular weight liquid mixtures, Macromolecules 14 (1981) 361–370. doi:`10.1021/ma50003a026`.

[534] J.J. Potoff, A.Z. Panagiotopoulos: Critical point and phase behavior of the pure fluid and a Lennard-Jones mixture, The Journal of Chemical Physics 109 (1998) 10914–10920. doi:`10.1063/1.477787`.

[535] J.J. Potoff, A.Z. Panagiotopoulos: Surface tension of the three-dimensional Lennard-Jones fluid from histogram-reweighting Monte Carlo simulations, The Journal of Chemical Physics 112 (2000) 6411–6415. doi:`10.1063/1.481204`.

[536] J. Powles: The liquid-vapour coexistence line for Lennard-Jones-type fluids, Physica A 126 (1984) 289–299. doi:`10.1016/0378-4371(84)90156-0`.

[537] J. Powles, W. Evans, N. Quirke: Non-destructive molecular-dynamics simulation of the chemical potential of a fluid, Molecular Physics 46 (1982) 1347–1370. doi:`10.1080/00268978200101981`.

[538] R. Privat, J.N. Jaubert: Classification of global fluid-phase equilibrium behaviors in binary systems, Chemical Engineering Research and Design 91 (2013) 1807–1839. doi:`10.1016/j.cherd.2013.06.026`.

[539] private communication of Valleau with Mecke, M. Universität Halle-Wittenberg, 1995. Data from Ref. [438]: Critical point data of the Lennard-Jones fluid (1994). doi:`10.1063/1.5021560`.

[540] private communication with Deiters, U.K. University of Cologne, 2019. Data from Ref. [138]: Computer simulation of the characteristic curves of pure fluids, Journal of Chemical & Engineering Data 61 (2016) 2720–2728. doi:`10.1021/acs.jced.6b00133`.

[541] private communication with Errington, J.R. University at Buffalo, 2019. Data from Ref. [163]: Direct calculation of liquid-vapor phase equilibria from transition matrix Monte Carlo simulation, The Journal of Chemical Physics 118 (2003) 9915–9925. doi:`10.1063/1.1572463`.

[542] private communication with Fischer, J. Universität für Bodenkultur, 2019. Data from Ref. [578]: Prediction of gas PVT data with effective intermolecular potentials using the Haar-Shenker-Kohler equation and computer simulations, Fluid Phase Equilibria 54 (1990) 237–246. doi:`10.1016/0378-3812(90)85082-L`.

[543] private communication with Köster, A. Universität Paderborn and Mausbach, P. Technical University of Cologne, 2019. Data from Ref. [341]: Premelting, solid-fluid equilibria, and thermodynamic properties in the high density region based on the Lennard-Jones potential, The Journal of Chemical Physics 147 (2017) 144502. doi:`10.1063/1.4990667`.

[544] private communication with Mairhofer, J. BASF, 2019. Data from Ref. [405]: Thermodynamic properties of supercritical n-m Lennard-Jones fluids and isochoric and isobaric heat capacity maxima and minima, The Journal of Chemical Physics 139 (2013) 154503. doi:`10.1063/1.4824626`.

[545] private communication with Mausbach, P. Technical University of Cologne, 2019. Additional unpublished data from Ref. [424]: Fluid properties from equations of state compared with direct molecular simulations for the Lennard-Jones system, AIP Conf. Proc. 1501 (2012) 954–960. doi:`10.1063/1.4769645`.

[546] private communication with Meier, K. Helmut-Schmidt-Universität, 2019. Data from Ref. [443]: Computer Simulation and Interpretation of the Transport Coefficients of the Lennard-Jones Model Fluid, Dissertation, University of the Federal Armed Forces Hamburg, 2002.

[547] private communication with Okumura, H. Keio University, 2019. Data from Ref. [509]: Liquid-vapor coexistence curves of several interatomic model potentials, The Journal of Chemical Physics 113 (2000) 9162–9168. doi:`10.1063/1.1320828`.

[548] private communication with Okumura, H. Keio University, 2019. Data from Ref. [510]: Reliable determination of the liquid-vapor critical point by the NVT plus test particle method, Journal of The Physical Society of Japan 70 (2001) 1990–1994. doi:`10.1143/JPSJ.70.1990`.

[549] private communication with Ustinov, E.A. Polytechnicheskaya St. Petersburg, 2019. Data from Ref. [674]: Efficient chemical potential evaluation with kinetic Monte Carlo method and non-uniform external potential: Lennard-Jones fluid, liquid, and solid, The Journal of Chemical Physics 147 (2017) 014105. doi:`10.1063/1.4991324`.

[550] private communication with Wheatley, R.J. University of Nottingham, 2019. Data from Ref. [711]: Calculation of high-order virial coefficients with applications to hard and soft spheres, Physical Review Letters 110 (2013) 200601. doi:`10.1103/PhysRevLett.110.200601`.

[551] S.P. Protsenko, V.G. Baidakov: Binary Lennard-Jones mixtures with highly asymmetric interactions of the components. 1. effect of the energy parameters on phase equilibria and properties of liquid-gas interfaces, Fluid Phase Equilibria 429 (2016) 242–253. doi:`10.1016/j.fluid.2016.09.009`.

[552] S.P. Protsenko, V.G. Baidakov, V.M. Bryukhanov: Binary Lennard-Jones mixtures with highly asymmetric interactions of the components. 2. effect of the particle size on phase equilibria and properties of liquid-gas interfaces, Fluid Phase Equilibria 430 (2016) 67–74. doi:`10.1016/j.fluid.2016.09.022`.

[553] S.E. Quiñones-Cisneros: Phase and critical behavior in type III phase diagrams, Fluid Phase Equilibria 134 (1997) 103–112. doi:`10.1016/S0378-3812(97)00001-0`.

[554] S.E. Quiñones-Cisneros, U.K. Deiters, R.E. Rozas, T. Kraska: New model for the correlation of the surface tension based on friction theory, The Journal of Physical Chemistry B 113 (2009) 3504–3511. doi:`10.1021/jp8073255`.

[555] A. Rahman: Correlations in the motion of atoms in liquid argon, Physical Review 136 (1964) A405–A411. doi:`10.1103/PhysRev.136.A405`.

[556] V. Ramakrishna, M. Patel: Eberhart model & surface tension of binary solutions near their critical solution temperature, Indian Journal of Chemistry 8 (1970) 256–260.

[557] W. Rathjen, J. Straub: Heat Transfer in Boiling, Academic Press, New York, 1977.

[558] O. Redlich, J.N.S. Kwong: On the thermodynamics of solutions. V. an equation of state. fugacities of gaseous solutions., Chemical Reviews 44 (1949) 233–244. doi:`10.1021/cr60137a013`.

[559] F.H. Ree: Analytic representation of thermodynamic data for the Lennard-Jones fluid, The Journal of Chemical Physics 73 (1980) 5401–5403. doi:`10.1063/1.439940`.

[560] P. Rehner, J. Gross: Predictive density gradient theory based on nonlocal density functional theory, Physical Review E 98 (2018) 063312. doi:`10.1103/PhysRevE.98.063312`.

[561] M. Robert, C. Stuart: Intrinsic structure of the critical liquid-gas interface, Physical Review Letters 49 (1982) 1434–1437. doi:`10.1103/PhysRevLett.49.1434`.

[562] D. Roccatano, A. Amadei, M.E.F. Apol, A. Di Nola, H.J.C. Berendsen: Application of the quasi-Gaussian entropy theory to molecular dynamics simulations of Lennard-Jones fluids, The Journal of Chemical Physics 109 (1998) 6358–6363. doi:`10.1063/1.477278`.

[563] A. Rohatgi: Webplotdigitizer, 2019. URL: `https://automeris.io/WebPlotDigitizer`, used december 2019.

[564] C. Romero, B. Giner, M. Haro, H. Artigas, C. Lafuente: Thermophysical study of 1,4-dioxane with cycloalkane mixtures, The Journal of Chemical Thermodynamics 38 (2006) 871–878. doi:`10.1016/j.jct.2005.09.004`.

[565] P. Rosales-Pelaez, I. Sanchez-Burgos, C. Valeriani, C. Vega, E. Sanz: Seeding approach to nucleation in the NVT ensemble: The case of bubble cavitation in overstretched Lennard Jones fluids, Phys. Rev. E 101 (2020) 022611. doi:`10.1103/PhysRevE.101.022611`.

[566] M.N. Rosenbluth, A.W. Rosenbluth: Further results on Monte Carlo equations of state, The Journal of Chemical Physics 22 (1954) 881–884. doi:`10.1063/1.1740207`.

[567] Y. Rosenfeld: Relation between the transport coefficients and the internal entropy of simple systems, Physical Review A 15 (1977) 2545–2549. doi:`10.1103/PhysRevA.15.2545`.

[568] A. Røsjorde, D. Fossmo, D. Bedeaux, S. Kjelstrup, B. Hafskjold: Nonequilibrium molecular dynamics simulations of steady-state heat and mass transport in condensation: I. local equilibrium, Journal of Colloid and Interface Science 232 (2000) 178–185. doi:`10.1006/jcis.2000.7203`.

[569] A. Røsjorde, S. Kjelstrup, D. Bedeaux, B. Hafskjold: Nonequilibrium molecular dynamics simulations of steady-state heat and mass transport in condensation. II. transfer coefficients, Journal of Colloid and Interface Science 240 (2001) 355–364. doi:`10.1006/jcis.2001.7611`.

[570] R. Roth, R. Evans, A. Lang, G. Kahl: Fundamental measure theory for hard-sphere mixtures revisited: the White Bear version, Journal of Physics: Condensed Matter 14 (2002) 12063. doi:`10.1088/0953-8984/14/46/313`.

[571] P.J. Rousseeuw, C. Croux: Alternatives to the median absolute deviation, Journal of The American Statistical Association 88 (1993) 1273–1283. doi:`10.1080/01621459.1993.10476408`.

[572] J.S. Rowlinson, F.L. Swinton: Liquids and Liquid Mixtures, Butterworth, London, 1982.

[573] J.S. Rowlinson, B. Widom: Molecular Theory of Capillarity, Dover Publications, New York, 1982.

[574] A. Rusanov, N. Kochurova, M. Aniskova: Surface tension data of cyclohexane (data taken from Ref. [1]), Vestnik St. Petersburg University 10 (1976) 76–79.

[575] G. Rutkai, A. Köster, G. Guevara-Carrion, T. Janzen, M. Schappals, C.W. Glass, M. Bernreuther, A. Wafai, S. Stephan, M. Kohns, S. Reiser, S. Deublein, M. Horsch, H. Hasse, J. Vrabec: ms2: A molecular simulation tool for thermodynamic properties, release 3.0, Computer Physics Communications 221 (2017) 343–351. doi:`10.1016/j.cpc.2017.07.025`.

[576] G. Rutkai, M. Thol, R. Span, J. Vrabec: How well does the Lennard-Jones potential represent the thermodynamic properties of noble gases?, Molecular Physics 115 (2017) 1104–1121. doi:`10.1080/00268976.2016.1246760`.

[577] B. Saager, J. Fischer: Predictive power of effective intermolecular pair potentials: MD simulation results for methane up to 1000 MPa, Fluid Phase Equilibria 57 (1990) 35–46. doi:`10.1016/0378-3812(90)80011-Y`.

[578] B. Saager, A. Lotfi, M. Bohn, V.N. Nguyen, J. Fischer: Prediction of gas PVT data with effective intermolecular potentials using the Haar-Shenker-Kohler equation and computer simulations, Fluid Phase Equilibria 54 (1990) 237 – 246. doi:`10.1016/0378-3812(90)85082-L`.

[579] A. Saboni, S. Alexandrova, M. Karsheva, C. Gourdon: Mass transfer from a contaminated fluid sphere, AIChE Journal 57 (2011) 1684–1692. doi:`10.1002/aic.12391`.

[580] R.J. Sadus: Molecular simulation of the phase behavior of fluids and fluid mixtures using the synthetic method, The Journal of Chemical Physics 137 (2012) 054507. doi:`10.1063/1.4739853`.

[581] R.J. Sadus: Intermolecular potential-based equations of state from molecular simulation and second virial coefficient properties, The Journal of Physical Chemistry B 122 (2018) 7757–7763. doi:`10.1021/acs.jpcb.8b05725`.

[582] R.J. Sadus, J.M. Prausnitz: Three-body interactions in fluids from molecular simulation: Vapor-liquid phase coexistence of argon, The Journal of Chemical Physics 104 (1996) 4784–4787. doi:`10.1063/1.471172`.

[583] M. Sahimi, B.N. Taylor: Surface tension of binary liquid-vapor mixtures: A comparison of mean-field and scaling theories, The Journal of Chemical Physics 95 (1991) 6749–6761. doi:`10.1063/1.461514`.

[584] K. Saito, Q. Peng, L. Qiao, L. Wang, T. Joutsuka, T. Ishiyama, S. Ye, A. Morita: Theoretical and experimental examination of SFG polarization analysis at acetonitrile-water solution surfaces, Physical Chemistry Chemical Physics 19 (2017) 8941–8961. doi:`10.1039/c6cp08856b`.

[585] E. Salomons, M. Mareschal: Atomistic simulation of liquid-vapour coexistence: Binary mixtures, Journal of Physics: Condensed Matter 3 (1991) 9215–9228. doi:`10.1088/0953-8984/3/46/021`.

[586] E. Salomons, M. Mareschal: Surface tension, adsorption and surface entropy of liquid-vapour systems by atomistic simulation, Journal of Physics: Condensed Matter 3 (1991) 3645–3661. doi:`10.1088/0953-8984/3/20/025`.

[587] I.C. Sanchez: Statistical thermodynamics of bulk and surface properties of polymer mixtures, Journal of Macromolecular Science, Part B 17 (1980) 565–589. doi:`10.1080/00222348008212827`.

[588] E. Sauer, J. Gross: Classical density functional theory for liquid fluid interfaces and confined systems: A functional for the perturbed-chain polar statistical associating fluid theory equation of state, Industrial & Engineering Chemistry Research 56 (2017) 4119. doi:`10.1021/acs.iecr.6b04551`.

[589] E. Schäfer, G. Sadowski, S. Enders: Interfacial tension of binary mixtures exhibiting azeotropic behavior: Measurement and modeling with PCP-SAFT combined with density gradient theory, Fluid Phase Equilibria 362 (2014) 151. doi:`10.1016/j.fluid.2013.09.042`.

[590] M. Schappals, A. Mecklenfeld, L. Kröger, V. Botan, A. Köster, S. Stephan, E.J. Garcia, G. Rutkai, G. Raabe, P. Klein, K. Leonhard, C.W. Glass, J. Lenhard, J. Vrabec, H. Hasse: Round robin study: Molecular simulation of thermodynamic properties from models with internal degrees of freedom, Journal of Chemical Theory and Computation 13 (2017) 4270–4280. doi:`10.1021/acs.jctc.7b00489`.

[591] M.R. Schenk, T. Köddermann, K.N. Kirschner, S. Knauer, D. Reith: Molecular dynamics in the energy sector: Experiment and modeling of the CO2/CH4 mixture, Journal of Chemical & Engineering Data 65 (2019) 1117–1123. doi:`10.1021/acs.jced.9b00503`.

[592] F. Schmitz, P. Virnau, K. Binder: Determination of the origin and magnitude of logarithmic finite-size effects on interfacial tension: Role of interfacial fluctuations and domain breathing, Physical Review Letters 112 (2014) 125701. doi:`10.1103/PhysRevLett.112.125701`.

[593] T. Schnabel, J. Vrabec, H. Hasse: Henry's law constants of methane, nitrogen, oxygen and carbon dioxide in ethanol from 273 to 498 K: Prediction from molecular simulation, Fluid Phase Equilibria 233 (2005) 134–143. doi:`10.1016/j.fluid.2005.04.016`.

[594] T. Schnabel, J. Vrabec, H. Hasse: Unlike Lennard-Jones parameters for vapor-liquid equilibria, Journal of Molecular Liquids 135 (2007) 170–178. doi:`10.1016/j.molliq.2006.12.024`.

[595] P. Schofield: Computer simulation studies of the liquid state, Computer Physics Communications 5 (1973) 17–23. doi:`10.1016/0010-4655(73)90004-0`.

[596] A.J. Schultz, D.A. Kofke: Comprehensive high-precision high-accuracy equation of state and coexistence properties for classical Lennard-Jones crystals and low-temperature fluid phases, The Journal of Chemical Physics 149 (2018) 204508. doi:`10.1063/1.5053714`.

[597] C. Secuianu, V. Feroiu, D. Geana: Phase behavior for carbon dioxide + ethanol system: Experimental measurements and modeling with a cubic equation of state, Journal of Supercritical Fluids 47 (2008) 109–116. doi:`10.1016/j.supflu.2008.08.004`.

[598] S. Senapati, M.L. Berkowitz: Computer simulation study of the interface width of the liquid/liquid interface, Physical Review Letters 87 (2001) 17. doi:`10.1103/physrevlett.87.176101`.

[599] J.V. Sengers, J.M.H.L. Sengers: Thermodynamic behavior of fluids near the critical point, Annual Review of Physical Chemistry 37 (1986) 189–222. doi:`10.1146/annurev.pc.37.100186.001201`.

[600] K.R.S. Shaul, A.J. Schultz, D.A. Kofke: The effect of truncation and shift on virial coefficients of Lennard-Jones potentials, Collection of Czechoslovak Chemical Communications 75 (2010) 447–462. doi:`10.1135/cccc2009113`.

[601] M.S. Shaw: A density of states transformation Monte Carlo method: Thermo-dynamics of the Lennard-Jones fluid, The Journal of Chemical Physics 89 (1988) 2312–2323. doi:`10.1063/1.455074`.

[602] V.K. Shen, R.D. Mountain, J.R. Errington: Comparative study of the effect of tail corrections on surface tension determined by molecular simulation, The Journal of Physical Chemistry B 111 (2007) 6198–6207. doi:`10.1021/jp070374f`.

[603] W. Shi, J. Johnson: Histogram reweighting and finite-size scaling study of the Lennard-Jones fluids, Fluid Phase Equilibria 187 (2001) 171–191. doi:`10.1016/S0378-3812(01)00534-9`.

[604] W. Shi, N.S. Siefert, B.D. Morreale: Molecular simulations of CO_2, H_2, H_2O, and H_2S gas absorption into hydrophobic poly(dimethylsiloxane) (pdms) solvent: Solubility and surface tension, The Journal of Physical Chemistry C 119 (2015) 19253–19265. doi:`10.1021/acs.jpcc.5b05806`.

[605] S.K. Shibata, S.I. Sandler: Critical evaluation of equation of state mixing rules for the prediction of high-pressure phase equilibria, Industrial & Engineering Chemistry Research 28 (1989) 1893–1898. doi:`10.1021/ie00096a024`.

[606] S.K. Shibata, S.I. Sandler: High pressure vapor-liquid equilibria of mixtures of nitrogen, carbon dioxide, and cyclohexane, Journal of Chemical & Engineering Data 34 (1989) 419–424. doi:`10.1021/je00058a014`.

[607] K.S. Shing, K.E. Gubbins, K. Lucas: Henry constants in non-ideal fluid mixtures, Molecular Physics 65 (1988) 1235–1252. doi:`10.1080/00268978800101731`.

[608] M.J. Shultz, C. Schnitzer, D. Simonelli, S. Baldelli: Sum frequency generation spectroscopy of the aqueous interface: Ionic and soluble molecular solutions, International Reviews in Physical Chemistry 19 (2000) 123–153. doi:`10.1080/014423500229882`.

[609] J.M. Simon, D. Bedeaux, S. Kjelstrup, J. Xu, E. Johannessen: Interface film resistivities for heat and mass transfersintegral relations verified by non-equilibrium molecular dynamics, The Journal of Physical Chemistry B 110 (2006) 18528–18536. doi:`10.1021/jp062047y`.

[610] M. Siskova, V. Secova: Surface tension of binary solutions of non-electrolytes. V. measurement of surface tensions of non-electrolyte solutions by means of a modified method of capillary rise, Collect. Czech. Chem. Commun. 35 (1970) 2702–2711. doi:`10.1135/cccc19702702`.

[611] B. Smit: Phase diagrams of Lennard-Jones fluids, The Journal of Chemical Physics 96 (1992) 8639–8640. doi:`10.1063/1.462271`.

[612] B. Smit, D. Frenkel: Calculation of the chemical potential in the Gibbs ensemble, Molecular Physics 68 (1989) 951–958. doi:`10.1080/00268978900102651`.

[613] W.R. Smith, D. Henderson, J.A. Barker: Approximate evaluation of the second-order term in the perturbation theory of fluids, The Journal of Chemical Physics 53 (1970) 508–515. doi:`10.1063/1.1674017`.

[614] G. Soave: Equilibrium constants from a modified Redlich-Kwong equation of state, Chemical Engineering Science 27 (1972) 1197–1203. doi:`10.1016/0009-2509(72)80096-4`.

[615] B. Song, J. Springer: Determination of interfacial tension from the profile of a pendant drop using computer-aided image processing: 1. theoretical, Journal of Colloid and Interface Science 184 (1996) 64–76. doi:`10.1006/jcis.1996.0597`.

[616] Y. Song, E.A. Mason: Statistical-mechanical theory of a new analytical equation of state, The Journal of Chemical Physics 91 (1989) 7840–7853. doi:`10.1063/1.457252`.

[617] J.M.G. Sousa, A.L. Ferreira, M.A. Barroso: Determination of the solid-fluid coexistence of the n-6 Lennard-Jones system from free energy calculations, The Journal of Chemical Physics 136 (2012) 174502. doi:`10.1063/1.4707746`.

[618] G.M. Sowers, S.I. Sandler: Equations of state from generalized perturbation theory: Part II. the Lennard-Jones fluid, Fluid Phase Equilibria 67 (1991) 127–150. doi:`10.1016/0378-3812(91)90052-9`.

[619] R. Span: Multiparameter Equations of State, Springer, Berlin, 2000.

[620] R. Span, W. Wagner: A new equation of state for carbon dioxide covering the fluid region from the triple-point temperature to 1100 K at pressures up to 800 MPa, Journal of Physical and Chemical Reference Data 25 (1996) 1509–1596. doi:`10.1063/1.555991`.

[621] R. Span, W. Wagner: On the extrapolation behavior of empirical equations of state, International Journal of Thermophysics 18 (1997) 1415–1443. doi:`10.1007/BF02575343`.

[622] R. Span, W. Wagner: Equations of state for technical applications. ii. results for nonpolar fluids, International Journal of Thermophysics 24 (2003) 41–109. doi:`10.1023/A:1022310214958`.

[623] R. Span, W. Wagner, E. Lemmon, R.T. Jacobsen: Multiparameter equation of state - recent trends and future challenges, Fluid Phase Equilibria 183-184 (2001) 1.

[624] S. Stephan, S. Becker, K. Langenbach, H. Hasse: Vapor-liquid interfacial properties of the binary system cyclohexane + CO2: Experiment, molecular simulation and density gradient theory, Fluid Phase Equilibria 518 (2020) 112583. doi:`10.1016/j.fluid.2020.112583`.

[625] S. Stephan, U.K. Deiters: Characteristic curves of the Lennard-Jones fluid, submitted (2020).

[626] S. Stephan, M. Dyga, H. Urbassek, H. Hasse: The influence of lubrication and the solid-fluid interaction on thermodynamic properties in a nanoscopic scratching process, Langmuir 35 (2019) 16948–16960. doi:`10.1021/acs.langmuir.9b01033`.

[627] S. Stephan, H. Hasse: Enrichment at vapour-liquid interfaces of mixtures: Establishing a link between nanoscopic and macroscopic properties, International Reviews in Physical Chemistry 39 (2020) 319–349. doi:`10.1080/0144235X.2020.1777705`.

[628] S. Stephan, H. Hasse: Influence of dispersive long-range interactions on properties of vapour-liquid interfaces of binary Lennard-Jones mixtures, Molecular Physics 118 (2020) e1699185. doi:`10.1080/00268976.2019.1699185`.

[629] S. Stephan, H. Hasse: Interfacial properties of binary mixtures of simple fluids and their relation to the phase diagram, Physical Chemistry Chemical Physics 22 (2020) 12544–12564. doi:`10.1039/d0cp01411g`.

[630] S. Stephan, H. Hasse: Molecular interactions at vapor-liquid interfaces: Binary mixtures of simple fluids, Physical Review E 101 (2020) 012802. doi:`10.1103/PhysRevE.101.012802`.

[631] S. Stephan, H. Hasse: unpublished data of binary mixtures of Lennard-Jones + dipolar fluids (2020).

[632] S. Stephan, H. Hasse: unpublished data of vapor-liquid interfacial properties of the binary systems toluene + CO2 and toluene + N2 (2020).

[633] S. Stephan, M. Horsch, J. Vrabec, H. Hasse: MolMod - an open access database of force fields for molecular simulations of fluids, Molecular Simulation 45 (2019) 806–814. doi:`10.1080/08927022.2019.1601191`.

[634] S. Stephan, K. Langenbach, H. Hasse: Enrichment of components at vapour-liquid interfaces: A study by molecular simulation and density gradient theory, Chemical Engineering Transactions 69 (2018) 295–300. doi:`10.3303/CET1869050`.

[635] S. Stephan, K. Langenbach, H. Hasse: Interfacial properties of binary Lennard-Jones mixtures by molecular simulations and density gradient theory, The Journal of Chemical Physics 150 (2019) 174704. doi:`10.1063/1.5093603`.

[636] S. Stephan, M.P. Lautenschlaeger, I.A. Alhafez, M.T. Horsch, H.M. Urbassek, H. Hasse: Molecular dynamics simulation study of mechanical effects of lubrication on a nanoscale contact process, Tribology Letters 66 (2018) 126. doi:`10.1007/s11249-018-1076-0`.

[637] S. Stephan, J. Liu, K. Langenbach, W.G. Chapman, H. Hasse: Vapor-liquid interface of the Lennard-Jones truncated and shifted fluid: Comparison of molecular simulation, density gradient theory, and density functional theory, The Journal of Physical Chemistry C 122 (2018) 24705–24715. doi:`10.1021/acs.jpcc.8b06332`.

[638] S. Stephan, D. Schaefer, K. Langenbach, H. Hasse: Mass transfer through vapor-liquid interfaces: A new molecular dynamics simulation method, submitted (2020).

[639] S. Stephan, J. Staubach, H. Hasse: Review and comparison of equations of state for the Lennard-Jones fluid, submitted (2020).

[640] S. Stephan, M. Thol, J. Vrabec, H. Hasse: Thermophysical properties of the Lennard-Jones fluid: Database and data assessment, J. Chem. Inf. Model. 59 (2019) 4248–4265. doi:`10.1021/acs.jcim.9b00620`.

[641] K. Stöbener, P. Klein, M. Horsch, K. Küfer, H. Hasse: Parametrization of two-center Lennard-Jones plus point-quadrupole force field models by multicriteria optimization, Fluid Phase Equilibria 411 (2016) 33–42. doi:`10.1016/j.fluid.2015.11.028`.

[642] J. Stoll, J. Vrabec, H. Hasse: Comprehensive study of the vapour-liquid equilibria of the pure two-centre Lennard-Jones plus pointdipole fluid, Fluid Phase Equilibria 209 (2003) 29–53. doi:`10.1016/S0378-3812(03)00074-8`.

[643] W.B. Streett, H.J. Raveché, R.D. Mountain: Monte Carlo studies of the fluid-solid phase transition in the Lennard-Jones system, The Journal of Chemical Physics 61 (1974) 1960–1969. doi:`10.1063/1.1682197`.

[644] D.E. Sullivan: Interfacial density profiles of a binary van der Waals fluid, The Journal of Chemical Physics 77 (1982) 2632–2638. doi:`10.1063/1.444137`.

[645] J. Sun, L.T. Zhang: Temperature control algorithms in dual control volume grand canonical molecular dynamics simulations of hydrogen diffusion in palladium, The Journal of Chemical Physics 127 (2007) 164721. doi:`10.1063/1.2794343`.

[646] T. Sun, A.S. Teja: An equation of state for real fluids based on the Lennard-Jones potential, The Journal of Physical Chemistry 100 (1996) 17365–17372. doi:`10.1021/jp9620476`.

[647] S.H. Sung, D. Chandler: Optimized cluster theory, the Lennard-Jones fluid, and the liquid-gas phase transition, Physical Review A 9 (1974) 1688–1697. doi:`10.1103/PhysRevA.9.1688`.

[648] S.K. Suri, V. Ramakrishna: Surface tension of some binary liquid mixtures, The Journal of Physical Chemistry 72 (1968) 3073–3079. doi:`10.1021/j100855a001`.

[649] J. Sýs, A. Malijevský: Equation of state of a Lennard-Jones 12-6 pairwise additive fluid, Collection of Czechoslovak Chemical Communications 45 (1980) 977–983. doi:`10.1135/cccc19800977`.

[650] Y. Tang, B.C.Y. Lu: A study of associating Lennard-Jones chains by a new reference radial distribution function, Fluid Phase Equilibria 171 (2000) 27–44. doi:`10.1016/S0378-3812(00)00346-0`.

[651] P. Tarazona, E. Chacón: Monte Carlo intrinsic surfaces and density profiles for liquid surfaces, Physical Review B 70 (2004) 235407. doi:`10.1103/PhysRevB.70.235407`.

[652] P. Tarazona, E. Chacón, F. Bresme: Intrinsic profiles and the structure of liquid surfaces, Journal of Physics: Condensed Matter 24 (2012) 284123. doi:`10.1088/0953-8984/24/28/284123`.

[653] P. Tarazona, E. Chacón, M. Reinaldo-Falagan, E. Velasco: Layering structures at free liquid surfaces: The Fisher-Widom line and the capillary waves, The Journal of Chemical Physics 117 (2002) 3941–3950. doi:10.1063/1.1495840.

[654] P. Tarazona, E. Chacón, E. Valasco: The Fisher-Widom line for systems with low melting temperature, Molecular Physics 101 (2003) 1595–1603. doi:10.1080/0026897031000068550.

[655] P. Tarazona, M.M. Telo da Gama, R. Evans: Wetting transitions at fluid-fluid interfaces I. the order of the transition, Molecular Physics 49 (1983) 283–300. doi:10.1080/00268978300101161.

[656] P. Tarazona, M.M. Telo da Gama, R. Evans: Wetting transitions at fluid-fluid interfaces II. the thickness of the wetting layer, Molecular Physics 49 (1983) 301–314. doi:10.1080/00268978300101171.

[657] M.J. Tardón, J.M. Garrido, H. Quinteros-Lama, A. Mejía, H. Segura: Molar isopycnicity in heterogeneous binary mixtures, Fluid Phase Equilibria 336 (2012) 84–97. doi:10.1016/j.fluid.2012.07.034.

[658] R. Taylor, R. Krishna: Multicomponent Mass Transfer, John Wiley & Sons, New York, 1993.

[659] P.I.C. Teixeira, B.S. Almeida, M.M. Telo da Gama, J.A. Rueda, R.G. Rubio: Interfacial properties of mixtures of molecular fluids: comparison between theory and experiment; methyl iodide + carbon tetrachloride and acetonitrile + carbon tetrachloride, The Journal of Physical Chemistry 96 (1992) 8488–8497. doi:10.1021/j100200a053.

[660] P.R. ten Wolde, D. Frenkel: Computer simulation study of gas-liquid nucleation in a Lennard-Jones system, The Journal of Chemical Physics 109 (1998) 9901–9918. doi:10.1063/1.477658.

[661] M. Thol, G. Rutkai, A. Köster, R. Lustig, R. Span, J. Vrabec: Equation of state for the Lennard-Jones fluid, Journal of Physical and Chemical Reference Data 45 (2016) 023101. doi:10.1063/1.4945000.

[662] M. Thol, G. Rutkai, R. Span, J. Vrabec, R. Lustig: Equation of state for the Lennard-Jones truncated and shifted model fluid, International Journal of Thermophysics 36 (2015) 25. doi:10.1007/s10765-014-1764-4.

[663] P.A. Thompson, M.O. Robbins: Shear flow near solids: Epitaxial order and flow boundary conditions, Physical Review A 41 (1990) 6830–6837. doi:10.1103/PhysRevA.41.6830.

[664] S.M. Thomson, K.E. Gubbins, J.P. Walton, R.A. Chantry, J.S. Rowlinson: A molecular dynamics study of liquid drops, The Journal of Chemical Physics 81 (1984) 530.

[665] H. Tong, C.M. Crowe: Detection of gross erros in data reconciliation by principal component analysis, AIChE Journal 41 (1995) 1712–1722. doi:10.1002/aic.690410711.

[666] G. Torrie, J. Valleau: Nonphysical sampling distributions in Monte Carlo free-energy estimation: Umbrella sampling, Journal of Computational Physics 23 (1977) 187–199. doi:`10.1016/0021-9991(77)90121-8`.

[667] S. Toxvaerd: Molecular dynamics simulation of prewetting, The Journal of Physical Chemistry C 111 (2007) 15620–15624. doi:`10.1021/jp073665x`.

[668] S. Toxvaerd, E. Praestgaard: Equation of state for a Lennard-Jones fluid, The Journal of Chemical Physics 53 (1970) 2389–2392. doi:`10.1063/1.1674336`.

[669] S. Toxvaerd, J. Stecki: Density profiles at a planar liquid-liquid interface, The Journal of Chemical Physics 102 (1995) 7163–7168. doi:`10.1063/1.469111`.

[670] H.G. Trieschmann: Oberflächenspannung und Solvatation, Zeitschrift für Physikalische Chemie 29 (1935) 328–334.

[671] S. Tripathi, W.G. Chapman: Microstructure of inhomogeneous polyatomic mixtures from a density functional formalism for atomic mixtures, The Journal of Chemical Physics 122 (2005) 094506. doi:`10.1063/1.1853371`.

[672] A. Trokhymchuk, J. Alejandre: Computer simulations of liquid/vapor interface in Lennard-Jones fluids: Some questions and answers, The Journal of Chemical Physics 111 (1999) 8510–8523. doi:`10.1063/1.480192`.

[673] T. Tsuruta, H. Tanaka, T. Masuoka: Condensation/evaporation coefficient and velocity distributions at liquid-vapor interface, International Journal of Heat and Mass Transfer 42 (1999) 4107–4116. doi:`10.1016/S0017-9310(99)00081-2`.

[674] E.A. Ustinov: Efficient chemical potential evaluation with kinetic Monte Carlo method and non-uniform external potential: Lennard-Jones fluid, liquid, and solid, The Journal of Chemical Physics 147 (2017) 014105. doi:`10.1063/1.4991324`.

[675] C. Vega, L.F. Rull, S. Lago: Location of the Fisher-Widom line for systems interacting through short-ranged potentials, Physical Review E 51 (1995) 3146–3155. doi:`10.1103/PhysRevE.51.3146`.

[676] P.J. in 't Veld, A.E. Ismail, G.S. Grest: Application of Ewald summations to long-range dispersion forces, The Journal of Chemical Physics 127 (2007) 144711. doi:`10.1063/1.2770730`.

[677] L. Verlet: Computer experiments on classical fluids. I. thermodynamical properties of Lennard-Jones molecules, Physical Review 159 (1967) 98–103. doi:`10.1103/PhysRev.159.98`.

[678] L. Verlet, D. Levesque: On the theory of classical fluids VI, Physica 36 (1967) 254–268. doi:`10.1016/0031-8914(67)90248-0`.

[679] O. Vilaseca, F. Llovell, J. Yustos, R.M. Marcos, L.F. Vega: Phase equilibria, surface tensions and heat capacities of hydrofluorocarbons and their mixtures including the critical region, The Journal of Supercritical Fluids 55 (2010) 755–768. doi:`10.1016/j.supflu.2010.10.015`.

[680] A. Villares, B. Giner, H. Artigas, C. Lafuente, F.M. Royo: Study of the surface tensions of cyclohexane or methylcyclohexane with some cyclic ethers, Journal of Solution Chemistry 34 (2005) 185–198. doi:`10.1007/s10953-005-2760-x`.

[681] A.I. Vogel: Physical properties and chemical constitution. part III. cyclopentane, cyclohexane, cycloheptane, and some derivatives. the multiplanar structure of the methylcyclohexane ring, Journal of The Chemical Society (1938) 1323–1338. doi:`10.1039/JR9380001323`.

[682] W. Voigt, V. Brendler, K. Marsh, R. Rarey, H. Wanner, M. Gaune-Escard, P. Cloke, T. Vercouter, E. Bastrakov, S. Hagemann: Quality assurance in thermodynamic databases for performance assessment studies in waste disposal, Pure and Applied Chemistry 79 (2007). doi:`10.1351/pac200779050883`.

[683] J. Vrabec, M. Bernreuther, H.J. Bungartz, W.L. Chen, W. Cordes, R. Fingerhut, C.W. Glass, J. Gmehling, R. Hamburger, M. Heilig, M. Heinen, M.T. Horsch, C.M. Hsieh, M. Hülsmann, P. Jäger, P. Klein, S. Knauer, T. Köddermann, A. Köster, K. Langenbach, S.T. Lin, P. Neumann, J. Rarey, D. Reith, G. Rutkai, M. Schappals, M. Schenk, A. Schedemann, M. Schönherr, S. Seckler, S. Stephan, K. Stöbener, N. Tchipev, A. Wafai, S. Werth, H. Hasse: Skasim – skalierbare HPC-software für molekulare simulationen in der chemischen industrie, Chemie Ingenieur Technik 90 (2018) 295–306. doi:`10.1002/cite.201700113`.

[684] J. Vrabec, J. Gross: Vapor-liquid equilibria simulation and an equation of state contribution for dipole-quadrupole interactions, The Journal of Physical Chemistry B 112 (2008) 51–60. doi:`10.1021/jp072619u`.

[685] J. Vrabec, H. Hasse: Grand Equilibrium: Vapour-liquid equilibria by a new molecular simulation method, Molecular Physics 100 (2002) 3375. doi:`10.1080/00268970210153772`.

[686] J. Vrabec, Y. lin Huang, H. Hasse: Molecular models for 267 binary mixtures validated by vapor-liquid equilibria: A systematic approach, Fluid Phase Equilibria 279 (2009) 120–135. doi:`10.1016/j.fluid.2009.02.017`.

[687] J. Vrabec, G.K. Kedia, G. Fuchs, H. Hasse: Comprehensive study of the vapour-liquid coexistence of the truncated and shifted Lennard-Jones fluid including planar and spherical interface properties, Molecular Physics 104 (2006) 1509. doi:`10.1080/00268970600556774`.

[688] J. Vrabec, G.K. Kedia, H. Hasse: Prediction of Joule-Thomson inversion curves for pure fluids and one mixture by molecular simulation, Cryogenics 45 (2005) 253–258. doi:`10.1016/j.cryogenics.2004.10.006`.

[689] J. Vrabec, G.K. Kedia, H. Hasse: Prediction of Joule-Thomson inversion curves for pure fluids and one mixture by molecular simulation, Cryogenics 45 (2005) 253–258. doi:`10.1016/j.cryogenics.2004.10.006`.

[690] J.D. van der Waals: Over de Continuiteit van Den Gas En Vloeistoftoestand. (On the Continuity of the Gas and Liquid State), Ph.D. thesis, Leiden University, 1873.

[691] J.D. van der Waals: Thermodynamische Theorie der Kapillarität unter Voraussetzung stetiger Dichteänderung, Zeitschrift für Physikalische Chemie 13 (1894) 657. doi:`10.1515/zpch-1894-1338`.

[692] T. Wadewitz, J. Winkelmann: Density functional theory: Structure and interfacial properties of binary mixtures, Berichte der Bunsengesellschaft für physikalische Chemie 100 (1996) 1825–1832. doi:`10.1002/bbpc.19961001112`.

[693] T. Wadewitz, J. Winkelmann: Application of density functional perturbation theory to pure fluid liquid-vapor interfaces, The Journal of Chemical Physics 113 (2000) 2447–2455. doi:`10.1063/1.482062`.

[694] D. Walther, B. Platzer, G. Maurer: High-pressure (vapour + liquid) equilibria of (carbon dioxide + methylbenzene or 1,2-dimethylbenzene or 1,3-dimethylbenzene or 1,4-dimethylbenzene) at temperatures between 313 K and 393 K and pressures up to 17.3 MPa, The Journal of Chemical Thermodynamics 24 (1992) 387–399. doi:`10.1016/S0021-9614(05)80157-0`.

[695] J. Walton, D.J. Tildesley, J.S. Rowlinson, J.R. Henderson: The pressure tensor at the planar surface of a liquid, Molecular Physics 48 (1983) 1357–1368. doi:`10.1080/00268978300100971`.

[696] J.Y. Wang, X.J. Zhang, Y.M. Liu, Y.Q. Hu: Interfacial tensions of imidazolium-based ionic liquids with n-alkanes and cyclohexane, Journal of Chemical & Engineering Data 56 (2011) 3734–3737. doi:`10.1021/je200349t`.

[697] V.B. Warshavsky, X.C. Zeng: Fundamental measure density functional theory study of liquid-vapor interface of dipolar and quadrupolar fluids, The Journal of Chemical Physics 139 (2013) 134502. doi:`10.1063/1.4822325`.

[698] H. Watanabe, N. Ito, C.K. Hu: Phase diagram and universality of the Lennard-Jones gas-liquid system, The Journal of Chemical Physics 136 (2012) 204102. doi:`10.1063/1.4720089`.

[699] J.D. Weeks, D. Chandler, H.C. Andersen: Perturbation theory of the thermodynamic properties of simple liquids, The Journal of Chemical Physics 55 (1971) 5422–5423. doi:`10.1063/1.1675700`.

[700] J.D. Weeks, D. Chandler, H.C. Andersen: Role of repulsive forces in determining the equilibrium structure of simple liquids, The Journal of Chemical Physics 54 (1971) 5237–5247. doi:`10.1063/1.1674820`.

[701] J. Werth: Molecular Modeling and Simulation of Vapor-Liquid Interfaces, Ph.D. thesis, Lehrstuhl für Thermodynamik, Technische Universität Kaiserslautern, 2016.

[702] S. Werth, M. Horsch, H. Hasse: Surface tension of the two center Lennard-Jones plus quadrupole model fluid, Fluid Phase Equilibria 392 (2015) 12–18. doi:`10.1016/j.fluid.2015.02.003`.

[703] S. Werth, M. Horsch, H. Hasse: Surface tension of the two center Lennard-Jones plus point dipole fluid, The Journal of Chemical Physics 144 (2016) 054702. doi:`10.1063/1.4940966`.

[704] S. Werth, M. Horsch, H. Hasse: Molecular simulation of the surface tension of 33 multi-site models for real fluids, Journal of Molecular Liquids 235 (2017) 126–134. doi:`10.1016/j.molliq.2016.12.062`.

[705] S. Werth, M. Kohns, K. Langenbach, M. Heilig, M. Horsch, H. Hasse: Interfacial and bulk properties of vapor-liquid equilibria in the system toluene+hydrogen chloride+carbon dioxide by molecular simulation and density gradient theory + PC-SAFT, Fluid Phase Equilibria 427 (2016) 219. doi:`10.1016/j.fluid.2016.07.016`.

[706] S. Werth, S.V. Lishchuk, M. Horsch, H. Hasse: The influence of the liquid slab thickness on the planar vapor-liquid interfacial tension, Physica A 392 (2013) 2359. doi:`10.1016/j.physa.2013.01.048`.

[707] S. Werth, G. Rutkai, J. Vrabec, M. Horsch, H. Hasse: Long-range correction for multi-site Lennard-Jones models and planar interfaces, Molecular Physics 112 (2014) 2227–2234. doi:`10.1080/00268976.2013.861086`.

[708] S. Werth, S. Stephan, M.T. Horsch, H. Hasse: Corrigendum to 'molecular simulation of the surface tension of 33 multi-site models for real fluids' [J. Mol. Liq. 235 (2017) 126-134], Journal of Molecular Liquids 286 (2019) 110877. doi:`10.1016/j.molliq.2019.110877`.

[709] S. Werth, K. Stöbener, M. Horsch, H. Hasse: Simultaneous description of bulk and interfacial properties of fluids by the Mie potential, Molecular Physics 115 (2017) 1017–1030. doi:`10.1080/00268976.2016.1206218`.

[710] T. van Westen, J. Gross: A critical evaluation of perturbation theories by Monte Carlo simulation of the first four perturbation terms in a Helmholtz energy expansion for the Lennard-Jones fluid, The Journal of Chemical Physics 147 (2017) 014503. doi:`10.1063/1.4991008`.

[711] R.J. Wheatley: Calculation of high-order virial coefficients with applications to hard and soft spheres, Physical Review Letters 110 (2013) 200601. doi:`10.1103/PhysRevLett.110.200601`.

[712] B. Widom: Some topics in the theory of fluids, The Journal of Chemical Physics 39 (1963) 2808. doi:`10.1063/1.1734110`.

[713] A.P. Willard, D. Chandler: Instantaneous liquid interfaces, The Journal of Physical Chemistry B 114 (2010) 1954–1958. doi:`10.1021/jp909219k`.

[714] J. Winkelmann: The liquid-vapour interface of pure fluids and mixtures: Application of computer simulation and density functional theory, Journal of Physics: Condensed Matter 13 (2001) 4739.

[715] K.W. Won, J.M. Prausnitz: Rectilinear diameter for saturated densities of binary mixtures, AIChE Journal 20 (1974) 200–202. doi:`10.1002/aic.690200136`.

[716] W.W. Wood: Physics of Simple Liquids, North Holland Publishing Company, Amsterdam, 1968.

[717] W.W. Wood, F.R. Parker: Monte Carlo equation of state of molecules interacting with the Lennard-Jones potential. I. A supercritical isotherm at about twice the critical temperature, The Journal of Chemical Physics 27 (1957) 720–733. doi:`10.1063/1.1743822`.

[718] E.H.M. Wright, B.A. Akhtar: Equilibrium studies of soluble films of short-chain monocarboxylic fatty acids at the organoliquid-vapour phase boundary, Trans. Faraday Soc. 66 (1970) 990–1003. doi:`10.1039/TF9706600990`.

[719] E.H.M. Wright, B.A. Akhtar: Soluble surface films of short-chain monocarboxylic acids on organic and aqueous substrates, J. Chem. Soc. B (1970) 151–157. doi:`10.1039/J29700000151`.

[720] A.J.M. Yang, P.D. Fleming, J.H. Gibbs: Molecular theory of surface tension, The Journal of Chemical Physics 64 (1976) 3732–3747. doi:`10.1063/1.432687`.

[721] Z. Yang, M. Li, B. Peng, M. Lin, Z. Dong: Dispersion property of CO2 in oil. 1. volume expansion of CO2 + alkane at near critical and supercritical condition of CO2, Journal of Chemical & Engineering Data 57 (2012) 882–889. doi:`10.1021/je201114g`.

[722] Z. Yang, M. Li, B. Peng, M. Lin, Z. Dong, Y. Ling: Interfacial tension of CO2 and organic liquid under high pressure and temperature, Chinese Journal of Chemical Engineering 22 (2014) 1302–1306. doi:`10.1016/j.cjche.2014.09.042`.

[723] J. Yao, R. Greenkorn, K. Chao: Monte Carlo simulation of the grand canonical ensemble, Molecular Physics 46 (1982) 587–594. doi:`10.1080/00268978200101411`.

[724] M. Yarrison, W.G. Chapman: A systematic study of methanol+n-alkane vapor-liquid and liquid-liquid equilibria using the CK-SAFT and PC-SAFT equations of state, Fluid Phase Equilibria 226 (2004) 195–205. doi:`10.1016/j.fluid.2004.09.024`.

[725] L.V. Yelash, T. Kraska: Volume-translated equations of state: Empirical approach and physical relevance, AIChE Journal 49 (2003) 1569–1579. doi:`10.1002/aic.690490620`.

[726] T.M. Yigzawe: Molecular Dynamics Simulation of the Thermodynamic Properties of Water and Atomistic Fluids, Dissertation, Swinburne University of Technology, Melbourne, 2012.

[727] T.M. Yigzawe, R.J. Sadus: Intermolecular interactions and the thermodynamic properties of supercritical fluids, The Journal of Chemical Physics 138 (2013) 194502. doi:`10.1063/1.4803855`.

[728] H.A. Zambrano, J.H. Walther, R.L. Jaffe: Molecular dynamics simulations of water on a hydropholic silicia surface at high air pressures, Journal of Molecular Liquids 198 (2014) 107–113. doi:`10.1016/j.molliq.2014.06.003`.

[729] X.C. Zeng, D.W. Oxtoby: Binary homogeneous nucleation theory for the gas-liquid transition: A nonclassical approach, The Journal of Chemical Physics 95 (1991) 5940–5947. doi:`10.1063/1.461615`.

[730] Z. Zhang: Parameter estimation techniques: a tutorial with application to conic fitting, Image and Vision Computing 15 (1997) 59–76. doi:`10.1016/S0262-8856(96)01112-2`.

[731] J.A. Zollweg, G.W. Mulholland: On the law of the rectilinear diameter, The Journal of Chemical Physics 57 (1972) 1021–1025. doi:`10.1063/1.1678352`.

[732] R.A. Zubillaga, A. Labastida, B. Cruz, J.C. Martinez, E. Sanchez, J. Alejandre: Surface tension of organic liquids using the OPLS/AA force field, Journal of Chemical Theory and Computation 9 (2013) 1611–1615. doi:`10.1021/ct300976t`.

[733] I. Zvereva, N. Smirnova: Dampf-Flüssig-Gleichgewicht und Oberflächenspannung in binären Dicyclohexyl- und Cyclohexylbenzolhaltigen-Systemen, Oniitekhim 2109 (1978) 1–11.

Appendix

A Additional Data

A.1 Simulation Results for LJTS Mixtures A - F

This Appendix contains the following points:

- MD density profile plots for the investigated LJTS mixtures A - F, cf. Fig. A.1 and A.2

- numeric values for the computed phase equilibria (Table A.1) and interfacial properties (Table A.2) for both MD and DGT for the LJTS mixtures A - F

- Henry's law constant data for the LJTS mixture D, E, and F, cf. Table A.3

Density Profiles from Molecular Simulations
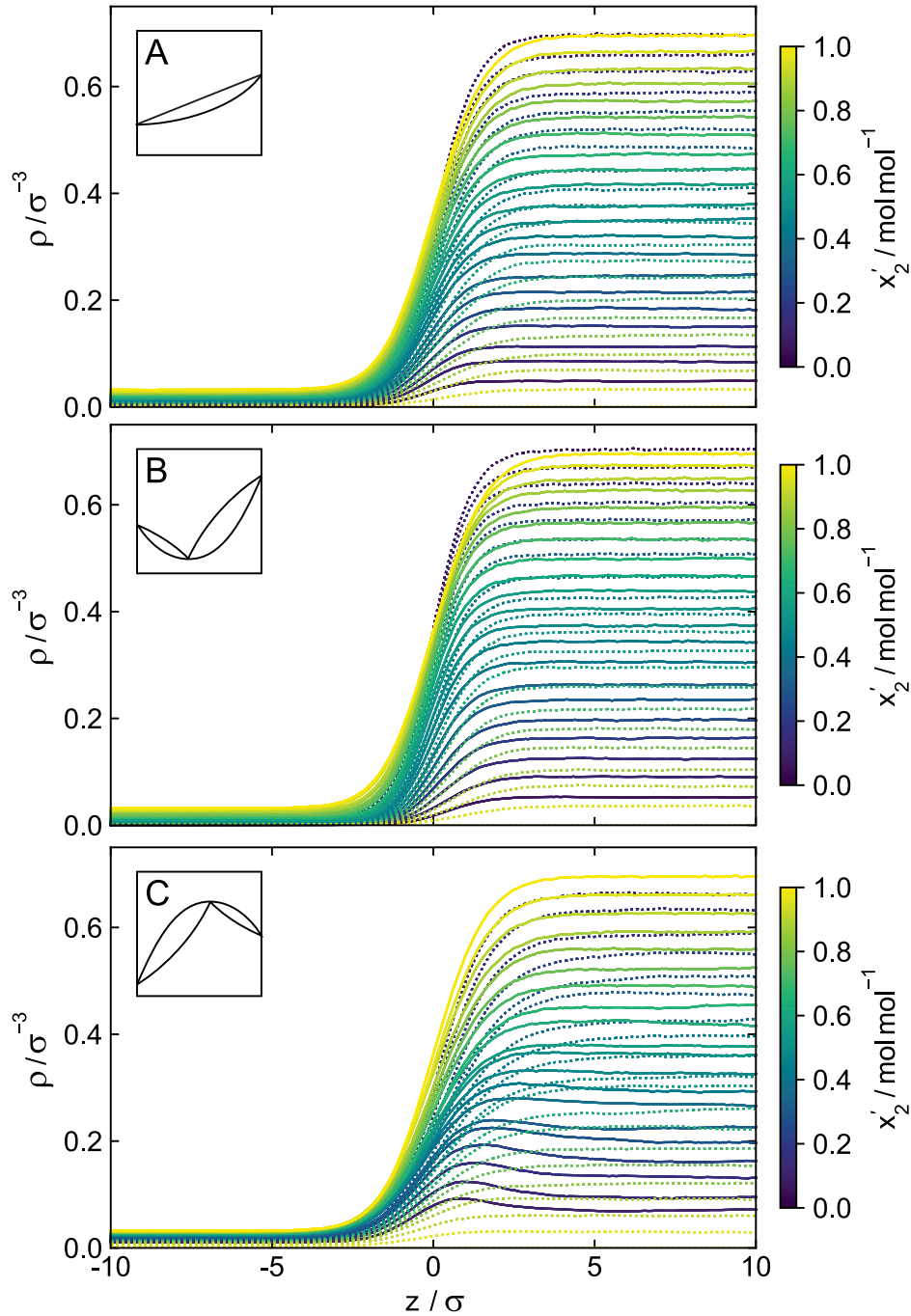
Figure A.1: Density profiles of the binary LJTS mixture A, B, and C as a function of the coordinate z normal to the interface at $T = 0.77\,\varepsilon k_{\mathrm{B}}^{-1}$. Results from MD. Dashed lines: high-boiling component 1, solid lines: low-boiling component 2. The color indicates the liquid phase composition.
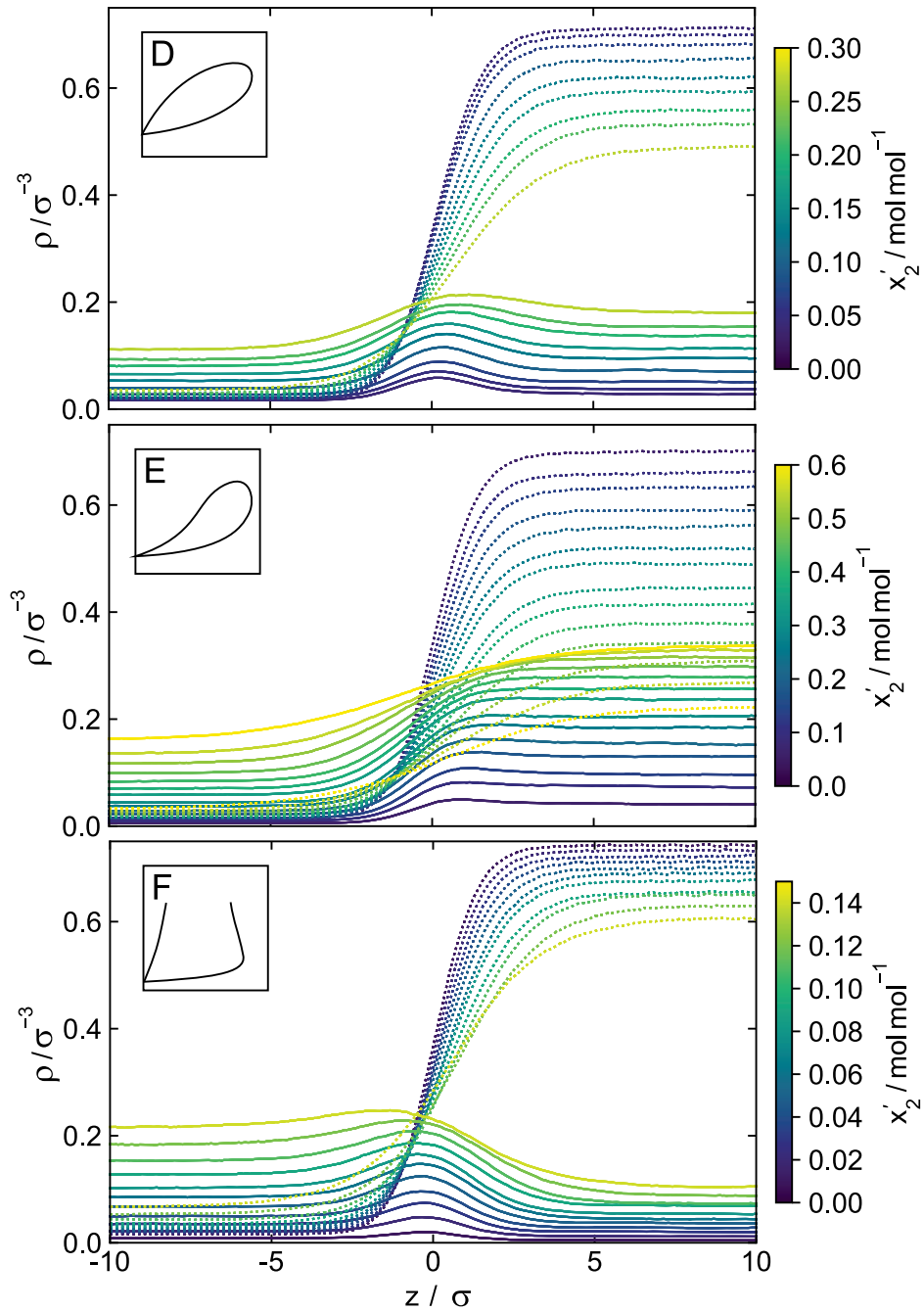
Figure A.2: Density profiles of the binary LJTS mixture D, E, and F as a function
of the coordinate z normal to the interface at $T = 0.77\,\varepsilon k_{\mathrm{B}}^{-1}$. Results
from MD. Dashed lines: high-boiling component 1, solid lines: low-boiling
component 2. The color indicates the liquid phase composition.

Tables of Numeric Values from the MD and DGT+PeTS Results

The numerical results from MD and the PeTS EOS for the vapor-liquid equilibrium of the studied mixtures are summarized in Table A.1. The numerical results for the interfacial properties are summarized in Table A.2.

Table A.1: MD and PeTS EOS results for the vapor-liquid equilibrium of the binary LJTS mixtures A - F for the temperature $T = 0.77 \, \varepsilon k_{\mathrm{B}}^{-1}$. The number in the parentheses indicates the statistical uncertainty in the last decimal digit.

$x_2' / \mathrm{mol \, mol^{-1}}$	$p \, / \, \varepsilon\sigma^{-3}$		$x_2'' \, / \, \mathrm{mol \, mol^{-1}}$		$\rho' \, / \, \sigma^{-3}$		$\rho'' \, / \, \sigma^{-3}$	
	MD	EOS	MD	EOS	MD	EOS	MD	EOS
LJTS Mixture A ($\varepsilon_2/\varepsilon_1 = 0.9$ and $\xi_{12} = 1$)								
0.000	0.0105(2)	0.0104	0.000	0.000	0.7486(4)	0.7480	0.015(2)	0.0150
0.064(2)	0.0110(3)	0.0110	0.110(12)	0.1102	0.7456(7)	0.7451	0.016(7)	0.0160
0.110(1)	0.0116(2)	0.0114	0.191(15)	0.1812	0.7435(8)	0.7430	0.017(9)	0.0167
0.154(2)	0.0119(3)	0.0118	0.257(13)	0.2450	0.7412(10)	0.7410	0.018(9)	0.0174
0.202(2)	0.0124(2)	0.0123	0.313(12)	0.3111	0.7391(9)	0.7387	0.018(9)	0.0181
0.246(2)	0.0129(4)	0.0127	0.366(18)	0.3662	0.7370(9)	0.7366	0.019(11)	0.0188
0.296(2)	0.0134(4)	0.0132	0.424(15)	0.4263	0.7346(9)	0.7342	0.020(11)	0.0196
0.334(1)	0.0137(3)	0.0136	0.466(18)	0.4691	0.7327(10)	0.7323	0.020(11)	0.0202
0.392(2)	0.0143(4)	0.0141	0.532(11)	0.5303	0.7297(10)	0.7294	0.021(10)	0.0211
0.436(1)	0.0146(3)	0.0145	0.573(11)	0.5742	0.7275(10)	0.7271	0.022(10)	0.0218
0.484(2)	0.0150(4)	0.0150	0.618(11)	0.6199	0.7249(11)	0.7247	0.023(11)	0.0226
0.527(2)	0.0156(4)	0.0154	0.653(12)	0.6584	0.7228(11)	0.7224	0.024(13)	0.0233
0.574(2)	0.0158(3)	0.0159	0.694(9)	0.6985	0.7202(11)	0.7199	0.024(12)	0.0241
0.617(2)	0.0163(4)	0.0163	0.726(14)	0.7345	0.7178(10)	0.7176	0.025(12)	0.0248
0.662(1)	0.0168(2)	0.0167	0.769(10)	0.7700	0.7154(10)	0.7151	0.026(10)	0.0256
0.714(2)	0.0173(3)	0.0172	0.813(6)	0.8097	0.7125(11)	0.7122	0.027(10)	0.0265
0.764(1)	0.0179(3)	0.0177	0.846(7)	0.8457	0.7096(11)	0.7093	0.028(9)	0.0273
0.808(2)	0.0183(4)	0.0181	0.881(8)	0.8761	0.7072(10)	0.7068	0.028(8)	0.0281
0.863(1)	0.0188(3)	0.0187	0.910(6)	0.9133	0.7039(12)	0.7035	0.029(9)	0.0291
0.904(1)	0.0192(2)	0.0191	0.939(5)	0.9404	0.7012(15)	0.7010	0.030(7)	0.0298
0.952(1)	0.0197(3)	0.0196	0.973(4)	0.9706	0.6985(10)	0.6981	0.031(6)	0.0307
1.000	0.0203(3)	0.0201	1.000	1.000	0.6955(9)	0.6951	0.032(3)	0.0316
LJTS Mixture B ($\varepsilon_2/\varepsilon_1 = 0.9$ and $\xi_{12} = 1.2$)								
0.000	0.0105(2)	0.0104	0.0000	0.0000	0.7486(4)	0.7480	0.015(2)	0.0150
0.069(1)	0.0097(2)	0.0097	0.019(4)	0.0184	0.756(6)	0.7564	0.0139(6)	0.0139
0.119(1)	0.0092(2)	0.0091	0.041(6)	0.0409	0.761(8)	0.7613	0.0132(6)	0.0130
0.163(1)	0.0087(2)	0.0086	0.066(7)	0.0696	0.764(7)	0.7647	0.0124(6)	0.0123
0.212(1)	0.0082(2)	0.0081	0.112(11)	0.1151	0.767(8)	0.7678	0.0116(6)	0.0115
0.256(1)	0.0079(2)	0.0077	0.171(13)	0.1682	0.769(8)	0.7698	0.0112(6)	0.0110
0.305(1)	0.0075(2)	0.0074	0.251(11)	0.2448	0.770(9)	0.7713	0.0106(7)	0.0105
0.343(1)	0.0073(2)	0.0073	0.304(11)	0.3139	0.771(8)	0.7720	0.0103(6)	0.0103
0.399(1)	0.0073(2)	0.0073	0.435(14)	0.4284	0.771(10)	0.7722	0.0103(7)	0.0103
0.442(1)	0.0075(2)	0.0075	0.525(23)	0.5223	0.770(9)	0.7716	0.0105(7)	0.0106
0.486(1)	0.0079(2)	0.0078	0.611(18)	0.6141	0.769(9)	0.7705	0.0111(7)	0.0111
0.528(1)	0.0085(2)	0.0083	0.697(19)	0.6944	0.767(8)	0.7688	0.0120(7)	0.0118
0.572(1)	0.0091(2)	0.0090	0.768(13)	0.7678	0.765(8)	0.7664	0.0129(7)	0.0128
0.614(1)	0.0099(3)	0.0098	0.828(9)	0.8247	0.762(8)	0.7636	0.0142(7)	0.0140
0.659(1)	0.0108(2)	0.0108	0.879(9)	0.8740	0.758(8)	0.7597	0.0156(8)	0.0155
0.712(2)	0.0122(3)	0.0121	0.914(8)	0.9170	0.753(8)	0.7541	0.0178(8)	0.0176
0.759(1)	0.0133(2)	0.0134	0.942(7)	0.9446	0.747(8)	0.7481	0.0196(8)	0.0197

$x_2'/\text{mol mol}^{-1}$	$p \ / \ \varepsilon\sigma^{-3}$		$x_2'' \ / \ \text{mol mol}^{-1}$		$\rho' \ / \ \sigma^{-3}$		$\rho'' \ / \ \sigma^{-3}$	
	MD	EOS	MD	EOS	MD	EOS	MD	EOS
0.804(1)	0.0148(3)	0.0147	0.961(6)	0.9635	0.740(7)	0.7414	0.0221(9)	0.0219
0.858(1)	0.0164(2)	0.0163	0.980(2)	0.9795	0.730(7)	0.7316	0.0247(8)	0.0246
0.900(1)	0.0177(1)	0.0174	0.988(3)	0.9879	0.722(6)	0.7228	0.0272(9)	0.0267
0.949(1)	0.0189(3)	0.0188	0.994(1)	0.9950	0.710(5)	0.7104	0.0294(9)	0.0292
1.000	0.0203(3)	0.0201	1.000	1.0000	0.695(3)	0.6951	0.0320(9)	0.0316
LJTS Mixture C ($\varepsilon_2/\varepsilon_1$ = 0.9 and ξ_{12} = 0.85)								
0.000	0.0105(2)	0.0104	0.000	0.000	0.7486(4)	0.7480	0.015(2)	0.0150
0.096(1)	0.0174(3)	0.0178	0.414(12)	0.4216	0.733(8)	0.7315	0.0259(1)	0.0272
0.136(2)	0.0189(3)	0.0197	0.465(11)	0.4832	0.727(13)	0.7247	0.029(1)	0.0306
0.183(3)	0.0204(4)	0.0212	0.512(9)	0.5276	0.720(13)	0.7170	0.032(1)	0.0335
0.226(2)	0.0213(3)	0.0222	0.541(10)	0.5551	0.714(17)	0.7102	0.034(1)	0.0355
0.276(3)	0.0221(3)	0.0230	0.573(12)	0.5771	0.707(18)	0.7026	0.035(1)	0.0371
0.316(4)	0.0224(3)	0.0235	0.577(10)	0.5901	0.701(18)	0.6968	0.036(2)	0.0381
0.377(5)	0.0231(5)	0.0239	0.599(11)	0.6051	0.694(25)	0.6889	0.038(3)	0.0390
0.425(5)	0.0234(2)	0.0242	0.612(11)	0.6150	0.690(23)	0.6834	0.038(1)	0.0396
0.473(4)	0.0238(3)	0.0244	0.629(12)	0.6238	0.684(22)	0.6789	0.041(9)	0.0400
0.520(5)	0.0241(2)	0.0245	0.643(9)	0.6327	0.682(19)	0.6752	0.039(2)	0.0403
0.572(5)	0.0241(4)	0.0247	0.651(15)	0.6435	0.680(25)	0.6724	0.039(1)	0.0406
0.614(3)	0.0241(6)	0.0248	0.664(11)	0.6535	0.674(24)	0.6710	0.045(20)	0.0408
0.668(2)	0.0243(3)	0.0248	0.676(9)	0.6689	0.670(17)	0.6704	0.040(2)	0.0409
0.722(4)	0.0242(12)	0.0247	0.708(9)	0.6888	0.672(25)	0.6713	0.047(25)	0.0408
0.772(2)	0.0238(4)	0.0246	0.730(9)	0.7124	0.678(12)	0.6733	0.039(1)	0.0404
0.816(2)	0.0238(17)	0.0243	0.762(9)	0.7392	0.667(45)	0.6759	0.053(22)	0.0398
0.873(2)	0.0236(4)	0.0236	0.803(6)	0.7870	0.684(11)	0.6806	0.038(1)	0.0384
0.912(1)	0.0228(3)	0.0229	0.844(6)	0.8311	0.686(8)	0.6845	0.037(2)	0.0370
0.956(1)	0.0217(3)	0.0217	0.915(10)	0.9009	0.691(6)	0.6896	0.035(1)	0.0347
1.000	0.0203(3)	0.0201	1.000	1.000	0.696(3)	0.6951	0.032(1)	0.0316
LJTS Mixture D ($\varepsilon_2/\varepsilon_1$ = 0.5 and ξ_{12} = 1)								
0.000	0.0105(2)	0.0104	0.0000	0.0000	0.7486(4)	0.7480	0.015(2)	0.0150
0.038(1)	0.0225(3)	0.0215	0.490(12)	0.4750	0.740(6)	0.7403	0.034(1)	0.03209
0.050(1)	0.0256(3)	0.0247	0.537(10)	0.5320	0.737(6)	0.7380	0.039(1)	0.03726
0.071(1)	0.0303(3)	0.0308	0.593(9)	0.6062	0.731(8)	0.7333	0.046(1)	0.04729
0.099(2)	0.0380(4)	0.0382	0.654(6)	0.6642	0.724(10)	0.7272	0.060(2)	0.06039
0.131(3)	0.0464(6)	0.0466	0.702(7)	0.7055	0.715(10)	0.7196	0.076(2)	0.07628
0.162(3)	0.0537(6)	0.0545	0.724(8)	0.7310	0.706(10)	0.7118	0.090(2)	0.09261
0.196(5)	0.0619(6)	0.0627	0.747(10)	0.7483	0.696(13)	0.7029	0.108(3)	0.11104
0.224(3)	0.0681(5)	0.0692	0.751(5)	0.7574	0.686(13)	0.6950	0.124(3)	0.12718
0.271(5)	0.0769(6)	0.0799	0.758(7)	0.7651	0.669(13)	0.6806	0.147(3)	0.15682
LJTS Mixture E ($\varepsilon_2/\varepsilon_1$ = 0.5 and ξ_{12} = 1.2)								
0.000	0.0105(2)	0.0104	0.0000	0.0000	0.7486(4)	0.7480	0.015(2)	0.0150
0.056(1)	0.0142(4)	0.0133	0.276(13)	0.2409	0.741(6)	0.7427	0.021(1)	0.0196
0.098(2)	0.0171(2)	0.0161	0.402(15)	0.3809	0.735(8)	0.7380	0.026(1)	0.0240
0.136(2)	0.0205(3)	0.0191	0.499(10)	0.4832	0.728(9)	0.7333	0.031(1)	0.0287
0.179(1)	0.0248(3)	0.0230	0.583(10)	0.5739	0.721(7)	0.7274	0.038(1)	0.0350
0.217(3)	0.0286(6)	0.0270	0.649(14)	0.6378	0.713(9)	0.7214	0.045(2)	0.0417
0.262(2)	0.0339(4)	0.0324	0.695(9)	0.6975	0.704(9)	0.7135	0.054(2)	0.0511
0.295(2)	0.0378(6)	0.0369	0.726(11)	0.7328	0.695(8)	0.7068	0.061(2)	0.0593
0.345(2)	0.0458(4)	0.0443	0.767(7)	0.7728	0.682(10)	0.6959	0.077(2)	0.0734
0.383(3)	0.0520(7)	0.0508	0.792(8)	0.7966	0.671(8)	0.6860	0.089(2)	0.0865
0.425(3)	0.0586(8)	0.0585	0.802(6)	0.8160	0.657(9)	0.6739	0.104(3)	0.1032
0.464(4)	0.0656(8)	0.0662	0.819(8)	0.8292	0.642(8)	0.6610	0.121(3)	0.1218
0.505(3)	0.0736(7)	0.0748	0.828(5)	0.8382	0.624(8)	0.6456	0.142(3)	0.1448
0.551(10)	0.0806(15)	0.0851	0.827(6)	0.8426	0.596(11)	0.6250	0.165(4)	0.1768

$x_2'/\text{mol mol}^{-1}$	$p\ /\ \varepsilon\sigma^{-3}$		$x_2''\ /\ \text{mol mol}^{-1}$		$\rho'\ /\ \sigma^{-3}$		$\rho''\ /\ \sigma^{-3}$	
	MD	EOS	MD	EOS	MD	EOS	MD	EOS
0.598(6)	0.0894(10)	0.0961	0.830(8)	0.8404	0.564(10)	0.5996	0.196(5)	0.2180
LJTS Mixture F ($\varepsilon_2/\varepsilon_1 = 0.5$ and $\xi_{12} = 0.85$)								
0.000	0.0105(2)	0.0104	0.0000	0.0000	0.7486(4)	0.7480	0.015(2)	0.0150
0.006(1)	0.0169(3)	0.0171	0.341(11)	0.3543	0.747(4)	0.7468	0.024(1)	0.0248
0.016(1)	0.0264(4)	0.0278	0.547(5)	0.5684	0.745(5)	0.7449	0.039(2)	0.0411
0.027(1)	0.0362(2)	0.0389	0.642(10)	0.6657	0.742(6)	0.7429	0.055(2)	0.0595
0.037(1)	0.0458(5)	0.0506	0.699(6)	0.7188	0.740(8)	0.7409	0.071(2)	0.0802
0.049(2)	0.0573(5)	0.0637	0.737(9)	0.7521	0.737(8)	0.7387	0.092(2)	0.1056
0.061(2)	0.0681(5)	0.0776	0.760(8)	0.7714	0.734(8)	0.7365	0.114(3)	0.1359
0.077(2)	0.0772(4)	0.0972	0.768(7)	0.7821	0.729(9)	0.7338	0.134(3)	0.1836
0.093(2)	0.0901(3)	0.1179	0.782(6)	0.7812	0.725(11)	0.7316	0.164(3)	0.2388
0.110(6)	0.1025(10)	0.1452	0.773(8)	0.7710	0.720(15)	0.7298	0.198(4)	0.3095
0.123(4)	0.1168(7)	0.1684	0.778(6)	0.7597	0.718(14)	0.7290	0.236(5)	0.3613
0.140(5)	0.1316(10)	0.2048	0.754(13)	0.7421	0.713(19)	0.7289	0.287(7)	0.4252

Table A.2: MD and DGT+PeTS EOS results for the vapor-liquid interfacial properties of the binary LJTS mixtures A - F for the temperature $T = 0.77\,\varepsilon k_\text{B}^{-1}$. The number in the parentheses indicates the statistical uncertainty in the last decimal digit.

$x_2'/\text{mol mol}^{-1}$	$\gamma\ /\ \varepsilon\sigma^{-2}$		$\Gamma_2^{(1)}\ /\ \sigma^{-2}$		E_2		$L_{10}^{90}\ /\ \sigma$	
	MD	DGT	MD	DGT	MD	DGT	MD	DGT
LJTS Mixture A ($\varepsilon_2/\varepsilon_1 = 0.9$ and $\xi_{12} = 1$)								
0.000	0.446(18)	0.4566	-	-	-	-	2.68(6)	2.33
0.064(2)	0.439(14)	0.4432	0.027(26)	0.0173	1.09(5)	1.00	2.72(4)	2.36
0.110(1)	0.423(16)	0.4339	0.056(20)	0.0290	1.06(2)	1.00	2.75(6)	2.38
0.154(2)	0.417(18)	0.4251	0.022(32)	0.0401	1.03(2)	1.00	2.76(4)	2.40
0.202(2)	0.410(13)	0.4154	0.065(47)	0.0519	1.03(2)	1.00	2.81(6)	2.42
0.246(2)	0.405(16)	0.4070	0.102(56)	0.0621	1.04(2)	1.00	2.88(8)	2.44
0.296(2)	0.393(15)	0.3973	0.007(57)	0.0737	1.01(2)	1.00	2.86(5)	2.46
0.334(1)	0.385(15)	0.3902	0.118(61)	0.0821	1.02(1)	1.00	2.90(7)	2.48
0.392(2)	0.376(11)	0.3794	0.100(62)	0.0945	1.02(1)	1.00	2.91(5)	2.52
0.436(1)	0.369(14)	0.3714	0.129(88)	0.1036	1.02(1)	1.00	2.96(8)	2.54
0.484(2)	0.361(16)	0.3627	0.096(85)	0.1133	1.02(1)	1.00	2.99(6)	2.56
0.527(2)	0.350(17)	0.3552	-0.018(18)	0.1216	1.01(2)	1.00	3.00(7)	2.58
0.574(2)	0.343(20)	0.3470	0.203(15)	0.1304	1.02(1)	1.00	3.08(7)	2.60
0.617(2)	0.327(15)	0.3395	0.211(12)	0.1384	1.02(1)	1.00	3.11(7)	2.62
0.662(1)	0.323(17)	0.3319	0.123(87)	0.1464	1.01(1)	1.00	3.12(7)	2.66
0.714(2)	0.317(18)	0.3230	0.177(13)	0.1553	1.01(1)	1.00	3.17(7)	2.66
0.764(1)	0.319(14)	0.3148	0.198(18)	0.1635	1.012(4)	1.00	3.22(11)	2.70
0.808(2)	0.302(14)	0.3077	0.316(15)	0.1704	1.011(4)	1.00	3.23(7)	2.72
0.863(1)	0.292(12)	0.2988	-0.099(14)	0.1789	1.007(4)	1.00	3.28(7)	2.74
0.904(1)	0.288(14)	0.2921	0.038(22)	0.1850	1.009(4)	1.00	3.28(7)	2.78
0.952(1)	0.283(15)	0.2846	0.452(37)	0.1918	1.008(1)	1.00	3.36(10)	2.80
1.000	0.273(18)	0.2920	-	-	-	-	3.38(6)	2.88
LJTS Mixture B ($\varepsilon_2/\varepsilon_1 = 0.9$ and $\xi_{12} = 1.2$)								
0.0000	0.446(18)	0.4566	-	-	-	-	2.68(6)	2.33
0.069(1)	0.474(16)	0.4792	-0.018(30)	-0.0224	1.08(5)	1.00	2.62(4)	2.26
0.119(1)	0.498(17)	0.4947	-0.044(42)	-0.0309	1.03(2)	1.00	2.56(5)	2.22
0.163(1)	0.523(21)	0.5069	-0.043(25)	-0.0336	1.04(1)	1.00	2.52(7)	2.18

$x'_2/\mathrm{mol\,mol^{-1}}$	$\gamma \;/\; \varepsilon\sigma^{-2}$		$\Gamma_2^{(1)} \;/\; \sigma^{-2}$		E_2		$L_{10}^{90} \;/\; \sigma$	
	MD	DGT	MD	DGT	MD	DGT	MD	DGT
0.212(1)	0.529(20)	0.5185	-0.044(44)	-0.0317	1.03(1)	1.00	2.49(8)	2.14
0.256(1)	0.527(18)	0.5262	-0.044(45)	-0.0260	1.02(1)	1.00	2.47(6)	2.10
0.305(1)	0.548(17)	0.5318	-0.046(46)	-0.0154	1.02(1)	1.00	2.42(5)	2.08
0.343(1)	0.545(17)	0.5337	-0.030(45)	-0.0044	1.02(1)	1.00	2.45(4)	2.08
0.399(1)	0.542(18)	0.5323	-0.03(7)	0.0164	1.01(1)	1.00	2.44(5)	2.08
0.442(1)	0.550(22)	0.5278	0.11(8)	0.0364	1.02(1)	1.00	2.43(5)	2.08
0.486(1)	0.547(20)	0.5202	0.07(7)	0.0599	1.01(1)	1.00	2.43(4)	2.10
0.528(1)	0.525(15)	0.5101	0.09(9)	0.0856	1.01(1)	1.00	2.50(6)	2.12
0.572(1)	0.515(21)	0.4965	0.14(8)	0.1163	1.02(1)	1.00	2.53(5)	2.14
0.614(1)	0.493(17)	0.4813	0.12(7)	0.1486	1.011(4)	1.00	2.60(5)	2.16
0.659(1)	0.476(16)	0.4622	0.18(8)	0.1879	1.012(4)	1.00	2.62(5)	2.22
0.712(2)	0.443(17)	0.4369	0.22(13)	0.2397	1.009(4)	1.00	2.77(7)	2.28
0.759(1)	0.419(19)	0.4123	0.34(5)	0.2918	1.011(3)	1.00	2.81(7)	2.34
0.804(1)	0.395(14)	0.3874	0.35(19)	0.3469	1.009(3)	1.00	2.90(7)	2.44
0.858(1)	0.357(15)	0.3564	0.46(11)	0.4213	1.009(3)	1.00	3.02(7)	2.52
0.900(1)	0.326(16)	0.3326	0.44(23)	0.4838	1.008(2)	1.00	3.14(6)	2.62
0.949(1)	0.300(16)	0.3045	0.51(43)	0.5648	1.008(3)	1.00	3.28(8)	2.72
1.0000	0.273(18)	0.2920	-	-	-	-	3.38(6)	2.88
LJTS Mixture C ($\varepsilon_2/\varepsilon_1$ = 0.9 and ξ_{12} = 0.85)								
0.000	0.446(18)	0.4566	-	-	-	-	2.68(6)	2.33
0.096(1)	0.363(14)	0.3625	0.144(46)	0.1476	1.28(8)	1.47	3.04(10)	2.68
0.136(2)	0.336(17)	0.3332	0.156(55)	0.2069	1.21(6)	1.43	3.18(9)	2.82
0.183(3)	0.308(16)	0.3064	0.25(8)	0.2673	1.19(7)	1.37	3.29(9)	2.94
0.226(2)	0.292(15)	0.2872	0.29(10)	0.3137	1.17(6)	1.32	3.40(9)	3.06
0.276(3)	0.275(18)	0.2703	0.39(11)	0.3515	1.13(6)	1.25	3.52(9)	3.14
0.316(4)	0.265(13)	0.2601	0.34(13)	0.3676	1.06(3)	1.19	3.51(9)	3.18
0.377(5)	0.252(16)	0.2489	0.37(6)	0.3651	1.05(2)	1.12	3.63(11)	3.22
0.425(5)	0.236(12)	0.2423	0.38(13)	0.3404	1.05(3)	1.07	3.65(11)	3.22
0.473(4)	0.234(15)	0.2374	0.19(12)	0.2996	1.03(2)	1.03	3.56(7)	3.22
0.520(5)	0.224(15)	0.2335	0.32(14)	0.2460	1.03(1)	1.01	3.75(16)	3.24
0.572(5)	0.223(14)	0.2303	-0.17(15)	0.1761	1.01(1)	1.00	3.68(9)	3.22
0.614(3)	0.230(12)	0.2284	0.16(13)	0.1131	1.02(1)	1.00	3.62(14)	3.22
0.668(2)	0.223(17)	0.2271	0.02(20)	0.0265	1.01(1)	1.00	3.67(11)	3.22
0.722(4)	0.224(14)	0.2275	-0.006(100)	-0.0665	1.02(2)	1.00	3.55(19)	3.20
0.772(2)	0.229(14)	0.2298	-0.10(19)	-0.1540	1.01(1)	1.00	3.70(7)	3.16
0.816(2)	0.231(10)	0.2336	0.09(14)	-0.2321	1.02(3)	1.00	3.59(22)	3.14
0.873(2)	0.241(13)	0.2418	-1.00(36)	-0.3343	1.01(1)	1.00	3.64(10)	3.08
0.912(1)	0.250(15)	0.2498	-0.26(33)	-0.4018	1.009(2)	1.00	3.57(5)	3.02
0.956(1)	0.253(12)	0.2619	-0.26(66)	-0.4774	1.009(3)	1.00	3.48(8)	2.94
1.000	0.273(18)	0.2920	-	-	-	-	3.38(6)	2.88
LJTS Mixture D ($\varepsilon_2/\varepsilon_1$ = 0.5 and ξ_{12} = 1)								
0.000	0.446(18)	0.4566	-	-	-	-	2.68(6)	2.33
0.038(1)	0.370(12)	0.3812	0.106(28)	0.0947	2.02(9)	2.11	3.05(6)	2.58
0.050(1)	0.347(17)	0.3611	0.143(27)	0.1190	1.88(6)	2.04	3.18(7)	2.66
0.071(1)	0.317(14)	0.3255	0.146(34)	0.1610	1.66(4)	1.92	3.27(9)	2.82
0.099(2)	0.276(10)	0.2844	0.202(33)	0.2083	1.57(5)	1.78	3.58(10)	3.02
0.131(3)	0.233(11)	0.2415	0.257(51)	0.2557	1.47(5)	1.65	3.90(12)	3.28
0.162(3)	0.191(16)	0.2043	0.27(6)	0.2952	1.37(4)	1.54	4.28(13)	3.54
0.196(5)	0.155(15)	0.1691	0.33(7)	0.3304	1.31(4)	1.45	4.74(18)	3.88
0.224(3)	0.131(9)	0.1431	0.34(6)	0.3542	1.25(3)	1.38	5.12(17)	4.20
0.271(5)	0.098(11)	0.1050	0.38(8)	0.3830	1.17(3)	1.28	5.9(5)	4.80
LJTS Mixture E ($\varepsilon_2/\varepsilon_1$ = 0.5 and ξ_{12} = 1.2)								
0.0000	0.446(18)	0.4566	-	-	-	-	2.68(6)	2.33

$x_2'/\mathrm{mol\,mol}^{-1}$	$\gamma\ /\ \varepsilon\sigma^{-2}$		$\Gamma_2^{(1)}\ /\ \sigma^{-2}$		E_2		$L_{10}^{90}\ /\ \sigma$	
	MD	DGT	MD	DGT	MD	DGT	MD	DGT
0.056(1)	0.406(22)	0.4157	0.056(23)	0.0480	1.17(6)	1.22	2.84(4)	2.45
0.098(2)	0.372(14)	0.3845	0.121(22)	0.0798	1.11(4)	1.17	3.00(7)	2.50
0.136(2)	0.337(14)	0.3557	0.091(31)	0.1069	1.07(3)	1.13	3.11(7)	2.55
0.179(1)	0.306(11)	0.3230	0.177(29)	0.1357	1.07(2)	1.10	3.30(7)	2.65
0.217(3)	0.277(18)	0.2937	0.18(4)	0.1602	1.06(2)	1.08	3.47(11)	2.75
0.262(2)	0.243(14)	0.2585	0.22(7)	0.1882	1.03(1)	1.05	3.76(9)	2.95
0.295(2)	0.213(15)	0.2323	0.222(31)	0.2082	1.02(1)	1.04	3.85(13)	3.05
0.345(2)	0.174(11)	0.1947	0.291(35)	0.2356	1.02(1)	1.02	4.33(12)	3.30
0.383(3)	0.150(11)	0.1657	0.25(7)	0.2554	1.02(1)	1.01	4.51(13)	3.50
0.425(3)	0.122(10)	0.1354	0.27(7)	0.2744	1.02(1)	1.01	4.94(17)	3.80
0.464(4)	0.098(11)	0.1084	0.28(4)	0.2889	1.01(1)	1.00	5.61(18)	4.20
0.505(3)	0.068(9)	0.0821	0.30(8)	0.2989	1.01(1)	1.00	6.60(63)	4.70
0.551(10)	0.044(11)	0.0552	0.26(12)	0.3005	1.015(4)	1.00	8.9(41)	5.50
0.598(6)	0.032(9)	0.0321	0.24(11)	0.2837	1.012(3)	1.00	9.2(16)	6.75
LJTS Mixture F ($\varepsilon_2/\varepsilon_1 = 0.5$ and $\xi_{12} = 0.85$)								
0.0000	0.446(18)	0.4566	-	-	-	-	2.68(6)	2.33
0.006(1)	0.420(16)	0.4296	0.035(10)	0.0352	2.42(16)	2.80	2.78(7)	2.45
0.016(1)	0.382(16)	0.3884	0.087(9)	0.0891	2.25(7)	2.64	2.99(5)	2.60
0.027(1)	0.349(20)	0.3474	0.14(3)	0.1426	2.12(7)	2.47	3.19(10)	2.80
0.037(1)	0.314(13)	0.3075	0.19(3)	0.1937	1.94(5)	2.28	3.43(9)	3.00
0.049(2)	0.267(15)	0.2662	0.24(3)	0.2440	1.84(3)	2.07	3.75(12)	3.20
0.061(2)	0.240(14)	0.2265	0.27(2)	0.2868	1.70(3)	1.86	4.05(12)	3.55
0.077(2)	0.203(19)	0.1793	0.28(3)	0.3213	1.61(2)	1.59	4.32(14)	3.90
0.093(2)	0.165(17)	0.1401	0.36(3)	0.3206	1.46(2)	1.38	4.83(23)	4.30
0.110(6)	0.144(20)	0.1037	0.33(4)	0.2783	1.36(2)	1.19	5.16(21)	4.55
0.123(4)	0.103(20)	0.0824	0.39(4)	0.2324	1.25(1)	1.10	6.11(47)	4.70
0.140(5)	0.077(23)	0.0604	0.38(8)	0.1702	1.15(2)	1.04	6.75(56)	4.85

Henry's law constant data

Table A.3: MD results for the Henry's law constants of the LJTS mixtures D, E, and F. The number in the parentheses indicates the statistical uncertainty in the last decimal digit.

$T\ /\ \varepsilon k_{\mathrm{B}}^{-1}$	$H_{2,1}\ /\ \varepsilon\sigma^{-3}$		
	D	E	F
0.63	0.2066(57)	0.0224(7)	0.9929(90)
0.68	0.2382(42)	0.0331(6)	0.9937(98)
0.73	0.2595(32)	0.0447(6)	0.9326(92)
0.78	0.2893(23)	0.0583(5)	0.8842(68)
0.83	0.3030(21)	0.0747(5)	0.8350(64)
0.88	0.3137(20)	0.0902(5)	0.7704(59)
0.93	0.3183(20)	0.1060(6)	0.7127(43)
0.98	0.3156(16)	0.1208(5)	0.6300(47)
1.03	0.3045(17)	0.1338(5)	0.5429(44)

A.2 Simulation Results for 90 LJTS Mixtures

This Appendix contains the following points:

- numeric values for the computed phase equilibria from both MD and the PeTS EOS (Table A.4) and the corresponding topology plots for the vapor pressure (cf. Fig. A.3) and the vapor phase composition (cf. Fig. A.4) as a function of the binary interaction parameter ξ and the ratio of the dispersion energies $\varepsilon_2/\varepsilon_1$

- Table A.5 report the Henry's law constants obtained from molecular simulations and the PeTS EOS

- Fig. A.6 shows the comparison for the configurational internal energy results obtained from the conformal solution theory and the PeTS EOS. Details on the CST are given in the main body of the article.
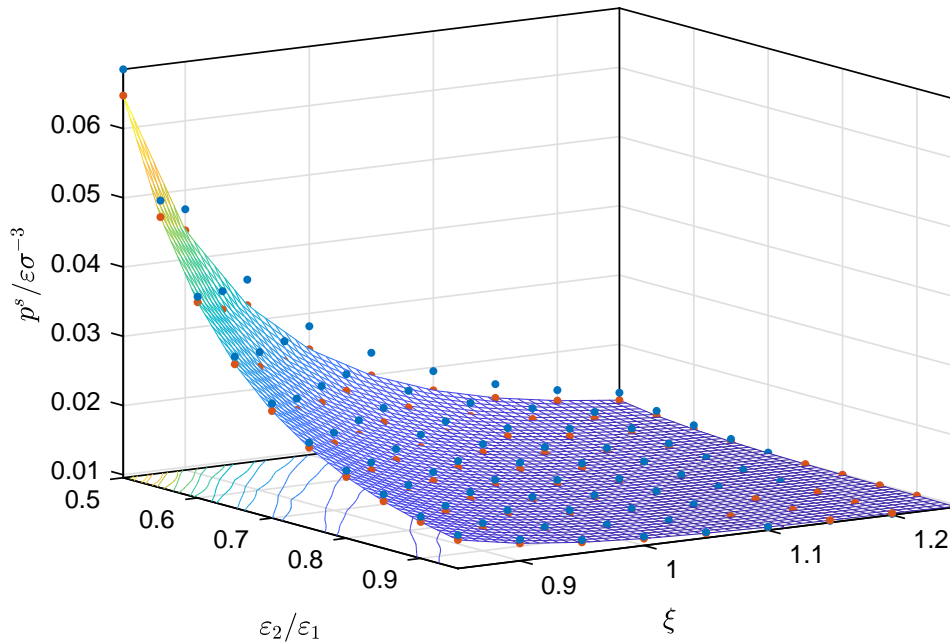
Figure A.3: Vapor pressure of binary LJTS mixtures at $T = 0.77\,\varepsilon k_{\mathrm{B}}^{-1}$ and $x_2' = 0.05\,\mathrm{mol\,mol^{-1}}$ as a function of the binary interaction parameter ξ and the ratio of the dispersion energies of the low and high-boiling component $\varepsilon_2/\varepsilon_1$. Blue points: MD, orange points: PeTS EOS [249]. The surface is a linear interpolation of the EOS results. The color of the surface is coded by its height position.
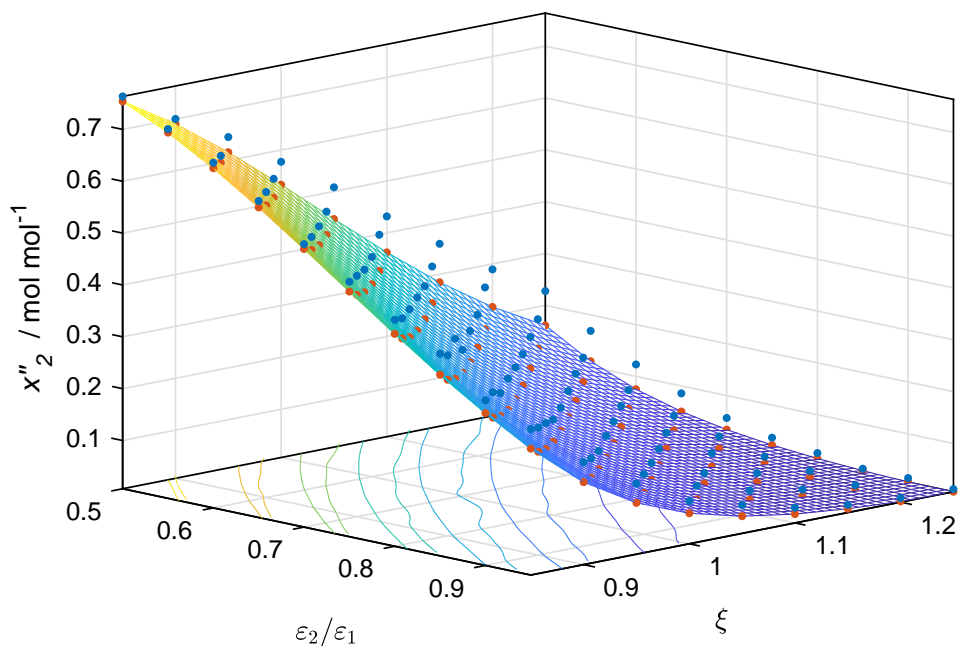
Figure A.4: Composition of the saturated vapor phase of binary LJTS mixtures at $T = 0.77\,\varepsilon k_{\mathrm{B}}^{-1}$ and $x_2' = 0.05\,\mathrm{mol\,mol^{-1}}$ as a function of the binary interaction parameter ξ and the ratio of the dispersion energies of the low and high-boiling component $\varepsilon_2/\varepsilon_1$. Blue points: MD, orange points: PeTS EOS [249]. The surface is a linear interpolation of the respective results. The color of the surface is coded by its height position.
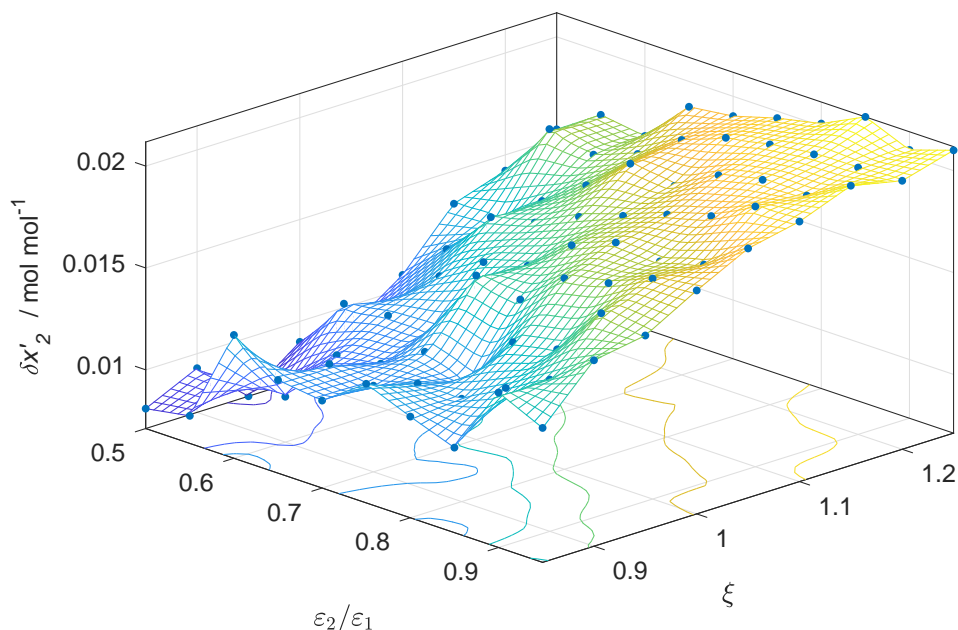
Figure A.5: Deviation from the liquid phase composition by MD to the initially prescribed concentration $x_2' = 0.05\,\mathrm{mol\,mol^{-1}}$ as a function of the binary interaction parameter ξ and the ratio of the dispersion energies of the low and high-boiling component $\varepsilon_2/\varepsilon_1$. The surface is a linear interpolation; the color of the surface is coded by its height position.
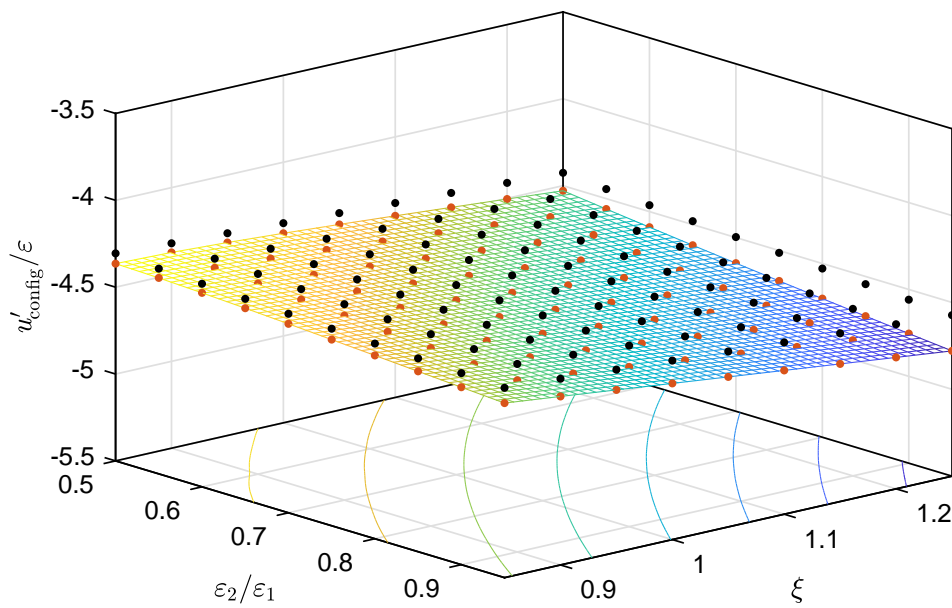
Figure A.6: Configurational internal energy of the saturated liquid phase u' calculated from the conformal solution theory by Eq. (56) (black points) and the PeTS EOS (orange points) as a function of the binary interaction parameter ξ and the ratio of the dispersion energies $\varepsilon_2/\varepsilon_1$ at $x_2' = 0.05\,\mathrm{mol\,mol^{-1}}$ and $T = 0.77\,\varepsilon k_\mathrm{B}^{-1}$. The shown surface is a linear interpolation of the data points. The color of the surface is coded by its height position. The absolute average deviation of the data from both methods is 2.3%.

Bulk VLE Numeric Values

Table A.4: MD and PeTS EOS results for the vapor-liquid equilibrium data at $T = 0.77\,\varepsilon k_{\mathrm{B}}^{-1}$ of the binary LJTS mixtures. DGT results were calculated at the liquid phase composition $x_2' = 0.05\,\mathrm{mol\,mol^{-1}}$. The MD liquid phase composition is listed in Table 5 and not repeated here. The number in the parentheses indicates the statistical uncertainty in the last decimal digit.

$\varepsilon_2/\varepsilon_1$	$x_2''/\mathrm{mol\,mol^{-1}}$		$p^s\ /\ \varepsilon\sigma^{-3}$		$\rho'\ /\ \sigma^{-3}$		$\rho''\ /\ \sigma^{-3}$	
	MD	EOS	MD	EOS	MD	EOS	MD	EOS
$\xi = 0.85$								
0.5	0.764(8)	0.754	0.0686(3)	0.0648	0.735(9)	0.7385	0.115(3)	0.1079
0.55	0.719(9)	0.712	0.0511(3)	0.0487	0.734(9)	0.7371	0.084(2)	0.0796
0.6	0.67(1)	0.662	0.0386(6)	0.0378	0.732(8)	0.7364	0.062(2)	0.0606
0.65	0.62(1)	0.605	0.0314(3)	0.0303	0.733(9)	0.7364	0.050(2)	0.0477
0.7	0.553(9)	0.543	0.0261(2)	0.0250	0.734(8)	0.7366	0.041(1)	0.0388
0.75	0.50(1)	0.480	0.0219(2)	0.0212	0.735(9)	0.7371	0.034(1)	0.0324
0.8	0.44(1)	0.417	0.0193(4)	0.0184	0.736(7)	0.7378	0.029(1)	0.0279
0.85	0.40(1)	0.356	0.0174(3)	0.0164	0.738(7)	0.7386	0.026(1)	0.0246
0.9	0.33(1)	0.301	0.0156(3)	0.0148	0.738(8)	0.7394	0.023(1)	0.0221
0.95	0.29(1)	0.251	0.0144(2)	0.0137	0.739(9)	0.7403	0.021(1)	0.0203
$\xi = 0.9$								
0.5	0.70(7)	0.691	0.047(1)	0.0442	0.734(8)	0.7372	0.075(2)	0.0696
0.55	0.648(7)	0.634	0.0369(7)	0.0342	0.734(8)	0.7368	0.058(2)	0.0533
0.6	0.60(1)	0.570	0.0295(3)	0.0274	0.734(7)	0.7369	0.046(1)	0.0422
0.65	0.528(7)	0.503	0.0243(3)	0.0226	0.735(8)	0.7373	0.037(1)	0.0345
0.7	0.47(1)	0.435	0.0208(4)	0.0192	0.736(7)	0.7379	0.032(1)	0.0290
0.75	0.41(1)	0.369	0.0180(6)	0.0168	0.737(8)	0.7387	0.027(1)	0.0252
0.8	0.36(1)	0.308	0.0161(3)	0.0150	0.738(7)	0.7395	0.024(1)	0.0224
0.85	0.30(1)	0.253	0.0146(4)	0.0138	0.739(9)	0.7405	0.022(1)	0.0204
0.9	0.25(1)	0.206	0.0136(2)	0.0128	0.741(7)	0.7414	0.020(1)	0.0189
0.95	0.205(9)	0.166	0.0126(3)	0.0121	0.742(8)	0.7424	0.019(1)	0.0177
$\xi = 0.95$								
0.5	0.645(9)	0.616	0.0360(4)	0.0323	0.735(8)	0.7372	0.056(2)	0.0494
0.55	0.583(6)	0.546	0.0285(5)	0.0256	0.735(7)	0.7374	0.044(2)	0.0390
0.6	0.51(1)	0.473	0.0235(7)	0.0211	0.735(7)	0.7379	0.036(1)	0.0318
0.65	0.45(1)	0.401	0.0200(3)	0.0180	0.737(7)	0.7386	0.030(1)	0.0269
0.7	0.387(9)	0.333	0.0173(3)	0.0157	0.738(8)	0.7395	0.026(1)	0.0234
0.75	0.349(3)	0.271	0.0154(3)	0.0142	0.739(7)	0.7405	0.023(1)	0.0209
0.8	0.262(7)	0.218	0.0140(3)	0.0130	0.740(8)	0.7415	0.021(1)	0.0192
0.85	0.22(1)	0.173	0.0129(4)	0.0122	0.742(8)	0.7425	0.019(1)	0.0179
0.9	0.17(1)	0.136	0.0119(3)	0.0116	0.743(7)	0.7436	0.017(1)	0.0169
0.95	0.143(8)	0.106	0.0115(3)	0.0111	0.744(7)	0.7447	0.017(1)	0.0163
$\xi = 1.0$								
0.5	0.577(4)	0.533	0.0281(6)	0.0248	0.735(8)	0.7379	0.043(2)	0.0374
0.55	0.500(9)	0.455	0.0227(3)	0.0203	0.735(7)	0.7385	0.034(1)	0.0303
0.6	0.43(1)	0.378	0.0193(2)	0.0172	0.737(7)	0.7393	0.029(1)	0.0256
0.65	0.37(1)	0.307	0.0168(3)	0.0150	0.738(8)	0.7402	0.025(1)	0.0223
0.7	0.29(1)	0.244	0.0145(2)	0.0136	0.739(8)	0.7413	0.021(1)	0.0200
0.75	0.25(1)	0.191	0.0132(3)	0.0125	0.741(7)	0.7424	0.019(1)	0.0184
0.8	0.19(1)	0.148	0.0122(3)	0.0118	0.742(7)	0.7435	0.018(1)	0.0172
0.85	0.15(1)	0.114	0.0118(2)	0.0112	0.744(8)	0.7446	0.017(1)	0.0164
0.9	0.123(8)	0.087	0.0112(2)	0.0109	0.745(8)	0.7458	0.016(1)	0.0158
0.95	0.089(9)	0.066	0.0109(1)	0.0106	0.747(7)	0.7469	0.016(1)	0.0154
$\xi = 1.05$								

$\varepsilon_2/\varepsilon_1$	$x_2'' / $ mol mol^{-1}		$p^s / \varepsilon\sigma^{-3}$		ρ' / σ^{-3}		ρ'' / σ^{-3}	
	MD	EOS	MD	EOS	MD	EOS	MD	EOS
0.5	0.51(1)	0.447	0.0232(5)	0.0199	0.736(7)	0.7390	0.035(1)	0.0297
0.55	0.43(1)	0.365	0.0192(3)	0.0167	0.737(7)	0.7398	0.029(1)	0.0249
0.6	0.35(2)	0.290	0.0162(2)	0.0146	0.738(7)	0.7409	0.024(1)	0.0216
0.65	0.29(1)	0.226	0.0144(2)	0.0132	0.740(7)	0.7420	0.021(1)	0.0194
0.7	0.24(2)	0.173	0.0132(2)	0.0122	0.741(8)	0.7431	0.019(1)	0.0178
0.75	0.18(1)	0.131	0.0121(2)	0.0115	0.743(7)	0.7443	0.018(1)	0.0168
0.8	0.140(8)	0.098	0.0114(2)	0.0110	0.745(7)	0.7455	0.017(1)	0.0160
0.85	0.106(9)	0.073	0.0109(1)	0.0107	0.747(7)	0.7467	0.016(1)	0.0155
0.9	0.080(9)	0.054	0.0106(2)	0.0104	0.748(8)	0.7479	0.015(1)	0.0151
0.95	0.062(8)	0.040	0.0104(3)	0.0102	0.750(7)	0.7491	0.015(1)	0.0148
$\xi = 1.1$								
0.5	0.43(1)	0.362	0.0194(3)	0.0167	0.737(8)	0.7403	0.029(1)	0.0247
0.55	0.35(1)	0.283	0.0163(5)	0.0144	0.738(7)	0.7414	0.024(1)	0.0213
0.6	0.28(2)	0.216	0.0141(3)	0.0130	0.740(7)	0.7425	0.021(1)	0.0190
0.65	0.22(1)	0.161	0.0128(3)	0.0120	0.742(8)	0.7438	0.019(1)	0.0175
0.7	0.17(1)	0.119	0.0120(3)	0.0113	0.744(8)	0.7450	0.017(1)	0.0165
0.75	0.13(1)	0.087	0.0112(3)	0.0108	0.745(7)	0.7463	0.016(1)	0.0158
0.8	0.094(9)	0.063	0.0109(1)	0.0105	0.747(7)	0.7476	0.016(1)	0.0153
0.85	0.066(7)	0.046	0.0104(2)	0.0103	0.749(8)	0.7488	0.015(1)	0.0149
0.9	0.051(6)	0.033	0.0101(2)	0.0101	0.751(6)	0.7501	0.015(1)	0.0147
0.95	0.037(4)	0.024	0.0101(2)	0.0100	0.753(8)	0.7513	0.015(1)	0.0145
$\xi = 1.15$								
0.5	0.36(1)	0.285	0.0165(4)	0.0145	0.738(6)	0.7418	0.024(1)	0.0213
0.55	0.29(1)	0.212	0.0145(3)	0.0129	0.740(7)	0.7430	0.021(1)	0.0189
0.6	0.22(2)	0.155	0.0130(3)	0.0119	0.742(7)	0.7443	0.019(1)	0.0173
0.65	0.16(1)	0.112	0.0116(3)	0.0112	0.744(7)	0.7456	0.017(1)	0.0163
0.7	0.12(1)	0.080	0.0111(2)	0.0107	0.746(8)	0.7469	0.016(1)	0.0156
0.75	0.087(9)	0.057	0.0107(3)	0.0104	0.748(6)	0.7483	0.015(1)	0.0151
0.8	0.07(1)	0.040	0.0104(3)	0.0102	0.750(7)	0.7496	0.015(1)	0.0148
0.85	0.046(8)	0.028	0.0100(2)	0.0101	0.752(7)	0.7509	0.014(1)	0.0146
0.9	0.033(4)	0.020	0.0099(1)	0.0100	0.754(7)	0.7522	0.014(1)	0.0144
0.95	0.022(5)	0.014	0.0098(2)	0.0099	0.756(8)	0.7535	0.014(1)	0.0143
$\xi = 1.2$								
0.5	0.29(2)	0.217	0.0145(4)	0.0130	0.740(7)	0.7433	0.021(1)	0.0190
0.55	0.212(9)	0.155	0.0128(2)	0.0118	0.742(7)	0.7446	0.019(1)	0.0173
0.6	0.16(1)	0.109	0.0119(2)	0.0111	0.744(8)	0.7460	0.017(1)	0.0162
0.65	0.112(8)	0.076	0.0111(2)	0.0107	0.746(7)	0.7474	0.016(1)	0.0155
0.7	0.08(1)	0.053	0.0105(1)	0.0104	0.748(7)	0.7489	0.015(1)	0.0150
0.75	0.060(8)	0.036	0.0103(2)	0.0102	0.750(7)	0.7503	0.015(1)	0.0147
0.8	0.039(7)	0.025	0.0100(2)	0.0100	0.752(8)	0.7516	0.014(1)	0.0145
0.85	0.030(6)	0.017	0.0099(2)	0.0099	0.754(7)	0.7530	0.014(1)	0.0143
0.9	0.021(4)	0.012	0.0097(2)	0.0099	0.756(6)	0.7543	0.014(1)	0.0142
0.95	0.015(4)	0.008	0.0097(2)	0.0098	0.758(7)	0.7556	0.014(1)	0.0142
$\xi = 1.25$								
0.5	0.228(9)	0.161	0.0130(2)	0.0119	0.741(7)	0.7449	0.019(1)	0.0175
0.55	0.17(1)	0.111	0.0118(2)	0.0111	0.744(7)	0.7463	0.017(1)	0.0162
0.6	0.12(1)	0.075	0.0112(3)	0.0106	0.746(7)	0.7478	0.016(1)	0.0155
0.65	0.086(8)	0.051	0.0107(2)	0.0103	0.748(7)	0.7493	0.016(1)	0.0150
0.7	0.057(8)	0.034	0.0102(2)	0.0101	0.751(7)	0.7508	0.015(1)	0.0146
0.75	0.037(5)	0.023	0.0098(2)	0.0100	0.753(7)	0.7522	0.014(1)	0.0144
0.8	0.026(4)	0.016	0.0098(2)	0.0099	0.755(6)	0.7536	0.014(1)	0.0143
0.85	0.014(3)	0.011	0.0097(2)	0.0098	0.757(7)	0.7550	0.014(1)	0.0142
0.9	0.015(4)	0.007	0.0096(2)	0.0098	0.759(6)	0.7564	0.014(1)	0.0141
0.95	0.012(5)	0.006	0.0095(3)	0.0097	0.760(7)	0.7575	0.014(1)	0.0139

Henry's Law Constant Numeric Values

The numeric values of the Henry's law constant calculated by both MD and the PeTS EOS for all 90 investigated mixtures are provided in Table A.5.

Table A.5: Henry's law constant calculated by both the PeTS EOS and computer experiment for 90 investigated LJTS mixtures (cf. section 3.4) at $T = 0.77\,\varepsilon k_{\mathrm{B}}^{-1}$.

$\varepsilon_2/\varepsilon_1$	PeTS	MD	$\varepsilon_2/\varepsilon_1$	PeTS	MD	$\varepsilon_2/\varepsilon_1$	PeTS	MD
$\xi = 0.85$			$\xi = 0.9$			$\xi = 0.95$		
0.5	0.95620	0.908(6)	0.5	0.62781	0.608(4)	0.5	0.41218	0.415(3)
0.55	0.70700	0.649(5)	0.55	0.45473	0.433(3)	0.55	0.29246	0.293(3)
0.6	0.52650	0.481(3)	0.6	0.33204	0.312(2)	0.6	0.20939	0.204(1)
0.65	0.39473	0.356(3)	0.65	0.24429	0.227(2)	0.65	0.15117	0.145(1)
0.7	0.29783	0.267(2)	0.7	0.18100	0.168(1)	0.7	0.10999	0.104(1)
0.75	0.22609	0.202(1)	0.75	0.13501	0.124(1)	0.75	0.08062	0.076(1)
0.8	0.17265	0.154(1)	0.8	0.10136	0.093(1)	0.8	0.05951	0.0554(4)
0.85	0.13258	0.118(1)	0.85	0.07657	0.070(1)	0.85	0.04422	0.0411(3)
0.9	0.10237	0.093(1)	0.9	0.05819	0.053(1)	0.9	0.03307	0.0305(2)
0.95	0.07946	0.071(1)	0.95	0.04447	0.040(1)	0.95	0.02488	0.0228(2)
$\xi = 1$			$\xi = 1.05$			$\xi = 1.1$		
0.5	0.27059	0.285(2)	0.5	0.17763	0.189(1)	0.5	0.11660	0.127(1)
0.55	0.18809	0.190(1)	0.55	0.12095	0.126(1)	0.55	0.07777	0.082(1)
0.6	0.13204	0.131(1)	0.6	0.08325	0.085(1)	0.6	0.05249	0.0541(4)
0.65	0.09354	0.092(1)	0.65	0.05787	0.0577(4)	0.65	0.03580	0.0361(2)
0.7	0.06683	0.0647(4)	0.7	0.04060	0.0398(3)	0.7	0.02467	0.0244(2)
0.75	0.04813	0.0467(3)	0.75	0.02873	0.0278(2)	0.75	0.01715	0.0167(1)
0.8	0.03493	0.0329(2)	0.8	0.02050	0.0196(1)	0.8	0.01203	0.0115(1)
0.85	0.02553	0.0238(2)	0.85	0.01474	0.0139(1)	0.85	0.00851	0.0080(1)
0.9	0.01879	0.0177(1)	0.9	0.01068	0.0099(1)	0.9	0.00607	0.0056(1)
0.95	0.01392	0.0128(1)	0.95	0.00779	0.0072(1)	0.95	0.00436	0.0040(1)
$\xi = 1.15$			$\xi = 1.2$			$\xi = 1.25$		
0.5	0.07653	0.085(1)	0.5	0.05023	0.0572(4)	0.5	0.03297	0.0374(3)
0.55	0.05001	0.0536(4)	0.55	0.03215	0.0348(2)	0.55	0.02067	0.0226(2)
0.6	0.03309	0.0345(2)	0.6	0.02086	0.0219(1)	0.6	0.01315	0.0139(1)
0.65	0.02215	0.0225(2)	0.65	0.01370	0.0140(1)	0.65	0.00847	0.0086(1)
0.7	0.01498	0.0149(1)	0.7	0.00910	0.0090(1)	0.7	0.00553	0.00547(4)
0.75	0.01024	0.0100(1)	0.75	0.00611	0.00593(4)	0.75	0.00365	0.00351(3)
0.8	0.00706	0.0067(1)	0.8	0.00414	0.00392(3)	0.8	0.00243	0.00228(2)
0.85	0.00491	0.0046(1)	0.85	0.00284	0.00263(2)	0.85	0.00164	0.00149(1)
0.9	0.00345	0.0032(1)	0.9	0.00196	0.00180(1)	0.9	0.00111	0.00099(1)
0.95	0.00244	0.0022(1)	0.95	0.00136	0.00121(1)	0.95	0.00080	0.00066(1)

A.3 Simulation Results for LJTS Mixtures A and G

This Appendix contains the following points:

- $p - T$ diagram of mixture G; including the state points whose density profiles intersect in two invariant points (see 3.6.4.4 for a discussion)

- the comparison of the difference of the component 2 bulk density in the VL_1E region $\Delta\rho_2 = \rho_2^{L1} - \rho_2^V$ (cf. Fig. A.8) and a discussion of these results

- exemplary screenshots of the MD simulation of the mixtures A and B (cf. Fig. A.9)

- the plots of the MD VL_1 density profiles from both investigated mixtures A and B at all five temperatures (cf. Fig. A.10 and Fig. A.11),

- plots of the DGT VL_1 density profiles for mixture B at all temperatures (cf. Fig. A.12)

- numeric values for the computed phase equilibria and interfacial properties for both MD and DGT for all studied temperatures for mixture A and G (Table A.6 and A.7 for the phase equilibria and Tables A.8 and A.9 for the interfacial properties)

$p - T$ Diagram of Mixture G
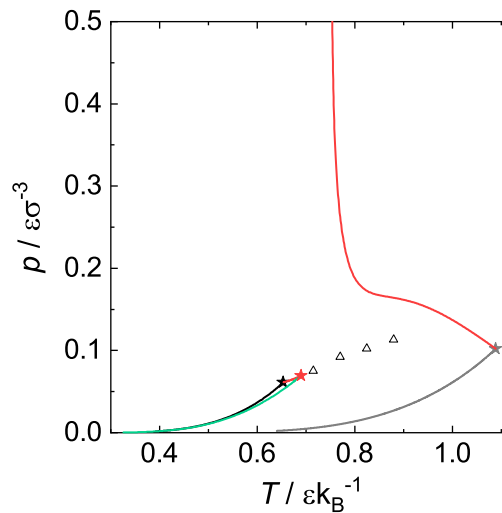
Figure A.7: Pressure-temperature diagram with characteristic curves for the mixture G – including the transition state points observed for the invariant intersection points. Pure component vapor pressure curves and critical points are the gray line and star (high-boiling component 1) and black line and star (low-boiling component 2). Red lines are critical lines of the mixture; the red star is the upper critical end point of mixture G (UCEP). The green line depicts the VL_1L_2E three-phase line. The open triangles indicate the state points $p^\star$ of which density profiles intersect multiple invariant points for a given temperature (see section 3.6.4.4 for a discussion).

Results for the Density Difference $\Delta\rho_2$

We have shown in an earlier work, cf. section 3.4 [630], that the difference of the component 2 bulk density in a VLE $\Delta\rho_2 = \rho_2^L - \rho_2^V$ is directly related to the arrangement of the surface excess at the vapor-liquid interface and thereby to the enrichment of the low-boiling component 2 at the interface. It was shown in section 3.4 that for $\Delta\rho_2 = 0$, all adsorption at a vapor-liquid interface contributes to the enrichment. Fig. A.8 shows $\Delta\rho_2$ in the VL_1E region for the mixtures A and G. As for the phase diagrams shown in the main body of the paper, the agreement between the computer experiment and the theory is almost perfect for the mixture A, but significant deviations are observed in the case of the mixture G. The PeTS EOS predicts $\Delta\rho_2 < 0$ for all temperatures in the entire composition range, whereas the molecular simulations predict small values $\Delta\rho_2 > 0$ for most state points. For mixture A, the function $\Delta\rho_2(x_2^{L1})$ is very different from that for mixture G. For mixture A, $\Delta\rho_2(x_2^{L1})$ shows an almost linear increase. The slope of $\Delta\rho_2(x_2^{L1})$ decreases with increasing temperature, which is simply due to the decreasing total density difference between both phases with increasing temperature.
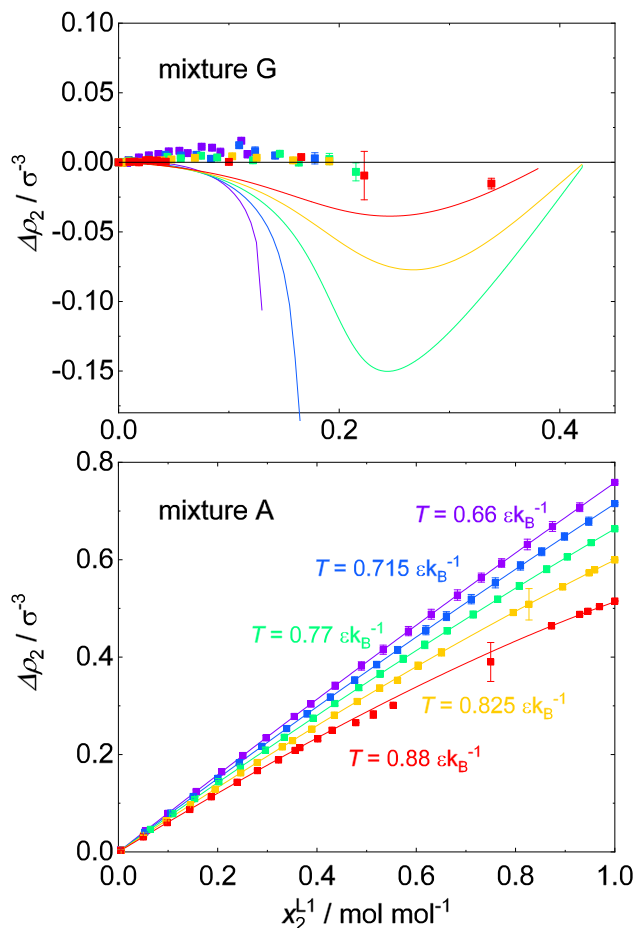
Figure A.8: Difference of the number density of the component 2 $\Delta\rho_2 = \rho_2^{L1} - \rho_2^V$ between both bulk phases. The temperatures in the top and bottom plot are color-coded using the same scale. Symbols are MD results and lines are the PeTS EOS.

In contrast, in mixture G $\Delta\rho_2(x_2^{L1})$ has a highly non-linear behavior. $\Delta\rho_2$ remains very close to zero at highly diluted mixtures $(x_2^{L1} \to 0)$ and then decreases with further

increasing concentration x_2^{L1}. This decay increases with decreasing temperature. Close to the VL_1L_2E line, $\Delta\rho_2$ drops almost vertically. The PeTS EOS predicts $\Delta\rho_2$ to exhibit a minimum at the three highest temperatures ($T = 0.77\,\varepsilon k_{\mathrm{B}}^{-1}$, $0.825\,\varepsilon k_{\mathrm{B}}^{-1}$, $0.88\,\varepsilon k_{\mathrm{B}}^{-1}$). By definition of the critical point, the densities and compositions of both phases must equalize upon approaching the very, i.e. $\Delta\rho_2 \to 0$ at the critical point, which is verified from the EOS results.

The poor agreement between MD and the EOS in the case of mixture G is likely due to the deviations observed in the bubble line in the phase diagrams at elevated pressures. Only the convex slope of $\Delta\rho_2(x_2^{L1})$ is captured consistently from both methods.

Simulation Screenshots

Fig. A.9 shows screenshots from the molecular dynamics simulation from mixture A and G at $T = 0.66\,\varepsilon k_{\mathrm{B}}^{-1}$ during the production phase of the simulation. The liquid phase composition is similar in both simulations – just above 10% mole fraction of the low-boiling component. It is evident that the vapor-liquid interface in the case of the asymmetric mixture G shows a strong surface excess of the low-boiling component 2 at the interface which is not present in the ideal mixture A.
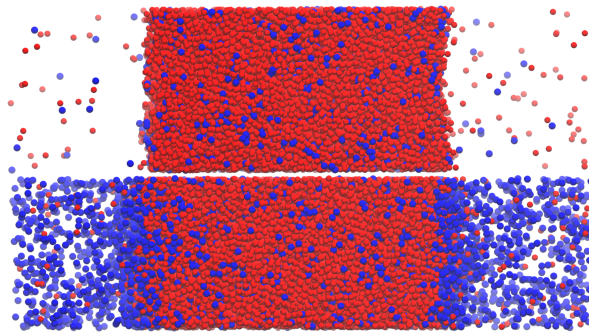
Figure A.9: Screenshots from the molecular simulations of mixture A (top) and mixture G (bottom) at $T = 0.66\,\varepsilon k_{\mathrm{B}}^{-1}$. The liquid phase compositions are $x_2^{L1} = 0.11$ mol mol^{-1} (top) and $x_2^{L1} = 0.12$ mol mol^{-1} (bottom). The high-boiling component 1 is indicated red, the low-boiling component 2 blue.

Density Profiles

Figure A.10: Density profiles of component 1 (dashed lines) and component 2 (full lines) for the mixture a obtained by MD. Results for all studied temperatures. The color-code indicates the liquid phase composition.
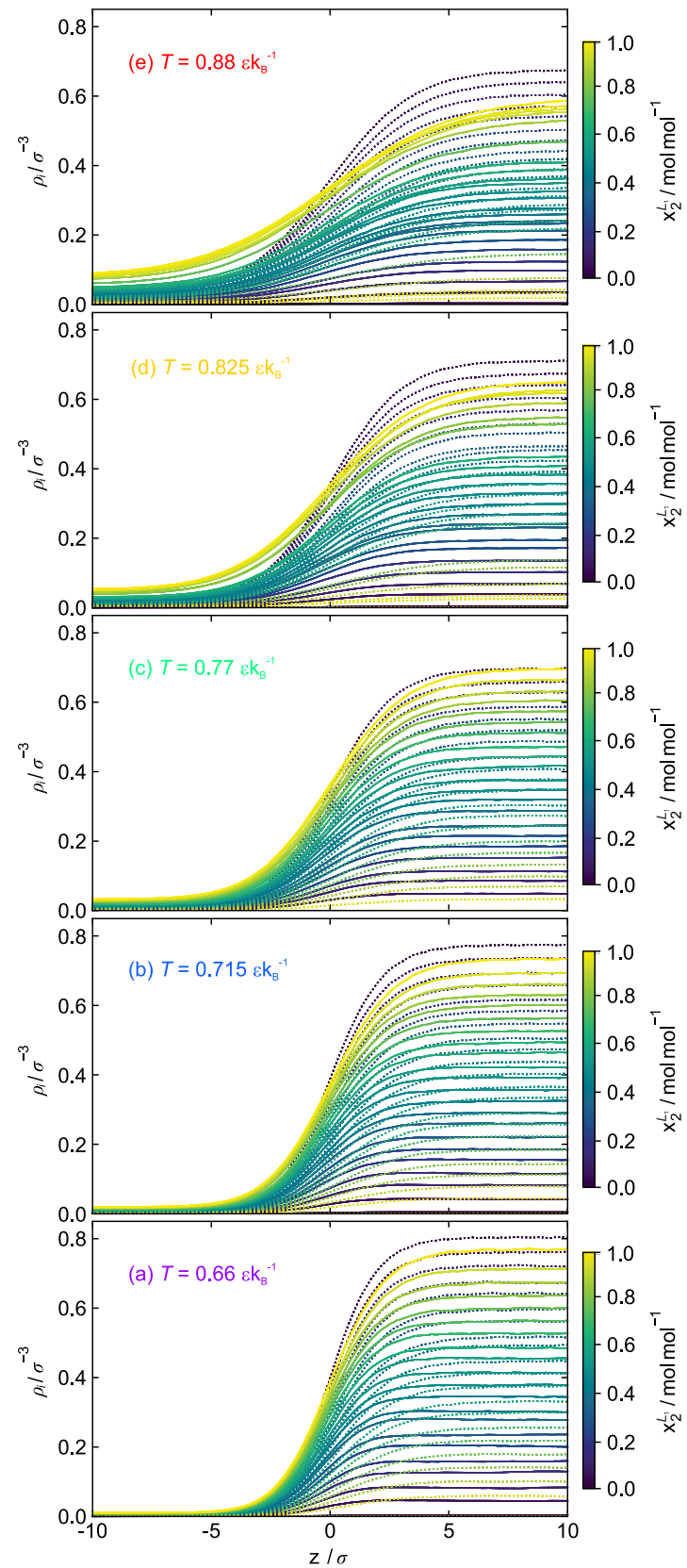
Figure A.11: *VL$_1$* density pro-
files of component
1 (dashed lines)
and component
2 (full lines) for
the mixture G
obtained by MD.
Results for all
studied tem-
peratures. The
color-code indi-
cates the liquid
phase composi-
tion. Red squares
indicate invari-
ant intersection
points of density
profiles.
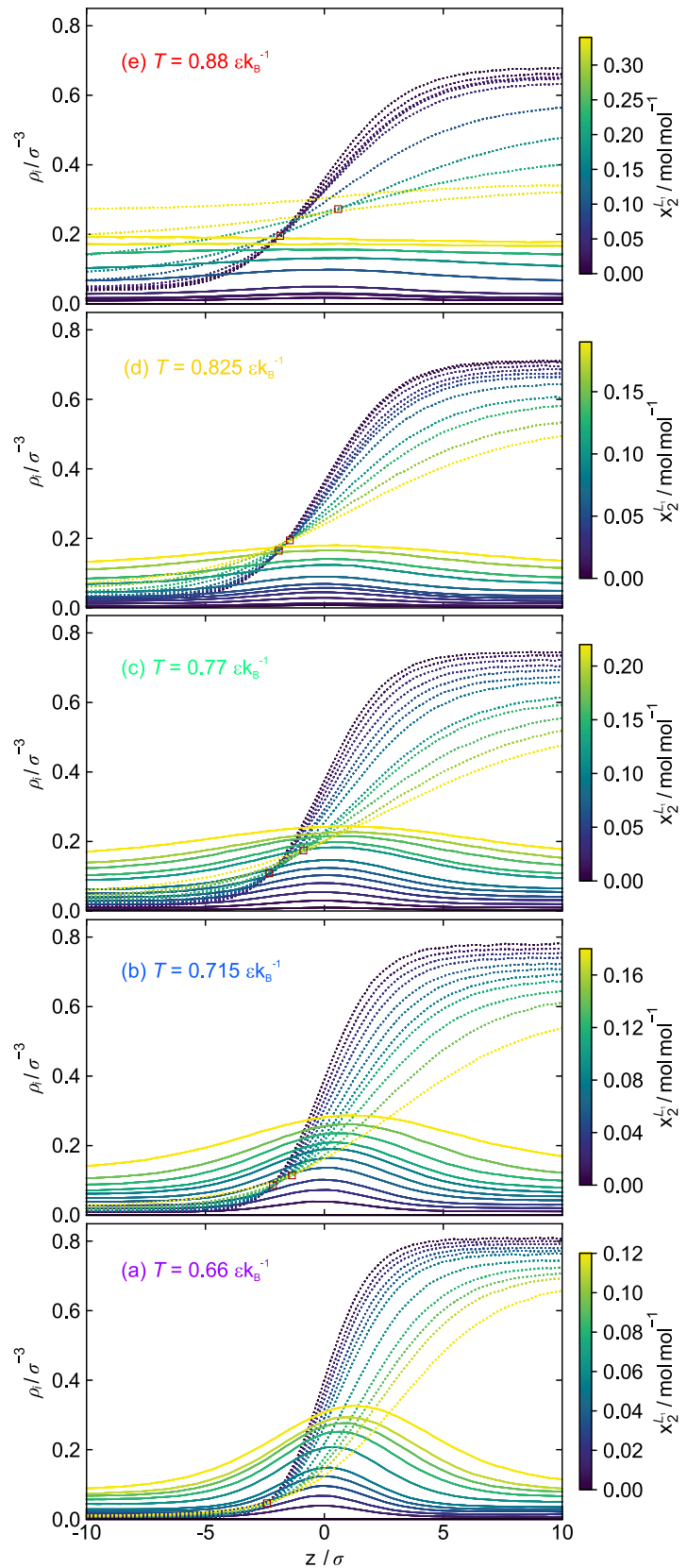
Figure A.12: Density profiles of component 1 (dashed lines) and component 2 (full lines) for the mixture A obtained by DGT. Results for all studied temperatures. The color-code indicates the liquid phase composition.
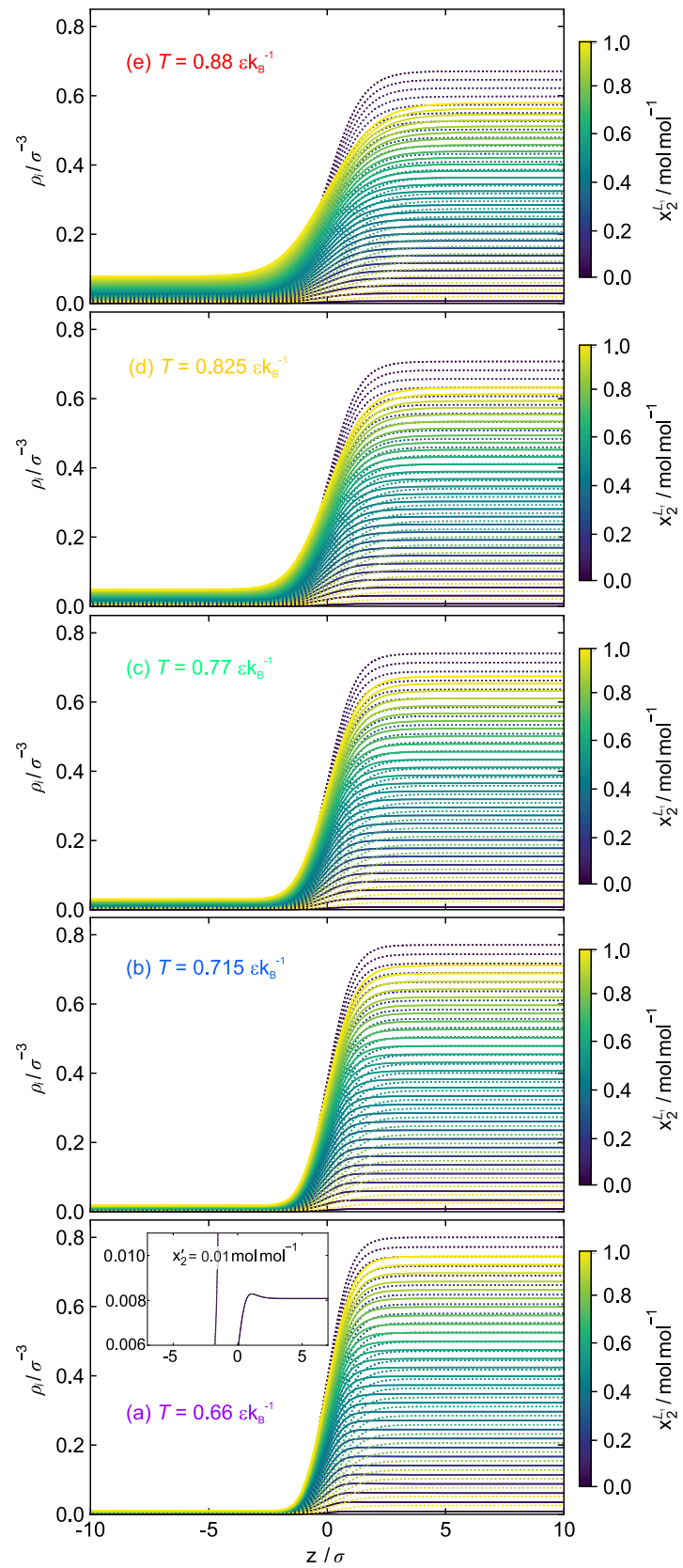
Numeric Values

Table A.6: MD and PeTS EOS results for the vapor-liquid equilibrium of the binary LJTS mixture A ($\varepsilon_2/\varepsilon_1 = 0.9$ and $\xi_{12} = 1$) for the temperatures $T/\varepsilon k_{\mathrm{B}}^{-1} = 0.66, 0.715, 0.825, 0.88$. The number in the parentheses indicates the statistical uncertainty in the last decimal digit.

$x_2'/\mathrm{mol\,mol}^{-1}$	$p \ / \ \varepsilon\sigma^{-3}$		$x_2'' \ / \ \mathrm{mol\,mol}^{-1}$		$\rho' \ / \ \sigma^{-3}$		$\rho'' \ / \ \sigma^{-3}$	
	MD	EOS	MD	EOS	MD	EOS	MD	EOS
$T = 0.66\,\varepsilon k_{\mathrm{B}}^{-1}$								
0.000	0.0030(1)	0.0029	0.00	0.00	0.808(4)	0.8084	0.0047(3)	0.0046
0.005(1)	0.0030(1)	0.0029	0.01(1)	0.0109	0.808(4)	0.8082	0.0047(3)	0.0046
0.055(1)	0.0030(1)	0.0031	0.11(1)	0.1110	0.806(8)	0.8065	0.0048(4)	0.0049
0.100(1)	0.0033(1)	0.0033	0.20(2)	0.1928	0.804(9)	0.8049	0.0052(5)	0.0052
0.157(2)	0.0034(2)	0.0035	0.27(2)	0.2846	0.80(1)	0.8028	0.0054(5)	0.0055
0.208(1)	0.0036(1)	0.0036	0.35(2)	0.3593	0.80(2)	0.8009	0.0058(5)	0.0058
0.251(1)	0.0038(1)	0.0038	0.42(2)	0.4160	0.80(1)	0.7993	0.0061(5)	0.0061
0.297(1)	0.0039(2)	0.0039	0.47(2)	0.4727	0.80(1)	0.7976	0.0063(5)	0.0063
0.354(1)	0.0042(2)	0.0041	0.53(2)	0.5364	0.80(1)	0.7954	0.0067(6)	0.0067
0.388(2)	0.0043(1)	0.0043	0.58(2)	0.5713	0.79(1)	0.7941	0.0070(6)	0.0068
0.437(2)	0.0045(1)	0.0044	0.62(2)	0.6187	0.79(1)	0.7922	0.0072(6)	0.0071
0.490(1)	0.0047(1)	0.0046	0.66(2)	0.6667	0.79(2)	0.7902	0.0075(6)	0.0074
0.533(1)	0.0047(2)	0.0048	0.69(3)	0.7036	0.79(2)	0.7884	0.0076(6)	0.0077
0.584(1)	0.0050(1)	0.0049	0.75(2)	0.7441	0.79(2)	0.7864	0.0081(6)	0.0080
0.630(2)	0.0051(1)	0.0051	0.77(1)	0.7784	0.78(1)	0.7845	0.0083(6)	0.0083
0.683(1)	0.0053(2)	0.0053	0.82(1)	0.8155	0.78(1)	0.7824	0.0086(6)	0.0086
0.731(1)	0.0055(2)	0.0054	0.84(1)	0.8474	0.78(1)	0.7804	0.0090(6)	0.0089
0.772(1)	0.0056(2)	0.0056	0.88(1)	0.8732	0.78(1)	0.7787	0.0091(6)	0.0091
0.824(2)	0.0059(2)	0.0058	0.90(1)	0.9046	0.78(1)	0.7765	0.0096(6)	0.0094
0.874(1)	0.0059(1)	0.0059	0.94(1)	0.9336	0.77(1)	0.7743	0.0097(6)	0.0097
0.929(1)	0.0062(2)	0.0061	0.96(1)	0.9635	0.77(1)	0.7719	0.0102(8)	0.0101
1.00	0.0064(2)	0.0063	1.00	1.00	0.769(3)	0.7692	0.0106(5)	0.0104
$T = 0.715\,\varepsilon k_{\mathrm{B}}^{-1}$								
0.000	0.0058(3)	0.0058	0.00	0.00	0.779(3)	0.7789	0.0087(4)	0.0087
0.0049(2)	0.0057(2)	0.0058	0.011(3)	0.0097	0.779(4)	0.7787	0.0086(5)	0.0087
0.053(1)	0.0061(2)	0.0061	0.10(1)	0.0988	0.777(7)	0.7768	0.0091(6)	0.0092
0.105(2)	0.0064(2)	0.0064	0.19(1)	0.1872	0.775(8)	0.7747	0.0097(6)	0.0097
0.151(1)	0.0067(2)	0.0067	0.26(1)	0.2567	0.773(10)	0.7728	0.0101(7)	0.0101
0.200(1)	0.0070(2)	0.0070	0.34(2)	0.3273	0.771(12)	0.7708	0.0107(7)	0.0106
0.243(1)	0.0073(2)	0.0072	0.39(1)	0.3836	0.769(11)	0.7690	0.0112(7)	0.0110
0.289(2)	0.0075(2)	0.0075	0.44(2)	0.4392	0.767(12)	0.7671	0.0115(7)	0.0115
0.339(1)	0.0079(2)	0.0078	0.49(2)	0.4957	0.765(12)	0.7649	0.0121(7)	0.0120
0.380(2)	0.0081(2)	0.0081	0.53(2)	0.5394	0.764(14)	0.7632	0.0125(8)	0.0124
0.427(2)	0.0083(2)	0.0083	0.58(2)	0.5866	0.761(12)	0.7611	0.0128(8)	0.0128
0.476(1)	0.0087(2)	0.0086	0.62(1)	0.6326	0.759(12)	0.7589	0.0133(8)	0.0133
0.520(1)	0.0088(2)	0.0089	0.68(1)	0.6718	0.757(12)	0.7570	0.0136(8)	0.0138
0.562(1)	0.0092(2)	0.0092	0.71(2)	0.7075	0.755(12)	0.7550	0.0143(8)	0.0142
0.619(2)	0.0095(2)	0.0095	0.75(1)	0.7530	0.753(14)	0.7524	0.0147(8)	0.0148
0.661(3)	0.0099(3)	0.0097	0.78(2)	0.7843	0.751(12)	0.7505	0.0154(8)	0.0152
0.711(1)	0.0101(2)	0.0100	0.82(1)	0.8204	0.749(13)	0.7481	0.0159(8)	0.0157
0.759(2)	0.0106(3)	0.0103	0.85(1)	0.8538	0.746(13)	0.7458	0.0166(8)	0.0162
0.810(1)	0.0109(2)	0.0106	0.88(1)	0.8870	0.744(10)	0.7433	0.0171(8)	0.0168
0.853(1)	0.0110(2)	0.0109	0.91(1)	0.9141	0.741(10)	0.7412	0.0174(12)	0.0172
0.899(1)	0.0112(3)	0.0112	0.94(1)	0.9418	0.739(8)	0.7389	0.0178(8)	0.0177
0.948(1)	0.0118(2)	0.0115	0.97(1)	0.9705	0.736(11)	0.7364	0.019(3)	0.0182

$x_2'/\mathrm{mol\,mol^{-1}}$	$p\ /\ \varepsilon\sigma^{-3}$		$x_2''\ /\ \mathrm{mol\,mol^{-1}}$		$\rho'\ /\ \sigma^{-3}$		$\rho''\ /\ \sigma^{-3}$	
	MD	EOS	MD	EOS	MD	EOS	MD	EOS
1.000	0.0119(2)	0.0117	1.00	1.00	0.734(3)	0.7342	0.0190(7)	0.0187
$T = 0.825\,\varepsilon k_{\mathrm{B}}^{-1}$								
0.000	0.0175(3)	0.0173	0.000	0.00	0.716(3)	0.7149	0.025(1)	0.0246
0.0055(3)	0.0176(3)	0.0173	0.010(3)	0.0092	0.715(4)	0.7146	0.025(1)	0.0247
0.051(1)	0.0181(4)	0.0180	0.082(8)	0.0820	0.713(6)	0.7122	0.026(1)	0.0257
0.096(1)	0.0188(3)	0.0186	0.151(7)	0.1500	0.710(7)	0.7098	0.027(1)	0.0268
0.145(1)	0.0195(2)	0.0193	0.213(9)	0.2189	0.707(9)	0.7072	0.028(1)	0.0279
0.195(2)	0.0201(3)	0.0200	0.29(1)	0.2844	0.705(9)	0.7044	0.029(1)	0.0291
0.246(1)	0.0210(2)	0.0207	0.35(1)	0.3485	0.702(9)	0.7015	0.031(1)	0.0303
0.280(1)	0.0214(4)	0.0212	0.38(1)	0.3878	0.700(10)	0.6996	0.031(1)	0.0311
0.330(1)	0.0222(4)	0.0219	0.44(1)	0.4445	0.697(9)	0.6966	0.033(1)	0.0323
0.351(2)	0.0224(3)	0.0222	0.47(1)	0.4668	0.696(10)	0.6954	0.033(1)	0.0328
0.390(2)	0.0231(3)	0.0228	0.51(1)	0.5078	0.69(1)	0.6931	0.035(3)	0.0338
0.435(2)	0.0236(3)	0.0234	0.55(1)	0.5531	0.69(1)	0.6903	0.035(1)	0.0350
0.481(2)	0.0243(3)	0.0241	0.60(1)	0.5974	0.69(1)	0.6875	0.036(2)	0.0361
0.526(2)	0.0248(3)	0.0247	0.63(1)	0.6389	0.68(1)	0.6846	0.037(1)	0.0373
0.562(4)	0.0253(7)	0.0253	0.66(1)	0.6709	0.68(1)	0.6823	0.043(2)	0.0383
0.604(2)	0.0259(3)	0.0259	0.71(1)	0.7065	0.68(1)	0.6796	0.040(2)	0.0394
0.651(1)	0.0267(4)	0.0266	0.74(1)	0.7458	0.68(1)	0.6764	0.041(2)	0.0407
0.795(2)	0.0289(3)	0.0287	0.86(1)	0.8577	0.667(7)	0.6663	0.045(1)	0.0448
0.83(4)	0.0294(5)	0.0292	0.88(3)	0.8808	0.664(8)	0.6640	0.046(2)	0.0457
0.895(1)	0.0304(4)	0.0302	0.928(4)	0.9289	0.658(8)	0.6589	0.049(3)	0.0478
0.948(1)	0.0313(4)	0.0310	0.965(3)	0.9653	0.655(5)	0.6547	0.050(1)	0.0494
0.959(1)	0.0313(4)	0.0312	0.973(3)	0.9729	0.654(5)	0.6538	0.050(1)	0.0498
1.000	0.0320(4)	0.0317	1.00	0.9934	0.651(3)	0.6514	0.052(1)	0.0508
$T = 0.88\,\varepsilon k_{\mathrm{B}}^{-1}$								
0.000	0.0271(4)	0.0270	0.00	0.00	0.679(3)	0.6782	0.039(1)	0.0384
0.0051(3)	0.0272(3)	0.0271	0.007(2)	0.0080	0.679(3)	0.6778	0.039(1)	0.0386
0.050(1)	0.0281(3)	0.0280	0.075(4)	0.0752	0.675(6)	0.6750	0.041(2)	0.0401
0.098(1)	0.0291(3)	0.0289	0.14(1)	0.1434	0.672(6)	0.6719	0.042(1)	0.0418
0.143(1)	0.0299(3)	0.0298	0.21(1)	0.2038	0.669(7)	0.6689	0.044(2)	0.0434
0.187(1)	0.0309(3)	0.0307	0.25(1)	0.2601	0.666(8)	0.6659	0.045(1)	0.0449
0.240(2)	0.0321(3)	0.0318	0.32(1)	0.3235	0.663(8)	0.6623	0.047(1)	0.0468
0.280(2)	0.0328(3)	0.0326	0.37(1)	0.3697	0.660(9)	0.6595	0.049(2)	0.0483
0.322(2)	0.0335(4)	0.0334	0.42(1)	0.4161	0.657(16)	0.6565	0.050(11)	0.0499
0.365(2)	0.0347(3)	0.0343	0.47(1)	0.4626	0.653(8)	0.6540	0.052(2)	0.0512
0.356(2)	0.0344(5)	0.0341	0.46(1)	0.4525	0.653(11)	0.6532	0.051(4)	0.0516
0.401(3)	0.0354(4)	0.0350	0.50(1)	0.4997	0.61(2)	0.6505	0.053(9)	0.0530
0.431(2)	0.0357(5)	0.0356	0.53(1)	0.5292	0.65(1)	0.6483	0.054(3)	0.0542
0.478(4)	0.0364(7)	0.0366	0.56(1)	0.5750	0.645(4)	0.6446	0.057(3)	0.0561
0.514(3)	0.0371(10)	0.0374	0.60(1)	0.6092	0.643(4)	0.6416	0.058(3)	0.0576
0.552(4)	0.0383(9)	0.0381	0.63(1)	0.6435	0.639(4)	0.6386	0.059(4)	0.0592
0.576(6)	0.0386(15)	0.0387	0.66(2)	0.6654	0.637(14)	0.6365	0.060(12)	0.0602
0.622(5)	0.0397(15)	0.0396	0.71(2)	0.7049	0.633(15)	0.6326	0.062(13)	0.0622
0.651(5)	0.0407(13)	0.0402	0.74(1)	0.7303	0.631(13)	0.6300	0.065(11)	0.0636
0.873(1)	0.0453(6)	0.0450	0.909(4)	0.9063	0.61(1)	0.6201	0.076(2)	0.0687
0.76(9)	0.0428(4)	0.0426	0.819(10)	0.8187	0.621(15)	0.6090	0.070(15)	0.0744
0.929(1)	0.0464(5)	0.0463	0.949(4)	0.9483	0.605(5)	0.6030	0.078(2)	0.0775
0.946(1)	0.0469(5)	0.0467	0.959(3)	0.9606	0.603(4)	0.6012	0.079(2)	0.0784
0.969(1)	0.0473(4)	0.0472	0.977(2)	0.9777	0.600(4)	0.5986	0.080(2)	0.0798
1.000	0.0478(7)	0.0477	1.00	1.00	0.597(3)	0.5963	0.081(2)	0.0810

Table A.7: MD and PeTS EOS results for the vapor-liquid equilibrium of the binary LJTS mixture G ($\varepsilon_2/\varepsilon_1 = 0.6$ and $\xi_{12} = 0.85$) for the temperatures $T/\varepsilon k_B^{-1} = 0.66, 0.715, 0.77, 0.825, 0.88$. The number in the parentheses indicates the statistical uncertainty in the last decimal digit.

$x_2'/\mathrm{mol\,mol^{-1}}$	$p / \varepsilon\sigma^{-3}$		$x_2'' / \mathrm{mol\,mol^{-1}}$		ρ' / σ^{-3}		ρ'' / σ^{-3}	
	MD	EOS	MD	EOS	MD	EOS	MD	EOS
$T = 0.66\,\varepsilon k_B^{-1}$								
0.000	0.0030(1)	0.0029	0.000	0.000	0.808(4)	0.8084	0.0047(3)	0.0046
0.009(1)	0.0066(2)	0.0074	0.534(16)	0.5874	0.806(5)	0.8070	0.0106(8)	0.0108
0.0077(5)	0.0072(2)	0.0067	0.580(18)	0.5503	0.807(5)	0.8067	0.0115(8)	0.0119
0.018(1)	0.0101(2)	0.0119	0.690(15)	0.7337	0.804(6)	0.8049	0.0164(9)	0.0197
0.027(1)	0.0135(3)	0.0161	0.759(9)	0.7953	0.803(7)	0.8032	0.022(1)	0.0274
0.036(1)	0.0168(2)	0.0201	0.803(8)	0.8294	0.801(8)	0.8015	0.029(1)	0.0351
0.045(1)	0.0199(3)	0.0242	0.824(9)	0.8527	0.799(9)	0.7997	0.035(1)	0.0438
0.055(2)	0.0235(3)	0.0283	0.848(8)	0.8687	0.797(11)	0.7978	0.042(1)	0.0532
0.063(3)	0.0271(5)	0.0315	0.863(8)	0.8777	0.796(11)	0.7963	0.050(2)	0.0609
0.075(2)	0.0295(4)	0.0366	0.872(6)	0.8886	0.793(12)	0.7938	0.056(2)	0.0750
0.085(2)	0.0329(4)	0.0403	0.880(8)	0.8941	0.791(14)	0.7919	0.064(2)	0.0865
0.092(5)	0.0364(6)	0.0432	0.891(6)	0.8974	0.789(13)	0.7903	0.074(2)	0.0967
0.111(2)	0.0387(3)	0.0504	0.889(9)	0.9019	0.785(20)	0.7864	0.081(2)	0.1295
0.117(4)	0.0430(4)	0.0525	0.901(5)	0.9020	0.784(18)	0.7853	0.095(3)	0.1429
$T = 0.715\,\varepsilon k_B^{-1}$								
0.000	0.0058(3)	0.0058	0.000	0.000	0.779(3)	0.7789	0.0087(4)	0.0087
0.0096(4)	0.0106(3)	0.0110	0.426(10)	0.4476	0.777(5)	0.7769	0.0160(8)	0.0167
0.0129(9)	0.0125(3)	0.0128	0.496(8)	0.5176	0.777(5)	0.7762	0.019(1)	0.0196
0.027(1)	0.0184(4)	0.0203	0.651(10)	0.6775	0.773(6)	0.7732	0.029(1)	0.0322
0.043(2)	0.0238(4)	0.0278	0.715(11)	0.7498	0.770(8)	0.7700	0.038(1)	0.0462
0.056(2)	0.0300(4)	0.0344	0.764(8)	0.7862	0.767(9)	0.7671	0.050(2)	0.0598
0.071(1)	0.0355(4)	0.0409	0.786(8)	0.8092	0.76(1)	0.7640	0.062(2)	0.0746
0.084(3)	0.0415(5)	0.0467	0.809(5)	0.8233	0.76(1)	0.7611	0.076(2)	0.0897
0.109(2)	0.0454(6)	0.0575	0.820(8)	0.8384	0.75(1)	0.7554	0.085(2)	0.1244
0.124(6)	0.0512(8)	0.0635	0.831(8)	0.8416	0.75(2)	0.7521	0.102(3)	0.1497
0.142(5)	0.0568(9)	0.0712	0.836(5)	0.8396	0.74(2)	0.7480	0.121(3)	0.1959
0.178(8)	0.0639(9)	0.1066	0.840(6)	0.7357	0.73(3)	0.7429	0.152(7)	0.5084
$T = 0.77\,\varepsilon k_B^{-1}$								
0.000	0.0105(3)	0.0104	0.000	0.000	0.749(3)	0.7480	0.0152(6)	0.0150
0.0045(3)	0.0128(3)	0.0130	0.164(6)	0.1821	0.748(4)	0.7470	0.0185(8)	0.0189
0.0097(6)	0.0151(3)	0.0160	0.272(13)	0.3193	0.746(5)	0.7458	0.022(1)	0.0234
0.0136(9)	0.0178(3)	0.0182	0.371(12)	0.3914	0.745(5)	0.7449	0.026(1)	0.0268
0.0271(9)	0.0242(3)	0.0257	0.517(8)	0.5446	0.742(6)	0.7418	0.036(1)	0.0389
0.044(1)	0.0308(3)	0.0349	0.607(9)	0.6416	0.737(8)	0.7378	0.047(2)	0.0551
0.056(1)	0.0371(4)	0.0411	0.652(9)	0.6810	0.734(8)	0.7349	0.059(2)	0.0670
0.075(2)	0.0435(7)	0.0501	0.696(9)	0.7194	0.729(9)	0.7305	0.071(2)	0.0863
0.089(1)	0.0499(4)	0.0570	0.717(5)	0.7387	0.73(1)	0.7268	0.085(2)	0.1031
0.122(3)	0.0617(6)	0.0715	0.747(6)	0.7607	0.72(1)	0.7186	0.115(3)	0.1464
0.146(3)	0.0666(6)	0.0820	0.753(11)	0.7641	0.71(1)	0.7123	0.129(3)	0.1889
0.163(4)	0.0731(6)	0.0894	0.767(7)	0.7598	0.70(2)	0.7078	0.150(4)	0.2276
0.191(8)	0.078(1)	0.1025	0.763(9)	0.7372	0.69(2)	0.7008	0.170(5)	0.3148
0.215(14)	0.084(1)	0.1165	0.757(15)	0.6988	0.68(3)	0.6953	0.204(8)	0.4069
$T = 0.825\,\varepsilon k_B^{-1}$								
0.000	0.0175(3)	0.0173	0.000	0.000	0.716(3)	0.7149	0.025(1)	0.0246
0.0041(3)	0.0200(4)	0.0198	0.114(6)	0.1091	0.714(3)	0.7139	0.029(1)	0.0282
0.0083(9)	0.0219(4)	0.0223	0.173(8)	0.1953	0.713(4)	0.7128	0.031(1)	0.0319
0.0177(6)	0.0275(4)	0.0279	0.308(9)	0.3301	0.711(5)	0.7103	0.040(1)	0.0404

$x_2'/\mathrm{mol\,mol^{-1}}$	$p\ /\ \varepsilon\sigma^{-3}$		$x_2''\ /\ \mathrm{mol\,mol^{-1}}$		$\rho'\ /\ \sigma^{-3}$		$\rho''\ /\ \sigma^{-3}$	
	MD	EOS	MD	EOS	MD	EOS	MD	EOS
0.029(2)	0.0327(5)	0.0343	0.40(1)	0.4314	0.707(6)	0.7074	0.048(2)	0.0507
0.038(1)	0.0371(5)	0.0397	0.46(1)	0.4906	0.704(6)	0.7049	0.055(2)	0.0598
0.048(1)	0.0413(4)	0.0449	0.51(1)	0.5341	0.701(7)	0.7023	0.062(2)	0.0692
0.069(2)	0.0501(5)	0.0561	0.57(1)	0.5971	0.695(9)	0.6964	0.078(2)	0.0910
0.103(2)	0.0633(5)	0.0727	0.62(1)	0.6477	0.68(1)	0.6868	0.106(3)	0.1297
0.125(3)	0.0713(6)	0.0829	0.65(1)	0.6629	0.68(1)	0.6801	0.125(3)	0.1589
0.158(6)	0.082(1)	0.0973	0.66(1)	0.6686	0.66(1)	0.6700	0.157(4)	0.2098
0.191(5)	0.090(1)	0.1110	0.67(1)	0.6585	0.65(2)	0.6597	0.184(5)	0.2701
$T = 0.88\,\varepsilon k_\mathrm{B}^{-1}$								
0.000	0.0271(4)	0.0270	0.000	0.000	0.679(3)	0.6782	0.039(1)	0.0384
0.0098(6)	0.0325(4)	0.0331	0.134(5)	0.1479	0.676(4)	0.6752	0.046(1)	0.0475
0.0143(5)	0.0350(3)	0.0359	0.181(6)	0.1993	0.674(4)	0.6739	0.050(2)	0.0517
0.0185(6)	0.0377(4)	0.0384	0.227(6)	0.2391	0.673(5)	0.6726	0.055(2)	0.0556
0.0248(9)	0.0401(4)	0.0421	0.259(8)	0.2902	0.670(4)	0.6707	0.058(2)	0.0616
0.027(2)	0.0411(7)	0.0437	0.274(8)	0.3088	0.669(6)	0.6698	0.060(2)	0.0642
0.029(1)	0.0425(4)	0.0445	0.293(6)	0.3182	0.669(5)	0.6694	0.062(2)	0.0656
0.0345(1)	0.0453(4)	0.0479	0.326(6)	0.3523	0.667(5)	0.6676	0.067(2)	0.0712
0.038(2)	0.0480(6)	0.0501	0.353(9)	0.3726	0.666(6)	0.6663	0.071(2)	0.0751
0.043(1)	0.0501(6)	0.0525	0.372(7)	0.3923	0.664(6)	0.6650	0.075(2)	0.0793
0.100(2)	0.0756(6)	0.0824	0.505(9)	0.5279	0.642(9)	0.6458	0.126(3)	0.1423
0.166(6)	0.0949(11)	0.1116	0.55(1)	0.5554	0.612(15)	0.6214	0.177(5)	0.2320
0.223(11)	0.1126(7)	0.1330	0.52(6)	0.5338	0.583(17)	0.5981	0.27(2)	0.3196

Table A.8: Interfacial properties of the binary LJTS mixture A ($\varepsilon_2/\varepsilon_1 = 0.9$ and $\xi_{12} = 1$) for the temperatures $T/\varepsilon k_{\mathrm{B}}^{-1} = 0.66$, 0.715, 0.825, 0.88. Results from MD and DGT+PeTS. Both methods are calculated at the same liquid phase composition. The number in the parentheses indicates the statistical uncertainty in the last decimal digit.

$x_2'/\mathrm{mol\,mol^{-1}}$	γ / $\varepsilon\sigma^{-2}$		$\Gamma_2^{(1)}$ / σ^{-2}		E_2		L_{10}^{90} / σ	
	MD	DGT	MD	DGT	MD	DGT	MD	DGT
$T = 0.66\,\varepsilon k_{\mathrm{B}}^{-1}$								
0.00	0.655(26)	0.6632	-	-	-	-	2.06(5)	1.94
0.005(1)	0.649(18)	0.6620	0.003(10)	0.002	1.32(13)	1.03	2.05(4)	1.94
0.055(1)	0.647(31)	0.6506	0.032(20)	0.019	1.11(5)	1.02	2.07(4)	1.96
0.100(1)	0.627(25)	0.6405	0.07(2)	0.034	1.08(2)	1.01	2.07(6)	1.96
0.157(2)	0.626(23)	0.6280	0.09(5)	0.052	1.06(2)	1.01	2.12(5)	1.98
0.208(1)	0.612(30)	0.6170	-0.11(4)	0.067	0.99(2)	1.00	2.11(5)	1.98
0.251(1)	0.604(24)	0.6080	0.07(3)	0.080	1.04(1)	1.00	2.16(4)	2.00
0.297(1)	0.590(19)	0.5984	0.11(7)	0.093	1.03(2)	1.00	2.16(5)	2.00
0.354(1)	0.582(28)	0.5869	0.08(4)	0.109	1.02(1)	1.00	2.19(3)	2.02
0.388(2)	0.568(24)	0.5803	0.08(7)	0.117	1.03(1)	1.00	2.22(6)	2.02
0.437(2)	0.565(26)	0.5708	0.16(8)	0.130	1.02(1)	1.00	2.23(3)	2.04
0.490(1)	0.559(20)	0.5606	0.01(13)	0.143	1.02(1)	1.00	2.22(4)	2.06
0.533(1)	0.542(23)	0.5523	0.04(12)	0.153	1.01(1)	1.00	2.25(5)	2.08
0.584(1)	0.534(20)	0.5429	0.11(21)	0.165	1.01(1)	1.00	2.28(6)	2.08
0.630(2)	0.524(27)	0.5345	0.03(20)	0.175	1.01(1)	1.00	2.29(5)	2.08
0.683(1)	0.517(23)	0.5251	-0.05(11)	0.186	1.01(1)	1.00	2.31(5)	2.10
0.731(1)	0.513(27)	0.5166	-0.04(12)	0.196	1.01(1)	1.00	2.33(6)	2.12
0.772(1)	0.499(28)	0.5095	0.1(2)	0.204	1.01(0)	1.00	2.36(5)	2.12
0.824(2)	0.494(23)	0.5006	-0.02(36)	0.214	1.01(1)	1.00	2.36(3)	2.14
0.874(1)	0.484(28)	0.4920	0.03(56)	0.223	1.01(1)	1.00	2.37(5)	2.14
0.929(1)	0.479(28)	0.4829	-0.23(84)	0.232	1.01(0)	1.00	2.39(5)	2.16
1.00	0.467(21)	0.4729	-	-	-	-	2.41(5)	2.18
$T = 0.715\,\varepsilon k_{\mathrm{B}}^{-1}$								
0.000	0.541(26)	0.5579	-	-	-	-	2.34(5)	2.12
0.0049(2)	0.543(20)	0.5568	0.004(3)	0.002	1.35(12)	1.01	2.31(5)	2.12
0.053(1)	0.537(21)	0.5463	0.01(2)	0.016	1.11(4)	1.00	2.35(4)	2.12
0.105(2)	0.526(24)	0.5350	0.03(3)	0.031	1.06(3)	1.00	2.37(5)	2.14
0.151(1)	0.511(22)	0.5255	0.03(4)	0.044	1.04(2)	1.00	2.40(4)	2.16
0.200(1)	0.502(23)	0.5152	0.10(7)	0.058	1.04(2)	1.00	2.44(4)	2.16
0.243(1)	0.497(23)	0.5064	0.06(7)	0.069	1.03(2)	1.00	2.44(7)	2.20
0.289(2)	0.484(22)	0.4973	0.03(7)	0.081	1.03(2)	1.00	2.47(7)	2.20
0.339(1)	0.482(16)	0.4876	0.11(10)	0.093	1.03(2)	1.00	2.52(5)	2.22
0.380(2)	0.474(24)	0.4797	0.09(11)	0.103	1.03(2)	1.00	2.51(5)	2.24
0.427(2)	0.465(18)	0.4707	0.10(07)	0.114	1.02(1)	1.00	2.53(5)	2.24
0.476(1)	0.453(21)	0.4616	0.08(5)	0.125	1.02(1)	1.00	2.58(6)	2.26
0.520(1)	0.445(22)	0.4535	0.12(9)	0.134	1.02(1)	1.00	2.59(7)	2.28
0.562(1)	0.439(27)	0.4458	0.05(9)	0.143	1.01(1)	1.00	2.63(7)	2.30
0.619(2)	0.429(21)	0.4356	0.2(3)	0.155	1.02(1)	1.00	2.66(7)	2.32
0.661(3)	0.424(25)	0.4283	0.04(23)	0.163	1.01(1)	1.00	2.68(6)	2.34
0.711(1)	0.414(25)	0.4197	-0.11(18)	0.172	1.01(1)	1.00	2.64(5)	2.34
0.759(2)	0.406(25)	0.4114	-0.04(30)	0.181	1.01(1)	1.00	2.67(6)	2.36
0.810(1)	0.398(26)	0.4028	0.09(27)	0.190	1.013(5)	1.00	2.74(5)	2.38
0.853(1)	0.387(25)	0.3957	0.02(34)	0.197	1.010(4)	1.00	2.76(7)	2.40
0.899(1)	0.382(23)	0.3882	-0.1(4)	0.205	1.009(4)	1.00	2.77(5)	2.42
0.948(1)	0.375(29)	0.3802	-0.8(8)	0.213	1.004(3)	1.00	2.83(7)	2.44

x_2'/mol mol^{-1}	γ / $\varepsilon\sigma^{-2}$		$\Gamma_2^{(1)}$ / σ^{-2}		E_2		L_{10}^{90} / σ	
	MD	DGT	MD	DGT	MD	DGT	MD	DGT
1.000	0.364(13)	0.3734	-	-	-	-	2.83(5)	2.44
$T = 0.825\,\varepsilon k_{\mathrm{B}}^{-1}$								
0.000	0.350(17)	0.3598	-	-	-	-	3.06(7)	2.62
0.0055(3)	0.347(14)	0.3587	0.00(1)	0.001	1.24(12)	1.00	3.09(8)	2.64
0.051(1)	0.343(16)	0.3497	0.04(2)	0.012	1.09(5)	1.00	3.17(8)	2.66
0.096(1)	0.329(14)	0.3408	0.01(3)	0.023	1.04(2)	1.00	3.18(7)	2.68
0.145(1)	0.323(17)	0.3314	0.04(5)	0.034	1.03(2)	1.00	3.26(9)	2.70
0.195(2)	0.311(15)	0.3221	0.01(4)	0.044	1.02(2)	1.00	3.30(9)	2.74
0.246(1)	0.306(14)	0.3125	0.03(7)	0.055	1.02(2)	1.00	3.33(9)	2.78
0.280(1)	0.302(19)	0.3064	0.08(7)	0.062	1.02(1)	1.00	3.35(7)	2.80
0.330(1)	0.282(20)	0.2973	0.07(5)	0.072	1.02(1)	1.00	3.39(7)	2.84
0.351(2)	0.285(17)	0.2936	0.07(9)	0.076	1.02(1)	1.00	3.47(10)	2.86
0.390(2)	0.280(20)	0.2867	0.03(10)	0.084	1.02(2)	1.00	3.46(6)	2.88
0.435(2)	0.272(20)	0.2788	0.06(7)	0.092	1.02(1)	1.00	3.50(9)	2.92
0.481(2)	0.263(20)	0.2709	0.08(8)	0.100	1.02(1)	1.00	3.53(8)	2.94
0.526(2)	0.253(18)	0.2632	0.05(12)	0.108	1.013(4)	1.00	3.62(12)	2.98
0.562(4)	0.253(16)	0.2572	0.05(10)	0.114	1.002(12)	1.00	3.54(12)	3.02
0.604(2)	0.242(19)	0.2503	0.05(23)	0.121	1.012(7)	1.00	3.75(12)	3.04
0.651(1)	0.237(19)	0.2425	-0.07(17)	0.129	1.008(7)	1.00	3.71(10)	3.08
0.795(2)	0.207(14)	0.2194	0.04(20)	0.150	1.007(3)	1.00	3.96(9)	3.20
0.83(4)	0.199(13)	0.2145	0.03(26)	0.154	1.007(3)	1.00	3.96(12)	3.22
0.895(1)	0.196(12)	0.2040	0.28(18)	0.163	1.008(4)	1.00	4.09(10)	3.30
0.948(1)	0.189(11)	0.1959	-0.08(33)	0.170	1.008(3)	1.00	4.16(12)	3.34
0.959(1)	0.189(15)	0.1942	0.35(31)	0.171	1.008(1)	1.00	4.20(16)	3.36
1.000	0.180(8)	0.1896	-	-	-	-	4.20(11)	3.40
$T = 0.88\,\varepsilon k_{\mathrm{B}}^{-1}$								
0.000	0.264(14)	0.2675	-	-	-	-	3.67(9)	3.04
0.0051(3)	0.253(14)	0.2665	0.002(7)	0.001	1.43(9)	1.00	3.68(8)	3.04
0.050(1)	0.247(8)	0.2582	0.006(13)	0.011	1.11(2)	1.00	3.75(12)	3.06
0.098(1)	0.239(12)	0.2494	0.03(3)	0.020	1.10(2)	1.00	3.83(9)	3.12
0.143(1)	0.233(15)	0.2412	0.05(2)	0.029	1.07(1)	1.00	3.90(11)	3.18
0.187(1)	0.226(11)	0.2334	0.02(4)	0.038	1.05(2)	1.00	3.95(10)	3.20
0.240(2)	0.213(14)	0.2242	0.01(4)	0.047	1.04(1)	1.00	4.01(9)	3.28
0.280(2)	0.208(13)	0.2174	0.07(5)	0.055	1.06(1)	1.00	4.04(13)	3.32
0.322(2)	0.204(13)	0.2102	0.08(4)	0.062	1.04(1)	1.00	4.03(15)	3.36
0.365(2)	0.197(15)	0.2029	0.09(4)	0.069	1.03(1)	1.00	4.17(11)	3.40
0.356(2)	0.202(16)	0.2045	0.08(5)	0.068	1.04(1)	1.00	4.18(12)	3.38
0.401(3)	0.194(17)	0.1970	0.05(7)	0.075	1.03(1)	1.00	4.22(19)	3.44
0.431(2)	0.188(17)	0.1921	0.04(7)	0.080	1.03(1)	1.00	4.26(13)	3.48
0.478(4)	0.180(18)	0.1845	0.05(6)	0.087	1.01(2)	1.00	4.37(16)	3.54
0.514(3)	0.174(19)	0.1787	-0.01(9)	0.093	1.00(3)	1.00	4.49(3)	3.58
0.552(4)	0.164(18)	0.1728	0.10(10)	0.098	1.02(2)	1.00	4.46(19)	3.64
0.576(6)	0.164(18)	0.1689	-0.07(6)	0.102	1.01(3)	1.00	4.6(4)	3.66
0.622(5)	0.156(16)	0.1619	-0.02(8)	0.108	1.01(2)	1.00	4.66(5)	3.74
0.651(5)	0.148(21)	0.1573	-0.08(7)	0.112	1.01(2)	1.00	4.7(3)	3.76
0.873(1)	0.113(8)	0.1245	0.20(19)	0.139	1.010(4)	1.00	5.2(2)	4.16
0.76(9)	0.119(11)	0.1411	0.31(32)	0.126	1.01(6)	1.00	5.03(2)	3.94
0.929(1)	0.108(10)	0.1165	0.19(20)	0.144	1.008(2)	1.00	5.38(19)	4.26
0.946(1)	0.103(11)	0.1141	0.0(3)	0.146	1.007(3)	1.00	5.38(24)	4.30
0.969(1)	0.103(12)	0.1109	-0.2(5)	0.148	1.008(3)	1.00	5.63(26)	4.36
1.000	0.097(13)	0.1080	-	-	-	-	5.70(26)	4.38

Table A.9: Interfacial properties of the binary LJTS mixture G ($\varepsilon_2/\varepsilon_1$ = 0.6 and ξ_{12} = 0.85) for the temperatures $T/\varepsilon k_{\mathrm{B}}^{-1}$ = 0.66, 0.715, 0.77, 0.825, 0.88. Results from MD and DGT+PeTS. Both methods are calculated at the same liquid phase composition. The number in the parentheses indicates the statistical uncertainty in the last decimal digit.

$x_2'/\mathrm{mol\,mol^{-1}}$	γ / $\varepsilon\sigma^{-2}$		$\Gamma_2^{(1)}$ / σ^{-2}		E_2		L_{10}^{90} / σ	
	MD	DGT	MD	DGT	MD	DGT	MD	DGT
$T = 0.66\,\varepsilon k_{\mathrm{B}}^{-1}$								
0.000	0.655(26)	0.6632	-	-	-	-	2.06(5)	1.94
0.009(1)	0.601(22)	0.6152	0.07(1)	0.075	4.6(6)	7.12	2.19(6)	2.06
0.0077(5)	0.609(28)	0.6222	0.07(1)	0.064	5.8(3)	7.10	2.18(5)	2.04
0.018(1)	0.573(24)	0.5659	0.12(1)	0.157	4.5(3)	7.22	2.28(5)	2.20
0.027(1)	0.536(25)	0.5201	0.19(2)	0.238	4.3(3)	7.23	2.45(5)	2.34
0.036(1)	0.493(34)	0.4768	0.25(2)	0.318	4.2(2)	7.08	2.58(6)	2.48
0.045(1)	0.477(35)	0.4317	0.31(3)	0.406	4.0(2)	6.74	2.73(3)	2.66
0.055(2)	0.430(30)	0.3871	0.35(2)	0.498	4.0(1)	6.32	2.92(4)	2.88
0.063(3)	0.393(30)	0.3535	0.48(4)	0.573	4.1(3)	5.98	3.15(8)	3.08
0.075(2)	0.366(37)	0.2988	0.53(4)	0.709	3.7(2)	5.38	3.31(10)	3.48
0.085(2)	0.328(31)	0.2594	0.64(6)	0.825	3.7(1)	4.93	3.59(7)	3.88
0.092(5)	0.295(17)	0.2285	0.75(5)	0.933	3.8(3)	4.58	3.00(14)	4.28
0.111(2)	0.260(19)	0.1493	0.75(6)	1.360	3.3(1)	3.67	4.30(17)	6.12
0.117(4)	0.215(32)	0.1253	1.08(5)	1.594	3.5(2)	3.38	5.08(16)	7.22
$T = 0.715\,\varepsilon k_{\mathrm{B}}^{-1}$								
0.000	0.541(26)	0.5579	-	-	-	-	2.34(5)	2.12
0.0096(4)	0.511(22)	0.5189	0.05(1)	0.056	3.7(4)	4.93	2.45(5)	2.22
0.0129(9)	0.494(17)	0.5055	0.08(1)	0.076	3.9(4)	4.90	2.50(7)	2.26
0.027(1)	0.452(25)	0.4496	0.14(2)	0.162	3.4(2)	4.73	2.69(5)	2.44
0.043(2)	0.413(18)	0.3944	0.18(2)	0.252	3.0(2)	4.48	2.89(7)	2.68
0.056(2)	0.363(32)	0.3466	0.30(3)	0.336	3.1(1)	4.19	3.19(9)	2.92
0.071(1)	0.319(31)	0.3008	0.38(4)	0.422	3.0(1)	3.87	3.44(8)	3.20
0.084(3)	0.273(29)	0.2608	0.44(3)	0.504	2.9(1)	3.56	3.9(1)	3.52
0.109(2)	0.257(19)	0.1891	0.50(5)	0.675	2.5(1)	2.95	4.0(1)	4.36
0.124(6)	0.208(26)	0.1514	0.64(6)	0.784	2.5(1)	2.59	4.6(2)	5.10
0.142(5)	0.172(22)	0.1061	0.77(6)	0.932	2.43(6)	2.11	5.4(2)	6.52
0.178(8)	0.112(24)	0.0330	0.96(7)	0.180	2.13(8)	1.02	6.8(4)	5.76
$T = 0.77\,\varepsilon k_{\mathrm{B}}^{-1}$								
0.000	0.454(20)	0.4567	-	-	-	-	2.68(4)	2.32
0.0045(3)	0.439(28)	0.4423	0.019(4)	0.019	2.8(4)	3.58	2.74(6)	2.38
0.0097(6)	0.411(18)	0.4258	0.03(1)	0.041	2.5(3)	3.53	2.78(7)	2.44
0.0136(9)	0.406(14)	0.4138	0.05(1)	0.057	2.9(4)	3.50	2.87(8)	2.48
0.0271(9)	0.366(23)	0.3734	0.10(1)	0.113	2.7(1)	3.36	3.01(6)	2.64
0.044(1)	0.331(22)	0.3250	0.14(3)	0.184	2.4(1)	3.15	3.2(1)	2.88
0.056(1)	0.303(20)	0.2935	0.20(3)	0.232	2.5(1)	3.00	3.5(1)	3.06
0.075(2)	0.270(22)	0.2485	0.27(2)	0.304	2.2(1)	2.76	3.7(1)	3.38
0.089(1)	0.219(22)	0.2154	0.29(2)	0.360	2.22(6)	2.56	4.0(1)	3.68
0.122(3)	0.170(18)	0.1507	0.45(3)	0.474	2.06(8)	2.12	4.9(2)	4.52
0.146(3)	0.150(17)	0.1090	0.49(5)	0.544	1.88(6)	1.80	5.1(2)	5.40
0.163(4)	0.115(16)	0.0834	0.59(6)	0.566	1.83(6)	1.58	6.1(3)	6.14
0.191(8)	0.088(19)	0.0492	0.60(6)	0.492	1.66(4)	1.26	6.7(4)	7.28
0.215(14)	0.063(18)	0.0282	0.68(11)	0.318	1.56(4)	1.07	8.0(7)	7.72
$T = 0.825\,\varepsilon k_{\mathrm{B}}^{-1}$								
0.000	0.350(17)	0.3598	-	-	-	-	3.06(7)	2.62
0.0041(3)	0.346(16)	0.3493	0.02(1)	0.013	2.5(2)	2.70	3.19(5)	2.68

$x_2'/\mathrm{mol\,mol^{-1}}$	$\gamma\ /\ \varepsilon\sigma^{-2}$		$\Gamma_2^{(1)}\ /\ \sigma^{-2}$		E_2		$L_{10}^{90}\ /\ \sigma$	
	MD	DGT	MD	DGT	MD	DGT	MD	DGT
0.0083(9)	0.335(13)	0.3387	0.02(1)	0.026	2.1(3)	2.67	3.19(8)	2.72
0.0177(6)	0.303(16)	0.3159	0.05(2)	0.054	2.2(1)	2.60	3.35(8)	2.82
0.029(2)	0.280(14)	0.2901	0.08(2)	0.087	2.1(2)	2.51	3.5(1)	2.96
0.038(1)	0.268(12)	0.2690	0.12(2)	0.115	2.1(1)	2.43	3.6(1)	3.10
0.048(1)	0.245(15)	0.2487	0.15(2)	0.142	2.0(1)	2.35	3.7(1)	3.24
0.069(2)	0.212(22)	0.2071	0.18(3)	0.198	1.8(1)	2.17	4.1(1)	3.56
0.103(2)	0.163(12)	0.1497	0.25(4)	0.278	1.74(6)	1.88	4.8(2)	4.24
0.125(3)	0.130(12)	0.1177	0.29(3)	0.320	1.64(6)	1.70	5.3(2)	4.78
0.158(6)	0.095(19)	0.0783	0.37(4)	0.358	1.54(7)	1.45	6.4(3)	5.74
0.191(5)	0.064(17)	0.0486	0.37(7)	0.349	1.42(4)	1.25	7.2(6)	6.82
$T = 0.88\,\varepsilon k_{\mathrm{B}}^{-1}$								
0.000	0.264(14)	0.2675	-	-	-	-	3.67(9)	3.04
0.0098(6)	0.236(13)	0.2481	0.01(1)	0.022	1.77(19)	2.08	3.81(8)	3.16
0.0143(5)	0.227(16)	0.2394	0.03(1)	0.032	1.81(13)	2.06	3.89(9)	3.20
0.0185(6)	0.225(15)	0.2316	0.05(1)	0.041	1.85(13)	2.03	4.0(1)	3.26
0.0248(9)	0.214(14)	0.2201	0.04(2)	0.055	1.69(12)	1.99	4.0(1)	3.36
0.027(2)	0.210(14)	0.2153	0.06(1)	0.060	1.62(17)	1.98	4.1(1)	3.38
0.029(1)	0.209(19)	0.2128	0.06(1)	0.063	1.72(11)	1.97	4.1(1)	3.40
0.0345(1)	0.201(18)	0.2028	0.08(1)	0.075	1.70(11)	1.93	4.3(1)	3.50
0.038(2)	0.192(10)	0.1961	0.09(3)	0.083	1.71(12)	1.91	4.4(2)	3.56
0.043(1)	0.184(9)	0.1891	0.09(2)	0.091	1.71(8)	1.88	4.4(1)	3.60
0.100(2)	0.105(16)	0.1085	0.19(3)	0.186	1.52(5)	1.55	5.7(2)	4.74
0.166(6)	0.056(14)	0.0476	0.22(5)	0.228	1.28(6)	1.24	7.5(6)	6.66
0.223(11)	0.021(18)	0.0187	0.19(8)	0.185	1.14(3)	1.07	10.3(20)	8.88

A.4 Simulation Results for the LJ Fluid

This Appendix contains the following points:

- Table A.10 summarizes the results for the vapor-liquid equilibrium data of the Lennard-Jones fluid obtained in this work using the Grand Equilibrium method [685] as implemented in $ms2$ [575]

- Table A.11 and A.12 report the vapor-liquid equilibrium bulk and interfacial properties, respectively, from the direct VLE simulations using the code $ls1$ $mardyn$ [506]

Table A.10: Simulation results for the VLE data of the LJ fluid. The columns are from left to right: vapor pressure, saturated liquid density, saturated vapor density, and the enthalpy of vaporization. The numbers in parentheses indicate the uncertainties of the last decimal digits.

T / $\varepsilon k_{\mathrm{B}}^{-1}$	p^s / $\varepsilon\sigma^{-3}$	ρ' / σ^{-3}	ρ'' / σ^{-3}	Δh_v / ε
0.69	0.001172(24)	0.847111(1)	0.001729(35)	6.766422(34)
0.7	0.001343(25)	0.8427(1)	0.001956(36)	6.762403(39)
0.72	0.001784(28)	0.834385(1)	0.002538(39)	6.652809(43)
0.74	0.002319(29)	0.825751(1)	0.003227(40)	6.641588(48)
0.76	0.002932(32)	0.817195(2)	0.003994(44)	6.528674(58)
0.78	0.003689(40)	0.8083(1)	0.004929(54)	6.513863(71)
0.8	0.004649(44)	0.799470(2)	0.006103(57)	6.395171(72)
0.82	0.005608(44)	0.7903(1)	0.007233(57)	6.278050(94)
0.84	0.006872(44)	0.7812(1)	0.008730(55)	6.25512(12)
0.86	0.008299(53)	0.7718(1)	0.010397(66)	6.13070(14)
0.88	0.009902(63)	0.7623(1)	0.012248(78)	6.10391(17)
0.9	0.011795(39)	0.7527(1)	0.014435(48)	5.97235(16)
0.92	0.013783(67)	0.7427(1)	0.016686(81)	5.84091(21)
0.94	0.016237(79)	0.7328(1)	0.01952(10)	5.80088(26)
0.96	0.018686(63)	0.7224(1)	0.02228(07)	5.66382(30)
0.98	0.021625(75)	0.7120(1)	0.02567(09)	5.51804(44)
1	0.024843(87)	0.7009(1)	0.02938(10)	5.46904(50)
1.02	0.02823(10)	0.6899(1)	0.03329(12)	5.31864(67)
1.04	0.03216(11)	0.6785(1)	0.03795(13)	5.15826(69)
1.06	0.03623(09)	0.6664(1)	0.04277(11)	4.9978(11)
1.08	0.04058(10)	0.6537(2)	0.04799(11)	4.8332(12)
1.1	0.04568(12)	0.6409(2)	0.05443(14)	4.7536(16)
1.12	0.05112(13)	0.6275(2)	0.06145(15)	4.5688(18)
1.14	0.05674(16)	0.6133(2)	0.06885(19)	4.3817(24)
1.16	0.06323(20)	0.5985(2)	0.07810(24)	4.1717(33)
1.18	0.06957(21)	0.5820(2)	0.08715(26)	3.9681(39)
1.2	0.07684(25)	0.5639(3)	0.09862(32)	3.7339(59)
1.22	0.08429(33)	0.5446(4)	0.11101(44)	3.3941(87)
1.24	0.09260(36)	0.5235(5)	0.12657(50)	3.122(11)
1.26	0.10129(44)	0.5007(5)	0.14451(62)	2.823(16)
1.28	0.11082(39)	0.4747(8)	0.17041(60)	2.350(21)

Table A.11: MD and EOS results for the vapor-liquid equilibrium of the pure Lennard-Jones fluid. The columns are from left to right: the temperature, the vapour pressure, saturated liquid and vapour density. The number in the parentheses indicates the statistical uncertainty in the last decimal digit. The EOS results were obtained by the LJ EOS presented in this work, see below.

$T \ / \ \varepsilon k_{\mathrm{B}}^{-1}$	$p \ / \ \varepsilon \sigma^{-3}$		$\rho'' \ / \ \sigma^{-3}$		$\rho' \ / \ \sigma^{-3}$	
	MD	EOS	MD	EOS	MD	EOS
0.69	0.00110(10)	0.0012	0.00164(20)	0.0018	0.847(12)	0.8468
0.74	0.00230(10)	0.0023	0.00320(40)	0.0032	0.826(12)	0.8255
0.79	0.00395(10)	0.0042	0.00522(40)	0.0055	0.804(11)	0.8036
0.84	0.0069(2)	0.0069	0.0087(6)	0.0088	0.781(11)	0.7811
0.89	0.0108(1)	0.0109	0.0133(7)	0.0134	0.758(10)	0.7578
0.94	0.0164(1)	0.0162	0.0198(9)	0.0195	0.7327(90)	0.7333
0.99	0.0233(3)	0.0233	0.0276(10)	0.0276	0.7065(80)	0.7073
1.04	0.0323(2)	0.0323	0.0380(10)	0.0380	0.6782(70)	0.6793
1.09	0.0437(1)	0.0434	0.052(1)	0.0515	0.6478(80)	0.6486
1.14	0.0572(4)	0.0570	0.070(2)	0.0691	0.6134(70)	0.6142
1.19	0.0736(7)	0.0733	0.094(2)	0.0925	0.5734(60)	0.5744
1.24	0.0931(5)	0.0925	0.128(3)	0.1249	0.5240(60)	0.5257
1.29	0.1164(3)	0.1150	0.189(4)	0.1753	0.4521(40)	0.4595

Table A.12: MD and DGT results for the vapor-liquid interfacial properties of the pure Lennard-Jones fluid. The columns are from left to right: the temperature, surface tension, and interfacial thickness. The number in the parentheses indicates the statistical uncertainty in the last decimal digit.

$T \ / \ \varepsilon k_{\mathrm{B}}^{-1}$	$\gamma \ / \ \varepsilon \sigma^{-2}$		$L_{10}^{90} \ / \ \sigma$	
	MD	DGT	MD	DGT
0.69	1.18(2)	1.207	1.88(2)	2.21
0.74	1.07(3)	1.083	2.06(5)	2.33
0.79	0.95(3)	0.961	2.24(3)	2.47
0.84	0.85(2)	0.844	2.43(3)	2.63
0.89	0.74(2)	0.730	2.72(5)	2.82
0.94	0.62(2)	0.620	3.04(3)	3.05
0.99	0.52(2)	0.515	3.38(5)	3.33
1.04	0.42(3)	0.415	3.84(5)	3.67
1.09	0.32(1)	0.320	4.43(9)	4.13
1.14	0.24(1)	0.232	5.23(8)	4.75
1.19	0.15(1)	0.153	6.5(1)	5.65
1.24	0.08(1)	0.083	8.4(2)	7.21
1.29	0.03(1)	0.028	14.3(9)	10.82

A.5 Simulation Results for LJ Mixtures A - F

This Appendix contains the following points:

- density profiles at the planar vapor-liquid interfaces of the investigated LJ mixtures. The results from both MD and DGT are shown for all investigated mixtures, cf. Figs. A.13 - A.16

- numeric values of the Henry's law constants from MD simulations for the LJ mixtures D, E, and F (Table A.13)

- numeric values of the phase equilibria (Table A.14) and interfacial properties (Table A.15) results of the LJ mixtures A - F. Results from both MD simulations and the EOS+DGT are reported

Density Profiles
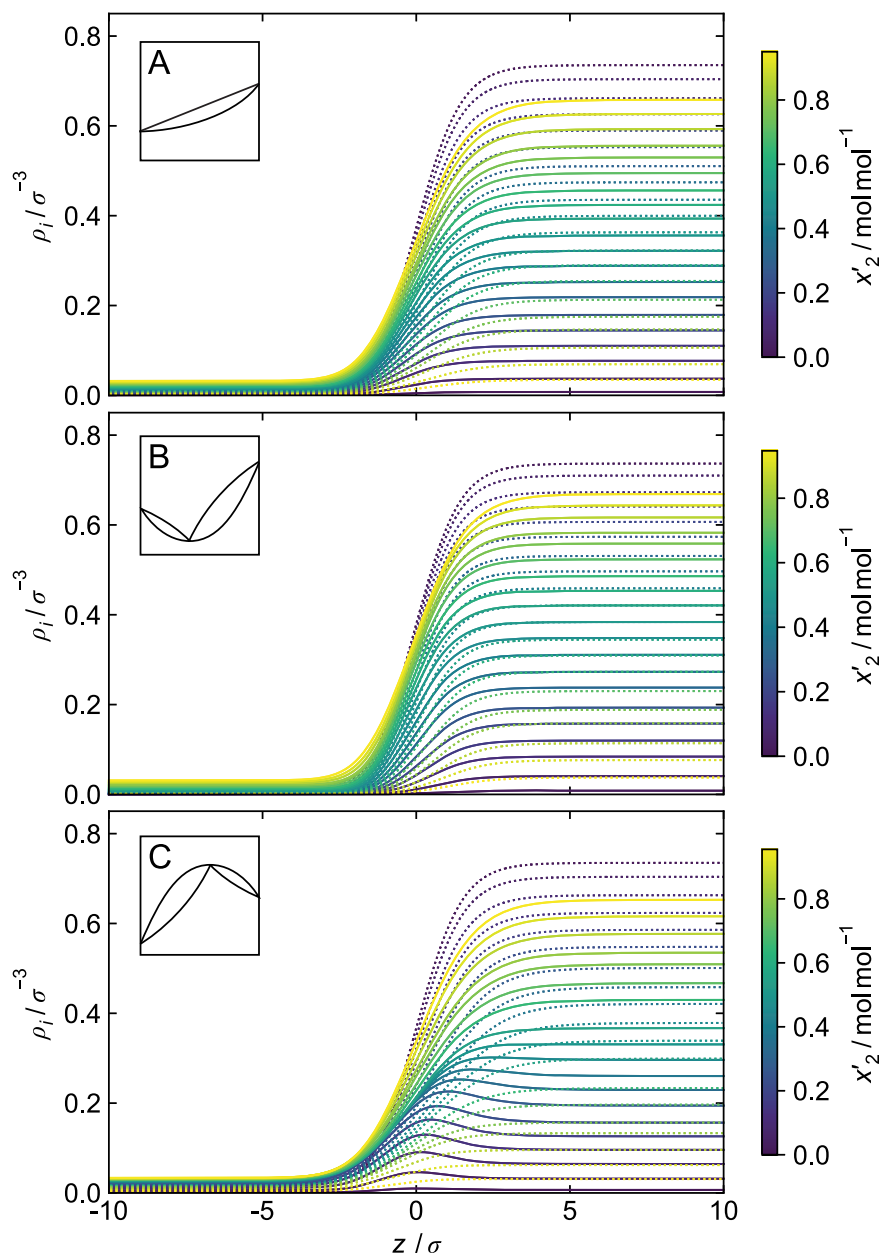
Figure A.13: Density profiles of the binary LJ mixtures A, B, and C at $T = 0.92\,\varepsilon k_{\mathrm{B}}^{-1}$. Results from DGT. Dashed lines: high-boiling component 1; solid lines: low-boiling component 2. The color indicates the liquid phase composition.
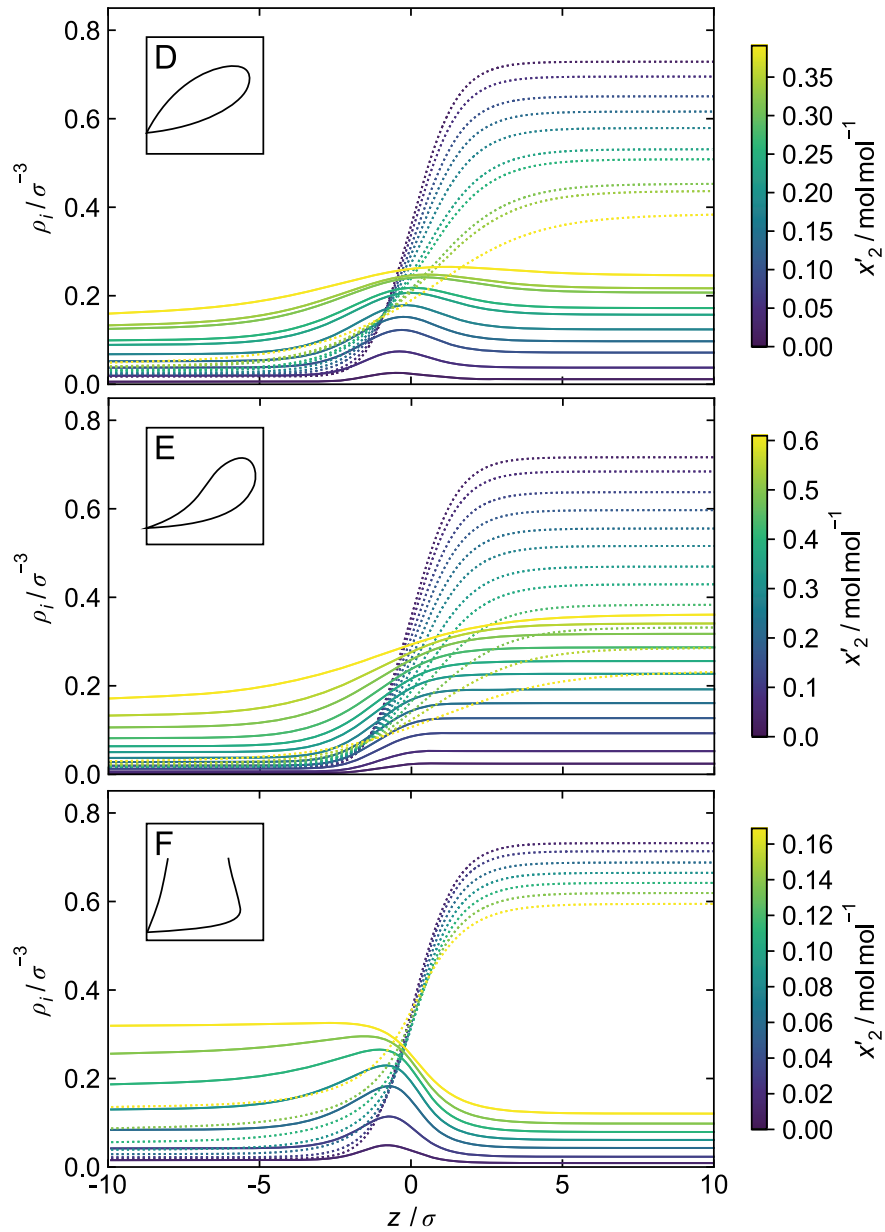
Figure A.14: Density profiles of the binary LJ mixtures D, E, and F at $T = 0.92\,\varepsilon k_{\mathrm{B}}^{-1}$. Results from DGT. Dashed lines: high-boiling component 1; solid lines: low-boiling component 2. The color indicates the liquid phase composition.
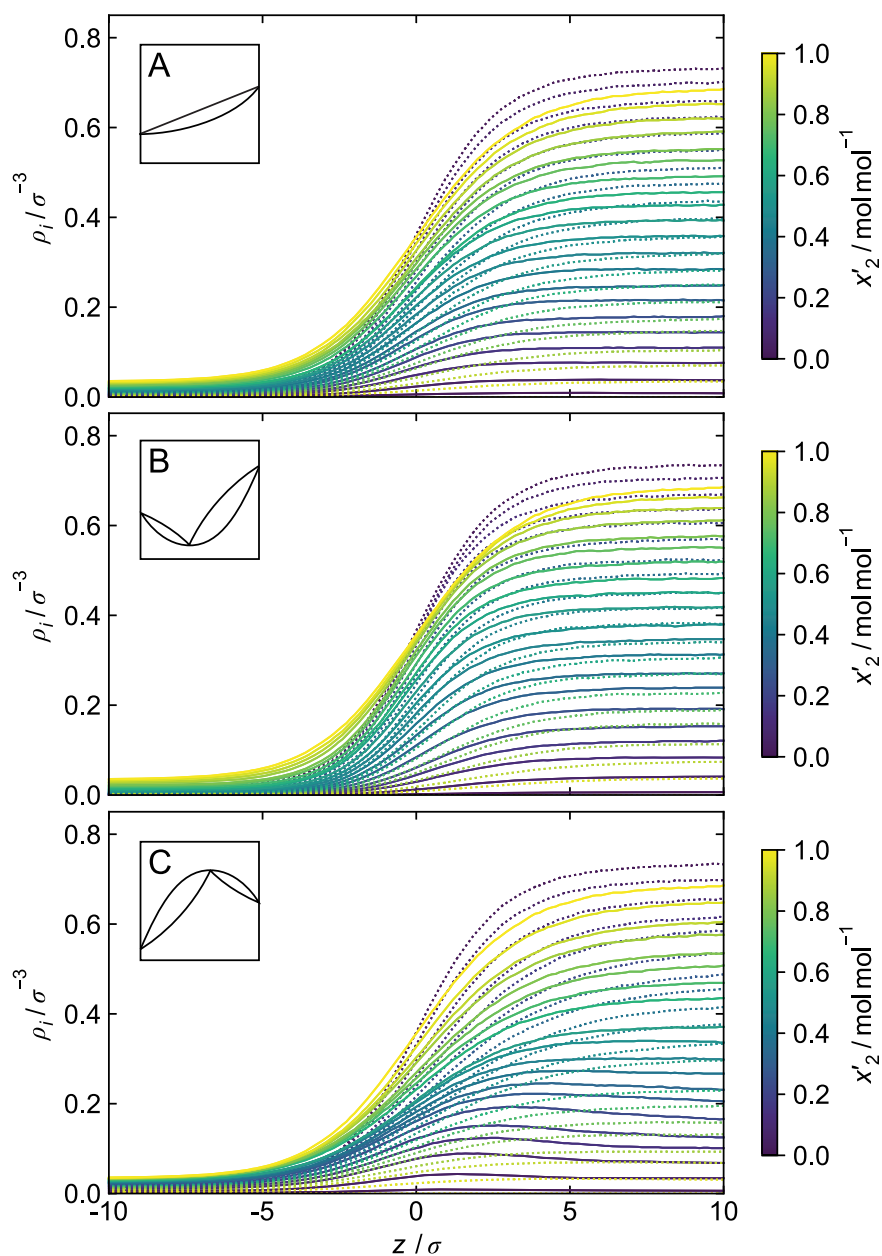
Figure A.15: Density profiles of the binary LJ mixtures A, B, and C at $T = 0.92\,\varepsilon k_{\mathrm{B}}^{-1}$. Results from MD. Dashed lines: high-boiling component 1; solid lines: low-boiling component 2. The color indicates the liquid phase composition.
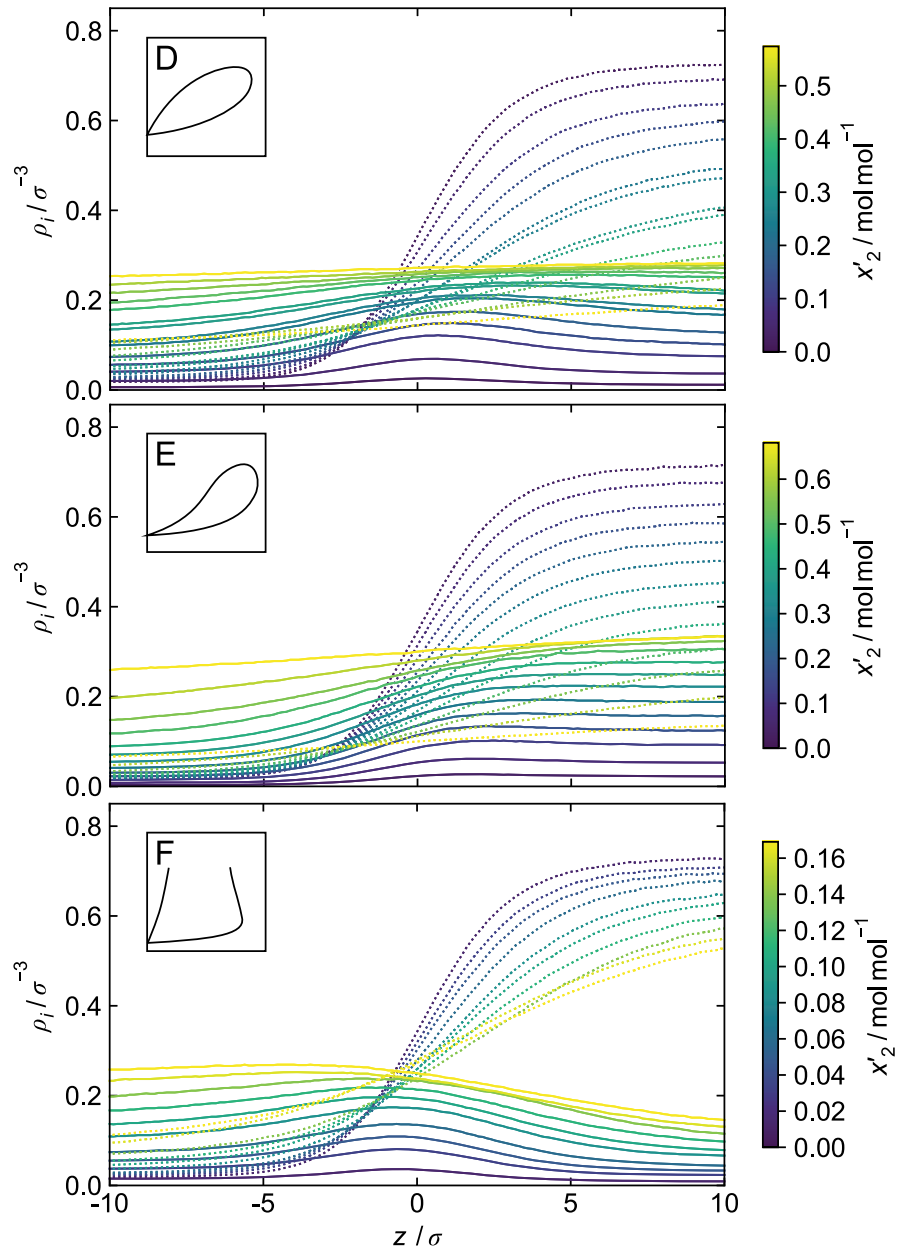
Figure A.16: Density profiles of the binary LJ mixtures D, E, and F at $T = 0.92\,\varepsilon k_{\mathrm{B}}^{-1}$. Results from MD. Dashed lines: high-boiling component 1; solid lines: low-boiling component 2. The color indicates the liquid phase composition.

Henry's Law Constant Numeric Values

Table A.13: MD results for the Henry's law constants of the LJ potential for the mixture D, E, and F. The number in the parentheses indicates the statistical uncertainty in the last decimal digit.

$T \ / \ \varepsilon k_\mathrm{B}^{-1}$	$H_{2,1} \ / \ \varepsilon\sigma^{-3}$		
	D	E	F
0.74	0.2283(47)	0.0261(6)	1.0999(98)
0.79	0.2538(48)	0.0353(7)	1.0593(90)
0.84	0.2796(27)	0.0468(5)	1.0209(96)
0.89	0.3053(28)	0.0601(5)	0.9902(91)
0.94	0.3302(24)	0.0752(5)	0.9629(73)
0.99	0.3464(21)	0.0903(5)	0.9157(58)
1.04	0.3541(20)	0.1054(5)	0.8538(53)
1.09	0.3664(16)	0.1199(5)	0.8143(48)
1.14	0.3663(17)	0.1357(5)	0.7472(46)
1.19	0.3653(17)	0.1505(5)	0.6912(37)
1.24	0.3539(18)	0.1626(5)	0.6180(39)
1.29	0.3290(26)	0.1703(8)	0.5262(56)

Bulk VLE Properties Numeric Values

Table A.14: MD and LJ EOS results for the vapor-liquid equilibrium of the binary LJ mixtures A - F for the temperature $T = 0.92\,\varepsilon k_{\mathrm{B}}^{-1}$. The number in the parentheses indicates the statistical uncertainty in the last decimal digit.

$x_2'/\mathrm{mol\,mol^{-1}}$	$p\ /\ \varepsilon\sigma^{-3}$		$x_2''\ /\ \mathrm{mol\,mol^{-1}}$		$\rho'\ /\ \sigma^{-3}$		$\rho''\ /\ \sigma^{-3}$	
	MD	EOS	MD	EOS	MD	EOS	MD	EOS
LJ Mixture A ($\varepsilon_2/\varepsilon_1 = 0.9$ and $\xi_{12} = 1$)								
0.000	0.0138(1)	0.0139	0.000	0.000	0.743(9)	0.743	0.0167(8)	0.0168
0.010(1)	0.0141(3)	0.0140	0.021(3)	0.018	0.742(4)	0.743	0.0171(8)	0.0170
0.050(1)	0.0145(4)	0.0145	0.089(6)	0.084	0.740(6)	0.741	0.0177(8)	0.0176
0.104(1)	0.0151(2)	0.0151	0.167(12)	0.168	0.738(8)	0.738	0.0184(8)	0.0185
0.150(2)	0.0157(2)	0.0157	0.239(13)	0.234	0.736(9)	0.736	0.0193(8)	0.0192
0.197(2)	0.0163(2)	0.0162	0.299(10)	0.298	0.733(9)	0.734	0.0201(9)	0.0200
0.245(3)	0.0167(3)	0.0168	0.364(14)	0.358	0.731(9)	0.732	0.0206(9)	0.0207
0.300(1)	0.0175(4)	0.0175	0.428(16)	0.424	0.728(11)	0.729	0.0217(12)	0.0216
0.347(1)	0.0178(3)	0.0180	0.473(14)	0.476	0.726(10)	0.727	0.0221(10)	0.0224
0.398(2)	0.0187(4)	0.0186	0.527(14)	0.530	0.723(11)	0.724	0.0233(10)	0.0233
0.446(2)	0.0195(4)	0.0192	0.581(15)	0.577	0.721(11)	0.722	0.0245(11)	0.0240
0.495(2)	0.0197(4)	0.0198	0.626(12)	0.623	0.718(10)	0.719	0.0248(11)	0.0249
0.550(1)	0.0206(2)	0.0205	0.670(7)	0.672	0.715(12)	0.716	0.0261(11)	0.0258
0.594(2)	0.0210(3)	0.0210	0.711(14)	0.710	0.713(11)	0.714	0.0267(11)	0.0266
0.642(2)	0.0214(3)	0.0216	0.747(9)	0.749	0.710(10)	0.711	0.0273(13)	0.0274
0.699(2)	0.0221(4)	0.0223	0.784(8)	0.794	0.706(10)	0.708	0.0282(11)	0.0284
0.752(2)	0.0230(4)	0.0229	0.831(10)	0.833	0.704(10)	0.705	0.0297(12)	0.0294
0.791(1)	0.0234(5)	0.0234	0.859(12)	0.862	0.701(10)	0.702	0.0302(11)	0.0301
0.848(2)	0.0242(3)	0.0241	0.901(9)	0.901	0.698(7)	0.699	0.0315(11)	0.0311
0.900(1)	0.0247(6)	0.0247	0.934(6)	0.936	0.694(7)	0.696	0.0322(11)	0.0321
0.950(1)	0.0253(2)	0.0253	0.968(2)	0.968	0.691(6)	0.693	0.0331(12)	0.0330
1.000	0.0259(3)	0.0259	1.000	1.000	0.688(3)	0.690	0.0342(12)	0.0340
LJ Mixture B ($\varepsilon_2/\varepsilon_1 = 0.9$ and $\xi_{12} = 1.2$)								
0.000	0.0138(1)	0.0139	0.000	0.000	0.743(9)	0.743	0.0167(8)	0.0168
0.0111(4)	0.0138(2)	0.0138	0.002(1)	0.002	0.744(4)	0.745	0.0167(8)	0.0166
0.0542(8)	0.0132(2)	0.0132	0.015(3)	0.014	0.749(6)	0.751	0.0159(6)	0.0158
0.1112(9)	0.0124(3)	0.0123	0.039(2)	0.038	0.754(7)	0.757	0.0149(6)	0.0148
0.1575(18)	0.0117(2)	0.0117	0.073(7)	0.067	0.758(8)	0.761	0.0139(7)	0.0139
0.2062(14)	0.0112(2)	0.0110	0.107(8)	0.110	0.761(8)	0.764	0.0133(7)	0.0131
0.2520(17)	0.0105(2)	0.0105	0.167(13)	0.164	0.763(8)	0.767	0.0125(7)	0.0124
0.3094(12)	0.0101(3)	0.0100	0.260(10)	0.252	0.765(9)	0.769	0.0120(7)	0.0118
0.3547(12)	0.0100(2)	0.0098	0.330(20)	0.335	0.765(8)	0.770	0.0118(7)	0.0116
0.4038(15)	0.0099(3)	0.0099	0.445(14)	0.436	0.765(9)	0.770	0.0117(7)	0.0116
0.4528(14)	0.0102(2)	0.0102	0.538(19)	0.540	0.765(9)	0.769	0.0121(7)	0.0120
0.4999(9)	0.0108(3)	0.0107	0.632(7)	0.636	0.763(8)	0.768	0.0128(7)	0.0126
0.5498(12)	0.0115(2)	0.0115	0.724(7)	0.726	0.761(8)	0.765	0.0137(8)	0.0137
0.5943(13)	0.0127(3)	0.0125	0.794(14)	0.793	0.758(8)	0.763	0.0152(7)	0.0149
0.6403(15)	0.0140(4)	0.0137	0.844(13)	0.850	0.754(8)	0.759	0.0169(8)	0.0164
0.6946(8)	0.0154(3)	0.0153	0.899(7)	0.900	0.749(7)	0.753	0.0187(8)	0.0186
0.7479(11)	0.0172(2)	0.0171	0.931(7)	0.935	0.742(8)	0.747	0.0211(8)	0.0210
0.7863(18)	0.0184(3)	0.0185	0.953(4)	0.954	0.737(7)	0.741	0.0228(9)	0.0229
0.8440(13)	0.0207(4)	0.0206	0.972(3)	0.974	0.727(7)	0.731	0.0261(9)	0.0259
0.8938(8)	0.0223(3)	0.0224	0.986(2)	0.986	0.717(6)	0.720	0.0284(9)	0.0286
0.9469(10)	0.0244(5)	0.0243	0.995(1)	0.994	0.704(5)	0.706	0.0317(10)	0.0313
1.0000	0.0259(3)	0.0259	1.000	1.000	0.688(3)	0.690	0.0342(12)	0.0340
LJ Mixture C ($\varepsilon_2/\varepsilon_1 = 0.9$ and $\xi_{12} = 0.85$)								

$x_2'/\text{mol mol}^{-1}$	$p \; / \; \varepsilon\sigma^{-3}$		$x_2'' \; / \; \text{mol mol}^{-1}$		$\rho' \; / \; \sigma^{-3}$		$\rho'' \; / \; \sigma^{-3}$	
	MD	EOS	MD	EOS	MD	EOS	MD	EOS
0.000	0.0138(1)	0.0139	0.000	0.000	0.743(9)	0.743	0.0167(8)	0.0168
0.0090(4)	0.0150(2)	0.0150	0.064(8)	0.073	0.741(4)	0.742	0.0183(9)	0.0183
0.0430(10)	0.0182(4)	0.0187	0.230(16)	0.257	0.736(6)	0.735	0.0225(9)	0.0231
0.0886(17)	0.0220(5)	0.0224	0.374(13)	0.388	0.728(9)	0.727	0.0279(12)	0.0284
0.1333(12)	0.0236(3)	0.0251	0.440(8)	0.460	0.721(11)	0.719	0.0302(12)	0.0323
0.1771(18)	0.0255(4)	0.0269	0.480(8)	0.505	0.714(12)	0.712	0.0331(15)	0.0352
0.2222(25)	0.0269(4)	0.0283	0.520(13)	0.537	0.707(13)	0.704	0.0352(13)	0.0375
0.2797(41)	0.0283(4)	0.0295	0.552(11)	0.564	0.699(18)	0.695	0.0375(14)	0.0394
0.3335(46)	0.0288(3)	0.0303	0.566(9)	0.582	0.692(19)	0.687	0.0383(15)	0.0407
0.3821(31)	0.0294(3)	0.0307	0.595(13)	0.595	0.686(15)	0.681	0.0396(17)	0.0415
0.4390(25)	0.0301(3)	0.0311	0.610(10)	0.608	0.680(20)	0.675	0.0411(31)	0.0422
0.4939(51)	0.0305(3)	0.0314	0.617(13)	0.620	0.676(16)	0.670	0.0413(16)	0.0428
0.5510(25)	0.0306(5)	0.0317	0.635(10)	0.634	0.672(20)	0.666	0.0419(27)	0.0432
0.6481(37)	0.0307(5)	0.0319	0.668(8)	0.661	0.668(17)	0.663	0.0417(14)	0.0435
0.7038(9)	0.0308(4)	0.0319	0.695(10)	0.681	0.668(14)	0.664	0.0423(27)	0.0435
0.7647(17)	0.0310(3)	0.0316	0.716(8)	0.710	0.670(12)	0.666	0.0422(16)	0.0431
0.8007(18)	0.0304(5)	0.0314	0.744(10)	0.731	0.670(11)	0.668	0.0412(16)	0.0426
0.8575(23)	0.0298(4)	0.0307	0.792(6)	0.775	0.675(9)	0.673	0.0402(14)	0.0414
0.9085(25)	0.0293(3)	0.0296	0.834(8)	0.830	0.679(10)	0.678	0.0392(14)	0.0396
0.9548(9)	0.0280(5)	0.0280	0.907(7)	0.901	0.683(6)	0.683	0.0373(14)	0.0372
1.0000	0.0259(3)	0.0259	1.000	1.000	0.688(3)	0.690	0.0342(12)	0.0340
LJ Mixture D ($\varepsilon_2/\varepsilon_1 = 0.5$ and $\xi_{12} = 1$)								
0.000	0.0138(1)	0.0139	0.000	0.000	0.743(9)	0.743	0.0167(8)	0.0168
0.015(1)	0.0193(4)	0.0190	0.259(13)	0.247	0.739(4)	0.740	0.024(1)	0.0232
0.051(1)	0.0310(3)	0.0305	0.504(10)	0.502	0.731(6)	0.733	0.039(1)	0.0383
0.099(2)	0.0467(6)	0.0452	0.646(9)	0.636	0.719(8)	0.722	0.061(2)	0.0590
0.136(3)	0.0573(6)	0.0559	0.692(7)	0.687	0.708(9)	0.713	0.078(2)	0.0755
0.176(3)	0.0681(5)	0.0669	0.724(7)	0.721	0.697(9)	0.703	0.096(2)	0.0941
0.228(4)	0.0827(8)	0.0803	0.744(6)	0.747	0.681(13)	0.688	0.125(2)	0.1191
0.253(3)	0.0872(6)	0.0863	0.749(7)	0.754	0.672(10)	0.680	0.134(3)	0.1315
0.314(9)	0.0988(3)	0.1002	0.761(5)	0.765	0.644(16)	0.660	0.161(6)	0.1638
0.332(6)	0.1031(9)	0.1040	0.760(7)	0.766	0.642(12)	0.653	0.173(3)	0.1738
0.391(6)	0.1144(9)	0.1157	0.757(10)	0.766	0.616(13)	0.629	0.208(4)	0.2086
0.424(3)	0.1193(7)	0.1217	0.756(7)	0.763	0.599(13)	0.614	0.224(4)	0.2299
0.467(6)	0.1267(7)	0.1288	0.749(11)	0.756	0.576(11)	0.592	0.255(5)	0.2594
0.498(15)	0.1326(17)	0.1334	0.731(43)	0.749	0.558(12)	0.574	0.293(15)	0.2823
LJ Mixture E ($\varepsilon_2/\varepsilon_1 = 0.5$ and $\xi_{12} = 1.2$)								
0.000	0.0138(1)	0.0139	0.000	0.000	0.743(9)	0.743	0.0167(8)	0.0168
0.032(1)	0.0161(2)	0.0158	0.146(8)	0.134	0.738(6)	0.740	0.020(1)	0.0192
0.071(2)	0.0197(3)	0.0184	0.312(11)	0.273	0.733(6)	0.737	0.024(1)	0.0227
0.127(1)	0.0248(3)	0.0232	0.462(9)	0.436	0.724(7)	0.730	0.031(1)	0.0289
0.175(1)	0.0301(4)	0.0282	0.557(7)	0.544	0.715(8)	0.724	0.038(1)	0.0357
0.225(2)	0.0357(4)	0.0342	0.633(7)	0.629	0.705(8)	0.716	0.046(1)	0.0441
0.271(1)	0.0430(5)	0.0409	0.691(7)	0.691	0.695(8)	0.708	0.057(2)	0.0536
0.326(2)	0.0518(6)	0.0499	0.740(7)	0.746	0.682(8)	0.697	0.071(2)	0.0671
0.373(2)	0.0612(4)	0.0586	0.777(9)	0.782	0.669(8)	0.685	0.086(2)	0.0811
0.428(3)	0.0714(9)	0.0699	0.803(5)	0.812	0.651(7)	0.670	0.105(2)	0.1005
0.489(1)	0.0847(4)	0.0836	0.825(5)	0.835	0.628(7)	0.649	0.131(3)	0.1270
0.544(3)	0.0971(7)	0.0971	0.834(8)	0.847	0.603(8)	0.626	0.160(4)	0.1568
0.610(3)	0.1116(7)	0.1135	0.835(6)	0.853	0.565(8)	0.592	0.204(5)	0.2010
0.681(6)	0.1290(8)	0.1309	0.826(8)	0.846	0.512(9)	0.541	0.275(7)	0.2650
LJ Mixture F ($\varepsilon_2/\varepsilon_1 = 0.5$ and $\xi_{12} = 0.85$)								
0.000	0.0138(1)	0.0139	0.000	0.000	0.743(9)	0.743	0.0167(8)	0.0168

$x_2'/\text{mol mol}^{-1}$	$p \ / \ \varepsilon\sigma^{-3}$		$x_2'' \ / \ \text{mol mol}^{-1}$		$\rho' \ / \ \sigma^{-3}$		$\rho'' \ / \ \sigma^{-3}$	
	MD	EOS	MD	EOS	MD	EOS	MD	EOS
0.012(1)	0.0273(4)	0.0279	0.446(8)	0.454	0.740(4)	0.741	0.033(1)	0.0341
0.032(1)	0.0455(5)	0.0502	0.629(5)	0.655	0.736(6)	0.737	0.058(2)	0.0642
0.048(2)	0.0591(5)	0.0689	0.688(8)	0.719	0.731(7)	0.733	0.078(2)	0.0924
0.059(2)	0.0726(4)	0.0812	0.721(6)	0.743	0.729(8)	0.731	0.099(2)	0.1129
0.084(4)	0.0947(7)	0.1104	0.758(6)	0.769	0.722(8)	0.726	0.138(3)	0.1691
0.101(3)	0.1084(6)	0.1310	0.766(7)	0.771	0.718(9)	0.723	0.165(3)	0.2159
0.110(4)	0.1248(6)	0.1419	0.769(6)	0.769	0.717(11)	0.721	0.202(4)	0.2429
0.137(3)	0.1419(8)	0.1817	0.762(5)	0.745	0.709(10)	0.717	0.246(4)	0.3435

Interfacial VLE Properties Numeric Values

Table A.15: MD and LJ EOS results for the vapor-liquid interfacial properties of the binary LJ mixtures A - F for the temperature $T = 0.92 \, \varepsilon k_{\text{B}}^{-1}$. The number in the parentheses indicates the statistical uncertainty in the last decimal digit.

$x_2'/\text{mol mol}^{-1}$	$\gamma \ / \ \varepsilon\sigma^{-2}$		$\Gamma_2^{(1)} \ / \ \sigma^{-2}$		E_2		$L_{10}^{90} \ / \ \sigma$	
	MD	DGT	MD	DGT	MD	DGT	MD	DGT
LJ Mixture A $(\varepsilon_2/\varepsilon_1 = 0.9$ and $\xi_{12} = 1)$								
0.000	0.665(21)	0.663	-	-	-	-	2.91(5)	2.95
0.010(1)	0.672(30)	0.661	0.005(13)	0.003	1.2(2)	1.0	2.90(5)	2.96
0.050(1)	0.660(22)	0.650	0.015(15)	0.014	1.07(4)	1.0	2.95(4)	2.98
0.104(1)	0.645(23)	0.636	0.040(23)	0.030	1.05(2)	1.0	2.98(6)	3.02
0.150(2)	0.622(24)	0.624	0.023(4)	0.042	1.03(3)	1.0	3.01(5)	3.06
0.197(2)	0.609(22)	0.612	0.042(4)	0.055	1.03(2)	1.0	3.01(5)	3.08
0.245(3)	0.599(23)	0.600	0.08(6)	0.067	1.03(1)	1.0	3.07(5)	3.12
0.300(1)	0.577(27)	0.586	0.04(5)	0.081	1.01(1)	1.0	3.11(5)	3.16
0.347(1)	0.575(26)	0.575	0.08(6)	0.093	1.02(1)	1.0	3.17(5)	3.2
0.398(2)	0.555(25)	0.562	0.09(9)	0.105	1.02(1)	1.0	3.21(7)	3.24
0.446(2)	0.542(18)	0.551	0.14(10)	0.116	1.02(1)	1.0	3.24(6)	3.28
0.495(2)	0.528(22)	0.539	0.14(6)	0.127	1.02(1)	1.0	3.28(6)	3.32
0.550(1)	0.512(18)	0.527	0.24(9)	0.140	1.02(1)	1.0	3.33(7)	3.34
0.594(2)	0.508(22)	0.516	0.31(10)	0.149	1.02(1)	1.0	3.37(5)	3.4
0.642(2)	0.486(20)	0.505	0.22(7)	0.159	1.01(1)	1.0	3.38(6)	3.42
0.699(2)	0.481(17)	0.492	0.16(18)	0.171	1.01(1)	1.0	3.39(6)	3.48
0.752(2)	0.468(23)	0.481	0.17(16)	0.181	1.01(1)	1.0	3.50(3)	3.52
0.791(1)	0.462(16)	0.472	0.08(17)	0.189	1.01(1)	1.0	3.50(4)	3.54
0.848(2)	0.449(25)	0.459	0.22(26)	0.200	1.01(1)	1.0	3.59(7)	3.6
0.900(1)	0.435(21)	0.448	0.28(28)	0.209	1.01(1)	1.0	3.58(6)	3.64
0.950(1)	0.425(19)	0.437	0.19(42)	0.218	1.01(1)	1.0	3.64(6)	3.68
1.000	0.424(21)	0.427	-	-	-	-	3.67(8)	3.70
LJ Mixture B $(\varepsilon_2/\varepsilon_1 = 0.9$ and $\xi_{12} = 1.2)$								
0.000	0.665(21)	0.663	-	-	-	-	2.91(5)	2.95
0.0111(4)	0.688(28)	0.669	-0.021(8)	-0.006	1.10(8)	1.0	2.90(4)	2.94
0.0542(8)	0.714(28)	0.692	-0.022(24)	-0.026	1.06(4)	1.0	2.84(5)	2.90
0.1112(9)	0.739(24)	0.722	-0.019(19)	-0.042	1.04(1)	1.0	2.77(3)	2.84
0.1575(18)	0.749(27)	0.744	-0.05(5)	-0.048	1.04(2)	1.0	2.77(3)	2.78
0.2062(14)	0.780(26)	0.764	-0.09(5)	-0.048	1.02(1)	1.0	2.73(4)	2.74
0.2520(17)	0.789(28)	0.779	-0.03(4)	-0.042	1.03(1)	1.0	2.67(3)	2.70

$x'_2/\mathrm{mol\,mol^{-1}}$	$\gamma\ /\ \varepsilon\sigma^{-2}$		$\Gamma_2^{(1)}\ /\ \sigma^{-2}$		E_2		$L_{10}^{90}\ /\ \sigma$	
	MD	DGT	MD	DGT	MD	DGT	MD	DGT
0.3094(12)	0.809(29)	0.791	-0.00(6)	-0.027	1.02(1)	1.0	2.65(4)	2.68
0.3547(12)	0.811(28)	0.796	0.02(2)	-0.010	1.02(1)	1.0	2.65(4)	2.68
0.4038(15)	0.808(29)	0.796	0.10(3)	0.014	1.02(1)	1.0	2.64(5)	2.68
0.4528(14)	0.800(25)	0.790	0.09(5)	0.043	1.02(1)	1.0	2.65(5)	2.70
0.4999(9)	0.786(25)	0.778	0.05(6)	0.077	1.02(1)	1.0	2.67(4)	2.72
0.5498(12)	0.768(22)	0.760	0.17(7)	0.118	1.01(1)	1.0	2.73(3)	2.76
0.5943(13)	0.743(33)	0.739	0.21(5)	0.160	1.01(1)	1.0	2.78(3)	2.80
0.6403(15)	0.715(26)	0.713	0.25(10)	0.209	1.01(1)	1.0	2.83(5)	2.86
0.6946(8)	0.684(26)	0.677	0.29(6)	0.275	1.01(1)	1.0	2.92(6)	2.94
0.7479(11)	0.644(23)	0.637	0.27(14)	0.348	1.01(1)	1.0	3.04(3)	3.06
0.7863(18)	0.604(25)	0.606	0.38(12)	0.407	1.01(1)	1.0	3.12(6)	3.14
0.8440(13)	0.558(20)	0.558	0.51(26)	0.506	1.01(1)	1.0	3.28(8)	3.28
0.8938(8)	0.510(18)	0.515	0.68(14)	0.600	1.01(1)	1.0	3.43(7)	3.44
0.9469(10)	0.471(26)	0.470	0.64(27)	0.710	1.01(1)	1.0	3.58(7)	3.58
1.0000	0.426(21)	0.427	-	-	-	-	3.67(8)	3.70
LJ Mixture C ($\varepsilon_2/\varepsilon_1 = 0.9$ and $\xi_{12} = 0.85$)								
0.000	0.665(21)	0.663	-	-	-	-	2.91(5)	2.95
0.0090(4)	0.662(35)	0.649	0.01(1)	0.016	1.31(17)	1.49	2.94(5)	3.00
0.0430(10)	0.604(17)	0.597	0.07(1)	0.078	1.33(10)	1.46	3.09(7)	3.16
0.0886(17)	0.555(23)	0.539	0.18(3)	0.157	1.34(10)	1.41	3.34(6)	3.36
0.1333(12)	0.515(22)	0.493	0.23(5)	0.229	1.25(4)	1.35	3.47(7)	3.54
0.1771(18)	0.479(20)	0.457	0.23(3)	0.290	1.17(5)	1.30	3.60(7)	3.72
0.2222(25)	0.442(23)	0.428	0.36(6)	0.340	1.20(6)	1.24	3.75(7)	3.84
0.2797(41)	0.414(26)	0.401	0.38(12)	0.381	1.11(4)	1.16	3.83(6)	3.98
0.3335(46)	0.406(22)	0.383	0.37(9)	0.393	1.05(2)	1.10	3.87(6)	4.04
0.3821(31)	0.380(22)	0.371	0.28(9)	0.381	1.04(2)	1.06	3.89(8)	4.08
0.4390(25)	0.370(22)	0.361	0.24(11)	0.340	1.03(2)	1.02	3.95(7)	4.10
0.4939(51)	0.351(21)	0.353	0.38(13)	0.279	1.03(1)	1.00	3.99(7)	4.12
0.5510(25)	0.345(18)	0.347	0.15(20)	0.197	1.01(2)	1.00	3.95(4)	4.14
0.6481(37)	0.342(19)	0.343	0.26(22)	0.027	1.02(1)	1.00	3.98(8)	4.16
0.7038(9)	0.342(15)	0.343	-0.13(13)	-0.084	1.01(1)	1.00	4.02(7)	4.14
0.7647(17)	0.338(21)	0.348	-0.14(27)	-0.213	1.01(1)	1.00	4.03(8)	4.12
0.8007(18)	0.354(25)	0.353	-0.09(20)	-0.293	1.01(1)	1.00	3.95(7)	4.12
0.8575(23)	0.366(20)	0.365	-0.04(32)	-0.421	1.01(1)	1.00	3.91(7)	4.06
0.9085(25)	0.373(15)	0.382	-1.25(30)	-0.536	1.01(1)	1.00	3.89(7)	3.96
0.9548(9)	0.393(24)	0.402	-0.72(63)	-0.639	1.01(1)	1.00	3.75(7)	3.86
1.0000	0.423(21)	0.427	-	-	-	-	3.67(8)	3.70
LJ Mixture D ($\varepsilon_2/\varepsilon_1 = 0.5$ and $\xi_{12} = 1$)								
0.000	0.665(21)	0.663	-	-	-	-	2.91(5)	2.95
0.015(1)	0.625(21)	0.620	0.05(1)	0.047	2.2(3)	2.26	3.08(6)	3.06
0.051(1)	0.540(20)	0.529	0.13(2)	0.139	1.8(1)	1.98	3.42(5)	3.38
0.099(2)	0.424(18)	0.427	0.26(3)	0.238	1.68(4)	1.72	3.99(8)	3.80
0.136(3)	0.354(13)	0.360	0.33(4)	0.302	1.52(3)	1.57	4.47(8)	4.18
0.176(3)	0.286(15)	0.296	0.38(4)	0.361	1.40(4)	1.44	5.0(2)	4.64
0.228(4)	0.206(17)	0.226	0.52(6)	0.423	1.30(4)	1.32	5.9(2)	5.34
0.253(3)	0.185(14)	0.196	0.48(3)	0.446	1.24(2)	1.27	6.2(2)	5.72
0.314(9)	0.133(13)	0.135	0.45(11)	0.488	1.14(2)	1.17	7.2(3)	6.82
0.332(6)	0.118(14)	0.119	0.49(9)	0.495	1.12(2)	1.14	7.7(3)	7.22
0.391(6)	0.073(13)	0.076	0.48(5)	0.511	1.06(1)	1.08	9.4(8)	8.76
0.424(3)	0.051(12)	0.056	0.42(7)	0.503	1.04(1)	1.05	10.5(12)	9.86
0.467(6)	0.036(15)	0.034	0.42(10)	0.472	1.03(1)	1.02	13.4(21)	12.00
0.498(15)	0.026(15)	0.023	0.30(17)	0.430	1.02(2)	1.01	14.8(35)	13.90
LJ Mixture E ($\varepsilon_2/\varepsilon_1 = 0.5$ and $\xi_{12} = 1.2$)								

$x_2'/\mathrm{mol\,mol^{-1}}$	$\gamma \;/\; \varepsilon\sigma^{-2}$		$\Gamma_2^{(1)} \;/\; \sigma^{-2}$		E_2		$L_{10}^{90} \;/\; \sigma$	
	MD	DGT	MD	DGT	MD	DGT	MD	DGT
0.000	0.665(21)	0.663	-	-	-	-	2.91(5)	2.95
0.032(1)	0.634(3)	0.637	0.013(14)	0.028	1.1(1)	1.03	3.03(3)	3.02
0.071(2)	0.592(16)	0.603	0.09(2)	0.060	1.2(1)	1.01	3.19(5)	3.14
0.127(1)	0.530(18)	0.551	0.14(3)	0.107	1.09(3)	1.00	3.36(6)	3.30
0.175(1)	0.469(20)	0.504	0.15(3)	0.147	1.05(2)	1.00	3.60(6)	3.48
0.225(2)	0.419(19)	0.453	0.19(4)	0.188	1.03(1)	1.00	3.77(4)	3.70
0.271(1)	0.362(14)	0.403	0.23(5)	0.227	1.03(1)	1.00	4.04(7)	3.94
0.326(2)	0.300(15)	0.343	0.25(4)	0.272	1.02(1)	1.00	4.43(6)	4.28
0.373(2)	0.250(13)	0.291	0.28(5)	0.310	1.01(1)	1.00	4.91(11)	4.64
0.428(3)	0.199(15)	0.231	0.31(8)	0.350	1.01(1)	1.00	5.5(2)	5.20
0.489(1)	0.134(12)	0.168	0.36(5)	0.388	1.01(1)	1.00	6.4(3)	6.02
0.544(3)	0.091(11)	0.116	0.31(6)	0.408	1.01(1)	1.00	7.4(3)	7.10
0.610(3)	0.054(9)	0.063	0.33(6)	0.397	1.01(1)	1.00	9.9(6)	9.10
0.681(6)	0.020(13)	0.023	0.29(8)	0.291	1.01(1)	1.00	16.1(26)	12.68
LJ Mixture F ($\varepsilon_2/\varepsilon_1$ = 0.5 and ξ_{12} = 0.85)								
0.000	0.665(21)	0.663	-	-	-	-	2.91(5)	2.95
0.012(1)	0.600(16)	0.587	0.07(1)	0.082	2.45(7)	3.18	3.15(5)	3.14
0.032(1)	0.519(17)	0.477	0.16(2)	0.199	2.22(3)	2.71	3.59(7)	3.52
0.048(2)	0.455(15)	0.394	0.21(2)	0.284	2.04(5)	2.38	3.92(7)	3.90
0.059(2)	0.400(18)	0.345	0.31(3)	0.333	1.91(4)	2.18	4.38(9)	4.18
0.084(4)	0.311(16)	0.242	0.38(3)	0.418	1.67(3)	1.77	5.1(1)	4.94
0.101(3)	0.268(20)	0.184	0.45(3)	0.443	1.56(2)	1.53	5.8(1)	5.50
0.110(4)	0.207(21)	0.158	0.53(5)	0.432	1.40(2)	1.42	6.6(3)	5.74
0.137(3)	0.166(14)	0.091	0.49(4)	0.322	1.28(1)	1.15	7.3(4)	6.14

A.6 Mass Transfer Simulations

Simulation Details

Fig. A.17 shows details of the mass transfer simulations (cf. chapter 6) that were carried out for the LJTS mixtures A and G at the temperature $T = 0.715\,\varepsilon k_{\mathrm{B}}^{-1}$. Only results from the production phase are shown. In the diagrams on the left side, the number of inserted and deleted particles of component 2 in the two control volumes is shown as a function of the simulation time. The mass flux $j_2 = \frac{\Delta N_2}{\Delta \tau\, a^2}$ was determined from the total number of inserted and removed particles during the production time $\Delta\tau$. The cross section of the simulation box is a^2 (see chapter 6 for details). Note that the control volumes regulate the chemical potential, which can result in the fact that each control volume inserts and deletes particles in some times steps. However, the cumulative number of inserted particles in the control volume CV+ and deleted particles in the control volume CV- during the production phase yield increasing and decreasing trends, respectively, cf. Fig. A.17. The number of inserted and deleted particles ΔN_2 was computed from the average of the inserted and deleted particles by the end of the production phase τ_{end}, i.e. $\Delta N_2 = \frac{N_2^{\mathrm{CV+}}(\tau_{\mathrm{end}}) + N_2^{\mathrm{CV-}}(\tau_{\mathrm{end}})}{2}$. In all cases, $N_2^{\mathrm{CV+}}(\tau_{\mathrm{end}})$ and $N_2^{\mathrm{CV-}}(\tau_{\mathrm{end}})$ deviate by no more than 10%.

The statistical uncertainty of the mass flux j_2 was determined from the average deviation of the lines through the origin with the slope $\frac{\Delta N_2}{\Delta\tau}$ and $-\frac{\Delta N_2}{\Delta\tau}$ and the corresponding primary data for $N_2^+(\tau)$ and $N_2^-(\tau)$, cf. Fig. A.17.

For mixture A, the results are as expected: symmetric straight lines through the origin for $N_2^+(\tau)$ and $N_2^-(\tau)$. The rate of low-boiling particles inserted in the left control volume approximately equals the rate of low-boiling particles being removed in the right control volume. The results for mixture G scatter much more than those for mixture A. This is mainly due to the higher vapor density and pressure in mixture G. Hence, the uncertainty obtained for the flux j_2 in mixture G is significantly larger than in mixture A (see chapter 6).

Since the insertion of particles is the more difficult step in a sense that also unfavorable configurations are sometimes accepted, the fluctuations are more pronounced for the inserting control volume, cf. Fig. A.17. Still, both shown cases can be considered quasi-stationary.

The interface positions shown in Fig. A.17 – right indicate that the liquid slab remains fairly constant in the simulation box. However, in the case of mixture A, the liquid slab slightly moves towards the inserting control volume during the production phase.

Several challenges were observed during the preliminary testing of the simulation method that are briefly summarized here. The choice of an appropriate difference of the chemical potential was particularly challenging. Large values of the difference of the chemical potential were found to cause strong perturbations – especially in the vapor phases – and, hence, cause nucleation of droplets or bubbles and also require long equilibration times to reach a quasi-stationary state. Furthermore, large differences of the chemical potential favor movements of the liquid film in the box. Small values of the differences of the chemical potential will on the other hand result in small values of the flux.
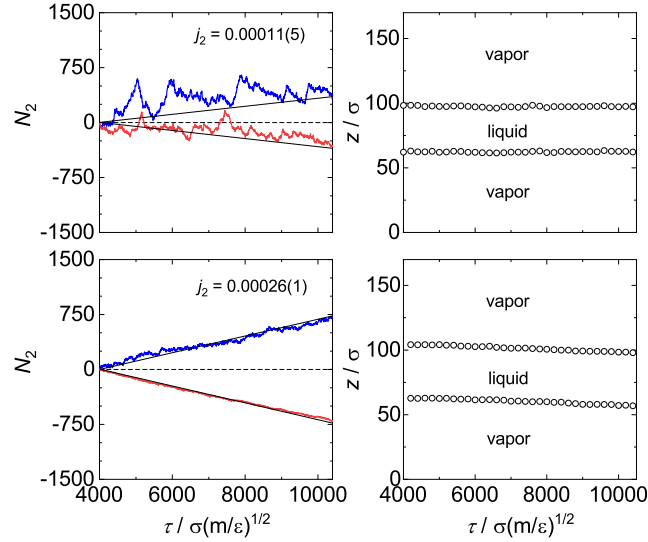
Figure A.17: Results from the production phase of the mass transfer simulations at $T = 0.715\,\varepsilon k_{\mathrm{B}}^{-1}$. Left: cumulative inserted and removed particles of the component 2 in the control volumes $N_2^+(\tau)$ (blue) and $N_2^-(\tau)$ (red); right: position of the interfaces as a function of the simulation time. Results of the mixture G are in the top; results of mixture A are bottom. Symbols indicate the total density at the interface $\rho_{\mathrm{interface}} = \rho_{\mathrm{V}} + 0.5\,(\rho_{\mathrm{L}} - \rho_{\mathrm{V}})$. The black lines indicate the obtained slopes $\frac{\Delta N_2}{\Delta \tau}$ and $-\frac{\Delta N_2}{\Delta \tau}$.

The number N_{MC} and frequency f_{MC} of GCMC steps applied in the control volumes (see chapter 6) were chosen based on preliminary tests. On the one side, the amount of MC steps has to be large enough to ensure that the prescribed chemical potential is regulated in the control volumes. On the other side, N_{MC} should be small as it significantly influences the required computational time and causes perturbations in the vapor phase. Also the frequency f_{MC} that MC and MD calculations are alternated has to be balanced between computational effort and the stability of the simulation.

Individual State Points in the Profiles

Fig. A.18 - top depicts a detailed comparison of the sampled state points from each bin (excluding the vicinity of the control volumes) from all profiles during the production phase from the mass transfer simulation at $T = 0.715\,\varepsilon k_{\mathrm{B}}^{-1}$. The averaged state points for the two vapor domains and the liquid domain agree very well with the equilibrium phase envelope computed from the PeTS EOS [249, 635]. The liquid bulk domain state points are connected to the two vapor domains by the state points in the interface. For the liquid bulk domain, the state points show an elliptic scatter pattern around a point on the phase equilibrium envelope. The scattering is dominated by a scattering in the pressure, which is simply due to the fact that the pressure shows stronger fluctuations in the liquid bulk than the vapor bulk, cf. the pressure profiles in Fig. 81. On the contrary for vapor bulk domains V_{left} and V_{right}, where the scattering of the individual bin state points is dominated by a scattering in the concentration. This is due to the fact that the relatively low number of particles in the vapor bins yields stronger fluctuations compared to the liquid bulk bins. Nevertheless, the three averaged state points from the bins in

the respective bulk domain from all profiles during the production phase (blue squares in Fig. A.18) are for both mixtures in excellent agreement with the phase equilibrium computed from the PeTS EOS [249, 635], which is known to give an excellent description of the phase equilibrium of LJTS mixtures [628–630].

Following Ref. [288], the local scalar pressure p in the heterogeneous system was simply computed by averaging the trace of the pressure tensor. The pressure across the interfaces smoothly connects the three bulk domains V_{left} – L – V_{right}. The pressure transition in the two interfaces differ, which is in line with differences in the enrichment, cf. Fig. 82.
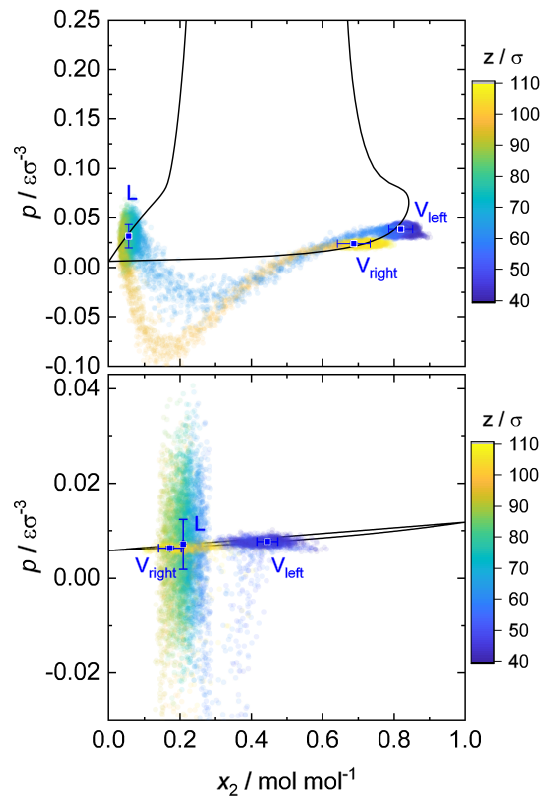
Figure A.18: Pressure – composition diagram for mixture G (top) and mixture A (bottom) at $T = 0.715\,\varepsilon k_B^{-1}$. The black line indicates the phase equilibrium computed with the PeTS EOS [249, 635]. The circles indicate state points sampled during the stationary phase of the simulation in the individual bins of the profiles – excluding the vicinity of the control volumes. The color corresponds to the z-position in the profile. The squares indicate the averaged state points computed in each bulk domain (liquid as well as left and right vapor).

The magnitude of the pressure and composition scattering in the bulk domains is similar for both mixtures: the state points in the vapor bulk domains (yellow and dark blue circles in Fig. A.18) exhibit stronger fluctuations in the composition, whereas the liquid bulk domain exhibits more pronounced pressure fluctuations (turquoise circles). For both mixtures, the pressure range in the interface and the scattering in the liquid domain exceeds the pressure range of the phase equilibrium.

Additional Results for Mixture A

Fig. A.19 shows the density profiles and isothermal $p - x$ diagrams of mixture A during the production phase of the mass transfer simulations at different temperatures. In all cases, no enrichment is found at the interface. The state points averaged for the three bulk domains are in excellent agreement with the respective phase equilibrium envelop.
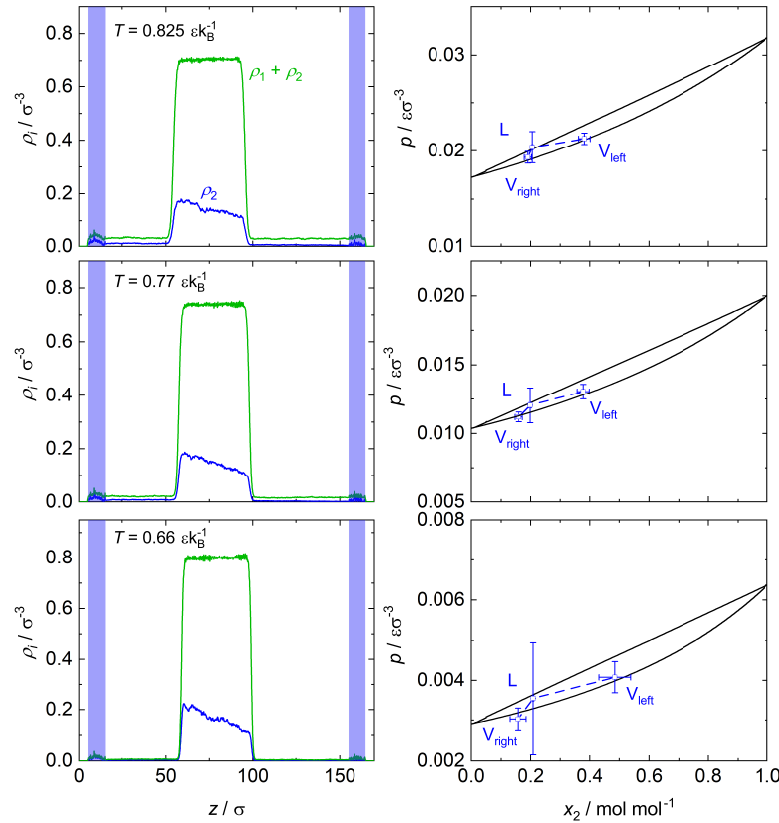
Figure A.19: Density profiles (left panels) and state points in the bulk domains (right panels) sampled during the production phase of the mass transfer simulations for mixture A at different temperatures. The blue shaded area indicates the elongation of the control volumes in z-direction.

Numeric Values from the Mass Transfer Simulations

Table A.16 reports the numeric values for the pressure, density, mole fraction, and velocity of component 2 obtained for all three bulk domains for both studied mixtures and the four considered temperatures.

Table A.17 reports the interface positions averaged during the production phase. The interface position was defined as the point in the interface with the total density $\rho_{\text{interface}} = \rho_V + 0.5\,(\rho_L - \rho_V)$, cf. Fig. A.17. The interface position was computed from each block averaged density profile; the reported values in Table A.17 are their mean values. The uncertainty was estimated as three times the standard deviation of the block average values, which confirms the assumption of a quasi-stationary state of the simulations.

Table A.16: Numeric values for the results from the mass transfer simulations in the three bulk domains V_{left}, L, and V_{right} (as defined in chapter 6). Results for mixture G and mixture A. Results for all four studied temperatures: pressure p; total density ρ in the bulk domains; mole fraction of the low-boiling component x_2 in the bulk domains; and average velocity u_2 of the component 2 particles in the fixed laboratory frame.

$T \,/\, \varepsilon k_{\mathrm{B}}^{-1}$	V_{left}		L		V_{right}	
	G	A	G	A	G	A
			$p \,/\, \varepsilon\sigma^{-3}$			
0.66	0.0335(25)	0.0041(4)	0.0262(19)	0.0036(14)	0.0187(7)	0.0030(3)
0.715	0.0387(15)	0.0077(5)	0.0316(21)	0.0071(13)	0.0239(14)	0.0063(3)
0.77	0.0440(21)	0.0131(5)	0.0376(20)	0.0121(13)	0.0300(15)	0.0112(4)
0.825	0.048(3)	0.0213(6)	0.0436(22)	0.0204(16)	0.0382(17)	0.0193(6)
			$\rho \,/\, \sigma^{-3}$			
0.66	0.06576(3)	0.00660(1)	0.79691(3)	0.80062(3)	0.03292(1)	0.00484(1)
0.715	0.06718(3)	0.01176(1)	0.76706(3)	0.77081(2)	0.04325(8)	0.00944(1)
0.77	0.07236(3)	0.01937(1)	0.73398(2)	0.73935(2)	0.04623(3)	0.01630(1)
0.825	0.07376(3)	0.03112(1)	0.69914(2)	0.70425(2)	0.05838(7)	0.02791(1)
			$x_2 \,/\, \mathrm{mol\,mol^{-1}}$			
0.66	0.895(10)	0.48(5)	0.057(5)	0.208(3)	0.81(4)	0.16(3)
0.715	0.829(9)	0.44(3)	0.056(3)	0.209(2)	0.68(6)	0.171(22)
0.77	0.711(13)	0.378(21)	0.058(4)	0.198(4)	0.60(3)	0.159(12)
0.825	0.567(22)	0.382(20)	0.055(3)	0.206(3)	0.49(4)	0.191(12)
			$u_2 \,/\, \sqrt{\varepsilon/\mathrm{M}}$			
0.66	0.0011(1)	0.0719(1)	0.0014(1)	0.0014(1)	0.0024(2)	0.3023(1)
0.715	0.0020(1)	0.0497(1)	0.0026(1)	0.0016(1)	0.0038(1)	0.1609(1)
0.77	0.0020(2)	0.0287(1)	0.0024(2)	0.0014(2)	0.0037(2)	0.0810(2)
0.825	0.0045(2)	0.0202(2)	0.0049(3)	0.0017(1)	0.0066(3)	0.0451(2)

Table A.17: Average position of the two vapor-liquid interfaces during the mass transfer simulations. Results for mixture G and mixture A. Results for all four studied temperatures. The uncertainty was estimated as three times the standard deviation of the block averages obtained during the simulation.

$T \,/\, \varepsilon k_{\mathrm{B}}^{-1}$	$z_{left} \,/\, \sigma$		$z_{right} \,/\, \sigma$	
	G	A	G	A
0.66	59(1)	58(1)	96(1)	98(1)
0.715	62(1)	56(2)	97(1)	99(2)
0.77	61(1)	56(2)	94(1)	96(2)
0.825	63(1)	52(2)	95(2)	94(2)

Comparison of Bulk Diffusion Coefficients

Figs. A.20 and A.21 compare the diffusivity ρD_{12} of the bulk phases from both mixtures G and A; results from Ref. [638]. Fig. A.20 shows the diffusivity for the liquid phase for both mixtures. Fig. A.21 shows the diffusivity for the vapor phase for both mixtures. The liquid phase results were obtained using *Green-Kubo* molecular simulations sampling slightly above the bubble line and the vapor phase results were obtained from the *Chapman-Enskog* theory for the saturated vapor phase [638].

The values of the diffusivity for both mixtures are approximately the same. This holds for both the liquid and the vapor phase. For the liquid and the vapor phase, there is a tendency that the diffusivity ρD_{12} for mixture G slightly exceeds that of mixture A.
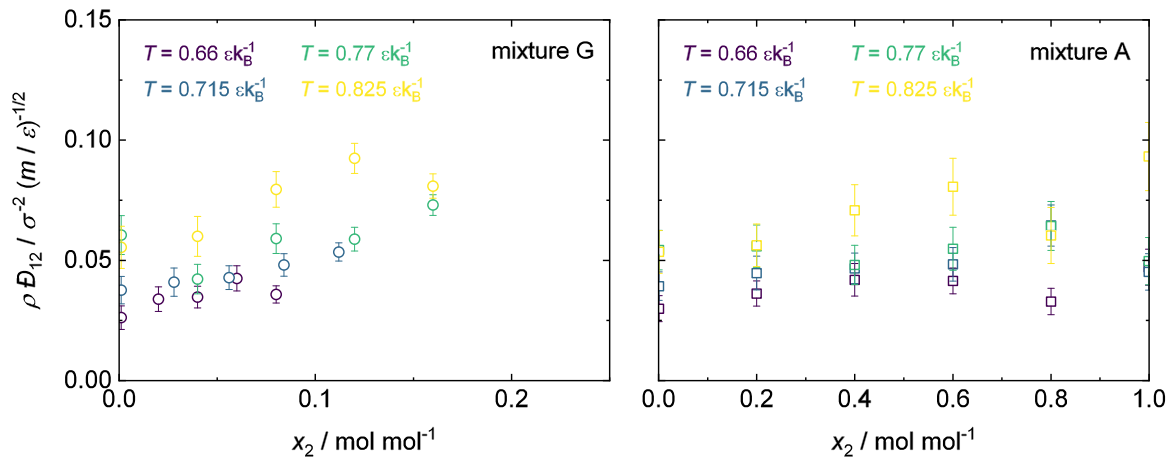
Figure A.20: Diffusivity $\rho Ð_{12}$ of the liquid phase at different temperatures. Results for mixture G (left) and mixture A (right) [638]. The color indicates the temperature.
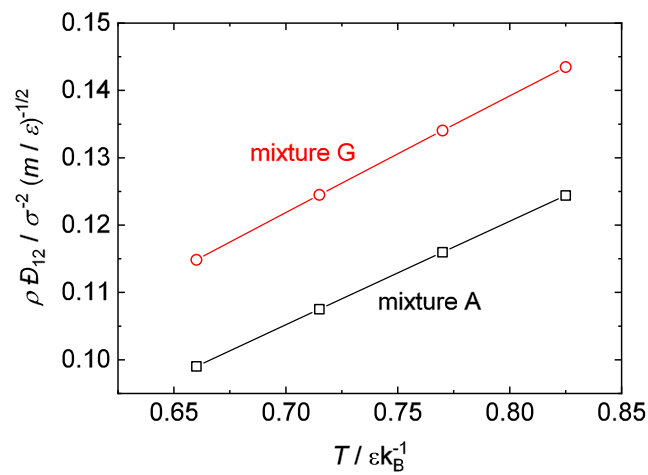
Figure A.21: Diffusivity $\rho Ð_{12}$ of the vapor phase for mixture G (circles) and A (squares) [638].

A.7 Results for the Mixture Cyclohexane + CO_2

This Appendix contains the following points:

- numeric values (results from MD and EOS) of the phase equilibria for the pure substances and the mixture of cyclohexane and CO_2, cf. Table A.18 - A.19 for the pure substances and Table A.20 for the binary mixture results at three temperatures

- numeric values of the interfacial properties obtained from MD and DGT; Tables A.21 and A.22 report the pure substance interfacial properties; Tables A.23 the mixture interfacial properties

- density profiles obtained from MD simulation of the binary mixture cyclohexane + CO_2 at three temperatures (Fig. A.22)

- numeric values of the of the experimental surface tension measurements, cf. Table A.24

Numeric Values of Phase Equilibria Results

Table A.18: MD and PCP-SAFT results for the vapor-liquid equilibrium of cyclohexane. The columns are from left to right: temperature, vapor pressure, and saturated liquid and vapor density, respectively. The number in the parentheses indicates the statistical uncertainty in the last decimal digit.

T / K	p / MPa		ρ' / mol l^{-1}		ρ'' / mol l^{-1}	
	MD	EOS	MD	EOS	MD	EOS
280	0.00524(4)	0.0054	9.349(34)	9.2530	0.0023(4)	0.0023
290	0.009(1)	0.0089	9.239(30)	9.1465	0.0039(7)	0.0037
303.15	0.0185(26)	0.0163	9.101(89)	9.0062	0.0075(16)	0.0065
313.15	0.0286(17)	0.0246	8.991(82)	8.8989	0.0112(21)	0.0096
323.15	0.0343(22)	0.0362	8.874(88)	8.7907	0.0131(29)	0.0137
333.15	0.0495(28)	0.0517	8.767(92)	8.6813	0.0185(33)	0.0190
343.15	0.0904(43)	0.0722	8.654(88)	8.5704	0.0334(41)	0.0259
353.15	0.1096(67)	0.0985	8.54(10)	8.4577	0.0392(43)	0.0347
363.15	0.1367(84)	0.1319	8.404(75)	8.3427	0.0476(44)	0.0455
373.15	0.1783(52)	0.1735	8.291(75)	8.2252	0.0615(55)	0.0588
390	0.278(9)	0.2657	8.075(27)	8.0200	0.0929(43)	0.0878
410	0.429(11)	0.4189	7.818(30)	7.7620	0.1402(65)	0.1356
430	0.650(11)	0.6309	7.536(34)	7.4838	0.211(10)	0.2020
450	0.945(11)	0.9143	7.227(42)	7.1790	0.308(18)	0.2929
470	1.327(18)	1.2829	6.882(59)	6.8381	0.440(34)	0.4171
490	1.812(14)	1.7517	6.494(98)	6.4465	0.629(71)	0.5882
510	2.438(11)	2.3374	5.91(31)	5.9783	0.995(276)	0.8309
530	3.155(27)	3.0593	5.33(35)	5.3783	1.435(348)	1.1991

Table A.19: MD and PCP-SAFT results for the vapor-liquid equilibrium of CO_2. The columns are from left to right: temperature, vapor pressure, and saturated liquid and vapor density, respectively. The number in the parentheses indicates the statistical uncertainty in the last decimal digit.

T / K	p / MPa		ρ' / mol l^{-1}		ρ'' / mol l^{-1}	
	MD	EOS	MD	EOS	MD	EOS
220	0.396(15)	0.607	26.60(17)	26.457	0.23(2)	0.360
230	0.864(24)	0.898	25.58(10)	25.685	0.56(10)	0.524
240	1.221(63)	1.282	24.51(16)	24.852	0.71(3)	0.743
250	1.89(12)	1.779	23.65(51)	23.939	1.13(7)	1.035
260	2.32(16)	2.407	22.83(21)	22.911	1.39(6)	1.423
270	3.20(16)	3.187	21.47(15)	21.718	2.02(12)	1.947
280	4.25(8)	4.144	20.18(23)	20.263	2.83(17)	2.681
290	5.08(19)	5.306	18.65(48)	18.327	3.48(21)	3.792

Table A.20: MD and PCP-SAFT results for the vapor-liquid equilibrium of the binary mixture cyclohexane + CO_2 at T = 303.15 K, 333.15 K, and 363.15 K. The columns are from left to right: the liquid phase concentration, the vapor phase concentration, the coexistence pressure, the liquid phase density, and the vapor phase density. The number in the parentheses indicates the statistical uncertainty in the last decimal digit. The given liquid phase composition holds for both the EOS and MD; for the EOS exactly and for MD with the reported uncertainty.

x'_{CO_2}/mol mol^{-1}	x''_{CO_2}/mol mol^{-1}		p / MPa		ρ' / mol l^{-1}		ρ'' / mol l^{-1}	
	MD	EOS	MD	EOS	MD	EOS	MD	EOS
T = 303.15 K								
0.0380(8)	0.9672(21)	0.9611	0.559(5)	0.4473	9.283(40)	9.196	0.228(6)	0.182
0.0618(14)	0.9777(16)	0.9745	0.906(11)	0.7120	9.411(48)	9.319	0.376(6)	0.294
0.0893(25)	0.9835(13)	0.9812	1.248(14)	1.0092	9.558(54)	9.465	0.527(8)	0.423
0.1711(21)	0.9893(6)	0.9883	2.213(21)	1.8511	10.02(9)	9.928	0.986(14)	0.815
0.2021(24)	0.9902(8)	0.9894	2.595(26)	2.1513	10.20(13)	10.115	1.182(15)	0.965
0.2526(35)	0.9909(9)	0.9906	3.097(24)	2.6163	10.53(17)	10.434	1.459(26)	1.211
0.3070(53)	0.9916(7)	0.9913	3.570(45)	3.0831	10.89(25)	10.801	1.739(21)	1.477
0.3655(50)	0.9915(4)	0.9918	4.033(33)	3.5423	11.29(38)	11.223	2.036(34)	1.761
0.4302(45)	0.9918(7)	0.9921	4.463(28)	3.9975	11.78(57)	11.727	2.341(43)	2.069
0.5039(46)	0.9914(10)	0.9923	4.868(42)	4.4477	12.38(72)	12.352	2.659(42)	2.408
0.5849(71)	0.9915(8)	0.9924	5.240(62)	4.8625	13.11(76)	13.107	2.983(72)	2.758
0.6711(44)	0.9912(6)	0.9924	5.487(53)	5.2253	13.91(84)	13.988	3.238(62)	3.105
0.7746(29)	0.9914(10)	0.9925	5.824(50)	5.6030	14.95(61)	15.119	3.625(85)	3.521
0.8692(14)	0.9911(7)	0.9929	6.164(55)	5.9897	15.84(28)	16.061	4.074(11)	4.030
T = 333.15 K								
0.0351(9)	0.9145(41)	0.9022	0.7039(87)	0.5694	8.928(36)	8.845	0.262(5)	0.212
0.0607(9)	0.9464(24)	0.9381	1.1717(83)	0.9436	9.046(40)	8.968	0.444(8)	0.356
0.0980(16)	0.9624(15)	0.9578	1.7852(87)	1.4835	9.233(48)	9.153	0.691(10)	0.572
0.1369(24)	0.9702(8)	0.9669	2.439(23)	2.0388	9.433(66)	9.354	0.968(13)	0.805
0.1770(17)	0.9740(11)	0.9720	3.149(15)	2.6035	9.648(73)	9.569	1.287(18)	1.055
0.2201(18)	0.9762(12)	0.9752	3.907(19)	3.1991	9.89(12)	9.811	1.654(18)	1.336
0.3324(38)	0.9785(11)	0.9788	5.365(37)	4.6910	10.54(24)	10.493	2.447(32)	2.130
0.3993(48)	0.9799(8)	0.9792	6.090(34)	5.5303	10.99(33)	10.938	2.893(49)	2.655
0.4648(50)	0.9774(11)	0.9790	6.971(51)	6.3094	11.39(53)	11.399	3.537(63)	3.215

$x'_{CO_2}/\text{mol mol}^{-1}$	$x''_{CO_2}/\text{mol mol}^{-1}$		p / MPa		ρ' / mol l^{-1}		ρ'' / mol l^{-1}	
	MD	EOS	MD	EOS	MD	EOS	MD	EOS
0.5592(74)	0.9764(17)	0.9775	7.798(70)	7.3493	12.01(66)	12.103	4.238(93)	4.121
0.6392(59)	0.9729(14)	0.9752	8.546(72)	8.1479	12.56(79)	12.712	5.06(16)	5.014
0.7332(25)	0.9687(16)	0.9706	9.196(46)	8.9922	13.01(84)	13.358	6.01(34)	6.303
T = 363.15 K								
0.0306(5)	0.8158(47)	0.7906	0.835(8)	0.6792	8.544(32)	8.474	0.288(6)	0.234
0.0479(8)	0.8688(30)	0.8513	1.210(11)	0.9900	8.621(39)	8.550	0.421(7)	0.343
0.0817(14)	0.9124(26)	0.9014	1.954(15)	1.5965	8.777(44)	8.702	0.692(10)	0.564
0.1454(24)	0.9434(25)	0.9347	3.286(34)	2.7419	9.068(71)	9.000	1.206(20)	1.006
0.1743(19)	0.9484(15)	0.9416	3.914(15)	3.2623	9.212(84)	9.141	1.466(25)	1.220
0.2188(24)	0.9506(15)	0.9484	4.858(25)	4.0623	9.42(11)	9.365	1.879(33)	1.566
0.2682(24)	0.9545(14)	0.9526	5.790(26)	4.9486	9.66(15)	9.624	2.313(36)	1.979
0.3068(32)	0.9536(14)	0.9544	6.598(36)	5.6392	9.85(21)	9.832	2.722(44)	2.325
0.3648(44)	0.9551(11)	0.9553	7.576(49)	6.6740	10.16(30)	10.157	3.248(56)	2.893
0.4279(51)	0.9533(25)	0.9545	8.680(49)	7.7873	10.46(45)	10.521	3.933(80)	3.586
0.5002(46)	0.9487(14)	0.9512	9.797(46)	9.0453	10.81(61)	10.946	4.68(22)	4.508
0.5859(59)	0.9415(23)	0.9431	10.865(76)	10.4977	11.15(90)	11.433	5.66(31)	5.837
0.6665(44)	0.9304(227)	0.9289	11.825(74)	11.7944	11.4(10)	11.811	6.73(47)	7.384

Numeric Values of Interfacial Properties Results

Table A.21: MD and DGT results for the vapor-liquid interfacial properties of cyclohexane. The columns are from left to right: the temperature, the surface tension, and the interfacial thickness. The number in the parentheses indicates the statistical uncertainty in the last decimal digit.

T / K	γ / mN m^{-1}		L_{10}^{90} / nm	
	MD	DGT	MD	DGT
280	28.72(37)	26.69	0.693(1)	0.80
290	27.64(15)	25.44	0.736(1)	0.82
303.15	25.78(13)	23.83	0.743(16)	0.85
313.15	24.69(23)	22.63	0.815(16)	0.87
323.15	23.69(15)	21.45	0.859(16)	0.90
333.15	22.78(21)	20.29	0.844(22)	0.92
343.15	21.06(25)	19.14	0.953(25)	0.95
353.15	19.81(15)	18.02	0.981(20)	0.98
363.15	18.53(19)	16.91	1.032(30)	1.01
373.15	17.47(15)	15.82	1.111(20)	1.05
390	15.66(18)	14.01	1.205(16)	1.11
410	13.19(15)	11.93	1.313(20)	1.21
430	11.18(15)	9.92	1.487(20)	1.32
450	9.07(10)	7.98	1.696(16)	1.47
470	7.08(9)	6.13	1.912(16)	1.66
490	5.08(17)	4.39	2.237(32)	1.94
510	3.20(12)	2.78	2.540(82)	2.36
530	1.76(11)	1.38	3.08(16)	3.14

Table A.22: MD and DGT results for the vapor-liquid interfacial properties of CO_2. The columns are from left to right: the temperature, the surface tension, and the interfacial thickness. The number in the parentheses indicates the statistical uncertainty in the last decimal digit.

T / K	γ / mN m^{-1}		L_{10}^{90} / nm	
	MD	DGT	MD	DGT
220	20.32(69)	15.66	0.81(2)	0.73
230	15.75(60)	13.42	1.09(8)	0.80
240	13.48(47)	11.24	1.14(4)	0.87
250	11.3(14)	9.13	1.49(25)	0.97
260	9.06(36)	7.10	1.43(4)	1.10
270	7.8(17)	5.16	1.75(12)	1.27
280	4.7(11)	3.34	2.14(23)	1.56
290	2.77(41)	1.70	2.58(48)	2.10

Table A.23: MD and DGT results for the vapor-liquid interfacial properties of the binary mixture cyclohexane + CO_2 at T = 303.15 K, 333.15 K, and 363.15 K. The columns are from left to right: the liquid phase concentration, the surface tension, the relative adsorption of CO_2 at the interface, the interfacial thickness, and the enrichment of CO_2. The number in the parentheses indicates the statistical uncertainty in the last decimal digit. The given liquid phase composition holds for both the DGT and MD; for the DGT exactly and for MD with the reported uncertainty.

x'_{CO_2}/mol mol^{-1}	γ / mN m^{-1}		$\Gamma_{CO_2}^{(C_6H_{12})}$ / μmol m^{-2}		L_{10}^{90} / nm		E_{CO_2}	
	MD	DGT	MD	DGT	MD	DGT	MD	DGT
T = 303.15 K								
0.0380(8)	24.24(17)	22.43	0.65(2)	0.57281011	0.83(1)	0.89	2.66(8)	2.68
0.0618(14)	23.26(29)	21.56	1.12(5)	0.94766042	0.87(1)	0.90	2.70(11)	2.64
0.0893(25)	22.24(22)	20.56	1.56(9)	1.39117202	0.90(2)	0.90	2.56(11)	2.60
0.1711(21)	18.95(23)	17.69	3.12(12)	2.79745698	0.96(2)	0.87	2.38(6)	2.46
0.2021(24)	17.80(15)	16.64	3.81(11)	3.36052806	0.98(2)	0.83	2.32(3)	2.40
0.2526(35)	16.08(12)	14.98	4.77(24)	4.30661582	1.00(3)	0.79	2.19(6)	2.29
0.3070(53)	14.28(14)	13.29	5.97(18)	5.36025348	1.03(2)	0.77	2.07(7)	2.17
0.3655(50)	12.41(16)	11.58	7.22(24)	6.51843965	1.11(3)	0.81	1.91(4)	2.03
0.4302(45)	10.56(16)	9.86	8.20(22)	7.81381184	1.23(2)	0.85	1.71(3)	1.87
0.5039(46)	8.74(19)	8.12	9.37(31)	9.27075818	1.28(3)	0.92	1.55(3)	1.68
0.5849(71)	7.23(13)	6.49	10.04(43)	10.7579958	1.46(3)	1.04	1.36(3)	1.49
0.6711(44)	5.83(18)	5.06	9.9(6)	11.9794891	1.61(3)	1.21	1.20(2)	1.30
0.7746(29)	4.22(24)	3.62	11.0(12)	12.3953079	2.02(8)	1.50	1.07(1)	1.12
0.8692(14)	3.00(16)	2.35	10.4(15)	11.2818141	2.30(9)	1.94	1.01(1)	1.01
T = 333.15 K								
0.0351(9)	20.85(19)	19.11	0.49(3)	0.43	0.96(3)	0.96	2.31(8)	2.32
0.0607(9)	19.77(28)	18.25	0.85(4)	0.76	1.00(3)	0.98	2.28(6)	2.28
0.0980(16)	18.56(23)	17.03	1.41(7)	1.24	1.04(3)	1.00	2.20(7)	2.21
0.1369(24)	17.01(35)	15.77	1.95(7)	1.76	1.10(2)	1.02	2.12(5)	2.15
0.1770(17)	15.60(23)	14.49	2.58(6)	2.30	1.13(3)	1.02	2.07(3)	2.08
0.2201(18)	14.08(28)	13.15	3.41(8)	2.90	1.19(2)	1.02	2.00(2)	2.00
0.3324(38)	10.65(27)	9.86	4.73(19)	4.52	1.34(3)	1.04	1.70(3)	1.80
0.3993(48)	9.19(49)	8.05	5.8(2)	5.49	1.39(3)	1.08	1.60(3)	1.67

| $x'_{CO_2}/mol\,mol^{-1}$	γ / mN m^{-1}		$\Gamma_{CO_2}^{(C_6H_{12})}$ / $\mu mol\,m^{-2}$		L_{10}^{90} / nm		E_{CO_2}	
	MD	DGT	MD	DGT	MD	DGT	MD	DGT
0.4648(50)	6.88(28)	6.42	6.3(4)	6.44	1.61(6)	1.19	1.45(3)	1.54
0.5592(74)	5.1(16)	4.34	6.6(5)	7.72	1.90(6)	1.44	1.26(3)	1.37
0.6392(59)	3.47(30)	2.84	7.5(7)	8.61	2.33(8)	1.83	1.15(1)	1.23
0.7332(25)	2.12(80)	1.43	5.3(11)	9.03	3.08(20)	2.64	1.04(1)	1.10
$T = 363.15\,K$								
0.0306(5)	17.52(29)	15.98	0.36(3)	0.31	1.10(2)	1.06	2.08(6)	2.05
0.0479(8)	17.01(24)	15.46	0.53(3)	0.49	1.13(2)	1.06	2.03(7)	2.02
0.0817(14)	15.84(39)	14.44	0.94(3)	0.84	1.19(3)	1.10	1.98(4)	1.97
0.1454(24)	13.79(30)	12.57	1.75(10)	1.51	1.28(3)	1.15	1.88(4)	1.87
0.1743(19)	12.84(23)	11.74	1.95(9)	1.82	1.33(2)	1.17	1.82(3)	1.83
0.2188(24)	11.22(28)	10.48	2.69(8)	2.29	1.40(2)	1.21	1.77(3)	1.76
0.2682(24)	9.67(51)	9.13	2.99(16)	2.81	1.50(3)	1.25	1.66(3)	1.68
0.3068(32)	8.59(31)	8.11	3.18(16)	3.22	1.61(3)	1.29	1.56(3)	1.63
0.3648(44)	7.16(40)	6.64	3.75(15)	3.81	1.71(4)	1.37	1.48(2)	1.54
0.4279(51)	5.54(33)	5.14	4.01(28)	4.40	1.91(5)	1.50	1.36(2)	1.44
0.5002(46)	4.12(81)	3.59	2.38(34)	4.96	2.19(6)	1.75	1.21(2)	1.33
0.5859(59)	2.69(35)	2.02	2.96(58)	5.29	2.6(1)	2.29	1.11(1)	1.21
0.6665(44)	1.65(29)	0.90	1.55(61)	4.92	2.9(2)	3.29	1.04(1)	1.11

Density Profiles
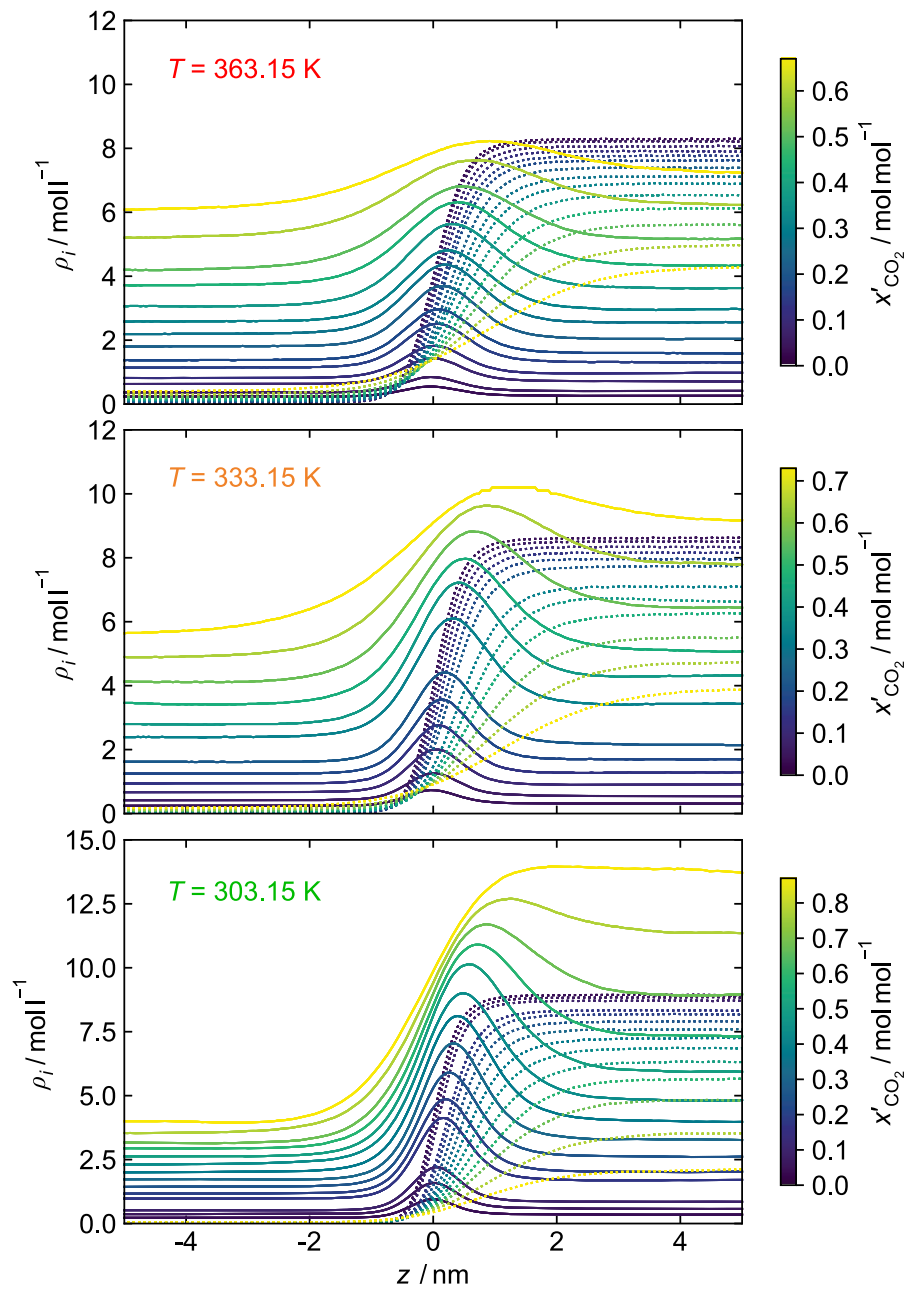
Figure A.22: Density profiles of the binary mixture cyclohexane + CO_2 at three different temperatures: 303.15 K (bottom), 333.15 K (middle), and 363.15 K (top) and different composition. Results from MD. Dashed lines are CO_2; solid lines are cyclohexane. The color indicates the liquid phase composition.

Results of Experimental Measurements

Table A.24: Experimental data of the surface tension of the binary mixture cyclohexane + CO_2 obtained with the pendant drop apparatus [624]. Absolute uncertainties U are $U(T) = 0.1\,\text{K}$, $U(p) = 0.0025\,\text{MPa}$ for $p > 2.5\,\text{MPa}$ and $U(p) = 0.01\,\text{MPa}$ for $p > 2.5\,\text{MPa}$. The relative uncertainty of the surface tension is $u(\gamma) = 0.041\,\gamma$.

T / K	p / MPa	γ / mN m^{-1}	T / K	p / MPa	γ / mN m^{-1}
303.15	0.573	21.63	343.15	0.526	17.79
	1.028	20.30		1.034	16.83
	2.014	17.40		2.065	14.93
	3.001	14.02		3.138	12.77
	4.032	10.21		4.093	11.13
	4.998	6.35		5.089	9.27
	5.991	2.59		5.974	7.61
313.15	0.529	20.72	353.15	0.539	16.87
	1.031	19.50		1.036	16.04
	2.106	16.68		2.083	14.22
	3.066	13.76		3.099	12.48
	4.065	11.01		4.109	10.74
	5.06	7.90		5.079	9.23
	6.47	3.13		6.028	7.63
323.15	0.561	19.74	363.15	0.584	16.06
	1.055	18.72		1.063	15.15
	2.065	16.35		2.078	13.59
	3.098	13.72		3.129	11.96
	4.106	11.26		4.126	10.40
	5.099	8.70		5.133	8.86
	6.107	6.10		6.027	7.57
333.15	0.512	19.07	373.15	0.583	14.83
	1.044	17.82		1.023	14.24
	2.122	15.56		2.076	12.78
	3.132	13.31		3.162	11.25
	4.131	11.09		4.129	9.85
	5.114	9.06		5.081	8.60
	6.053	7.07		5.954	7.49

B Details on Data Analysis and Data Assessment

B.1 Details on the Assessment of LJ Computer Experiment Data

This Appendix contains the following points:

- additional information on the EOS test for the assessment of the homogeneous state points.

- additional information on the compressibility factor test, the Clausius-Clapeyron test, and the deviation test of the VLE bulk data, cf. Fig. A.24, A.25, and A.26, respectively. All available VLE data (both confirmed and discarded) are shown and discussed in detail.

- additional information on the surface tension data, cf. Fig. A.27.

- list of clear outliers (eight data point) from the seven best VLE datasets (Refs. [163, 164, 298, 299, 395, 452, 510, 541, 548] and this work), cf. Table A.25.

Details on the Assessment of Homogeneous States Data

Fig. A.23 shows the results of the EOS test on the homogeneous state points as the percentage of the overall confirmed data as a function of the parameter $P_{\max}$. The chosen value of $P_{\max} = 4$ is indicated, which entails approximately 90% confirmed data. For smaller $P_{\max}$ values, the EOS test becomes more stringent as more data points are characterized as outliers. For larger $P_{\max}$ values, the EOS test becomes more lenient (i.e. more conservative) and less data points are identified as outliers. Evidently, the EOS test converges for large $P_{\max}$ values to approximately $N_{\text{conf}} = 98\%$, which means that these 2% of all homogeneous data are particularly gross outliers.
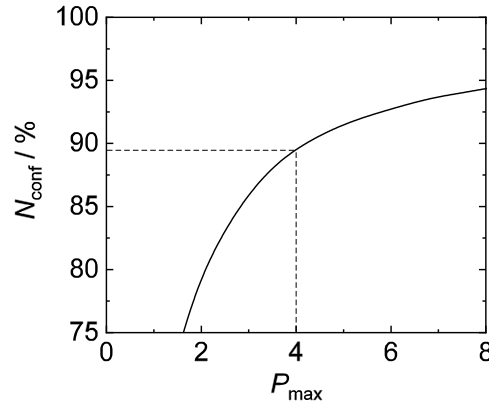
Figure A.23: Percentage of overall confirmed data as a function of the parameter P_{max} for the homogeneous data EOS test. N_{conf} is the confirmation rate of all homogeneous data. The dashed line indicates the value $P_{max} = 4$ chosen for the identification of outliers as they are specified in the database.

Details on the Assessment of VLE Bulk data

The results of the three VLE tests for all datasets (both confirmed and discarded) are shown in Figs. A.24, A.25, and A.26. Fig. A.24 shows the results of the compressibility factor test for all VLE data, Fig. A.25 shows the results of the Clausius-Clapeyron test for all VLE data, and Fig. A.26 shows the deviations from all VLE data and the base correlations (see section 4.2 for details).

Datasets that were discarded according the criteria for the compressibility factor test (cf. Fig. A.24) outlined in the main part of this work are those from *Adams* [6], *Adams* [7], *Anisimov et al.* [23], *Baidakov et al.* [31], *Baidakov et al.* [39], *Betancourt-Cárdenas et al.* [53], *Kioupis et al.* [324], *Martin and Siepmann* [410], *Panagiotopoulos* [514], *Panagiotopoulos et al.* [516], *Smit and Frenkel* [612], and *Trokhymchuk and Alejandre* [672].

For the datasets from the literature that report all VLE properties required for the Clausius-Clapeyron test, the RHS of Eq. (73) was computed and is shown in Fig. A.25 for comparison. Large deviations from the base correlation and the most precise datasets (Refs. [298, 299, 395, 452] and this work) were found for the data of *Adams* [6], *Adams* [7], *Kioupis et al.* [324], *Betancourt-Cárdenas et al.* [53], *Panagiotopoulos* [514], *Panagiotopoulos et al.* [516], and *Smit and Frenkel* [612]. According the criteria outlined in the main part of this work, these datasets were discarded.

Fig. A.26 shows the deviation plots for each VLE property (p^s, ρ', ρ'', and Δh_v) for all VLE datasets considered in this work. The following datasets contain two or more data points with deviations larger than 5%, i.e. are out of the range of Fig. A.26: *Adams* [6], *Adams* [7], *Anisimov et al.* [23], *Baidakov et al.* [31], *Baidakov et al.* [39], *Baidakov et al.* [37], *Betancourt-Cárdenas et al.* [53], *Guo et al.* [230], *Guo and Lu* [229], *Galliero et al.* [189], *Hunter and Reinhardt* [283], *Holcomb et al.* [268], *Janeček* [297], *Kioupis et al.* [324], *Kofke* [331], *Lee et al.* [363], *Martin and Siepmann* [410], *Mecke et al.* [440], *Okumura and Yonezawa* [509, 547], *Panagiotopoulos* [514], *Panagiotopoulos et al.* [516], *Potoff and Panagiotopoulos* [534], *Smit and Frenkel* [612], and *Trokhymchuk and Alejandre* [672]. These pronounced deviations were found in most cases for the vapor
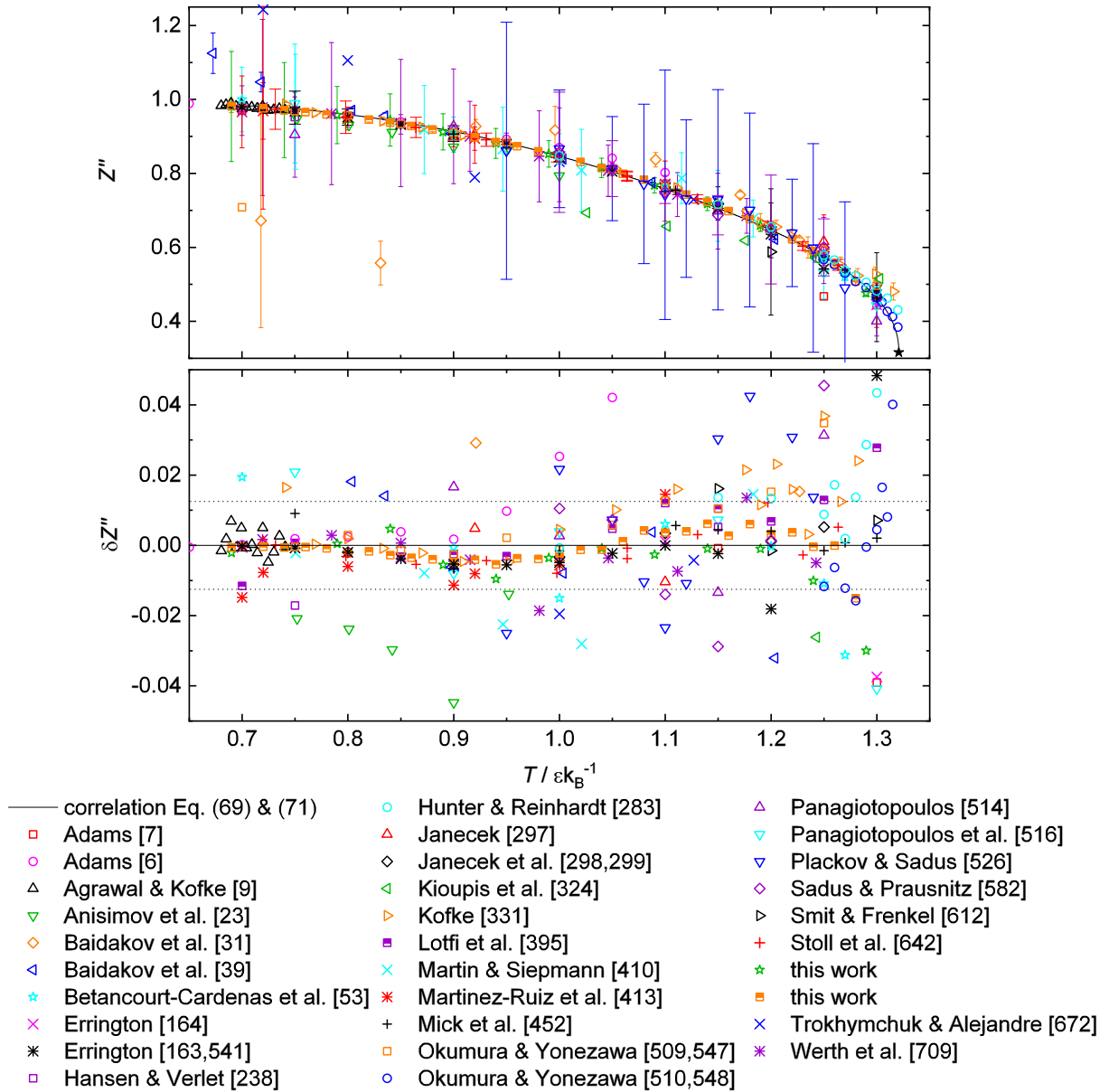
Figure A.24: Compressibility factor test for the vapor-liquid equilibrium data of the Lennard-Jones fluid according to *Nezbeda* [494, 495]: saturated vapor phase compressibility factor Z'' as function of the temperature T (top) and the relative deviation of Z'' from correlations (69) and (71) (bottom). The dotted line indicates the range of 2.5 times the confidence interval of the most precise data, as discussed in section 4.2. Error bars are omitted in the bottom plot to avoid visual clutter. For clarity, the out-of-range data points are omitted in both, the top and bottom plot. The black filled star indicates the compressibility factor at the critical point according the base correlation.
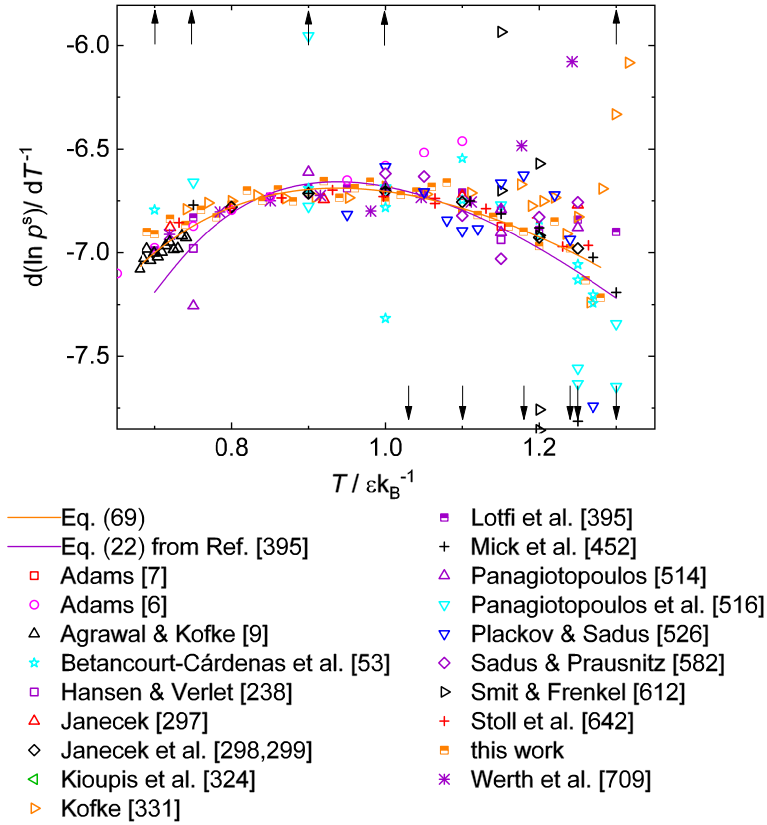
Figure A.25: Clausius-Clapeyron test according to Eq. (73). Symbols indicate the RHS and the lines the LHS of Eq. (73). The orange line indicates Eq. (69). The purple line is Eq. (22) from Ref. [395]. For clarity, the numeric values of the out-of-range data points are omitted in the plot; they lie in the range of $d(\ln p^s)/d(T^{-1}) = -31$ to -0.8.

pressure and the saturated vapor density. Deviations of data points that exceed 5% in the saturated liquid density or the enthalpy of vaporization were only found for the data from *Panagiotopoulos* [514], *Smit and Frenkel* [612], *Kofke* [331], *Kioupis et al.* [324], *Hunter and Reinhardt* [283], *Mecke et al.* [440], and *Lee et al.* [363]. Datasets exhibiting particularly large deviations from Eqs. (69) - (72) at multiple state points are those from *Anisimov et al.* [23], *Baidakov et al.* [31], *Baidakov et al.* [39], *Galliero et al.* [189], *Hunter and Reinhardt* [283], *Kioupis et al.* [324], *Lee et al.* [363], *Panagiotopoulos* [514], and *Trokhymchuk and Alejandre* [672]. To avoid visual clutter, these out-of-range data points are not shown in Fig. A.26. This confirms the findings from the compressibility factor and the Clausius-Clapeyron tests, where these datasets could be applied.

The datasets of *Hunter and Reinhardt* [283], *Potoff and Panagiotopoulos* [534], *Shi and Johnson* [603] (only saturated densities reported) show small, but distinct systematic deviations to the base correlation and the seven most precise datasets.
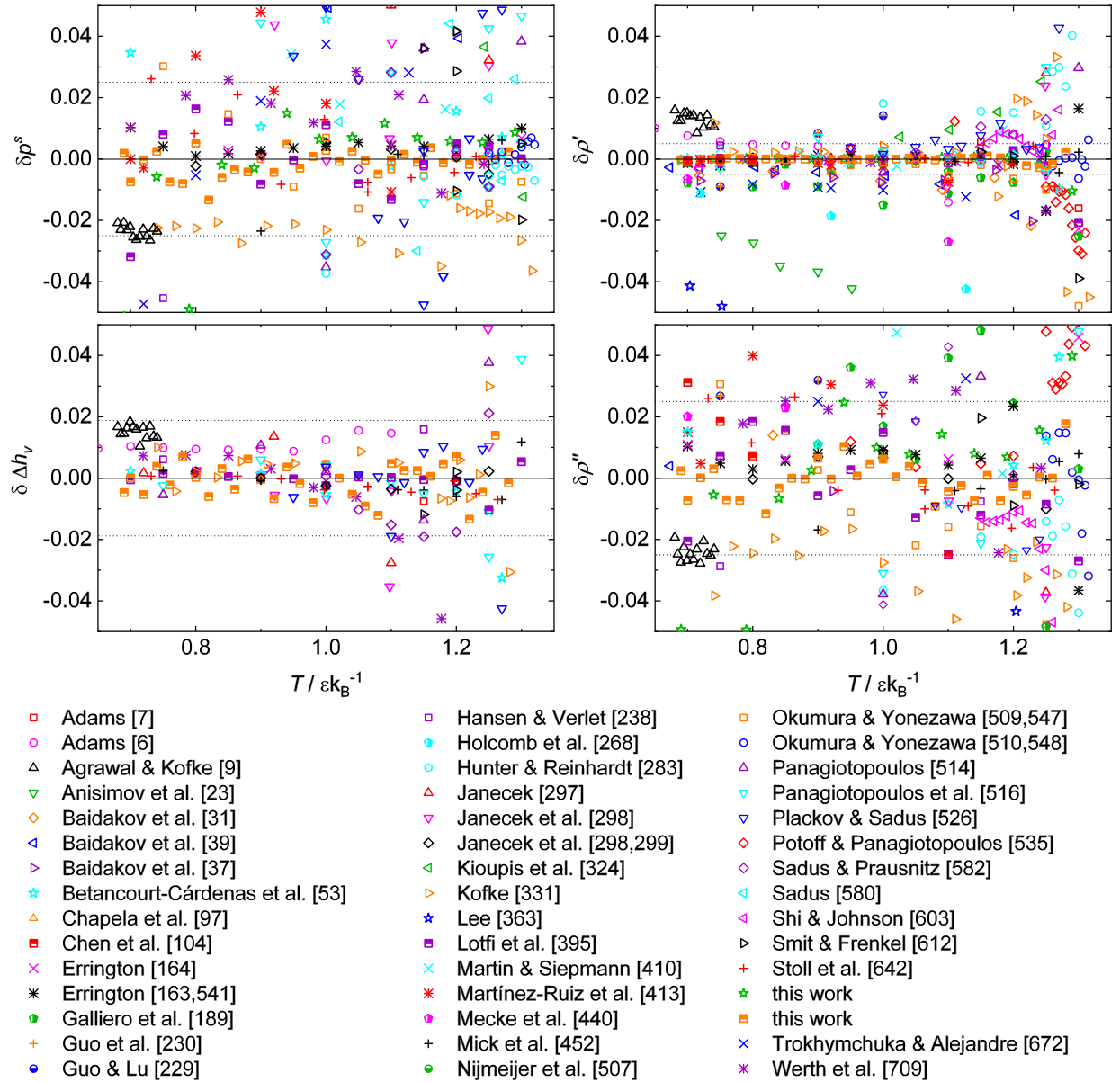
□ Adams [7]	□ Hansen & Verlet [238]
○ Adams [6]	⬠ Holcomb et al. [268]
△ Agrawal & Kofke [9]	○ Hunter & Reinhardt [283]
▽ Anisimov et al. [23]	△ Janecek [297]
◇ Baidakov et al. [31]	▽ Janecek et al. [298]
◁ Baidakov et al. [39]	◇ Janecek et al. [298,299]
▷ Baidakov et al. [37]	◁ Kioupis et al. [324]
✦ Betancourt-Cárdenas et al. [53]	▷ Kofke [331]
△ Chapela et al. [97]	★ Lee [363]
■ Chen et al. [104]	■ Lotfi et al. [395]
✕ Errington [164]	✕ Martin & Siepmann [410]
✳ Errington [163,541]	✳ Martínez-Ruiz et al. [413]
⬠ Galliero et al. [189]	⬠ Mecke et al. [440]
+ Guo et al. [230]	+ Mick et al. [452]
● Guo & Lu [229]	● Nijmeijer et al. [507]

□ Okumura & Yonezawa [509,547]
○ Okumura & Yonezawa [510,548]
△ Panagiotopoulos [514]
▽ Panagiotopoulos et al. [516]
▽ Plackov & Sadus [526]
◇ Potoff & Panagiotopoulos [535]
◇ Sadus & Prausnitz [582]
◁ Sadus [580]
◁ Shi & Johnson [603]
▷ Smit & Frenkel [612]
+ Stoll et al. [642]
★ this work
■ this work
✕ Trokhymchuka & Alejandre [672]
✳ Werth et al. [709]

Figure A.26: Relative deviations of the vapor-liquid equilibrium data for the vapor pressure p^s, saturated liquid density ρ', saturated vapor density ρ'', and enthalpy of vaporization Δh_v from correlations (69) - (72) as a function of the temperature T. Error bars were omitted to avoid visual clutter. The dotted lines indicates the range of 2.5 times the confidence interval of the most precise data δx, as discussed in section 4.2. For clarity, the out-of-range data points are omitted in the deviation plots.

Details on the Assessment of VLE Interfacial Data

Fig. A.27 shows the surface tension of the LJ fluid from all considered data. The surface tension results reported by *Trokhymchuk and Alejandre* [672] and the MC results of *Galliero et al.* [189] are slightly but noticeably below the mutually best agreeing datasets. The data of *Anisimov et al.* [23] show large deviations, which is likely a result of the employed LJ potential version.

The surface tension data of *Potoff and Panagiotopoulos* [535] shows distinct deviations from the above mentioned data of best mutual agreement – especially close to the critical point. The same was found for the saturated densities data of *Potoff and Panagiotopoulos* [535]. This is in line with the relatively low critical temperature reported by Ref. [535].

Identified Outliers in Best VLE Datasets

Table A.25 summarizes the identified outliers in the datasets that were identified to be the best VLE datasets: *Errington* [163, 541], *Janeček et al.* [298, 299], *Lotfi et al.* [395], *Mick et al.* [452], *Okumura and Yonezawa* [510, 548], and this work.

Table A.25: Identified outliers in the best VLE datasets: *Errington* [163, 541], *Janeček et al.* [298, 299], *Lotfi et al.* [395], *Mick et al.* [452], *Okumura and Yonezawa* [510, 548], and this work.

Reference	$T \, / \, \varepsilon k_{\mathrm{B}}^{-1}$	$p^s \, / \, \varepsilon\sigma^{-3}$	$\rho' \, / \, \sigma^{-3}$	$\rho'' \, / \, \sigma^{-3}$	$\Delta h_v \, / \, \varepsilon$
Mick et al. [452]	0.75	0.0022(1)	0.8208(2)	0.0030(1)	6.595(3)
	1.25	0.0967(4)	0.514(2)	0.135(2)	3.30(3)
this work[a]	1.08	0.040583(62)	0.65371(20)	0.047992(74)	4.8332(12)
Lotfi et al. [395]	0.7	0.00131(6)	0.84266(18)	0.00193(10)	6.758(4)
Errington [164]	1.3	0.1212(10)	0.4271(13)	0.2096(13)	-
Errington [163, 541]	1.3	0.1215841(996)	0.4442(51)	0.193072(5552)	-
	1.25	0.0975052(672)	0.5049(12)	0.143990(335)	-

[a] data point is slightly off the statistical uncertainties regarding the self-consistency Clausius-Clapeyron test (see Fig. A.25).
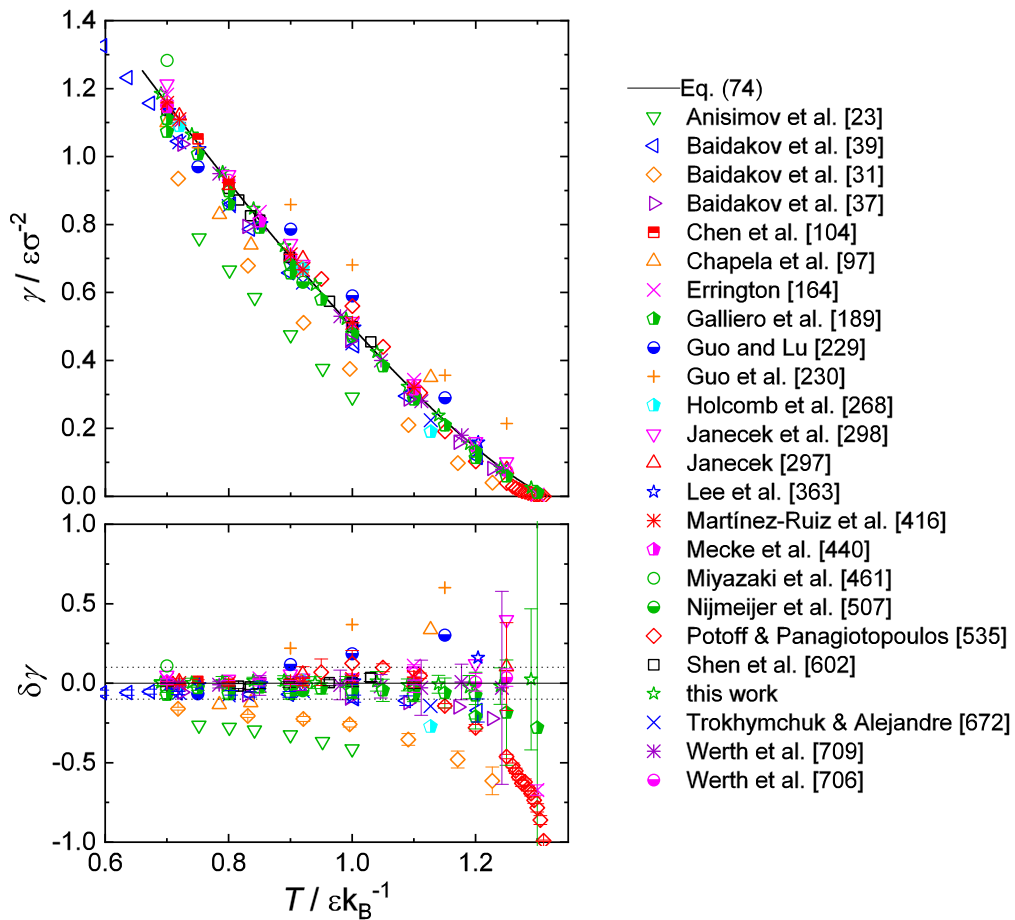
Figure A.27: Surface tension of the LJ fluid as a function of the temperature (top) and the corresponding relative deviation plot (bottom). The black line indicates Eq. (74). Symbols indicate computer experiment data. For clarity, numerical values for out-of-range data points in the vicinity of the critical temperature in the deviation plot are omitted. The dotted lines indicates the range of 2.5 times the confidence interval of the most precise data as discussed in section 4.2.

B.2 Details on the Assessment of LJ EOS

This Appendix contains the following points:

- remarks on the implementation of the Lennard-Jones (LJ) equations of state (EOS)

- remarks on the considered LJ EOS

- critical data of the Lennard-Jones fluid

- behavior of $p - \rho$ isotherms in the two-phase region

- comparison of spinodal reference data with selected LJ EOS

Implementations of the LJ EOS

All 20 considered LJ EOS were implemented in Matlab and validated using data reported in the respective original publications. Benchmark values for the validation of the implementation of the EOS were unfortunately not in all cases available. Several authors only reported graphical results computed from their LJ EOS or numeric values with few significant digits. Interestingly, in most cases, publications reporting empirical LJ EOS provide excellent test-data and even in some cases a source code, whereas theoretically-based LJ EOS generally provide only sparse support for potential users.

Hess [258] proposed several LJ EOS in his publication. We have employed the EOS described by Eqs. (7), (10), (11), (15), (18), and (20) of Ref. [258].

Van Westen and Gross [710] compared several approaches; we have used the LJ EOS termed 'BH3 corr'.

Typos were identified in two publications [554, 710]. We could reproduce the results reported in these publications only after correcting them. The corrections are briefly described in the following. The LJ EOS of *Quiñones-Cisneros et al.* [554] was implemented in accordance with the implementation in Ref. [134]. Two typos were thereby identified in the original publication [554]. Eq. (15) from Ref. [554] was changed in our implementation to

$$p_{\mathrm{r}}^* = \frac{T^* \rho^{*2} b + (...)}{1 - b\rho^*} \ , \tag{136}$$

and Eq. (17) from Ref. [554] to

$$p_{\mathrm{dis}}^* = (...)\, \rho^{*\,1.9} \exp[-(...)\rho^{*\,3}] \ . \tag{137}$$

The LJ EOS of *van Westen and Gross* [710] was implemented after correcting two typos: the last term in Eq. (26) and an inverted sign in Eq. (41). Accordingly, the following equations were used for the LJ EOS of *van Westen and Gross* [710] in the present work:

$$y_d^{\mathrm{hs}} = \exp((...) + C(\eta)x^3) \, , \tag{138}$$

$$a_3 = +\beta^3(...) \ . \tag{139}$$

Also the LJ EOS of *Betancourt-Cárdenas et al.* [53] was implemented in the present work, but results reported in the original publication could not be reproduced. However, the deviations computed from our implementation of the LJ EOS of *Betancourt-Cárdenas et al.* [53] are in agreement with those reported by *Guerin* [227] for the same LJ EOS. Nevertheless, the LJ EOS from Ref. [53] was discarded from the present study.

In cases where LJ EOS yield complex numbers for a given property and data point, only its real part was used.

Remarks on the Considered LJ EOS

This section reports details on the LJ EOS considered in chapter 4. Fig. A.28 gives an overview of the number of citations of the respective publications.
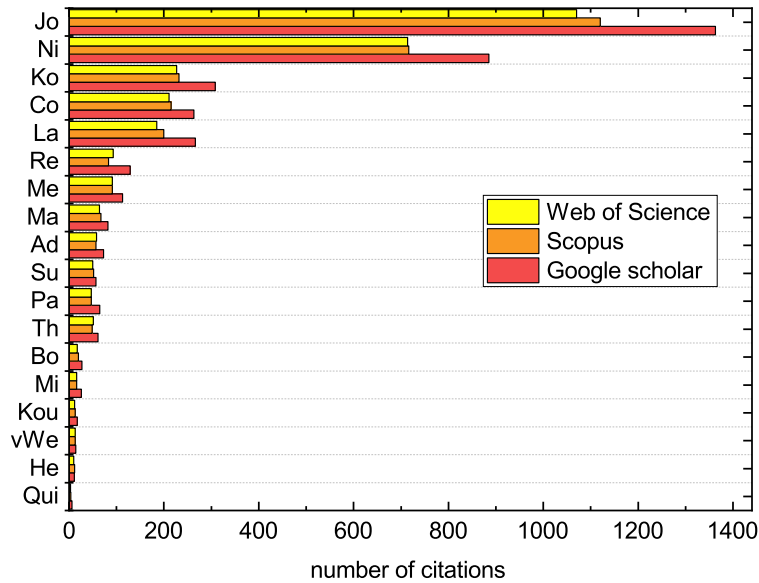
Figure A.28: Number of citations of the publications reporting LJ EOS that were considered in the present work. The abbreviations refer to Table I of the main body of this work. The data was taken in April 2020.

In the following, for each of the 20 considered LJ EOS, some central features are summarized, based on the original publications: range of validity, type of data used for the parametrization, and number of parameters used for the optimization. The latter is given in the form ($\#P_{real}$ | $\#P_{exp}$), where $\#P_{real}$ indicates the number of parameters that are real numbers (classical parameters) and $\#P_{exp}$ indicates parameters that are exponents that were also fitted or selected. The sequence of the LJ EOS corresponds to that used for the discussion of the LJ EOS in the main body of this work.

- LJ EOS of *Cotterman et al.* [128] (Co, 1986)
  - reported range of validity: not stated
  - reference data used for parametrization: second virial coefficient and first and second-order perturbation term data
  - number of parameters (15 | 13)

- LJ EOS of *Paricaud* [519] (Pa, 2006)
  - reported range of validity: not stated
  - reference data used for parametrization: hard sphere radial distribution function
  - number of parameters (34 | 9)

- LJ EOS of *Lafitte et al.* [353] (La, 2013)
  - reported range of validity: not stated
  - reference data used for parametrization: first and second-order perturbation term data and VLE data of the Mie fluid
  - number of parameters (62 | 12)

- LJ EOS of *van Westen and Gross* [710] (vWe, 2017)
  - reported range of validity: not stated
  - reference data used for parametrization: first, second, and third-order perturbation term data
  - number of parameters (43 | 19)

- LJ EOS of this work (th, 2020)
  - reported range of validity: $0.66 < T < 5\,\varepsilon k_{\mathrm{B}}^{-1}$ and $\rho < 1.25\,\sigma^{-3}$
  - reference data used for parametrization: second and third virial coefficient, VLE of the LJ fluid, and Helmholtz energy and its density and inverse temperature derivatives at homogeneous states
  - number of parameters (18 | 8)

- LJ EOS of *Koutras et al.* [343] (Kou, 1992)
  - reported range of validity: not stated
  - reference data used for parametrization: second virial coefficient and pvT data
  - number of parameters (15 | 8)

- LJ EOS of *Kolafa and Nezbeda* [334] (Ko, 1994)
  - reported range of validity: $0.68 < T < 10\,\varepsilon k_{\mathrm{B}}^{-1}$
  - reference data used for parametrization: second virial coefficient, pvT data, and internal energy data at homogeneous states
  - number of parameters (36 | 32)

- LJ EOS of *Mecke et al.* [438, 439] (Me, 1996)
  - reported range of validity: $0.7 < T < 10\,\varepsilon k_{\mathrm{B}}^{-1}$
  - reference data used for parametrization: second and third virial coefficient, pvT data, internal energy data at homogeneous states, and VLE data of the LJ fluid
  - number of parameters (38 | 70)

- LJ EOS of *Hess* [258] (He, 1999)
  - reported range of validity: not stated
  - reference data used for parametrization: -
  - number of parameters (0 | 0)

- LJ EOS of *Boltachev and Baidakov* [62] (Bo, 2003)
  - reported range of validity: $0.7 < T < 35\,\varepsilon k_{\mathrm{B}}^{-1}$ and $p < 0.5\,\varepsilon\sigma^{-3}$
  - reference data used for parametrization: not reported explicitly
  - number of parameters (39 | 33)

- LJ EOS of *Gottschalk* [217] (Go, 2019)

- reported range of validity: $T < 140\,\varepsilon k_{\mathrm{B}}^{-1}$ and $\rho < 2.5\,\sigma^{-3}$

- reference data used for parametrization: virial coefficients, and Helmholtz energy and its density and inverse temperature derivatives at homogeneous states

- number of parameters (167 | 38)

- LJ EOS of *Quiñones-Cisneros et al.* [554] (Qui, 2009)
  - reported range of validity: $0.7 < T < 6\,\varepsilon k_{\mathrm{B}}^{-1}$

  - reference data used for parametrization: not stated

  - number of parameters (16 | 15)

- LJ EOS of *Nicolas et al.* [505] (Ni, 1979)
  - reported range of validity: $0.5 < T < 6\,\varepsilon k_{\mathrm{B}}^{-1}$ and (depending on T) $0 < \rho < 1.2\,\sigma^{-3}$

  - reference data used for parametrization: second virial coefficient and pvT and internal energy data

  - number of parameters (33 | 43)

- LJ EOS of *Adachi et al.* [4] (Ad, 1988)
  - reported range of validity: not stated

  - reference data used for parametrization: second virial coefficient and pvT data

  - number of parameters (33 | 43)

- LJ EOS of *Miyano* [460] (Mi, 1993)
  - reported range of validity: $0.45 < T < 100\,\varepsilon k_{\mathrm{B}}^{-1}$ and $0 < \rho < 1.2\,\sigma^{-3}$

  - reference data used for parametrization: second virial coefficient, pvT data, and internal energy data

  - number of parameters (33 | 43)

- LJ EOS of *Johnson et al.* [302] (Jo, 1993)
  - reported range of validity: $0.7 < T < 6\,\varepsilon k_{\mathrm{B}}^{-1}$

  - reference data used for parametrization: second virial coefficient, pvT data, and internal energy data

  - number of parameters (33 | 43)

- LJ EOS of *Sun and Teja* [646] (Su, 1996)
  - reported range of validity: $0.45 < T < 6\,\varepsilon k_{\mathrm{B}}^{-1}$

  - reference data used for parametrization: second virial coefficient, pvT data, and internal energy data

  - number of parameters (33 | 43)

- LJ EOS of *May and Mausbach* [423, 425] (Ma, 2012)

- reported range of validity: not stated

- reference data used for parametrization: second virial coefficient, pvT data and internal energy data

- number of parameters (33 | 43)

- LJ EOS of *Ree* [559] (Re, 1980)
  - reported range of validity: $0.76 < T < 2.698\,\varepsilon k_{\mathrm{B}}^{-1}$ and $0.05 < \rho < 0.96\,\sigma^{-3}$

  - reference data used for parametrization: pvT data

  - number of parameters (15 | 22)

- LJ EOS of *Thol et al.* [661] (Th, 2016)
  - reported range of validity: $0.661 < T < 9\,\varepsilon k_{\mathrm{B}}^{-1}$ and $p < 65\,\varepsilon\sigma^{-3}$

  - reference data used for parametrization: Helmholtz energy and its density and inverse temperature derivatives at homogeneous states

  - number of parameters (67 | 52)

Critical Data of the Lennard-Jones Fluid

Table A.26 reports the critical data obtained from the LJ EOS. For the sake of completeness, also critical parameters from LJ EOS are reported that were not employed in the evaluation of the present work. These results are compared in Fig. A.29 to the critical data obtained from computer experiments reported in the literature. That data was discussed and evaluated in Ref. [640], cf. chapter 4. We report the compilation of the available primary data on the critical data of the LJ fluid (both EOS and computer experiment) in Fig. A.29. The presumed true critical data values are $T_c = 1.321 \pm 0.007\,\varepsilon k_{\mathrm{B}}^{-1}$ and $\rho_c = 0.316 \pm 0.005\,\sigma^{-3}$ and $p_c = 0.129 \pm 0.005\,\varepsilon\sigma^{-3}$. Evidently, some computer experiment data and LJ EOS show significant deviations from those.

Table A.26: Critical data obtained from Lennard-Jones equations of state.

publication		year	$T_c \ / \ \varepsilon k_B^{-1}$	$\rho_c \ / \ \sigma^{-3}$	$p_c \ / \ \varepsilon\sigma^{-3}$
Levesque & Verlet [370]		1969	1.3700	0.3100	0.1403
			1.3600	0.3300	0.1616
Nicolas et al. [505]	Ni	1979	1.3500	0.3500	0.1417
Ree [559]	Re	1980	1.41	0.33	0.177
Sys & Malijevsky [649]		1980	1.35	0.33	0.147
Cotterman et al. [128]	Co	1986	1.3305	0.3222	0.1413
Adachi et al. [4]	Ad	1988	1.2731	0.2842	0.1188
Song & Mason [616]		1989	1.3057	0.2625	0.1225
Koutras et al. [343]	Kou	1992	1.355	0.29	0.147
Miyano [460]	Mi	1993	1.3500	0.3200	0.1420
Johnson et al. [302]	Jo	1993	1.3130	0.3100	0.1299
Kolafa & Nezbeda [334]	Ko	1994	1.3396	0.3108	0.1405
Mecke et al. [438, 439]	Me	1996	1.3280	0.3107	0.1352
Sun & Teja [646]	Su	1996	1.3130	0.3100	0.1299
Amadai et al. [21]		1999	1.35	0.337	0.149
Hess [258]	He	1999	1.4187	0.2851	0.1499
			1.2800	0.2500	0.1056
			1.3300	0.3000	0.1357
Gross & Sadowski [223] (PC-SAFT)[†]		2001	1.2757	0.2824	0.1147
Boltachev & Baidakov [62]	Bo	2003	1.3082	0.2962	0.1262
Paricaud [519]	Pa	2006	1.3859	0.3112	0.1602
Betancourt-Cardenas et al. [53]		2008	1.3532	0.3162	0.1508
Betancourt-Cardenas et al. [53][††]			1.3531	0.3166	0.1669
Quiñones-Cisneros et al. [554]	Qui	2009	1.3321	0.3236	0.1387
May & Mausbach [423, 425]	Ma	2012	1.3145	0.3160	0.1300
Lafitte et al. [353]	La	2013	1.3122	0.3003	0.1306
Thol et al. [661]	Th	2016	1.3200	0.3100	0.1301
van Westen & Gross [710]	vWe	2017	1.3535	0.3196	0.1544
Gottschalk [217]	Go	2019	1.3276	0.3164	0.1356
this work	th	2020	1.3352	0.3105	0.1383

[††] critical point obtained from the implementation from this work
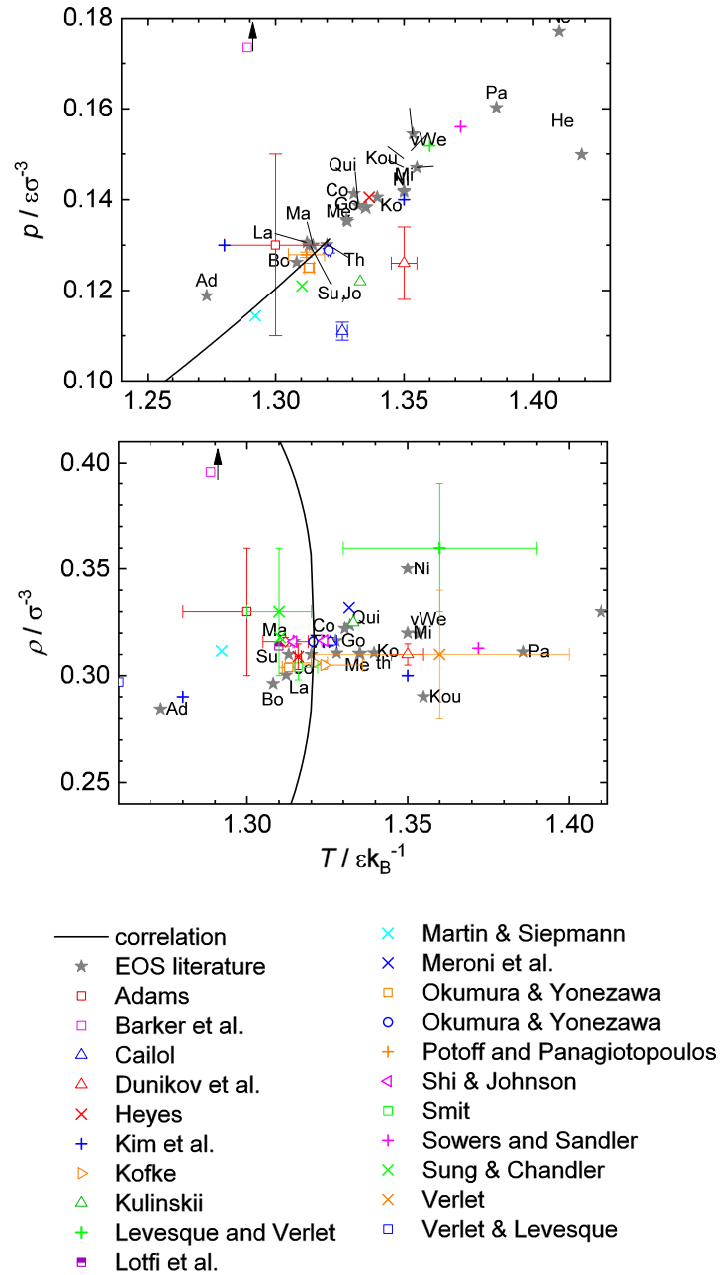[†] original parameters of the PC-SAFT monomer [223]

Figure A.29: Critical point of the LJ fluid. Top: critical pressure over tempera-
ture. Bottom: critical density over temperature. Each combination
of a gray star & abbreviation indicates the critical parameters from an
LJ EOS. The abbreviations are linked with Table A.26. Colored sym-
bols are critical parameters obtained from computer experiment of Refs.
[7, 46, 84, 148, 259, 323, 331, 350, 370, 395, 410, 450, 509, 510, 534, 559,
603, 611, 618, 647, 677, 678], cf. Table 9.

Behavior of $p - \rho$ Isotherms in the Two-Phase Region

Fig. A.30 shows the vapor-liquid two-phase region in a $p - \rho$ diagram for the characterization of the van der Waals loops. Fig. A.30 shows results from from computer experiments in the metastable region (symbols) at four temperatures and the corresponding isotherms computed from the LJ EOS of *Thol et al.* [661], *Gottschalk* [217], and the LJ EOS from the present work. The LJ EOS of *Thol et al.* [661] and *Gottschalk* [217] exhibit strong oscillations in the two-phase region. Furthermore, Fig. A.30 shows that isotherms yield significant negative pressure in the unstable region – as expected. However, the LJ EOS of *Thol et al.* [661] and *Gottschalk* [217] yield isotherms with multiple zero crossings in the two-phase region.
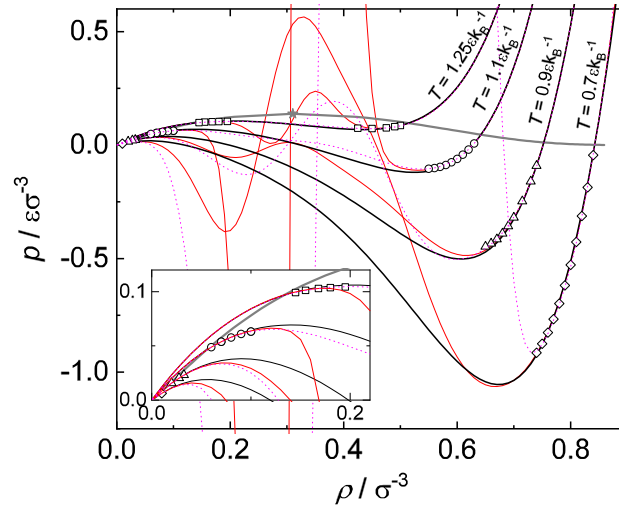

Figure A.30: Thermal properties of the LJ fluid: isotherms in the $p - \rho$ diagram obtained with from the LJ EOS from the present work (black lines), the LJ EOS from *Thol et al.* [661] (red lines), *Gottschalk* [217] (pink dotted lines) and molecular simulation results from *Stephan et al.* [640] (open symbols) for $T/\varepsilon k_{\mathrm{B}}^{-1} = 0.7,\ 0.9,\ 1.1,\ 1.25$. The gray solid line and star indicate the VLE and critical point obtained from the LJ EOS from the present work.

Comparison of Spinodal Reference Data with Selected LJ EOS

Fig. A.31 shows the spinodal of the LJ fluid in the $p - T$ and $T - \rho$ diagram. Results from computer experiments are compared with the LJ EOS of *Johnson et al.* [302], *Lafitte et al.* [353], and the present work. The reference data obtained from computer experiments [37, 380] shows significant scattering. The depicted LJ EOS agree with that reference data within that scattering. The same holds for most other considered LJ EOS (see main body of the present work and the attached electronic Supplementary Material [639]). Only for the LJ EOS of *Thol et al.* [661] and *Gottschalk* [217], no meaningful spinodal could be computed due to the oscillations present in the two-phase region, cf. Fig. A.30.
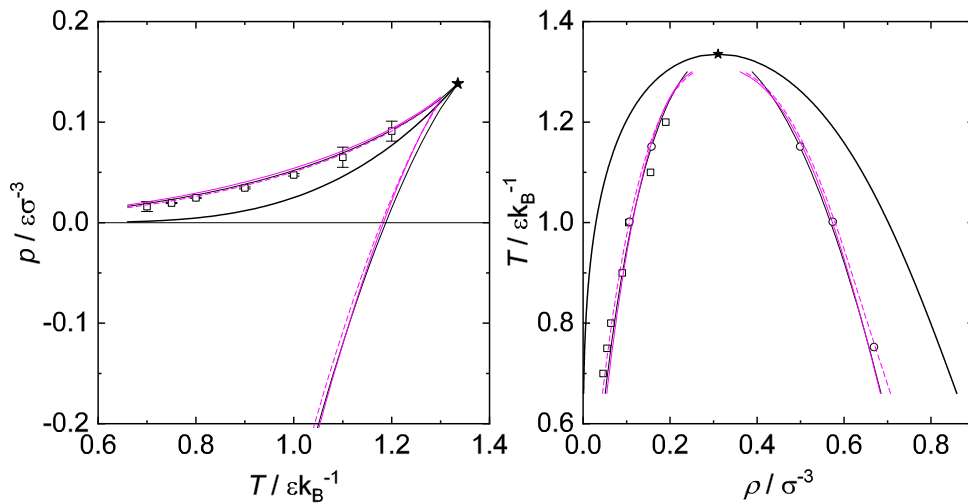

Figure A.31: Spinodal (thin lines) computed from the LJ EOS of *Johnson et al.* [302] (pink dashed line), *Lafitte et al.* [353] (pink solid line), and from the present work (black solid line) compared to corresponding molecular simulations data (open symbols): squares are results from *Linhart et al.* [380] and circles are from *Baidakov et al.* [37]. The binodal and critical point shown were also computed from the LJ EOS from the present work (black thick line and star).

B.3 Details on Enrichment Data from the Literature

This Appendix contains the following points:

- details on the digitalization procedure of the enrichment data from the literature, cf. chapter 9

- summary of the VLE data employed for testing the empirical enrichment model, cf. chapter 9

Details on the Digitalization Procedure

Since the vast majority of publications (cf. Table 25 in the main body of this work) report on density profiles $\rho_i(z)$ only graphically, the enrichment E_2 (cf. Eq. (122)) had to be extracted from that data manually. Therefore, screenshots of the $\rho_i(z)$ plots were extracted from a given publication and required data for the computation of the enrichment E_2 was metered using the *Web Plot Digitizer* [563]. A database was established (see attached spread sheet file [627]) based on that data.

Each data point j consists of the following data obtained from a given publication reporting vapor-liquid interfacial density profiles (cf. Table 25) or databases [1]:

- The temperature T_j and

- the liquid bulk phase mole fraction $x'_{2,j}$ to specify the state point.

- The enrichment $E_{2,j}$ and the difference of the bulk densities $\Delta\rho_{2,j}$ measured from the density profile $\rho_{2,j}(z)$ of the respective low-boiling component 2.

- The standard deviation from five repeated 'measurements' for all manually digitalised data.

- The partition coefficient $K_{2,j}^{5\%}$ at $x'_2 = 0.05\,\mathrm{mol\,mol}^{-1}$ at T_j (either taken from the same publication reporting the density profiles or taken from the Dortmund Data Base [1] or NIST database [381]).

- The critical density $\rho_{c,1}$ of the high-boiling component 1 (also either taken from the same publication reporting the density profiles or taken from the Dortmund Data Base [1] or NIST database [381]).

To compute $E_{2,j}$ and $\Delta\rho_{2,j}$, the three points $\max(\rho_2(z))$, ρ'_2, and ρ''_2 were measured from a given $\rho_2(z)$ plot. If the concentration of the low-boiling component 2 in the liquid phase $x'_{2,j}$ – to specify the state point – was not explicitly reported, it was computed from

$$x'_2 = \frac{\rho'_2}{\rho'_1 + \rho'_2}\,, \tag{140}$$

which additionally required the measuring of the bulk phase density ρ'_1 of the high-boiling component 1. In some cases, neither the high-boiling component density profile $\rho_1(z)$, nor the bulk phase composition was reported. In such cases, $x'_{2,j}$ was taken from reported phase diagrams.

Each digitalization was repeated five times; the actual value for each required property was taken from the mean value of the individual measurements and an uncertainty

caused by the digitalization was estimated from the standard deviation of the repeated values. The mean value of the absolute uncertainty was $\delta E_2 = \pm 0.11$.

For some mixtures, the required VLE data was not available in databases – especially the model mixtures. In such cases, x_2'' at $x_2' = 0.05\,\mathrm{mol\,mol^{-1}}$ for the computation of $K_{2,j}^{5\%}$ was also obtained by digitalization from phase diagrams reported in respective publications.

Challenges emerged, when plots for density profiles were small, the resolution was low, and the line width and symbol size were particularly large or hard to detect precisely. This became particularly a problem for density profiles at very low concentrations of the low-boiling component such that ρ_2' and ρ_2'' practically collapse with the abscissa of the respective plot. In such cases the value of ρ_2' and/ or ρ_2'' can get in the size of a pixel during the digitalization. Since such state points often correspond to large enrichment, the digitalization yields large uncertainties for such data – in both E_2 and x_2'. Sometimes, the density profiles would also not be plotted to the exact bulk density values, i.e. the end of the density profiles would still posses a gradient $\mathrm{d}\rho_i/\mathrm{d}z \neq 0$.

VLE Data Employed for the Enrichment Model

For the test-dataset, the required VLE data (see list above) was taken either from the publication that reported the density profiles or it was taken from the Dortmund Data Base [1] or NIST database [381]. In practically all cases, the partition coefficient was not exactly available at the prescribed $x_2' = 0.05\,\mathrm{mol\,mol^{-1}}$ and the given T. For the liquid phase composition, the vast majority of data points was available at $x_2' = 0.05 \pm 0.005\,\mathrm{mol\,mol^{-1}}$. For the temperature, most data points were available within 2% of the required temperature. Fig. A.32 shows the histogram of the available VLE data for the considered systems (cf. Table 25 in the main body of the present work). The enrichment model was only applied, if the available VLE data did not deviate more than 10% from the temperatures the density profiles were reported for and data on the partition coefficient was available within $x_2' = 0.05 \pm 0.015\,\mathrm{mol\,mol^{-1}}$. This was only the case for less than 1% of the data points of the entire database on enrichment data.
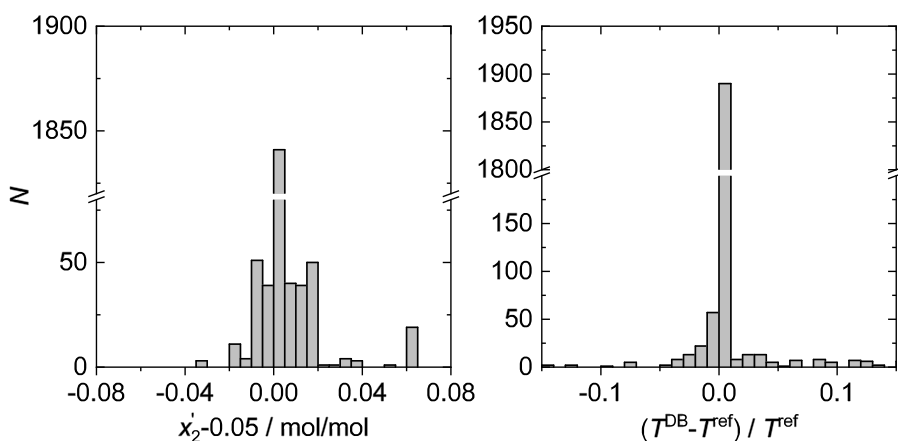

Figure A.32: Histogram of the available VLE data for the prediction of the enrichment of the literature data. Left: histogram for the absolute deviation of the prescribed liquid phase concentration. Right: histogram of the relative deviation of the required temperature. 'DB' indicates the temperature of VLE data taken from databases as input for the enrichment model; 'ref' indicates the temperature of the reference data, cf. Table 25.

C Parametrization of New Lennard-Jones Equation of State

C.1 PC-SAFT Monomer Model

The LJ EOS developed in the present work is a re-parameterization of the PC-SAFT [223] monomer model, i.e. a spherical particle with soft repulsive and dispersive interactions. The universal constants of the PC-SAFT EOS [223] have been optimized several times in the literature [53, 222, 249, 375, 376]. *Gross and Sadowski* [222], who developed the original version of the PC-SAFT EOS adjusted the universal constants to hard chain computer experiment data [222] and n-alkane VLE properties [223]; *Liang and Kontogeorgis* [375, 376] fitted the parameters to VLE and speed of sound data of different real substances, and *Heier et al.* [249] fitted the parameters to VLE data of the Lennard-Jones truncated and shifted fluid. To include the PC-SAFT monomer model in the comprehensive comparison of the present work, its universal constants were re-parametrized such as to match computer experiment data of the Lennard-Jones fluid.

As most other theoretically-based LJ EOS, the PC-SAFT monomer model is based on perturbation theory [43, 44, 237, 252, 613]. The PC-SAFT monomer model uses the perturbation theory of *Barker and Henderson* [42, 43], according to which the Helmholtz energy of the LJ fluid can be written as

$$\tilde{a} = \tilde{a}_{\text{id}} + \tilde{a}_{\text{res}} = \tilde{a}_{\text{id}} + \tilde{a}_{\text{ref}} + \tilde{a}_{\text{pert}} , \tag{141}$$

where $\tilde{a}_{\text{ref}}$ and $\tilde{a}_{\text{pert}}$ are the Helmholtz energy contribution of the reference system and the perturbation, respectively.

The Helmholtz energy of the hard sphere fluid of the PC-SAFT monomer is adopted from *Boublík* [67] and *Mansoori et al.* [407] as

$$\tilde{a}_{\text{ref}} = \tilde{a}_{\text{hs}} = \zeta_0^{-1} \left(\frac{3\zeta_1\zeta_2}{(1-\zeta_3)} + \frac{\zeta_2^3}{\zeta_3(1-\zeta_3)^2} + \left(\frac{\zeta_2^3}{\zeta_3^2} - \zeta_0 \right) \ln(1-\zeta_3) \right) , \tag{142}$$

where ζ_n is defined as

$$\zeta_n = \frac{\pi}{6}\rho d^n \quad \text{with} \quad n = 0, 1, 2, 3 , \tag{143}$$

where $\zeta_3 = \eta$ is the packing fraction and ρ is the number density.

Following *Barker and Henderson* [41], the purely repulsively interacting reference fluid is that of a hard sphere, with an effective temperature-dependent hard sphere diameter

d as

$$d(T) = \int_0^1 \left(1 - \exp\left(-\frac{u_{\mathrm{LJ}}(r)}{k_{\mathrm{B}}T}\right)\right)\mathrm{d}r . \tag{144}$$

This temperature-dependent diameter gives the repulsive hard sphere term its softness. The PC-SAFT monomer model simplifies Eq. (144) to an algebraic equation proposed by *Chen and Kreglewski* [108] to avoid the numerical integration to

$$d(T) = 1 - c_1 \cdot \exp\left(-\frac{c_2}{k_{\mathrm{B}}T}\right). \tag{145}$$

The perturbation contribution $\tilde{a}_{\mathrm{pert}}$ is modeled up to second-order in the PC-SAFT monomer model, i.e.

$$\tilde{a}_{\mathrm{pert}} = \tilde{a}_1 + \tilde{a}_2 . \tag{146}$$

As described in detail in Refs. [41, 42], applying the *local compressibility-version* of *Barker and Henderson's* perturbation theory, the first- and second-order perturbation terms can be written as

$$\tilde{a}_1 = -2\pi\rho \int_1^\infty u_{\mathrm{pert}}(r)\, g_0(r)r^2\mathrm{d}r , \quad \text{and} \tag{147}$$

$$\tilde{a}_2 = -\pi\rho T \left(\frac{\partial\rho}{\partial p}\right)_T \frac{\partial}{\partial\rho}\left[\rho\int_1^\infty u_{\mathrm{pert}}(r)^2 g_0(r)\, r^2\mathrm{d}r\right]. \tag{148}$$

Following the ansatz of *Gross and Sadowski* made in their PC-SAFT equation of state [222, 223], the integrals in Eq. (147) and (148) are simplified into a power series expansion in the packing fraction:

$$\int_1^\infty u_{\mathrm{pert}}(r)\, g_0(r)r^2\mathrm{d}r = I_1 = \sum_{i=0}^N a_i\eta^i \tag{149}$$

$$\frac{\partial}{\partial\rho}\left[\rho\int_1^\infty u_{\mathrm{pert}}(r)^2 g_0(r)\, r^2\mathrm{d}r\right] = I_2 = \sum_{i=0}^N b_i\eta^i \tag{150}$$

The parameters c_1, c_2, a_i, and b_i ($i = 1..N$) are the state-independent universal constants of the PC-SAFT monomer model. We chose $N = 7$ for the present work. The 18 model parameters were adjusted in the present work to data of the LJ fluid. Only a subset of the computer experiment data compiled in Ref. [640] was used for that purpose. It comprises consistent comprehensive data for the VLE and homogeneous fluid states [625, 640, 661].

The optimization was guided by the idea that a good representation of VLE properties should be accompanied by a good representation of bulk properties. Therefore, the dataset used for the parametrization was a combination of the homogeneous state data and vapor-liquid equilibrium data. Not the full set of simulation data compiled in Ref. [640] that was used for testing the EOS as described in the main part of the paper was also used for the re-parameterization of the PC-SAFT monomer term. The large and consistent set of simulation data of *Thol et al.* [661] for homogeneous stable states was selected here, as it provides the residual Helmholtz energy $\tilde{a}^{\mathrm{res}} = a^{\mathrm{res}}/k_{\mathrm{B}}T$ and its derivatives with respect to the inverse temperature and the density for each state

point. The vapor pressure and the saturated densities were taken from the correlations from section 4.2 that describe the most precise computer experiment data within their combined scattering. Furthermore, data for the second and third virial coefficient in the range $T = 1.32 .. 5 \, \varepsilon k_{\mathrm{B}}^{-1}$ with a discretization step of 0.005 were used for the parametrization.

The employed parametrization strategy uses elements from multi-criteria optimization to account for conflicts between the different objectives and is based on recent work of our group [64, 65, 182, 641, 683].

C.2 Parametrization

In this section, the optimization procedure that was employed to determine the new universal constants of the PC-SAFT monomer term for the modeling of the LJ fluid is described. The optimization was guided by the idea that a good representation of VLE properties should be accompanied by a good representation of bulk properties. Therefore, the dataset used for the parametrization was a combination of the homogeneous state data and vapor-liquid equilibrium data, cf. Table A.27.

Table A.27: Dataset used for the parametrization of the LJ EOS from the present work. The two last columns indicate the number of data points and the temperature range of that data.

Data	Source	#	$T \, / \, \varepsilon k_{\mathrm{B}}^{-1}$
free energy and free energy derivatives at homogeneous states; $\tilde{a}_{00}^{\mathrm{res}}$, $\tilde{a}_{10}^{\mathrm{res}}$, $\tilde{a}_{01}^{\mathrm{res}}$, $\tilde{a}_{11}^{\mathrm{res}}$, $\tilde{a}_{20}^{\mathrm{res}}$, $\tilde{a}_{02}^{\mathrm{res}}$	*Thol et al.* [661]	167	0.7 .. 5
VLE p^s, ρ', ρ''	this work	61	0.69 .. 1.29
2$^{\mathrm{nd}}$, 3$^{\mathrm{rd}}$ virial coefficient B, C	this work	736	1.32 .. 5

In contrast to the main body of this work, for simplicity, the fluid state was divided in only four regions k: liquid, gas, and supercritical (sc) for the homogeneous region, and the vapor-liquid equilibrium (VLE). The liquid, gas, and supercritical region were simply defined here with respect to the critical point, i.e. homogeneous state points with ($T < T_{\mathrm{c}}$ and $\rho < \rho_{\mathrm{c}}$) belong to the gas region, for ($T < T_{\mathrm{c}}$ and $\rho > \rho_{\mathrm{c}}$) they belong to the liquid region, and for ($T > T_{\mathrm{c}}$) they belong to the supercritical region. The employed reference data (cf. Table A.27) was assigned accordingly. Following this classification, the virial coefficients that were used here are from the supercritical region.

The objective functions were defined using the *Huber loss* [241, 281, 730] as

$$f_{jk}(\underline{x}) = \frac{1}{N_{jk}} \sum_{l=1}^{N_{jk}} c_{jkl} \left[\left(1 + \left(100 \cdot \frac{Y_{jkl}^{\mathrm{ref}} - Y_{jkl}(\underline{x})}{Y_{jkl}^{\mathrm{ref}}} \right)^2 \right)^{0.5} - 1 \right], \tag{151}$$

where j indicates the property, k the fluid region, and l the data point; $\underline{x}$ is the parameter vector, c_{jkl} was calculated from the uncertainty of the data points as explained

below, and N_{jk} is the number of data points of property j in a region k. The properties are $j = (\tilde{a}_{00},\ \tilde{a}_{10},\ \tilde{a}_{01},\ \tilde{a}_{11},\ \tilde{a}_{20},\ \tilde{a}_{02},\ B,\ C,\ \rho',\ \rho'',\ p^s)$, and the regions are $k = $ (liquid, gas, sc, VLE). The employed *Huber loss* function behaves like the ordinary convex 'squared' loss in the vicinity of the origin but like an 'absolute' loss elsewhere, which makes it robust against regions of particularly large deviations [241, 281, 730] (which is found to be the case for the PC-SAFT monomer equation in the supercritical region, see below).

The resulting objective space is a $\mathbb{R}^{23}$-space (B, C, ρ', ρ'', p^s are only applicable in a single region). The parameter space is a $\mathbb{R}^{18}$-space; the parameters are c_1, c_2, a_i, and b_i with $i = 0..7$, as described in the main text.

For the homogeneous state data from *Thol et al.* [661], the values c_{jkl} were computed from

$$c_{jkl} = \frac{\delta_{jkl}^{-1}}{\frac{1}{N_{jk}}\sum_{l=1}^{N_{jk}} \delta_{jkl}^{-1}}\ , \tag{152}$$

where δ_{jkl} is the statistical uncertainty reported by *Thol et al.* [661]. The denominator in Eq. (152) normalizes the data point specific penalty δ_{jkl}^{-1} by the mean value of δ_{jkl}^{-1} of the corresponding thermophysical property j and fluid region k. For the VLE region data, the values c_{jkl} were computed from the reported uncertainty of the respective correlations [640], i.e. $\delta_{p^s} = 0.01$ for the vapor pressure, $\delta_{\rho'} = 0.002$ for the saturated liquid density, and $\delta_{\rho''} = 0.01$ for the saturated vapor density [640]. Hence, all data points l of a VLE property $j = p^s$, ρ', ρ'' had the same c_{jkl} value, which was defined as

$$c_{j,k=\text{VLE},l} = \frac{\delta_j^{-1}}{\frac{1}{3}\sum_{j=1}^{3}\delta_j^{-1}}\quad \text{for}\quad j = p^s,\ \rho',\ \rho''\ . \tag{153}$$

Again, the denominator normalizes the uncertainties in the region. For the virial coefficients, c_{jkl} were set to unity, since such data is exact for a given intermolecular potential.

To reduce the objective space from a $\mathbb{R}^{23}$ to a space with lower dimension, the 11 considered properties j were lumped into a single objective function for each fluid region k:

$$f_k = \sum_{j=1}^{11} w_j\, f_{jk}\ . \tag{154}$$

For each region, the weights w_j were determined as follows: a single optimization run was carried out for each property j. The weight w_j was determined as the reciprocal value of the resulting objective function value, i.e. $w_j = f_j^{-1}$.

After applying the lumping described by Eq. (154), the objective space is a $\mathbb{R}^4$, with the objectives f_{VLE}, f_{gas}, f_{liq}, and f_{sc}. An ad hoc optimization procedure was applied to find a good compromise between these conflicting objectives, in which elements from single objective optimization, namely the lumping of the objective functions, were combined with elements from multi-criteria optimization (MCO). The MCO routine was adapted from previous work of our group [182]. Sets of best compromises were determined simply by varying weights in objective functions (see below), assuming the set is convex. The

following objective function was used in a hierarchical, iterative manner:

$$f = w_{\mathrm{VLE}} f_{\mathrm{VLE}} + w_{\mathrm{bulk}} \big(\underbrace{w_{\mathrm{gas}} f_{\mathrm{gas}} + w_{\mathrm{liquid}} f_{\mathrm{liquid}} + w_{\mathrm{sc}} f_{\mathrm{sc}}}_{f_{\mathrm{bulk}}} \big). \tag{155}$$

In a first step, the weights w_{VLE} and w_{bulk} were set to unity. Then the weights w_{gas}, w_{liq}, and w_{sc} were varied and for each triplet, an SCO was carried out. The resulting f_{gas}, f_{liq}, and f_{sc} can be considered as a point in the set of best compromises, see Fig. A.33 - right, for an example of the results, which form a surface in the $\mathbb{R}^3$ objective space. For each point in this set, also the corresponding set of weights w_{gas}, w_{liq}, and w_{sc} is known, and, additionally, also f_{VLE} is known (not shown in Fig. A.33 - right). It turns out that the set in the $\mathbb{R}^3$ has a sharp 'Pareto knee', i.e. a region in which small gains in one objective can only be achieved by high losses in at least one of the other objectives. A point from that Pareto knee was chosen, leading to a certain triplet of values f_{gas}^*, f_{liq}^*, and f_{sc}^*. The corresponding triplet (w_{gas}^*, w_{liq}^*, and w_{sc}^*) also yields a value for f_{VLE}^*. The results for the deviations in the bulk properties were then lumped as indicated in Eq. (155), leading to a number for f_{bulk}^*. The actions described so far relate a given choice of w_{VLE} and w_{bulk} to certain values of f_{VLE} and f_{bulk}.

This enables an optimization on a higher level, namely by finding best compromises between f_{VLE} and f_{bulk}. This is done following the ideas presented above by varying the weights w_{VLE} and w_{bulk}. In that optimization, the weights w_{gas}, w_{liq}, and w_{sc} were kept constant. A typical result is shown in Fig. A.33 - left. It has the typical shape of a Pareto set in the $\mathbb{R}^2$. Also from this set, a solution must be chosen. Here, we did not select a solution from the Pareto knee, but the one, in which the number obtained for f_{VLE} is not lower than what can be expected from the corresponding experimental uncertainties to avoid an overfitting. Using the the weights w_{VLE} and w_{bulk} from that point, all steps, starting from step 1, were repeated until convergence was achieved in about 5 iterations. The final solution is depicted in Fig. A.33 - left by a square; the corresponding detailed results for f_{gas}, f_{liq}, and f_{sc} are also depicted by a square in Fig. A.33 - right.

Fig. A.33, right reveals that the average deviation in each of the regions converges to a certain minimal value. That value is found when the weights for the other regions are set to zero. These minimal values are approximately: $f_{\mathrm{liquid}}^{\mathrm{min}} = 0.3\%$, $f_{\mathrm{gas}}^{\mathrm{min}} = 0.2\%$, and $f_{\mathrm{sc}}^{\mathrm{min}} = 3.5\%$. While the absolute numbers of the f_j should not be over-interpreted (they follow from the definition of Eq. 151) their relative values indicate strengths and weaknesses. The high number for f_{sc} indicates that it is difficult to heal the poor performance of the PC-SAFT monomer term for the sc region by any parameterization (as long as also VLE properties are taken into account).

The square in Fig. A.33 indicates the chosen model. The final 18 parameters of the new LJ EOS are summarized in Table A.28.
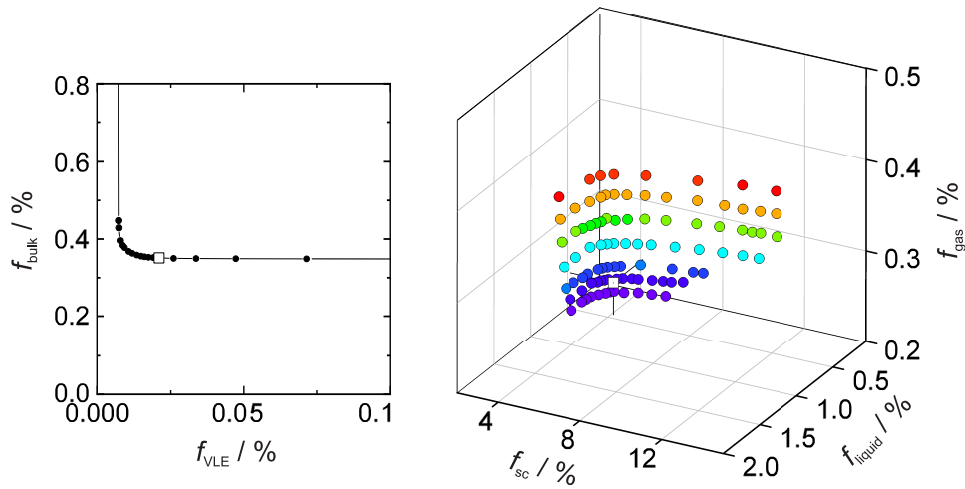
Figure A.33: Results from the optimization procedure that was applied for determining the parameters of the LJ EOS from the present work. Different objective spaces are shown. Left: objective functions for the bulk properties and the VLE properties; right: objective functions for homogeneous state properties in the gas, liquid, and supercritical (sc) region. The results in both plots have the form of Pareto sets. The white square indicates the chosen model. The color coding corresponds to the value of the deviation f_{gas}.

Table A.28: Parameters of the new LJ EOS based on the PC-SAFT monomer model, cf. main body of this work.

parameter	value	parameter	value	parameter	value
a_0	0.8589806535	b_0	0.6408575395	c_1	0.11428861
a_1	0.6349673926	b_1	3.2950236588	c_2	2.91331917
a_2	6.3970881521	b_2	-2.0716729542		
a_3	-39.4901329694	b_3	-201.2263717300		
a_4	109.8420725518	b_4	1151.6799275262		
a_5	-173.3316886409	b_5	-3855.8452492581		
a_6	139.7734440081	b_6	8261.2413758352		
a_7	-37.2039395551	b_7	-7537.8336347463		

Declaration

This dissertation contains material that has been published previously or that is included in submitted publications. In the following, these publications are listed together with a statement on the contributions of the author of the present dissertation.

- M. Heier, S. Stephan, J. Liu, W.G. Chapman, H. Hasse, K. Langenbach: Equation of state for the Lennard-Jones truncated and shifted fluid with a cut-off radius of 2.5σ based on perturbation theory and its applications to interfacial thermodynamics, Molecular Physics 116, 15 (2018) 2083-2094,
  DOI: 10.1080/00268976.2018.1447153.

  The author carried out the DGT calculations and wrote the corresponding parts of the manuscript.

- S. Stephan, J. Liu, K. Langenbach, W.G. Chapman, H. Hasse: Vapor-Liquid Interface of the Lennard-Jones Truncated and Shifted Fluid: Comparison of Molecular Simulations, Density Gradient Theory, and Density Functional Theory, Journal of Physical Chemistry C 122 (2018) 24705,
  DOI: 10.1021/acs.jpcc.8b06332.

  The author performed the DGT and MD simulations, developed and performed the oscillatory layering structure analysis method and performed its evaluation. Jinlu Liu performed the DFT calculations. The author wrote the manuscript.

- S. Stephan, K. Langenbach, H. Hasse: Interfacial Properties of Binary Lennard-Jones Mixtures by Molecular Simulation and Density Gradient Theory, Journal of Chemical Physics 150 (2019) 174704,
  DOI: 10.1063/1.5093603.

  The author performed the MD simulations as well as the EOS and DGT calculations and evaluated the data. The author wrote the manuscript.

- S. Stephan, H. Hasse: Molecular Interactions at Vapor-Liquid Interfaces: Binary Mixtures of Simple Fluids. Physical Review E 101 (2020) 012802,
  DOI: 10.1103/PhysRevE.101.012802.

  The author carried out the MD simulations and the DGT calculations and developed the conformal solution theory for interfacial properties. The author wrote the manuscript.

- S. Stephan, H. Hasse: Interfacial Properties of Binary Mixtures of Simple Fluids and their Relation to the Phase Diagram. Physical Chemistry Chemical Physics 22 (2020) 12544-12564,
  DOI: 10.1039/d0cp01411g.

The author carried out the code development for the calculation of the phase equilibria and performed the MD simulations and the DGT calculations. The author performed the post processing and analysis of the data and wrote the manuscript.

- S. Stephan, M. Thol, J. Vrabec, H. Hasse: Thermophysical Properties of the Lennard-Jones Fluid: Database and Data Assessment, Journal of Chemical Information and Modeling 59, 10 (2019) 4248-4265,
  DOI: 10.1021/acs.jcim.9b00620.

  The author collected and reviewed the data, developed the EOS test, performed the data assessment, and established the database. The author wrote the manuscript.

- S. Stephan, J. Staubach, H. Hasse: Review and Comparison of Equations of State for the Lennard-Jones Fluid, (submitted)
  The author developed the new Lennard-Jones equation of state based on the PC-SAFT monomer, developed the EOS assessment procedure, and performed the evaluation. The author wrote the manuscript.

- S. Stephan, U.K. Deiters: Characteristic Curves of the Lennard-Jones Fluid, (submitted)
  The author computed the characteristic curves, virial coefficients, and characteristic state points and performed the evaluation of the equations of state. The author wrote the manuscript.

- S. Stephan, H. Hasse: Influence of Dispersive Long-Range Interactions on Properties of Vapour-Liquid Equilibria and Interfaces of Binary Lennard-Jones Mixtures, Molecular Physics 188, 9-10 (2020) e1699185,
  DOI: 10.1080/00268976.2019.1699185.

  The author carried out the MD simulations and performed the EOS and DGT calculations. The author wrote the manuscript.

- S. Stephan, K. Langenbach, H. Hasse: Enrichment of Components at Vapor-Liquid Interfaces: A Study by Molecular Simulation and Density Gradient Theory, Chemical Engineering Transactions 69 (2018) 295-300,
  DOI: 10.3303/CET1869050.

  The author carried out parts of the MD and the DGT calculations and wrote the manuscript.

- S. Stephan, S. Becker, K. Langenbach, H. Hasse: Vapor-Liquid Interfacial Properties of the System Cyclohexane + CO2: Experiments, Molecular Simulation and Density Gradient Theory, Fluid Phase Equilibria 518 (2020) 112583,
  DOI: 10.1016/j.fluid.2020.112583.

  The author carried out the MD, PC-SAFT and DGT calculations. The author implemented the PCP-SAFT equation of state and the density gradient theory in a Matlab code. The author modified the experimental equipment and performed pendant drop measurements. The author wrote the manuscript.

- S. Stephan, H. Hasse: Enrichment at Vapour-Liquid Interfaces of Mixtures: Establishing a Link between Nanoscopic and Macroscopic Properties, International Reviews in Physical Chemistry 39, 3 (2020) 319-349,
  DOI: 10.1080/0144235X.2020.1777705.

  The author established the enrichment database, developed the empirical enrichment model, and performed the evaluation. The author wrote the manuscript.

- S. Stephan, D. Schaefer, K. Langenbach, H. Hasse: Mass Transfer Through Vapor-Liquid Interfaces: A New Molecular Dynamics Simulation Method (submitted)
  The author developed the simulation method and carried out the mass transfer simulations together with Dominik Schaefer. The author wrote the manuscript.

Furthermore, the author contributed to the following publications that are relevant for this thesis and cited therein:

- M. Schappals, A. Mecklenfeld, L. Kröger, V. Botan, A. Köster, S. Stephan, E.J. Garcia, G. Rutkai, G. Raabe, P. Klein, K. Leonhard, C. Glass, J. Lenhard, J. Vrabec, H. Hasse: Round Robin Study: Molecular Simulation of Thermodynamic Properties from Models with Internal Degrees of Freedom, Journal of Chemical Theory Computation 13 (2017) 4270,
  DOI: 10.1021/acs.jctc.7b00489.

- G. Rutkai, A. Köster, G. Guevara-Carrion, T. Janzen, M. Schappals, C. Glass, M. Bernreuther, A. Wafai, S. Stephan, M. Kohns, S. Reiser, S. Deublein, M. Horsch, H. Hasse, J. Vrabec: ms2: A Molecular Simulation Tool for Thermodynamic Properties, release 3.0, Computer Physics Communications 221 (2017) 343,
  DOI: 10.1016/j.cpc.2017.07.025.

- M.P. Lautenschlaeger, S. Stephan, H.M. Urbassek, B. Kirsch, J.C. Aurich, M. Horsch, H. Hasse: Effects of Lubrication on the Friction in Nanometric Machining Processes: A Molecular Dynamics Approach, Applied Mechanics and Materials 869 (2017) 85,
  DOI: 10.4028/www.scientific.net/AMM.869.85.

- M.P. Lautenschlaeger, S. Stephan, M. Horsch, B. Kirsch, J.C. Aurich, H. Hasse: Effects of Lubrication on Friction and Heat Transfer in Machining Processes on the Nanoscale: A Molecular Dynamics Approach, Procedia CIRP, 67 (2018) 296,
  DOI: 10.1016/j.procir.2017.12.216.

- J. Vrabec, M. Bernreuther, H.-J. Bungartz, W.-L. Chen, W. Cordes, R. Fingerhut, C. Glass, J. Gmehling, R. Hamburger, M. Heilig, M. Heinen, M. Horsch, C.-M. Hsieh, M. Hülsmann, P. Jäger, P. Klein, S. Knauer, T. Köddermann, A. Köster, K. Langenbach, S.-T. Lin, P. Neumann, J. Rarey, D. Reith, G. Rutkai, M. Schappals, M. Schenk, A. Schedemann, M. Schönherr, S. Seckler, S. Stephan, K. Stöbener, N. Tchipev, A. Wafai, S. Werth, H. Hasse: SkaSim – Scalable HPC Software for Molecular Simulation in the Chemical Industry, Chemie Ingenieur Technik 90 (2018) 295,
  DOI: 10.1002/cite.201700113.

- S. Stephan, M.P. Lautenschlaeger, I. Alabad Alhafez, M. Horsch, H.M. Urbassek, H. Hasse: Molecular Dynamics Simulation Study of Mechanical Effects of Lubrication on a Nanoscale Contact Process. Tribology Letters 66 (2018) 126,
  DOI: 10.1007/s11249-018-1076-0.

- S. Stephan, M. Horsch, J. Vrabec, H. Hasse: MolMod – an Open Access Database of Force Fields for Molecular Simulations of Fluids, Molecular Simulation 45, 10 (2019) 806-814,
  DOI: 10.1080/08927022.2019.1601191.

- S. Stephan, M. Dyga, H.M. Urbassek, H. Hasse: The Influence of Lubrication and the Solid-Fluid Interaction on Thermodynamic Properties in a Nanoscopic Scratching Process, Langmuir 35, 51 (2019) 16948-16960,
  DOI: 10.1021/acs.langmuir.9b01033.

- A. Kulkarni, E.J. Garcia, A. Damone, M. Schappals, S. Stephan, M. Kohns, H. Hasse: A Force Field for Poly(oxymethylene) Dimethyl Ethers (OMEn), Journal of Chemical Theory and Computation 16, 4 (2020) 2517-2528,
  DOI: 10.1021/acs.jctc.9b01106.

- F. Diewald, M.P. Lautenschlaeger, S. Stephan, K. Langenbach, C. Kuhn, S. Seckler, H.-J. Bungartz, H. Hasse, R. Müller: Molecular Dynamics and Phase Field Simulations of Droplets on Surfaces with Wettability Gradient, Computer Methods in Applied Mechanics and Engineering 361 (2020) 112773,
  DOI: 10.1016/j.cma.2019.112773.

Student theses

The following student theses were prepared under the supervision of the author of the present doctoral thesis in the frame of his research:

- D. Hoebbel: Molecular Simulation Study of the Enrichment of Components at Vapour-liquid Interfaces. Student thesis, Laboratory of Engineering Thermodynamics (LTD), TU Kaiserslautern (2018).

- C. Balzer: Study of the Influence of Dipolar Interactions on the Enrichment of Components at Vapour-Liquid Interfaces. Bachelor thesis, Laboratory of Engineering Thermodynamics (LTD), TU Kaiserslautern (2018).

- C. Gross: Investigation of the Enrichment of Light Boiling Components at Vapour-Liquid Interfaces by Molecular Simulation. Student thesis, Laboratory of Engineering Thermodynamics (LTD), TU Kaiserslautern (2018).

- D. Schäfer: Molecular Simulation of the Mass Transfer Through Vapour-Liquid Interfaces with the 'Dual Control Volume' Method. Master thesis, Laboratory of Engineering Thermodynamics (LTD), TU Kaiserslautern (2019).

- M. Bubel: Parameterization of a Model for the Description of the Enrichment of Light Boiling Components at Fluid Interfaces. Bachelor thesis, Laboratory of Engineering Thermodynamics (LTD), TU Kaiserslautern (2019).

- J. Staubach: Development of an Equation of State for the Lennard-Jones + Quadrupole Fluid and Investigation of its Interfacial Properties. Student thesis, Laboratory of Engineering Thermodynamics (LTD), TU Kaiserslautern (2019).

- K. Köhler: Investigation of vapour-liquid interfacial properties. Bachelor thesis, Laboratory of Engineering Thermodynamics (LTD), TU Kaiserslautern (2020).

- A. Cazade: Molecular Simulation of Mass Transport through Vapour-Liquid Interfaces. Master thesis, Laboratory of Engineering Thermodynamics (LTD), TU Kaiserslautern (2020).

- C. Balzer: Investigation of vapour-liquid interfacial properties by experiment, molecular simulation and density gradient theory (toluene+CO_2 and toluene+N_2). Master thesis, Laboratory of Engineering Thermodynamics (LTD), TU Kaiserslautern (2020).

Curriculum vitae

Name:	Simon Stephan
Place of birth:	Darmstadt
Nationality:	German

Education

1995 – 1999	Elementary school in Roth, Germany
1999 – 2008	Gymnasium Wilhel-Löhe Schule in Nuremberg, Germany
	Degree: Allgemeine Hochschulreife
2009 – 2015	Diplomstudium at TU Dresden
	Program: mechanical engineering (Maschinenbau)
	Degree: Dipl.-Ing.

Professional

08/2008 – 04/2009	Civil service at the Jugendbildungsstätte Asel/Ostfriesland
03/2015 – 08/2015	Academic visitor at the University of Reading
	Dr. Patrick Ilg
02/2015 – 05/2019	PhD student at the Laboratory of Engineering Thermodynamics
	TU Kaiserslautern
	Prof. Dr.-Ing. Hans Hasse
01/2017 – 03/2017	Research stay at the Rice University
	Prof. Dr. Walter G. Chapman